Analytical CHEMISTRY

Chemical Oceanography

1065 A

From the people who pioneered major innovations in nitrogen and sulfur analysis . . .

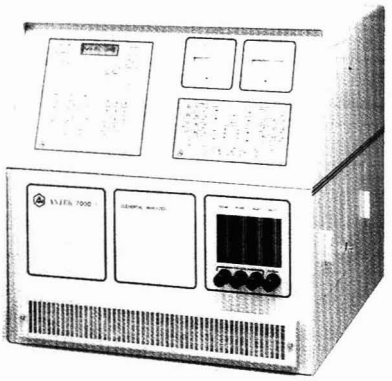

Model 7000

Nitrogen/Sulfur Analyzers

perform nitrogen and/or sulfur determinations on gas, liquid, and solid samples in as little as one minute.

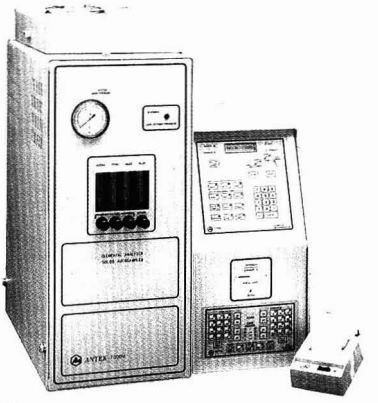

Model 7000V SA

Nitrogen/Sulfur Analyzer with Solids Autosampler

automated system for total nitrogen and/or sulfur analyses of solid samples and viscous liquids up to 500 mg.

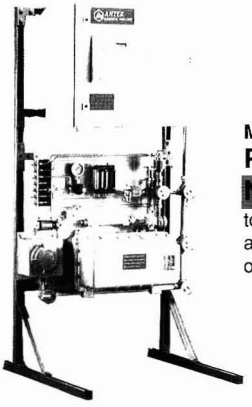

Model 6000

Process/On-line Nitrogen/Sulfur Analyzers

total nitrogen and/or total sulfur analyzers for industrial applications. Available in NEMA 4 enclosure, purged housing, or explosion proof housing.

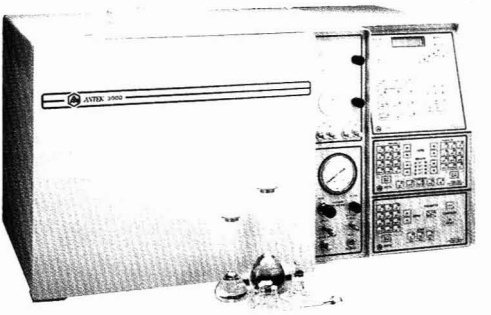

Model 3000

Gas Chromatograph

microprocessor-controlled, modular GC. Choose from many detector, injector, and controller configurations; packed, capillary, or wide bore columns.

ANTEK INSTRUMENTS, INC.

For more information or for a free catalog call

World Headquarters:
300 Bammel Westfield Rd., Houston, TX 77090, USA,
(713)580-0339, (800)365-2143, FAX (713)580-0719
European Office:
Wacholderstrasse 7, 4000 Düsseldorf 31, F.R.Germany
0203-74325, FAX 0203-741545, TLX 841 8551136 ANDU D

CIRCLE 5 ON READER SERVICE CARD

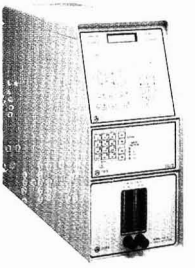

Model 705D

Nitrogen Specific GC Detector

only GC detector available that is ***totally*** specific for nitrogen. Proven chemiluminescent detector, installed on ANTEK 3000 GC or retrofitted on most commercial GCs.

A revolutionary new technology: The Elemental Fingerprint

This complete 2 dimensional emission spectrum was produced by the IRIS (shown below), the first ICP spectrometer ever to be implemented with CID array technology.

IRIS can view and store every line of every element in the sample. The lines of each given element are identified with colored brackets (e.g. C, yellow; Co, red; Fe, green).

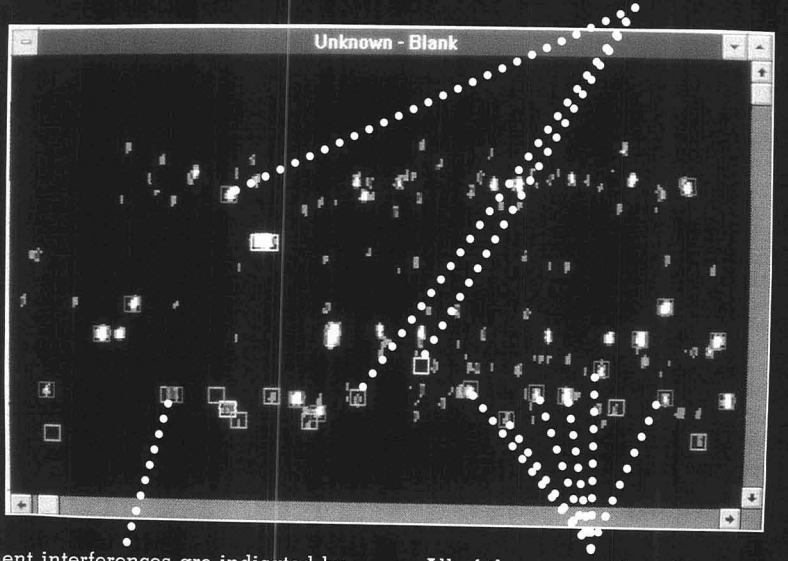

Interelement interferences are indicated by overlapped brackets. Overlapped lines may be ignored or corrections may be made.

All of the unencumbered lines of a given element may be used to achieve a more accurate and reproducible determination.

For literature or a demonstration of the many exciting new opportunities offered by the IRIS, please call (508) 520-1880, or write Thermo Jarrell Ash, 8E Forge Parkway, Franklin, MA 02038.

CIRCLE 110 ON READER SERVICE CARD

Thermo Jarrell Ash Corporation

A Subsidiary of Thermo Instrument Systems Inc.

For Performance Evaluation, accepted laboratory standards shouldn't be acceptable.

In the past, you've probably relied on EPA standards to evaluate the performance of your lab. However, these "accepted" standards compare your results to only one other lab. Is that really the best way to evaluate your quality control?

We don't think so. That's why APG created the P.E.T. (Proficiency Environmental Testing) program—to provide a wider range of comparative performance data against which to evaluate your lab's performance. This national interlaboratory Performance Evaluation program compares your results on blind samples with those of labs throughout the U.S. and gives you a confidential evaluation of your performance. More than 500 labs throughout the U.S. and Canada use this unique program, because they've found that Performance Evaluation is the most reliable measure of quality.

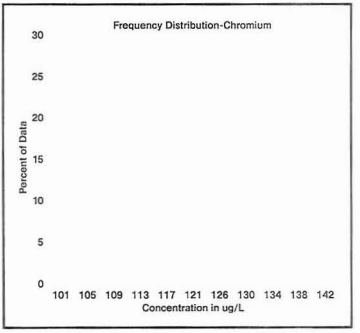

Call for more information on our P.E.T. program. And on our Setpoint Standards which are more than acceptable. They're essential.

APG *The Measure of Quality*

Analytical Products Group, Inc.

2730 Washington Blvd., Belpre, OH 45714
Fax: 1-614-423-5588

1-800-272-4442

CIRCLE 1 ON READER SERVICE CARD

NOVEMBER 15, 1992
VOLUME 64
NUMBER 22

The Audit Bureau
ANCHAM
64(23) 1049A–1096A/2665–2888 (1992)
ISSN 0003-2700

Analytical CHEMISTRY

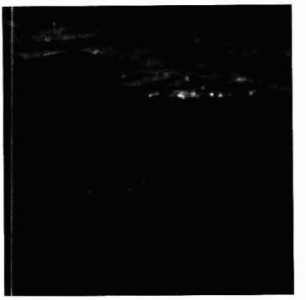

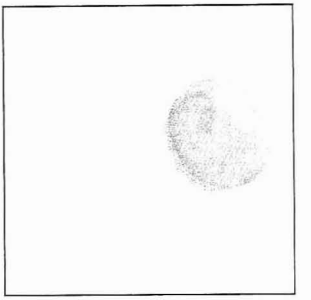

COVER: PHOTO OF DSV *ALVIN* BY ROD CATANACH COURTESY WOODS HOLE OCEANOGRAPHIC INSTITUTION

Matheson and the Environment

Special gas mixtures for environmental compliance, emissions monitoring, safety and industrial hygiene.

Backed by Matheson's more than 65 years of experience.

The 1990 revision of the Clean Air Act places increasing restrictions on the discharge of pollutants into the atmosphere and demands more proof of compliance. Penalties for noncompliance will increase. Compliance requires verification by accepted analytical procedures. Analytical data is acceptable only if instrumentation is calibrated with reliable standards. Questionable quality of calibration mixtures is intolerable. Accuracy and consistency must be assumed and verified.

Matheson, the world leader in specialty gases, has successfully prepared accurate calibration gas mixtures of every variety for over 65 years. With greater emphasis on pollution abatement and more demanding compliance requirements, analytical reliability becomes increasingly critical. Matheson's experience is your guarantee that the calibration mixture you receive will meet the requirement.

If you are involved with compliance testing, air quality monitoring or industrial hygiene - insist on reliability and consistency. Insist on Matheson.

Matheson
Gas Products
World Leader in Specialty Gases & Equipment

30 Seaview Drive,
Secaucus, NJ 07096-1587

Calibration Gas Mixtures Available from Matheson

EPA Protocol and NBS Traceable Calibration Mixtures in all Allowable Concentration Ranges

Pollutant	Balance Gas
Carbon Dioxide	Nitrogen or Air
Carbon Monoxide	Nitrogen or Air
Hydrogen Sulfide	Nitrogen or Air
Methane	Nitrogen or Air
Nitric Oxide	Nitrogen
Nitrogen Oxide	Nitrogen or Air
Oxygen	Nitrogen
Propane	Nitrogen or Air
Sulfur Dioxide	Nitrogen or Air
SO_2/O_2	Nitrogen
SO_2/NO	Nitrogen
SO_2/CO_2	Nitrogen
SO_2/NO/CO	Nitrogen

Certified Calibration Gas Mixtures for Industrial Hygiene

Pollutant	Balance Gas	Concentration Ranges
Carbon Dioxide	Air	2000 ppm - 2.5%
Carbon Monoxide	Air	20 - 4000 ppm
Ethylene Oxide	Nitrogen	1 -100 ppm
n-Hexane	Air	500 ppm
Hydrogen	Air	0.8 - 2%
Hydrogen Sulfide	Nitrogen	10 - 95 ppm
Methane	Air	1 - 3%
Nitric Oxide	Nitrogen	5 - 30 ppm
Oxygen	Nitrogen	5%
Pentane	Air	1000 ppm - 0.75%
Pentane and O_2	Nitrogen	0.75%/15%
Pentane, O_2 and CO	Nitrogen	0.75%/15%/60 ppm
Propane	Air	0.5 - 1.0%

Toxic Organic Mixtures (allowable combinations of the following components in Nitrogen in ***ppm or ppb*** concentrations)

Acetone	cis-1,2-Dichloroethylene
Acetonitrile	1,2-Dibromoethane
Benzene	Halocarbon 11
Benzyl Chloride	Methyl Ethyl Ketone
1,3-Butadiene	Tetrachloroethylene
Carbon Tetrachloride	Toluene
Chlorobenzene	1,1,1-Trichloroethane
Chloroform	o-Xylene
Dichlorobenzenes	Vinyl Chloride
1,1-Dichloroethane	Vinylidene Chloride
1,2-Dichloroethane	

CIRCLE 72 ON READER SERVICE CARD

Analytical CHEMISTRY

ANALYTICAL CHEMISTRY (ISSN 0003-2700) is published semimonthly by the American Chemical Society, 1155 Sixteenth St., N.W., Washington, DC 20036. Second-class postage paid at Washington, DC, and additional mailing offices. Postmaster: Send address changes to ANALYTICAL CHEMISTRY, Member & Subscriber Services, P.O. Box 3337, Columbus, OH 43210.

Canadian GST Reg. No. R127571347.

Subscription and Business Information

1992 subscription rates include air delivery outside the U.S., Canada, and Mexico. Canadian subscriptions are subject to 7% GST.

	Members	Nonmembers (personal)	Nonmembers (institutional)
U.S.	$ 33	$ 76	$ 373
Canada and Mexico	69	112	409
Europe	117	233	457
Other countries	150	266	490

Nonmember rates in Japan: Rates above do not apply to nonmember subscribers in Japan, who must enter subscription orders with Maruzen Company Ltd., 3–10. Nihonbashi 2-chrome, Chuo-ku, Tokyo 103, Japan. Tel: (03) 272-7211.

For multi-year and other rates, call toll free 800-227-5558 in the U.S. and Canada; in the Washington, DC, metropolitan area and outside the U.S., call 202-872-4363; fax 202-872-4615.

Single issues, current year, $16.00 except review issue, $40.00, and LabGuide, $50.00; **back issues and volumes and microform editions** available by single volume or back issue collection. For information or to order, call the number listed for subscription orders by phone; or write the Microform & Back Issues Office at the Washington address.

Subscription orders by phone may be charged to VISA, MasterCard, or American Express. Call toll free 800-333-9511 in the continental U.S.; in the Washington, DC, metropolitan area and outside the continental U.S., call 202-872-8065. Mail orders for new and renewal subscriptions should be sent with payment to American Chemical Society, Department L-0011, Columbus, OH 43268-0011.

Changes of address must include both old and new addresses with ZIP code and a recent mailing label. Send all address changes to the ACS Columbus address. Please allow 6 weeks for change to become effective. **Claims for missing numbers** will not be allowed if loss was due to failure of notice of change of address to be received in the time specified; if claim is dated (a) North America—more than 90 days beyond issue date, (b) all other foreign—more than 180 days beyond issue date. Hard copy claims are handled at the ACS Columbus address.

ACS membership information: Lorraine Bowlin (202-872-4567)

Articles

*Corresponding author

continued on p. 1057 A

SCALE UP RELIABILITY
Simple, Economical and Direct

Produced to the Same Exacting Specifications, E. Merck Silica Based Chromatography Products Provide the Highest Performance with Identical Selectivity and Guaranteed Reproducibility Regardless of the Method and Size of Your Sample

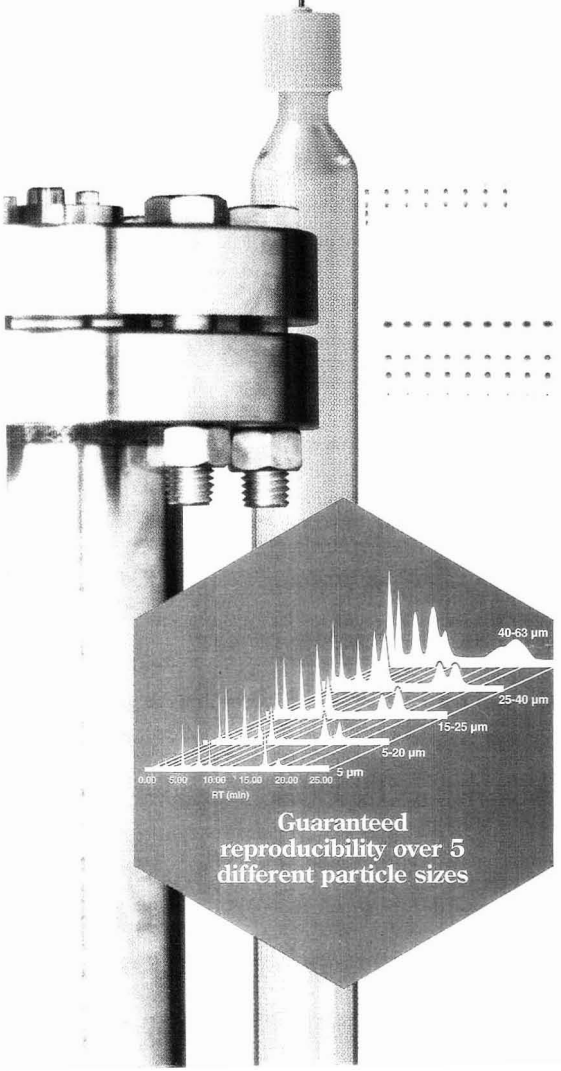

...Makes the Transfer from Analytical to Prep and Production Scale Easy, Reliable, and Reproducible

Use HPTLC to Economically Scan Chemistries to Determine the Best Selectivity

E. Merck HPTLC plates are available in a wide range of bonded phases which provide a fast, easy, and direct method for product screening. HPTLC can be particularly useful for "In-Process" control during prep LC with Lobar® Prepacked Columns.

Lobar Prepacked Glass LC Columns Offer Convenience, Economy, and Performance for Preparative Chromatography in the Lab

Lobar Glass Columns are packed with E. Merck LiChroprep® materials which are guaranteed to provide identical selectivity. They are a convenient and cost-effective alternative to HPLC for isolating prep quantities of product. Available in three sizes to accommodate a variety of loading capacities.

LiChroprep Packing Materials Guarantee Selectivity and Reproducibility for Scale Up

E. Merck has produced LiChroprep packing materials with the same guaranteed selectivity for over 20 years. Available in four different particle size ranges, scale up reproducibility is guaranteed.

ORDER DIRECT

For more information call 800/922-1084 or write:

EM SEPARATIONS

A Division of EM Industries, Inc.

480 Democrat Road • Gibbstown, New Jersey 08027
(609) 224-0742 • (800) 922-1084 • FAX: (609) 423-4389

CIRCLE 28 ON READER SERVICE CARD

Analytical CHEMISTRY

Editorial Information

Instructions for authors of AC RESEARCH are published in the January 1 issue, p. 107. Guidelines for the INSTRUMENTATION, REPORT, ANALYTICAL APPROACH, and A/C INTERFACE features are available from the Washington editorial office. Please consult these instructions and guidelines prior to submitting a manuscript for consideration for publication.

Manuscripts for publication in AC RESEARCH (4 copies of text and illustrative material) should be submitted to the Editor at the University of North Carolina address. Please include a signed copyright status form; a copy of this document appears on p. 111 of the January 1 issue. Manuscripts for publication in the A-page section should be submitted to the Washington editorial staff.

For individual reprints of AC RESEARCH or A-page articles, please contact the authors directly. Bulk reprints of individual articles are available from ACS. For information, write or call the Distribution office at the ACS Washington address (202-872-4539; fax 202-872-4615).

ACS Division of Analytical Chemistry
Chair, Joseph L. Glajch (508-671-8413)
Secretary, Sarah Rutan (804-367-1298)

ACS Information

Library Services	202-872-4515
Education Division	202-872-4388
Meetings Dept.	202-872-4397
Member Services	202-872-4414
Employment Services	202-872-6120
Public Outreach	202-872-4091

Supplementary material is noted in the table of contents with a ■. It is available as photocopy ($10.00 for up to 3 pages and $1.50 per page for additional pages, plus $2.00 for foreign postage) or as 24X microfiche ($10.00, plus $1.00 for foreign postage). Canadian residents should add 7% GST. See supplementary material notice at end of journal article for number of pages. Orders *must* state whether for photocopy or for microfiche and give complete title of article, names of authors, journal, issue date, and page numbers. Prepayment is required and prices are subject to change. Order from Microforms & Back Issues Office at the ACS Washington address.

The paper used in this publication meets the minimum requirements of American National Standard for Information Sciences—Permanence of Paper for Printed Library Materials, ANSI Z39.48-1984.

Journals Department
American Chemical Society
2540 Olentangy River Road
P.O. Box 3330
Columbus, OH 43210
614-447-3600, Ext. 3171
TELEX 6842086; Fax 614-447-3745

Member & Subscriber Services
American Chemical Society
P.O. Box 3337
Columbus, OH 43210
614-447-3776
800-333-9511

continued on p. 1059 A

Choice Offerings.

Choice of injector.

Rheodyne's Series-25 line of injectors for HPLC offers you four models:

1. For biotechnology and ion chromatography, the Model 9125.
2. For low-dispersion and microbore chromatography, the 8125.
3. For general applications, the widely used 7125 or the new 7725.

Choice of loading.

Each injector offers two ways of loading sample:

1. You can partially fill the loop. The syringe sets the volume without wasting sample.
2. Or you can completely fill the loop. The loop sets the volume without need to read syringe calibrations. There are ten loop sizes from 5 µL to 5 mL.

A new choice.

Rheodyne's new model 7725 has all the capabilities of the 7125, plus five advanced features:

1. Continuous flow during switching.
2. Front-end pressure screw for easy maintenance.
3. Wide port angles for improved access to fittings.
4. 2-µL loop accessory.
5. Optional internal position switch.

For information phone your Rheodyne dealer. Or contact Rheodyne, Inc., P.O. Box 996, Cotati, California 94931, U.S.A. Phone (707) 664-9050. Fax (707) 664-8739.

Circle Reader Service Card No. 95

RHEODYNE

Analytical CHEMISTRY

LabGuide

The LabGuide is published as the August 15 issue of ANALYTICAL CHEMISTRY. Begun 38 years ago by the JOURNAL, the annual LabGuide edition is designed to be the ultimate buyers' resource for chemists. Its comprehensive coverage includes 2250 categories of laboratory products and services from more than 1700 companies.

The 1993 edition features a record 40,000 informative listings detailing manufacturers and distributors of each product and service. Each listing includes the company's phone number for fast action; a more complete listing of the company's address and branch offices is located in a separate section at the back of the book. Sections include Instruments, Equipment, and Supplies (including new subsections on chromatography and spectroscopy); Chemicals and Standards; and Research, Analytical, and Consulting Services.

Putting together such a comprehensive and useful guide would be impossible without the suggestions and guidance of our advisory board. Current members include Duane Bartak (University of North Dakota), Bob Hosely (Mettler Instruments), Paul Preidecker (Gilson), K. C. Warawa (Hewlett-Packard), Ann Cerino (Perkin Elmer), H. M. Kingston (Duquesne University), Tim Heil (Radian), Susan Olesik (Ohio State University), Rodger Stringham (Merck), Bob Wright (Battelle Pacific Northwest Laboratories), and Sherman Hamel (Parr Instruments).

Instrumentation in Analytical Chemistry 1988–1991

This recently published book continues a series begun as *Instrumentation in Analytical Chemistry* in 1973 by Alan J. Senzel, and continued by Stuart A. Borman in the 1980s as *Instrumentation in Analytical Chemistry: Volume 2* and *Instrumentation in Analytical Chemistry: 1982–86*. Like its predecessors, *Instrumentation in Analytical Chemistry 1988–1991* is designed to provide readers with updated overviews of analytical techniques and instrumentation drawn from articles originally published in ANALYTICAL CHEMISTRY's A pages.

The volume begins with an introduction by Royce Murray designed to help readers put into perspective the methodological and instrumental developments that have occurred during the period. The book is divided into six topical areas: Robotics, Computers, and Laboratory Data Management; Atomic and Molecular Spectroscopy; Electroanalytical Chemistry and Chemical Sensors; Separations; Mass Spectrometry; and Surface Analysis. Each section begins with a short introduction designed to provide a context for interpreting the articles that follow and to answer questions such as "What are recent changes in this field?" and "Why are these techniques important?". Copies of *Instrumentation in Analytical Chemistry 1988–1991* are available in clothbound ($44.95), paperbound ($28.95), and student ($16.95) editions from the ACS Distribution Office, Dept. 390, 1155 16th St., N.W., Washington, DC 20036 (800-ACS-5558).

The LECO ICP-3000

flexibility and resolution with operational ease

The LECO ICP-3000 employs a fully solid-state RF source to provide 2 kw of power at a software selectable 27 or 40 mHz.

High resolution Echelle optics, with polychromator preselection of wavelengths ranging from 190 to 800 nm, provides the ultimate in resolution.

Cost effective programmable wavelength sets permit efficient simultaneous operation. The ICP-3000 can also be programmed for sequential operation using the same optics.

Photodiode imaging detection permits collection of the entire profile with simultaneous background correction.

Microsoft Windows™ operational software allows easy selection of operational parameters. Integral features of the software include CLP quality control and quality assurance protocols for interference checking, internal standardization, spike recovery testing, check standard analysis and an extensive list of procedures that assure the accuracy of your analysis.

For more information on how the ICP-3000 can add productivity and resolution to your laboratory contact:

LECO®

LECO® Corporation
3000 Lakeview Avenue
St. Joseph, MI 49085-2396

Phone: (616) 983-5531
Facsimile: (616) 983-3850

CIRCLE 64 ON READER SERVICE CARD

UPCOMING RESEARCH

Secondary Ion Emission from Solutions: Time Dependence and Surface Phenomena

Secondary ion images from droplets of various glycerol solutions show that, in some cases, emission of solute-characteristic ions is not homogeneous across the surface of the droplet. This can account for time-variant signals in SIMS and in FAB.

M. Scott Kriger and Kelsey D. Cook*, Department of Chemistry, University of Tennessee, Knoxville, TN 37996-1600 and **R. T. Short and Peter J. Todd***, Analytical Chemistry Division, Oak Ridge National Laboratory, Oak Ridge, TN 37831-6365

Digital Chemical Analysis of Dilute Microdroplets

Concentration detection limits for fluorescent molecules in small samples can be reduced substantially by counting the analyte molecules. Experimental results with β-phycoerythrin molecules are presented to demonstrate this concept.

Kin C. Ng, William B. Whitten, Stephen Arnold, and J. Michael Ramsey*, Oak Ridge National Laboratory, Oak Ridge, TN 37831

Influence of Tyrosine on the Dual Electrode Electrochemical Detection of Cu(II)–Peptide Complexes

Tyrosine increases the anodic sensitivity of Cu(II)–peptide complexes: A detection limit of 40–100 fmol (in 20 μL) for bioactive peptides results. Cathodic sensitivity is decreased because of intramolecular electron transfer reactions.

Hweiyan Tsai and Stephen G. Weber*, Department of Chemistry, University of Pittsburgh, Pittsburgh, PA 15260

Surface Concentrations of Indium, Phosphorus, and Oxygen in Indium Phosphide Single Crystals after Exposure to Gamble Solution

Rutherford backscattering and X-ray photoelectron spectroscopy are used to probe the surface of single crystals of indium phosphide that are exposed to synthetic lung fluid. The indium concentration is depleted to a depth of 1000 Å, and the oxygen content in this layer increases by 24%.

Tami B. Dittmar and Quintus Fernando*, Department of Chemistry, University of Arizona, Tucson, AZ 85721 and **J. A. Leavitt and L. C. McIntyre, Jr.,** Department of Physics, University of Arizona, Tucson, AZ 85721

Integrated Approach to Surfactant Environmental Safety Assessment: Fast Atom Bombardment Mass Spectrometry and Liquid Scintillation Counting To Determine the Mechanism and Kinetics of Surfactant Biodegradation

Static FABMS and liquid scintillation counting are used to determine, at the molecular level, the fate of a novel cationic surfactant in a live sludge matrix. The data are used to assess the environmental safety of the surfactant and the accuracy of various environmental fate models.

J. R. Simms, D. A. Woods, D. R. Walley, and T. Keough*, The Procter and Gamble Company, Miami Valley Laboratories, P. O. Box 398707, Cincinnati, OH 45239-8707 and **B. S. Schwab and R. J. Larson,** The Procter and Gamble Company, Ivorydale Technical Center, Cincinnati, OH 45217

Quantitative Determination of Sulfonated Aliphatic and Aromatic Surfactants in Sewage Sludge by Ion-Pair/Supercritical Fluid Extraction and Derivatization Gas Chromatography/Mass Spectrometry

Aliphatic and aromatic sulfonated surfactant are quantitatively extracted from sewage sludge as ion pairs using supercritical CO_2. The ion pairs are derivatized in the injection port of the gas chromatograph and determined by GC/MS. Precision is 5% RSD.

Jennifer A. Field*, David J. Miller, Thomas M. Field, Steven B. Hawthorne, and Walter Giger, Swiss Federal Institute for Water Resources and Water Pollution Control (EAWAG), CH-8600 Dübendorf, Switzerland, and Energy and Environmental Research Center, University of North Dakota, Grand Forks, ND 58202

Capillary Isoelectric Focusing with Universal Concentration Gradient Imaging System Using Charge-Coupled Photodiode Array

The system includes a 4-cm-long capillary, a He–Ne laser, and a 1024-pixel CCD. Subpicomole levels of proteins with isoelectric points ranging from 4.7 to 8.8 are separated and detected in 1–2 min.

Jiaqi Wu and Janusz Pawliszyn*, Department of Chemistry, University of Waterloo, Waterloo, Ontario N2L 3G1, Canada

Extension of Sedimentation/Steric Field-Flow Fractionation into Submicrometer Range: Size Analysis of 0.2–15-μm Metal Particles

Strong sedimentation forces and high flow rates drive the minimum diameter for steric FFF to submicrometer levels. Accordingly, sedimentation/steric FFF can fractionate 0.2–15-μm metal particles and yield size distributions in 1–12 min.

Myeong Hee Moon and J. Calvin Giddings*, Field-Flow Fractionation Research Center, Department of Chemistry, University of Utah, Salt Lake City, UT 84112

These articles are scheduled to appear in AC RESEARCH in the near future.

*Corresponding author

Quality you can count on!

We're the Laboratory Products Association. When you buy from an LPA member company you can count on choosing from the best products & prices, the broadest line of laboratory products, guaranteed delivery & service from well established and dependable companies.

& still counting...

By purchasing from an LPA member company you tap an invaluable source of leading manufacturers & distributors serving the scientific community. Our membership is constantly growing & expanding its network of information & services; all with the goal of providing you with what you need.

LPA

Laboratory Products Association • 225 Reinekers Lane • Suite 625 • Alexandria • Virginia • 22314-2876 • 703 836 1360

For an application package use Reader Circle #66
For information about LPA companies & their commitment to customers use Reader Circle #67

Biemann and Hunt Receive Edman Award

Klaus Biemann of the Massachusetts Institute of Technology (MIT) and Donald F. Hunt of the University of Virginia were awarded the 1992 Edman Award, sponsored by the Millipore Corp. Biemann was recognized for achievements in protein sequence analysis using MS; Hunt was recognized for achievements in applying MS to the microsequence analysis of proteins. The award was presented Sept. 22 at the 9th International Conference on Methods in Protein Sequence Analysis in Otsu, Japan.

Biemann received his Ph.D. at the University of Innsbruck in 1951 and taught there until joining the chemistry faculty at MIT in 1955. He is well known for his contributions to GC/MS, computers in MS, and structure elucidation of natural compounds. He was ANALYTICAL CHEMISTRY's Associate Editor for MS between 1986 and 1990.

Hunt received his Ph.D. from the University of Massachusetts in 1967. He joined the chemistry faculty at the University of Virginia in 1968 and was promoted to professor in 1978. Hunt's research interests include ion–molecule reactions, chemical ionization MS, and structural characterization of biological compounds.

Ford Foundation Fellowships

The National Research Council (NRC) will award approximately 25 Ford Foundation Postdoctoral Fellowships for Minorities to help young teacher–scholars who show great promise to achieve recognition in their fields and to develop professional associations that will make them more effective in academic research. The fellowships are targeted for minority groups traditionally underrepresented in the behavioral and social sciences, the humanities, engineering, mathematics, physical sciences, and biological sciences, and for interdisciplinary programs composed of two or more of the eligible disciplines.

To qualify, the individual must be a citizen or national of the United States at the time of application and a member of one of the following minority groups: native American Indian or Alaskan native (Eskimo or Aleut), black/African American, Mexican American/Chicano, native Pacific islander (Micronesian and Polynesian), or Puerto Rican. Individuals must be already engaged in a teaching or research career or planning such a career. They must have earned their Ph.D. or Sc.D. by Jan. 8, 1993, and must have held it for not more than seven years as of that date.

The proposed fellowship institution must be one other than that from which the individual applies; all applicants must have a faculty member or other scholar at that institution who will act as their host. Qualifying institutions include universities, museums, libraries, government or national laboratories, privately sponsored not-for-profit institutes, government-chartered not-for-profit research organizations, and centers for advanced study. Applicants wishing to affiliate with institutions outside the United States must submit evidence of the particular benefits that would accrue from affiliation with a foreign institution. Tenure is for nine or 12 months and begins on Sept. 1, 1993. The stipend is $25,000 with a $3000 travel allowance.

Applications will be evaluated on the basis of academic records; letters of recommendation; and indications of competence, including competence as a teacher, if applicable. A plan of study or research that will further the individual's career in higher education must be submitted. Applicants will be notified in April 1993.

For application material, contact the Fellowship Office, National Research Council, 2101 Constitution Ave., Washington, DC 20418 (202-334-2860). Deadline is Jan. 8, 1993.

Nominations for 1994 Dimick Award

Nominations are requested for the Keene P. Dimick Award for Chromatography, which is presented annually for noteworthy accomplishments in GC and SFC. This $5000 award, administered by the Society for Analytical Chemists of Pittsburgh (SACP), is presented at a Pittsburgh Conference symposium. Selection is based on overall accomplishments in the fields of GC and/or SFC, including scientific publications, as well as beneficial influence on other scientists. There are no restrictions on age, nationality, sex, or affiliation.

Nominations can be made by sending five copies of a nomination letter and a complete résumé of the candidate to Eli Absey, Keene Dimick Award Committee, SACP, 300 Penn Center Blvd., Suite 332, Pittsburgh, PA 15235-5503 (412-825-3220). Deadline for nominations is Jan. 15, 1993.

For Your Information

The deadline for receipt of nominations for the National Science Foundation's 18th Alan T. Waterman Award is Dec. 31. The award, presented annually to an outstanding young scientist, mathematician, or engineer, consists of a grant for up to $500,000 over a three-year period. The winner will be announced in May 1993. For further information, contact Susan Fannoney, National Science Foundation, 1800 G St., N.W., Washington, DC 20550 (202-357-7512).

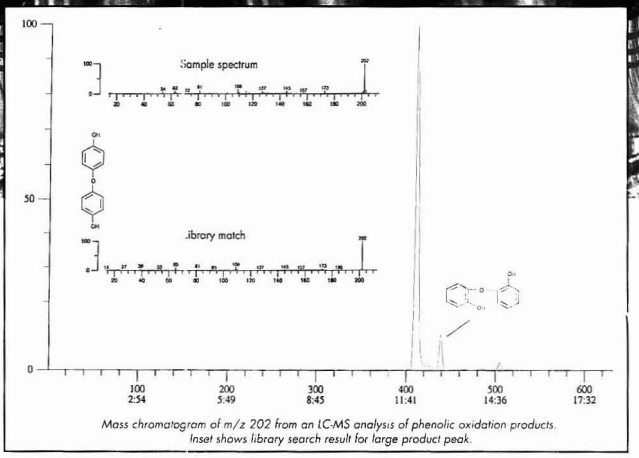

Mass chromatogram of m/z 202 from an LC-MS analysis of phenolic oxidation products. Inset shows library search result for large product peak.

Fully Automated LC-MS from Kratos Analytical

- For rapid screening of single samples, there's nothing faster.
- For repetitive or quantitative LC-MS, there's nothing easier.
- For limited sample quantities, there's nothing more sensitive.

Kratos has combined PROFILE, the world's most advanced automated mass spectrometry system with the power of Shimadzu's latest LC autosamplers to provide multi-sample LC-MS capabilities.

Just think.... fully automated LC-MS analysis.... spectra directly from samples in solution, load in your NMR samples for instance.... dilution series in situ, add derivatizing reagents all within the autosampler.... and process data with one of the fastest MS data systems around....

....all completely automatically.

Kratos combines reliability with innovation to provide the highest performance and quality in mass spectrometry instrumentation.

If you would like to know more about increasing your LC-MS capability or about any other Kratos MS products, write or call for our free information pack, now:

KRATOS ANALYTICAL

when analysis quality counts

535 East Crescent Avenue, Ramsey, NJ 07446.
Tel: (201) 825-7500. Fax: (201) 825-8659.

CIRCLE 60 ON READER SERVICE CARD

REPORT

Analytical Chemistry in Oceanography

Kenneth S. Johnson[1], Kenneth H. Coale, and Hans W. Jannasch[2]
Moss Landing Marine Laboratories
P.O. Box 450
Moss Landing, CA 95039

Chemical measurements in the ocean involve a unique set of challenges related to the distinctive composition of seawater, the large spatial and temporal scales over which measurements are made, and the frequent need to perform analyses while at sea under difficult conditions. These problems are not familiar to many analytical chemists, in part because it is unusual to find chemical oceanographers or geochemists in close contact with their chemistry colleagues (*1*).

Chemical oceanography has been practiced primarily in departments or institutions oriented toward marine or environmental sciences. Our chemical understanding of the oceans is, however, directly linked to the development of the latest analytical tools and advances in chemistry and engineering. A report soon to be issued by the National Research Council states that a significant increase is needed in our abilities to observe ocean chemistry and to study the biological, physical, and chemical (biogeochemical) processes that control the flow of chemicals through the ocean and its linkage with the atmosphere (*2*). Rapid improvements in the methods of chemical analysis available to oceanographers are needed, particularly with respect to sensors that can operate in situ and unattended for long periods of time on deep-sea moorings. These advances will require much closer cooperation between the analytical chemistry and chemical oceanography communities.

Increasing attention has been focused on ocean chemistry because of civilization's impact on the flow of chemicals through the sea. On a local scale, nutrient loading from sources such as sewage plants or runoff from farmland (e.g., ammonia, nitrates, and phosphates) can lead to increased rates of plant production, or eutrophication, in surface waters. Eutrophication is linked to toxic phytoplankton blooms (e.g., red tides) and greater oxygen demand in the subsurface waters. Increasing anoxia in the water column attributable to eutrophication has had a negative impact on marine resources in both the New York Bight (*3*) and the Chesapeake Bay (*4*). A single episode of anoxia in the New York Bight resulted in a $60 million loss to surfclam fishery alone (*3*). In many cases, the impacts of these perturbations are not recognized or understood because we lack records of natural chemical variability in the marine environment or an adequate means to monitor it (*5*).

On a global scale, the flow of chemicals through the ocean system is closely linked to the Earth's climate. The ocean holds 60 times more inorganic carbon than does the atmosphere, and perturbations in the flow of CC_2 through the ocean are related to changes in atmospheric CO_2 and global temperature (*6*). Release of CO_2 from the burning of fossil fuels, which has resulted in a 30% increase in atmospheric CO_2 since 1850, has the potential to produce even greater climatic changes than were experienced over the last glacial cycle (*7*). Much of this CO_2 will enter the ocean, but the rates of CO_2 absorption in seawater are not yet well known (*8*). Rapid changes in ocean circulation may produce large CO_2 fluxes between the ocean and the atmosphere (*9*); small changes in ocean chemistry may also draw large amounts of CO_2 from the atmosphere and regulate climate (*10*).

Despite the importance of these cy-

[1]Also affiliated with Monterey Bay Aquarium Research Institute, 160 Central Ave., Pacific Grove, CA 95039
[2]Present address: Monterey Bay Aquarium Research Institute

0003-2700/92/0364-1065A/$03.00/0

cles, there are large gaps in our most fundamental understanding of the processes that drive the flow of chemicals through the ocean. For example, we do not understand what combination of processes controls the rates at which phytoplankton fix dissolved CO_2 into organic carbon in large areas of the ocean (*11*). Yet this "biological pump" is one of the most significant processes that acts to redistribute dissolved and particulate chemicals throughout the sea.

Our goal in this REPORT is to highlight some of the current issues and problems in chemical oceanography. It will focus on both the oceanographic questions and the analytical methods used to address them. This article will concentrate primarily on the determination of dissolved chemicals. However, cycling of particles in the marine environment is an equally important subject that cannot be easily separated from studies of dissolved chemicals (*12*). The areas in which significant advances in analytical technology are required will be emphasized. We do not pretend to offer a comprehensive treatment of this subject in so few pages, but we hope to offer the analytical chemist a sense of the enormous challenge facing the chemical oceanographer, with an appreciation for the complexity of the marine system and the power of analytical chemistry to unravel the ocean's secrets.

Background

The analytical challenges involved in studying ocean chemistry are formidable. Only seven ions are present in seawater at concentrations > 1 mM. These major ion electrolytes constitute > 99.5% of the dissolved chemicals in seawater and dramatically affect the rates and equilibria of chemical reactions in the sea. Hidden within this matrix of major ions are infinitesimally small quantities of the remaining elements (Figure 1). Determination of these trace chemicals is often complicated by the major ion matrix. Despite their low concentration, the remaining elements may have a significant influence on global chemical cycling. A single iron atom, for instance, is required for each 100,000 molecules of CO_2 that are fixed into organic carbon. Lack of iron, therefore, may control the fate of enormous amounts of carbon in the ocean (*10, 11*).

The sea is also a weak organic soup that contains up to 300 μM dissolved organic carbon (DOC), of which < 10% has been identified (*13*). Much of the remaining organic carbon is humic material, a poorly characterized substance of high molecular weight with extensive unsaturation and polymerization.

Seawater cannot be considered as an assemblage of dissolved elements and compounds alone. Particles of every size drift, sink, and swim through the sea. Furthermore, many of the particles studied by geochemists are actually living organisms. A typical milliliter of surface seawater contains on the order of 10 million viruses, 1 million bacteria, 100,000 phytoplankton, and 10,000 zooplankton. All of these living and nonliving particles affect the cycling of chemicals in the sea. Many elements and compounds are passively adsorbed to the exterior of particles, whereas others are actively taken up and transformed by the biota. Biologically mediated reactions are one of the major forces that control the chemical cycling of dissolved trace elements in the ocean (*13*).

The natural cycles of many chemicals are characterized by large temporal changes in concentration. Daily variability in the surface waters is driven by photosynthesis, respiration, photochemical reaction, tidal

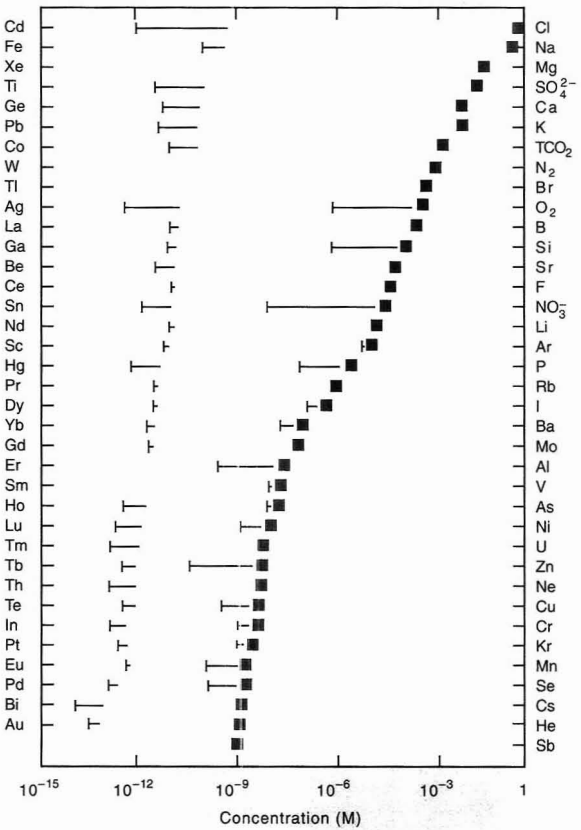

Figure 1. Plot of concentrations of seawater components, spanning 15 orders of magnitude.

The horizontal bar spans the range of concentrations that have been detected in open ocean waters. In many cases, low concentrations represent detection limits and even lower concentrations are likely to occur. Yellow squares refer to the left *y*-axis; dark blue squares refer to the right *y*-axis. TCO_2 refers to total inorganic carbon. Concentrations are taken from current literature.

mixing, and overturn of the water column initiated by solar heating. Variations in concentration also occur on a seasonal cycle because of changes in light, temperature, vertical mixing rates, and growth of phytoplankton. Interannual changes in chemical distributions over large areas of the ocean basins occur because of climatic processes such as the well-known weather phenomenon "El Niño" (*14*).

For example, concentrations of nitrate near the sea surface can be high at the end of winter because of frequent storms that bring deep, nutrient-rich water to the surface. Solar heating during the spring produces a density stratification that stabilizes the water column. This thermal stratification allows phytoplankton to remain within the sunlit portion of the water column (euphotic zone) where they grow rapidly and consume the available plant nutrients such as nitrates, phosphates, and silicates.

After such spring blooms, which usually last only a few weeks, photosynthetic rates are controlled by physicochemical processes (e.g., upwelling, diffusion, and atmospheric deposition) that slowly resupply nutrients to the sunlit surface layer. Biological processes such as grazing and microbial decomposition also release nutrient elements stored in cells (*15*). Fall and winter storms vigorously mix plant nutrients into surface waters, but productivity does not increase until the water column again stabilizes during the spring. The few weeks of high primary production during the spring bloom can dominate the annual carbon production cycle (*15*). The chemical composition of the deep water is more stable, but changes can be detected over longer time scales of seasons to years (*16, 17*).

Chemical distributions also show large variations over all spatial scales. Concentrations may increase or decrease from the surface to the sea floor (average ocean depth is 3800 m), depending on whether the chemical cycle is dominated by release from or uptake by sinking particles (*18*). Large vertical concentration gradients can be found over distances of a few meters. Furthermore, water circulates between each of the major ocean basins in a distinctive pattern. This produces a unique lateral distribution of dissolved chemicals on a scale whose length is tens of thousands of kilometers for many chemicals. In addition, important chemical variability may occur over distances of < 1 mm because of the presence of microenvironments such as anoxic fecal pellets found in oxygenated surface waters (*19*). Reduced compounds produced in these environments may have an impact on chemical cycles.

Thus the challenge for the chemical oceanographer is to develop or apply analytical methodologies with the sensitivity and specificity to determine a wide variety of chemical substances within a complex medium over a large range of temporal and spatial scales. To discriminate analytes against the large background of major ions, efficient methods of chemical separation must be employed. Time-series measurements over periods from seconds to years are required to interpret ongoing chemical processes in the ocean. Chemical measurements must often be made over length scales from millimeters to thousands of kilometers.

Chemical tracers of ocean circulation

Chemical and biological coupling in the ocean are often regulated by the physical processes that transport water, plankton, and chemicals in the sea. To some degree, the major circulation of seawater can be described as a conveyor belt (Figure 2) (*20*). A strong density gradient (pycnocline) at a depth of 50–200 m, caused by a rapid temperature decrease with increasing depth, isolates the surface wind-mixed layer from the colder and denser deep waters. The major source of the deep water below the pycnocline is in the high latitudes of the North Atlantic. From there it flows south through the Atlantic to the Antarctic circumpolar current, then north through both the Indian and Pacific oceans. Deep water returns to the surface ocean by turbulent mixing and upwelling in zones located on the eastern coastal margins and equatorial belt of the major ocean basins. The average time needed to replace the deep waters of the entire ocean system is 500 years, and deep water in the North Pacific is thought to be about 1500 years old (*21*).

Much of our knowledge of advective and diffusive processes in the ocean is obtained from measurements of chemical tracers rather than from direct measurements of the motion of water masses (*18*). Circulation tracers are chemicals whose concentrations change in a well-defined manner with time. They are excellent tools for the study of deep circulation because they integrate the turbulent fluctuations that dominate the flow of water in the deep sea. Without the information pro-

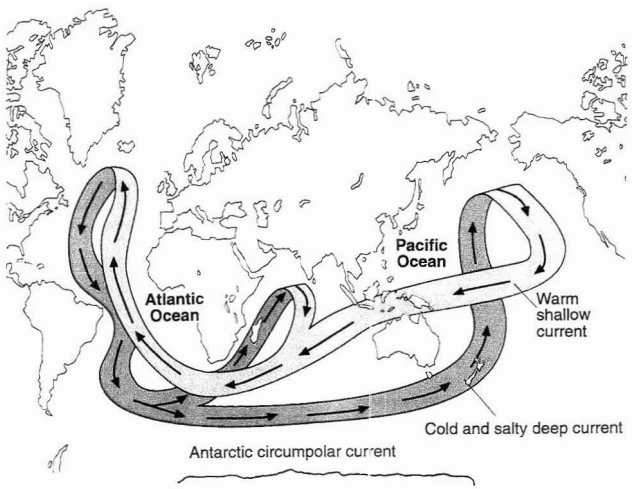

Figure 2. Conveyor belt of oceanic surface and deep-water currents, illustrating the major pattern of deep-sea circulation deduced from chemical tracer measurements.

(Adapted with permission from Reference 20, courtesy Joe LaMonnier.)

vided by circulation tracers, an inordinately large number of velocity measurements would be required to describe the time-averaged circulation of the ocean.

The general circulation of seawater along the conveyor was initially deduced from measurements of biochemically reactive tracer compounds such as oxygen and plant nutrients. Determination of the rates at which seawater flows along the conveyor requires measurements of radiotracers with appropriate half-lives or chemicals with well-known, time-dependent source functions. These tracers exist only in extremely low concentrations. Their utility has come about mainly through advances in analytical instrumentation and contamination control.

Two examples of chemical tracers that can be used to determine the patterns and rates of deep-sea circulation are chlorofluorocarbons (CFCs) and ^{14}C. CFCs were first produced in the 1930s, and their concentrations in the atmosphere have increased almost exponentially since that time. CFCs dissolved in surface seawater are in equilibrium with the atmosphere; present-day concentrations are ~5 pM for CCl_3F (Freon-11) and CCl_2F_2 (Freon-12) (*22*). The increase in CFC concentrations has been paralleled by a changing ratio of Freon-11 to Freon-12. This time-dependent ratio makes it possible to determine when a seawater sample was last in equilibrium with the atmosphere. CFC measurements have now been used to trace the flow of water as it enters the deep sea. For example, CFC measurements show that water leaving the surface of the North Atlantic during winter reaches the equator in 23 years and is diluted only fivefold during this time (*23*).

Detection of low CFC concentrations in seawater became feasible only after the invention of the electron capture detector (ECD) for GC and the adoption of strict procedures to control contamination from the atmosphere and the CFC-rich laboratory environment. Samples are purged, cold-trapped, and analyzed by GC using an ECD. Because of the high sensitivity of this approach, ECD-based analyses can accurately measure CFCs down to concentrations of 0.005 pM (grams per cubic kilometer) in seawater (*22*).

Further development of CFC measuring techniques is still needed. For example, Freon-113 (CCl_2FCClF_2) has been produced in large quantities only during the past two decades. A method for its determination will allow better temporal resolution when dating water that has left the surface in the past 20 years, when the atmospheric Freon-11/12 ratio has been relatively constant. Freon-113 concentrations are, however, below the detection limit of most current measurement techniques, primarily because of contamination problems.

The utility of ^{14}C, another oceanic tracer, has recently been enhanced by new analytical techniques. ^{14}C, which has a half-life of 5720 years, is naturally produced in the stratosphere by cosmic-ray interaction with nitrogen. Unlike CFCs, which can be tracked in the environment for no more than 60 years, ^{14}C can be used to determine the time elapsed since a water mass left the surface in the oldest portions of the oceanic conveyor (*21*). ^{14}C measurements have not been made routinely, however, because decay-counting techniques require that inorganic carbon be stripped and concentrated from > 200 L of seawater for each analysis. This is an expensive process that requires specialized sampling apparatus at sea and time-consuming analyses. The development of accelerator MS has eliminated the need for decay counting (*24*) and will revolutionize the ability of oceanographers to date deep seawater samples. At present, accelerator MS can be used to measure ^{14}C concentrations by direct atomic counting of the inorganic carbon extracted from 200 mL of seawater. A national accelerator MS facility for oceanographic research has just begun operation at the Woods Hole Oceanographic Institution. However, difficult contamination problems still exist in the determination of natural levels of ^{14}C in samples collected on research vessels where large spikes of $^{14}CO_2$ are used to determine rates of primary productivity.

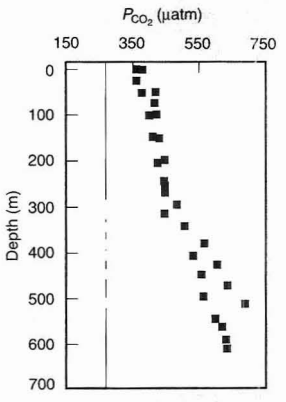

Figure 3. Atmospheric CO_2 increase reflected in the P_{CO_2} of the North Atlantic Ocean at a station between Florida and Bermuda.

Measured P_{CO_2} values (dark blue squares) increase with depth because of remineralization of organic carbon. Correction of the measured values for respiration (yellow squares), using the observed depletion of oxygen, demonstrates that shallower waters are equilibrated with the modern atmosphere (P_{CO_2} = 350 µatm); older, deep water is equilibrated with the pre-industrial atmosphere, which had a P_{CO_2} of only 270 µatm. (Data from Reference 26.)

Inorganic carbon

The concentration of CO_2 in the atmosphere has increased rapidly since the industrial revolution because of the burning of fossil fuels and the destruction of tropical rain forests. It is predicted that this concentration will double during the 21st century. Concentrations of CO_2 in the upper ocean must also have increased. Total inorganic carbon in the ocean is defined as

$$[TCO_2] = [HCO_3^-] + [CO_3^{2-}] + [CO_2]_{aq}$$

However, direct measurements of the increase in TOC are not yet feasible because its spatial and temporal variability requires a massive number of samples to assess the TCO_2 inventory of a single ocean.

The rate at which CO_2 is absorbed from the atmosphere by the ocean is not well known, and considerable variability exists in recent estimates of the amount of fossil fuel CO_2 that has entered the ocean (*8*). Measurements of a time-dependent change in the ratio of $^{13}C/^{12}C$ in seawater, because of dilution of oceanic carbon by fossil fuel carbon with a different isotopic composition, demonstrate that the ocean is receiving fossil fuel carbon (*25*). A direct assessment of CO_2 uptake by the ocean is critically important because it will allow limits to be placed on the magnitudes of other global carbon sources (e.g., tropical forest clearing) and sinks (e.g., uptake by boreal forests) (*8*).

In lieu of direct measurements of the rate at which CO_2 enters the ocean because of fossil fuel burning, oceanographers have attempted to measure the change in TCO_2 or P_{CO_2} as seawater flows along the conveyor. Old water that has moved far along the conveyor should have equilibrated with the pre-industrial atmosphere and have a lower P_{CO_2}

and TCO_2. However, respiration of organic carbon and dissolution of $CaCO_3$ from particles sinking into the deep sea also increase the P_{CO_2} and TCO_2 as seawater ages. The TCO_2 concentration increases by ~20% during the time water spends in the deep sea. Respiration of organic carbon produces the largest change in TCO_2 in the deep sea (≈70%). If concentrations of TCO_2 and titration alkalinity, defined as

$$TA = [HCO_3^-] + 2[CO_3^{2-}] + [B(OH)_4^-] + [OH^-] - [H^+]$$

are measured with a precision better than 0.1%, it is possible to detect the change in P_{CO_2} and TCO_2 concentrations because of the increase in CO_2 in the recent atmosphere. Such measurements have been used to detect the extent of penetration of fossil fuel CO_2 into the Atlantic Ocean (Figure 3) (*26, 27*).

The analytical difficulties in routinely measuring the TCO_2 concentration and the TA or pH with errors < 0.1% throughout the ocean are substantial. Recently, significant progress was made in measuring TCO_2 levels of seawater with a routine precision of 0.1% with the development of a coulometric titration procedure that could be used aboard ship (*28*). This has become the standard analytical procedure for global ocean science programs. It will be difficult, however, to achieve interlaboratory agreement at the 99.9% level until seawater standards for TCO_2 become readily available.

Measurements of TCO_2 alone cannot completely define the state of the inorganic carbon system in seawater. One additional chemical parameter, such as pH, P_{CO_2}, or TA must also be determined. As with the coulometric TCO_2 determination, these measurements must be made with extremely high precision and accuracy to detect the small temporal changes occurring in the ocean. The spectrophotometric determination of pH by using indicator dyes may be the simplest measurement that can be made to fully define the seawater carbonate system (*29*). The narrow pH range of seawater (7.4–8.9) is well suited to spectrophotometric measurement with an acid–base indicator of the appropriate pK_a. Precision better than 0.001 pH can be obtained on a routine basis. Such a system may form the basis for an optical sensor that can be deployed on oceanographic moorings for long periods of time to observe changes in oceanic carbon chemistry.

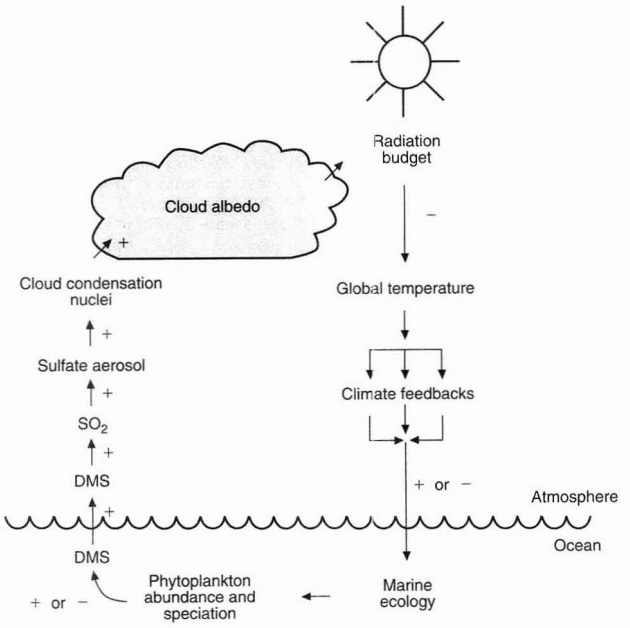

Figure 4. Proposed role of phytoplankton in the ocean–atmosphere sulfur cycle.

Production of DMS in the ocean leads to increased atmospheric DMS. This link may serve as a negative feedback mechanism for global warming. (Adapted with permission from Reference 36.)

Organic compounds

Large gaps occur in our most fundamental knowledge of DOC compounds in seawater. The total concentration of DOC is classically determined by chemical oxidation of organic molecules with persulfate or by ultraviolet photooxidation and subsequent determination of the CO_2 that is produced. This technique yields ocean DOC concentrations that are quite low (30–100 μM). However, results obtained with recently developed high-temperature combustion methods have suggested that the total DOC concentration in seawater has been underestimated by a factor of 2 or more (*30*). DOC values obtained by high-temperature combustion methods in surface waters can reach 300 μM. The excess, relative to that obtained by low-temperature oxidation, amounts to a pool of organic carbon that is greater in mass than the total amount of carbon stored on land in soils and vegetation, when averaged over the volume of the ocean (*31*).

Although many investigators have turned their analytical efforts toward the recently developed high-temperature combustion method, a recent interlaboratory comparison failed to resolve the discrepancies among the various methods for DOC analysis. Other laboratories have reported confirmation of a much larger DOC pool (*31*), but the original paper reporting the high-temperature combustion method has been withdrawn, leaving the field in a state of disarray. Much work in this important area remains to be done.

Temporal variability of individual organic compounds or compound classes, their spatial distributions, and their roles in biogeochemical cycles are not well understood. Studies of a few specific organic molecules, however, have demonstrated the tremendous influence that these compounds can have, both in controlling global processes and as tools for studying physical and chemical processes in the ocean.

For example, recent work by Brassell et al. has shown the potential of long-chain (n-C_{37}) unsaturated alkenone biomarkers as indicators of surface temperatures in ancient oceans (*32*). Phytoplankton of the class *Prymnesiophyceae* biosynthesize

these alkenones, apparently storing them in cell membranes. The degree of unsaturation is used to regulate membrane fluidity as a function of temperature. Measurements in plankton cultures, in suspended particulate matter, and in surface sediments at different locations in the ocean demonstrate that the ratio of the 37-carbon alkadienone to that of the 37-carbon alkatrienone is linearly related to the temperature of the water in which these phytoplankton live (*32, 33*).

These alkenones are refractory in marine sediments, and their ratio apparently is preserved for > 650,000 years. Determination of the alkenone compounds in ancient sediments, dated by isotopic measurements, can be used to reconstruct the surface temperature of the ocean during past glacial and interglacial periods (*34*). The carbon isotopic ratios of these biomarker compounds in sediment cores can be used to estimate the magnitude and direction of the atmosphere–sea CO_2 flux in ancient oceans (*35*). This analysis has been possible only through the coupling of capillary GC with isotope ratio MS for measuring isotopes of specific compounds in a complex mixture.

Trace organic compounds may also have a large impact on global chemical cycles. For example, dimethylsulfide (DMS) produced in the ocean is believed to play a critical role in the global sulfur cycle and the radiation balance of the Earth (Figure 4) (*36*). Dimethylsulfoniopropionate (DMSP), the precursor to DMS, is produced in the surface layer of the ocean by some phytoplankton (Figure 5) (*37*). DMSP apparently is used to regulate the internal osmotic pressure of the plankton cell; it decomposes to DMS, which is quite stable in seawater. DMS is lost primarily through transport across the sea surface to the atmosphere and also to microbial consumption.

The radicals $OH^{\cdot}$ and $NO_3^{\cdot}$ react with DMS in the atmospheric boundary layer to produce methanesulfonic acid, sulfur dioxide and, ultimately, sulfate. Biogenic DMS entering the atmosphere from the oceans may add sulfur at a concentration roughly equivalent to the input from sulfur dioxide derived from fossil fuel combustion. The sulfate aerosol provides the most significant source of nuclei for cloud condensation in the remote marine atmosphere. The concentration of cloud condensation nuclei is now directly linked to the abundance of methanesulfonic acid (*38*) and presumably the flux of DMS from the sea. Ocean cloud cover has also been correlated with the concentration of phytoplankton (*39*). It has been suggested, in fact, that phytoplankton may regulate the production of DMS in such a manner as to control the Earth's albedo and its climate (*40*).

The identification and quantitation of individual dissolved organic compounds at low nanomolar to picomolar concentrations continues to be the chief obstacle in studies of organic carbon cycling. Current methods of analysis require large samples or a time-consuming chromatographic separation and, even then, concentrations are still often near detection limits. The determination of DMS involves purging and cold-trapping a sample with liquid nitrogen, which is difficult to maintain on long research cruises (*41*). Advances in MS that provide detection limits in the picomolar range (*42*) promise to expand the number of compounds that can be detected. The development of other analytical schemes that do not introduce isotopic fractionation effects is still required. Much of the development needs to be focused on methods that can be used aboard ship or in situ for real-time measurements of large numbers of samples and a limited suite of compounds, rather than a few measurements of large numbers of compounds (*37*).

Trace elements

Many trace elements are required micronutrients in the enzyme and electron transport systems present in all living organisms. Plant growth is limited by trace element availability in many terrestrial systems, yet the role of these elements in limiting phytoplankton growth in the ocean has remained largely speculative. Recent advances in analytical methods, sample collection, and processing techniques have led to dramatic new understanding of the marine biogeochemical behavior of trace elements in seawater. The first accurate measurements of the total dissolved concentrations of most trace elements were made only in the past 15 years (*43*), demonstrating that most trace elements are present at low nanomolar to picomolar concentrations in surface waters. In many cases, their vertical distribution in the oceanic water column mimics that of the major plant nutrients such as nitrates, phosphates, and silicates (Figure 6) (*44*).

Experiments using phytoplankton cultures indicate that iron as well as zinc, manganese, copper, and cadmium can exert strong selective pressures that may regulate the differences in species composition of phytoplankton between metal-rich coastal and metal-poor open ocean environments (*45*). Recent studies with natural plankton samples demonstrate that iron may limit primary production in otherwise potentially productive regions of the world's oceans (*46*). Addition of only 1 nM Fe to surface seawater samples, which typically contain < 0.1 nM Fe, can cause a significant increase in primary production. Estimates of the potential productivity of ocean waters, based on phytoplankton cellular Fe:N:C ratios and dissolved iron and nitrate in surface waters, indicate that substantial increases in global carbon fixation could be realized if modest amounts of iron were added at the equator and at high latitudes. This scenario, known as the "Iron Hypothesis" (*11*), has recently received much public attention because of the potential for iron fertilization

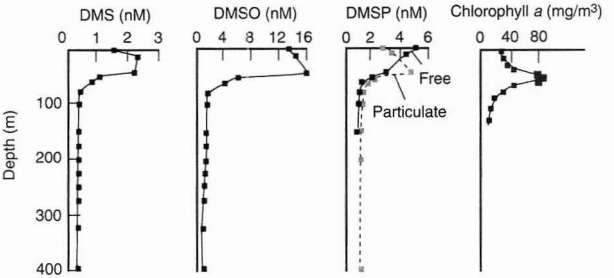

Figure 5. Vertical profiles of organosulfur compounds.

Distributions of DMS, DMSO (dimethylsulfoxide), DMSP, and chlorophyll *a* demonstrate that phytoplankton are the source of organosulfur compounds. (Adapted with permission from Reference 37.)

of the oceans to offset the effects of increased atmospheric CO_2 and global warming. This hypothesis is still the subject of much scientific debate, mainly because very few laboratories can accurately measure iron in seawater at ambient concentrations or perform uncontaminated enrichment experiments.

Two major advances have made it possible to determine total concentrations of dissolved trace elements in seawater. First was the realization of the extraordinary efforts required to carry a seawater sample through each step of the sampling and analytical processes without contamination (*43*). Second was the adaptation of analytical methodologies with sufficient sensitivity and selectivity to determine trace metals at extremely low concentrations.

The analytical methods most commonly used in oceanography involve preconcentration and separation steps with use of ion-exchange resins or chelation and solvent extraction. Even after concentration by factors of 100 to 1000, most trace elements in seawater can be detected only by using graphite furnace atomic absorption spectrometry (GFAAS) or thermal ionization MS (TIMS). Inductively coupled plasma MS is becoming widely accepted for oceanographic analyses because it is highly sensitive, can determine multiple elements, and requires small samples. It is especially useful for measuring the refractory elements, such as titanium and the rare earths (*47*).

These developments led to dramatic decreases in the reported concentrations of most trace elements dissolved in seawater; in some cases, the reported concentrations dropped several orders of magnitude. These changes led to the concept of oceanographic consistency as a criterion for accepting trace chemical measurements (*48*). This concept states that element concentrations measured in the open ocean should show smooth variations that are related to known physical, chemical, and biological processes. Trace element concentrations change smoothly because of the long time scale for mixing of seawater (> 100 years) and the long distances between strong sources of trace elements at the oceans' margins and interior. Oceanographic consistency has been a highly successful means of identifying reliable trace measurements. Only recently, the techniques developed for oceanographic analyses have been extended to measurements taken in freshwater systems. These measurements, using methods developed by chemical oceanographers, demonstrate that dissolved metal concentrations are overestimated in freshwater lakes and rivers by as much as 3 orders of magnitude (*49*).

Measurements of total element concentrations, however, are insufficient to define chemical behavior. The chemical speciation of an element will determine its biological availability, toxicity, and geochemical reactivity in seawater. The oxidation states of a variety of trace elements (e.g., arsenic, tin, antimony, and tellurium) have been successfully determined by using techniques such as selective hydride generation coupled with AAS or GC (*50*).

Complexation of metals by organic and inorganic ligands can also have a marked effect on the reactivity of chemicals in the ocean. Copper, for example, is present in surface seawater at concentrations of < 1 nM. It is bound by an unidentified ligand, which appears to be produced by organisms in the upper ocean, that has a high specificity for the metal (*51*). The ligand is also present at concentrations of ~1 nM and regulates the copper(II) aquo-ion concentration. Concentrations of the copper aquo-ion are calculated to be on the order of 1×10^{-14} M, which is undetectable by any analytical method now available (Figure 7). Studies of this system must be performed at total metal and ligand concentrations < 1 nM. Electrochemical methods such as differential pulse anodic stripping voltammetry (DPASV) at a thin mercury film/glassy carbon electrode or differential pulse cathodic stripping voltammetry (DPCSV) methods using a hanging mercury drop electrode are employed most often in these studies (*52, 53*).

Much of the focus in the analytical chemistry of trace metals in seawater is on the development of methods that can be used aboard ship to produce large data sets (*53*). Shipboard methods have, in general, precluded AAS and MS because the instruments are sensitive to the constant vibrations. Instead, a variety of methods have been developed, including atomic fluorescence (for mercury) (*54*), GC (for aluminum, beryllium, arsenic, and selenium) (*55*), and flow injection analysis (FIA) using chemiluminescence and fluorometric detection (for a suite of met-

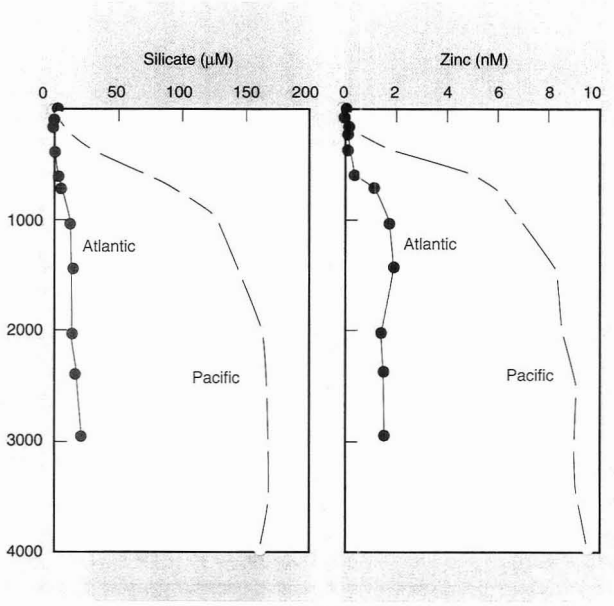

Figure 6. Profiles of total dissolved zinc and silicate in the North Atlantic and North Pacific oceans.

Zinc distributions are similar to those of the plant nutrient silicate—depleted at the surface and enriched at depth. Biological activity depletes dissolved zinc to subnanomolar levels. The interocean differences are the same for the two analytes, indicating a constant composition of sinking plankton as seawater passes along the oceanic conveyor. (Data from Reference 44.)

als, including cobalt and manganese [*56*, *57*]). DPASV and DPCSV are also used at sea for the determination of zinc, cadmium, copper, lead, cobalt, nickel, and iron (*53*). Many of these techniques can discriminate between the various chemical forms of the element (e.g., the oxidation state and the degree of complexation by organic ligands), which more accurately reflects the chemical reactivity and the biological availability or toxicity of the metal (*51*). However, shipboard sampling (with the possible exception of surface water pumping) permits only a few samples to be collected, and the possibility of contamination still exists. Future work must focus on in situ measurements of metal concentrations where greater sampling resolution and less likelihood of contamination can be achieved.

Radioisotopes

More than 60 radionuclides occur naturally in the marine environment, in addition to the fission products of thermonuclear power generation and weapons detonation. Of the natural radionuclides, 14 are produced by cosmic rays and 49 by decay of primordial isotopes. Radioisotopes have the unique feature of allowing oceanographers to elucidate rates of mixing and chemical transformations in the ocean.

The parent/product activity ratios of the natural uranium and thorium decay series isotopes have proved particularly useful in studies of dissolved metal–particle interactions (*58*). The primordial isotope ^{238}U exists principally as the dissolved $^{238}UO_2(CO_3)_3^{4-}$ species in seawater and shows a low affinity for chemical reaction or sorption onto sinking particles. Uranium therefore is distributed in a uniform manner throughout the water column. In contrast, ^{234}Th, the immediate product of ^{238}U, exists as the hydrolysis product $^{234}Th(OH)_n^{(4-n)+}$ and is highly particle reactive. Radioactive disequilibria between the dissolved ^{234}Th and its ^{238}U parent (shown in the shaded region of Figure 8) can be used to calculate rates at which thorium is scavenged from the dissolved to the particulate phase and the rate at which particles are removed from the water column. These measurements show the importance of interactions with plankton in removing metals from the surface ocean (Figure 8) (*59*). By measuring other elements associated with particles carrying thorium, various elemental removal rates can be calculated.

The determination of ^{234}Th has typically been achieved through a long coprecipitation, ion-exchange, and electrodeposition process. This is followed by alpha particle counting of a ^{230}Th yield tracer using silicon surface barrier detectors and beta particle counting of the ^{234}Pa product of ^{234}Th using low-background, anticoincidence, gas-flow proportional detectors (*60*). The particles and processes that remove thorium are heterogeneously distributed in the surface waters, and many measurements are required to characterize these rates accurately. Furthermore, ^{234}Th has only a 24.1-day half-life, and some of the activities are very low (< 0.2 decay per minute per liter), necessitating that the isotopes in samples collected on long cruises be separated and counted at sea. The other isotopes of thorium that are useful in determining rates of metal interactions with particles, ^{230}Th and ^{232}Th, have long half-lives and require thousands of liters to be processed for each sample before the isotopes can be measured by conventional methods of alpha particle detection.

These difficulties have prompted several recent analytical advances in thorium isotope detection. First, thorium can be extracted in situ by pumping seawater through cartridges filled with acrylic fibers that have been impregnated with manganese oxide (*58*), thus eliminating the need to process thousands of liters of seawater aboard ship. Second, ^{234}Th emits a gamma particle that can be detected with use of a low-background well-type germanium–lithium detector. The acrylic fibers on which thorium is concentrated can be melted into a puck and inserted directly into the detector to obtain ^{234}Th activities while still at sea (*61*). Third, TIMS is now being used to detect the longer-lived thorium and other uranium-series radionuclides. The direct determination of the molecular abundance of ^{230}Th and ^{232}Th by using TIMS greatly improves the detection limit, which reduces the volume of water needed for an analysis from 1000 to about 10 L (*62*). Further improvements in concentration and detection techniques will increase the utility of radioisotopes as tracers of chemical processes within the oceans.

Chemical sensors and analyzers

A long-term series of chemical observations is required to identify the processes that lead to natural vari-

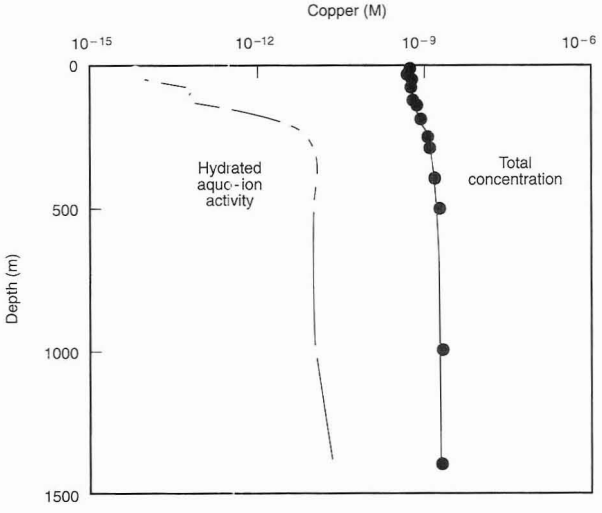

Figure 7. Vertical profiles of total dissolved copper (right) and the Cu(II) aquo-ion (left) activity in the North Pacific Ocean.

Organic ligands produced near the surface suppress the Cu(II) ion activity in the upper ocean by > 3 orders of magnitude relative to the value in organic-free seawater. (Adapted with permission from Reference 51.)

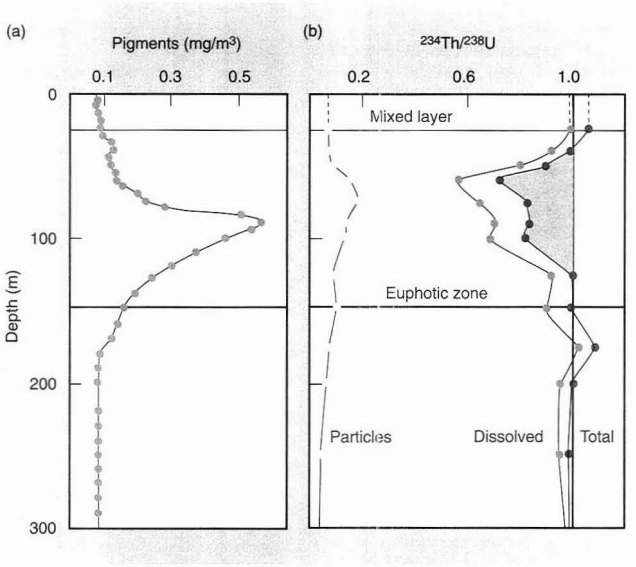

Figure 8. Vertical profiles of (a) phytoplankton pigments and (b) activity ratio of $^{234}Th:^{238}U$ in the dissolved and particulate (> 0.45 μm) fractions in the central North Pacific.

(a) Phytoplankton are concentrated near 100 m because nutrient concentrations are too low at shallower depths, and there is insufficient light below 150 m to support growth. (b) Low dissolved ^{234}Th activities in the 100-m region (highest biological activity) are an indication of the role of phytoplankton in removing metals from surface waters. (Adapted with permission from Reference 59.)

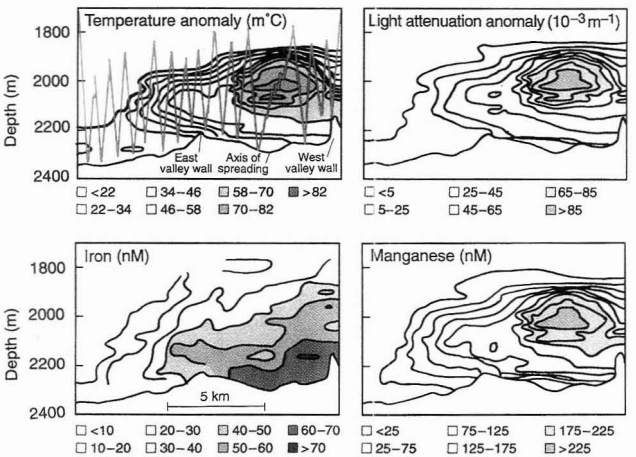

Figure 9. Temperature anomaly, light attenuation anomaly, dissolved iron, and dissolved manganese measured in situ over a hydrothermally active segment of the Juan de Fuca Ridge.

The sawtooth line in the temperature anomaly plot (1000 m °C = 1 °C) shows the tow path of the instrument package. More than 3700 determinations for iron and manganese were performed at depths > 2000 m in real time, enabling the acquisition of chemical data at similar resolution to physical measurements. (Adapted with permission from Reference 69.)

ability in ocean chemistry and to assess the human impacts on biogeochemical cycles. Analysis of temporal trends in chemical concentrations in the ocean now requires that a ship be on station to collect the samples. The cost of operating a modern research vessel capable of working on the high seas ($7000 to $18,000 per day) makes this a prohibitively expensive undertaking, and long-term oceanographic studies are done at very few locations (*63*). As a result, our understanding of ocean processes is severely limited.

The high production that occurs during the few weeks of a spring bloom may never be sampled by scientists constrained by ship schedules and finite budgets. Wintertime sampling in many high-latitude areas of the ocean is completely lacking because of extremely unfavorable weather conditions. Few long-term series of oceanographically consistent data have been collected with automated chemical measurement systems. Difficulties with sensor drift and biofouling have compromised their use on deep-sea moorings where sensors must operate unattended for months at a time, although recent progress has been made (*64*). A new generation of chemical measurement systems must be developed for long-term (1–12 months) operation on oceanographic moorings.

Two approaches are being tested for the design of chemical measurement systems that can operate in the deep sea. One method uses chemical sensor systems in which the analyte interacts with the active surface of the sensor by diffusion. The second approach is to adapt continuous-flow chemical analyzers, which transport sample and reagents mechanically, for in situ operations over long periods of time. Both techniques have significant advantages and disadvantages.

Sensor systems, such as electrodes, fiber-optic sensors, and chemical field-effect transistors promise to play an important role in the future (*65*). These systems are mechanically simple and can potentially be manufactured at low cost. Fiber-optic systems also allow the electronics to be placed in a remote location. The only chemical sensors regularly used are oxygen and pH electrodes. These sensors have been particularly valuable for measurements of small-scale (< 1 mm) chemical gradients across the sediment–water interface (*66*). Development of other chemical sensor systems has been hindered be-

cause they usually require a reversible chemistry that will respond rapidly to changes in dissolved chemical concentration and yet have sufficient sensitivity and selectivity to detect dissolved chemicals present at a concentration of 0.1 μM. Few such chemistries are known.

It is also possible to determine the concentrations of a suite of dissolved chemicals in situ by using unsegmented, continuous-flow analyzers (*67*). These submersible chemical analyzers (scanners) are based on the principles of FIA, although without the injection valve. Continuous-flow analyzers modified to operate underwater can use many of the chemistries developed for use in the laboratory with little modification required. Scanners are the only instruments available that can be used to determine dissolved nutrient elements in situ. Nitrate concentrations from the surface to depths of 2000 m have been determined in situ with a scanner tethered to a research vessel (*68*). The concentration of nitrate is determined classically by reducing it to nitrite and forming an azo dye. Measurements of redox reactive species such as sulfide, manganese, and iron also have been made in deep-sea hydrothermal systems at depths of 2500 m with scanners mounted on manned submersibles or towed from a research vessel (Figure 9) (*69*).

Scanner systems can easily be calibrated in situ by substituting standards for the seawater input at regular intervals. Analyzer systems are, however, inherently more complex than sensor systems. This has a marked impact on their long-term reliability and operating life. Significant progress in reducing the complexity of scanner systems has been made by replacing mechanical pumps with osmotic pumps (*70*).

Conclusions

Our vision of the ocean is seen through lenses crafted by the tools of our discipline. The picture of ocean chemical cycles developed by oceanographers has been focused by advances in analytical chemistry. In many ways, however, our knowledge of ocean chemistry still remains very superficial. The influence of organisms, one of the most important factors in controlling the composition of seawater, is often treated by chemical oceanographers as a black box. This lack of knowledge arises because ocean chemistry is undersampled on all time and space scales.

The ocean is a dynamic system with fronts, eddies, and biological patchiness that requires continuous observations (*71*). The present generation of instrumentation is oriented primarily toward analyses of discretely collected samples in ship- and shore-based laboratories. The need for a new generation of chemical observing systems to better monitor the changing ocean is now widely recognized. Global science initiatives, including the Joint Global Ocean Flux Study (*72*) and the Ridge Interdisciplinary Global Experiments (*73*), have identified developments in chemical sensing that are required to meet their scientific objectives. Many of these needs are outlined in a National Research Council report (*2*). What is now needed is an exchange of ideas and technology between the chemical oceanographer and analytical chemist to foster the development of new techniques for a clearer vision of the global ocean and our planet as a whole.

We wish to acknowledge the contributions of our many colleagues at Moss Landing Marine Laboratories and Monterey Bay Aquarium Research Institute. They have inspired and encouraged our work on marine analytical chemistry. Greg Cutter, Stuart Wakeham, and one anonymous reviewer had many useful comments on an early version of this report. We apologize to those chemical oceanographers whose areas of study were not presented or mentioned only briefly here, but we thank all who have made this field what it is today. This work is supported by Office of Naval Research grant N00014-89-J-1070 and National Science Foundation grant OCE8923057.

References

(1) Bard, A.; Goldberg, E. D.; Spencer, D. W. *Appl. Geochem.* **1988**, *3*, 3.
(2) *Chemical Measurement Technologies for Ocean Sciences*; National Research Council: Washington, DC, in press.
(3) Falkowski, P. G.; Hopkins, T. S.; Walsh, J. J. *J. Mar. Res.* **1980**, *38*, 479.
(4) Officer, C. B.; Biggs, R. B.; Taft, J. L.; Cronin, L. E.; Tyler, M. A.; Boynton, W. R. *Science* **1984**, *223*, 22.
(5) *Managing Troubled Waters: The Role of Marine Environmental Monitoring;* National Research Council: Washington, DC, 1990.
(6) *The Carbon Cycle and Atmospheric CO_2: Natural Variations Archean to Present*; Sundquist, E. T.; Broecker, W. S. Eds.; American Geophysical Union: Washington, DC, 1985.
(7) Lorius, C.; Jouzel, J.; Raynaud, D.; Hansen, J.; Le Treut, H. *Nature* **1990**, *347*, 139.
(8) Sarmiento, J. L.; Sundquist, E. T. *Nature* **1992**, *356*, 589.
(9) Broecker, W. S.; Denton, G. H. *Geochim. Cosmochim. Acta* **1989**, *53*, 2465.
(10) Martin, J. H. *Paleoceanogr.* **1990**, *5*, 1.
(11) Martin, J. H.; Gordon, R. M.; Fitzwater, S.; Broenkow, W. W. *Deep-Sea Res.* **1989**, *36*, 649.
(12) *Marine Particles: Analyses and Characterization*; Hurd, D. C.; Spencer, D. W., Eds.; Geophysical Monograph No. 63; American Geophysical Union: Washington, DC, 1991.
(13) Chester, R. *Marine Geochemistry*; Unwin Hyman: London, 1990.
(14) Barber, R. T.; Chavez, F. P. *Science* **1983**, *222*, 1203.
(15) Platt, T.; Sathyendranath, S.; Ulloa, O.; Harrison, W. G.; Hoepffner, N.; Goes, J. *Nature* **1992**, *356*, 229.
(16) Brewer, P. G.; Broecker, W. S.; Rhinnes, P. R.; Jenkins, W. J.; Rooth, C. G.; Swift, J. H.; Takahashi, T.; Williams, R. T. *Science* **1983**, *222*, 1237.
(17) Sansone, F. J.; Smith, S. V.; Price, J. M.; Walsh, T. W.; Daniel, T. H.; Andrews, C. C. *Nature* **1988**, *332*, 714.
(18) Broecker, W. S.; Peng, T-H. *Tracers in the Sea*; Eldgio Press: Palisades, NY, 1982.
(19) Alldredge, A. L.; Cohen, Y. *Science* **1987**, *235*, 689.
(20) Broecker, W. S. *Nat. Hist. Mag.* **1987**, *97*, 74.
(21) Stuiver, M.; Quay, P. D.; Ostlund, H. G. *Science* **1983**, *219*, 849.
(22) Gammon, R. H.; Cline, J.; Wisegarver, D. *J. Geophys. Res.* **1982**, *87*, 9441.
(23) Weiss, R. F.; Bullister, J. L.; Gammon, R. H.; Warner, M. J. *Nature* **1985**, *314*, 608.
(24) Nelson, D. E.; Korteling, R. G.; Stott, W. R. *Science* **1977**, *198*, 507.
(25) Quay, P. D.; Tilbrook, B.; Wong, C. S. *Science* **1992**, *256*, 74.
(26) Brewer, P.; Goyet, C., Monterey Bay Aquarium Research Institute, personal communication, 1992.
(27) Brewer, P. G. *Geophys. Res. Lett.* **1978**, *5*, 997.
(28) Johnson, K. M.; Sieburth, J. M.; Williams, P.J.L.; Braendstroem, L. *Mar. Chem.* **1987**, *21*, 117.
(29) Robert-Baldo, G.; Morris, M. J.; Byrne, R. H. *Anal. Chem.* **1985**, *57*, 2564.
(30) Sugimura, Y.; Suzuki, Y. *Mar. Chem.* **1988**, *24*, 105.
(31) Martin, J. H.; Fitzwater, S. E. *Nature* **1992**, *356*, 699.
(32) Brassell, S. C.; Eglinton, G.; Marlowe, I. T.; Pflaumann, U.; Sarnthein, M. *Nature* **1986**, *320*, 129.
(33) Prahl, F. G.; Wakeham, S. G. *Nature* **1987**, *330*, 367.
(34) Eglinton, G.; Bradshaw, S. A.; Rosell, A.; Sarnthein, M.; Pflaumann, U.; Teiedemann, R. *Nature* **1992**, *356*, 423.
(35) Jasper, J. P.; Hayes, J. M. *Nature* **1990**, *347*, 462.
(36) Andreae, M. *Mar. Chem.* **1990**, *30*, 1.
(37) Lee, C.; Wakeham, S. G. In *Chemical Oceanography*; Riley, J. P., Ed.; Academic: London, 1988; Vol. 9, pp. 1–51.
(38) Ayers, G. P.; Gras, J. L. *Nature* **1991**, *353*, 834.
(39) Falkowski, P. G.; Kim, Y.; Kolber, Z.; Wilson, C.; Wirick, C.; Cess, R. *Science* **1992**, *256*, 1311.
(40) Charlson, R. J.; Lovelock, J. E.; Andreae, M. O.; Warren, S. G. *Nature* **1987**, *326*, 655.
(41) Andreae, M. O.; Barnard, W. R. *Anal. Chem.* **1983**, *55*, 608.
(42) Burlingame, A. L.; Millington, D. S.; Norwood, D. L.; Russell, D. H. *Anal. Chem.* **1990**, *62*, 268 R.
(43) Bruland, K. W. In *Chemical Oceanography*; Riley, J. P.; Chester, R., Eds.; Academic: London, 1983; Vol. 8, pp. 157–220.
(44) Bruland, K. W.; Franks, R. P. In *Trace Metals in Sea Water*; Wong, C. S.; Boyle, E.; Bruland, K. W.; Burton, J. D.; Goldberg, E. D., Eds.; Plenum: New York, 1983; pp. 395–414.
(45) Bruland, K. W.; Donat, J. R.; Hutchins, D. A. *Limnol. Oceanogr.* **1991**, *36*, 1555.

(46) *What Controls Phytoplankton Production in Nutrient-Rich Areas of the Open Sea?* Chisholm, S. W.; Morel, F.M.M., Eds.; *Limnol. Oceanogr.* **1991**, *36*, 1507–1965.
(47) Orians, K. J.; Boyle, E. A.; Bruland, K. W. *Nature* **1990**, *348*, 322.
(48) Boyle, E. A.; Sclater, F. R.; Edmond, J. M. *Earth Planet. Sci. Lett.* **1977**, *37*, 38.
(49) Windom, H. L.; Byrd, J. T.; Smith, R. G.; Huan, F. *Environ. Sci. Technol.* **1991**, *25*, 1137.
(50) Cutter, L. S.; Cutter, G. A.; San Diego-McGlone, M.L.C. *Anal. Chem.* **1991**, *63*, 1138.
(51) Coale, K. H.; Bruland, K. W. *Limnol. Oceanogr.* **1988**, *33*, 1084.
(52) Van Den Berg, C.M.G. In *Chemical Oceanography*; Riley, J. P., Ed.; Academic: London, 1988; Vol. 9, pp. 197–245.
(53) Donat, J. R.; Bruland, K. W. In *Trace Metals in Natural Waters*; Steinnes, E.; Salbu, B., Eds.; CRC Press: Boca Raton, FL, in press; Chapter 12.
(54) Gill, G. A.; Bruland, K. W. *Environ. Sci. Technol.* **1990**, *24*, 1392.
(55) Measures, C. I.; Edmond, J. M. *Anal. Chem.* **1989**, *61*, 544.
(56) Sakamoto-Arnold, C. M.; Johnson, K. S. *Anal. Chem.* **1987**, *59*, 1789.
(57) Chapin, T. P.; Johnson, K. S.; Coale, K. H. *Anal. Chim. Acta* **1991**, *249*, 469.
(58) Bacon, M. P.; Anderson, R.F. *J. Geophys. Res.* **1982**, *37*, 2045.
(59) Coale, K. H.; Bruland, K. W. *Limnol. Oceanogr.* **1987**, *32*, 189.
(60) Coale, K. H.; Bruland, K. W. *Limnol. Oceanogr.* **1985**, *30*, 22.
(61) Buesseler, K. O.; Cochran, J. K.; Bacon, M. P.; Livingston, H. D.; Casso, S. A.; Hirschberg, D.; Hartman, M. C.; Fleer, A. P. *Deep-Sea Res.* **1992**, *39*, 1103.
(62) Chen, J. H.; Edwards, R. L.; Wasserburg, G. J. *Earth Planet. Sci. Lett.* **1986**, 80, 241.
(63) Karl, D. M.; Winn, C. D. *Environ. Sci. Technol.* **1991**, *25*, 1977.
(64) Wallace, D.W.R.; Wirick, C. D. *Nature* **1992**, *356*, 694.
(65) Goyet, C.; Walt, D. R.; Brewer, P. G. *Deep-Sea Res.* **1992**, *39*, 1015.
(66) Reimers, C. E. *Deep-Sea Res.* **1987**, *34*, 2019.
(67) Johnson, K. S.; Beehler, C. L.; Sakamoto-Arnold, C. M. *Anal. Chim. Acta* **1986**, *179*, 245.
(68) Johnson, K. S.; Sakamoto-Arnold, C. M.; Beehler, C. L. *Deep-Sea Res.* **1990**, *36*, 1407.
(69) Coale, K. H.; Chin, C. S.; Massoth, G. J.; Johnson, K. S.; Baker, E. T. *Nature* **1991**, *352*, 325.
(70) Jannasch, H. W.; Johnson, K. S. In *Proceedings of the MarChem '91 Workshop on Marine Chemistry*; Martin, S. J.; Codispoti, L. A.; Johnson, D. H., Eds.; Office of Naval Research Report No. OCNR 12492-510; Office of Naval Research: Arlington, VA.
(71) Dickey, T.; Marra, J.; Granata, T.; Langdon, C.; Hamilton, M.; Wiggert, J.; Siegel D.; Bratkovich, A. *J. Geophys. Res.* **1991**, *96*, 8643.
(72) *Global Ocean Flux Study*; National Academy Press: Washington, DC, 1984.
(73) *Ridge Inter-Disciplinary Global Experiments: Initial Science Plan*; Ridge Office, University of Washington: Seattle, 1989.

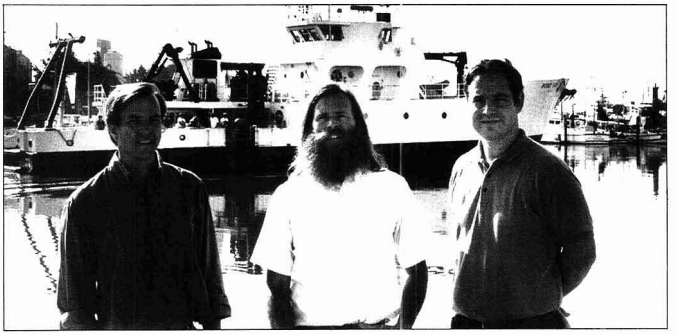

The authors in front of the National Science Foundation's research vessel, R/V Point Sur, *operated by Moss Landing Marine Laboratories (MLML).*

Kenneth S. Johnson (left) is professor of chemical oceanography at MLML of the California State University and a senior scientist at the Monterey Bay Aquarium Research Institute (MBARI). He received his B.S. degrees in chemistry and oceanography from the University of Washington in 1975 and a Ph.D. in oceanography from Oregon State University in 1979. His research interests include the development of automated methods for shipboard and in situ trace chemical analysis and application of these systems to the study of chemical cycling in the ocean.

Kenneth H. Coale (center) is a research scientist and adjunct professor at MLML. He received his B.S. degree and his Ph.D. (1988) from the University of California, Santa Cruz. His research interests include trace element biogeochemistry in marine and freshwater systems, the application of naturally occurring U/Th series radionuclides to study chemical cycling and age dating of marine specimens, and the development of analytical methods for shipboard and in situ determination of trace metals in seawater.

Hans W. Jannasch (right) is an assistant scientist at MBARI. Before his joint postdoc at MBARI and MLML, he received his Sc.B. degree in chemistry from Brown University in 1978 and a Ph.D. in chemical oceanography from the University of Washington in 1990. His research interests include trace metal scavenging, behavior of marine particles, and the development of in situ chemical instrumentation.

Environmental Sampling for Trace Analysis

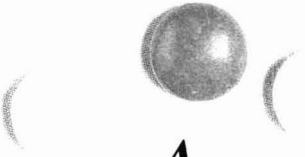

A Classroom Experiment You Can Sink Your Teeth Into!

Ray E. Clement
Ontario Ministry of the Environment
Laboratory Services Branch
125 Resources Rd.
P.O. Box 213
Rexdale, Ontario, Canada M9W 5L1

Hundreds of millions of dollars are spent worldwide each year on environmental issues—based directly on the results of chemical analyses. One would think that students in chemistry and engineering programs, who will be employed in the environmental field, should receive basic training in evaluating the reliability of such chemical analyses. However, it is unfortunately true that far too few of these graduates will have such training. Many new environmental programs being introduced in our colleges and universities emphasize the study of environmental issues rather than the scientific tools needed to investigate these issues.

Few undergraduate programs emphasize the type of laboratory instruction in analysis that is needed to understand how reliable chemical data are generated. Although most analytical textbooks and courses discuss the importance of accurate sampling, students are seldom offered practical examples of the consequences of poor sampling. They may think that an analytical result generated by a million-dollar state-of-the-art instrument is a number "carved in stone." And because such analyses are expensive, they believe there is no need for replication.

Can students learn the basic principles of environmental sampling and analysis from a simple classroom experiment? To find out, a sampling experiment was conducted at Mohawk College (Canada) in a class of students who were not chemistry majors. Although the experiment was originally designed to illustrate sampling difficulties and analytical errors that can occur in trace environmental determinations, it became apparent that it could also be used to describe many analytical concepts—including the importance of sample treatment and the need for selective detection. Most important, it clearly demonstrates the reality of errors in analytical measurements. Because the experiment is simple, interactive,

REPORT

and directly analogous to the analytical principles described above, it is highly effective and even enjoyable.

Design of the experiment

Nestlé manufactures a candy product called Smarties (available in Canada), which are button-shaped chocolate candies that have multicolored hard outer coatings. Individual Smarties are relatively uniform in shape and weight, and in appearance differ only in the color of the outer coating. (Any brand of multicolored candy can be substituted.) In the sampling experiment, different colors were used to represent different atoms and molecules. Green was used to signify PCB molecules, blue represented Pb, brown designated Fe, and red symbolized chlorinated dioxin molecules. In addition, purple and pink represented unknown molecules. A soil matrix was depicted by combining yellow and orange candies. The manufacture of a sample where the matrix predominated was difficult, because the Smarties, as marketed, are fairly evenly distributed among the various colors. To avoid having to purchase kilogram quantities of Smarties, a second type of candy similar in appearance to Smarties was purchased. This candy, called Reese's Pieces (manufactured by Hershey), comes in orange, yellow, and brown. The brown Reese's Pieces also represented Fe.

After combining the Smarties and Reese's Pieces, the number of candies of each color were counted. Because the individual molecules and components of the soil matrix are almost uniform in size and shape, we assumed for the purpose of this experiment that the molecular weights of all the individual candy pieces were the same. Therefore, by counting the number of candies of the same color, the concentration of the molecule or atom represented by that colored candy could be determined in units of parts per hundred (pph) (Table I).

Two volunteers from the class were selected to run the experiment. Student A was instructed to sample the contents of the plastic container in which the candies were brought to class by grabbing a small handful. After the first grab sample was taken, student A was told to make a second small grab and to keep this sample separate from the first. Student B was given the same instructions, except he was told to take large handfuls. The class was then told to determine the concentrations of all of our target analytes in parts per hundred—based on the four grab

ALLEN PHOTO/JEFF WATTS

0003-2700/92/0364-1076A/$03.00/0

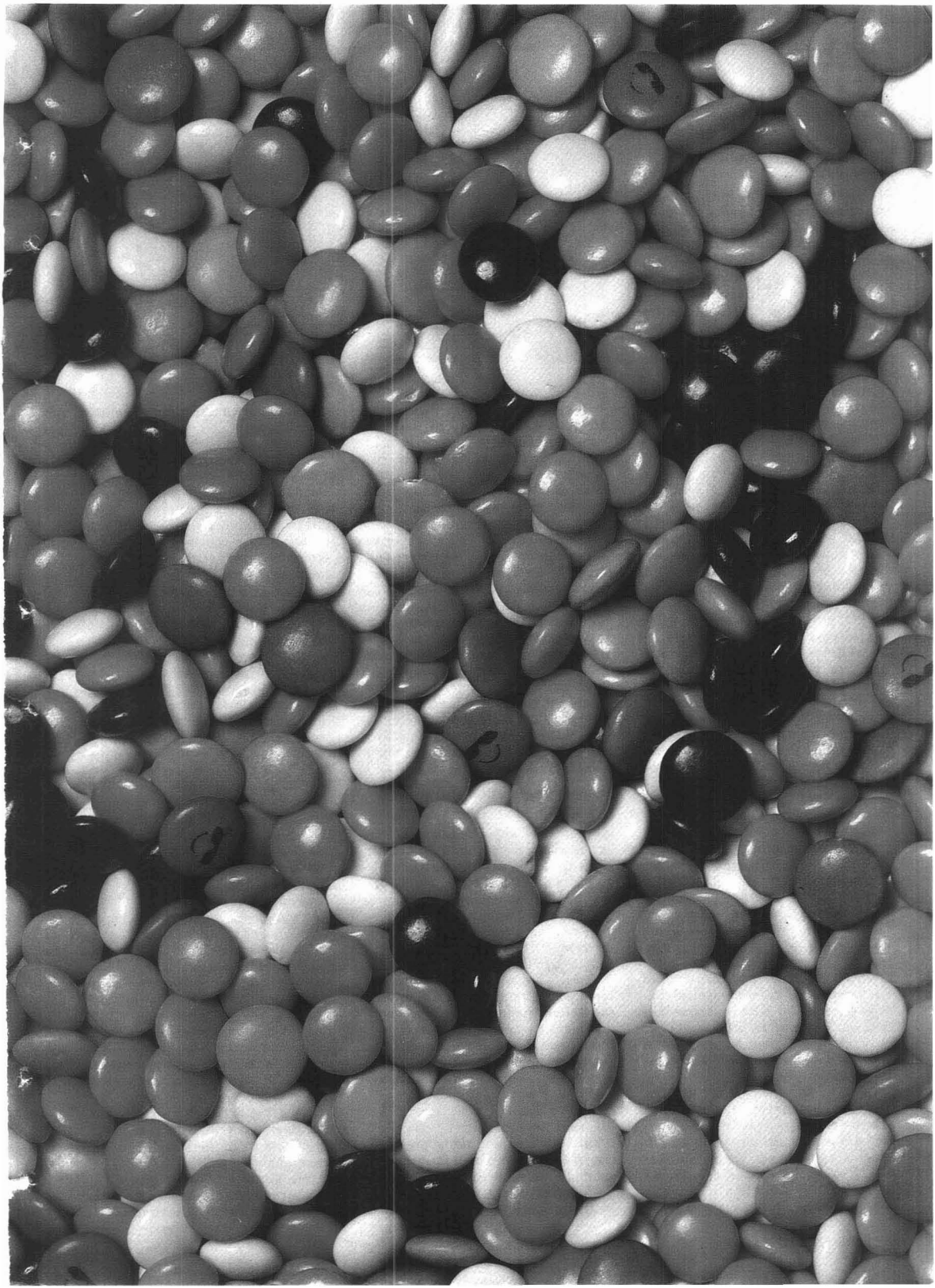

samples. An overhead projector was used to record the results.

Effect of sample size and replication on precision and accuracy

The actual experimental data from this classroom experiment are shown in Table II. Quite a large difference can be seen in the replicate results from student A, who collected total sample sizes of seven candies for each replicate. Unfortunately, the analyte with the highest concentration, Fe, was not detected in either replicate sample. PCBs, Pb, and the two unknown substances were detected in the first sample, each at 14 pph; only one of the unknowns was found in the second sample, at 28 pph.

Clearly, the differences between the replicates are significant. The result of selecting a small sample size was to increase (make worse) the detection limit of the determination. The comparison of individual results to the actual values seems pretty poor. However, when the averages of the values of the two determinations are taken, it can be seen that the estimates are much closer to the actual values; generally the estimated concentrations are within a factor of about 2—not too bad for trace analysis. Only the results for Fe and the unidentified pink analyte are way off. In the case of dioxin, the method is not sensitive enough to detect such an ultratrace analyte.

Real-life trace environmental analysis is conceptually not so different from this example; when methodology is used that can barely detect analytes, it is not uncommon for the analytes to be observed in some samples but not in others, even though all samples were thought to be the same. For example, in a six-laboratory round-robin study of chlorinated dibenzo-*p*-dioxins and chlorinated dibenzofurans introduced into blank water samples, a significant variation in laboratory results was noted (*1*). The reported concentrations of one compound, introduced at a concentration of 50 parts per quadrillion, varied from 37 to 62 parts per quadrillion, and two laboratories of the six could not detect the compound at all.

One way to improve detection limits in environmental analysis is to obtain a larger sample. Student B selected replicate samples of 75 and 70 candies, respectively. The data in Table II show the dramatic improvement in the estimation of analyte concentrations by using a 10-fold greater sample size. In these larger handfuls each analyte in the "soil" was detected in both replicates except for "dioxin," which was observed in only one sample. The concentrations of all analytes are more accurate and more precise for the large-sample-size experiment with the single exception of PCBs, where the mean concentration as determined from the first sampling experiment (small sample size) was closer to the actual value. As in the first sampling experiment, the mean estimates from two determinations were closer to the correct values than the estimates from an individual sampling event (with the single exception of PCBs, where both replicates from student B produced low estimates). The closeness of the mean analyte values from student B to the actual concentrations is quite reassuring.

Table I. "Contaminant" concentrations

Color	"Contaminant"	Actual no. of "molecules" [a]	Actual concentration (pph)
Green	PCBs	46	5.11
Blue	Pb	28	3.11
Brown	Fe	106	11.78
Purple	Unknown	30	3.33
Pink	Unknown	40	4.44
Red	Dioxin	10	1.11
Yellow/orange	Soil matrix	640	—

[a] Total no. of units is 900.

Sample preparation and analyte detection

A number of important concepts relating to sample preparation and analyte detection can be illustrated by this simulated soil-sampling experiment. Before sampling, the class was asked if any special sample preparation were needed. Almost everyone suggested that the sampling container should be well mixed before samples were withdrawn. It was also important (for this specific experiment) that the sampler take a "blind" sample; otherwise, the sample selected could be biased toward the sampler's favorite color. Although it is not recommended that samplers in the real world do their work with their eyes closed, it is certainly possible that the samples they collect could be biased and not representative of the population of interest. For example, water stream samples may be collected at the most convenient location, which may be outside of a contaminant plume that is emitted from a plant.

Some sample "cleanup" was needed before analytes could be accurately detected. In this experiment, cleanup consisted of sorting the candies into groups according to color, after which they could be assayed by counting. For the large sample, an accurate quantitative determination could not be made without this sorting step, although without cleanup it is still possible to do a qualitative determination of the analytes present by recording the different colors observed.

The physical separation of the candies into different colors is analogous to various chromatographic separation methods that are the basis of most real cleanup schemes. Note that the cleanup is more difficult to perform with the large sample. In real life, it is not difficult to overload cleanup methods by choosing sample sizes greater than those for which the cleanup is designed. In such cases, choosing a large sample size will increase rather than reduce the detection limits achievable. In this experiment the detection limits were not good for the small-sized samples taken initially, but sample cleanup and analysis were much easier. Thus the students learn to choose analysis methods that are sufficient for the specific application, and not to reach automatically for the most sensitive state-of-the-art method available. In addition, the analysis of the larger sample was more costly, because sample preparation and analyte detection took more time to complete.

The detector in this experiment was the human eye. By observing the various colors in the sample, the different analytes were identified (qualitative analysis). By counting the number of candies in each color group, quantitative estimates of

Table II. "Contaminant" data

Analyte	Student A: #1		Student A: #2		Student B: #1		Student B: #2		Mean conc. (pph)		Actual conc. (pph)
	No.	Conc. (pph)	No.	Conc. (pph)	No.	Conc. (pph)	No.	Conc. (pph)	A	B	
PCBs (green)	1	14	0	ND	2	2.7	1	1.4	7	2.1	5.11
Pb (blue)	1	14	0	ND	2	2.7	5	7.1	7	4.9	3.11
Fe (brown)	0	ND	0	ND	9	12	8	11.4	ND	11.7	11.78
Unknown (purple)	1	14	0	ND	3	4.0	1	1.4	7	2.7	3.33
Unknown (pink)	1	14	2	28	2	2.7	4	5.7	21	4.2	4.44
Dioxin (red)	0	ND	0	ND	0	ND	2	2.8	ND	1.4	1.11
Soil matrix (yellow/ orange)	3	—	5	—	57	—	49	—			
Total	7	—	7	—	75	—	70	—			

ND indicates not detected

their concentrations were determined. A serendipitous illustration of some of the difficulties in analyte detection could be made because the test sample was made up of a mixture of Smarties and Reese's Pieces. Although they appeared to be similar, Reese's Pieces are a bit smaller than Smarties. This size difference is not critical for the "soil matrix" itself, but it is important for the detection of the brown-colored candies used to represent Fe. Therefore the method of detection (color) by itself cannot distinguish between the two brown analytes. A determination of physical properties (size) is also needed to avoid an overestimation of Fe in the sample.

This situation frequently occurs in ultratrace environmental analysis. Another possible explanation for the two brown candies is that they both represent Fe, but in different forms (e.g., ferric and ferrous Fe). It is often important to know which specific form of an analyte is present in the environment and, as illustrated in this experiment, this can be very difficult. In this case, a second method of detection (taste) can be used to distinguish between the Smarties and Reese's Pieces. (Note that taste is destructive detection; observation of color is nondestructive detection.)

Other observations and limitations

At this time some readers may be noting that the concentrations detected are inaccurate because the students conducted sampling without replacement. In other words, the candies taken from the container by the first sampler were not replaced; consequently, the actual concentrations of the candies in subsequent samplings were affected by this omission. This is true, but by selecting a large original population size, this factor is not significant (at least for the purposes of this experiment).

In real environmental sampling, the amount of analyte removed from the area sampled (e.g., field, lake, or ambient air) is trivial when compared with the total amount of analyte present. In fact, in real environmental sampling one samples such a small amount of the whole area to be tested that a single sample quite likely is not representative of the area under investigation. Therefore when conducting actual environmental sampling it is important to analyze several samples thought to be representative of the area of interest. The average concentration from several samples will almost always give a more accurate estimate of the real analyte concentration than a single sample. Also, the amount by which the concentrations of the analyte differ between the various replicate samples will permit an estimate of the magnitude of the error in the determination.

The sampling experiment with candies represents an idealized situation in which the entire population is present in a plastic container, and therefore the concentrations of the various analytes could be determined exactly. In the environment, it is not possible to know the exact concentration of any analyte in the population. The best we can do is to estimate analyte concentrations by using a rigorous and careful sampling program, with judicious use of replication to determine the precision of our estimates. The population used in this experiment is also static; the exact numbers of the various colored candies could change only if some were removed by accident or design. The environment represents a dynamic situation in which analyte concentrations depend on weather conditions, time of day, type of industrial and natural processes occurring, and many other factors (some of which may be unknown).

Because of the assumption that all of the colored candies represented individual analyte molecules or atoms, the calculation of analyte concentrations was greatly simplified. In real life these analytes have unique molecular and atomic weights as well as physical and chemical properties. Therefore they respond differently to the detector used. (We can't count the true numbers of atoms or molecules in a sample.) To determine concentrations in real life, we must find the detector response to analytes by evaluating standards prepared with known concentrations of these analytes. For this soil-sampling experi-

Analytical Abstracts Now on CD-ROM!

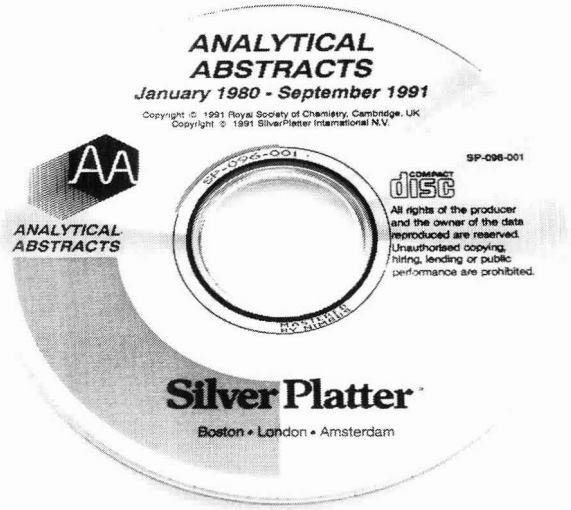

Available in Macintosh™ and IBM Compatible Formats

This valuable source of current awareness information in analytical chemistry is now available on a single SilverPlatter CD-ROM.

Analytical Abstracts on CD-ROM features:

- Approximately 140,000 items from 1980 onwards
- Easy to use SilverPlatter software
- Quarterly updates with more than 3,000 items
- Unlimited searching – no additional costs

Special Discount for Hardcopy Subscribers

Contact us today for further information and a FREE demo disk.

Judith Barnsby, Royal Society of Chemistry,
Thomas Graham House, Science Park, Milton Road,
Cambridge CB4 4WF, United Kingdom
Tel: +44 (0) 223 420066 Fax: +44 (0) 223 423623
Telex: 818293 ROYAL

ROYAL SOCIETY OF CHEMISTRY
Information Services

ment, the concentrations of the two unknown analytes could not be determined until their identities were established.

An interesting problem was presented to the students after the initial sampling experiment was completed. They were asked to sample the population to find a single poisoned candy that had been thrown in. In the absence of a specific detector that could selectively detect the poison (nobody volunteered to perform a taste test!), the students favored disposal of the entire population. This specific situation seldom occurs in an environmental analysis, but it is now obvious that the objectives of a sampling experiment should be clearly stated before any work is performed. The methods selected for any application depend on the specific results desired.

Conclusions

In the 30 minutes it took to conduct this experiment, students received a better understanding of the principles of environmental sampling and analysis than if they had read a textbook on the subject. Hands-on experiments capture the interest and attention of the students and encourage them to use their imaginations. Nobody is suggesting that the students are now experts in environmental sampling and analysis, but after this experiment they are better prepared to consider the details of such methods used for environmental investigations. The most important lesson is that sampling and analysis methods are used to estimate the concentrations of analytes, and the answers obtained are subject to error. Proper methods are required to give the most accurate and precise results.

After the experiment and discussion, the remaining candies were passed around the class for individual sampling and detection by taste. The students unanimously agreed that the soil-sampling experiment was literally one they could sink their teeth into.

Reference

(1) Tashiro, C.; Clement, R. E.; Davies, S.; Oliver, B.; Munshaw, T.; Fenwick, J.; Chittim, B.; Foster, M. G. *Chemosphere* **1990**, *20*(10–12), 1313–17.

Suggested reading

Principles of Environmental Sampling; Keith, L. H., Ed.; ACS Professional Reference Books; American Chemical Society: Washington, DC, 1988.

Keith, L. H. *Environmental Sampling and Analysis: A Practical Guide*; Lewis Publishers: Chelsea, MI, 1992.

Ray E. Clement received a Ph.D. in analytical chemistry (1981) from the University of Waterloo under the supervision of F. W. Karasek. He then joined the Ontario Ministry of the Environment where he is a senior scientist in the R&D department. He has authored more than 100 publications, most of which concern trace determination of chlorinated dioxins and furans in environmental samples.

BOOKS

Chromatography and Separations

Trace and Ultratrace Analysis by HPLC. Satinder Ahuja. xi + 419 pp. John Wiley & Sons, 605 Third Ave., New York, NY 10158. 1992. $75

Reviewed by Lane Sander, Organic Analytical Research Division, Chemical Science and Technology Laboratory, National Institute of Standards and Technology, Gaithersburg, MD 20899

Trace and Ultratrace Analysis by HPLC provides a broad examination of many topics of interest to analysts who use LC to determine contaminants at part-per-million or part-per-billion levels. The nine chapters deal with each stage of the analytical process, including sample preparation techniques, chromatographic method development, and approaches for selective detection and optimization of sensitivity. Each chapter provides a review of the pertinent literature and is supplemented with an extensive reference list. The final chapter, which constitutes about one-fourth of the text, is devoted to applications of trace analysis.

The emphasis of this monograph is on analyses relating to the pharmaceutical and biomedical disciplines, and this is perhaps its greatest strength. Numerous examples of methods for the determination of drugs, nutrients, steroids, amino acids, and other compounds of biological significance are presented. Less detail is provided for environmental analyses.

Chapter 2 presents a concise treatment of many of the most important mathematical relationships associated with chromatographic theory. This section is well executed and would make excellent supplemental reading for a course in separations science. Especially useful are a review of the factors affecting detection limits and a discussion of the sources of noise in chromatographic systems.

Instrumentation is discussed in subsequent chapters, and emphasis is placed on considerations for optimizing system performance. Sample preparation is described in some detail; however, there are some notable omissions that may have resulted from the emphasis on biomedical applications. For example, although Soxhlet extractions are routinely used in environmental analyses of sediments and particulate matter, this technique is not mentioned. Also omitted is a discussion of supercritical fluid extractions.

Solid-phase extraction (SPE) is treated more comprehensively, and two useful flow diagrams are provided to assist in the selection of SPE cartridges. Chromatographic method development is discussed for three of the major modes of operation: reversed-phase, normal-phase/adsorption, and ion pair chromatography. Also described are approaches for controlling selectivity to optimize a separation, including computer-based optimizations.

One of the most useful sections of the book is the final chapter on applications of trace analysis. The examples are organized into sections by analyte class; for example, analgesics are reviewed separately from antibiotics and alkaloids. Throughout the text, data are extracted from the literature and presented in tabular form.

This book describes many aspects and problems that may be encountered in trace-level determinations, and it should be particularly useful to analysts concerned with biomedical and related applications.

Unified Separation Science. J. Calvin Giddings. 320 pp. John Wiley & Sons, 605 Third Ave., New York, NY 10158. 1991. $55

Reviewed by K. G. Wahlund, Department of Technical Analytical Chemistry, University of Lund, Chemical Center, P.O. Box 124, S-22100 Lund, Sweden

This unique book is the result of the author's wish to develop separations science, and especially analytical separations, as a unified discipline rather than as a collection of apparently different and unrelated techniques. Whereas many other writers approach separations science by describing a specific technique, Giddings starts with a general description of transport, flow, and equilibrium that applies to all separation techniques and then uses his description to classify all methods.

The classification scheme is based on the way that flow interacts with fields in obtaining separations. Electrophoresis, sedimentation, field-flow fractionation (FFF), and chromatography are then described in relation to the classification. Realizing that most separations require some mass transport, the author develops the mathematics and the physical chemistry of transport phenomena in a general way so that the different methods can be put into this framework.

It is the author's intent to present the fundamental basis of different separation techniques rather than to give technical recipes on how to do the separations. In this way, the book aims at an educational, long-range perspective. Even though the text goes into the very fundamentals of the physicochemical basis of separations, the author never lets mathematics live its own life but always uses it in combination with vivid language to give the reader a sound physical insight and understanding of complex phenomena.

A list of key words from the contents describes the physicochemical phenomena treated in the book: mechanical and molecular equilibrium, molecular interaction and polarity scales, entropy effects in porous media, transport driven by equilibrium, mechanical versus molecular transport, flow mechanics, viscosity, flow in capillaries and packed beds, convective and electroosmotic flow, laminar and turbulent flow, friction coefficients, diffusion, Gaussian zones, random processes, zone broadening, steady-state zones, and resolution.

In addition to complete author and subject indexes, there are two separate lists of titles and references to the author's own publications in the separations field. These lists are ex-

LEGAL NOTICE

U.S. POSTAL SERVICE
STATEMENT OF OWNERSHIP, MANAGEMENT AND CIRCULATION

(Required by 39 U.S.C. 3685)

1A. Title of publication: Analytical Chemistry
1B. Publication no.: 00032700
2. Date of filing: Oct. 1, 1992
3. Frequency of issue: Semimonthly
3A. No. of issues published annually: 24
3B. Annual subscription price: $33.00
4. Complete mailing address of known office of publication:
American Chemical Society
1155 16th Street, N.W.
Washington, D.C. 20036
5. Mailing address of headquarters of the publisher: ACS, 1155 16th Street, N.W.
Washington, D.C. 20036
6A. Publisher: ACS, 1155 16th Street, N.W.
Washington, DC 20036:
6B. Editor: Royce W. Murray
Department of Chemistry
University of North Carolina
Chapel Hill, NC 27514
6C. Managing Editor: Mary Warner, ACS
1155 16th Street, N.W., Wash., DC 20036
7. Owner:
American Chemical Society
1155 16th Street, N.W.
Washington, D.C. 20036
8. Not applicable
9. The purpose, function, and nonprofit status of this organization and the exempt status for Federal income tax purposes has not changed during the preceding 12 months.
10. Extent and nature of circulation

	Average No. Copies Each Issue During Preceding 12 Months	Actual No. Copies of Single Issue Published Nearest to Filing Date
A. Total no. copies printed	21,667	30,340
B. Paid Circulation		
1.Sales through dealers and carriers, street vendors and counter sales	0	0
2.Mail subscriptions	18,714	26,174
C. Total paid circulation	18,714	26,174
D. Free distribution by mail, carrier or other means, samples, complimentary, and other free copies	1,458	1,698
E. Total distribution	20,172	27,872
F. Copies not distributed		
1.Office, use, left over, unaccounted, spoiled after printing	1,495	2,468
2.Return from news agents	0	0
G. Total	21,667	30,340

11. I certify that the statements made by me above are correct and complete

Head, Journals Department-ACS
Charles R. Bertsch

BOOKS

tensive, because Giddings has worked on almost every aspect of the theory and optimization of chromatography-like separations. References are cited up to 1989.

The book is intended primarily as a textbook for graduate analytical separations courses but is also useful as a reference for researchers. The unusual clarity of language and reasoning are the author's hallmark, and the student will benefit from the many worked-out exercises. Giddings' areas of expertise (chromatographic zone spreading, migration, and optimization of resolution and speed) are treated in detail, as are newer separation techniques such as FFF and capillary electrophoresis. Indeed, any worker in analytical separations, be it a graduate student or an experienced researcher, can use this book as a knowledge base for almost every important aspect of the field.

HPLC in the Pharmaceutical Industry: Drugs in the Pharmaceutical Sciences, Vol. 47. G. W. Fong and S. K. Lam, Eds. vii + 309 pp. Marcel Dekker, 270 Madison Ave., New York, NY 10016. 1991. $100

Reviewed by L. A. Pachla, Sterling Winthrop Research Division, Analytical Sciences, 25 Great Valley Parkway, Malvern, PA 19355

The purpose of this book is to present and better understand the latest advances in the pharmaceutical analysis field. The 11 chapters, written by experts in both academia and industry, are subdivided into four parts.

Part One, "Contemporary LC Techniques in Pharmaceutical Analysis," contains three chapters. In Chapter 1, Kucera and Licato (19 references) discuss high-speed LC using 3-μm packings. They include theoretical aspects of high-speed LC systems; instrument design; and column, detector, connection, electronic, and data acquisition variances. Chapter 2, by Raglione and Hartwick (36 references), is devoted to microbore LC. Topics include advantages of the technique as well as high separation efficiency, solvent and packing economics, thermal equilibria, and detector considerations. In Chapter 3 (70 references), Chow discusses column switching.

Part Two, "Specialized Detection Techniques," contains four chapters. Chapter 4, by Kissinger and Radzik (111 references), focuses on LC-EC. In addition to explaining principles of electrochemistry in thin-layer solutions, they discuss selectivity and applications to electroactive and inactive components. Chapter 5, by Quint and Newton (12 references), is devoted to radiochemical analysis. In Chapter 6 (16 references), Huber and Fiedler discuss photodiode array detectors. Chapter 7, by Kalasinsky and Kalasinsky (44 references), concerns LC/FT-IR.

Part Three is entitled "Automation in Pharmaceutical Analysis." Chapter 8, by Hanson (18 references), describes the application of LC to dissolution testing. This chapter focuses on identification of the individual components of dissolution testing, instrumentation, and the opportunities provided by LC. In Chapter 9, Felder (42 references) concludes the section with a discussion on robotics in the pharmaceutical laboratory.

Part Four, "HPLC of Peptides, Proteins, and Enantiomeric Drugs," contains two chapters. Chapter 10, by Bui (101 references), describes different mechanistic modes for separating enantiomers of pharmaceutical interest. Theoretical and applied aspects of conversion to diasteriomers, as well as the chiral aspects of ion pairing, stationary, and mobile phases, are also discussed. In Chapter 11, Benedek and Swadesh (215 references) describe the separation of peptides and proteins, reversibility of denaturation, concepts in refolding and the influences of physical forces, sources of heterogeneity, and protein adsorption and confirmation.

The book presents the theory of the technology and many examples of practical applications to everyday pharmaceutical problems. It should be on the shelf of every pharmaceutical library.

Fundamentals and Applications of Chromatography and Related Differential Migration Methods. E. Heftmann, Ed. xxxvi + 552 pp. Elsevier Science Publishers, 52 Vanderbilt Ave., New York, NY 10017. 1992. $180

Reviewed by Nebojsa Avdalovic, Dionex, 1228 Titan Way, Sunnyvale, CA 94088-3603

This fifth edition is a completely revised text on chromatography and related separation methods. The new chapters describe supercritical fluid chromatography (SFC), countercurrent chromatography (CCC), affinity chromatography, and field-flow fractionation (FFF).

The book contains 11 chapters. Some well-written chapters in the fourth edition were omitted; however, chapters on the history of chromatography and electrophoresis should remain a valuable reference for the new generation of readers. There are some useful additions, such as the list of chromatography and electrophoresis vendors.

The first chapter, by Snyder, deals with the theory of chromatography and describes the essential, basic mathematical relationships using qualitative explanations and easily understood physical analogies. If needed, the reader can find more detailed information in the classical volume written by Snyder and Kirkland, entitled *Introduction to Modern Liquid Chromatography.*

The next two chapters, which discuss CCC and planar chromatography, are easy to understand; however, the reader is left with the impression that these two powerful techniques still reside in the domain of highly specialized laboratories. In addition, the success of CCC separations rests heavily on choosing the two-phase solvent system that provides the proper partition coefficient values for the chosen compounds. In essence, the nature of the sample to be analyzed must be known. If the literature contains some information on the sample's physicochemical properties, the analyst is in a good position. A similar situation exists for the separation of chemical substances using isotachophoresis (ITP). Table 2.3 lists some of the most recent applications of CCC for those interested in using this separation technique.

Chapter 4 is a concise review of all major aspects of LC. It provides enough detail to understand the basic relationship between particle size and packing of LC columns, the essentials of isocratic and gradient separations as well as the types of columns, and an excellent yet simple explanation of the different types of pumps and their performance problems. The description of sample handling, columns, and connectors is up to date and informative, as is the short review of detectors. However, the description of optimization procedures, options, and packing materials is a bit meager and does not cover some of the major accomplishments in polymer chemistry and developments in polymeric support. To make this chapter more interesting, Pappe has added a succinct, accurate description of new forms of chromatography such as capillary and open

chemical systems, capillary zone electrophoresis, and micellar electrochromatography.

The chapter on ion-exchange chromatography is an abbreviated version of an older text edited by Walton and Rocklin. In my view, this text should be updated to cover some of the exciting applications, especially in the area of carbohydrate analysis of glycoproteins. The chapters on size exclusion and affinity chromatography provide much useful information and some insightful interpretation of the most recent developments related to macromolecule characterization and isolation.

The chapter on GC is well written but is too extensive for a review-type text. The new chapter on FFF, however, takes a balanced approach and is highly informative. The chapter on electrophoresis contains brief but significant information on pulsed-field and capillary electrophoresis, in addition to mentions of older techniques. The SFC chapter is well written and up to date, but because of the enormous interest in supercritical fluid extraction, a description of this technique should have been included.

This volume is an excellent orientation to chromatography theory and basic applications. Although it may not be of great use to practicing chromatographers, anyone unfamiliar with a particular technique will find it a great review text; it can provide a quick orientation, regardless of whether the individual is interested in detection, separation, or theory. I recommend this text as a supplement to the existing reference books in industrial and research libraries.

Books Received

Analytical Methods in Toxicology. H. M. Stahr. xxxvi + 328 pp. John Wiley & Sons, 605 Third Ave., New York, NY 10158. 1991. $70

This handbook provides guidelines for handling and analyzing hazardous substances. The front matter, which discusses chemistry laboratory policy, elapsed time for analysis, sample requirements, safety practices, and the safe handling of radioisotopes, also provides a list of abbreviations. The book is divided into six sections based on type of analysis: inorganics; mycotoxins; pesticides; rodenticides; antibiotics, drugs, vitamins, and feed additives; and miscellaneous analyses such as those for petroleum products or bacteria in water, ethylene glycol or oxalic acid in tissues and body fluids, urease activity in soy flour and feeds, and coal tar. The 11 appendices contain information on general laboratory techniques and list conversion factors, dilutions, and normal concentrations. A subject index is also included.

Transition Metal Nuclear Magnetic Resonance. P. S. Pregosin, Ed. xi + 351 pp. Elsevier Science Publishers, 52 Vanderbilt Ave., New York, NY 10017. 1991. $189

Volume 13 of the Studies in Inorganic Chemistry Series, this book contains a collection of review articles on the measurement, use, and understanding of transition-metal NMR spectra. Approaches to studying the transition-metal nuclei and the type of information that can be obtained from them are described. Correlations between NMR data and physical characteristics of the molecules are also discussed.

Potentiometric Water Analysis, 2nd ed. Derek Midgley and Kenneth Torrance. xiv + 586 pp. John Wiley & Sons, 605 Third Ave., New York, NY 10158. 1991. $125

This volume surveys the theoretical and practical aspects of potentiometry and ion-selective electrodes for the analysis of water. The first part of the book covers theory and background, with discussions of new electrodes and updates on general methods and procedures. The second part covers analytical methods. Each analytical methods chapter includes information such as the reagents required, worked examples, and possible sources of error. Six appendices contain information on theoretical values of the Nernstian slope, Debye–Huckel A and B coefficients for electrolytes in water, equipment manufacturers, a function table, data sources, and a table of weights and measures conversions. A subject index is also included.

Protein Structure Determination. Clarence H. Suelter, Ed. ix + 310 pp. John Wiley & Sons, 605 Third Ave., New York, NY 10158. 1991. $75

This book is volume 35 of the Methods of Biochemical Analysis Series. The determination of the secondary and tertiary structure of proteins is discussed in four chapters: "Theoretical and Empirical Approaches to Protein Structure Prediction and Analysis," "Protein–Ligand Interaction as a Method To Study Surface Properties of Proteins," "Fluorescence Techniques for Studying Protein Structure," and "The Use of Monoclonal Antibodies and Limited Proteolysis in Elucidation of Structure–Function Relationships in Proteins." Author and subject indexes for this volume and for the complete series are included.

Sampling. G. E. Baiulescu, P. Dumitrescu, and P. G. Zugravescu. 184 pp. Prentice Hall, Englewood Cliffs, NJ 07632. 1991. $85

Sampling processes and problems are reviewed in this book. Although samples are not discussed in depth, the analytical processes and the meaning of sampling are considered. Other topics include separation methods and sample history and homogeneity. A list of references and a subject index are included.

Activation Spectrometry in Chemical Analysis. Susan J. Parry. xii + 243 pp. John Wiley & Sons, 605 Third Ave., New York, NY 10158. 1991. $80

This book describes activation spectrometry, which is the basis of activation analysis. After an introductory chapter, the book is divided into sections on principles, techniques, and applications. The section on principles gives a background of the subject without discussing the underlying detailed physics. The techniques section describes sampling and preparation of material, how to make standards, and which reference materials to use. Two chapters in this section discuss irradiation and counting techniques. Biomedical, environmental, geological, and industrial applications of the technique are covered in the final section. Each chapter contains a list of references, and a subject index is included.

Concise Encyclopedia of Biological and Biomedical Measurement Systems. Peter A. Payne, Ed. xiii + 490 pp. Pergamon Press, 395 Saw Mill River Rd., Elmsford, NY 10523. 1991.

Biological and biomedical measurement systems as well as the biological systems and subsystems on which the measurements are made are detailed in 85 articles. Arranged alphabetically, each article contains a bibliography of additional reading. The requirements of the physical scientist who must understand the measurement methods and their effects on the system being measured are emphasized. Advances in medical imaging are also covered. A list of the articles, a list of contributors, and a subject index are included.

NEW PRODUCTS

Instrumentation

Hydrocarbon analyzer. Model 51 heated total hydrocarbon analyzer features flame ionization detection and a microprocessor-based design for auto-zeroing, auto-calibration, and auto-ranging over the 0.1–10,000-ppm concentration range. All components in contact with the sample (detector, pump head, 7-μm filter, transport lines, and back-pressure regulator) are heated to 200 °C to prevent sample condensation. Thermo Environmental Instruments **401**

Elemental analyzers. NA 1500 Series 2 and EA 1108 organic elemental analyzers have flexible designs that permit direct oxygen measurement and simultaneous determination of nitrogen, carbon, hydrogen, and sulfur at concentrations ranging from 100 ppm to 100% in organic or inorganic materials. The NA 1500 Series 2 is available in N/protein, N/C, and N/C/S configurations; the EA 1108 is available in CHN, CHNS, and CHN-O versions. Fisons Instruments **402**

Evaporator. Organomation S-Evap Model 12060 analytical evaporator features eight glass condensers with individual solvent recovery flasks that can evaporate eight samples in < 15 min and provide ≥ 95% recovery of Freon by volume. The design, which prevents Freon from being exhausted through the hood, lets users segregate contaminated Freon and reduce waste. Organomation Associates **403**

Optical analyzer. Lambda LS-2000C cooled multichannel optical analyzer is based on a proprietary 2048-element photodiode/CCD array. Dual thermoelectric coolers allow operation of the array at 0 °C with only air cooling and at −10 °C with water cooling. Applications include general spectroscopy, light source characterization, fluorescence studies, process control, quality control, environmental monitoring, and biomedical measurements. Alton Instruments **404**

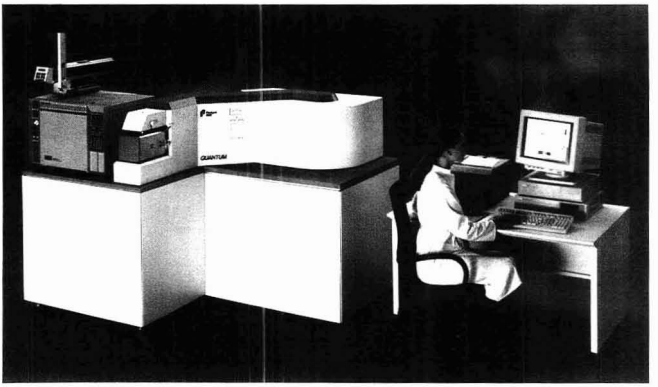

Mass spectrometer. Quantum integrated target compound analyzer, based on a high-performance mass spectrometer, is designed for fully automated and unattended ultratrace determination of compounds such as halogenated dibenzodioxins and dibenzofurans in water, soil, and food. Femtogram detection limits can be achieved, and system operation can be customized and documented. Finnigan MAT **407**

Microplate reader. Model 3550-UV microplate reader has a spectral range of 340–750 nm and can be used to analyze test systems that produce a chromogenic product or light scattering. Applications include enzyme immunosorbent assays, protein determination, cell viability, DNA detection, NAD/NADH assay, kinetic ELISA, and kinetic enzyme analysis. Bio-Rad Laboratories **405**

Homogenizer. Digi-System bench-scale, programmable homogenizer is designed for repeatable, highly accurate processing of volumes ranging from 0.03 mL to 20 L. Homogenization, emulsion, suspension, and high-shear mixing processes can be handled. An optical sensor maintains programmed speed throughout changes in sample viscosity. Omni International **406**

Conductivity monitor. Model ICM-180 flow-through conductivity monitor for HPLC and IC features a cell with a dead volume of < 20 μL. It is useful in optimizing protein separation using both classical column and HPLC apparatus and in converting standard HPLC systems to perform IC. Lazar Research Laboratories **408**

LC. Flow 2P and Flowprep adjustable flow dividers split the outlet of a chromatographic column into multiple flow streams. Designed for preparative chromatography, post-column derivatization, and multiple-detector applications, the dividers handle rates up to 2 mL/min (Flow 2P) and 20 mL/min (Flowprep). Lab Connections **409**

ICP spectrometer. Super Sequential ICP/echelle spectrometer combines simultaneous and sequential ICP designs to increase sample throughput and reduce analysis cost. The instrument can be programmed to carry out quality control checks, calculate recoveries on spiked samples, and check laboratory standards without user intervention. Leeman Labs **410**

PRESENTING

The Absolute Detector.™

Powerful. Precise. Productive.

Brought to you by the people who *invented* laser light scattering, the miniDAWN® is an inexpensive, easy-to-use multi-angle light scattering detector that can be coupled to almost any HPLC line for absolute macromolecular characterization. It determines molecular weights and sizes for a broad range of polymers without making assumptions about your samples. It can also reveal a wealth of information that goes unseen by UV, RI and other detection technologies.

Solves aggregation and calibration problems. You can use the miniDAWN to see what your samples are doing *in solution* as well as to distinguish among protein and microgel aggregation states without column calibration.

From the #1 Light Scattering Company. With installations in more than 25 countries, Wyatt Technology is the pioneer and world's leading manufacturer of laser light scattering instrumentation for absolute macromolecular characterization. Call us today to get your free 10-page brochure on the miniDAWN. You'll see immediately that the miniDAWN is *absolutely* smarter and faster than any other detector on the market.

SPECIAL U.S.A. INTRODUCTORY OFFER:

20% DISCOUNT IF ORDERED BEFORE DECEMBER 31, 1992. CALL TODAY!

(805) 963-5904

Wyatt Technology CORPORATION

802 East Cota Street
Santa Barbara, California 93103
Telephone: (805) 963-5904
Fax: (805) 965-4898

CIRCLE 120 ON READER SERVICE CARD

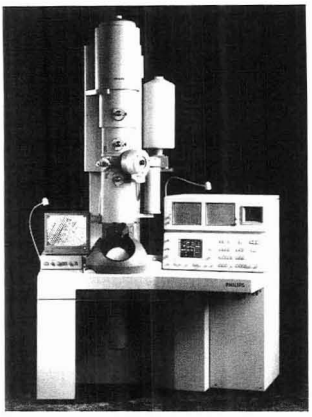

TEM. CM200 FEG series of transmission electron microscopes combines the essential technologies of field emission and a range of objective lenses as well as a fully automated goniometer. Philips Analytical **411**

Viscosity. Visco 3 viscosity measuring system is designed for the determination of viscosity of newtonian fluids. By coupling a timer equipped with optical sensors to time the meniscus between two points, the system can accurately measure viscosities over the range 0.5–100,000 cP. Jupiter Instrument **412**

HPCPC. Series 1000 column module can be used in place of a packed analytical LC column to perform preparative liquid–liquid partition chromatography. Centrifugal force is used to immobilize the stationary phase, allowing separations to be performed at any pH without adsorptive or catalytic effects. Sanki Laboratories **413**

Software

Statistics. SigmaStat incorporates a command that helps users select the most appropriate statistical package for their data, handles missing and unbalanced data, and checks that the user's data fit the assumptions underlying the selected statistical methods. The package calculates a range of descriptive statistics, including mean, standard deviation, standard error of mean, range, maximum, minimum, normality, median, percentiles, sum of squares, skewness, and kurtosis. Jandel Scientific **414**

GC. 700 Series GC software handles from one to six detectors on up to three independent gas chromatographs. Designed for PC compatibles, the software offers fast data file handling, integration, and reporting; hardware control via built-in relay flags; and batch automation capabilities. Axxiom Chromatography **415**

Manufacturers' Literature

Trace analysis. "Sample Preparation for Trace Analysis Methods: An Alternative Approach" details the use of microdiluters to reduce preparation time, cost, and waste by describing two sample preparation approaches prior to LC analysis: a traditional volumetric method and a semiautomated microdiluter approach. Hamilton **416**

Chromatography workstation. Brochure describes AI-450 workstation system capabilities and an up-

dated software package that automates LC, GC, IC, SFC, and CE instruments. Sample scheduling, group reports, calibration capabilities, and automatic data file validation for compliance with GLP standards are described. 8 pp. Dionex **417**

Atomic spectroscopy. Vol. 1, No. 2 of "The Spectroscopist" newsletter includes technical updates on TJA products and articles covering topics such as analysis of lanthanum oxide, determination of refractory elements in ores, and multielement AA spectrometry. 21 pp. Thermo Jarrell Ash **418**

GC. "Sample Handling in GC" describes a range of methods and automatic samplers for extracting analytes directly into the gas phase at ambient or elevated temperatures. The brochure includes information on the HS 40 headspace sampler and the ATD 400 thermal desorber and discusses methods for handling water, soil, and air samples. 6 pp. Perkin Elmer **419**

ESCA. Brochure highlights features of the Escalab 220i, which combines high-resolution XPS imaging, high-performance XPS, and multitechnique capability in a single instrument. Discussion of the microfocused X-ray monochromator and the Eclipse data system is also included. 8 pp. Fisons Instruments **420**

PCR. CE Application Note 2, "Capillary Gel Electrophoresis of PCR Products: Easy Sample Preparation Method," details a dialysis technique designed for use before injection. Salts are removed by membrane dialysis, thereby increasing the signal of amplified products. 4 pp. J&W Scientific **421**

For more information, please circle the appropriate numbers on one of our Readers' Service Cards.

Catalogs

Labware. "Platinum Labware" lists laboratory products such as dishes, crucibles, beakers, tongs, inoculating loops, electrodes, anodes, XRF fusion ware, gauze, and reshapers. Information on the properties of platinum, platinum alloys, and iridium as well as the use and care of platinum labware is included. 23 pp. Engelhard **422**

SRMs. NIST Standard Reference Materials Catalog 1992–93 lists all SRMs and RMs in three major categories: chemical composition, physical properties, and engineering materials. Certified materials include metals, ores, glass, plastics, food, and environmental and clinical standards. 162 pp. NIST **423**

Electrophoresis. Instruments for vertical, horizontal, pulsed field, and 2D electrophoresis and products for blotting, densitometry, dialysis, elution, fluorometry, gel drying, and sequencing are listed in the 1992–1993 catalog. Hoefer **424**

IR and UV–vis. Catalog 592 covers accessories for IR and UV–vis spectrophotometers, including cells for FT-IR and dispersive instruments, polished crystals, specular reflectance units, and gas cells. 30 pp. McCarthy Scientific **425**

LABORATORY SERVICE CENTER

INDEX TO ADVERTISERS IN THIS ISSUE

CIRCLE INQUIRY NO.	ADVERTISERS	PAGE NO.
3	*Alltech Associates, Inc. Chromad	1091A
1	Analytical Products Group, Inc. CJC Advertising	1052A
5	Antek Instruments, Inc.	IFC
12	*Brookhaven Instruments Corporation	1085A
25, 26	*EG&G Princeton Applied Research Kilgore Associates	1075A
28	EM Separations Scientific Marketing Services, Inc.	1056A
46, 47	*Hewlett-Packard Company Brooks Communications, Inc.	OBC
60	*Kratos Analytical	1064A
66, 67	Laboratory Products Association LaMotte Company	1062A
64	Leco Corporation Lecom	1060A
68	Macherey-Nagel GmbH & Co., KG MP Design Werbeagentur	1083A
72	*Matheson Gas Products Kenyon Hoag Associates	1054A
78	*National Institute of Standards & Technology	1085A
85	*Perkin-Elmer Corporation Keiler Advertising	1083A
95	Rheodyne, Inc. Bonfield Associates	1058A
112	Teledyne Hastings-Raydist TRL Productions	1081A
110	Thermo Jarrell Ash Corporation Noon Advertising, Inc.	1051A
116, 117	*Wheaton The Wheaton Agency	1087A
120	*Wyatt Technology Corporation	1089A

Directory section, see page 1092A.
** See ad in ACS LabGuide.*

Advertising Management for the American Chemical Society Publications

CENTCOM, LTD.

President
James A. Byrne
Executive Vice President
Benjamin W. Jones

Robert L. Voepel, *Vice President*
Joseph P. Stenza, *Production Director*

1599 Post Road East
P.O. Box 231
Westport, Connecticut 06881-0231
(Area Code 203) 256-8211
Fax No. 203-256-8175

DIRECTOR, ADVERTISING SALES, LABORATORY PRODUCTS
Bruce E. Poorman

ADVERTISING PRODUCTION MANAGER
Jane F. Gatenby

SALES REPRESENTATIVES

Philadelphia, Pa. . . . CENTCOM, LTD. GSB Building, Suite 405, 1 Belmont Ave., Bala Cynwyd, PA. 19004. Telephone: 215-667-9666, FAX: 215-667-9353

New York/New Jersey . . . Dean A. Baldwin, John F. Raftery, CENTCOM, LTD., Schoolhouse Plaza, 720 King Georges Post Road, Fords, NJ 08863, Telephone: 908-738-8200, FAX: 908-738-6128

Westport, CT./Boston, MA. . . . Edward M. Black, CENTCOM, LTD., 1599 Post Road East, P.O. Box 231, Westport, CT 06881-0231. Telephone: 203-256-8211, FAX: 203-256-8175

Cleveland, OH./Atlanta, GA. . . . Bruce E. Poorman, CENTCOM, LTD., 325 Front St., Suite 2, Berea, OH 44017. Telephone: 216-234-1333, FAX: 216-234-3425

Chicago, IL./Houston, TX. . . . Michael J. Pak, CENTCOM, LTD., 540 Frontage Rd., Northfield, IL. 60093. Telephone: 708-441-6383, FAX: 708-441-6382

West Coast/Denver, CO. . . .Paul M. Butts, Jay S. Francis, CENTCOM, LTD., Suite 808, 2672 Bayshore Parkway, Mountain View, CA 94043. Telephone: 415-969-4604, FAX: 415-969-2104

United Kingdom, Scandinavia and Europe (Except: Germany, Switzerland, Austria) . . . Malcolm Thiele, Technomedia Ltd., Wood Cottage, Shurlock Row, Reading RG10 OQE, Berkshire, England. Telephone: 0734-343302, FAX: 0734-343848

France, Belgium, The Netherlands, Spain, and Italy . . .Ivonne Melcher, Bel Air Building 331A, 58 Rue Pottier, 78150, Le Chesnay, France. Telephone: (1)34-62-00-03, FAX: (1)34-62-95-07

Germany, Switzerland, Austria . . . InterMedia Partners, GmbH, Katernberger Strasse 247, 5600 Wuppertal #1, Germany. Telephone: (0202) 711091, FAX: (0202) 712431

Tokyo, Japan . . . Sumio Oka, International Media Representatives Ltd., 1-11-5-502, Tamazutsumi, Setagaya-ku, Tokyo 158 Japan. Telephone: 502-0656, Telex #22633, FAX: 5706-7349

Asia (Except Japan) . . . Bruce E. Poorman, CENTCOM, LTD., 325 Front St., Suite 2, Berea, OH 44017. Telephone: 216-234-1333, FAX: 216-234-3425

South America . . .Bruce E. Poorman, CENTCOM, LTD., 325 Front St., Suite 2, Berea, OH 44017. Telephone: 216-234-1333, FAX: 216-234-3425

AC RESEARCH

High-Performance Capillary Electrophoresis of SDS–Protein Complexes Using UV-Transparent Polymer Networks

Katalin Ganzler, K. S. Greve, A. S. Cohen, and B. L. Karger*

Barnett Institute, Northeastern University, Boston, Massachusetts 02115

Andras Guttman and N. C. Cooke

Beckman Instruments, Inc., 2500 Harbour Boulevard, Fullerton, California 92634

This paper demonstrates the use of UV-transparent replaceable polymer networks for the separation of SDS–protein complexes on the basis of molecular weight. First, the use of linear (i.e. non-cross-linked) polyacrylamide is shown to provide molecular separation of SDS–protein complexes. A study reveals such columns to yield significantly greater lifetime than cross-linked gels because of the flexibility of the noncovalently attached polymer chains. However, column lifetime was still found to be limited (~20–40 injections), and detection at 214 nm was problematical because of the absorbance of polyacrylamide. UV-transparent polymer networks of dextran and PEG were substituted for polyacrylamide with successful molecular weight sieving of SDS–protein complexes at 214 nm. Due to their low to moderate viscosities, these networks could be routinely replaced leading to the possibility of hundreds of injections with a single column. Migration time reproducibilities of 0.5% *RSD* or less were found with replacement of the network. Using dextran, calibration plots of peak area vs concentration of standard protein were linear over the range of 0.5 μg/mL up to at least 0.25 mg/mL. Furthermore, plasma samples could be directly utilized because of the strong solvating power of SDS. Rapid separation of protein mixtures are demonstrated with these UV-transparent polymer networks.

INTRODUCTION

Electrophoresis is a widely used analytical method for the separation of biopolymers.[1,2] However, conventional slab gel electrophoresis can be time-consuming and difficult to quantitate and automate. Capillary electrophoresis, an instrumental approach, combines the high resolving power of electrophoresis with the possibility of rapid separation, quantitative analysis, and automated instrument control.[3–6]

In the presence of excess sodium dodecyl sulfate (SDS) and a reducing agent, e.g., 2-mercaptoethanol, most proteins are fully denatured and, regardless of their size or shape, hydrophobically bind a constant amount of SDS per unit weight (1.4 g of SDS/g of protein).[7] The adsorbed SDS masks the intrinsic charge of the protein, resulting in a detergent–protein complex of approximately constant charge per unit mass and in a similar denatured shape for each complex.[8] As a consequence, the free solution mobilities of the SDS–protein complexes are practically identical. However, in a sieving medium the electrophoretic mobility of each complex is found to be proportional to the log effective molecular radius and thus, to the log molecular weight of the polypeptide chain.[8,9] Although there are exceptions to this rule (e.g., histones, glycoproteins), the relationship is generally useful for a large number of proteins,[7] and the method of SDS–polyacrylamide gel electrophoresis (SDS–PAGE) has been widely adopted for purity analysis and molecular weight estimation. SDS–PAGE is also utilized as an orthogonal technique to isoelectric focusing in the powerful separation method of 2D gel electrophoresis.[10]

Previously we have shown SDS–PAGE separations of proteins in cross-linked polyacrylamide gel-filled capillaries.[11] Hjerten also briefly illustrated SDS–PAGE,[12] and recently, using ethylene glycol as a stabilizer, SDS–PAGE in cross-linked gels in capillary electrophoresis has been demonstrated.[13] Separately, we showed that molecular weight separations could be obtained using non-cross-linked gels (linear poly-

* Author to whom reprint requests should be sent.

(1) Chrambach, A. *The Practice of Quantitative Gel Electrophoresis*; VCH: Deerfield Beach, FL, 1985; pp 64–66.

(2) Andrews, A. T. *Electrophoresis - Theory, Techniques and Biochemical and Clinical Application*, 2nd ed.; Clarendon Press: Oxford, NY, 1986.

(3) Jorgenson, J. W.; Lukacs, K. D. *Science* **1983**, *222* 266–272.

(4) Karger, B. L.; Cohen, A. S.; Guttman, A. *J. Chromatogr.* **1989**, *492*, 585–613.

(5) Gordon, M. J.; Huang, X.; Pentoney, S. L.; Zare, R. N. *Science* **1988**, 242, 224–228.

(6) Novotny, M. V.; Cobb, K. A.; Liu, J. *Electrophoresis* **1990**, *11*, 735–749.

(7) Weber, K.; Osborn, M. *J. Biol. Chem.* **1969**, *244*, 4406–4412.

(8) Reynolds, J. A.; Tanford, C. *Proc. Nat. Acad. Sci. U.S.A.* **1970**, *66*, 1002–1007.

(9) Shapiro, A. L.; Vinuela, E.; Maizel, J. V. *Biochem. Biophys. Res. Commun.* **1967**, *28*, 815–820.

(10) *Two Dimensional Gel Electrophoresis of Proteins: Methods and Applications*; Celis, J. E., Bravo, R., Eds.; Academic Press: New York, 1984.

(11) Cohen, A. S.; Karger, B. L. *J. Chromatogr.* **1987**, *397*, 409–417.

(12) Hjerten, S. *Electrophoresis* '83; Hirai, H., Ed.; Walter de Gruyter & Co.: New York, 1984; pp 71–79.

(13) Tsuji, K. *J. Chromatogr.* **1991**, *550*, 823–830.

0003-2700/92/0364-2665$03.00/0

acrylamide) for SDS–protein complexes,[14] in agreement with earlier results in the classical slab techniques.[15,16] Others have also briefly demonstrated SDS–protein complex separations with linear polyacrylamide.[17,18]

The first part of this paper further explores the use of linear polyacrylamide for the separation of SDS–protein complexes. It will be shown that column stability is substantially better with this matrix than with cross-linked gels. However, even with linear polyacrylamide, column lifetime can be limited, particularly at the high fields employed. In addition, the absorbance of polyacrylamide at 214 nm is significant, affecting the linear dynamic range and detection limit. Higher absorbance wavelengths can be utilized, but at the expense of detection limits.

To overcome these limitations, this paper then describes the separation of SDS–protein complexes using a UV-transparent polymer matrix (dextran or poly(ethylene glycol)) (i.e. low UV absorption at 214 nm) of low to moderate viscosity. As a term for such sieving matrices, as well as polyacrylamide, we will follow that suggested by Bode: "polymer network".[19] Excellent linear relationships of peak area versus injected amount of solute over a broad concentration range will be shown. Furthermore, as with the use of polymer networks for DNA separations or for protein separations under nondenaturing conditions,[20–24] the relatively low viscosity of the buffer media results in a significant extension of column lifetime via simple replacement of the network when necessary. Reproducibilities in migration times of generally less than 0.5% RSD will be shown. Finally, examples of separations of complex biological samples are presented to demonstrate the general applicability of the method.

EXPERIMENTAL SECTION

Instrumentation. High-performance capillary electrophoresis of SDS–protein complexes was performed in fused-silica capillaries (Polymicro Technologies, Phoenix, AZ) of 75- or 100-μm i.d. and 375-μm o.d., with different column lengths. In the case of the PEG-filled columns, 100-μm-i.d. capillaries have been used. A detection window of ca. 2-mm length was prepared, as described previously.[25] The samples were separated on both a manual and an automated instrument. The manual HPCE apparatus consisted of a 30-kV high-voltage direct current power supply (Model PS/EG 30, Glassman, Whitehouse Station, NJ) and a UV detector (Model Spectra Focus, Spectra Physics, Inc., San Jose, CA) used at 214 and 280 nm, respectively. The sample loading was controlled by a timer (Model PU-15 SEC, Industrial Timer Co., Waterbury, CT). Column cooling was achieved using a laboratory fan. The electropherograms were acquired and stored on an IBM PC/XT (Boca Raton, FL) via an analog to digital interface (Model 970, P. E. Nelson, Cupertino, CA). The automated system was a Beckman P/ACE, version 2100 (Beckman Instruments, Fullerton, CA), with System Gold version 6.01 to control the instrument, again at 214 and 280 nm. The conductivity of the buffers was measured using a Model 1481-40 conductivity meter (Cole-Palmer Instrument Co., Chicago, IL). The UV spectra of the buffers and the polymer networks were determined with a Beckman DU-60 spectrophotometer in the scan mode from 200 to 300 nm, using a quartz cuvette with a light path of 0.5 cm.

Materials. Protein samples were purchased from Sigma (St. Louis, MO) and Pharmacia (Piscataway, NJ), unless otherwise noted. Sodium dodecyl sulfate (SDS), *N,N,N′,N′*-tetramethylethylenediamine (TEMED), ammonium persulfate (APS), 2-mercaptoethanol, and prestained molecular weight standards were obtained from Bio-Rad (Richmond, CA). Cerium(IV) sulfate tetrahydrate was purchased form EM Science (Gibbstown, NJ). Ultra pure electrophoresis grade TRIS-base, acrylamide, *N,N′*-methylenebisacrylamide (Bis), histidine (HIS), cacodylic acid (CACO), 2-amino-2-methyl-1-3-propanediol (AMPD), and 2-(cyclohexylamino)ethanesulfonic acid (CHES) were supplied by Schwarz/Mann Biotech (Cambridge, MA). All dextran polymer samples were obtained from Sigma except as noted, and poly(ethylene glycol) polymers were from Aldrich (Milwaukee, WI). Caution should be exercised in handling acrylamide and CACO, as they can be toxic.

All buffer and acrylamide solutions were filtered through an 0.2-μm pore-size filter (Schleicher & Schuell, Keene, NH) and vacuum degassed before use. In the case of acrylamide polymerization, the vacuum degassing was followed by a helium-purge step in order to minimize the amount of dissolved oxygen, a possible terminator of the polymerization reaction.[1]

Columns. The capillaries were pretreated using [(methacryloxy)propyl]trimethoxysilane (Petrarch Systems, Bristol, PA) and acrylamide solutions (6% T, 0% C), as described previously.[26] In the case of dextran or PEG polymer network columns, a dextran layer was added to the linear acrylamide coating using Ce^{IV} ions as a free radical source under acidic conditions.[27]

Polyacrylamide. As described previously, the polymerization of the acrylamide solution was accomplished in the capillaries after initiation with APS and TEMED.[11] Gel columns of 3–5% T, 0.5–2.4% C and 8–20% T, 0% C were used during the study. The ends of the capillary were placed in 3-mL buffer reservoirs containing platinum wire electrodes. In the case of non-cross-linked polyacrylamide gels, the reservoirs were filled with electrodialyzed linear polyacrylamide, 6% T.

UV-Transparent Polymer Networks. Stock solutions of dextran (MW 10 000–2 000 000) were made in the specific separating buffer containing 0.05 M AMPD–CACO and 0.1% SDS (wt % = wt of polymer/volume of buffer × 100). For PEG (MW 100 000), the buffer was 0.10 M TRIS–CHES and 0.1% SDS. The pH of both buffers was adjusted with CACO or CHES to a value of 8.6–8.8. The polymer network was carefully degassed prior to filling the capillaries. It was easy to remove and refill the capillary by means of a syringe or by pressure (P/ACE).

Samples. The SDS–protein samples were prepared according to the standard method of Weber and Osborn[7] using 10 min of boiling. The sample buffer contained 0.06 M TRIS–HCl, pH 6.6 with 1% SDS and 5% 2-mercaptoethanol. The SDS:protein ratio was in general 1.6:1.

RESULTS AND DISCUSSION

Linear Polyacrylamide. As noted, linear polyacrylamide has been previously used for the SDS–PAGE separation of proteins in slab gels.[15,16] This matrix can also be employed in HPCE. Based on the buffer systems and polymerization procedures selected, monomer concentrations between 8 and 16% proved to be advantageous for proteins in the molecular weight range of 14 000–96 000. As an example of the separations possible, Figure 1 shows the rapid SDS–PAGE resolution of five standard proteins in a 12% T linear polyacrylamide polymer network with a field of 560 V/cm. Figure 1B illustrates a separation of growth hormone and the

(14) Ganzler, K.; Cohen, A. S.; Karger, B. L. Poster No. PT-31, HPCE '91, San Diego, CA.
(15) Bode, H. J. *Anal. Biochem.* **1977**, *83*, 204–210.
(16) Tietz, D.; Gottlieb, M. H.; Fawcett, J. S.; Chrambach, A. *Electrophoresis* **1986**, *7*, 217–220.
(17) Manabe, T.; Terabe, S. Poster No. PT-23, HPCE '91, San Diego, CA.
(18) Widhalm, A.; Schwer, C.; Blass, D.; Kenndler, E. *J. Chromatogr.* **1991**, *546*, 446–451.
(19) Bode, H. J. *Electrophoresis* '79; Walter de Gruyter & Co.: New York, 1980; pp 39–52.
(20) Heiger, D. N.; Cohen, A. S.; Karger, B. L. *J. Chromatogr.* **1990**, *516*, 33–48.
(21) Hjerten, S.; Valtcheva, L.; Elenbring, K.; Eaker, D. *J. Liq. Chromatogr.* **1989**, *12*, 2471–2499.
(22) Zhu, M.; Hanson, D. L.; Bird, S.; Garrison, F. *J. Chromatogr.* **1989**, *480*, 311–319.
(23) Schwartz, H. E.; Ulfelder, K. J.; Sunzeri, F. J.; Busch, M. P.; Brownlee, R. G. *J. Chromatogr.* **1991**, *559*, 267–283.
(24) Bocek, P.; Chrambach, A. *Electrophoresis* **1991**, *12*, 1059–1061.
(25) Guttman, A.; Cohen, A. S.; Heiger, D. H.; Karger, B. L. *J. Chromatogr.* **1990**, *62*, 137–141.
(26) Hjerten, S. *J. Chromatogr.* **1985**, *347*, 191–198.
(27) McDowall, D. J.; Gupta, B. S.; Stannett, V. T. Progr. *Polym. Sci.* **1984**, *10*, 1–15.

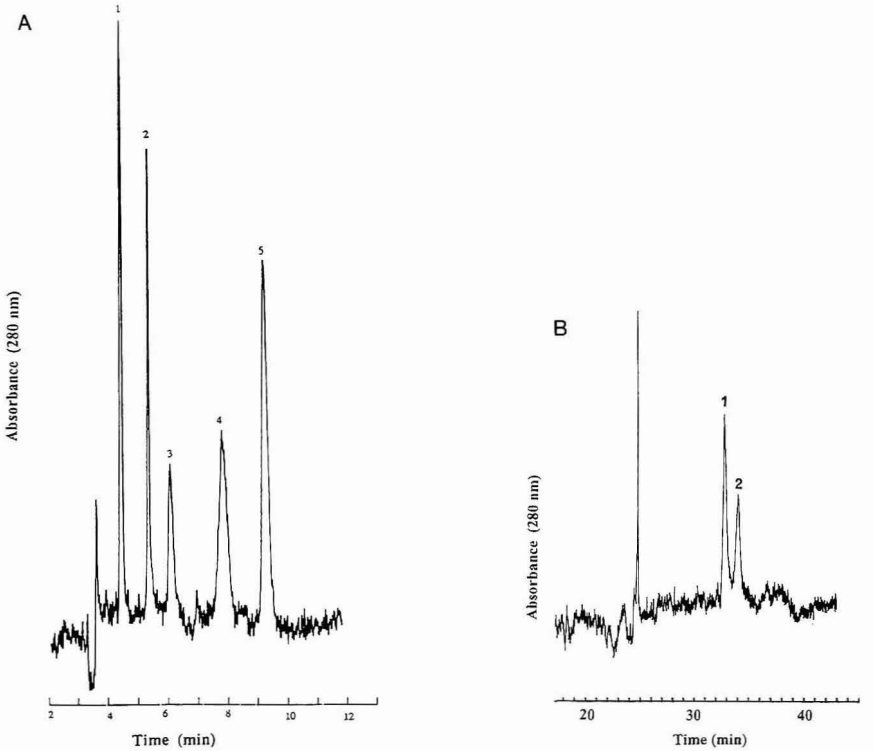

Figure 1. (A) Separation of SDS–protein complexes in linear polyacrylamide networks. Conditions: buffer, 0.12 M TRIS–0.12 M histidine, pH 8.8, 0.1% SDS; gel, 12% T, 0% C; effective length, 15 cm; applied electric field, 560 V/cm; current, 44 μA; injection, 6 s at 400 V/cm; detection, 280 nm, 0.005 AUFS manual system; solutes, (1) lysozyme; (2) carbonic anhydrase; (3) ovalbumin; (4) bovine serum albumin; (5) phosphorylase B. (B) Separation of recombinant human growth hormone (rhGH) from its dimer. (rhGH was the kind gift of Genentech.) Conditions: buffer, 0.12 M TRIS–0.12 M histidine, pH 8.8, 0.1% SDS; gel, 8% T, 0% C; effective length, 12 cm; applied electric field, 350 V/cm; current, 30 μA; injection, 10 s at 350 V/cm; detection, 280 nm, 0.005 AUFS manual system; solutes, (1) recombinant human growth hormone; (2) dimer.

covalently attached dimer (exposure in solution for 2 days) on an 8% T, 0% gel, with an applied field of 350 V/cm. Similar separations, albeit at lower fields, were obtained for cross-linked gels of 1–2.4% C.

Straight-line plots of log mobility vs % T (monomer concentration) for individual SDS–proteins (Ferguson plots)[1,2] with linear polyacrylamide networks were found to be similar to those on the cross-linked gels. Furthermore, the slopes of the Ferguson plots (K_R) were found to be proportional to the molecular weight of the proteins (r^2 = 0.990). Thus, the separations in Figure 1 are based on molecular weight of the proteins under the given conditions.

As noted previously, an important consideration is the number of injections possible with the polyacrylamide networks, since the matrices cannot be easily replaced. As a measure of relative stability, we have utilized the collapse time of the network. The collapse time is a measure of the time at a given applied electric field until the appearance of bubble formation or gel collapse, as measured by a loss in current. The collapse time is thus indicative of the resistance of the gel to the stress occurring at the given field. This value can provide an estimate of the relative running time of the polymer-filled capillary. The collapse time is particularly relevant when SDS is in the buffer since hydrophobic adsorption of SDS to the polymer chains may be possible. Such a partially charged polymer, if SDS adsorption were to occur, would be expected to stretch under the applied field.

The collapse time of the polymer network columns proved to be strongly dependent on polymer composition and on electric field strength, as shown in Figure 2A. The lower the amount of cross-linker, the more stable was the column. For example, the collapse time of a 5% T, 1% C polymer network or gel column proved to be roughly double that of a 5% T, 2.4% C gel under electric fields of 150–300 V/cm. Upon addition of 2–propanol (1% v/v) to the buffer, the collapse time of the cross-linked acrylamide-filled capillary could be extended by a factor of 2. Figure 2B illustrates a separation of prestained SDS–protein complexes from molecular weight 43 000 to 220 000 using a 5% T, 1% C column to which 1% 2-propanol was added to the buffer for increased stability. The peak spliting of myosin may be a consequence of differences in the extent of staining. At the applied field of 180 V/cm, ~10–15 injections were possible before collapse. If the polymer network were allowed to relax between runs for ~15 min, the number of injections could be extended to 20 or more before collapse. It is also to be noted that several other additives could be used to improve the lifetime of the capillaries, e.g. urea[11,28] and ethylene glycol.[13,15] Nevertheless, the number of injections with cross-linked polyacrylamide was limited.

In order to increase the lifetime of the columns, we removed the cross-linker (B's) from the polymer matrix. As can be

(28) Swank, P.; Munkres, K. D. *Anal. Biochem.* **1971**, *39*, 462–477.

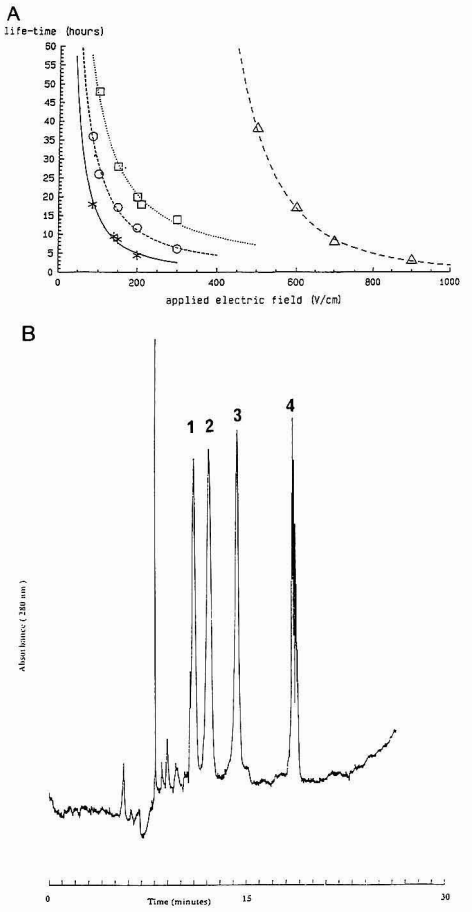

Figure 2. (A) Effect of the electric field on the collapse time of acrylamide network capillaries. Conditions: buffer, 0.12 M TRIS–0.12 M histidine, pH 8.8, 0.1% SDS; gel composition, (*) 5% T, 2.4% C; (O) 5% T, 1% C; (□) 5% T, 1% C, plus 1% 2-propanol; (Δ) 13% T, 0% C. The electric field was applied continuously on the manual system. See text for definition of collapse time. (B) Separation of high molecular weight SDS–protein standards in cross-linked polyacrylamide gel. Conditions: buffer, 0.12 M TRIS–0.12 M histidine, pH 8.8, 0.1% SDS, 1% 2-propanol; polymer, 5% T, 1% C; effective length, 20 cm; applied electric field, 180 V/cm; current, 16 μA; injection, 9 s at 150 V/cm; detection, 280 nm, 0.01 AUFS manual system; solutes, prestained high molecular weight proteins; (1) ovalbumin, (2) bovine serum albumin, (3) β-galactosidase, (4) myosin.

seen in Figure 2A, a considerable increase in the collapse time was observed. This increase could be explained by the fact that the viscoelastic properties and thus the stress resistance of the polymer network depended on the polymer network density and on the mechanism of the network formation.[29] In cross-linked gels, the network structure is formed by covalent bonds between the polymer chains. On the other hand, for linear polyacrylamide, the network

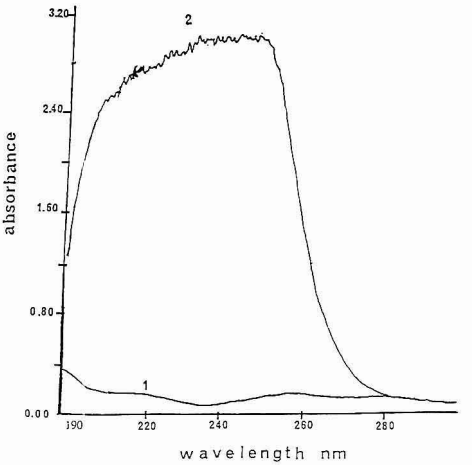

Figure 3. Comparison of the UV spectra of (1) polyacrylamide (3% T, 0% C electrodialyzed) and (2) dextran (20% w/v, MW 2 000 000). Conditions: solvent, distilled water; scan, from 190 to 300 nm; scan speed, 500 nm/min; light path, 0.5 cm.

structure is formed by physical interactions, e.g. by van der Waals forces and by hydrogen bonds.[29,30] These physical interactions are in dynamic equilibrium; at any time, some will open, while others will close, providing a more flexible structure than crosslinked gels.

As further seen in Figure 2A at a given polymer concentration, the higher the applied electric field (and thus stress), the lower was the collapse time of the polymer network. This observation was similar for both the cross-linked and for the linear polymers. In the case of cross-linked gels, however, the collapse of the gel structure occurred at a much lower electric field.

The above results demonstrate the improvement in separation of SDS–protein complexes using linear polyacrylamide. However, while successful in the separation, the matrix still had limitations in use, such as high detection limits and the still relatively limited column lifetime. Because of the necessary high applied fields, the typical number of injections for linear polyacrylamide was ~20–40. Therefore, we sought an alternative approach using UV transparent polymers (i.e. low UV absorption at 214 nm). In the next section we show two possibilities to overcome the abovementioned limits using a hydrophilic, branched polymer (dextran) and a linear polymer (poly(ethylene glycol)). As noted in the introduction, important advantages of this approach are the lower detection limits and the ability to replace the matrix when desired.

Dextran. Figure 3 shows the comparison of UV spectra of a polymer network of dextran of MW 2×10^6 (20% w/v in water) and linear polyacrylamide (3% T, 0% C in water). The spectra indicate a significant difference at 214 nm for the two polymers, with polyacrylamide having a much greater absorbance. Note that the absorbance for this latter polymer would be even greater as the percent T is increased. Therefore, the ability to utilize polyacrylamide at 214 nm is severely limited. However, it is well-known that extinction coefficients of proteins at 214 nm are 20–50 times larger than at 280 nm.[31]

(29) Rogovina, L. Z. Comparison of the Formation and Properties of Physical and Chemical Networks Prepared in Swollen State. In *Physical Networks*; Buchard, W., Ross-Murphy, S. B., Eds.; Elsevier Applied Science: Amsterdam, 1988.

(30) Bektunov, E. A.; Bakanowa, Z. K. H. *Synthetic Watersoluble Polymers in Solution*; Huthig, Wepf, Eds.; Verlag: Basel, 1981.

(31) Deutscher, M. P. *Guide to Protein Purification*; *Methods* in Enzymology, Vol. 182; Academic Press: San Diego, CA, 1990.

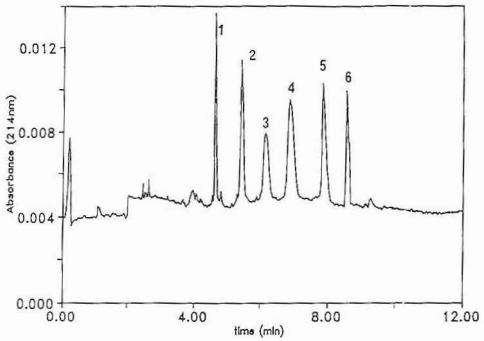

Figure 4. Separation of standard SDS–protein complexes in dextran polymer network. Conditions: buffer, 0.06 M AMPD–CACO pH 8.8, 0.1% SDS; polymer, 10% w/v dextran (MW 2 000 000); effective length, 18 cm; applied electric field, 400 V/cm; current, 30 μA; injection, 2 s at 300 V/cm; detection, 214 nm, 0.01 AUFS, automated system; peaks, (1) myoglobin; (2) carbonic anhydrase; (3) ovalbumin; (4) bovine serum albumin; (5) β-galactosidase; (6) myosin.

Table I. Relative Mobility of SDS–Protein Complexes to SDS–Phosphorylase B as a Function of the MW of Dextran[a]

	relative mobility dextran MW		
protein	72 000	500 000	2 000 000
lysozyme	3.5	6.4	6.7
carbonic anhydrase	2.2	4.3	4.7
ovalbumin	1.5	2.6	2.8
bovine serum albumin	0.6	1.2	1.4

[a] Conditions: 10% dextran; 0.06 M AMPD–CACO; pH 8.8; 0.1% SDS; 300 V/cm; 20 μA; effective length = 20 cm.

Furthermore, at 214 nm there is less variability in the absorbance of proteins than at 280 nm. The disadvantage of the lower wavelength region is that many chromophores absorb, and thus pure buffers must be carefully selected. Besides dextran, other polymer networks that can be utilized at 214 nm include PEG (see later) and agarose.

The selection of buffers for SDS separation includes consideration of UV absorbance at 214 nm and conductivity of the solution in order to minimize Joule heating. In terms of both conductivity and UV absorbance AMPD–CACO and TRIS–CHES buffers with 0.1% SDS were found to be useful. For the sample buffer, TRIS–HCl at pH 6.2 with 1% SDS was used for sample focusing via the pH change upon injection, resulting in a mobility change of buffer components.[32]

Figure 4 shows the separation of standard SDS–proteins in a 10% w/v dextran polymer network (MW 2 000 000). As can be seen, both the selectivity and the efficiency are comparable to that of the linear polyacrylamide. Straight-line relationships between the mobility and the logarithm of the protein molecular weight were observed with an r^2 value of 0.992. Ferguson plots of the separations were also similar to those obtained in linear acrylamide. The slopes of the plots, K_R, were again proportional to the molecular weight of the proteins ($r^2 = 0.985$), indicating that the separation was due to molecular weight differences.

The effect of the molecular weight of the dextran on the molecular weight selectivity of the SDS–protein complexes was also studied. Table I presents the influence of the molecular weight of dextran on the size selectivity of SDS–protein complexes (as measured by the relative mobility with phosporylase B as the internal standard). It can be seen that the higher the molecular weight of the dextran, the higher the selectivity obtainable. In this work, MW 2 000 000 was thus selected for study.

(32) Laemmli, U. K. *Nature* **1970**, *227*, 680.

Table II. Reproducibility of Migration Times Using 10% Dextran (MW 2 × 10⁶) Network[a]

protein[b]	RSD (%)	n
(A) Replacing the Matrix after Each Run		
MYO	0.12	12
CA	0.13	12
OVA	0.30	12
BSA	0.38	12
PHB	0.22	12
(B) Consecutive Injections		
MYO	2.3	10
CA	2.2	10
OVA	2.4	10
BSA	2.6	10
PHB	2.7	10

source	myoglobin	phosphorylase B
(C) Different Batches of Dextran, Average Migration Time (n = 15)		
Sigma 1	8.7 ± 0.37	13.9 ± 0.37
Sigma 2	8.4 ± 0.12	13.4 ± 0.12
Sigma 3	8.1 ± 0.24	12.7 ± 0.24
Pharmacia	8.3 ± 0.20	13.4 ± 0.20

[a] Conditions: Buffer 0.06 M AMPD–CACO pH 8.8; 0.1% SDS; applied electric field 300 V/cm; 20 μA; effective length = 15 cm. [b] MYO = myoglobin, CA = carbonic anhydrase, OVA = ovalbumin, BSA = bovine serum albumin, PHB = phosphorylase B.

The reproducibility of the migration times using the 10% w/v dextran polymer network (MW 2 000 000) is presented in Table II. Replacement of the polymer matrix after each run resulted in a significantly lower RSD of the migration times than consecutive injection runs (~0.3% vs ~2.5%). The batch-to-batch reproducibility of different dextran samples purchased from various suppliers was compared as well. The average RSD values of migration times were similar in each batch. However, the batch-to-batch variation of migration times was found to be approximately 3–5%, probably due to the different polymer molecular weight distributions of the batches. The linear calibration of mobility vs log MW of the proteins nevertheless remained constant. Since one would necessarily calibrate a particular system, the variation from batch to batch is quite acceptable.

Using dextran (or PEG) as a separation matrix, the lifetime of the column could be significantly extended since the polymer is readily replaceable in the column by applying pressure. Figure 5 shows one example of this characteristic in which standard SDS–protein complexes are separated, with the dextran network replaced after each run. It can be seen that even after 300 runs the column is still quite useable. In this example the polymer network was directly replaced without a wash step. Depending on the sample injected, wash steps, of course, can be utilized for improved run-to-run reproducibility.

Because of the strong solubilizing power of SDS, dirty or complex samples could be directly injected into the column. Figure 6 demonstrates this characteristic in the injection of rat plasma treated in the standard denaturing SDS condition (see the Experimental Section). It can be seen that the same peak pattern is obtained for the first and twenty-third injection, with the dexran polymer network replaced after each run. A multipeak pattern is observed because of the complexity of the sample and the detection wavelength at 214 nm.

An advantage of the capillary electrophoretic approach relative to the slab gel method is the potential for quantitation

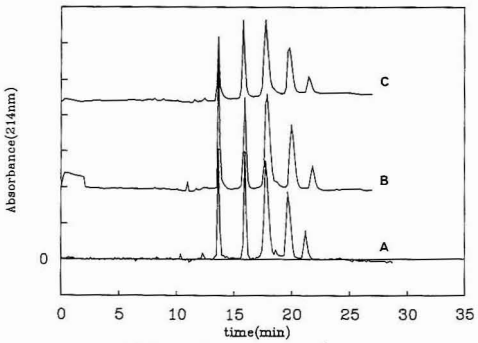

Figure 5. Column lifetime studies using the replaceable dextran polymer network. Conditions: see Figure 4 (except effective length, 30 cm; applied electric field, 300 V/cm, 20 μA; electropherograms, (A) 100th injection; (B) 200th injection; (C) 300th injection). In B and C the baseline has been shifted for purposes of clarity.

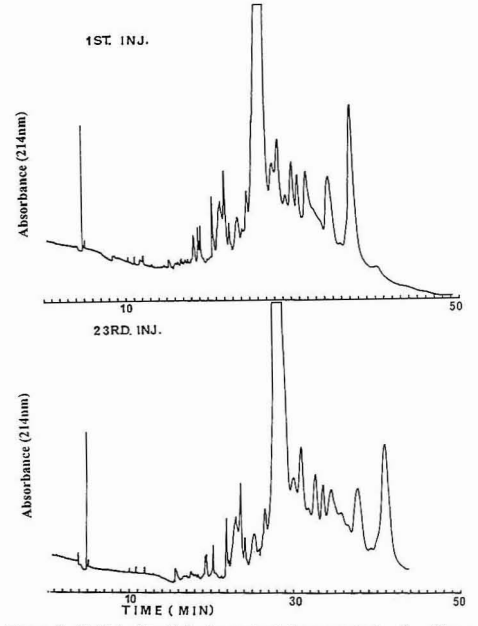

Figure 6. Multiple direct injections of rat plasma sample. Conditions: see Figure 5. (A) 1st injection; (B) 23rd injection.

of the SDS–protein complexes. As we have noted, detection at 214 nm is advantageous, relative to high-wavelength absorbance. This is shown in Figure 7 for detection of standard proteins at 280 and 214 nm, respectively. The separation and injection conditions were identical except for the detection wavelength. It can be observed that at 280 nm the proteins are barely visible, whereas at 214 nm, acceptable signals are obtained.

A calibration curve was constructed on the manual instrument for SDS–myoglobin on a 10% w/v dextran polymer network column. The concentration of the protein in the sample buffer was varied, while electrokinetic injection was kept constant at 300 V/cm for 2 s. The plot of peak area vs sample concentration was linear (r^2 = 0.999) up to at least

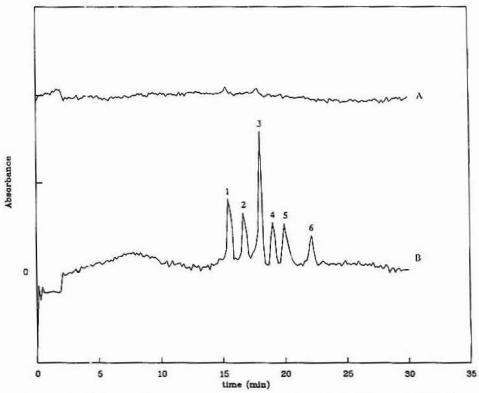

Figure 7. Comparison of protein detection at 280 and 214 nm. Conditions: buffer, 0.1 M TRIS–CHES pH 8.2, 0.1% SDS; polymer, 10% w/v dextran (MW 2 000 000); effective length, 30 cm; applied electric field, 300 V/cm; current, 15 μA; injection, 3 s at 300 V/cm; detection, (A) 280 nm, 0.005 AUFS (baseline shifted for clarity), (B) 214 nm, 0.01 AUFS, automated system; peaks, (1) α-lactalbumin; (2) trypsinogen; (3) carbonic anhydrase; (4) glyceraldehyde-3-phosphate dehydrogenase; (5) ovalbumin; (6) bovine serum albumin. Electropherogram was redrawn using Lotus 1,2,3.

0.25 mg/mL and intersecting the origin. A sample concentration of 0.5 μg/mL led to a S/N ratio of ~2 under the given injection conditions. Linear calibration using pressure injection on the automated system could also be utilized. Using the 10% w/v dextran polymer network, a calibration curve for myoglobin in dog plasma was next constructed. Treating the plasma under standard SDS denaturing conditions, a calibration plot of peak area vs sample concentration was again linear (r^2 = 0.981) up to at least 0.25 mg/mL and intersecting the origin. The minimum detectable concentration (S/N = 2) was, however, 15 μg/mL. The 30-fold worse detection limits relative to the standard solution was undoubtedly a consequence of the background signal of the plasma itself.

Finally, Figure 8 shows the separation of the light and heavy chains of human IgG using the manual system. The molecular weights determined from the calibration plot of mobility vs log MW were 23 kDa for the light and 52 kDa for the heavy chain. These molecular weights are in the expected ranges.

PEG. As originally employed by Bode,[19] poly(ethylene glycol) (PEG) can also be used as a polymer network for sieving with good UV transparency. Whereas dextran is a branched polymer, PEG is linear, and it has been found that much lower polymer concentrations should be employed, due to solubility and viscosity considerations. Using the previously described dextran coating, a 3% PEG (MW 100 000) polymer network was able to achieve a rapid separation of standard SDS–protein complexes (using pressure injection) from 14 to 94 kD with detection at 214 nm (Figure 9). Orange green dye, a small molecule, was added as an internal standard.

As in the case of dextran, plots of log mobility vs % w/v PEG (Ferguson plots) were linear with an intercept at approximately the free solution mobility of the SDS–protein complex. The slopes of the plots K_R vs protein molecular weight were again linear (r^2 = 0.986), indicating a molecular weight based separation mechanism.

Reproducibility of migration times for SDS–protein standards was found comparable to that of dextran in Table II. An experiment was conducted of the proteins in Figure 9 in which 100 injections were made with replacement of the PEG polymer network after each run. To obtain migration time

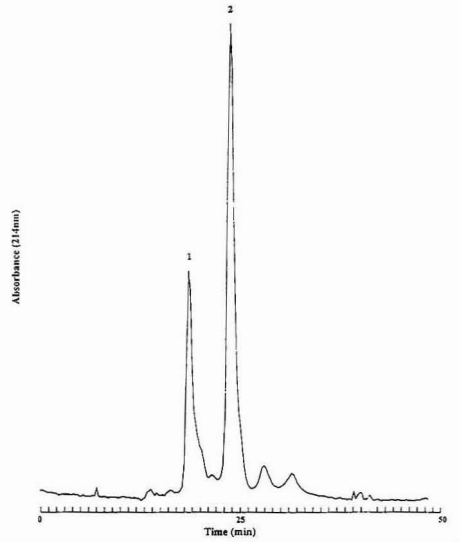

Figure 8. SDS–protein complex separation of light (1) and heavy (2) chains of human IgG. Manual system. Other conditions: see Figure 6.

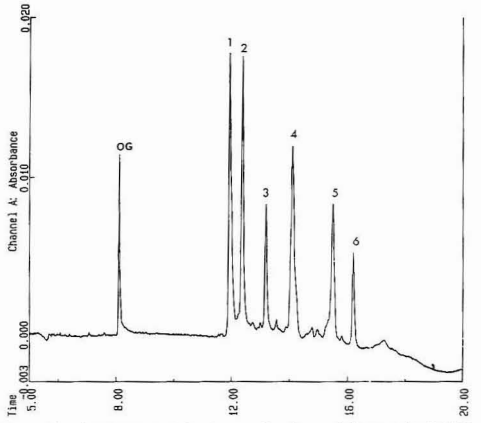

Figure 9. Separation of the low molecular weight standard SDS–protein complexes using a PEG polymer network. Conditions: buffer, 0.1 M TRIS–CHES, 0.1% SDS, pH 8.8; polymer, 3% w/v PEG 100 000; effective length, 40 cm; 100-μm i.d.; applied electric field, 300 V/cm; injection, pressure mode for 20 s; detection, 214 nm, 0.01 AUFS, automated system; peaks, (OG) internal standard-Orange G; (1) α-lactalbumin; (2) soybean trypsin inhibitor; (3) carbonic anhydrase; (4) ovalbumin; (5) bovine serum albumin; (6) phosphorylase B.

reproducibility, each tenth injection was included, with the result of 0.4–0.5% RSD for the six proteins. In addition, at least 300 injections with replacement of the network after each run were possible with little degradation.

As a further example of the applicability of UV-transparent polymer networks, Figure 10A shows the separation of an *E. coli* extract from a fermentation broth in which the sample has been treated in the standard SDS-denaturing procedure. As with plasma, multiple injections could be made without loss in performance. Figure 10B shows the separation of two SDS-reduced F_{ab} fragments of a monoclonal antibody.

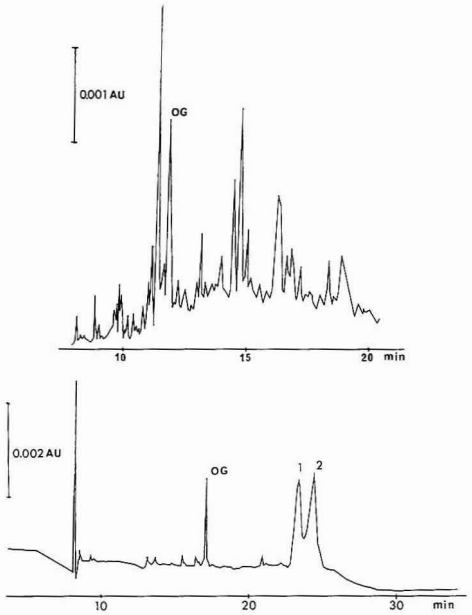

Figure 10. Electropherogram of an SDS–*E. coli* crude extract using capillary PEG polymer network. Conditions: see Figure 9. OG: internal standard-Orange G. Electropherogram was redrawn using Lotus 1,2,3. (B) Separation of reduced F_{ab} fragments of a monoclonal antibody. Conditions: see Figure 9, except applied electric field, 200 V/cm; peaks, (OG) internal standard-Orange G.

CONCLUSIONS

SDS–protein complexes have been resolved on the basis of molecular weight using UV transparent polymer networks. In contrast to polyacrylamide, detection at 214 m is readily achieved using either dextran or PEG. The columns can be utilized for at least 300 runs without loss in performance, due to the ability to replace the network by pressure. Indeed, even replacing after each run, the migration time reproducibility is in general less than 0.5% RSD. The method provides a rapid estimation of protein molecular weight, and quantitative analysis using either electrokinetic or pressure injection is possible. Finally, complex sample matrices can be injected into the column without significant column degradation.

ACKNOWLEDGMENT

The authors gratefully acknowledge Beckman Instruments and the NIH under GM15847 for support of this work. The authors further thank Ken Olson, Genentech, Inc., for the recombinant growth hormone sample and William Henzel, also of Genentech, for the F_{ab} fragment sample. Contribution No. 531 from the Barnett Institute.

RECEIVED for review May 11, 1992. Accepted July 30, 1992.

Registry No. PEG, 25322-68-3; dextran, 9004-54-0; polyacrylamide, 9003-05-8.

Solid-Phase Method for the Purification of DNA Sequencing Reactions

Xinchun Tong and Lloyd M. Smith*

Department of Chemistry, University of Wisconsin, Madison, Wisconsin 53706

A solid-phase method for the purification of the single-stranded DNA molecules produced in enzymatic sequencing reactions has been developed. A primer oligonucleotide is synthesized containing a biotin moiety at an internal position. This primer is utilized in enzymatic extension reactions, and the resulting products are bound to streptavidin-coated magnetic beads. Contaminating species such as protein, salts, template DNA, and unincorporated or degraded deoxy and dideoxy nucleotide triphosphates may be removed by washing the beads after immobilizing them in the sample tube with a fixed magnet. The resulting pure single-stranded DNA fragments are removed from the solid support by heating in 10 mM EDTA, 95% formamide, loading dye at 90 °C, and may then be directly loaded onto a polyacrylamide gel for sequence analysis. This method was used to investigate the effect of various contaminants upon DNA sequence data.

INTRODUCTION

DNA sequence analysis continues to play a central role in modern molecular biology. Automated methods for sequencing promise eventually to remove the burden of routine DNA sequencing from the research laboratory, as well as permitting the successful performance of very large scale projects such as the analysis of the Human Genome.[1,2]

Although some apsects of sequencing have been effectively automated, others remain to be addressed. For example, although the separation and detection of DNA fragments in polyacrylamide gels has been automated,[3,4] most of the steps preceding this separation, such as the generation of subclones, growth and purification of template DNAs, and so on, are still largely performed manually. Much of the reason for this lies in the nature of the procedures involved. Traditional methods for sequencing are not readily amenable to automation, involving procedures such as the growth and plating of bacterial cultures, biochemical extractions, and centrifugations. In general, these processes need to be redesigned in ways that are more compatible with automation.

One generic approach to many of these problems is offered by solid-phase chemistry. Solid-phase methods have a long history in molecular biology, in for example, the Southern and Northern hybridization procedures.[5] More recently, solid-phase chemistries for DNA and peptide synthesis, and even total gene assembly, have been developed, with revolutionary consequences for the field.[6,7] These procedures are intrinsically amenable to automation and eliminate the problems with purification of intermediates that plague conventional approaches. Uhlen and co-workers have pioneered the use of such methods for problems in DNA sequence analysis, exploiting the high affinity and stability of biotin–avidin chemistry to permit the immobilization and sequence analysis of double-stranded PCR products.[8-10]

In this paper we describe a solid-phase DNA sequencing method for the purification of the single-stranded DNA molecules produced in enzymatic sequencing reactions. A primer oligonucleotide labeled at the 5′ terminus with ^{32}P and containing a biotin group at an internal position is utilized in the enzymatic extension reactions, and the resulting products are bound to streptavidin-coated magnetic beads. The template strand and other reaction contaminants are removed by denaturation and washing of the beads, and the remaining pure single-stranded fragments are eluted by heating in a EDTA/formamide mixture. In contrast to previously described methods, in which the biotinylated strand remains attached to the support particle, in this approach the biotinylated molecules are removed from the support particle and directly analyzed. This allows the purification method to be utilized for the sequence analysis of the single-stranded M13 template DNAs most widely used in enzymatic DNA sequencing. This solid-phase strategy was used to investigate the effects of template DNA, polymerase, glycerol, and salts upon DNA sequence data.

EXPERIMENTAL SECTION

Enzyme, DNA Template, and Oligonucleotide Primer. *Bst* DNA polymerase was obtained from Bio-Rad (Richmond, CA). Single-stranded M13mp19 template DNA was prepared by standard methods. A modified M13 sequencing primer (denoted B-BT) with the sequence 5′-CAT* GAC GTT GTA AAA CGA CGG CCA GT-3′ was synthesized by the University of Wisconsin Biotechnology Center on an Applied Biosystems 380A DNA synthesizer (Foster City, CA). T* is the product obtained from use of the modified nucleoside phosphoramidite amino-modifier-dT (Glen Research, Sterling, VA), which has a primary amino group attached to thymine with a 10-atom spacer arm. This amino group was coupled to NHS-LC-Biotin (Pierce, Rockford, IL) as described.[11] The biotinylated primer (denoted Bio-B-BT) was purified by reverse-phase high-performance liquid chromatography and 5′ end-labeled using polynucleotide kinase (USB, Cleveland, OH) and [γ-^{32}P] at 5000 Ci/mmol (Amersham, Arlington Heights, IL).

Magnetic Beads. Streptavidin-coupled magnetic beads (Dynabeads M-280, Dynal, Inc., Great Neck, NY) were utilized as a solid support. A $^1/_2$-in. × $^1/_2$-in. neodymium–iron–boron magnet (Bunting Magnetics, Newton, KS) was used to immobilize the beads during the supernatant removal and washing steps.

(1) Hood, L. E.; Hunkapiller, M. W.; Smith, L. M. *Genomic* **1987**, *1*, 201–212.
(2) Smith, L. M.; Hood, L. E. *Bio/Technology* **1987**, *5*, 933–939.
(3) Smith, L. M.; Sanders, J. Z.; Kaiser, R. J.; Hughes, P.; Dodd, C.; Connell, C. R.; Heiner, C.; Kent, S. B. H.; Hood, L. E. *Nature* **1986**, *321*, 674–679.
(4) Prober, J. M.; Trainor, G. L.; Dam, R. J.; Hobbs, F. W.; Robertson, C. W.; Zagursky, R. J.; Cocuzza, A. J.; Jensen, M> A.; Baumeister, K. *Science* **1987**, *238*, 336–341.
(5) Gillespie, D.; Spiegelman, S. *J. Mol. Biol.* **1965**, *12*, 829–842.
(6) Atkinson, T.; Smith, M. In *Oligonucleotide synthesis-A practical approach*; Gait, M. J., Ed.; IRL Press: Oxford, 1984; pp 35–81.
(7) Stewart, J. M.; Young, J. D. *Solid phase synthesis*; W. H. Freeman: San Francisco, 1969.
(8) Stahl, S.; Hultman, T.; Olsson, A.; Moks, T.; Uhlen, M. *Nucleic Acids Res.* **1988**, 16, 3025–3038.
(9) Hultman, T.; Stahl, S.; Hornes, E.; Uhlen, M. *Nucleic Acids Res.* **1989**, *17*, 4937–4946.
(10) Hornes, E.; Korsnes, L. *Genet. Anal.* **1990** *7*, 145–150.
(11) *Dynabeads M-280 Technical Handbook: Magnetic DNA Technology 6.*

0003-2700/92/0364-2672$03.00/0

Table I. Protocol for Solid-Phase DNA Sequencing

1.	label tubes A, C, G, T and aliquot 2 μL of the appropriate d/ddNTP mix to each tube; keep on ice
2.	mix the following cocktail (10 μL per set of four reactions): 1.0 μL of ssM13mp19 template DNA (2.0 μg/μL = 0.8 pmol/μL); 1.5 μL 10 × SB (100 mM $MgCl_2$, 100 mM Tris pH 8.5); 0.8 μL primer (0.8 pmol); 6.7 μL of H_2O
3.	annealing: 65 °C (heating block) 2 min, 37 °C (heating block) 5 min, RT (air) 10 min
4.	add 0.5 μL of *Bst* DNA polymerase
5.	remove 2.5 μL of cocktail and add it to each nucleotide mix tube and immediately place at 65 °C for 5 min
6.	remove tubes from heating block and add 2 μL of 10 mM EDTA, 95% formamide
7.	heat tubes at 90 °C for 5 min; place on ice
8.	binding: to each tube add 2.0 μL of 5 × BB (5 × TES, 1% Tween-20) 2.0 μL of beads (in 1 × TES) sit at room temperature for 15 min
9.	immobilize beads with a magnet, wash twice with 10 μL of 1 × TES, once with 10 μL of H_2O
10.	elute DNA fragments from beads in 6.5-μL stop solution (10 mM EDTA, 95% formamide, 0.05% bromophenol blue) at 90 °C for 5 min
11.	pipette off the supernatant and load on gel

The beads were prewashed in 1 × TES (10 mM Tris-HCl, 1 mM EDTA, 1 M NaCl, pH 8.2) three times and resuspended at 10 μg/μL in 1 × TES. These beads are reported by the manufacturer to possess 0.3 pmol of biotin-binding sites per microgram of beads.

Single-Stranded Sequencing Reactions. DNA sequencing reactions were performed by mixing 0.8 pmol of template DNA, 0.8 pmol of 5′-^{32}P end-labeled primer, and 1.5 μL of 10 × SB (SB, or sequence buffer, is 10 mM $MgCl_2$ and 10 mM Tris-HCl pH 8.5).[12] Water was added to give a total volume of 10 μL. This mixture was placed at 65 °C (heating block) for 2 min, at 37 °C (heating block) for 5 min, and at room temperature (air) for 10 min to anneal the primer to the template. A 0.5-μL portion of *Bst* DNA polymerase (1 unit/μL, Bio-Rad, Richmond, CA) was added, and 2.5 μL of the resultant enzyme/DNA mixture was placed in each of four tubes containing 2.0 μL of d/ddNTP mixture (see below). The sequencing reactions were placed at 65 °C for 5 min, followed by the addition of 2.0 μL of a solution containing 10 mM EDTA (diluted from a 0.5 M solution of disodium EDTA which had been adjusted to pH 8.2 with NaOH) and 95% formamide to stop the reaction. They were denatured by heating at 90 °C for 5 min and immediately placed on ice before either loading on an acrylamide gel for analysis or binding to magnetic particles for purification. The following nucleotide mixtures were used: 250 mM each of 3 dNTPS, one of 240 mM ddGTP, 480 mM ddATP, 500 mM ddTTP, or 200 mM ddCTP, and 25 mM of the corresponding dNTP.

Solid-Phase Procedures. The newly synthesized DNA fragments were bound to streptavidin-coated magnetic beads by adding 2.0 μL of the bead suspension and 2.0 μL of 5 × BB (BB, or binding buffer, is 1 × TES and 0.2% Tween-20) to each reaction tube. The tube was placed at room temperature for 15 min to allow binding to take place. The supernatant was removed, and the beads were washed using the magnet to immobilize the beads in the tubes. The beads were washed twice with 10 μL of 1 × TES buffer and once with 10 μL of H_2O. The DNA fragments were eluted from the beads in 6.5 μL of stop solution (10 mM EDTA, 95% formamide, 0.05% bromophenol blue) at 90 °C for 5 min. Approximately 1.5 μL of supernatant were loaded on a 6% denaturing polyacrylamide gel for sequence analysis. Table I is a protocol for solid-phase DNA sequencing, in which steps 1–7 describe the DNA sequencing reactions. Kodak XAR-5 film (Rochester, NY) was used for autoradiography, and scintillation counting was performed on a Beckman LS6000SE (Fullerton, CA).

(12) Mead, D. A.; McClary, J. A.; Luckey, J. A.; Kostichka, A. J.; Witney, F. R.; Smith, L. M. *BioTechniques* **1991**, *11*, 76–87.

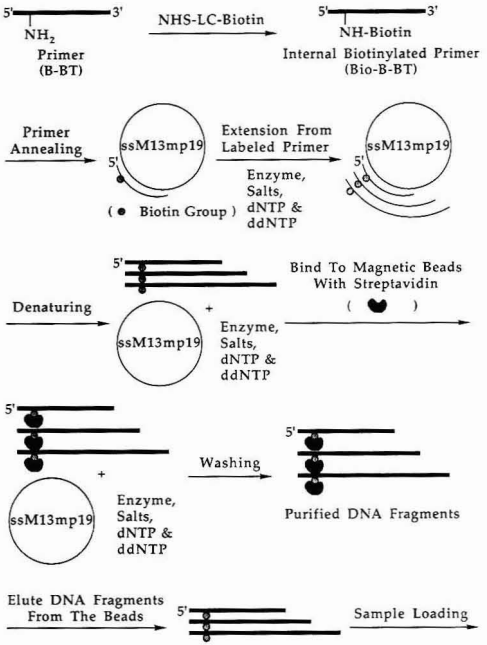

Figure 1. A schematic drawing of the basic concept for solid-phase DNA sequencing.

RESULTS AND DISCUSSION

Basic Concept. A diagram outlining this approach to solid-phase DNA sequencing is shown in Figure 1. Sequencing reactions are performed in solution by standard procedures, except that a biotinylated primer is employed. In this work the primer was a 26mer biotinylated at an amino-modified T nucleoside three bases from the 5′ end. The primer sequence was chosen to be complementary to the M13 sequence at all positions other than the modified T, which replaced a C normally at that position. The choice of an internal position for the biotin group left the 5′ terminus of the primer free for labeling with ^{32}P using polynucleotide kinase.

The sequencing reactions are denatured to separate the newly synthesized fragments from the template strand, and the fragments are captured on streptavidin-conjugated magnetic beads in a 15-min incubation at room temperature. The inclusion of the detergent Tween-20 in the binding buffer was found to be important for minimizing nonspecific binding. Contaminating species are removed by washing the beads after immobilizing them in the sample tube with a fixed magnet. The resulting pure single-stranded DNA fragments are eluted from the solid support by heating at 90 °C in 10 mM EDTA and 95% formamide, and may be loaded directly onto a denaturing polyacrylamide gel for sequence analysis.

Binding and Elution Efficiency. A central issue in this solid-phase procedure is the efficiency of capture and elution of the extension reaction products. In order to quantify and optimize these efficiencies, biotinylated primers labeled at the 5′ terminus with ^{32}P were bound to and eluted from beads with radioactive counting of the beads and supernatants. The

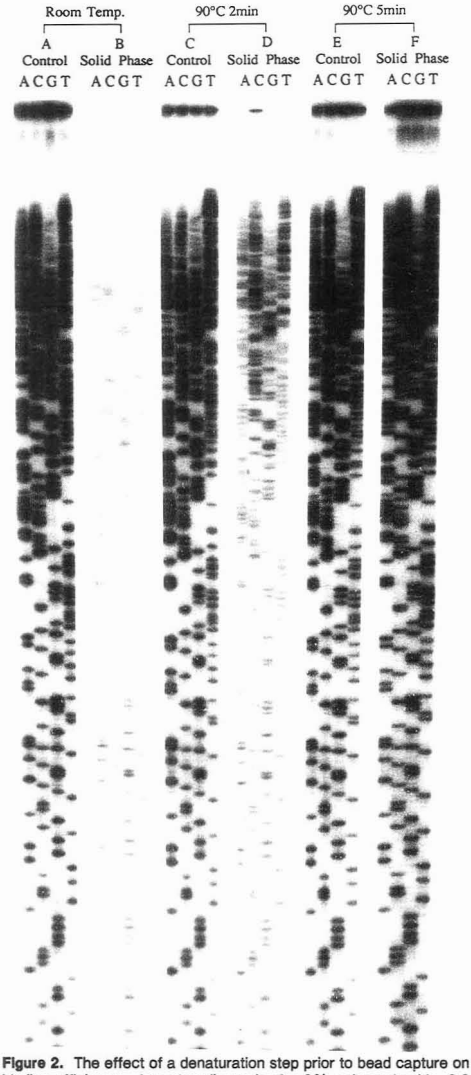

Figure 2. The effect of a denaturation step prior to bead capture on binding efficiency. An autoradiograph of a 6% polyacrylamide, 8.3 M urea gel shows the products of sequencing single-stranded M13mp19 with *Bst* DNA polymerase. Sets B, D, and F were sequencing reactions obtained using the solid-phase method in which a denaturation step subsequent to the extension reactions but prior to bead capture is omitted (B), at 90 °C for 2 min (D), and at 90 °C for 5 min (F), then to which 2.0 μL of 10 μg/μL beads suspended in 1 × TES and 2.0 μL of 5 × TES, 1% Tween-20 were subsequently added. Following binding and washing procedures (described in Table I), the DNA fragments were eluted from the beads in 3.0 μL of stop solution. Sets A, C, and E show control reactions that were denatured in the same way but to which no beads were subsequently added. The comparable intensity of the sequence ladders in lanes E and F is indicative of a binding efficiency of about 50%, as the control reactions were twice as dilute; 1.5 μL of the sequencing reactions were loaded on the gel for each of set A–F.

variables examined in the binding reaction were temperature, salt concentration, the primer/bead ratio, and incubation time. Varying the temperature from ambient to 65 °C had little effect upon the binding efficiency. The binding efficiency was 89% in 1 × TES, 0.2% Tween-20 compared to 74% in 10 mM Tris-HCl, pH 8.2, 0.2% Tween-20. An 8-fold variation in the primer/bead ratio (0.0025–0.02 pmol of primer/μg of beads) had no significant effect upon binding efficiencies, nor did incubation times of longer than 15 min.

Table II. Elution Efficiency

temp (°C), time (min)	elution solution	elution efficiency (%)
90, 10	10 mM EDTA, pH 8.2 and 95% formamide	96.8
90, 5	10 mM EDTA, pH 8.2 and 95% formamide	96.4
90, 2	10 mM EDTA, pH 8.2 and 95% formamide	96.8
65, 5	10 mM EDTA, pH 8.2 and 95% formamide	96.4
65, 2	10 mM EDTA, pH 8.2 and 95% formamide	97.9
37, 10	10 mM EDTA, pH 8.2 and 95% formamide	41.9
90, 10	H_2O	7.3
90, 10	10 mM EDTA, pH 8.2	52.0
90, 10	95% formamide	35.9
90, 10	30 mM NaOAc, pH 9 and 95% formamide	95.5
90, 10	80 mM NaOAc, pH 9 and 95% formamide	97.3
90, 10	140 mM NaOAc, pH 9 and 95% formamide	95.4

In early experiments the binding efficiencies obtained for sequencing reactions were substantially lower than those found for the free biotinylated oligonucleotides. Experiments were performed to evaluate whether this lower efficiency was due to interference in binding from the template strand. Figure 2 shows the effect of a denaturation step prior to bead capture. Reactions B, D, and F show the sequencing ladders obtained using the solid-phase protocol in which a denaturation step subsequent to the extension reactions but prior to bead capture is either omitted (B), 2 min at 90 °C (D), or 5 min at 90 °C (F). Reactions A, C, and E show control reactions treated the same way but to which no beads were subsequently added. In this experiment the control reactions were dissolved in twice the volume as the solid-phase reactions, but the same volumes were applied to the gel. The data show clearly that the denaturation step is critical to obtaining a good efficiency of binding to the beads. The comparable intensity of the sequence ladders in lanes E and F is indicative of a binding efficiency of about 50%, as the control reactions were twice as dilute. This was confirmed by cutting out the gel region and measuring the radioactivity by scintillation counting. The modest effect of the 2-min denaturation relative to the 5-min denaturation is probably due to the time required to bring the sample tube to temperature after placing it in a hot block.[13] The need for a denaturation step prior to binding presumably reflects some form of steric hindrance between the template DNA and the streptavidin-coated magnetic particle, although this has not been investigated in detail.

In order to further increase the binding efficiency, the denaturation conditions were investigated. As expected, more stringent denaturation conditions produced by lower salt concentrations and/or added formamide increased the binding efficiency. It was also found to be important to place the reactions on ice immediately after denaturation, presumably to inhibit renaturation prior to bead capture. The best conditions found employed a 5-min denaturation at 90 °C in the presence of 29% formamide and 3.0 mM EDTA followed

(13) D'Cunha, J.; Berson, B. J.; Brumley, B. L.; Wagner, P. R.; Smith, L. M. *BioTechniques* **1990**, *9*, 80–90.

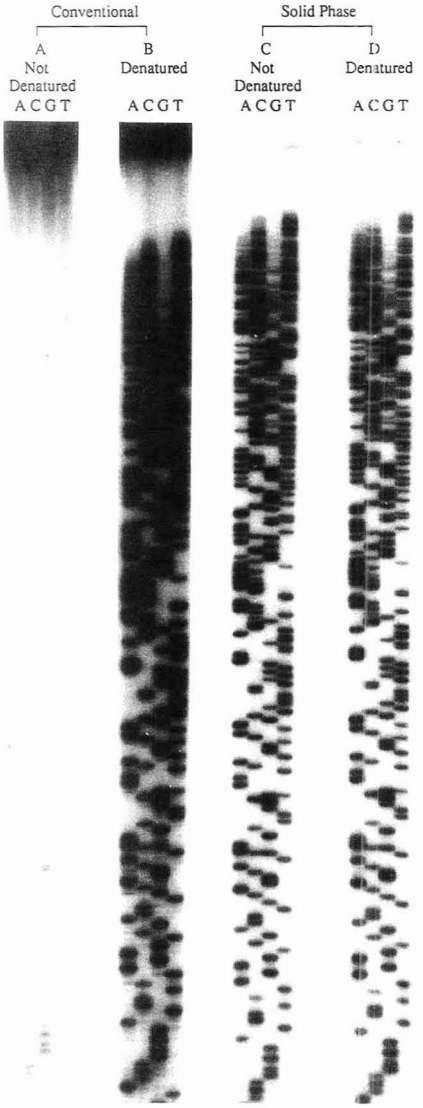

Figure 3. Sequence data examining the effect of a sample denaturation step prior to loading on the sequencing gel in both solid-phase purified DNA fragments and conventional sequencing reactions. Sets A and B: conventional sequencing reactions were denatured by heating at 90 °C for 5 min and immediately placed at room temperature for longer than 1 h (A), or on ice (B). Sets C and D: the sequencing reactions employing a biotinylated primer (see text) were denatured by heating at 90 °C for 5 min and immediately placed on ice before binding to magnetic particles for purification (step 7 of Table I protocol). They were then eluted from the beads in 10 mM EDTA, 95% formamide, 0.05% bromophenol blue and (C) were placed at room temperature for longer than 1 h or (D) were heated at 90 °C for 5 min and placed on ice. The radioactive signal evident in the well of Figure 2 lane F but absent in the wells of Figure 3 lanes C and D is presumably due to rehybridization of the sequencing products to the template DNA. This template DNA is not removed by the step employed for the experiments of Figure 2, but was removed by the procedure employed for Figure 3.

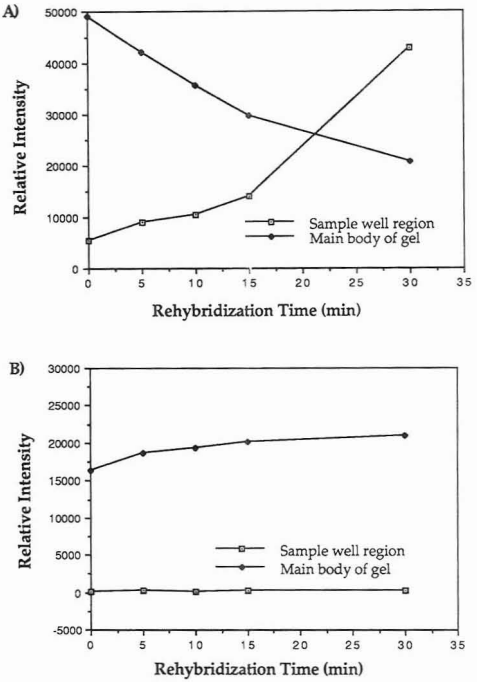

Figure 4. Plots of radioactivity of sequencing reactions versus rehybridization time for rehybridization experiments in conventional (A) and solid-phase purified (B) DNA sequencing reactions. Sequencing reactions performed as described in Table I were denatured by heating at 90 °C for 5 min and placed on ice for 5 min (step 10 of Table I protocol) and then left at room temperature for 0, 5, 10, 15, or 30 min. Aliquots (1.5 μL) were loaded on a 6% polyacrylamide, 8.3 M urea gel and individually electrophoresed into the gel matrix immediately after loading of each reaction and then separated by electrophoresis. The region of the gel corresponding to the sample well, and the separated DNA fragment was excised and quantified by scintillation counting.

by immediate incubation on ice (see Table I for protocol) and resulted in a binding efficiency of ~80%.

The degree of nonspecific binding of DNA to the streptavidin-coated beads was determined in mock binding experiments using unbiotinylated B-BT primers. Some nonspecific binding (12.4%) was observed in early experiments using TES as a binding buffer, but was rendered negligible (0.9%) by inclusion of the detergent Tween-20 in the binding buffer.

In order to have a high overall efficiency, both the binding and the elution efficiencies must be high. A variety of conditions were investigated for elution of the immobilized DNA fragments. As before, initial studies were performed with radiolabeled biotinylated primer oligonucleotides. The results are shown in Table II. A 10 mM EDTA, 95% formamide solution gave efficient elution for temperatures of 65 °C or greater. Even at a temperature of 90 °C for 10 min, very poor elution efficiency was observed in water alone, only a 52% efficiency in 10 mM EDTA alone, and only a 36% efficiency in 95% formamide alone. It was suspected that the effect of the EDTA might simply be to provide ionic strength to the elution buffer. To test this hypothesis other salts were tested in the elution buffer. Sodium acetate at 30 mM or higher concentration also gave good elution efficiency (Table II). Other salts such as triethylammonium acetate and Tris buffer of varying concentrations improved elution efficiency, but for reasons that are unclear led to some

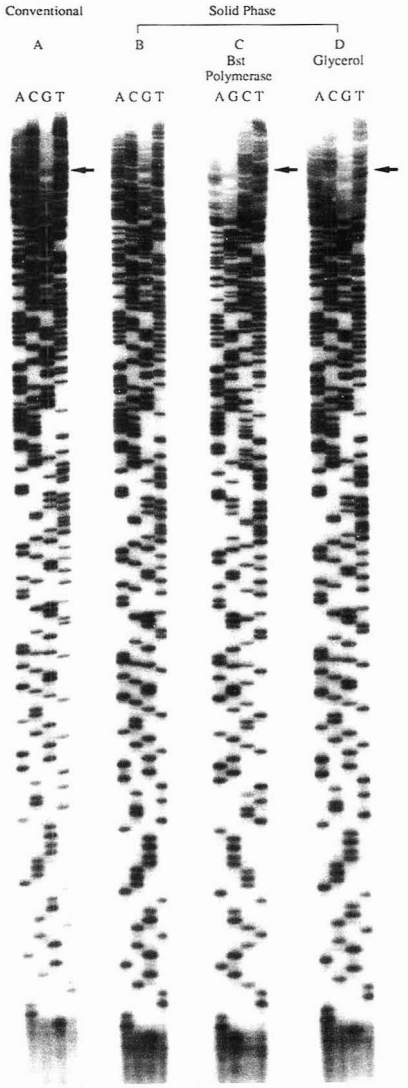

Figure 5. The influence of glycerol on sequence data. Set A was a control conventional sequencing reaction which includes approximately 0.019 units/μL or 5 ng/μL of *Bst* DNA polymerase and 1% glycerol. B–D were solid-phase purified DNA sequencing reactions prepared as described in Table I, to which were added nothing (B), *Bst* DNA polymerase (0.057 units/μL or 15 ng/μL, C), or glycerol (3%, D).

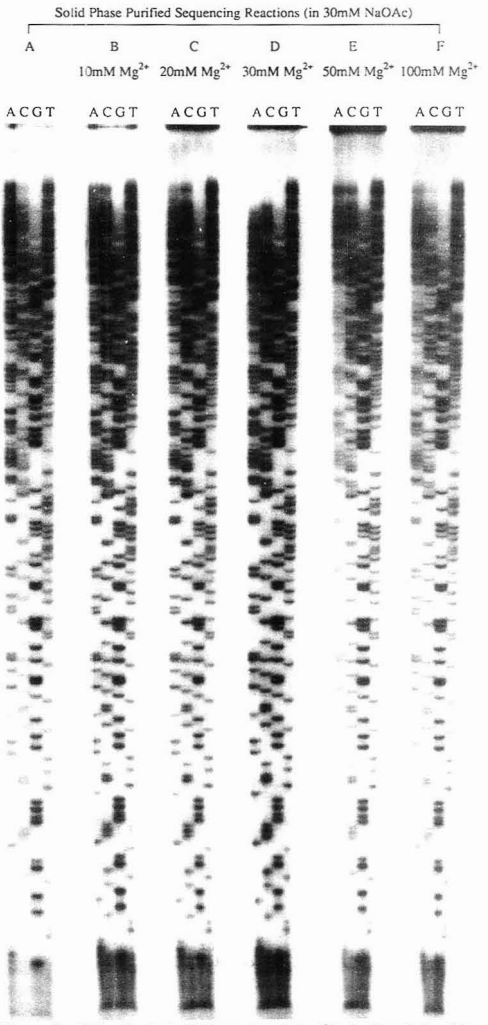

Figure 6. Salt effects in DNA sequencing. Single-stranded solid-phase DNA sequencing reactions produced according to the protocol in Table I, except that DNA fragments were eluted in 3.0 μL of 30 mM NaOAc, 95% formamide by heating at 90 °C for 10 min. Additional salts as indicated were added to the supernatants removed from the beads. These samples were dried on a SpeedVac Concentrator (Savant) and resuspended in 3.0 μL 95% formamide, 0.05% bromophenol blue. Aliquots (1.5 μL) were loaded on a 6% polyacrylamide, 8.3 M urea gel and separated by electrophoresis.

difficulties with reproducibility. The pH of the elution buffer may also have an effect upon elution efficiency, but this issue was not examined in detail. The mechanism of elution is presumed to involve the denaturation of streptavidin, causing a loss of biotin-binding activity.

Denaturation Experiments. Figure 3 presents data showing the effect of a sample denaturation step immediately prior to gel loading upon both solid-phase purified DNA fragments and conventional sequencing reactions. Two observations may be made. First, data obtained from the solid-phase purified material did not suffer from the absence of a denaturation step, in marked contrast to data obtained from conventional reactions treated similarly. Second, the large mass of radioactive material present in the well of the conventional sequencing reactions is absent in the wells on which the solid-phase purified material was applied. Both these observations presumably reflect the absence of a DNA template strand to which the newly synthesized fragments can bind. Rehybridization of the newly synthesized fragments to the template strand increases their effective molecular weight greatly, preventing them from entering the gel and

thus producing the large amount of radioactive signal in the sample well. Independent evidence confirming the efficient removal of the template DNA strand in the solid-phase procedure was obtained in agarose gel electrophoresis experiments (data not shown).

In further experiments, unpurified and purified sequencing reactions were left at room temperature for varying amounts of time after a denaturation step. They were then loaded on a sequencing gel, the products separated by electrophoresis, and the regions of the gel corresponding to the sample well and the separated DNA fragments were excised and quantified by scintillation counting. The results are shown in Figure 4. Whereas for unpurified reactions the counts present in the sample well increased with time while those present in the gel decreased, for the solid-phase purified reactions the counts present in both regions remained roughly constant.

Effects of Additional Components upon Sequencing Reactions. Since the solid-phase procedure described above yields pure single-stranded DNA fragments, it can be used to determine the effects of other components upon sequence data. Experiments were performed in which various components were added to solid-phase purified DNA sequencing reactions prior to their electrophoretic separation. The components examined were DNA template, DNA polymerase, glycerol, and both sodium chloride and magnesium chloride. The effect of DNA template was as described above. Figure 5A,B shows control conventional and solid-phase purified sequencing reactions, and Figure 5C shows the effect of added DNA polymerase, whose only apparent effect was to produce a "bulge" in the sequence ladders near the top of the gel. It was suspected that glycerol present in the *Bst* storage buffer might be responsible for this effect.[14] This hypothesis was tested by addition of glycerol to solid-phase purified sequencing reactions and found to be correct as shown in Figure 5D. Apart from the effect of the glycerol, the *Bst* polymerase did not appear to have an adverse effect upon the sequence data.

Another major contaminant often present in sequencing reactions is salts. In protocols generally employed in fluorescence-based automated DNA sequencing, for example,[15,16] an ethanol precipitation step to concentrate samples and remove salt is required prior to gel loading. Thus, the effects of added NaCl, $MgCl_2$, EDTA, and Tris-HCl upon sequence data were examined. In the addition experiments involving $MgCl_2$, the purified DNA molecules were eluted from the support in 30 mM NaOAc, 95% formamide to avoid interactions with the EDTA normally employed in elution. Interestingly, neither added sodium chloride up to 200 mM in concentration nor Tris-HCl up to 400 mM had any discernable effect upon the sequence data (not shown). In contrast, both $MgCl_2$ (Figure 6) and EDTA (not shown) caused a "focusing" of the sequencing ladders, that is a narrowing together of the four lanes evident near the bottom of the autoradiogram. This "focusing" phenomenon was accompanied by a slow movement of the blue loading dye into the gel matrix from the wells and diffusion of the dye at the beginning of electrophoresis, followed by a subsequent sharpening later in the separation. It was initially surprising that these effects were specific to the salts employed and were thus not a function solely of either ionic strength or ionic conductivity. One explanation consistent with these observations, however, is that since EDTA molecules, either free or bound to Mg^{2+}, have a relatively low electrophoretic mobility, they remain near the top of the gel much longer than do the fast moving chloride ions introduced with either sodium chloride or Tris-HCl. Their presence in the gel decreases the field strength locally, causing the marker dye to migrate slowly as well as bending the electric field lines and causing the "focusing" effect observed.

In summary, we have described a simple system for the purification of DNA sequencing reactions on a solid phase. The ability to generate pure single-stranded DNA fragments for analysis permits the effect of contaminants upon sequence data to be determined, increases signal by eliminating rehybridization of the synthesized fragments to template which does not enter the gel, and offers a simple alternative approach to the automated production of clean samples for large-scale DNA sequencing. It is expected to prove useful in capillary electrophoretic methods for DNA sequencing[17,18] in which contaminants are believed to substantially decrease capillary gel stabilities and lifetimes. The utility of this method for sample preparation in automated fluorescence-based DNA sequencing methods is also under investigation.

ACKNOWLEDGMENT

This work was supported by NIH Grant GM 42366. We wish to thank Mr. Robert L. Brumley, Jr. for many helpful discussions in the course of this work, and Ms. Amy Doubles for technical assistance.

RECEIVED for review May 11, 1992. Accepted August 17, 1992.

Registry No. Streptavidin, 9013-20-1.

(14) Fuller, C. W. *United States Biochemical Corp. Editorial Comments* **1989**, *16* (2), 19.
(15) *Applied Biosystems Taq DyeDeoxy Terminator Cycle Sequencing Kit User's Manual*; Part Number 901497, 11 & A1–A3.
(16) *Applied Biosystems 373A DNA Sequencing System User's Manual*, Section 3, 10.
(17) Drossman, H.; Luckey, J. A.; Kostichka, A. J.; D'Cunha, J.; Smith, L. M. *Anal. Chem.* **1990**, *62*, 900–903.
(18) Luckey, J. A.; Drossman, H.; Kostichka, A. J.; Mead, D. A.; D'Cunha, J.; Norris, T. B.; Smith, L. M. *Nucleic Acids Res.* **1990**, *18*, 4417–4421.

Video Analysis of DNA Sequence Homologies

Michael Ludwig* and Robert J. Hartzman

Georgetown University School of Medicine, Department of Pediatrics, Washington, DC 20007, and C. W. "Bill" Young Marrow Donor Recruitment and Research Program, Naval Medical Research Institute, Bethesda, Maryland 20889-5055

A method for the rapid quantitative analysis of dot blot assays is presented. A video camera, an NTSC compatible frame grabber board, and an AT personal computer are used to read photographic exposures of the assay plate. Image processing and image analysis techniques are used to calculate the orientation of the dot raster and then to compensate for the effect of variations in field illumination on measurements of local contrast. Local contrast (between dots and background) is an exponential function of the amount of hybridization between blotted DNA and complimentary oligonucleotide probes. The amount of hybridization between blotted DNA and oligonucleotide probes of known sequence is the criteria used to establish HLA-DR tissue types. Although the assay described here utilizes a chemiluminescent reaction, this algorithm may be used to read any assay that produces a rectangular raster of dots.

INTRODUCTION

Dot blot assays are a standard technique for measuring the amount of biological material bound to a membrane.[1] At the C. W. "Bill" Young Marrow Donor Recruitment and Research Program, dot blots are used to evaluate the DNA sequence of human leukocyte antigen (HLA) genes isolated from potential bone marrow donors. The HLA types of donors are entered into a national data base that is used to match the donors with patients requiring bone marrow transplants. A large number of tests are needed to complete the typing of a single individual, hence the requirement for an inexpensive, rapid, accurate, and easy to use method for reading the assay.

Dot blot assays are commonly evaluated either visually or by densiometric scanning.[2,3] Advancements in commercial filtering apparatus have greatly eased sample preparation procedures. However, the tedius, time-consuming, and error-prone tasks of manual analysis and data entry underscore the need for automated analysis. Previous attempts to automate reading have assumed the presence of mainframe computers, required extensive user intervention,[3,4] or utilized dedicated systems running proprietary software.

In the dot blot assay, the DNA blotted at each dot position was tested against probes of known sequence. Measurements of the degree of hybridization between the probe and blotted DNA were used to evaluate the HLA-DR tissue types of potential bone marrow donors. Our goals in developing this video system were to (1) quickly and accurately read the large numbers of assays produced daily and (2) introduce a measure of numeric consistency that was lacking in visual assessments of the assay.

The dot blots were read using a video camera and an image acquisition board to capture the image of a photographic exposure of an assay plate. The analogue NTSC signal from the video camera was digitized by the frame grabber. Approximately 5 s was required to read and save a single exposure. The results can be observed immediately on the PC screen and may be ported to many commercial database programs for further analysis.

EXPERIMENTAL SECTION

The dot blot assays were prepared according to standard protocols.[5] Figure 1 illustrates the preparation of a single (positive) dot. Human DNA was amplified using polymerase chain reaction (PCR) to produce DNA complementary to the sequence of interest. The amount of DNA (absorption coefficient = 0.020 $cm^2/\mu g$ at 260 nm) after PCR was measured with a Spectronic 601 absorption spectrophotometer (Milton Roy, Rochester NY). The PCR was slowly filtered through Zeta-Probe membranes (Bio-Rad, Richmond CA). For the calibration experiments, it was assumed that all of the applied DNA adhered to the membrane. This assumption is valid since our maximum target size was 0.09 μg of DNA, while Bio-Rad has loaded targets containing up to 7.5 μg. The surface area of the membranes was sufficiently high to accommodate all of the applied DNA.

Samples containing up to 0.0858 μg of PCR-amplified DNA (in 10X SSPE—1.5 M NaCl, 0.1 M Na_2HPO_4–$7H_2O$, 10 mM EDTA) were individually blotted to the membrane in a 96-well vacuum filtering apparatus (Bio-Rad). The 96-well microtiter plate sets the 8 × 12 dot raster pattern. The dot positions are labeled A1 (row 1 column 1) to H12 (row 8 column 12). After blotting, the DNA was denatured with 0.5 M NaOH, cross-linked to the membrane with a 30-s 1200-μJ exposure in a UV Stratalinker 1800 (Stratagene, La Jolla, CA), dried, and rewet in 2X SSPE. The membrane was incubated for 60 min in a solution of 0.33% (v/v) 20X SSPE, 0.1% (v/v) Denhardt's solution (5.0 g of Ficoll Hypaque, 5.0 g of polyvinylpyrrolidone, and 5.0 g of bovine serum albumin in 500 mL of water), 0.2 g of sarcosine, 0.4 mL of 10% SDS, 20.0 mg of salmon sperm DNA (Sigma Chemical Corp., St. Louis, MO), and a digoxigenin-labeled sequence-specific 18 base pair oligonucleotide.[5] The probe concentration in the reaction mixture was 100 pM. The membranes were then washed (pH 7.5, 50–60 °C) to remove nonhybridized and nonspecifically bound oligonucleotide.

Detection of digoxigenin-linked oligonucleotide was accomplished as follows. First, nonspecific antibody binding was blocked using a buffered solution of 2% nonfat dry milk (pH 7.5, Boehringer Mannheim, Indianapolis, IN). The membranes were then incubated with a solution of anti-digoxigenin-Ab-alkaline phosphatase conjugated antibody (Boehringer Mannheim). The blots were transferred in a darkroom to a solution of Lumiphos-530 (Boehringer Mannheim) and placed in a film cassette. After a final 30-min incubation, the blots were exposed to X-ray film (Kodak X-OMAT scientific imaging film) for timed intervals and developed. Chemiluminescence resulting from the enzymatic cleavage of Lumiphos could then be seen as a dark spot against a clear background.

Figure 2 shows the equipment required for the video analysis. The developed films were placed on an illuminated copy stand. A black and white CCD video camera (Cohu, San Diego, CA)

* To whom correspondence should be addressed.

(1) Kafatos, F. C.; Jones, C. W.; Efstratiadis, A. *Nucleic Acids Res.* **1979**, *7*, 1541–1552.
(2) Thomas, P. S. *Proc. Natl. Acad. Sci. U.S.A.* **1980**, *77*, 5201–5205.
(3) Williams, R. L.; Cascio, D.; Wight, P. A.; Spindler, S. R. *DNA* **1985**, *4*, 255–262.
(4) Taub, F. E.; DeLeo, J. M.; Thompson, E. B. *DNA* **1983**, *2*, 309–327.
(5) Georgetown University and Naval Medical Research Institute Bone Marrow Typing Standard Operating Procedure. Naval Medical Research Institute: Bethesda, MD, 1991.

0003-2700/92/0364-2678$03.00/0

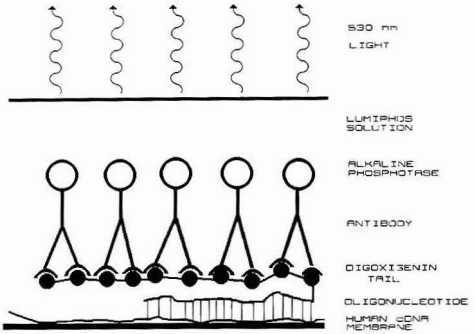

Figure 1. DNA sequence homology test. Human cDNA is linked to a membrane by UV light. A digoxigenin-linked oligonucleotide probe will bind to the cDNA if they are homologous. Next, the membrane is washed with alkaline phosphatase bound digoxigenin antibody. Finally, the membrane is placed in a solution of Lumiphos 530. The enzymatic cleavage of Lumiphos produces light.

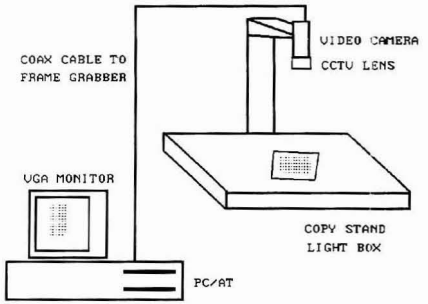

Figure 2. Setup for the video analysis of dot blot assays.

with a Fujinon HF16A CCTV lens was focused on the film. An AT personal computer (Dell Computer Corp., Austin, TX) and a 3Mb P-360 power grabber (Dipix Technologies, Ontario, Canada) was used to capture and analyze the images. The P-360 is a singlet-slot PC-based video digitizer that uses the TMS320C30 (Texas Instruments, Austin, TX) floating point digital signal processor. The P-360 digitized the NTSC (RS-170 2:1 interlace, 60 Hz) video signal. In the calibration experiments, neutral-density filters were placed between the CCTV lens and the film exposure to simulate changes in room lighting.

RESULTS AND DISCUSSION

Program Algorithm. Figure 3 is a flowchart for image acquisition and analysis. The steps requiring user intervention are shown in solid boxes, while the steps automatically carried out are in dotted boxes.

The program requires that the first exposure read in each session must be a previously prepared template. This template is simply a developed film image of a microtitre plate with positive spots in diagonally opposite corners (the A1 and H12 positions). These positions were forced positive by using DNA-linked digoxigenin bound to the membrane instead of PCR-amplified DNA solution. There are no other spots on the template.

The template is used to establish the geometric parameters required for alignment and to optimize the overall video levels used in reading the ensuing exposures. The program sets the video levels by repeatedly calculating the histogram of the acquired image and adjusting the gain (white clipping level) and offset (black clipping level) of the video amplifier stage

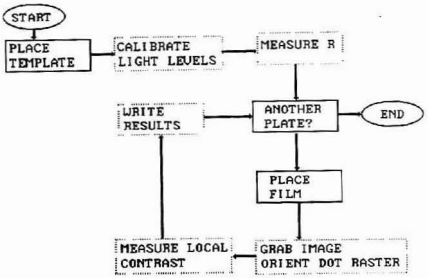

Figure 3. Flowchart for the video analysis. Steps requiring user intervention are in solid boxes. Steps automatically performed are in dotted boxes.

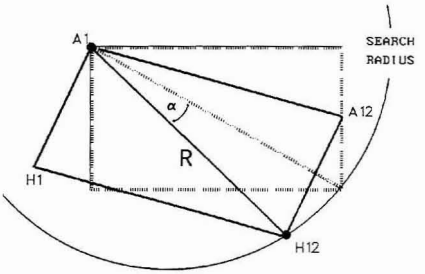

Figure 4. Alignment of a 96 well assay exposure. Pixels are search along R until a second "dot" is found identifying the H12 corner. The angle of rotation (α) and the known geometry of the plate are used to calculate the positions of each well.

of the P-360 until overflow and underflow are eliminated. The video calibration takes about 10 s.

The diagonal distance between the two template spots (R in Figure 4) is measured after the template is read. R is measured by creating a binary image of the template gray image.[6] The binary image contains only those pixels below a threshold gray value. Contiguous pixels in the binary image represent the objects that are observed in the image. The size and shape of each group of pixels in the binary image is calculated to determine whether it is one of the reference spots. Once the two reference points are found, R is equal to the distance between them.

Since R is a function of the size of the image on the CCD it depends on the distance between the camera and the film exposure. R is measured at the start of each session and must be remeasured if the camera is moved. Other geometrical parameters required for the determination of plate orientation include the length, width, and the number of rows and columns contained in the dot raster. These parameters are set by the geometry of the microtitre plates used and may be chosen at the beginning of the session. Thus, assays using different raster patterns are easily accommodated.

After R has been measured, the dot blot films are successively placed on the copystand. As with the template, each exposure must have dark spots in the A1 and H12 positions. In addition, the A12 and H1 positions must be blank.

Figure 4 shows how the dot raster in an image is aligned. A binary image of the plate is created from the captured gray value image. The objects in the binary image are subject to size and shape tests to determine whether they are potentially one of the reference spots. If the size and shape tests are

(6) Gonzales, R. C.; Wintz, P. *Digital Image Processing*; Addison-Wesley: Reading, MA, 1987.

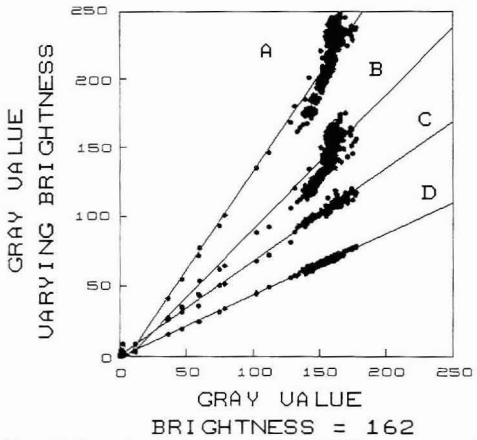

Figure 5. Comparison of the average gray values of image areas read for a single plate under varying lighting and amplifier conditions. The slopes of these lines were used to construct Figure 6. Plate brightness values: curve A = 209, B = 149, C = 114, D = 75.

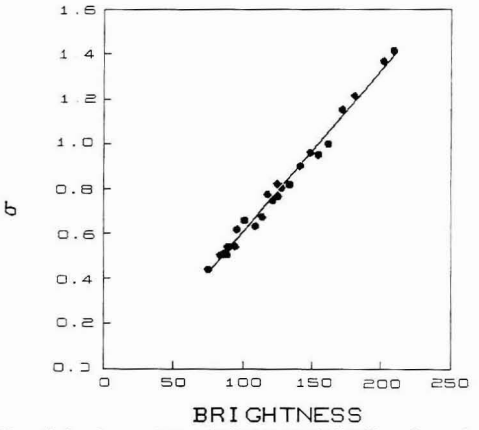

Figure 6. Local contrast correction factors as calculated from observed image brightness.

passed, the pixels at a radius R from the center of the spot are searched. If the object is indeed one of the reference spots, there will be one (and only one) position at the radius R that is covered by another object that also passes the size and shape tests. The identify and search process is repeated until both reference spots are located.

Once the corner positions are identified, the rest of the exposure orientation is calculated by determining the angle between R and the diagonal of an imaginary "perfectly aligned" exposure. Figure 4 shows an exposure randomly placed within the camera field of view (solid rectangle) and the outline of an exposure placed so that its edges are aligned with the camera field of view (dotted rectangle). Using A1 as the origin and the known microtitre plate geometry, the positions of the remaining 94 wells are calculated by a two-dimensional rotation of coordinates through α.

At this point the program signals the user that one of the following has occurred:

(1) Both reference points have been located. In this case, the exposure will be automatically read. The results appear on the screen and the user is prompted to save them. If saved, the results are written to a file for detailed analysis at a later time.

(2) The program is unable to locate two reference points. This may occur if (A) either A1 or H12 is out of the field of view of the CCTV lens and (B) the reference points are of too low contrast to appear in the binary image. The binary image is displayed, so these two cases are easily distinguished. The exposure may be reread after moving it into the field of view or increasing the binary threshold.

(3) The reference points are present, but some positions fall out of the field of view of the camera. Alternatively, the program can tell if the exposure has been placed upside down (the reference points are in A12 and H1 giving a very large value for α). In either case, the user is given the opportunity to reposition the exposure.

The local contrast at each spot position is read by sampling a 6 × 6 pixel area at the calculated well position. The background surrounding each spot is sampled by reading up to 864 pixels (a 30 × 30 pixel area excluding the 36 "spot" pixels) surrounding the calculated spot position. The standard deviation of both the spot and background pixel intensities are also calculated. Thus, nonuniform spots and uneven background shadings are easily detected. In addition, dark pixels far from the calculated dot center position—belonging to dots that are too large or smudged—may be identified and automatically filtered from the background. In practice, the spots produced by the alkaline phosphotase reaction are uniform. Physical disruptions of the membrane during filtering, washing, or pipetting are the primary cause of nonuniform spot density and irregularities of shape.

Quantitative Calibration. Measurements of local contrast vary widely with changes in room-lighting conditions. The value of any pixel in an acquired image is also a function of the gain and offset settings of the frame grabber amplifier. Figure 5 is a plot of the average gray values of image areas—regions defined by the 36 pixels at calculated dot locations (as described above) and the 864 pixels surrounding each dot location that comprise the local backgrounds. The image brightness is defined as the average value of the pixels located outside the boundaries of the microtitre plate. Under normal room illumination the image brightness value was 162. The lines labeled A (very bright lighting, brightness = 209) through D (dark lighting, brightness = 75) are plots of the average gray value of each image area acquired with a brightness level of 162 against the corresponding values of that area obtained under other lighting conditions. In Figure 5, readings from strongly positive dots appear near the origin while readings from the local backgrounds are clustered at higher gray values. Faint dots are distributed along the lines connecting the origin and the background readings.

Figure 6 shows the slopes of a series of such lines as a function of image brightness. Using Figure 6, variations in local contrast caused by fluctuations in room lighting and video settings may be corrected by measuring the image brightness and applying the calculated correction factor to each gray value measurement. The corrected value for local contrast (δ) at each spot position is

$$\delta = (B - P)/\sigma \qquad (1)$$

where B is the value of the surrounding (background) pixels, P is the value at the calculated spot position, and σ is the correction factor read from Figure 6.

Figure 7 shows the quantitative analysis for the hybridization of an oligonucleotide probe. The relative contrast

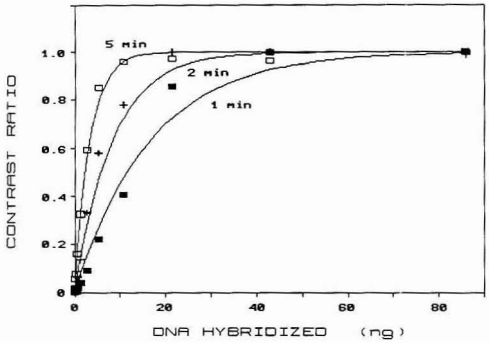

Figure 7. Dot contrast plotted versus applied DNA at varying exposure durations.

between spots containing known amounts of amplified DNA (δ_d) and a saturated reference spot (δ_r) is

$$\delta_d/\delta_r = 1 - e^{-C_d t} \quad (2)$$

where t is the film exposure time and c_d is the amount of DNA applied. The amount of hybridized DNA at any spot position may be found by comparing its local contrast value with the local contrast at the saturated A1 and H12 reference positions:

$$C_d = -\ln\left(1 - \frac{\delta_d}{\delta_r}\right)/t \quad (3)$$

The A1 and H12 positions are forced positive (saturated black) by using digoxigenin-labeled DNA instead of the usual PCR solution. These positions define the upper limit for local contrast measurements on a given exposure.

Increasing the exposure time of the X-ray film will decrease the detection limit of hybridized DNA. It was possible to detect 84 ± 40 pg of hybridized DNA with a 5-min exposure time. This limit represents the faintest detectable dot produced by a 5-min film exposure time under the conditions used to prepare the assay. On the basis of the average amount of PCR-amplified DNA applied to a spot position during a sequence homology assay, this corresponds to the detection of about 0.1% of the total possible hybridization. The upper detection limit can be further decreased by using less DNA spotted at each position and longer exposure times. This will prevent increases in dot size and smearing due to overexposure.

As implied in Figure 7 and eq 3, the detection limit is not a linear function of exposure time. Further, the limit of detection is a function of many experimental variables, each influencing how well hybridization occurs between the probe and the target DNA and how well the blotted DNA adheres to the membrane. The temperature during incubation, the pH of the wash medium, turbulence and shear induced during the wash and filtration steps, the molecular weight of the probe, photographic exposure time, and the inherent sequence homology between the probe and the blotted DNA each contribute to the experimental uncertainty to varying degrees. We have therefore found it necessary to prepare a concurrent internal standard membrane (from the nonvariable HLA-DR region) for each panel of bone marrow donors. This internal standard serves as a measure of the maximum strength of response at each dot position in the assay.

SEQUENCE HOMOLOGIES

To demonstrate the utility of the dot blot analyzer, PCR-amplified DNA from a panel of 94 individuals was anlayzed. DNA was blotted onto 17 membranes as discussed above. Each membrane was tested for hybridization by a different oligonucleotide probe. The probes were complementary to known sequences of the variable region of HLA-DR. In addition, a membrane was prepared using a probe complimentary to the nonvariable region of the HLA-DR gene. This membrane is used as a measure of the total amount of DNA-amplified PCR spotted onto the membrane at each position.

After development, the films were read and the data were used to assign donor HLA-DR types. The type assignments made using video data were identical to the types assigned after visual inspection of the assays. The entire panel (over 1700 dots) was read, and the data were stored in a commercial database in less than 10 min. Typically, visual inspection of the assays, corroborating the results, and manual data entry take 12–16 h of technician time.

As demonstrated above, the video analysis is capable of quantitative analysis. When the assay is read visually, however, quantitative information is not used for type assignments of HLA-DR regions. This is due to the large number of dots that must be evaluated before an assignment is made and the subjectivity of evaluating dot densities by eye. With visual inspection, type assignments are usually made on the basis of the presence of a few dots and must be verified by accomplished technicians who "know the probes". Cross reactivity (nonspecific probe hybridization) impedes both quantitative and qualitative approaches to type assignments. We are developing methods for type assignments that combine the quantitative readings obtained by the video analysis with our accumulated experience. These methods are based on a statistical correlation of donor responses with the expected responses from known types.

ACKNOWLEDGMENT

Support for this research was provided by the Naval Medical Research Institute Work Unit 63706N.M2022.001.1110. The work was done as part of the C. W. "Bill" Young Marrow Donor Recruitment and Research Program. The authors are grateful to Amy Cigan, Caroline Carter, Alicia Reyes, and Pat Mero for preparing the dot blot assays and to Lee Husted for his valuable suggestions and contributions concerning the user interface. Views presented in this paper are those of the authors: no endorsement by the Department of the Navy has been given or should be inferred.

RECEIVED for review May 18, 1992. Accepted August 24, 1992.

Determination of Manganese in Seawater Using Flow Injection Analysis with On-Line Preconcentration and Spectrophotometric Detection

Joseph A. Resing* and Michael J. Mottl

Department of Oceanography, School of Ocean and Earth Science and Technology, University of Hawaii at Manoa, 1000 Pope Road, Honolulu, Hawaii 96822

A highly sensitive method for the rapid determination of dissolved Mn(II) and total dissolvable Mn in seawater has been developed. The method uses on-line concentration of Mn(II) onto 8-hydroxyquinoline immobilized onto a vinyl polymer gel. The Mn(II) is then eluted from the gel by acid and its concentration determined by spectrophotometric detection of the malachite green formed from the reaction of leucomalachite green and potassium periodate with Mn(II) acting as a catalyst. The limit of detection is 36 pmol/L when concentrating 15 mL of seawater. The accuracy of the method was proven using NASS-2 standard seawater. The method has a precision of ≈5% for Mn(II) concentrations of ≈400 pmol/L. Analysis time is ≈5.5 min per sample.

The use of Mn as a tracer has improved the understanding of eolian, coastal, riverine, and hydrothermal inputs to the ocean.[1-6] Because of the importance of hydrothermal activity in understanding the geochemical cycles of elements in the ocean, the accurate and precise determination of Mn in seawater is important.[7,8] Within the last 15 years, the advent of relatively contamination-free sampling has resulted in the improved understanding of Mn in its biogeochemical cycle.[9]

Mn has been determined in seawater by methods emphasizing both matrix elimination and preconcentration, using Chelex-100[10] and Chelex-100-type resins,[11] 8-hydroxyquinoline,[12] electrolytic oxidation,[13] and other resins.[14,15] Detection methods have included inductively coupled plasma atomic emission spectroscopy (ICP-AES), ICP-mass spectroscopy, graphite furnace atomic absorption spectrophotometry, and colorimetry. 8-Hydroxyquinoline has been immobilized on several substrates, resulting in resins that will concentrate Mn and exclude most of the seawater matrix.[12,16-19] 8-Hydroxyquinoline immobilized on vinyl polymer gel[17] has been used in flow injection analysis (FIA) for the on-line preconcentration of cobalt and manganese.[20,21] This resin has also made it possible to concentrate samples for other trace metals automatically and on-line with various methods of detection. The advantages of on-line concentration include the relative ease of sample handling and a significant reduction in contamination. Among spectrophotometric detection methods, kinetic catalytic methods[22-25] are more sensitive than equilibrium methods because each analyte ion produces more than one color molecule. Because catalytic methods are time dependent, they are not suited for batch analysis. FIA lends reproducibility to both reagent addition and reaction times[26] and thus is ideal for catalytic methods.

The method presented here uses 8-hydroxyquinoline immobilized onto vinyl polymer gel.[17] This resin was packed into a column and placed on-line with a leucomalachite green (LMG) flow injection analysis (FIA) method. The LMG FIA method is a modification of the LMG autoanalyzer (AA) method of Olafsson.[25] Olafsson's method describes the reaction of LMG with potassium periodate to form malachite green which is detected at 620 nm. The reaction is catalyzed by Mn(II). Olafsson's AA method is not sensitive enough to measure open-ocean Mn profiles.

EXPERIMENTAL SECTION

Apparatus. The flow injection manifold used for this work is shown in Figure 1. The manifold consists of two four-channel peristaltic pumps (Haake Buchler Instruments Multistaltic Pump), a pneumatically actuated eight-port valve, two 1-m and one 10-m knitted reaction coils, a column heater (Dionex), a variable-wavelength spectrophotometer (Dionex VDM-1), an integrator (Spectraphysics Model 4270), and a chart recorder. The spectrophotometer has a 6-μL flow cell with a 2.5-mm path length. The flow cell was modified by replacing the 0.3-mm inside diameter (i.d.) entrance and exit tubing with 0.5-mm i.d. Teflon tubing. Columns of 8-HOQ resin are constructed using $^1/_8$-in. (3.2-mm) i.d. thick wall tubing, as shown in Figure 2. The column ends are fabricated by placing $^1/_8$-in. (3.2 mm) outside diameter

(1) Bender, M. L.; Klinkhammer, G. P.; Spencer, D. W. *Deep Sea Res.* **1977**, *24*, 799–812.
(2) Bishop, J. K.; Fleisher, M. Q. *Geochim. Cosmochim. Acta* **1987**, *51*, 2807–2825.
(3) Heggie, D.; Klinkhammer, G.; Cullen, D. *Geochim. Cosmochim. Acta* **1987**, *51*, 1059–1070.
(4) Hodge, V.; Johnson, S. R.; Goldberg, E. D. *Geochem. J.* **1978**, *12*, 7–20.
(5) Jickells, T. D.; Church, T. M.; Deuser, W. G. *Global Biogeochem. Cycles* **1987**, *1*, No. 1, 117–130.
(6) Martin, J. H.; Knauer, G. A. *Nature* **1985**, *314*, 524–526.
(7) Lupton, J. E. *J. Geophys. Res. Lett.* **1990**, *95*, No. B8, 12829–12842.
(8) Von Damm, K. L.; Edmond, J. M.; Grant, B.; Measures, C. I. *Geochim. Cosmochim. Acta* **1985**, *49*, 2197–2220.
(9) Topping, G. *Sci. Total Environ.* **1986**, *49*, 9–25.
(10) Kingston, H. M. Interagency Energy/Environment R&D Program Report EPA-600/7-79-174; EPA: Washington, DC, 1979.
(11) Siriracks, A.; Kingston, H. M.; Riviello, J. M. *Anal. Chem.* **1990**, *62*, 1185–1193.
(12) Sturgeon, R. E.; Berman, S. S.; Willie, S. N.; Desaulniers, A. H. *Anal. Chem.* **1981**, *53*, 2337–2340.
(13) Nakayama, E.; Isshiki, K.; Sohrin, Y.; Karatani, H. *Anal. Chem.* **1989**, *61*, 1392–1396.
(14) Isshiki, K.; Tsuji, F.; Kuwamoto, T.; Nakayama, E. *Anal. Chem.* **1987**, *59*, 2491–2495.
(15) Sakai, Y.; Mori, N. *Talanta* **1986**, *33*, No. 2, 161–163.
(16) Willie, S. N.; Sturgeon, R. E.; Berman, S. S. *Anal. Chim. Acta* **1983**, *149*, 59–66.
(17) Landing, W. M.; Haraldsson, C.; Paxeus, N. *Anal. Chem.* **1986**, *58*, 3031–3035.
(18) Persaud, G.; Cantwell, F. *Anal. Chem.* **1992**, *64*, 89–94.
(19) McLaren, J. W.; Mykytiuk, A. P.; Willie, S. N.; Berman, S. S. *Anal. Chem.* **1985**, *57*, 2907–2911.
(20) Chapin, T.; Johnson, K.; Coale, K. *EOS* **1990**, *71*, No. 2, 143.
(21) Sakamoto-Arnold, C. M.; Johnson, K. S. *Anal. Chem.* **1987**, *59*, 1789–1794.
(22) Rentsch, O. M.; Werner, G. *Anal. Chim. Acta* **1983**, *147*, 267–275.
(23) Cordoba, H. M.; Viñas, C. P.; Sanchez-Pedreño, C. *Talanta* **1986**, *33*, No. 2, 135–139.
(24) Hirayama, K.; Unohara, N. *Anal. Chem.* **1988**, *60*, 2573–2577.
(25) Olafsson, J. *Sci. Total Environ.* **1986**, *49*, 101–113.
(26) Ruzika, J.; Hansen, E. H. In *Flow Injection Analysis*; Elving, P. J., Winefordner, J. D., Kolthof, I. M., Eds.; John Wiley & Sons: New York, 1981.

0003-2700/92/0364-2682$03.00/0

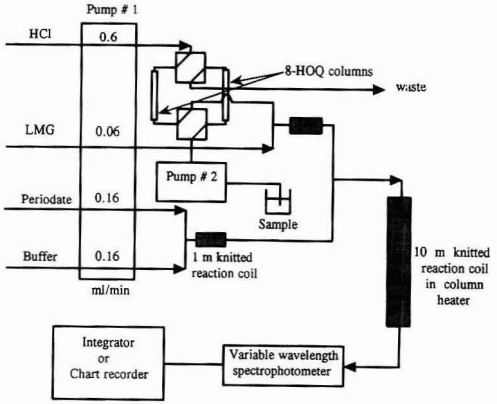

Figure 1. FIA manifold for preconcentration/LMG detection of Mn^{2+} in seawater.

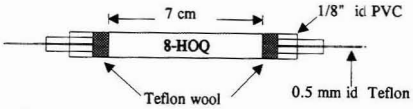

Figure 2. 8-Hydroxyquinoline column.

(o.d.) tubing inside the column tubing. This connection is secured with cyclohexanone. The $^1/_8$-in. o.d. tubing is $^1/_{16}$-in. i.d. (1.6 mm) and securely fits the outside diameter of the 0.5-mm i.d. Teflon manifold tubing. The ends are secured with cable ties. All manifold tubing is 0.5-mm i.d. Teflon tubing except for the column and the peristaltic pump tubing, which are poly(vinyl chloride) (PVC). The knitted reaction coils are fabricated by a modification to the method of Selavka et al.[27] using 0.5-mm i.d. Teflon tubing. The 10-m knitted reaction coil is placed in the column heater, and the heater is set at 50 °C. The detector is set to measure absorbance at 620 nm and the rise time is 3 s.

Reagents. Tris(hydroxymethyl)aminomethane (Aldrich ultrapure grade), potassium periodate (Aldrich ultrapure grade), sodium hydroxide (Johnson Matthey 99.996% pure), Brij-35 (Alpkem), and leucomalachite green (Aldrich) were used as received. Subboiling quartz-distilled 6 M hydrochloric acid (HCl) and glacial acetic acid were prepared from reagent grade acids. All reagents were made with subboiling quartz-distilled water (SBDW), except where noted. All plasticware was high-density polyethylene unless noted. Bottles were acid-washed by filling them ~80% full with 10% HCl (made in ≥16 MΩ deionized water). The bottles were heated to 60 °C for >18 h, removed from the oven, and inverted for >18 h at room temperature. The bottles were then rinsed three times with deionized water and twice under a laminar flow hood with SBDW. Other plasticware was acid-washed by soaking in 10% HCl at 60 °C for >24 h, followed by five rinses with SBDW. All filtration was done using acid-washed 0.2-μm polycarbonate filters (47-mm Nucleopore) on acid-washed polysulfonate filtration devices (250-mL, Nalgene). The use of 0.4-μm polycarbonate filters (47-mm Nucleopore) was also found to be sufficient. Most reagent preparation was done under class-100 laminar flow conditions to reduce contamination.

Potassium periodate (0.01 M) was prepared by dissolving 1.25 g of KIO_4 and ~0.5 g of NaOH in 500 mL of SBDW. To ensure complete dissolution, the reagent was stirred overnight using a Teflon stir bar and magnetic stirrer. The reagent was then aged for a minimum of 24 h and filtered. This reagent was found to degrade slowly over time but was useable for >3 weeks.

Ammonium acetate buffer (2 M) was prepared by placing 900 mL of 2 M acetic acid in a 1-L bottle. NH_3 was added by isopiestic distillation in a large glass desiccator[28] until the solution was pH ≥ 4.27. The pH was then adjusted to exactly 4.27 with 2 M acetic acid. A 1-mL aliquot of Brij-35 was added to 1 L of buffer. This solution was stable indefinitely. Buffers for pH optimization experiments were made by adding more NH_3 to the 2 M acetic acid. The exact pH of interest was then obtained by adding 2 M acetic acid.

HCl (0.036 M).

Leucomalachite green was prepared by adding 1 mL of 6 M HCl to 100 mL of SBDW in a dark 500-mL bottle. To this was added 60 mg of LMG. This solution was stirred slowly (so as not to entrain bubbles) for several hours. The solution was then brought up to 500-mL final volume and stirred slowly overnight. The solution was filtered prior to use. This reagent was found to be stable for at least 1 month.

Tris buffer (2 M) was prepared by placing 121 g of tris(hydroxymethyl)aminomethane in a Teflon bottle with 400 mL of SBDW. After Tris was completely dissolved, 6 M HCl was added until a pH of 7.8 was reached (~97 mL). This solution was then "cleaned" by passing it over a 100-mm 8-HOQ column at 0.25 mL/min. This reagent was stable indefinitely.

Tris buffer modifier (saturated) was prepared by adding 121 g of tris(hydroxymethyl)aminomethane into a 250-mL Teflon bottle. This mixture was brought up to 250 mL with SBDW and was stirred on a hot plate (T < 45 °C) until all of the Tris was dissolved. This reagent was allowed to cool for 24 h, and the supernatant was poured into a 250-mL Teflon bottle. Finally, 10 g of sodium hydroxide was dissolved into this solution. This reagent was found to be stable indefinitely.

pH 7.8 rinse was prepared by combining 1 mL of Tris buffer with 500 mL of SBDW. The rinse was made fresh daily.

8-Hydroxyquinoline immobilized onto vinyl polymer gel was obtained from Dr. William Landing at Florida State University. It was prepared by a modification of the procedure of Landing et al.[17]

Procedure. The manifold is set up as described previously. The peristaltic pump is run at speed 6 (speeds range from 1 to 10). This speed results in flow rates that are comparable to the rated values for the FIA manifold tubing.

The preconcentration technique is used for Mn^{2+} concentrations from 0 to 20 nmol/L. There are two columns in the system (Figure 1). Column 1 is loaded while column 2 is eluted. Seawater at pH = 7.8 ± 0.2 is loaded onto column 1 by peristaltic pump 2 at 3.7 mL/min. The effluent from column 1 is collected and its volume measured in a graduated plastic buret. In just over 4 min, 15.0 mL has passed over column 1; at this point the inlet tubing is switched to the pH = 7.8 rinse. The rinse is then pumped for ~1.5 min, causing 5.0 mL of rinse to be pumped across column 1. By actuating the valve, column 1 is placed in line with the detection system and column 2 is ready for sample loading. The procedure is repeated for column 2. The pH = 7.8 rinse that remains in the peristaltic pump tubing from the previous sample serves to rinse the acid from the second column prior to sample loading. About 4 min elapses from placing column 1 on-line to peak detection.

Stored samples had been acidified with 4 mL of 6 M HCl/L of sample. These samples were adjusted to pH = 7.8 by adding ~0.5 mL of matrix modifier to 60 mL of sample.

Standardization. Deep Pacific ocean seawater (>2000 m depth, Mn^{2+} ~270 pmol/L) was used to make standards. When the concentrations of interest were lower than 270 pmol/L, seawater effluent from the columns was collected. This low-Mn seawater was spiked and used for standards. Standard additions were used to determine the concentration of background Pacific Ocean seawater. The standard curve that was generated by these standard additions was applied to other samples. The additions were linear over the range of 0.025–0.5 nmol/L. Standardization from 0.5 to 20 nmol/L for a 15-mL sample size required a parabolic least-squares fit to the data ($Y = AX^2 + BX + C$). Samples >20 nmol/L required the preconcentration of less seawater or the use of the direct injection method. Figure 3 shows a parabolic fit for a standard curve produced at sea aboard the *RV New Horizon*.

(27) Selavka, C. M.; Jiao, K.-S.; Krull, I. S. *Anal. Chem.* **1987**, *59*, 2221–2224.

(28) Riley, J. E. *Anal. Chem.* **1978**, *50*, 541–543.

(29) Bruland, K. W. In *Chemical Oceanography*; Riley, J. P., Chester, R., Eds.; Academic Press: London, 1983; Chapter 8.

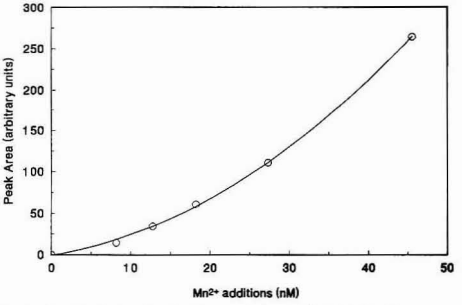

Figure 3. Parabolic standard curve ($Y = AX^2 + BX + C$).

This standard curve covers the range from 1 to 45 nmol using a 5-mL sample size.

^{54}Mn Tracer Experiments. Tracer studies were done using Pacific Ocean seawater (>2000-m depth, Mn^{2+} ~270 pmol/L) spiked with ^{54}Mn. These experiments were designed to optimize column performance. All experiments were run by flowing the desired amount of spiked seawater at a given rate across the column of interest. The column was then rinsed with DIW, and the ^{54}Mn was eluted with acid. Fractions were collected of the seawater effluent, the rinse effluent, and the acid effluent. Fractions were collected using a fraction collector (Gilson, Model 201). The ^{54}Mn in the fractions was detected using a Bicron NaI well-type detector and an EG&G Ortec 4096 multichannel analyzer.

Mg Uptake Experiments. The amount of Mg retained on the columns was determined by collecting the acid effluent during elution of the columns. Mg concentrations were determined using flame atomic absorption spectrometry.

RESULTS AND DISCUSSION

Besides the addition of the preconcentration column, other significant modifications to the autoanalyzer (AA) method of Olafsson[25] were made. These include reagent flow rates, the order of reagent mixing, and the preparation of reagents. The system was optimized for use with columns and was tested for response to pH and salinity of a Mn-spiked sample. Potential interference from other elements was also tested. Finally, the system was used to measure Mn^{2+} in seawater samples that had previously been analyzed by other methods.

System Optimization by Direct Injection. Olafsson's method[25] for AA was directly adapted to FIA using direct injection with a 150-μL sample loop. From this initial setup, modifications were made to improve the system.

Olafsson[25] added reagents to the acidified seawater carrier stream in the following order: buffer, periodate, and LMG. The modified order chosen here is shown in Figure 1, in which the acid and LMG streams merge first and this combined stream then merges with a combined periodate/buffer stream. It was observed that LMG is more soluble in an acidic medium; thus, by mixing the LMG with the acid stream first, the LMG is more likely to remain dissolved and is simultaneously diluted. By the time the buffer/periodate stream combines with the acid/LMG stream, the rise in pH is less likely to cause LMG to precipitate.

Other modifications to the FIA-adapted method of Olafsson include filtering the LMG reagent to remove particles assumed to be undissolved LMG, and aging and filtering the potassium periodate reagent. Because this latter reagent has a pH >10, any Mn contaminant in the reagents is likely to precipitate from solution. The presence of particles assumed to be either MnO_2 or reprecipitated potassium periodate had been noted on the filters. These modifications significantly decreased baseline noise and spurious signals. They also cured the frequent detector clogging that had plagued the FIA system when configured and operated according to Olafsson's method. We also changed the molarity of the buffer from 1 to 2 M, which decreased dependence on sample pH and improved baseline stability. Addition of the surfactant Brij-35 to the buffer decreased peak width and peak tailing, decreasing in turn the analysis time and increasing precision.

Table I. ^{54}Mn Recovery Studies for Sample Volume Pumped across a 60-mm Column

fraction size (mL)	tot. amt loaded (mL)	cumulative % bleed
20.5	20.5	0.7
20.5	41.0	2.3
19.0	60.0	4.4
5 (rinse)		4.9

Finally, we changed the pumping rates and ratios of the reagent streams in the flow system, so that the overall flow rate is less than that used by Olaffson. This change increased reaction time and decreased dispersion.[26] A total flow rate of 1 mL/min was desired to allow for adequate mixing in the mixing coil.[27] The relative ratio of acid to LMG was maintained. The ratio of acid to buffer was decreased to make the system less dependent on sample pH and to improve baseline stability. The ratio of acid to periodate was changed due to the initial availability of pump tubing in the laboratory. This change did not affect the system and has been maintained. It was also found that an increase in the periodate concentration did not effect sensitivity or baseline noise.

System Optimization for Preconcentration. *Column Optimization.* The 8-HOQ columns were designed to produce good analytical precision, 100% Mn^{2+} recovery, sharp peaks, and high loading rates. A balance was sought between column length and radius. Parameters were optimized using the FIA system and also ^{54}Mn retention studies. It was found that columns <3.2-mm i.d. significantly restricted sample loading, whereas columns with >3.2-mm i.d. produced broad, tailing peaks. A 40-mm column (3.2-mm i.d.) loaded at 3.7 mL/min yielded very reproducible results in preliminary work. We then used ^{54}Mn tracer studies with 20-mL samples to optimize the column further for loading rate and column length. At a flow rate of 1.6 mL/min any column >40 mm long yielded 100% retention of ^{54}Mn. At 3.7 mL/min, close to 100% retention was observed for a 60-mm column and 100% recovery was obtained from an 80-mm column.

Because the 60-mm column showed less than 100% retention, it was important to demonstrate that the column's capacity had not been exceeded. To do this, a 60-mL seawater sample was spiked with ^{54}Mn and 200 nmol/L Mn^{2+}. The seawater effluent was collected in three separate fractions (~20 mL each) to characterize potential bleed as a function of the amount of seawater loaded. The results, shown in Table I, demonstrate that this sample did not exceed the column's capacity although ~5% of the ^{54}Mn bled from the column. This test also demonstrates the feasibility of loading greater amounts of sample to improve sensitivity.

Because the preconcentration procedure requires only a 15-mL sample and the above results used ≥20 mL of sample, a 60-mm column loaded at 3.7 mL/min was assumed to yield 100% recovery. Nonetheless, a 70-mm column was chosen to ensure that 100% of the Mn would be retained for analysis.

Reaction pH. The addition of the 8-HOQ column significantly altered the system's response to pH (Figure 4). It was expected that the pH response would be the same as that for direct injection, but that was not the case. Figure 4 shows system response versus effluent stream pH for the preconcentration method, the direct injection method, and Olafsson's AA method. The pH of maximum response for each method is preconcentration pH ~ 4.15, direct injection pH ~ 4.5,

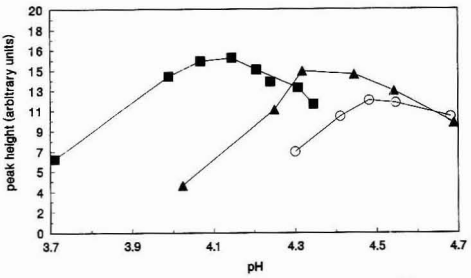

Figure 4. Response of system to effluent stream pH: (■) preconcentration peak height (cm); (▲) auto analyzer (from Olafsson[25]) peak height (recorder units × 10); (○) direct injection peak height (cm).

Table II. System Response as a Function of Salinity ($[Mn^{2+}]$ = 4 nM)

salinity (psu)	response pk ht (cm)	% of column sites occupied by Mg
34.0	14.4	97
17.0	14.5	95
8.5	13.7	95
4.4	13.4	
3.0		93
1.7	14.1	
1.0		82
0.56	15.1	86
0.27		73
0	1.5	0

and AA pH ~ 4.35.[25] In the case of AA versus direct injection the difference in response is likely to be caused by the addition of the surfactant Brij-35. On a qualitative level, it appeared that for the direct injection system at higher pH the peaks were broader and there was more peak tailing and baseline drift. It is believed that the addition of the surfactant has decreased the peak tailing and broadening, resulting in a shift of maximum response versus pH. Because AA relies on the measurement of peak height, significant peak broadening at elevated pH may have decreased the signal obtained by Olafsson, thereby resulting in a lower pH for maximum response. Other explanations for the pH offset may include the difference in the flow rates and reagent ratios and the use of an all Teflon system versus a mostly glass AA system.

The lower pH for the maximum response of the preconcentration system, compared with the direct injection system, may be an artifact of measurement. The removal of acid from the acid flow stream during the elution of the Mn^{2+} and Mg^{2+} from the column creates a local area of H^+-depleted carrier resulting in a higher pH in the area that contains the Mn^{2+} peak. A second factor that would lead to locally elevated pH is the elution of the pH = 7.8 rinse used to flush seawater from the column. Because the volume containing the actual peak is small, it was not possible to measure its pH. The pH of the bulk effluent from the spectrophotometer was measured instead. While the pH of the bulk effluent at maximum response is lower than that for direct injection, the actual pH of the flow stream in the area containing the peak may be higher and therefore closer to the pH of maximum response for the direct injection system.

System Optimization: Sample. *Salinity of Sample.* One of the main problems with the method of Olafsson[25] is the presence of a significant salinity effect. He found that at a salinity of 17.5 practical salinity units (psu) the signal produced by Mn^{2+} was reduced to 60% of that obtained at a salinity of 35 psu. The salinity response found in the direct injection method used here is similar to that found by Olafsson. When the 8-HOQ columns are added to the system, however,

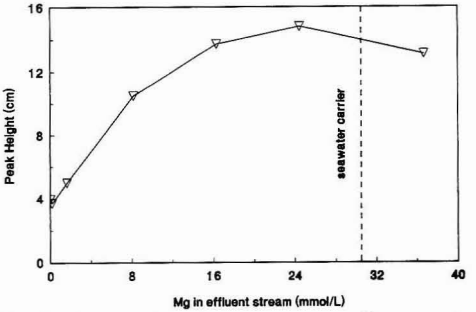

Figure 5. Response of direct injection system to Mg^{2+} concentration in the flow stream. Mg^{2+} was added to the buffer stream. If seawater (34 psu ~ 50 mmol of Mg^{2+}) was used as the carrier stream instead of SBDW, the resulting concentration of the reaction stream effluent would be 30 mmol/L in Mg^{2+}.

Table III. Response of the System to the pH of the Sample

pH	pk ht (cm)	pH	pk ht (cm)
1.77	0	7.80	13.64
4.90	3.83	8.04	13.10
6.65	12.94	8.06	13.26
7.15	13.20	8.25	12.10
7.46	12.97		

there is only a negligible salinity effect (Table II). Above a salinity of 1 psu, there is <3% variation in the system's response to a 4 nM Mn standard. Below 1 psu, the response is highly variable and significantly less at 0 psu. It was apparent that the 8-HOQ column was retaining part of the seawater matrix. To test this, the direct injection system's response was tested for the addition of the major cations in seawater, and it was found that the salinity effect for direct injection was due almost exclusively to enhancement of the signal by Mg^{2+}. Figure 5 shows the effect of Mg^{2+} additions to the direct injection system (using acidified SBDW for the acid reagent). 8-HOQ has been used to bind aqueous Mg^{2+} for quantitative analysis.[18] It is shown in Table II that above a salinity of 3 psu >93% of the column sites are occupied by Mg. When the column is eluted, both Mn^{2+} and Mg^{2+} are eluted into the analytical stream. Below this salinity, decreasing amounts of Mg^{2+} are retained by the column, and this is the likely cause in the variation observed for the response of the system at these salinities. In conclusion, the use of the 8-HOQ column has virtually eliminated any salinity effect for the system above a salinity of ~3 psu.

pH of Sample. Prior to this work, the optimal pH for transition-metal complexation with 8-HOQ and 8-HOQ immobilized on different substrates had been determined to be 8.0.[12,17] Table III shows the response of the preconcentration system to sample pH. This response agrees fairly well with the optimal pH of other workers. From these results, a pH of 7.8 ± 0.2 was chosen for sample loading for preconcentration.

Interferences. The method presented here was tested for Co, Cu, Ni, Zn, Fe, and I^- as potential interferants to the determination of a 3.6 nmol/L Mn standard in seawater (Table IV). These ions posed no significant interferences at concentrations >20× their oceanic concentrations. The Mn concentration of the standard covers the range 1–10× its background concentration in seawater.[30] Co at 1700× its background seawater concentration caused a significant reduction in signal. This concentration is unlikely to be

(30) Statham, P. J.; Burton, J. D. *Earth Planet. Sci. Lett.* **1986**, *79*, 55–65.

Table IV. Interferences from Various Elements ([Mn] = 3.5 nmol/L)

element added (concn)	ratio of concn of element added to its open-ocean concn	ratio of concn of element added to the concn of Mn^{2+} detected	% Mn^{2+} found
Co^{2+} (3.4 nmol/L)	170:1	1:1	101
Co^{2+} (34 nmol/L)	1700:1	10:1	73
Zn^{2+} (150 nmol/L)	25:1	40:1	101
Cu^{2+} (160 nmol/L)	40:1	45:1	101
Ni^{2+} (170 nmol/L)	20:1	50:1	100
Fe^{3+} (50 nmol/L)	50:1	14:1	98
Fe^{3+} (3.6 μmol/L)	3600:1	1000:1	84
NaI (88 μmol/L)	~175:1[a]	25 000:1	104

[a] Ratio of NaI to total iodine in seawater.

Table V. Determination of Mn in North Atlantic Standard Seawater-2 (NASS-2)

	concn (pmol/kg)	% error
NASS-2 day 1 $n = 6$	335 ± 5	1.5
NASS-2 day 2 $n = 4$	332 ± 18	5.42
NASS-2 day 3 $n = 4$	388 ± 10	3.0
NASS-2 certified value	404 ± 127	31.4

encountered in any uncontaminated seawater sample. Iron showed no significant interference at >50× its background oceanic concentration, a molar ratio of 50:1 Fe:Mn. At 10:1 Fe:Mn Olafsson[25] found a 7% reduction in response, while at a ratio of 50:1 he found a 57% reduction. The present method showed a 16% reduction in response at a ratio of 1000:1 Fe:Mn. This significant improvement results from both the addition of the surfactant Brij-35 and the reduction in pH of the flow stream. It was noted here that elevated Fe concentrations caused some reaction byproduct to adhere to the wall of the manifold tubing. It is assumed that less of this byproduct adheres to the wall because of the addition of Brij-35 and a lower eluant stream pH. NaI at ~175× the background concentration of iodine in seawater produced a small positive interference and a small shoulder on the front side of the peak. This level of interference is far less than that observed by Olafsson, probably because the 8-HOQ resin does not retain I^-. The shoulder seen in the present work may have been caused by residual NaI in the column.

Precision and Accuracy. To test the accuracy of this method, the Mn^{2+} concentration was determined for North Atlantic Standard Seawater-2 (NASS-2), as is shown in Table V. The method yields results that are well within 1 standard deviation of the certified value for Mn^{2+} in NASS-2. Table IV further shows a range in daily precision at the 0.35 nmol/L level from 1.5% to 5.4%.

The limit of detection of this method is calculated as 3 times the standard deviation of 10 replicates of Pacific Ocean seawater (~0.255 nmol/L ± 0.012, ~2000-m depth), yielding a detection limit of 0.036 nmol/L. A further attempt was made to resolve the limit of detection by extracting all of the Mn from seawater and making additions just above the proposed limit of detection. By so doing, a peak representing 0.02 nmol/L could be resolved from the blank. The lowest concentrations of Mn reported to date in seawater are <0.2 nmol/L.[30,31] While the present method is able to determine Mn concentrations at that level, increasing the amount of sample preconcentrated may allow for an even more precise measurement at these low levels.

(31) Landing, W. M.; Bruland, K. W. *Earth Planet. Sci. Lett.* **1980**, *49*, 45–56.

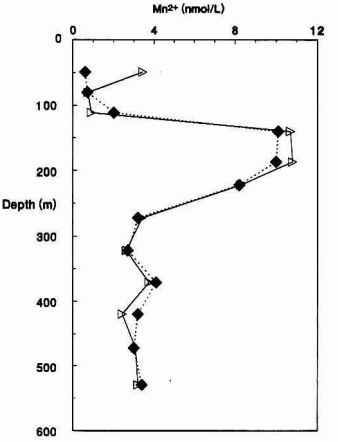

Figure 6. Hydrothermal plume profile from Macdonald Seamount: (△) Mn^{2+} determined by this method; (♦) Mn^{2+} determined by direct injection GFAAS.

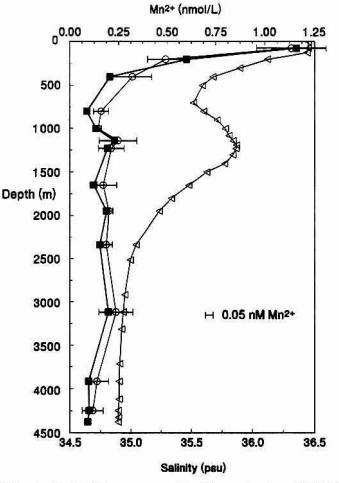

Figure 7. International Oceanographic Commission (IOC) baseline cruise profile, station 4, dissolved Mn: (■) Mn^{2+} by this method; (○) IOC average value; (△) salinity.

Application and Intercomparison. The method was validated further by determining Mn in samples that had been analyzed by other methods. The Mn profile in Figure 6 is a hydrothermal plume profile from Macdonald Seamount.[32] The Mn^{2+} concentration was determined both by direct injection graphite furnace atomic absorption spectrophotometry[32,33] and by the present method. The two methods agree fairly well. The 50-m-deep sample was most likely contaminated prior to analysis by this method. The Mn^{2+} profile shown in Figure 7 is from station 4 from the International Oceanographic Commission (IOC) baseline study and intercomparison cruise. Figure 7 compares the values for total dissolved Mn^{2+} (filtered through 0.4-μm filters and acidified with 4 mL of 6 M HCl/L), as determined using

(32) Sedwick, P. N. Personal communication.

(33) Carnrick, G. R.; Slavin, W.; Manning, D. C. *Anal. Chem.* **1981**, *53*, 1866–1872.

this method, with the average values determined by participants in the IOC exercise.[34] The two data sets agree favorably; the Mn^{2+} values determined here by FIA are generally within 1 standard deviation of the average values from the intercomparison. This profile demonstrates conclusively the ability of this method to measure background seawater concentrations accurately and precisely.

Finally, it should be reported that this method was used successfully for shipboard Mn detection aboard the *RV New Horizon* on a 30-day cruise designed to locate hydrothermal vents on the East Pacific Rise from 9 to 11° N. Measurements were complete within a few hours of sample recovery, greatly aiding the scientific objectives of this cruise.

CONCLUSIONS

Mn determination by FIA with on-line preconcentration has greatly simplified Mn determination in seawater. This method is rapid, easy to use, and selective and sensitive enough to measure Mn^{2+} concentrations in the open ocean. This method is also shown to be less expensive than methods requiring the use of a GFAAS, ICP, or ICP-MS. The total cost of instrumentation is less than $10 000 U.S. While other flow injection methods have been developed for metal ion analysis in seawater, they have either lacked sensitivity or required specialized equipment. The most successful and sensitive of the methods so far have used chemiluminescence reactions to determine Mn in seawater.[13,20] These methods in particular suffer from significant interference problems. The use of chemiluminescence detection has other disadvantages which include the relatively high price of the detectors, the need for a photomultiplier cooler to decrease instrumental background noise, and lack of other general uses for the detector. By comparison, the present method employs a spectrophotometer, which is more of a "general use" instrument.

(34) Landing, W. Personal communication.

ACKNOWLEDGMENT

The authors would like to gratefully acknowledge reviews of this work by Chris Measures, Frank Sansone, Eric DeCarlo, and two anonymous reviewers. This work was funded by the National Science Foundation, OCE87-12475 (to M.J.M.) and OCE90-20405 (to M.J.M.), the Office of Naval Research, N00014-90-J-1805 (to Francis J. Sansone), and the University of Hawaii (to M.J.M.). This work was presented in part at the American Geophysical Union 1991 Fall meeting, San Francisco, CA. School of Ocean and Earth Science and Technology Contribution No. 3016.

RECEIVED for review April 16, 1992. Accepted August 24, 1992.

Registry No. H_2O, 7732-18-5; Mn, 7439-96-5; 8-quinolinol, 148-24-3.

Characterization of a Gold Minigrid Cell for Fourier Transform Infrared Spectroelectrochemistry: Experimental vs Digitally Simulated Response

Philip B. Graham† and David J. Curran*

Department of Chemistry, University of Massachusetts, Amherst, Massachusetts 01003

A cell capable of recording Fourier transform infrared (FTIR) spectra of the region near a gold minigrid electrode surface during electrochemical experiments was developed and characterized using the ferri/ferrocyanide couple as a test system. The IR cell was of the total internal reflection type. The absorbance–time response to potential step and potential sweep experiments was investigated and the experimentally determined response compared to a digital simulation of the response at different distances from the electrode surface. This allowed the distance from the electrode surface to the point of observation to be estimated. Spectra were obtained during potential sweep experiments at sweep rates up to 200 mV/s.

INTRODUCTION

The use of infrared spectroscopy to obtain spectra of electrochemically generated species was first described more than 20 years ago.[1] One of the disadvantages of the IR region in comparison to the UV region is the inherently lower extinction coefficients and consequential need for higher concentrations of species in order to obtain a similar signal-to-noise ratio. Infrared monitoring of electrochemical processes imposes restraints on the cell design in terms of materials, path length, and solvent systems.

Most IR spectroelectrochemical cell designs can be grouped into the following five categories:

(i) Cells based on internal reflection elements that also function as electrodes.[1-3] A substantial compromise between optical and electrode properties is required.

(ii) Internal reflection cells with a thin, optically transparent electrode film deposited on the surface of the reflection element.[4-7] With this design there is an inherent compromise between the conductivity of the electrode film (usually carbon or a vapor-deposited metal) and it's optical transparency.

(iii) Cells with a gold minigrid working electrode sandwiched between two IR transparent windows,[8-14] normally sodium chloride. Construction is often difficult because of the fragile nature of the salt windows and the difficulty of obtaining a good seal. Response times are very long; typically on the order of 30 s.

(iv) Barrel–plunger type cells with a platinum disk working electrode were developed by Pons[15] and applied extensively.[16-24] Advantages of this design are the capability to "tune" the solution thickness depending on the nature of the solvent and analyte and to separately observe surface and solution species by selective polarization.

(v) A high-conversion flow-through electrode immediately prior to a conventional IR cell.[25] This method uses a flowing stream to carry the electrogenerated species from the electrode to the IR cell. In this case a trade-off between conversion efficiency and residence time in the electrode is necessary.

An older cell design by Laser and Ariel[26] is apparently unique in the literature and allows the favorable electrochemical properties of the gold minigrid electrode to be combined with an internal reflection germanium crystal. The more recent introduction and widespread use of Fourier transform instrumentation has led to a number of publications[9-13] dealing with IR spectroelectrochemistry. These all involve thin-layer cell designs for applications to a number of organic, inorganic, or organometallic systems.

One of the inherent drawbacks of electrochemical studies is the nonspecific nature of the data obtained. Current–time responses, for instance, can only by inference provide information on the reactants and products of electrochemical transformations. Reactions following electron transfer are even less easily studied. It is therefore desirable to have a means of directly observing reactions at or near the electrode surface on a time scale that allows useful information to be obtained. The cell described here is an attempt to meet this

† Present address: Eli Lilly & Co., P.O. Box 685, Lafayette, IN 47902.

(1) Marks, H. B.; Pons, B. S. *Anal. Chem.* **1966** *38* (1), 119.
(2) Yaniger, S. I.; Vidrine, D. W. *Appl. Spectrosc.* **1986**, *40* (2), 174–180.
(3) Tallant, D. R.; Evans, D. H. *Anal. Chem.* **1969**, *41* (6), 835–8.
(4) Mattson, J. S.; Smith, C. A. *Anal. Chem.* **1975**, *47* (7), 1122–25.
(5) Bancroft, E. E.; Sidwell, J. S.; Blount, H. N. *Anal. Chem.* **1981**, *53*, 1390–94.
(6) Genies, E. M.; Lapowski, M. *J. Electroanal. Chem. Interfacial Electrochem.* **1987**, *220*, 67–82.
(7) Gottesfield, S.; Ariel, M. *J. Electroanal. Chem. Interfacial Electrochem.* **1972**, *34*, 327–344.
(8) Heineman, W. R.; Burnett, J. N.; Murray, R. W. *Anal. Chem.* **1968**, *40* (13), 1974.
(9) Bullock, J. P.; Boyd, D. C.; Mann, K. R. *Inorg. Chem.* **1987**, *26*, 3084–86.
(10) Enger, S. K.; Weaver, M. J.; Walton, R. A. *Inorg. Chim. Acta* **1987**, *129*, L1–L3.
(11) Heath, G. A.; Yellowlees, L. J.; Braterman, P. S. *J. Chem. Soc., Chem. Commun.* **1981**, *6*, 287.
(12) Coombe, V. T.; Heath, G. A.; MacKenzie, A. J.; Yellowlees, L. J. *Inorg. Chem.* **1984**, *23* (21), 3423.
(13) Brisdon, B. J.; Enger, S. K.; Weaver, M. J.; Walton, R. A. *Inorg. Chem.* **1987**, *26*, 3340–44.
(14) Kadish, K. M.; Mu, X. H.; Lin, X. Q. *Electroanalysis* **1989**, *1*, 35–41.
(15) Pons, S.; Davidson, T.; Bewick, A. *J. Electroanal. Chem. Interfacial Electrochem.* **1982**, *140*, 211–16.
(16) Pons, S.; Davidson, T.; Bewick, A. *J. Am. Chem. Soc.* **1983**, *105*, 1802–05.
(17) Pons, S.; Datta, M.; McAleer, J. F.; Hinman, A. S. *J. Electroanal. Chem. Interfacial Electrochem.* **1984**, *160*, 369–76.
(18) Foley, J. K.; Pons, S. *Anal. Chem.* **1985**, *57* (8), 945A–956A.
(19) Foley, J. K.; Pons, S.; Smith, J. J. *Langmuir* **1985**, *1*, 697–701.
(20) Korzeniewski, C.; Pons, S. *J. Vac. Sci. Technol. B* **1985**, *3* (5), 1421–24.
(21) Daschbach, J.; Heisler, D.; Pons, S. *Appl. Spectrosc.* **1986**, *40* (4), 489–91.
(22) Bkhoo, S.; Foley, J. K.; Korenziewski, C.; Pons, S. *J. Electroanal. Chem. Interfacial Electrochem.* **1987**, *233*, 223.
(23) Bewick, A.; Pons, S.; Kunmatsu, S.; Russell, J. W. *J. Electroanal. Chem. Interfacial Electrochem.* **1984**, *160*, 47.
(24) Bewick, A.; Pons, S. *Advances in Infrared and Raman Spectroscopy*; Wiley-Hayden: London, U.K., 1985.
(25) Clark, B. R.; Evans, D. H. *J. Electroanal. Chem. Interfacial Electrochem.* **1976**, *69*, 181.
(26) Laser, D.; Ariel, M. *J. Electroanal. Chem. Interfacial Electrochem.* **1973**, *41*, 381.

0003-2700/92/0364-2688$03.00/0

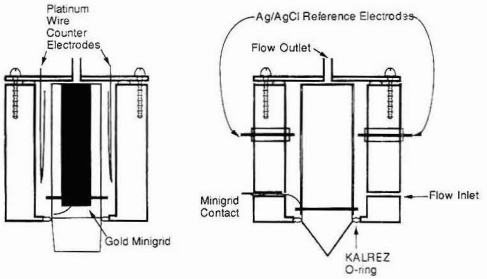

Figure 1. Vertical cross section of cell.

objective and to overcome some of the difficulties associated with other spectroelectrochemical cell designs. The ferro/ferricyanide couple in aqueous media is used as a test system with a gold minigrid electrode on a ZnSe prism in a FTIR spectrometer.

EXPERIMENTAL SECTION

Construction of the Infrared Cell. The main body of the cell was constructed of Teflon and was modeled after a commercially available stainless steel FTIR cell: PLC-19M, Harrick Scientific Co., Ossining, NY. It was machined to fit the base plate of Harrick nine reflection prism liquid cell. The prism was 45 mm long and 9 mm square. The body was secured to the base plate by means of four hexagonal-key screws. Four standard flow line fittings were drilled in the body of the cell so flow lines, reference electrodes, and the contact to the gold minigrid could be secured. The base of the zinc selenide prism (Harrick Scientific) was sealed with an O-ring between the Teflon body and base plate. The top cover was secured with eight cross-head screws and sealed by means of an O-ring (Viton). This material is unsuitable for use with some organic solvents such as THF, in which case Kalrez (Du Pont) O-rings could be used.

The manufacturer (Buckbee-Mears) supplies the gold minigrid as a sheet packed between two polycarbonate sheets. Leaving this assembly intact, a strip of gold minigrid (7.0 cm × 0.7 cm) was cut out using an Exacto knife. The gold minigrid could be easily positioned on the prism surface when moistened with either water or acetone. Acetone was preferred as it would quickly evaporate leaving the minigrid in place. A Teflon clip, constructed locally (9 mm × 11 mm), was slid from the bottom of the prism over the gold minigrid by squeezing its oversize sides. Then a folded 0.1-mm-diameter gold wire was placed between the minigrid and Teflon clip. A small Teflon wedge on one of the unused prism faces secured this clip in place. The gold wire was threaded through one of the lower flow line fittings for later contact. The prism with minigrid in place was lowered into the Teflon body and the smaller lower O-ring placed around the bottom of the prism. The base plate was then secured and the seal checked for leaks. The minigrid contact wire was threaded through a 0.3-mm-i.d. Teflon flow line inside a male flow line fitting. A small piece of 0.8-mm-i.d. tygon tubing sealed the flow line to the copper contact wire. The remaining lower threaded fitting was used for the flow inlet to the cell. The two upper threaded fittings secured the silver/silver chloride reference electrodes which were prepared by coating the silver wires in aqua regia for 10 min until a coating of silver chloride was visible. The silver wires had previously been partially coated with heat shrink Teflon and force-fit into a standard male flow line connection (1/4-28, Ranin Instrument Co. Inc., Woburn MA). The two reference electrodes were shorted together, as were the two counter electrodes. Vertical cross-section views of the assembled cell are given in Figure 1 to show adjacent sides of the prism.

After securing the top plate and exit flow line fitting the cell was checked for leaks by pumping water through the cell at about 5 mL/min. Leaking fittings were reflanged or repaired with Teflon tape when necessary.

Data Collection. Sequential collection of spectra can be achieved with the Mattson Cygnus 100 FTIR spectrometer, either by using the software for gas chromatography–FTIR or by collecting data directly into the spectrometer's on-board buffer. The latter was used when high rates of data acquisition were required. Data collection time and the interval between spectra were determined by monitoring of the mirror position using an oscilloscope.

Operation of the Cell. The cell, once assembled, was mounted on adjustable rails in the spectrometer. Electrical contacts and flow line connections were made through holes drilled in the cell compartment cover. The holes were light-proofed using appropriate rubber grommets. The MCT or TGS detector output was optimized by adjusting the cell position while displaying the real-time interferogram. When using the MCT detector the iris was adjusted to an indicated value of 0% which, with a wire gauze attenuator placed over the source outlet to the sample compartment, gave a peak-to-peak output voltage of around 13 V. This is close to the maximum acceptable value before saturation of the detector occurs.

For initial studies, the TGS detector was used; however, the poor sensitivity and long response time (maximum mirror velocity = 0.63 cm s^{-1}) limited its application to bulk electrolysis and very slow (2 mV s^{-1}) potential sweeps. The MCT detector could be very simply installed in the spectrometer allowing mirror velocities up to 2.53 cm s^{-1}.

A Masterflex pump (Cole-Parmer) was used to introduce ferricyanide solutions into the cell without the need to break the spectrometer purge. Between runs the cell was emptied and then refilled with fresh solution.

A Princeton Applied Research Model 174 potentiostat and Fisher Recordall Model 4520 strip chart recorder were used to conduct the electrochemical part of the experiment.

Digital Simulation of Response. A program to digitally simulate the concentration–time behavior at different distances from the surface of a planar electrode was written in turboPascal and could be executed on an IBM or IBM-compatible personal computer. The program listing is available from the authors.

The program is based on a model of diffusion between "boxes" of solution.[27] Essentially the solution is divided into segments of size X extending in a perpendicular direction away from the electrode surface. The concentration at the surface, in the first segment, can be calculated from the electrode potential using the Nernst equation. Various procedures can be selected to vary the surface concentration to mimic a particular electrochemical technique. The program selects a value for the variable T, the time interval between successive calculations of the concentration–distance profile. An important assumption of this model is that diffusion during the time interval T can only occur between neighboring segments, which means the model diffusion coefficient (D_M), as defined in eq 1 below, must have a value less than 0.5.

$$D_M = (D_0 T)/(X)^2 \quad (1)$$

D_0 is the diffusion coefficient for ferricyanide. In this program T is calculated based on a value of 0.45 for D_M. A result of this restriction is that for $X = 1$ μm, T must be approximately 0.7 ms. Another value that is set is "maxdist" which represents the number of segments that are needed to completely encompass the diffusion layer. This is calculated according to eq 2

$$\text{maxdist} = (4D_0 t)^{1/2}/X \quad (2)$$

Since a very large number of calculations are performed and much data is produced, only a fraction of that data is saved in the output file. A two-dimensional array with three rows is used to calculate successive concentration–distance profiles. The first two rows store the present and most recent profiles, while the third can be used for storing the derivative data (if needed) before writing to an output file.

(27) Kissinger, P. T.; Heineman, W. R. *Laboratory Techniques in Electroanalytical Chemistry*; Marcell Dekker: New York, 1984; Chapter 16.

Table I. Diffusion Profile Averaging Times for Different Grid Sizes

no. of wires/in.	hole size[a] (μm)	wire size[a] (μm)	diffusion averaging[b] time (s)
333	66	10	0.91
1000	18	7.6	0.065
2000	7.6	5.0	0.012

[a] Buckbee–Mears information sheet. [b] Calculated using eq 3.

RESULTS AND DISCUSSION

Potential Step Experiments. The dimensions of the three grid sizes investigated are shown in Table I. The diffusion profile averaging time is the time necessary for the developing diffusion layers from neighboring wires to coalesce. At this point the grid behaves as a planar electrode of somewhat diminished surface area. For the 1000 and 2000 lines (wires) per inch grids this process is rapid on the time sacle of these experiments and during potential step or potential sweep experiments the electrode essentially behaves in a planar manner. If the electrode to prism distance is 15 μm (a typical value for the 2000 lines per inch grid (lpi)) then the time (t) for the diffusion layer thickness (δ) to extend 15 μm will be approximately 150 ms based on eq 3. By this time,

$$\delta = (2Dt)^{1/2} \tag{3}$$

however, significant changes in concentration of reactant and product will have occurred. The much larger holes of the 333 lpi grid suggest that even if perfect contact between the grid and the prism was achieved a considerable amount of the region of observation would be at least 20 μm from the electrode surface, thereby significantly reducing the speed of the response. As will be discussed later, zero clearance is not achieved in practice so that the distance involved is even greater.

An assumption of the digital simulation model is that the wall of the cell is effectively at an infinite distance from the electrode surface. However it was possible that the behavior of the absorbance–time response might correspond to a thin-layer situation, as exists between the prism and electrode. A digital simulation of the response to a potential step in a thin-layer cavity was conducted. The results show rapid achievement (under 2 s) of maximum absorbance, at distances less than 30 μm. The experimental data is not in good agreement with the thin-layer model, but is well represented by the semiinfinite linear diffusion case. This is due to access to the bulk of solution by the layer of solution between the prism and grid, through what is essentially a porous electrode. The electrode is only 3–5 μm thick. By comparison the average distance to the walls of the cell from the electrode is on the order of 3000 μm.

The chief effect of reducing the grid size is to reduce the average distance of the point of observation from the electrode surface. This in turn leads to a faster absorbance response to a potential step into the diffusion limited region. Figure 2 shows the normalized absorbance response for three grid sizes during the 20 s immediately following a potential step into a region where reduction of ferricyanide is diffusion limited. The absorbance reached after a set time is characteristic of the distance from the electrode to the point of observation. This is illustrated in Figure 3 which shows the calculated absorbance-time response, at different distances from the electrode surfaces, for a potential step to a diffusion limiting potential. These curves are obtained from eq 4 below

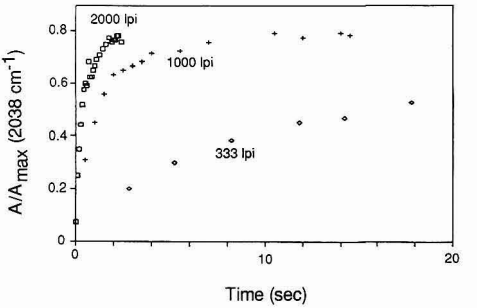

Figure 2. Absorbance response to potential step for three grid sizes.

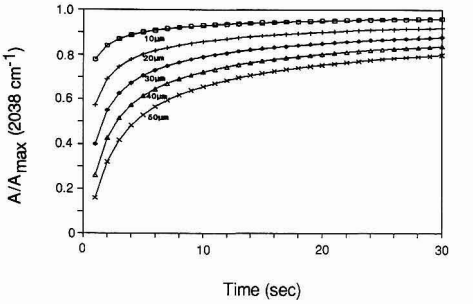

Figure 3. Simulated response at 10, 20, 30, 40, and 50 μm from the electrode surface after a potential step.

where x is the distance away from the electrode surface, t is the time since the potential step, and c_o^b is the bulk concentration of product. The error function in eq 4 was approximated using a McLaurin series[28] and the necessary number of iterations performed to achieve convergence.

$$C_o(x,t) = C_o^b \mathrm{erf}[x/2(D_o t)^{1/2}] \tag{4}$$

To confirm that the digital simulation program was performing satisfactorily, it was used to generate concentration–time response curves for a simple potential step experiment. These curves were indistinguishable from those produced using eq 4. The digital simulation data was calculated to four significant figures, and comparison with data from eq 4 (calculated to six significant figures) indicated no differences between the two data sets. This is an important test as algorithims to describe the concentration–distance–time profile in more sophisticated electrochemical experiments are exceedingly complex.[27]

Since the response curve is characteristic of the distance from the electrode to the point of observation, it is possible to estimate how close the minigrid is to the prism surface by means of curve fitting. To obtain a normalized concentration (or absorbance)–time curve it is necessary to know the maximum possible absorbance (A_{max}). This is the absorbance if all of the reactant is converted into product in the region of observation. A_{max} can be determined readily with the ferrocyanide ($\nu_{CN} = 2038\ cm^{-1}$)/ferricyanide ($\nu_{CN} = 2116\ cm^{-1}$) couple as both ions are stable. If the reduction of 5 mM ferricyanide solution is under study, the cell is mounted in the spectrometer and filled with the product, a 5 mM solution of ferrocyanide. The absorbance at 2038 cm^{-1} is measured, and by correcting the absorbance for the area of the prism not covered by the grid, A_{max} can be calculated (eq 5). The correction, shown below, is achieved by multiplying the

(28) Boas, M. L. *Mathematical Methods in the Physical Sciences*; John Wiley & Sons: New York, 1983.

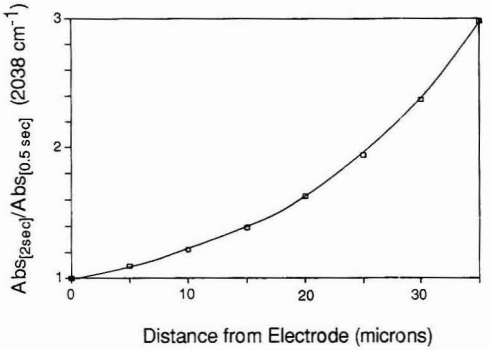

Figure 4. Ratio of absorbance at 2 and 0.5 s after a potential step, as a function of distance from the electrode surface.

$$A_{max} = [A(soln)](electrode\ area)/(prism\ area) \quad (5)$$

absorbance of the ferrocyanide solution by the proportion of the prism surface covered by the minigrid. The area of the minigrid is 4.9 cm^2 while the area of the prism exposed to the solution is 6.75 cm^2. This value of A_{max} can also be obtained during experiments on a long time scale. A_{max} should be determined for each installation of the grid and for each time the cell is aligned in the spectrometer. For a 5 mM solution of ferrocyanide the value of A_{max} (calculated from the absorbance at 2038 cm^{-1}) was found to vary between 0.012 and 0.015 absorbance units, depending on cell alignment during installation.

Another way in which as estimate of the prism–minigrid distance can be made is to calculate the ratio of the absorbance 2 s after the potential step to the absorbance after just 0.5 s. At the surface this ratio would be unity as the surface concentration of product is at its maximum value for all times after the step. This ratio increases as the point of observation is moved further from the electrode surface (Figure 4). The principle advantage of this approach is that it is not necessary to know A_{max} in advance.

Figure 5 shows data points for a potential step from +350 to 0 mV, at a 2000 lpi grid, using 5 mM ferricyanide and monitoring the formation of ferrocyanide at 2038 cm^{-1}. Spectra were collected at 80-ms intervals. The solid line represents the predicted response at 15 μm from the electrode surface. The ratio of the absorbance at 2 s to the absorbance at 0.5 s is $0.0089/0.0069 \approx 1.3$. From Figure 4 a prism–minigrid distance of 13 μm is predicted. The prism–minigrid distances obtained from curve fitting and the absorbance ratio method, for 1000 and 2000 lpi grids, are shown in Table II.

The digital simulation of the response curve for a potantial step experiment provides a convenient method to estimate the electrode prism distance in the cell. As was noted earlier the grid could be positioned on the prism using acetone or water. The presence of the fluid lubricates the grid and allows it to be readily positioned. Because a layer of fluid must exist between the grid and prism during operation, zero clearance between the grid and prism is not likely to be achieved.

Linear Potential Sweep. Figure 6 shows the digital simulation of the change of concentration (and absorbance) during a 20 mV s^{-1} linear potential sweep for a reversible system at the electrode surface and at selected distances from the surface. As the point of observation is moved away from the electrode surface the slope of the rising part of the curve decreases as does the absorbance achieved at a given potential. The degree to which this distortion occurs depends on the

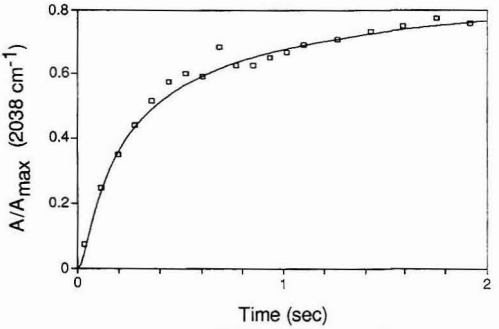

Figure 5. Potential step at a 2000 lpi grid compared to a simulated response at 15 μm from the electrode surface.

Table II. Estimation of Electrode–Prism Distance

no. of wires/in.	observation distance from curve fitting (μm)	observation distance from absorbance ratio[a] (μm)
333	90	
1000	26	22
2000	15	13

[a] Determined from Figure 4. Data not available for 333 wires/in. grid.

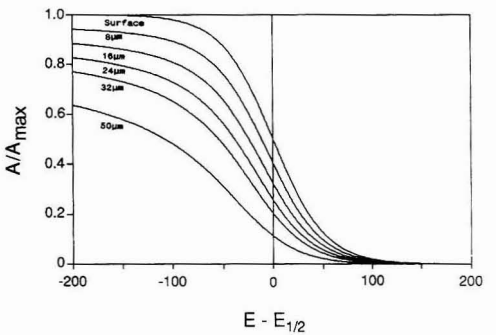

Figure 6. Digital simulation of 20 mV/s potential sweep at 0, 8, 16, 24, 32, and 50 μm from the electrode surface.

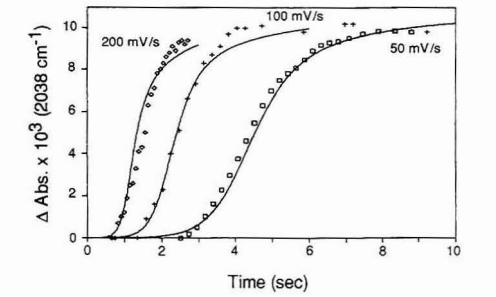

Figure 7. Potential sweep data at a 2000 lpi grid compared to digital simulation at 15 μm from the electrode surface.

potantial sweep rate as well as the distance from the electrode surface.

The data points in Figure 7 show the experimentally obtained response to a 50, 100, and 200 mV s^{-1} sweep. The solid lines are the simulated response at a distance of 15 μm

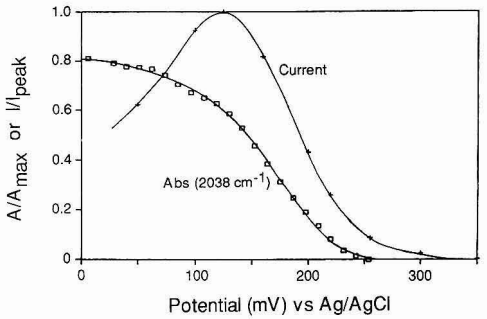

Figure 8. Normalized absorbance–potential and current–potential data for a 50 mV/s sweep.

from the electrode surface. This distance was determined from a potential step experiment conducted immediately afterwards.

Figure 8 shows the absorbance and current response to a 50 mV s^{-1} potential sweep. This figure shows that the absorbance does not level out until past the peak current. This is to be expected since the normalized surface concentration of product at this potential is 0.75. Ninety-five percent conversion to product at the surface is not obtained until approximately 75 mV past the peak potential.

Cyclic Potential Sweep. The absorption–potential response for a 2 mV/s cyclic sweep at a 333 lpi minigrid (Figure 9a) and a 2000 lpi grid (Figure 9b) show significantly different responses. This is expected as the concentrations observed for the 2000 lpi grid are close to the surface value at a distance of 15 μm, particularly during a slow potential sweep experiment. In other words, electrolysis is essentially complete in the region of observation. For the 333 lpi grid the prism–electrode distance was about 90 μm so the absorbances do not reflect the surface concentrations well.

The forward sweep data from Figure 9b were used to produce an optical analog[26] of the Nernst plot with a slope of 64 mV/decade, which is close to the expected value of 59 mV/decade for a reversible one-electron transfer. In this case the ratio of the concentration of oxidized to reduced species at the electrode surface is determined from the observed absorbance (A) and the maximum absorbance (A_{max}).

The response of the cell to potential sweep experiments depends on the prism electrode distance and the sweep velocity. At slow sweep rates and small prism–electrode distances the observed concentrations are a good indication of the electrode surface concentration. Increasing the sweep rate or prism–electrode distance results in a shallower absorbance–potential profile.

CONCLUSIONS

By placing a gold-minigrid electrode on the surface of an infrared internal reflection element a cell can be constructed

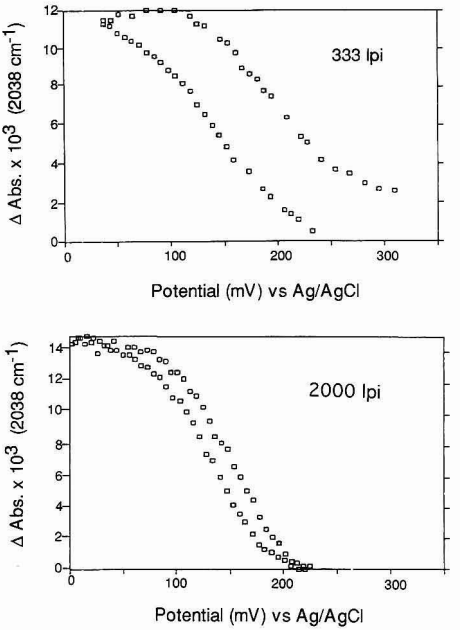

Figure 9. Cyclic sweep at 2 mV/s: (top) 333 lpi grid, (bottom) 2000 lpi grid.

that allows observation of the region of solution close to the electrode surface. This cell design combines the advantages of a low-resistance electrode with the favorable optical properties of zinc selenide. Relatively high (200 mV/s) scan rates were achievable due to the low electrode and cell resistance. Vapor-deposited gold film electrodes are not capable of this performance and cannot be easily replaced in the event of fouling. This design allows easy replacement of the electrode.

The absorbance–time response is very dependent on the distance from the electrode to the point of observation. This relationship was investigated using digital simulation of the absorbance response and by experimental observation. The shorter this distance the closer the absorbance response mimics the electrode surface concentration. When the 2000 lines per inch grid was used it behaved as though the distance from the electrode to the surface of the infrared crystal was around 15 μm.

RECEIVED for review April 23, 1992. Accepted August 13, 1992.

Registry No. Gold, 7440-57-5.

Equivalence of Staircase and Linear Sweep Voltammetries for Reversible Systems Including Conditions of Convergent Diffusion

Uruthirapasupathy Kalapathy and Dennis E. Tallman*

Department of Chemistry, North Dakota State University, Fargo, North Dakota 58105-5516

The question of the equivalence of staircase (SCV) and linear sweep (LSV) voltammetries for reversible electron transfer is reexamined using highly accurate numerical computation. When diffusion is rectilinear, such as for macroelectrodes or for microelectrodes at very high sweep rates, the shape of the SCV is rather strongly dependent on α, the fraction of the way along the step at which the current is sampled. The closest agreement with LSV under such conditions appears to be for α equal 0.30. When diffusion is convergent, such as for microelectrodes at low to moderate sweep rates, the shape of the SCV is much less dependent on α and a range of values can yield LSV equivalent voltammograms, although $\alpha = 0.30$ would provide the best equivalence over all sweep rates.

INTRODUCTION

Staircase voltammetry (SCV) may eventually replace linear sweep voltammetry (LSV) for routine diagnostic and analytical measurements. Indeed, modern computer-based electrochemical instrumentation employs a digital-to-analog converter to permit direct computer control of electrode potential.[1] Such instruments necessarily change electrode potential in discrete steps, the magnitude of the step being governed by such considerations as voltammogram resolution (or definition) and sweep rate. Since with SCV it is often possible to sweep through the desired potential range using only 50–100 steps, very high sweep rates can be achieved, even with computer-based instrumentation.[1] Furthermore, SCV is better able to discriminate against charging current than is LSV since the actual current measurement is made under potentiostatic conditions.[2,3]

As pointed out by Osteryoung and co-workers,[4] the slow acceptance of SCV is probably a result of the additional complexity associated with quantitatively describing the voltammogram. Unlike LSV for which the response is determined uniquely by the sweep rate, V (assuming the initial potential is chosen at zero current), the SCV response is determined by three parameters: ΔE, the step height; τ, the width or duration of each step (note that sweep rate $V = \Delta E/\tau$); and α, the fraction of the way along the step at which the current is measured.[5,6] SCV at microelectrodes (having at least one dimension on the order of micrometers) offers even greater challenges since convergent diffusion can lead to the additional dependence of voltammetric response on electrode geometry.[7] These challenges can and will be met with increasingly sophisticated computational strategies, a few of which are already beginning to appear.[7-9]

A question first raised by Reilley et al.[10] and also by Perone et al.[6] and subsequently investigated in some detail by Osteryoung and co-workers[4,11-13] is the extent to which the voltammetric response from the discrete technique SCV can be made equivalent to that from the continuous technique LSV. Such equivalence, established through proper choice of the SCV current sampling parameter, α, would facilitate direct comparison of voltammograms obtained by each of the two techniques as well as permit voltammograms obtained by SCV to be interpreted using the wealth of theory developed for LSV. There is no a priori reason to expect that an exact equivalence between SCV and LSV should exist, except in the limit $\Delta E \rightarrow 0$ whereupon the staircase waveform collapses to a linear ramp and the two techniques become identical. However, there does appear to be a very close correspondence between the two techniques for particular values of α.[6,10,11]

Perone and co-workers[6] have suggested an α of 0.3 results in nearly equivalent SCV and LSV voltammograms. The first step of the staircase waveform used in their work occurs at $T = 0$ and has the same amplitude (ΔE) as each succeeding step. Their computation, based on the theory of Christie and Lingane,[3] uses a summation formula which is equivalent to a limiting form of the convolution approach we use in this paper.[9] Osteryoung and co-workers[11] suggest an α of 0.25 using a Walsh series approximation for a staircase potential profile which begins with a first step at $T = 0$ having half the amplitude ($\Delta E/2$) of each succeeding step. For further comparison, the early treatment of Christie and Lingane employed a staircase potential function with a first-step amplitude of zero (i.e., the first step is delayed by τ).[3] The nature of the first step is of little consequence when the voltammogram is initiated from a potential of zero current and is displayed in the form of current versus potential. However, a display of current versus time would exhibit a small dependence on the nature of the first step.

In related work, a theoretical study of linear sweep and staircase anodic stripping voltammetry by Stojek and co-workers[14] found that $\alpha = 0.35$ provides the best agreement in the vicinity of the peak maximum, with lower values of α

* To whom correspondence should be addressed.

(1) Tallman, D. E.; Shepherd, G.; MacKellar, W. J. *J. Electroanal. Chem. Interfacial Electrochem.* **1990**, *280*, 327.
(2) Barker, G. C. *Advances in Polarography*; Longmuir, I. Si., Ed.; Pergamon Press: New York, 1960; p 144.
(3) Christie, J. H.; Lingane, P. J. *J. Electroanal. Chem. Interfacial Electrochem.* **1965**, *10*, 176.
(4) Seralathan, M.; Osteryoung, R. A.; Osteryoung, J. G. *J. Electroanal. Chem. Interfacial Electrochem.* **1987**, *222*, 69.
(5) Zipper, J. J.; Perone, S. P. *Anal. Chem.* **1973**, *45*, 452.
(6) Miaw, L-H. L.; Boudreau, P. A.; Pichler, M. A.; Perone, S. P. *Anal. Chem.* **1978**, *50*, 1988.
(7) Kalapathy, U.; Tallman, D. E.; Hagen, S. *J. Electroanal. Chem. Interfacial Electrochem.* **1992**, *325*, 65.
(8) Aoki, K.; Tokuda, K.; Matsuda, H.; Osteryoung, J. *J. Electroanal. Chem. Interfacial Electrochem.* **1986**, *207*, 25.
(9) Cope, D. K.; Tallman, D. E. *J. Electroanal. Chem. Interfacial Electrochem.* **1991**, *303*, 1.
(10) Suprenant, H. L.; Ridgway, T. H.; Reilley, C. N. *J. Electroanal. Chem. Interfacial Electrochem.* **1977**, *75*, 125.
(11) Seralathan, M.; Osteryoung, R.; Osteryoung, J. *J. Electroanal. Chem. Interfacial Electrochem.* **1986**, *214*, 141.
(12) Bilewicz, R.; Osteryoung, R. A.; Osteryoung, J. *Anal. Chem.* **1986**, *58*, 2761.
(13) Stojek, Z.; Osteryoung, J. *Anal. Chem.* **1991**, *63*, 839.

0003-2700/92/0364-2693$03.00/0

providing the best agreement in prepeak regions of the voltammogram. The optimum value of α appeared to depend little on the thickness of the mercury phase. An experimental study of linear sweep and staircase voltammetry of adsorbed species by Stojek and Osteryoung[13] revealed a strong dependence of the staircase voltammograms on α, and an optimum α was not suggested. However, data presented for the reduction of adsorbed midazolam indicated a possible equivalence for $^1/_4 < \alpha < {}^1/_2$.[13]

Work currently in progress in our laboratory involves staircase and cyclic staircase voltammetry at microelectrodes, with emphasis on electrode geometries having high perimeter-to-area ratio such as the band and the ring. These investigations have led us to reassess the conditions for which SCV and LSV become equivalent, or nearly so, for reversible systems, under both rectilinear and convergent diffusion conditions. In this paper we provide the computational background for staircase voltammetry at microelectrodes and provide evidence, based on accurate (0.1%) numerical calculations, that the best equivalence between SCV and LSV occurs when the current is sampled at $\alpha = 0.30$. In this work, as in the preveious work cited above, the influence of charging current is not considered. For SCV at microelectrodes, the small (rc) cell time constant results in rapid decay of the charging current, and the results reported here should have direct practical application.

COMPUTATIONAL METHODS

For a reversible electron transfer reaction of the type

$$O + ne^- \Leftrightarrow R$$

the current at any arbitrary electrode geometry in response to any arbitrary potential modulation is given by[8,9]

$$i_R(t) = \frac{d}{dt}\int_0^t i_d(t-u)\theta(u)\,du \tag{1}$$

where $i_R(t)$ is the time- (and potential-) dependent reversible current in response to a potential–time function $\theta(t)$, and $i_d(t)$ is the transient diffusion-limited current at the electrode in response to a large potential step. Equation 1 was derived with the assumption that mass transport within the cell occurs only by semiinfinite (convergent) diffusion and also that no ohmic loss occurs in the cell. The only other restriction on the use of eq 1 is that the diffusion coefficients of the oxidized and reduced species be equal ($D_O = D_R = D$). In this work we assume only species O is present initially and eq 1 is written accordingly, but extension of the computation to cases where both O and R are initially present is straightforward.[9]

All variables in eq 1 are dimensionless and have the following definitions in terms of physical variables:

$$i(t) = I(T)/nFDC^*L \tag{2a}$$

$$t = DT/L^2 \tag{2b}$$

$$\theta(t) = (1 + \exp[nf(E(T) - E^{\circ\prime})])^{-1} \tag{2c}$$

where $I(T)$ is physical current as a function of physical time T, D is the diffusion coefficient (for both O and R), C^* is the bulk concentration of O, and $E(T)$ is the time-dependent physical potential, with $E^{\circ\prime}$, n, and $f = F/RT$ all having their conventional electrochemical meanings. L is a characteristic electrode length, taken in this work to be $(A/\pi)^{1/2}$ where A is the physical electrode area (thus, for a disk electrode, L equals the electrode radius). This choice for L leads to area-normalized variables,[9] permitting direct comparisons of current densities at electrodes of differing geometry.

For convergent diffusion, the values of $i_d(t)$ used in the numerical solution of eq 1 were computed using the integral equation method (IEM)[15] and were numerically accurate to within 0.1%. Details of the IEM as applied to various electrode geometries have been published elsewhere.[15-18] As discussed previously,[7] the IEM offers particular advantages for generating the values of $i_d(t)$ used in the numerical solution of eq 1. Nonetheless, any suitably accurate method could be used to obtain $i_d(t)$, such as a finite difference method or perhaps even experiment. For rectilinear diffusion, the values of $i_d(t)$ used in the numerical solution of eq 1 were computed using the dimensionless form of the Cottrell equation

$$i_d(t) = (\pi/t)^{1/2} \tag{3}$$

with $i_d(t)$ and t defined as in eq 2.

Linear Sweep Voltammetry. For linear sweep voltammetry at a sweep rate V starting from an initial potential E_I and sweeping negatively, the potential (E) as a function of time (T) is given by

$$E(T) = E_I - VT \tag{4}$$

In dimensionless form eq 4 becomes

$$e(t) = e_i - bt \tag{5a}$$

with

$$e(t) = nfE(T) \tag{5b}$$

$$e_i = nfE_I \tag{5c}$$

and

$$b = nfVL^2/D \tag{5d}$$

where b is a dimensionless sweep rate for electrodes of constant area (hence, constant L^2).

The potential–time function $\theta(t)$ in eq 2c can now be written in the form[7]

$$\theta(t) = (1 + a\exp(-bt))^{-1} \tag{6a}$$

where a is a function of the dimensionless initial potential (e_i) relative to the formal potential ($e^{\circ\prime} = nfE^{\circ\prime}$) and is given by

$$a = \exp[nf(E_I - E^{\circ\prime})] = \exp[e_i - e^{\circ\prime}] \tag{6b}$$

All LSVs and SCVs in this paper were computed using an initial potential $e_i - e^{\circ\prime} = 8.0$, corresponding to $a = 2981$.

The numerical integration and differentiation of eq 1 were carried out as previously described,[7] with the exception that 1600 time intervals (or points) were used in the numerical solution to reduce numerical error associated with discretization of the linear sweep to less than 0.1%.[7] The computer program for solving the linear sweep case (originally written in WATFOR-87 FORTRAN) was rewritten and compiled in QuickBASIC, resulting in a much faster run-time module. The computation of a 1600 point voltammogram from a disk file of $i_d(t)$ values required less than 3 min on a 25-MHz 80386-based personal computer with a 80387 math coprocessor.

(14) Penczek, M.; Stojek, Z.; Buffle, J. *J. Electroanal. Chem. Interfacial Electrochem.* **1989**, *270*, 1.

(15) Coen, S.; Cope, D. K.; Tallman, D. E. *J. Electroanal. Chem. Interfacial Electrochem.* **1986**, *215*, 29.

(16) Cope, D. K.; Scott, C. H.; Kalapathy, U.; Tallman, D. E. *J. Electroanal. Chem. Interfacial Electrochem.* **1990**, *280*, 27.

(17) Cope, D. K.; Tallman, D. E. *J. Electroanal. Chem. Interfacial Electrochem.* **1990**, *285*, 79.

(18) Cope, D. K.; Scott, C. H.; Tallman, D. E. *J. Electroanal. Chem. Interfacial Electrochem.* **1990**, *285*, 49.

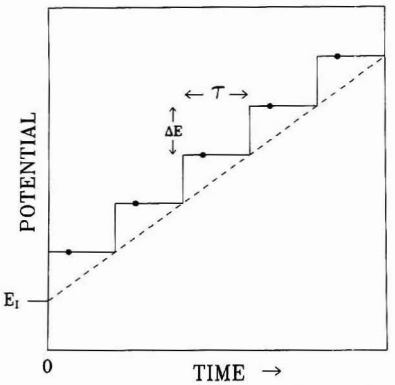

Figure 1. The potential–time waveform for staircase voltammetry (solid line, illustrating five steps, each of height ΔE and duration τ) and linear sweep voltammetry (dashed line, having equivalent sweep rate $V = \Delta E/\tau$ and identical initial potential, E_I). The point on each step of the staircase waveform denotes the time at which current is measured and corresponds to a current sampling parameter α of 0.30 (see text).

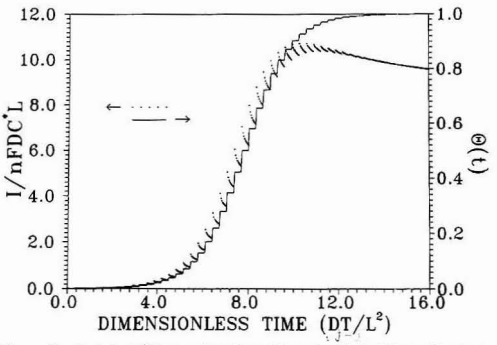

Figure 2. A plot of $\theta(t)$ as a function of time (solid line) for a 50-step staircase waveform having $a = 2981$, $\delta e = 0.32$, and $\lambda = 0.32$ (see eq 9 and text). The points represent the computed current for a ring electrode having $\gamma = 10$ (see text). Eight values of current were computed for each step at intervals of $^1/_8$ the step duration ($\alpha = n/8$ for $n = 1$–8).

Staircase Voltammetry. Starting from an initial potential E_I and stepping negatively with N steps, each step of size ΔE and duration τ, the staircase potential (E) as a function of time (T) is expressed by

$$E(T) = E_I - \Delta E \sum_{n=1}^{N} S_0\{T - (n-1)\tau\} \tag{7}$$

where $S_0\{\nu\}$ is the unit step function such that $S_0\{\nu\} = 0$ for $\nu < 0$ and $S_0\{\nu\} = 1$ for $\nu > 0$. The waveform described by eq 7 is shown in Figure 1 along with the linear sweep waveform of eq 4. In particular, note that the first step is a full step and occurs at $T = 0$, consistent with the waveform described by Perone et al.[5,6]

In dimensionless form eq 7 becomes

$$e(t) = e_i - \delta e \sum_{n=1}^{N} S_0\{t - (n-1)\lambda\} \tag{8}$$

where $e(t)$, e_i, and t are as defined earlier, δe is a dimensionless step potential ($\delta e = nf\Delta E$), and λ is a dimensionless step duration ($\lambda = D\tau/L^2$). Sweep rates for LSV and SCV are considered equal when $V = \Delta E/\tau$ (or, equivalently, when $b = \delta e/\lambda$), although any given sweep rate in SCV can be obtained from many combinations of ΔE and τ.

The potential–time function $\theta(t)$ in eq 2c can now be written for staircase voltammetry in the form

$$\theta(t) = [1 + a \exp(-\delta e \sum_{n=1}^{N} S_0\{t - (n-1)\lambda\})]^{-1} \tag{9}$$

The shape of this function is shown in Figure 2 for $a = 2981$, $\delta e = 0.32$, $\lambda = 0.32$, and $N = 50$, corresponding to a dimensionless sweep rate $b = \delta e/\lambda$ of 1.0. Of particular importance to the solution of eq 1 is the observation that $\theta(t)$ is piecewise constant over the range of t, leading to considerable simplification in the solution of the equation.

The integral of eq 1 may be written as a sum of integrals, each taken over a range of constant $\theta(t)$. Thus, the current at time t on the pth step, the step beginning at t_{p-1} and ending at t_p such that $t_{p-1} < t < t_p$ with $t_0 = 0$, is given by

$$i_R(t) = \frac{d}{dt}\left[\sum_{k=1}^{p-1}\int_{t_{k-1}}^{t_k} i_d(t-u)\theta(t_k)\,du + \int_{t_{p-1}}^{t} i_d(t-u)\theta(t_p)\,du\right] \tag{10}$$

Since each $\theta(t_k)$ is a constant over the range t_{k-1} to t_k, each may be moved outside its corresponding integral, in which case each term in the summation of eq 10 is of the form

$$\text{term}_k = \theta(t_k)\frac{d}{dt}\int_{t_{k-1}}^{t_k} i_d(t-u)\,du \tag{11}$$

which can be solved exactly, yielding

$$\text{term}_k = \theta(t_k)(-i_d(t-t_k) + i_d(t-t_{k-1})) \tag{12}$$

Since $i_d = 0$ at $t \le 0$, the last term in eq 10 simplifies to

$$\text{term}_p = \theta(t_p) i_d(t-t_{p-1}) \tag{13}$$

Altogether, the exact solution to eq 10 and, thus, to eq 1 for staircase voltammetry is given by

$$i_R(t) = i_d(t-t_{p-1})\theta(t_p) - \sum_{k=1}^{p-1}(i_d(t-t_k) - i_d(t-t_{k-1}))\theta(t_k) \tag{14}$$

where the sum is vacuous for $p = 1$. The symmetry of the convolution integral (i.e., replacing $i_d(t-u)\theta(u)$ in eq 1 by $i_d(u)\,\theta(t-u)$) leads to the following equivalent expression (which may also be obtained by applying summation by parts to eq 14:

$$i_R(t) = i_d(t)\theta(t_1) + \sum_{k=1}^{p-1} i_d(t-t_k)(\theta(t_{k+1}) - \theta(t_k)) \tag{15a}$$

which, for $E_I \gg E^{o\prime}$ such that $\theta(t_0) \approx 0$ may be written in the form

$$i_R(t) = \sum_{k=1}^{p} i_d(t-t_{k-1})(\theta(t_k) - \theta(t_{k-1})) \tag{15b}$$

We emphasize that both eqs 14 and 15 are exact solutions to eq 1 for staircase voltammetry and are, therefore, valid for convergent diffusion conditions. For rectilinear diffusion, i_d is replaced by the Cottrell equation (eq 3) in which case eqs 14 and 15 reduce to forms equivalent to eqs 5, 6 and 1, 2, respectively, of ref 5.

The SCV computations of this work were performed using eq 15 rather than eq 14. This choice was motivated by the observation that eq 14 requires differences between i_d values computed numerically (for the convergent diffusion case) from the IEM as described above and could, therefore, result in some loss of computational accuracy. On the other hand, eq 15 requires differences between $\theta(t)$ values computed ana-

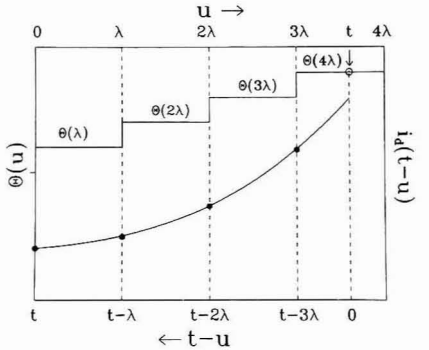

Figure 3. Illustration of the use of eq 15 for computing the reversible current $i_R(t)$ at time t (denoted by the arrow and open circle) on the fourth step ($p = 4$) of a staircase. The upper curve is $\theta(u)$; the lower curve is $i_d(t-u)$. The solid points on the i_d curve represent the four values of i_d used in eq. 15 to obtain eq 16. For illustrative purposes, the singularity in i_d as $t - u \rightarrow 0$ has been removed.

lytically from eq 9, and such differences can be computed with much greater precision.

Figure 3 illustrates the implementation of eq 15 to compute the current at time t (indicated by the arrow) on the fourth step of a staircase waveform. For this example, the current is given by

$$i_R(t) = i_d(t)\theta(\lambda) + i_d(t-\lambda)(\theta(2\lambda) - \theta(\lambda)) + i_d(t-2\lambda)(\theta(3\lambda) - \theta(2\lambda)) + i_d(t-3\lambda)(\theta(4\lambda) - \theta(3\lambda)) \quad (16)$$

Note that the first $i_d(t)$ value occurs at $t = \alpha\lambda$ (at $t - 3\lambda$ in the example of Figure 3) with subsequent values at intervals of λ. In general, the computation of a voltammogram for a staircase of N steps with current sampled at α requires N values of $i_d(t)$ at dimensionless times of

$$t_k = \alpha\lambda + (k-1)\lambda \qquad k = 1, 2, ..., N \quad (17)$$

The IEM is a fast and convenient method for computing these $i_d(t)$ values for convergent diffusion at a variety of planar electrode geometries (vide supra).

The program for computing staircase voltammograms was written in QuickBASIC and is available from the authors upon request. The program reads the appropriate $i_d(t)$ values from a disk file and computes a 50-step SCV in less than 1 s on the personal computer described above. The computation time increases approximately as the square of the number of steps. The numerical error in the computed SCVs is much less than 0.1% for the rectilinear diffusion case, where both $i_d(t)$ and $\theta(t)$ can be computed exactly, and is ca. 0.1% for the convergent diffusion case, where the error is determined primarily by the error in the numerically generated $i_d(t)$ values.

RESULTS AND DISCUSSION

Figure 2 displays the computed current–time response to a staircase waveform applied to a ring microelectrode having $\gamma = 10$ (γ is a dimensionless measure of ring shape given by $(R_2 + R_1)/2(R_2 - R_1)$ where R_1 and R_2 are the inner and outer ring radii, respectively[7]). For each step, the current was computed eight times in α increments of $^1/_8$, illustrating the jump and subsequent decay of current following each step. The dimensionless sweep rate ($b = \delta e/\lambda = 1$) used in Figure 2 is approximately midway between that required to achieve steady-state behavior ($b \leq 10^{-3}$) and that required for rectilinear diffusion behavior ($b > 10^4$) at typical ring and disk microelectrodes.[7]

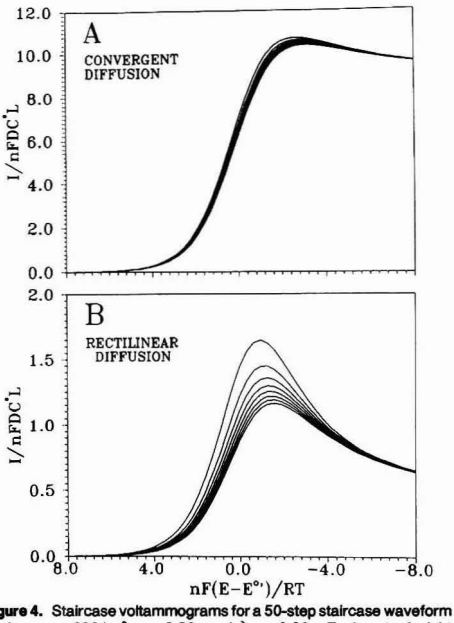

Figure 4. Staircase voltammograms for a 50-step staircase waveform having $a = 2981$, $\delta e = 0.32$, and $\lambda = 0.32$. Each set of eight voltammograms corresponds to α ranging from $^1/_8$ (top curve) to 1 (bottom curve) in increments of $^1/_8$. (A) For convergent diffusion conditions at a ring microelectrode of $\gamma = 10$ (constructed from points of equal α in Figure 2). (B) For rectilinear diffusion conditions.

The eight SCVs for the ring microelectrode in Figure 2, obtained by connecting points of equal α are displayed in Figure 4A, illustrating the influence of α on voltammogram shape at a sweep rate $b = 1$. The maximum current, I_{MAX}, and the potential at half the maximum current, $E_{M/2}$, are both functions of α, with I_{MAX} increasing and $E_{M/2}$ shifting to more positive potential (for a reduction) as α decreases. For comparison, the SCVs for rectilinear diffusion (or macroelectrode behavior) are displayed in Figure 4B under otherwise identical conditions. In agreement with previous work,[5] these voltammograms display a much greater dependence of I_{MAX} and $E_{M/2}$ on α and exhibit this strong dependence on α at all sweep rates (assuming diffusion remains rectilinear at the lowest sweep rates, as is usually the case at sufficiently large electrodes). In contrast, the staircase voltammograms computed in this work for convergent diffusion (microelectrodes) exhibit a dependence on α which is a function of sweep rate, being rather insensitive to α at very low sweep rates (approaching steady state) and becoming increasingly more sensitive to α at higher sweep rates as diffusion to the electrode becomes increasingly rectilinear.

The primary focus of this work is a reassessment of the conditions under which staircase and linear sweep potential waveforms produce essentially equivalent voltammograms for reversible electron transfer. We have employed the computational approach outlined earlier in this paper to examine SCVs as a function of the current sampling parameter (α), the sweep rate ($\delta e/\lambda$), and the number of steps comprising the staircase (N) for both rectilinear and convergent diffusion conditions and have critically compared each SCV with the corresponding LSV computed for the equivalent sweep rate. Because of the high computational accuracy of the methods employed, we are able to attribute significance to small differences in voltammograms which might otherwise be

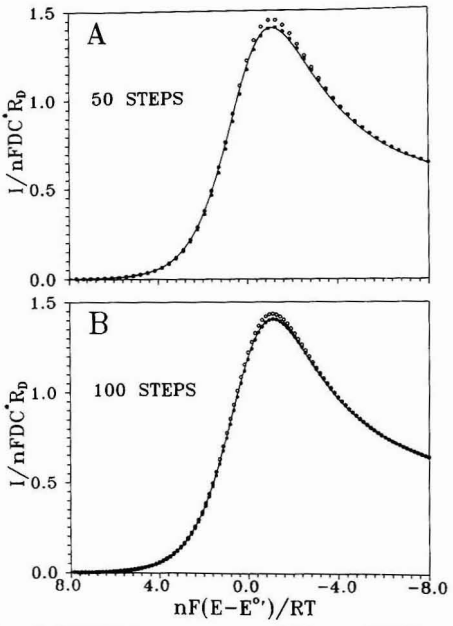

Figure 5. Comparisons of linear sweep and staircase voltammograms for equivalent sweep rates ($b = 1$) under rectilinear diffusion conditions. The solid curve is the LSV. The points are the SCVs for $\alpha = {}^{3}/_{10}$ (filled circles) and $\alpha = {}^{1}/_{4}$ (open circles). (A) 50 steps of height $\delta e = 0.32$ and duration $\lambda = 0.32$. (B) 100 steps of height $\delta e = 0.16$ and duration $\lambda = 0.16$.

considered within computational error or experimental uncertainty. We have previously demonstrated the excellent agreement obtainable for convergent diffusion conditions between experimental LSVs and ones computed using the methods employed in this work.[7]

Rectilinear Diffusion. Figure 5A illustrates the agreement between a 50-step SCV obtained with $\alpha = 0.30$ (solid points) and the corresponding LSV (solid line) at a sweep rate $b = 1$ for rectilinear diffusion. For comparison, the SCV obtained with $\alpha = 0.25$ is also displayed in Figure 5A by the open circles. Clearly, the best fit in the vicinity of the peak maximum is for $\alpha = 0.30$. The values of i_{MAX} and $E_{M/2}$ for each voltammogram are summarized in Table I. Differences in computed i_{MAX} of greater than 0.2% are considered significant. The deviations between the $\alpha = 0.25$ SCV and the LSV (Table I) are in agreement with those reported by Osteryoung et al.[11] Typical experimental uncertainties of a few percent would make it difficult to establish the best choice of α from experiment.[11]

The dimensionless step height (δe) for the SCVs of Figure 5A is 0.320, corresponding to a ΔE of 8.2/n mV at 25 °C. The use of fewer than 50 steps (i.e., a larger δe) to span the potential range of Figure 5 would lead to rather poor voltammogram resolution. Even for the 50-step voltammogram of Figure 5A, the estimation of $E_{M/2}$ from the voltammogram is subject to an estimated uncertainty of 0.5 mV (see footnote *b*, Table I). Nonetheless, the agreement among the $E_{M/2}$ values is within 1–2 mV.

The sum of the squares (or sumsquare) of the differences between corresponding points on a LSV and a SCV taken over the entire potential range of Figure 5 is an indicator of the overall agreement between two voltammograms. For the 50-step voltammogram of Figure 5A, this sumsquare is 0.0081 for $\alpha = 0.30$ and 0.018 for $\alpha = 0.25$, indicating better overall agreement for $\alpha = 0.30$.

Figure 5B displays the 100-step SCVs for the same sweep rate (thus, half the step duration, λ) and same current sampling parameters as in Figure 5A. Again, $\alpha = 0.30$ (sumsquare = 0.0040) results in better agreement with LSV than does $\alpha = 0.25$ (sumsquare = 0.018) over the entire voltammogram, as well as in the vicinity of the current maximum (Figure 5B and Table I). The deviation between LSV and SCV at any α is expected to decrease as the number of steps in the staircase increases, a trend which is observed in Figure 5 and Table I. Results obtained for 200-step voltammograms (not shown) follow this same pattern of dependence upon α.

For rectilinear diffusion, the deviation between LSV and SCV at fixed α and ΔE is expected to be independent of sweep rate and, thus, independent of variations in the step duration τ.[11] Our computations reveal virtually identical behavior to that described above over many orders of magnitude in sweep rate (for example, see Table I for $b = 1000$). In contrast, the deviation between LSV and SCV under convergent diffusion conditions is dependent on sweep rate, as demonstrated in the next section.

The reason for the discrepancy between the optimum α obtained for rectilinear diffusion in this work (0.30) and that obtained by Osteryoung and co-workers (0.25)[11] is not clear. Their SCV waveform differs from ours in that their first step is half the amplitude of all succeeding steps. Their mathematical evaluation of α was apparently based on this first step (or interval) which may unduly exaggerate the influence of their first (half-amplitude) step. Indeed, the nature of the first step should be relatively inconsequential for the SCV of a solution initially containing only one component of a redox system, as long as the initial potential is sufficiently removed from the formal potential such that the initial current is zero and as long as the voltammogram is displayed as current versus potential (not time). To verify this expected behavior, we performed SCV calculations for conditions identical to those in Figure 5A but employing the Osteryoung-type waveform[11] having a first step of half amplitude. Of course, the points from these calculations fell at potentials midway between those of Figure 5A, but using interpolation these voltammograms overlapped those of Figure 5A to within computation error (<0.1%).

Convergent Diffusion. The relative insensitivity of SCV to α at a disk microelectrode under convergent diffusion conditions ($b = 1$) is illustrated in Figure 6A (50-step SCV) and Figure 6B (100-step SCV). Both $\alpha = 0.30$ (solid points) and $\alpha = 0.25$ (open circles) produce voltammograms in excellent agreement with the LSV (solid line) at this sweep rate. The differences in the values of i_{MAX} and $E_{M/2}$ for the voltammograms (Table II) are nearly within computational error. For the 50-step SCV of Figure 6A, the sumsquare for $\alpha = 0.30$ is 0.013 and for $\alpha = 0.25$ it is 0.0088. For the 100-step SCV of Figure 6B, the sumsquare for $\alpha = 0.30$ is 0.0096 and for $\alpha = 0.25$ it is 0.0071. On the basis of overall fit, $\alpha = 0.25$ may be slightly preferred. However, there is little to distinguish between these two choices of α at this sweep rate.

At lower sweep rates ($b < 1$, not shown) the staircase voltammograms become even less dependent upon α. Indeed, as $b \to 0$ the step period τ becomes sufficiently long that time-independent (steady-state or perhaps quasi steady-state[19]) current is established very early in the step duration (at very small α), and the current, hence the voltammogram, becomes independent of α. At higher sweep rates ($b > 1$) the dependence of the voltammogram on α increases as diffusion

(19) Cope, D. K.; Tallman, D. E. *J. Electroanal. Chem. Interfacial Electrochem.* **1990**, *285*, 85.

Table I. A Comparison of Linear Sweep and Staircase Voltammetries under Conditions of Rectilinear Diffusion

method	no. of Steps, N	sweep rate, b	α	i_{MAX}[a]	$n(E_{M/2} - E^{\circ\prime})$,[b] mV
LSV		1		1.403	28.1
SCV	50	1	0.30	1.404 (<0.1%)	26.4
SCV	50	1	0.25	1.445 (3.0%)	27.3
SCV	100	1	0.30	1.404 (<0.1%)	27.3
SCV	100	1	0.25	1.435 (2.3%)	27.9
LSV		1000		44.41	28.2
SCV	100	1000	0.30	44.40 (<0.1%)	27.3
SCV	100	1000	0.25	45.37 (2.2%)	27.9

[a] $i_{MAX} = I_{MAX}/nFDC^*L$ has a computational error of ca. 0.1% for LSV and less than 0.1% for SCV. Each number in parentheses is the relative difference between that SCV value and the corresponding LSV value of i_{MAX}. [b] Estimated from the computed voltammogram for a temperature of 25 °C with an uncertainty of ca. 0.1 mV for LSV, ca. 0.3 mV for 100-step SCV, and ca. 0.5 mV for 50-step SCV. For SCV, the limited number of points defining the voltammogram influence this uncertainty.

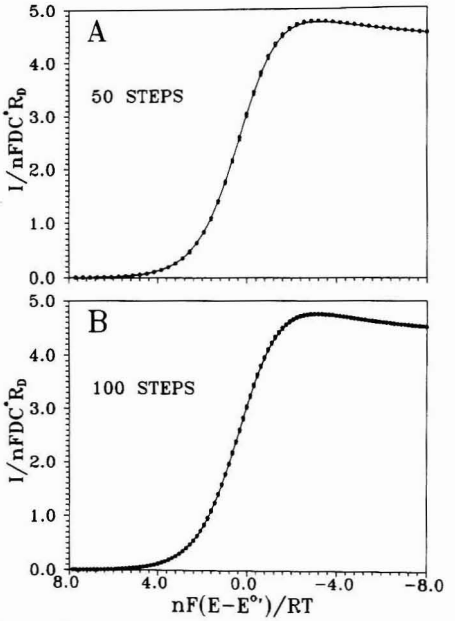

Figure 6. Comparisons of linear sweep and staircase voltammograms for equivalent sweep rates ($b = 1$) under convergent diffusion conditions at a disk microelectrode. The solid curve is the LSV. The points are the SCVs for $\alpha = {}^3/_{10}$ (filled circles) and $\alpha = {}^1/_4$ (open circles). (A) 50 steps of height $\delta e = 0.32$ and duration $\lambda = 0.32$. (B) 100 steps of height $\delta e = 0.16$ and duration $\lambda = 0.16$.

becomes increasingly rectilinear, eventually reaching a dependence on α identical to that summarized by Figure 5 and Table I. For example, at $b = 1000$, diffusion to the microdisk electrode is sufficiently (though not completely[7]) rectilinear that $\alpha = 0.30$ again provides the best agreement with LSV (Table II).

The dependence of SCV on α and variation of the dependence with sweep rate, described above for a microdisk electrode, is somewhat dependent on microelectrode geometry. Compared to a disk electrode, thin band and thin ring electrodes (geometries having higher perimeter-to-area ratio) exhibit transient currents which are *less* time- (sweep rate-) dependent at shorter times (or higher sweep rates, $b > 1$), a consequence of the more significant contribution from convergent diffusion at such geometries at short time.[7,19] On the other hand, compared to a disk electrode, transient currents at ring and band electrodes are *more* time- (sweep rate-) dependent at longer times (or lower sweep rates, $b < 1$), due to slower attainment of the steady-state (in the case of thin rings) or the absence of a true steady-state (in the case of bands).[7,19] Therefore, SCVs at ring and band electrodes are expected to be somewhat more sensitive to α at low sweep rates and somewhat less sensitive to α at high sweep rates, compared to the microdisk behavior. Such influences of electrode geometry on the choice of α necessary to obtain LSV equivalence are quite subtle, and we have not explored this behavior in detail. For SCV at ring microelectrodes (e.g., Figure 4A), we do find that $\alpha = 0.30$ provides the best agreement with LSV, and we conjecture that this value of α is optimum for all electrode geometries.

The Influence of α on Staircase Voltammograms. The discussion thus far has focused on just two values of α, namely 0.25 and 0.30. It is of interest to examine (in a more quantitative way than is possible from Figure 4) the influence of α on staircase voltammograms as α varies over a much wider range. The large numer of variables involved (α, b, N, γ) precludes a comprehensive display of such results, so we restrict our discussion to a 50-step staircase applied to a microdisk electrode ($N = 50$, $\gamma = 0.5$). Table III summarizes the influence of α on the wave height, i_{MAX}, and wave position, $n(E_{M/2} - E^{\circ\prime})$, of staircase voltammograms obtained at a sweep rate $b = 1$ for rectilinear diffusion (thus, for any electrode geometry) and for convergent diffusion at the disk electrode. For ease of comparison, the corresponding linear sweep results are included in this table along with the percent difference in i_{MAX} between each SCV and the corresponding LSV (in parentheses).

For rectilinear diffusion, the variation of i_{MAX} with α is substantial, ranging from ca. 23% higher than the LSV wave height at $\alpha = 0.1$ to ca. 17% lower than the LSV height at $\alpha = 1.0$. The position of the wave on the potential axis shifts negatively (for a reduction) by ca. 10 mV over this range of α (see Figure 4 and Table III). The maximum current from staircase voltammetry at any fixed α is proportional to the square root of the sweep rate, $b^{1/2}$, provided the SCV sweep rate ($\Delta E/\tau$) is varied by changing the step duration τ rather than the step amplitude ΔE (i.e., the number of steps, N, remains constant; see Table I). Since (for rectilinear diffusion) both LSV and SCV exhibit this same $b^{1/2}$ dependence for all b, the same *relative* i_{MAX} differences between SCV and LSV and the same wave positions, provided as a function of α in Table III, are observed at any sweep rate, b. Thus, the same incongruities between LSV and SCV at each α will be observed at any sweep rate and at any electrode geometry for which rectilinear diffusion conditions exist.

For convergent diffusion at the disk microelectrode at a sweep rate $b = 1$ (Table III), the variation of i_{MAX} with α is much weaker than observed for the rectilinear diffusion case, ranging from 2.2% higher than the LSV wave height at $\alpha = 0.1$ to 1.3% lower than the LSV wave height at $\alpha = 1.0$.

Table II. A Comparison of Linear Sweep and Staircase Voltammetries under Conditions of Convergent Diffusion

method	no. of steps, N	sweep rate, b	α	i_{MAX}[a]	$n(E_{M/2} - E^{o\prime})$,[b] mV
LSV		1		4.748	12.7
SCV	50	1	0.30	4.756 (0.2%)	11.9
SCV	50	1	0.25	4.767 (0.4%)	12.6
SCV	100	1	0.30	4.751 (<0.1%)	12.2
SCV	100	1	0.25	4.758 (0.2%)	12.8
LSV		1000		46.83	27.5
SCV	100	1000	0.30	46.80 (<0.1%)	26.6
SCV	100	1000	0.25	47.76 (2.0%)	27.2

[a] $i_{MAX} = I_{MAX}/nFDC^*L$ has a computational error of ca. 0.1% for both LSV and SCV. Each number in parentheses is the relative difference between that SCV value and the corresponding LSV value of i_{MAX}. [b] See footnote b of Table I.

Table III. Influence of the Current Sampling Parameter α on the Wave Height and Wave Position of Staircase Voltammograms

method	no. of steps, N	sweep, rate, b	α	i_{MAX}[a]	$n(E_{M/2} - E^{o\prime})$,[b] mV
		Rectilinear Diffusion			
LSV		1		1.403	28.1
SCV	50	1	0.1	1.727 (+23.1%)	30.8
SCV	50	1	0.2	1.505 (+7.3%)	28.1
SCV	50	1	0.3	1.404 (<+0.1%)	26.4
SCV	50	1	0.4	1.342 (−4.3%)	25.1
SCV	50	1	0.6	1.258 (−10.3)	23.4
SCV	50	1	0.8	1.202 (−14.3)	22.2
SCV	50	1	1.0	1.161 (−17.2%)	21.2
		Convergent Diffusion (Disk Electrode)			
LSV		1		4.748	12.7
SCV	50	1	0.1	4.852 (+2.2%)	16.7
SCV	50	1	0.2	4.783 (+0.7%)	13.5
SCV	50	1	0.3	4.756 (+0.2%)	11.9
SCV	50	1	0.4	4.738 (−0.2%)	10.8
SCV	50	1	0.6	4.715 (−0.7%)	9.4
SCV	50	1	0.8	4.699 (−1.0%)	8.5
SCV	50	1	1.0	4.685 (−1.3%)	7.8

[a] See footnote a of Tables I and II. Each number in parentheses is the relative difference between that SCV value and the corresponding LSV value of i_{MAX}. [b] See footnote b of Table I.

However, the wave position is nearly as sensitive to α at this sweep rate as for the rectilinear diffusion case, shifting negatively by ca. 9 mV over this range of α. Of course, for convergent diffusion, the relative differences in i_{MAX} between SCV and LSV and the wave positions are sweep rate dependent (see Table II). As $b \rightarrow 0$, the SCV current at any α approaches the steady-state value (for a disk, $i_{MAX} \rightarrow 4.00$) and $n(E_{M/2} - E^{o\prime}) \rightarrow 0$, the same limiting behavior as is observed for LSV.[7,20] Thus, LSV and SCV become increasingly equivalent for any α as the zero sweep rate limit is approached. As $b \rightarrow \infty$ and diffusion becomes increasingly rectilinear, the incongruities between LSV and SCV at each α approach those tabulated for rectilinear diffusion in Table III.

CONCLUSIONS

Computed staircase voltammograms of reversible systems with $\alpha = 0.30$ are remarkably similar to linear sweep voltammograms over a wide range of sweep rates and diffusion conditions. This optimum value of α was determined numerically for rectilinear diffusion conditions where SCV is most sensitive to variations in α. This optimum α was then found to provide excellent equivalence (within computational error) between SCV and LSV for convergent diffusion conditions as well. Thus, $\alpha = 0.30$ appears to be a better choice than $\alpha = 0.25$[11] for maintaining such equivalence over a wide range of sweep rates and for a wide variety of electrode geometries and sizes. Admittedly, the differences between SCVs obtained experimentally at these two values of α will often be within the experimental error, particularly for measurements made at microelectrodes at low to moderate sweep rates. At macroelectrodes and at microelectrodes employed at high sweep rates, the differences can approach a few percent and may be comparable to the experimental error. The computational approach used in this work allows us to attribute significance to such differences and to establish the best overall choice for α.

Finally, we address the implications of the requirement for equal diffusion coefficients ($\delta^2 = D_R/D_O = 1$) embodied in eq 1.[9] Indeed, for rectilinear diffusion, the computation of linear sweep and staircase voltammograms can be performed exactly without the need to assume equal diffusion coefficients.[5,9,11,21] The results so obtained are identical to those presented here, the only change being the replacement of the formal potential ($E^{o\prime}$) appearing in this work by the half-wave potential ($E_{1/2} = E^{o\prime} + RT/nF \ln \delta$). Therefore, all conclusions pertaining to the choice of α remain valid for the unequal diffusion coefficient case.

For convergent diffusion, the exact solution appears more difficult,[9] and the assumption of equal diffusion coefficients leads to eq 1, making the solution tractable.[9] Replacing $E^{o\prime}$ by $E_{1/2}$ as described above for the rectilinear diffusion case would likely account for some (perhaps even most) of the effect of unequal diffusion coefficients. However, theoretical considerations indicate that not only wave position on the potential axis (as in the rectilinear diffusion case) but also

(20) Aoki, K.; Akimoto, K.; Tokuda, K.; Matsuda, H.; Osteryoung, J. *J. Electroanal. Chem. Interfacial Electrochem.* **1984**, *171*, 219.

(21) Nicholson, R. S.; Shain, I. *Anal. Chem.* **1964**, *36*, 706.

wave shape are influenced by unequal diffusion coefficients.[9] Such influences are likely to be similar for LSV and SCV which (along with the observation that SCV under convergent diffusion conditions exhibits less dependence on the choice of α) leads us to conjecture that $\alpha = 0.30$ will produce staircase voltammograms equivalent to linear sweep voltammograms even for unequal diffusion coefficients at microelectrodes under convergent diffusion conditions. Confirmation of this conjecture will require very careful experimentation and/or further advances in microelectrode theory.

ACKNOWLEDGMENT

This research was supported by the National Science Foundation through Grant No. CHE-9108921. The authors are grateful to Professor Davis Cope of the NDSU Mathematics Department for fruitful discussions related to this problem.

RECEIVED for review April 23, 1992. Accepted August 13, 1992.

Flow Electroanalysis of Compound Semiconductor Thin Films: Application to the Compositional Assay of Cathodically Electrosynthesized Cadmium Selenide

Noseung Myung, Chang Wei, and Krishnan Rajeshwar*

Department of Chemistry, Box 19065, The University of Texas at Arlington, Arlington, Texas 76019-0065

A flow electroanalysis procedure is described to determine the composition of compound semiconductor thin films. Electrosynthesized samples of CdSe + Se + Cd have been used as a model system to illustrate our analysis protocol. The analytical data are chemical state selective in that free Cd and Cd present as CdSe are differentiated. A combination of chemical and electrochemical stripping of CdSe + Se + Cd from the support Ti electrodes is used for the selective monitoring of the species at a downstream Hg thin film electrode. Thus, the free CdSe is then chemically stripped and the Se(IV) retained at a filter cell to avoid interference with the bound Cd assay. Finally, the total selenium content of the film is determined via cathodic stripping voltammetry.

INTRODUCTION

Group II–VI (12–16) compound semiconductors (such as CdSe) are important in a wide spectrum of optoelectronic device applications ranging from solar cells to "smart" goggles.[1] Thin films of these materials hitherto have been synthesized by a variety of techniques including vacuum evaporation, chemical vapor deposition, sputtering, and electrodeposition. In all of these synthesis scenarios, compositional variability and nonstoichiometry are frequent problems. Thus, "free" elements (e.g., Cd and Se) often are present in admixture with the targeted compound semiconductor. While a wide range of analytical techniques has been used for the compositional analyses of compound semiconductors, electroanalytical methods are conspicuous by the lack of their widespread use contrasting the trend with other types of analytes in general. However, there do exist a few isolated examples of the use of electroanalytical methods such as polarography, cyclic voltammetry, and chronoamperometry for the compositional assay of compound semiconductors.[2-4]

In this report, we describe a new flow electroanalysis (FEA) technique based on selective stripping and analysis of components from a compound semiconductor matrix. Unlike the electroanalytical methods which have been previously employed for this purpose,[2-4] we use a combination of stripping (both chemical and electrochemical) to facilitate *selective* monitoring of species from the semiconductor matrix. Further, our methodology is "chemical state selective" (differentiating, for example, free Cd and Cd present as CdSe), unlike techniques such as atomic spectroscopies which yield only the *total* species content.[5] We illustrate our analysis protocol with the Cd–Se system.

We further note the applicability of our analysis approach to other (nonsemiconductor) situations. Thus, new methods for analysis of Se are important for a variety of considerations.[6] In this vein, the FEA technique that we propose herein constitutes an extension of the electrochemical stripping methods previously described for Se(IV) using *nonflow* methodology.[6-10]

EXPERIMENTAL SECTION

Instrumentation. A Bioanalytical Systems Model 100A instrument equipped with an IBM personal computer and a Hewlett–Packard Model 7475A digital plotter was used for differential pulse stripping voltammetry (DPSV) and for CdSe thin film deposition. An EG&G Princeton Applied Research Model 273 system equipped with a Houston Instrument RE0089 X–Y recorder was used for cyclic voltammetry (CV). An Electrosynthesis Inc. Model 415 potentiostat was used to control the potential of the filter cell electrode (cf. Figure 1); this potential was monitored on a Fluke Model 37 multimeter. Solution to the FEA system was delivered by a Masterflex peristaltic pump.

FEA System and Thin Film Synthesis Cell. The system is depicted in Figure 1 along with the functions of the various components. The FEA system features a filter cell and a detector cell further downstream. The filter cell (3.84-cm diameter, 5.86-cm length) was custom built with Plexiglass and comprised a Hg-coated reticulated vitreous carbon (RVC) working electrode (100 ppi, 0.48-cm diameter, 2-cm length, Electrosynthesis Inc.), an Ag/AgCl/3 M KCl reference, and a stainless steel counter electrode. Electrical contact to the RVC was provided by a glassy carbon electrode. The detector cell (5.4 cm × 3.19 cm × 5.02 cm) was also custom built with Plexiglass and consisted of a Hg thin film electrode (MTFE) on a glassy carbon support, an Ag/AgCl/3 M KCl reference, and a Pt counter electrode. The solution flow channel (1.5-mm diameter at the detector cell) was drilled through the cell body. Further details of the filter and detector cells are available from the authors. The synthesis cell consisted mainly of a Ti foil (Alfa) working electrode (immersed area 5.2 cm^2) atop which CdSe thin flims were electrodeposited at selected potentials. The cells were interconnected within the FEA system and with the synthesis cell via 1.6-mm-i.d. tubing (Masterflex).

Chemicals. $Hg(NO_3)_2$, $CdSO_4$ (ACS Certified Grade), and SeO_2 (Ultrapure) were from Johnson-Matthey Electronics. KCl from MCB and HCl from Malinkdrodt were used to prepare the Clark and Lubs buffer at pH 2. All the other chemicals were of Analar grade purity. Double-distilled water was used for the preparation of all solutions and for electrochemical syntheses and analyses. All solutions were carefully deaerated with ultrapure N_2 prior to and during measurements.

Procedures. The RVC electrode in the filter cell was pretreated by switching the potential between −1.0 and +1.0 V for 10 min at least three times in 0.05 M H_2SO_4. This procedure has been described by a previous author[11] to result in a clean and reproducible surface free of adsorbed impurities. Deposition of

* Author for correspondence.

(1) Rajeshwar, K. *Adv. Mater.* **1992**, *4*, 23–29.
(2) Whitnack, G. C.; Donovan, T. M.; Ritchie, M. H. *J. Electroanal. Chem. Interfacial Electrochem.* **1967**, *14*, 205–208.
(3) Darkowski, A.; Cocivera, M. *Talanta* **1986**, *33*, 187–189.
(4) (a) Rao, G. S. R.; Reddy, S. J. *J. Ind. Chem. Soc.* **1984**, *31*, 306–311. (b) *Thin Solid Films* **1984**, *120*, 205–213. (c) *Acta Chim. Hung.* **1985**, *118*, 241–248.
(5) Lin, W.-Y.; Mishra, K. K.; Mori, E.; Rajeshwar, K. *Anal. Chem.* **1990**, *62*, 821–825.
(6) For example, Adeloju, S. B.; Bond, A. M.; Briggs, M. H.; Hughes, H. C. *Anal. Chem.* **1983**, *55*, 2076–2082.
(7) Andrews, R. W.; Johnson, D. C. *Anal. Chem.* **1975**, *47*, 294–299.
(8) Adeloju, S. B.; Bond, A. M.; Hughes, H. C. *Anal. Chim. Acta* **1983**, *148*, 59–69.
(9) Ferii, T.; Morabito, R.; Petronio, B. M.; Pitti, E. *Talanta* **1989**, *36*, 1259–1263.
(10) Van den Berg, C. M. G.; Khan, S. H. *Anal. Chim. Acta* **1990**, *231*, 221–229.
(11) Wang, J. *Electrochim. Acta* **1981**, *26*, 1721–1726.

0003-2700/92/0364-2701$03.00/0

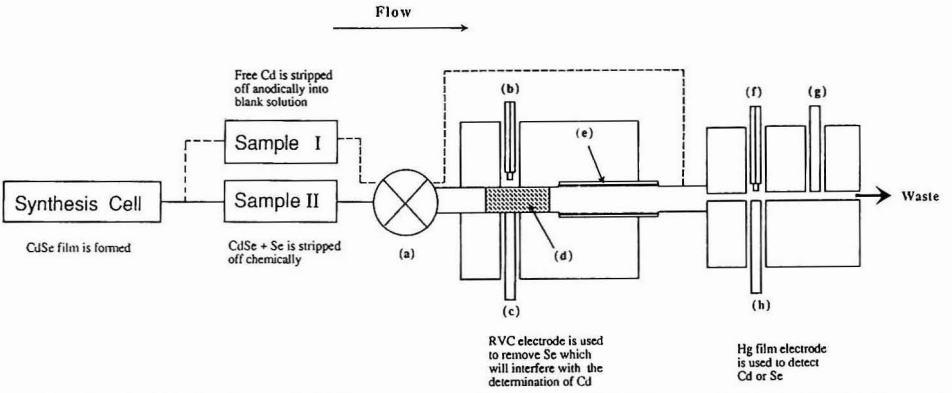

Figure 1. A schematic of the flow electroanalysis (FEA) system: (a) pump; (b,f) reference electrodes; (c) electrical lead to RVC, glassy carbon electrode; (d) Hg-coated RVC cylinder; (e) stainless steel counter electrode; (g) Pt counter electrode; and (h) MTFE. An outline of the sample preparation and analytical procedure is also given.

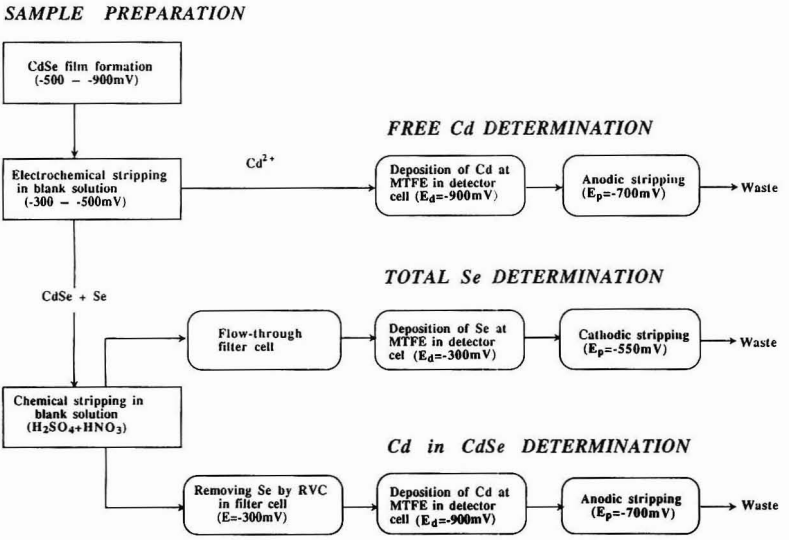

Figure 2. A more detailed perspective on the FEA procedure. E_d is the film deposition potential and E_p is the peak potential in the DPSV scan.

Hg, both in the filter cell and for preparation of the MTFE in the detector cell, was done at the beginning of each day. For the former, a 1 mM $Hg(NO_3)_2$ solution in 0.05 M H_2SO_4 was pumped through the cell at 0.322 mL/min for 15 min with the RVC held at −500 mV. Similar conditions except for the use of a 0.1 mM solution were utilized for preparation of the MTFE.

A 0.5 M H_2SO_4 matrix containing 0.4 M $CdSO_4$ and 4 mM SeO_2 was used for the cathodic electrodeposition of CdSe[12,13] at various potentials ranging from −500 to −900 mV. A potentiostatic mode was employed and the deposition time was 5 min.

The analyte preparation and analysis procedure is schematized in Figure 2. Anodic stripping of the "free" Cd (present in admixture with CdSe) was done after thoroughly washing the thin-film loaded Ti foil which was then transferred to the Clark and Lubs pH 2 buffer which served as the "blank" solution. Stripping was done at potentials ranging from −300 to −500 mV into the blank which was subsequently made up to 50 mL. This procedure generates the sample designated "I" in Figure 1. The free Cd content of the film was then determined at the downstream detector cell (Figure 1) by anodic stripping voltammetry (in a stationary mode). Preconcentration of the cadmium at the MTFE was done at −900 mV for 1 min at a flow rate of 0.26 mL/min. In the second stage of the analytical procedure (sample II, Figure 1), the CdSe and free Se were chemically stripped from the Ti support into the blank solution (Figure 2). For this, a few drops of concentrated HNO_3 and concentrated H_2SO_4 were used, and the pH of the solution was then adjusted to 2 with 1:1 NH_4OH.[3] Final sample solutions were made up to 100 mL using the Clark and Lubs pH 2 buffer as blank and subsequently diluted with blank as required prior to quantitation.

Since Se interferes with the quantitation of Cd (cf. Figures 1 and 2) (also see below), a potential of −300 mV was applied to the RVC to "immobilize" the Se(IV) within it as Se^0. The Cd in CdSe was then determined as before (Figure 2). Finally, the total Se content (free Se + Se present at CdSe) was determined by cathodic stripping voltammetry after preconcentrating it at

(12) Mishra, K. K.; Rajeshwar, K. *J. Electroanal. Chem. Interfacial Electrochem.* **1989**, *273*, 169–182.
(13) Krishnan, V.; Ham, D.; Mishra, K. K.; Rajeshwar, K. *J. Electrochem. Soc.* **1992**, *139*, 23–27.

Table I. Nominal Errors in the Quantitative Analyses of Cadmium and Selenium

element	concentration (M)	RSD (%)	N
Se	8×10^{-6}	6.30	5
	4×10^{-6}	11.02	5
	8×10^{-7}	8.60	5
	1×10^{-7}	12.70	4
Cd	5×10^{-6}	1.64	5
	1×10^{-6}	2.44	5
	5×10^{-7}	5.27	5
	1×10^{-7}	3.94	5

the MTFE at −300 mV for 1 min at 0.26 mL/min flow rate. The solution was then switched to the blank for the stripping analyses. This had to be done to avoid distortion of the Se stripping peak by the Cd as revealed in exploratory runs. [Note, however, that Cd will not otherwise interfere with the deposition of Se(IV) at the MTFE at −300 mV.]

All quantitations were based on measurement of peak heights in the stripping voltammograms. The reproducibility was checked by running at least four replicates for both standards and the unknown. Nominal errors for the standards are summarized in Table I. The data shown in Figure 8 below contain averaged values from such replicate runs.

CAUTION. Cadmium and selenium-containing solutions are toxic, and adequate care needs to be exercised in the handling and disposal of these solutions. A chemical hood is also recommended for the analyses in view of the toxicity of the electrochemically generated H_2Se.

RESULTS AND DISCUSSION

Background and Development of Analysis Protocol. As discussed by us elsewhere[12,13] and by other authors,[14-17] two electrochemical routes can be envisioned for the cathodic formation of CdSe:

$$SeO_2 + 4H^+ + 4e^- = Se^0 + 2H_2O \quad (1a)$$

$$Cd^{2+} + 2e^- = Cd^0 \quad (1b)$$

$$Cd^0 + Se^0 = CdSe \quad (1c)$$

$$SeO_2 + Cd^{2+} + 6e^- + 4H^+ = CdSe + 2H_2O \quad (2)$$

Reaction 1 involves the sequential reduction of Se(IV) to the elemental state followed by assimilation of Cd^{2+} ions in an "underpotential" $2e^-$ step to generate CdSe.[18] On the other hand, reaction 2 involves the $6e^-$ reduction of Se(IV) to selenide followed by precipitation with Cd^{2+}. A representative CV scan for a Ti foil in 0.05 M H_2SO_4 containing 4 mM SeO_2 and 0.4 M $CdSO_4$ is contained in Figure 3. The inset amplifies the negative-going scan to bring out the fine structure associated with Se(IV) reduction and CdSe formation. Differentiation of the aforementioned two routes requires mechanistic data beyond the scope of this study and the information contained in Figure 3. Instead, we merely present the CV data as a framework for our choice of the thin film deposition potentials for subsequent FEA and anticipate that films deposited at the positive end of the −500 to −600 mV range would be Se-rich. Further, the sharp onset of cathodic current flow at potentials negative of ~−700 mV along with

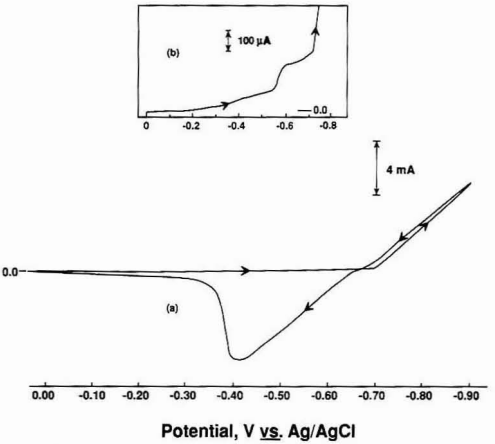

Figure 3. Cyclic voltammogram for 0.5 M H_2SO4 containing 4 mM SeO_2 and 0.4 M $CdSO_4$ on Ti foil. Potential scan rate: 10 mV/s.

the anodic wave on the return scan are attributable to reaction 1b.[12] Thus, the samples generated at deposition potentials negative of ~−700 mV are expected to be Cd-rich. We note the almost "ohmic" nature of the current flow at high potential scan rates (i.e. at high current levels)—a manifestation of the resistance exerted by the Ti foil (and associated surface oxides). Our CV data are in broad agreement with earlier measurements from this laboratory[12] once such differences attributable to the support electrode material are taken into account. Preliminary measurements with glassy carbon electrodes yielded rather erratic results in terms of thin film quality and stoichiometry. Thus, our choice of Ti largely was prompted by the excellent adhesion and morphology of group II–VI (12–16) semiconductor thin films when electrosynthesized on this support material. It is our experience that glassy carbon, while the material of choice for voltammetry and mechanistic studies on chalcogenides,[1,19] is not suitable as a support for semiconductor thin films.

Next, we consider the electrosynthesized thin films to contain, aside from CdSe, also free Se and Cd as a general test case. Figure 4 outlines the possible candidate routes that are available for the FEA of this matrix. The prerequisite is an effective means of dislodging the CdSe + Se + Cd from the thin-film matrix into the flow stream. As the scheme in Figure 4 shows, initial anodic stripping of the free Cd^0 as Cd^{2+} (reaction 1b) constitutes the first optimal step. (In Figure 4, the routes marked with X have been ruled out after careful consideration.) This then leaves CdSe + Se which are chemically stripped for the FEA. Anodic striping of CdSe is not feasible because it occurs at very positive potentials (>~1.50 V) where the Ti support is also oxidized (cf. Figure 5). After quantitation of the Cd present as CdSe, the Se(IV) is immobilized at the MTFE as "HgSe" and then quantitated by *cathodic* stripping voltammetry. The anodic route is not possible here because of the susceptibility of Hg to oxidation at the potentials relevant to the anodic stripping of Se^0 (cf. Figure 5). These measurements yield the *total* selenium content of the film. Finally, the "free" Se is quantitated by subtracting the equivalent amount, bound to Cd, from the total amount. The inherent assumption here is that the Cd-Se as electrosynthesized is stoichiometric or nearly so (i.e. Cd and Se are present in essentially 1:1 mole ratio). This assumption is substantiated by findings in a companion paper

(14) (a) Kazacos, M. S.; Miller, B. *J. Electrochem. Soc.* **1980**, *127*, 869–873. (b) *Ibid.* **1980**, *127*, 2378–2381.
(15) Tomkiewicz, M.; Ling, I.; Parsons, W. S. *J. Electrochem. Soc.* **1982**, *129*, 2016–2022.
(16) Darkowski, A.; Grabowski, A. *Solar Energy Mater.* **1991**, *23*, 75–82.
(17) Kressin, A. M.; Doan, V. V.; Klein, J. D.; Sailor, M. J. *Chem. Mater.* **1991**, *3*, 1015–1020.
(18) Krõger, F. A. *J. Electrochem. Soc.* **1978**, *125*, 2028–2034.
(19) Mori, E.; Baker, C. K.; Reynolds, J. R.; Rajeshwar, K. *J. Electroanal. Chem. Interfacial Electrochem.* **1988**, *252*, 441–451.

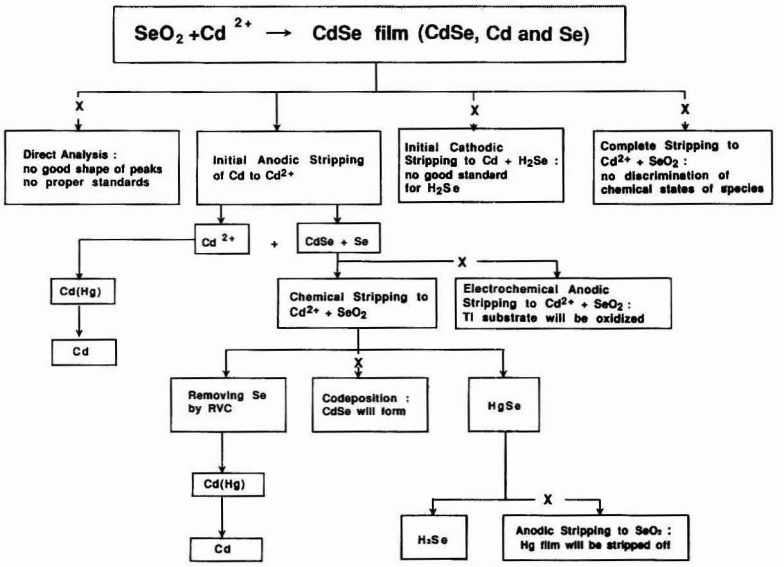

Figure 4. An outline of possible routes and optimal pathways for the analysis of CdSe + Se + Cd thin films.

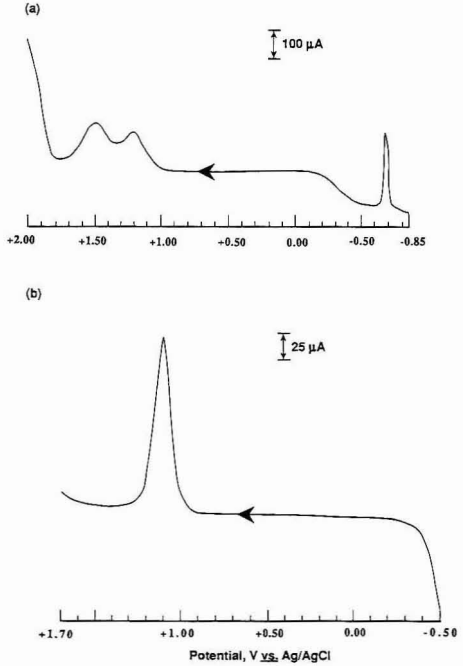

Figure 5. Linear sweep voltammograms for 0.05 M H_2SO_4 matrix containing (a) 10 mM $CdSO_4$ and 4 mM SeO_2 on glass carbon electrode. Potential scan rate: 5 mV/s, 2-min deposition at −850 mV. (b) 4 mM SeO_2 on glassy carbon electrode Potential scan rate: 5 mV/s, 1-min deposition at −500 mV.

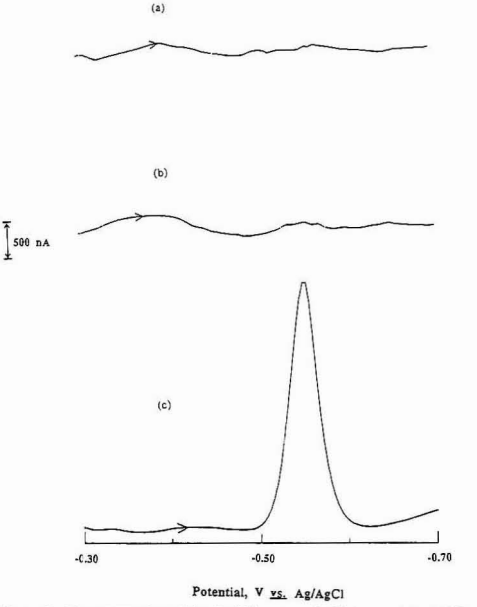

Figure 6. Demonstration of the Se(IV) removal efficiency at the RVC filter cell electrode: (a) Blank. (b) 4.0 × 10^{-5} M SeO_2 in Clark and Lubs buffer, 1-min deposition at −300 mV. Potential scan rate, 4 mV/s; solution flow rate, 0.26 mL/min; filter cell potential, −300 mV. (c) 4.0 × 10^{-6} M SeO_2 without filter cell. Potential scan rate, 4 mV/s; solution flow rate, 0.26 mL/min.

from this laboratory.[20] Furthermore, sample calculations also quickly reveal that deviations from stoichiometry typical of "doping" of semiconductor materials would exert only a negligible perturbation on the scale of compositional variations in the CdSe + Se + Cd system.

The LSV scan in Figure 5a for a thin-film matrix containing CdSe + Se + Cd also illustrates the unsatisfactory

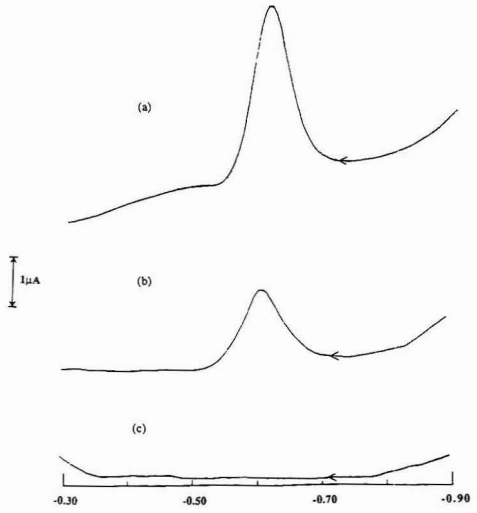

Figure 7. The influence of Se(IV) in the flow stream on Cd quantitation. The electrolyte contained 1.0×10^{-6} M $CdSO_4$ and 4.0×10^{-6} M SeO_2 and the flow rate was 0.26 mL/min. Film deposition at the MTFE was for 1 min at −900 mV. Potential scan rate, 4 mV/s: (a) with filter cell at −300 mV; (b) without filter cell; (c) blank.

nature of the "direct analysis" route (Figure 4) (based on the anodic stripping of CdSe + Se + Cd) *even if the support electrode material were electrochemically stable.* Thus, the Se and CdSe stripping features at a glassy carbon electrode overlap in the 1.00–1.80 V potential range, and no suitable calibration standards are available, especially for the latter. (The anodic peak at ~−700 mV in Figure 5a is assignable to reaction 1b).

DPSV of Cd and Se and Filter Cell Efficiency Considerations. The filter efficiency of a Hg-coated RVC electrode has been well-studied by previous authors.[21] Figure 6 contains some data pertinent to this aspect. With the filter cell electrode poised at −300 mV, removal of Se(IV) from the flow stream essentially is complete as shown by the comparison of the three scans in Figure 6. The cathodic stripping of selenium at a MTFE has been studied by previous authors.[6,8] The scan in Figure 6c is representative of the cathodic DPSV profiles observed for Se(Hg) in this study.

Figure 7 contains anodic DPSV data which illustrate why it is necessary to "filter out" Se from the flow stream prior to quantitation of the Cd present as CdSe. When the filter cell is isolated from the flow stream [i.e. when Se(IV) coexists with Cd^{2+} ions], the Cd stripping (analytical) peak (Figure 7b) is reduced to ca. half of its correct amplitude (Figure 7a).

Thin-Film Composition as a Function of the Electrosynthesis Potential. The FEA protocol, as described above, was applied to a series of samples electrosynthesized at five potentials spanning the −500 to −900 mV range. The results are contained in Figure 8. Clearly, the thin film composition is very sensitive to the electrosynthesis potential. The targeted CdSe content is maximum between −600 and

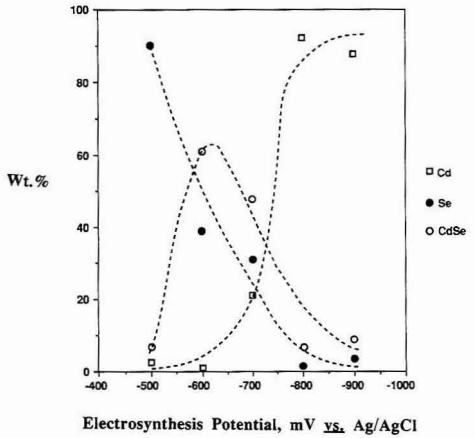

Figure 8. Effect of electrosynthesis potential on the composition of "CdSe" thin films at a Ti foil, as determined by FEA. The dashed lines have been simply drawn through the data as a guide.

−700 mV. On the other hand, the free Se drops from ~90% (weight basis) at −500 mV to nearly 0% at −900 mV, while the free Cd content of the matrix shows an almost exactly reverse trend. With reference to the CV data presented earlier in Figure 3, samples electrosynthesized along the current plateaux in the −0.60 to −0.70 V range (cf. inset in Figure 3) contain the maximal amount of CdSe. It must be noted that these comments pertain to the samples in the *as-deposited state.* Subsequent thermal treatment constitutes a secondary route to facilitate further conversion of the free Cd and Se to CdSe.[5,22]

We have recently presented[20] electrochemical quartz crystal microgravimetry (EQCM) data on the Cd–Se system which show *broadly* similar trends. However, any quantitative comparisons between analytical results from the two studies have to take into account the facts that (a) the support electrode materials are different, namely Au in ref 20 and Ti in the present study, and (b) a much lower concentration of Cd^{2+} was employed in ref 20, viz. 10 mM vis-à-vis 400 mM in this study. Thus, a correspondingly lower content (39%) of free Cd was noted at −900 mV in the previous study. Similarly, the underpotential deposition of Cd, known to occur at the Au surface,[23] provides for a more efficient electrogeneration of CdSe (than that seen in Figure 8) at potentials around −500 mV.

Finally, it is worth emphasizing an important advantage of electroanalytical methods (such as FEA) for semiconductor compositional analyses, namely *selective* monitoring of various component species via control of the potential (or equivalently, current). This is an advantage that other (ex situ) techniques such as photoelectron spectroscopies, electron probe microanalyses, and atomic spectroscopies do not offer.

ACKNOWLEDGMENT

This research was funded, in part, by a grant from the Texas Higher Education Coordinating Board, Advanced Technology Program. We also thank Vepa Krishna for assistance with initial set-up of the FEA system.

RECEIVED for review May 26, 1992. Accepted August 24, 1992.

Registry No. Cadmium, 7440-43-9; selenium, 7782-49-2; cadmium selenide, 1306-24-7.

(20) Wei, C.; Bose, C. S. C.; Rajeshwar, K. *J. Electroanal. Chem.* **1992**, *327*, 331–336.
(21) Wang, J.; Dewald, H. D. *Anal. Chem.* **1983**, *55*, 933–936.
(22) Lin, W-Y.; Mishra, K. K.; Segal, R.; Rajeshwar, K. *J. Phys. Chem.* **1991**, *95*, 3975–3979.
(23) Gregory, B. W.; Norton, M. L.; Stickney, J. L. *J. Electroanal. Chem. Interfacial Electrochem.* **1990**, *293*, 85–101.

Stripping Voltammetry with Preconcentration through Chemical Reactions Coupled to Charge Transfer in an Ionomer-Coated Electrode: Application to the Determination of a Nitrosoamine

Waldemar Gorski† and James A. Cox*

Department of Chemistry, Miami University, Oxford, Ohio 45056

A cathodic stripping voltammetric method for the determination of an aromatic nitrosoamine, 4-nitroso-*N,N*-diethylaniline (NDEA), was developed using a glassy carbon indicator coated with a cation-exchange membrane film. The preconcentration step was shown to involve reduction of the analyte by an ECE mechanism, the product of which couples with NDEA subsequently introduced to the film. This condensation product is reduced at a lower potential than NDEA. The resulting differential pulse stripping current is directly proportional to the solution concentration over the range 5–810 nM NDEA. The detection limit by this method is 3 nM with a 10-min preconcentration of the condensation product followed by a 5-min preoxidation at 800 mV. A comparable stripping method based on the direct reduction of NDEA has a detection limit of 0.1 μM.

INTRODUCTION

Analytical applications of voltammetry at modified electrodes have been slow to appear although several investigations have shown promising results.[1] Among the more interesting possibilities is to use an ionomer-coated electrode or a surface that has been modified by incorporating a chelating agent as the preconcentrator for a stripping voltammetry experiment.[2-6] The advantage over classifical stripping analysis is that the electrode process does not need to be reversible since the preconcentration is by a chemical-exchange process. For example, Cr(VI) was preconcentrated from acid solution by ion exchange at a poly(4-vinylpyridine) film on glassy carbon and determined on the basis of the current produced when it was reduced during a negative-going linear potential scan.[3] The working range with a 60-s preconcentration was 10^{-6}–10^{-8} M. Inclusion of fluoride in the supporting electrolyte and application of 0.9 V vs SCE during the preconcentration prevented the accumulation of Cr(III) oxides which would otherwise passivate the electrode surface.

Adsorptive stripping voltammetry also shares the attribute of not requiring electrochemical reversibility.[7,8] Wang et al.[8] determined proteins such as trypsin and chymotrypsin using preconcentration by adsorption at open circuit followed by linear scan voltammetry to yield an analytical signal due to reduction of the analyte.

The present study is part of a program to devise improved methods for the determination of trace levels of nitrosoamines in water. By using an acidified sample in conjunction with an electrode coated with a cation-exchange film, an ion-exchange stripping voltammetric method can be envisioned. Indeed, others have reported the preferential uptake of aromatic cations over alkali metal ions into Nafion films, presumably because of strong nonspecific interaction between the organic compound and the backbone of the perfluorosulfonated membrane.[9] Based on previous reports,[10,11] reduction of the immobilized NDEA was predicted. As detailed herein, we found that a superior approach was to preconcentrate the NDEA as the product of a condensation reaction which can be promoted within the film by an electrochemical pretreatment step. This product is reduced at a less-negative potential than is NDEA; moreover, the sensitivity of the method based on a chemical preconcentration step is greater than that for the method which utilizes direct preconcentration and subsequent reduction of NDEA.

The use of a chemical conversion of an organic analyte in the preconcentration step constitutes, to our knowledge, a new variation of stripping voltammetry. In perhaps the most-related study, Fogg and Lewis derivatized amines to assist in the preconcentration step of an adsorptive stripping voltammetry procedure.[12]

EXPERIMENTAL SECTION

Chemicals. 4-Nitroso-*N,N*-diethylaniline (Sigma) was used without further purification. Nafion (equivalent weight 1100 g) was purchased from Aldrich as a 5% (wt) solution in lower aliphatic alcohols and 10% water. Methanol (Fisher), used for dilution of the Nafion solution to 2.5%, was of spectral purity.

Stock solutions of 4-nitroso-*N,N*-diethylaniline (NDEA), $c_{NDEA} = 6 \times 10^{-x}$ M (where $x = 2$, 4, or 6), were prepared in 0.05 M HCl (Fisher). Distilled water, purified with a Sybron/Barnstead NANOpure cartridge system, was used in all of the experiments. As NDEA is highly toxic, all solutions of the compound were prepared in a fume hood.

Experimental Techniques and Instrumentation. Cyclic and differential pulse voltammetric measurements were made with an EG&G PAR Potentiostat/Galvanostat Model 273A connected with a MC-GPIB interface board (National Instruments) installed on an IBM PS/2 Model 55 SX computer and controlled by EG&G PAR Model 270 electrochemical software. Voltammograms were recorded on a Hewlett-Packard 7470A digital plotter.

* Author to whom correspondence should be addressed.
† On leave from the Department of Chemistry, Warsaw University, Pasteura 1, Warsaw 02093, Poland.

(1) Cox, J. A.; Jaworski, R. K.; Kulesza, P. J. *Electroanalysis* **1991**, *3*, 869–877.
(2) Oyama, N.; Anson, F. C. *Anal. Chem.* **1980**, *52*, 1192–1198.
(3) Cox, J. A.; Kulesza, P. J. *Anal. Chim. Acta* **1983**, *154*, 71–78.
(4) Espenscheid, M. W.; Martin, C. R. *Electroanalysis* **1989**, *1*, 93–95.
(5) Cheek, G. T.; Nelson, R. F. *Anal. Lett.* **1978**, *A11*, 393–402.
(6) Guadalupe, A. R.; Abruña, H. D. *Anal. Chem.* **1985**, *57*, 142–149.
(7) Paleček, E.; Postbieglová, I. *J. Electroanal. Chem. Interfacial Electrochem.* **1986**, *214*, 359–371.
(8) Wang, J.; Villa, V.; Tupia, T. *Bioelectrochem. Bioenerg.* **1988**, *19*, 39–47.
(9) Nagy, G.; Gerhardt, G. A.; Oke, A. F.; Rice, M. E.; Adams, R. N.; Moore, R. B., III; Szentirmay, M. N.; Martin, C. R. *J. Electroanal. Chem. Interfacial Electrochem.* **1985**, *188*, 85–94.
(10) Leedy, D. W.; Adams, R. N. *J. Electroanal. Chem. Interfacial Electrochem.* **1967**, *14*, 119–122.
(11) Kemula, W.; Krygowski, T. M. In *Encyclopedia of Electrochemistry of the Elements*; Bard, A. J., Ed.; Marcel Dekker: New York, 1979; Vol. XIII, Chapter XIII-3 and references therein.
(12) Fogg, A. G.; Lewis, J. M. *Analyst* **1986**, *111*, 1443–1444.

0003-2700/92/0364-2706$03.00/0

Differential pulse voltammograms (DPVs) were recorded using a negative-going dc scan at a rate 4 mV s^{-1}. The step time was 0.5 s. The pulse amplitude and the current sampling time were varied in the ranges of 20–200 mV and 5–50 ms, respectively.

A conventional three-electrode cell, with a Pt wire counter electrode, a Ag/AgCl/3 M NaCl reference electrode (Bioanalytical Systems, Inc., BAS), and a 3-mm-diameter glassy carbon (GC) disk (BAS) working electrode, was used.

Procedures. The glassy carbon surface was prepared as follows. First, it was polished with an Alpha A polishing cloth (Mark V Lab) using successively smaller particles (1.0-, 0.3-, and 0.05-μm diameter) of alumina suspended in 17.6 MΩ water. The surface was sonicated for 2 min in a closed beaker of distilled water after each polishing step. A final sonication was performed in methanol for 15 min and in water for 5 min. The surface was then air-dried.

The dry GC electrode was coated by adding 10 μL of the 2.5% Nafion solution and evaporating the solvent. The area covered by the film was ca. 6 mm in diameter. Two methods of drying the Nafion films were used. The first involved evaporating the solvent for 15 min under ambient conditions of ca. 20% relative humidity ("dry-cured" film). In the second method, which was based on a recent report,[13] the GC electrode with the added Nafion solution was placed immediately into a closed desiccator which was partially filled with water; it was dried for 48 h under the resulting 85% relative humidity conditions ("wet-cured" films).

Freshly-coated electrodes were preconditioned by immersing in 2 M HCl for 45 min and subsequently cycling the potential between +0.800 and −0.300 V in 0.05 M HCl (background electrolyte) until a steady-state voltammogram was achieved (usually 30 min). This pretreatment procedure was repeated prior to performing a sequence of experiments with the objective of characterizing the electrode performance or of elucidating the mechanism. When applying the electrode to NDEA determinations, sequential standard additions were used, so treatment between experiments was not employed.

All procedures for the determination of NDEA involved a 15-min preconcentration step during which the solution studied was stirred for the first 10 min. The preconcentration into the Nafion film was performed either at open circuit (OC mode) or with the electrode polarized for 10 min at −300 mV and then for 5 min at +800 mV (electrolytic mode). After the preconcentration step, a differential pulse polarogram was obtained by scanning from +800 to −300 mV. The typical range of NDEA concentrations studied was from 5.0×10^{-9} to 8.7×10^{-6} M; however, in some experiments it was extended up to 1.5×10^{-4} M NDEA.

Background currents were obtained by following the procedures described above except that the solutions contained only 0.05 M HCl. These currents were subsequently subtracted from those measured in the presence of NDEA.

All experiments were done at room temperature (20 ± 1 °C) in deaerated solutions under an argon blanket.

RESULTS AND DISCUSSION

A cyclic voltammogram of NDEA recorded at a bare GC electrode in acidic aqueous solution is shown in Figure 1a. The shape is essentially the same as that reported by Leedy and Adams[10] for the cyclic voltammetry of 4-nitroso-*N*,*N*-dimethylaniline (NDMA) on a carbon-paste electrode. They demonstrated that the electrolysis mechanism for NDMA was an ECE-type. Specifically, they proposed that NDMA is reduced in a two-electron step (E) to [*p*-(*N*,*N*-dimethylamino)phenyl]hydroxylamine which dehydrates (C) to form *N*,*N*-dimethyl-*p*-phenylenediimine. Under the same cathodic peak, the imine is further reduced in a two-electron step (E) to the corresponding diamine. The diamine undergoes a quasireversible oxidation at a potential about 400 mV less negative than the peak for the reduction of NDMA. In fact, the electrochemical reductions of aromatic nitroso compounds generally occur by ECE mechanisms.[11] Since the replacement

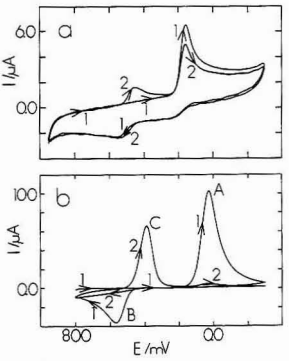

Figure 1. Cyclic voltammograms for 1.1×10^{-4} M NDEA on (a) bare GC electrode at a scan rate of 50 mV s^{-1} and (b) for 1.5×10^{-4} M NDEA on dry-cured GC/Nafion electrode after preconcentration with the OC mode at a scan rate of 4 mV s^{-1}. Background electrolyte, 0.05 M HCl. Numbers at curves indicate order of the trials.

of the methyl with an ethyl group should not markedly change the voltammetric behavior, this mechanism is assigned to the reduction of NDEA in Figure 1a.

When the bare GC electrode, after several potential cycles in NDEA solution, is removed, rinsed with water, and transferred to 0.05 M HCl, the pair of peaks centered at about 500 mV is still observed, but the currents are diminished. Apparently, adsorption is involved in the electrode process.

In a solution of 0.05 M HCl, NDEA, for which the pK_A is 4.48,[14] exists primarily as a cation which can be sorbed by a Nafion layer on a GC electrode. Because of strong, nonspecific interactions between organic compounds and the membrane backbone,[9] cationic NDEA can preconcentrate even in the presence of a large excess of inorganic cations. A cyclic voltammogram of NDEA bound in a Nafion layer on a GC electrode is shown in Figure 1b. An important characteristic is that the current of cathodic peak A (Figure 1b) is diminished after the first cycle by a factor of more than 20. Apparently, most of the nitroso compound present in the Nafion layer is irreversibly reduced during the first potential excursion to values more negative than 200 mV. As a result, peaks A and B, which are coupled, both practically vanish with cycling. The only voltammetric peak which is sustained at steady state is cathodic peak C (Figure 1b).

Peak C was not characterized in the study of the electrochemistry of NDMA in homogeneous solution,[10] but the related chemistry can be surmised from other studies on the oxidation of compounds related to the diamine. For example, the oxidative dimerization of aniline to an azo compound was demonstrated by surface-enhanced Raman spectroscopy (SERS).[15] Using SERS in conjunction with cyclic voltammetry, Shi et al.[16] demonstrated that nitroso intermediates in the reduction of *p*-nitrobenzoic acid condense with an aromatic hydroxylamine to form an azoxy compound. The latter reaction, as well as coupling between aromatic nitroso compounds and aromatic amines to form azo compounds, is well-known.[17] Therefore, it is suggested that peak B results in the formation of an azo compound, the four-electron reduction of which leads to peak C.[18] The proposed mech-

(13) Striebel, K. A.; Scherer, G. G.; Haas, O. *J. Electroanal. Chem. Interface Electrochem.* **1991**, *304*, 289–296.

(14) Gornostaev, L. M.; Skvortsov, N. K.; Belyaev, Yu. E.; Ionin, B. I. *Zh. Org. Khim.* **1974**, *10*, 2484–2486.

(15) Gao, P.; Gosztola, D.; Weaver, M. J. *J. Phys. Chem.* **1989**, *93*, 3753–3760.

(16) Shi, C.; Zhang, W.; Birke, R. L.; Gosser, D. K., Jr.; Lombardi, J. R. *J. Phys. Chem.* **1991**, *95*, 6276–6285.

(17) Boyer, J. H. In *The Chemistry of the Nitro and Nitroso Groups*; Feuer, H., Ed.; Interscience: New York, 1969; Chapter 5.

anism for the cyclic voltammetry of NDEA sorbed into the Nafion film at a glassy carbon electrode is summarized as follows. At about 30 mV during the first negative-going scan, NDEA is reduced (peak A, Figure 1b) by the process

$$\text{NDEA} + 2e^- + 2H^+ \rightarrow \text{PHA} \quad (1)$$

$$\text{PHA} \rightarrow H_2O + \text{PDI} \quad (2)$$

$$\text{PDI} + 2e^- + 2H^+ \rightarrow \text{PDA} \quad (3)$$

where PHA is [(*N*,*N*-diethylamino)phenyl]hydroxylamine, PDI is *N*,*N*-diethyl-*p*-phenylenediimine, and PDA is *N*,*N*-diethyl-*p*-phenylenediamine. During the reverse scan, PDA is oxidized at about 570 mV (peak B, Figure 1b)

$$2\,\text{PDA} \rightarrow 4e^- + 4H^+ + \text{EAAB} \quad (4)$$

where EAAB is 4,4′-(*N*,*N*-diethylamino)azobenzene. During the second negative-going cycle, EAAB is reduced at about 400 mV (peak C, Figure 1b) stepwise to PDA

$$\text{EAAB} + 2e^- + 2H^+ \rightarrow \text{EAHAB} \quad (5)$$

$$\text{EAHAB} + 2e^- + 2H^+ \rightarrow 2\,\text{PDA} \quad (6)$$

where EAHAB is 4,4′-(*N*,*N*-diethylamino)hydrazobenzene. Only a single, narrow peak is developed, which suggests that reaction 6 is facile relative to reaction 5.

The above mechanism is supported by the results of stripping voltammetry experiments performed in the concentration range, 5.0 nM to 0.51 μM NDEA. Here, differential pulse voltammetry was used in conjunction with preconcentration into the Nafion layer in order to obtain faradaic currents above the background level.

A series of experiments was performed at a Nafion-coated GC electrode (dry-cured) on a solution of 0.05 M HCl to which NDEA was added by sequential spikes. Prior to each trial, the indicator electrode was contacted to the sample solution for 15 min in the OC mode. After each pulse-stripping measurement step, the sample was spiked to the next concentration of NDEA, and the OC preconcentration was initiated. Based upon our recent study of the transport of an aromatic cation through a cation-exchange membrane (Nafion),[19] preconcentration of protonated NDEA by an ion-exchange mechanism was expected even though the ionic strength of the sample was high relative to the NDEA concentration. The stripping voltammogram which results is shown in Figure 2. The first appearance of a faradaic peak was with a NDEA concentration of 30 nM. The stripping potential corresponded to peak C rather than to peak A of Figure 1b. The threshold concentration for the appearance of peak A, which is due to the direct reduction of NDEA (reaction 1), is in the 0.1–0.3 μM range (Figure 2). These observations are consistent with the hypothesis that peak C is due to the reduction of an azo compound formed by condensation of the parent nitrosoamine and a diamine which is present in the film from the ECE reduction of NDEA in the previous trial.

$$\text{NDEA} + \text{PDA} \rightarrow \text{EAAB} \quad (7)$$

Such reactions are well-known.[17] By reaction 7, the PDA that accumulates in the film during a sequence of experiments, which does not include a rather lengthy (ca. 45 min) acid-wash step between trials, chemically converts the sorbed NDEA to an azo compound. The azo compound is more easily reduced than the parent NDEA.

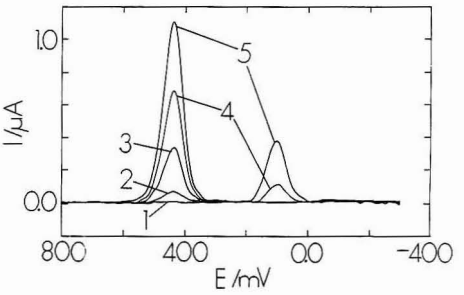

Figure 2. Background corrected DPVs on a dry-cured GC/Nafion electrode after preconcentration with the OC mode in a solution spiked with increasing amounts of NDEA. C_{NDEA}: (1) 5×10^{-9}; (2) 3×10^{-8}; (3) 1.1×10^{-7}; (4) 3.1×10^{-7}; and (5) 5.1×10^{-7} M. Background electrolyte, 0.05 M HCl. Pulse amplitude, 50 mV; pulse time, 50 ms.

The mechanistic study provides a guideline for describing conditions for the determination of trace levels of NDEA. The peak at 440 mV (Figure 2) permits detection at lower concentration than does that for the direct reduction of NDEA. This experimental observation is probably indicative of the relative mobilities of these compounds in Nafion.

In order to use the reduction of EAAB for analytical purposes, the preconcentration step must include conversion of NDEA to EAAB. With a modified electrode that was not previously used or which was acid-washed between experiments, open circuit preconcentration will give a low result for the first trial since PDA, which is needed in reaction 7, is not present in the film during the preconcentration step. Two or three trials on a given sample are generally sufficient to load the film with the necessary amount of PDA by reactions 1–3. The electrolytic preconcentration mode described in the Experimental Section does not require a pretreatment of a new or acid-washed film. During the first 10 min of preconcentration at −300 mV, NDEA is converted to PDA by reactions 1–3. The electrode is then polarized at 800 mV for 5 min. The azo compound is formed by reaction 4. Additional NDEA which is sorbed into the film during the period at 800 mV and while the stripping potential scan is applied will not be detected at peak C when a new or acid-washed film is used; however, this quantity will be small relative to that accumulated at −300 mV. That the sample is stirred only during the 10-min preconcentration at −300 mV accounts for this difference in the amount of NDEA sorbed.

Prior to optimizing the preconcentration and stripping steps, the influence of the drying step on the performance of the Nafion-coated GC electrode was examined. This investigation was inspired by a recent report of improved ion-exchange behavior for hydrophobic cations when a Nafion film is wet-cured.[13] A comparison of the stripping voltammetry of NDEA at wet- and dry-cured Nafion is shown in Figure 3. At the wet-cured film, the analytical signal is more than twice the value observed with the dry-cured film. Also significant is the fact that the peak for the reduction of NDEA is attenuated at the wet-cured film; it is not observed above the background until the NDEA concentration exceeds 1 μM. Although it is not surprising that the peak for the direct reduction of NDEA is small, the data in Figure 3 suggest that the coupling reaction of NDEA is more efficient in the

(18) Thomas, F. G.; Boto, K. G. In *The Chemistry of Hydrazo, Azo and Azoxy Groups*; Patai, S., Ed.; John Wiley: London, 1975; Chapter 12.

(19) Cox, J. A.; Poopisut, N. *Anal. Chem.* **1992**, *64*, 423–426.

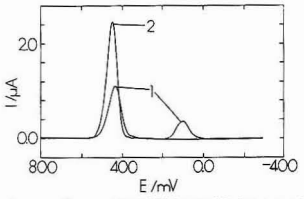

Figure 3. Background corrected DPVs on (1) dry-cured and (2) wet-cured GC/Nafion electrode recorded after loading in NDEA solution under conditions corresponding to curve 5 in Figure 2. Experimental conditions as in Figure 2.

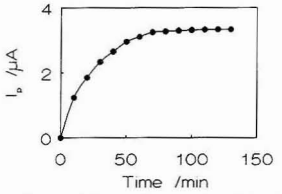

Figure 4. Dependence of the peak current on the preconcentration time in a solution of 1×10^{-7} M NDEA. Other experimental conditions are those in Figure 5.

wet-cured film. In all subsequent experiments the wet-cured Nafion was used.

In order to establish the optimum analytical procedure, the following experimental parameters were varied: preconcentration potential, pulse amplitude, and current sampling time. First, using stripping conditions of 4 mV s^{-1} dc scan rate, 50-mV pulse amplitude, and 50-ms current-sampling time, the OC and electrolytic preconcentration modes were compared. In all cases, the film contained PDA from previous experiments. That is, the acid-washing steps described in the Experimental Section was not used in this part of the study. The peak current at 440 mV (Figure 3) comprised the analytical signal. In the 5–100 nM DNEA range, the sensitivities of the electrolytic and OC modes were the same, but above 100 nM the former was more sensitive. The electrolytic mode was employed in subsequent work. Using pulse amplitudes of 20, 50, and 100 mV, the peak currents were 18.5 ± 0.2, 63 ± 1, and 162 ± 3 μA (n = 5), respectively, with a 1.5×10^{-4} M NDEA solution and a 10-ms current-sampling time. This observation is consistent with the general behavior of differential pulse voltammetry.[20] With amplitudes above 100 mV, further increases in sensitivity were not significant. Also expected was the observation that shorter sampling times yielded higher sensitivities. Below 10 ms, the greater background current offsets the increase in sensitivity. The subsequent experiments were performed with a 100-mV pulse amplitude and a 10-ms current-sampling time.

The sensitivity of the method is a function of preconcentration time. As shown in Figure 4, the analytical peak current increases with preconcentration times at −300 mV up to 1 h. At that point, when 0.1 μM NDEA is the sample, the film is apparently saturated. A preconcentration time of 10 min at −300 mV was selected because, as shown below, a useful sensitivity was obtained without deleterious effects such as fouling, which may occur with high loadings of the Nafion layer.

Stripping voltammograms obtained under the optimized conditions are shown in Figure 5. A linear least squares fit of peak current vs concentration over the range 5.0–810 nM NDEA (eight points) under the Figure 5 conditions yielded the following: slope, 19.3 ± 0.1 nA/nM; intercept, 0.02 ± 0.02 μA; and correlation coefficient, r, 0.9999. Here, the NDEA concentration was increased by sequential standard addition. The detection limit was 3.0 nM using the criteria of the concentration that yields a background-corrected signal of 3 times the standard deviation of the blank.

(20) Hasebe, K.; Osteryoung, J. *Anal. Chem.* **1975**, *47*, 2412–2418.

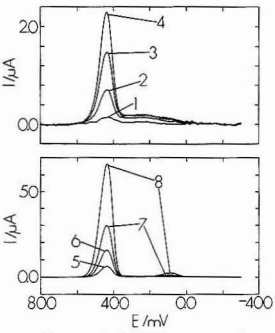

Figure 5. Background corrected DPVs on a wet-cured GC/Nafion electrode after preconcentration with the electrolytic mode in a solution spiked with increasing amounts of NDEA. C_{NDEA}: (1) 5×10^{-9}; (2) 3×10^{-8}; (3) 7×10^{-8}; (4) 1.1×10^{-7}; (5) 3.1×10^{-7}; (6) 8.1×10^{-7}; (7) 1.81×10^{-6}; and (8) 4.77×10^{-6} M. Background electrolyte, 0.05 M HCl; pulse amplitude, 100 mV; pulse time, 10 ms.

The wet-cured Nafion-coated GC electrode was stable in the present study. A single electrode was used for 3 weeks without any change in behavior when cleaned in 2 M HCl and stored in 0.05 M HCl after a series of experiments. Concentrations above 10 μM NDEA were not used during this period, however.

As a test for matrix effects on the method, a calibration curve was obtained by spiking Miami University tap water with various concentrations of NDEA. Each solution contained 0.05 M HCl. In the range 5.0–810 nM, a linear least squares fit of current vs concentration (eight points) yielded the following: slope, 13.6 ± 0.1 nA nM^{-1}; intercept, −0.01 ± 0.02 μA; and correlation coefficient, r, 0.9998. The detection limit was 8 nM NDEA. The lower slope probably reflects an influence of multicharged inorganic cations on the sorption of protonated NDEA. The water sample had a total hardness of 344 ± 4 mg/L (five trials with a EDTA titration with results expressed as $CaCO_3$). If the decrease in sensitivity of 30% is unacceptable, quantifying the concentration by sequential standard addition can be employed.

The water sample used in the above study had a sodium ion content of (5.0 ± 0.4) 10^{-4} M based on five trials by flame atomic absorption spectrometry. Because of the high affinity of Nafion for aromatic cations relative to alkali metals,[9] the sodium ion concentration was not expected to influence the sensitivity. This was verified by performing an experiment that compared the responses of 20 nM NDEA in supporting electrolytes containing 0, 0.05, 0.10, and 0.15 M NaCl in addition to 0.05 M HCl. Five trials under the conditions in Figure 5 were performed on each solution. The respective peak currents were 0.44 ± 0.03, 0.43 ± 0.03, 0.46 ± 0.03, and 0.49 ± 0.03 μA. The currents in the presence of NaCl are not significantly different at the 95% confidence level (t-test) except for the 0.15 M NaCl case, where the departure from the mean current for the experiments in the absence of NaCl, 0.05 μA, is slightly out of the 95% confidence interval, 0.44 ± 0.043 μA.

In conclusion, the reported stripping analysis procedure is promising for the determination of nanomolar levels of aromatic nitrosoamines. The method may be well-suited to other classes of aromatic compounds which form cations in acidic solution and are reduced by a mechanism involving

coupled following chemical reactions to form electroactive products. With analytes for which it is suited, this procedure may be more selective and less subject to matrix effects than comparable electrochemical techniques such as differential pulse voltammetry (with or without preconcentration) and adsorptive stripping voltammetry. However, more practical applications of the described mechanism may result if the chemistry is initiated and quantified in a dual-indicator electrode amperometric cell for high-performance liquid chromatography. That possibility is presently being explored.

ACKNOWLEDGMENT

This work was supported by Grant No, R816507-01-0 from the U.S. Environmental Protection Agency.

RECEIVED for review May 27, 1992. Accepted August 24, 1992.

Registry No. NDEA, 120-22-9; carbon, 7440-44-0; water, 7732-18-5.

Trace Element Analysis Using X-ray Absorption Edge Spectrometry

Masaharu Nomura

Photon Factory, National Laboratory for High Energy Physics, Oho, Tsukuba 305, Japan

The sensitivity of X-ray absorption edge spectrometry has been improved by using synchrotron radiation as the light source and analytical method developed for EXAFS. Qualitative and quantitative information is obtained free from any interferences which are experienced in many physicochemical methods and free from any empirical information except the thickness of sample cell by using this method nondestructively. Excellent linearity is shown on Ag–Cd (200–1 ppm Cd in 1000 ppm Ag) and Cu–Zn systems. Minimum detection limit is 0.5 ppm for cadmium and 2 ppm for zinc, respectively.

INTRODUCTION

The concept of X-ray absorption edge spectrometry (XAES) was developed in 1925 by Glocker and Frohnmayer.[1] They measured absorbances at several energies above and below the absorption edge sought and determined the concentration of the element from the estimated variation of absorbance at the absorption edge (hereafter called as edge-jump). This method has many advantages compared with other spectrochemical analytical methods. Elemental selectivity, the little matrix effect, and interference are the most important ones. However, as this method had taken a long time owing to weak white radiation and rather poor X-ray optics, usually measurements were carried out at two energies bracketing the absorption edge using characteristic X-rays instead of measurements at several energies[2] thereafter (bracketing method). For example, copper and nickel Kα lines were used in order to determine the concentration of cobalt in a solution. The bracketing method suffered some matrix effect because it cannot distinguish the change of edge-jump (concentration of target element) from the change of energy dependence of absorbance, the change of matrix composition. Making the matter worse, this method cannot give correct result if some absorption edges exit between two observed energies.

Although the X-ray fluorescence analysis is popular, it suffers serious matrix effects and interferences. Also it is not easy to analyze a small amount of an element in a large amount of the previous element in atomic number such as zinc in copper. On the contrary, the sensitivity of XAES was rather low compared with that of X-ray fluorescence analysis. The low sensitivity of XAES was restricted by the statistical error of the signal and the error of the background estimated from only a few data points.

Recently X-ray absorption fine structure (XAFS) has become a powerful tool for structure and electronic state analysis with the help of intense synchrotron radiation. The experimental method of XAFS is exactly the same as original XAES and can give the direct information about edge-jump, which makes the matrix effect negligible. Also the analytical method of XAFS is well suited for extracting minute variation of absorbance in a spectrum. By using these techniques the sensitivity of XAES has been much improved. Here two examples, cadmium in 1000 ppm silver solution and zinc in 0.3 mol/L copper solution, are shown. Both examples indicate the superiority and high sensitivity of XAES.

EXPERIMENTAL SECTION

Silver–cadmium solutions were obtained by mixing weighed amounts of silver and cadmium standard solutions for atomic absorption analysis (1000 ppm, Kanto Chemical Co., Inc.). Copper solution was prepared by dissolving copper(II) oxide (2.39 g) for elemental analysis (Merck) in reagent-grade perchloric acid (34.8 g, Kanto Chemical Co., Inc.) and then diluting to 100 mL with pure water. The copper concentration was 0.3 mol/L. Copper–zinc solutions were obtained by mixing this copper solution and zinc standard solution for atomic absorption analysis (1000 ppm, Kanto Chemical Co., Inc.). The content of zinc in the perchloric acid and the pure water was measured by means of ICP analysis. They were less than the detection limits, 1.5 and 0.01 μg/mL, respectively.

High monochromaticity is required for X-rays, and the control of thickness and uniformity of samples is important in X-ray absorption experiments.[3] X-ray absorption spectra were obtained by using XAFS facility at beamline 10B of Photon Factory in the National Laboratory for High Energy Physics. X-rays were monochromatized by a Si(311) channel-cut monochromator.[4] Higher orders were less than 7×10^{-4} around the copper K absorption edge and less than 2×10^{-5} at the silver edge. To make tha matter better, the ionization chamber becomes less sensitive with the increase of photon energy. Sample solutions were poured into cells made of acryl whose thicknesses were 45 mm for Ag–Cd and 2 mm for Cu–Zn mixtures. Each cell has 0.5-mm-thick acryl windows. The sample cell was placed between two ionization chambers, one monitoring incoming flux (I_0) and another the transmitted flux (I) through sample, and then apparent absorbance, ln (I_0/I), was calculated. This apparent absorbance must be distinguished from the true one because it contains instrumental factors such as the detection efficiencies of the detectors as a function of energy.[5] However, edge-jump reflects the true one because the detection efficiencies can be assumed constant within a narrow energy region.

DATA ANALYSIS

Two absorption edges, copper and zinc or silver and cadmium, were recorded in a spectrum. Spectra were analyzed according to usual manner used in data analysis of EXAFS[3] except the handling of the second edge. At first the preedge absorption of the lighter element was removed by fitting it to a second-order polynomial. Then EXAFS wiggle ($\chi(k)$) was extracted from postedge total absorption by using eq 1. The discontinuity in absorption derived from the heavier element is also included in $\chi(K)$. Here $\mu_0(E)$ is the smooth

$$\chi(k) = \{\mu(E) - \mu_0(E)\}/\mu_0(E) \quad (1)$$

(1) Glocker, R.; Frohnmayer, W. *Ann. Phys.* **1925**, *76*, 369–395.
(2) Hakkila, E. A.; Waterbury, G. R. *Adv. X-ray Anal.* **1960**, *3*, 11–39.
(3) Lee, P. A.; Citrin, P. H.; Eisenberger, P.; Kincaid, B. M. *Rev. Mod. Phys.* **1981**, *53*, 769–806.
(4) Nomura, M.; Koyama, A. *X-ray Absorption fine structure*; Hasnain, S. S., Ed.; Ellis Horwood: Chichester, 1991; pp 667–669.
(5) Nomura, M. *KEK Rep.* **1985**, No. 85-7.

0003-2700/92/0364-2711$03.00/0

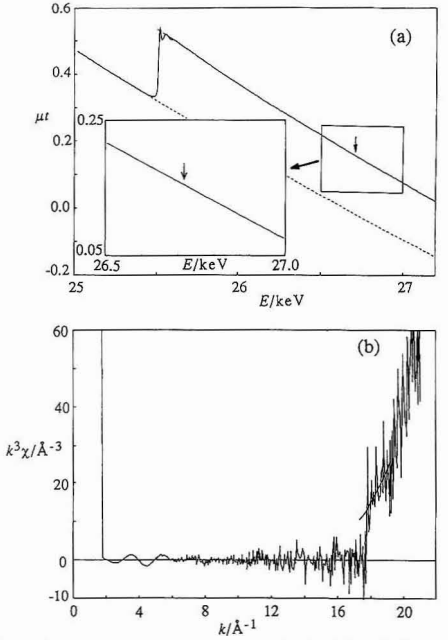

Figure 1. (a) Raw XAES spectrum of a mixed solution of silver and cadmium, Cd/Ag = 1/500, and the concentration of silver is 1000 ppm. Enlarged plot is shown in an inset, but no absorption edge ascribable to cadmium (the position indicated by an arrow) can be observed. (b) $k^3\chi(k)$ of the spectrum. A discontinuity due to cadmium absorption edge can be observed clearly at k = 17.8 Å^{-1}.

background of $\mu(E)$ which was obtained by applying a cubic spline fit between two absorption edges. At the same time, the horizontal axis was changed from energy (E) to wave vector (k) according to $k = [0.263(E - E_0)]^{1/2}$. The energy of the absorption edge of the lighter element is chosen as E_0. Though this conversion is essential in the case of EXAFS analysis, it is not always necessary for quantitative analysis. Generally $\chi(k)$ is multiplied by k^3 in order to enhance weak EXAFS signal at high k region.

The edge-jump of the lighter element is directly obtained from the extrapolation of $\mu_0(E)$ and that of the heavier one is similarly obtained when the edge-jump was easily observed in the raw spectrum. However, it is obtained from the variation of $\{k^3\chi(k)\}\mu_0(k)/k^3$ when the edge-jump is too little in the raw spectrum. This data handling process is shown in Figure 1. An absorption edge can be distinguished from the oscillation of EXAFS because the former is steeper change in μt than the latter one.

Theoretical mass absorption coefficients were cited from refs 6–8. In case of ref 8, the mass absorption coefficients below an edge were calculated by using C2 and D2, whereas those above the edge were calculated by using C1 and D1. The difference of absorption coefficient was within 10% and that of edge-jump was less than 5% among three tables. Therefore mass absorption coefficients were cited from the McMaster's table.[6]

(6) McMaster, W. H.; Kerr Del Grande, N.; Mallett, J. H.; Hubell, J. H. *Compilation of X-ray Cross Sections*; National Information Service: Springfield, 1969.
(7) Sasaki, S. *KEK Rep.* **1990**, No. 90-16.
(8) Lonsdale, K., Ed. *International tables for x-ray crystallography*; Kynoch Press: Birmingham, 1968; Vol. 3.

Quantitative information on the concentration of minor elements were determined by means of two methods. The first is the direct comparison of observed and calculated edge-jumps (edge-jump method). If the density and the thickness of the sample is already known, the concentration can be calculated from eq 2. Here $\Delta\ln(I_0/I)$ is the observed edge-

$$\Delta\ln(I_0/I) = \Delta\mu_{M_i} W_i \rho d = \Delta\mu_{M_i} c_i d = \Delta\mu_i \qquad (2)$$

jump, ρ the density (g/cm^3), d the thickness of the sample (cm), $\Delta\mu_{M_i}$ the variation of the authentic mass absorption coefficient at the absorption edge (cm^2/g) and W_i the mass fraction of ith element, respectively. Information on density of the solution can be omitted if mass concentration, c_i (g/mL), is required.

The second method is to get the ratio of edge-jumps of minor and major elements in a solution and then calculate the concentration of the minor element according to eq 3 (ratio method). As the concentration of the major element,

$$\Delta\mu_i/\Delta\mu_j = \{\Delta\mu_{M_i} W_i\}/\{\Delta\mu_{M_j} W_j\} \qquad (3)$$

W_j, can be determined easily by means of other analytical methods, that of the minor element can be determined also easily. In this method information on the density and the thickness of the sample is not required.

RESULTS AND DISCUSSION

Cadmium in Silver. X-ray absorption spectrum of blank showed no edge jump larger than noise level, 0.0002, at silver K absorption edge, which corresponds to 1 ppm silver in a 4.5-cm-long water or a 4-nm-thick silver layer. Also no absorption edge greater than noise level, 0.0001, was observed at cadmium K absorption edge in the spectrum of silver standard solution.

The raw X-ray absorption spectrum of a silver–cadmium mixture (Cd/Ag = 0.0021 in mole ratio) is shown in Figure 1a with its preedge background (broken line). The steep rise of absorbance at 25.5 keV indicates the silver K absorption edge by the major component. An enlarged spectrum between 26.5 and 27 keV is inset in the figure. An arrow indicates the expected position of cadmium absorption edge (26.7 keV), but no edge-jump can be found. Figure 1b expresses the $k^3\chi(k)$ as a function of wave vector k. The position of cadmium K absorption edge is 17.8 Å^{-1} in k space, and clear discontinuity of $k^3\chi$ is found in the figure. This jump reflects the absorption by minor cadmium component. A smooth line is drawn above the cadmium edge, and edge-jump is calculated as described before.

On the analysis of edge-jump method, the density of the solutions was assumed as 1 g/cm^3, and 4.5 cm was used as the path length. Numerical results are listed in Table I and show good agreement between observed and calculated ones through 3 orders. This result indicates that XAES does not require any working curve when the density and thickness of the sample is correctly estimated. The minimum detection limit is defined as the edge-jump becomes the same as noise level in the spectrum and is about 0.0005 μg/mg of solution, 0.5 ppm. There is no upper limit of concentration if appropriate cell length is chosen.

The result of the ratio method is also written in Table I and indicates high linearity of this analysis and excellent agreement with calculated ratio of edge-jumps. Therefore the working curve is not necessary in this method too. Furthermore, information about the path length and density is not necessary in this case. This is a merit of the ratio method because it is not easy to estimate the correct thickness of powdery samples.

Table I. Results on Silver–Cadmium Solution[a]

mole ratio Cd/Ag	w(Cd), μg/mg of solution	$\Delta\mu t$(Ag)		$\Delta\mu t$(Cd)		$\Delta\mu t$(Cd)/$\Delta\mu t$(Ag)	
		obs	calc	obs	calc	obs	calc
0.197	0.17	0.178	0.172	0.032	0.0325	0.18	0.189
0.097	0.092	0.196	0.188	0.017	0.0175	0.089	0.0931
0.049	0.048	0.205	0.197	0.0088	0.0091	0.043	0.0460
0.020	0.021	0.211	0.203	0.0039	0.0039	0.019	0.0193
0.010	0.010	0.213	0.205	0.0023	0.0020	0.011	0.0097
0.010	0.010	0.211	0.205	0.0023	0.0020	0.011	0.097
0.0058	0.0060	0.214	0.206	0.0011	0.0011	0.0052	0.0055
0.0021	0.0022	0.214	0.207	0.00039	0.00042	0.0018	0.0020
0.0012	0.0012	0.216	0.207	0.00020	0.00023	0.00091	0.0011

[a] The density of the solution was assumed as 1 g/cm^3 and the cell length was 4.5 cm. Calculations are based on the mass absorption coefficients in ref 6.

Table II. Results on Copper–Zinc Solutions

mole ratio[a] Zn/Cu	w(Zn),[b] μg/mg of solution	$\Delta\mu t$(Cu)		$\Delta\mu t$(Zn)		$\Delta\Delta\mu t$(Zn)[c]
		obs	calc	obs	calc	
0.012	0.17	0.844	0.794	0.0093	0.0087	0.0006
0.0059	0.092	0.776	0.866	0.0059	0.0048	0.0011
0.0059	0.092	0.794	0.866	0.0059	0.0048	0.0011
0.0030	0.049	1.032	0.908	0.0035	0.0025	0.0010
0.0012	0.020	1.078	0.935	0.0021	0.0010	0.0011
0.00	0.00	1.10	0.954	0.0010	0.00	0.0010
0.00	0.00	1.07	0.954	0.0011	0.00	0.0011

[a] Mole ratio of intentionally added zinc to copper. [b] Concentration of intentionally added zinc. [c] $\Delta\Delta\mu t(\mathrm{Zn}) = \Delta\mu t(\mathrm{Zn})_{obs} - \Delta\mu t(\mathrm{Zn})_{calc}$. The density of the solutions was assumed as 1.137 g/cm^3 and the cell length was 0.2 cm. Calculations are based on the mass absorption coefficients in ref 6.

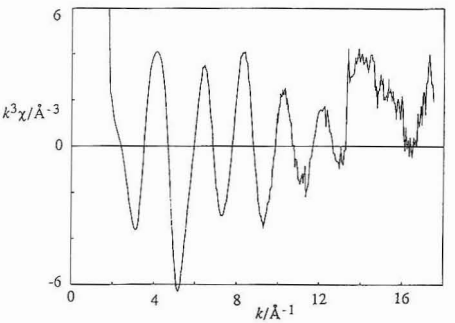

Figure 2. $k^3\chi(k)$ of the copper solution prepared from copper oxide. An absorption edge due to zinc can be clearly observed at k = 13.4 Å^{-1}.

Zinc in Copper. X-ray absorption spectrum of the blank showed a weak edge-jump at copper absorption edge, 0.0007, which corresponds to 3-nm-thick copper foil or 2×10^{-4} mol/L copper solution in 2-mm-thick water. This jump will be due to the impurity contained in the window of ionization chambers. No indication of a zinc absorption edge greater than 0.000 04 was observed in the spectrum, which corresponds to 0.2-nm-thick zinc foil or 2-mm-thick 0.65 μg/mL zinc aqueous solution.

Figure 2 shows the $k^3\chi(k)$ of a 0.3 mol/L copper solution in which no zinc was added intentionally. Here a discontinuity of $k^3\chi$ is clearly observed at k = 13.4 Å^{-1}, though no discontinuity was observed in the raw μt. This discontinuity corresponds to the absorption edge of zinc. The edge-jump of zinc is 0.0010.

Edge-jump method was applied to several mixture solutions of copper and zinc and compared with calculated edge-jumps based on the quantity of intentionally added zinc. The results are listed in Table II with the differences between observed and calculated edge-jumps ($\Delta\Delta\mu t$(Zn)). The difference in edge-jump was almost constant through a wide concentration range, and its average was 0.0010, which agrees well with the edge-jump of the copper solution without adding any zinc solution. This difference indicates that zinc impurity was contained in the copper solution and/or in the windows of the sample cell or ionization chambers. The latter possibility can be denied by the small edge-jump found in blank spectra.

In order to assure this idea, a 0.15 mol/L copper solution was prepared from the copper oxide keeping the concentration of perchloric acid. The edge-jump of zinc was 0.0005, which was about a half of that found in 0.3 mol/L copper solution: the edge-jump is proportional to copper concentration. This result also supports the conclusion that the origin of zinc is copper solution or copper oxide itself and excludes the possibility of the contamination in windows. The concentration of zinc is calculated as 21 μg/mL.

Inductively coupled plasma atomic emission (ICP) analysis on the copper solution were carried out using two facilities. They gave the copper content as 8.9 and 10.1 μg/mL. The reason of the difference between XAES and ICP results is not clear. The interference of two emission lines, copper and zinc, can be excluded from the spectra of reference samples, pure copper and zinc solutions. The random error in edge-jump of zinc is ca. 0.0001, which is determined by the noise in $k^3\chi$ and corresponds to 2 μg/mL. This error can be reduced by integrating the signal for a longer period around the edge. The mixing of XAES and XAFS signals at the zinc absorption edge may cause a certain systematic error. Though a rather rough energy step (≈6 eV) was used in this study, finer steps can improve the discrimination of both signals. On the other hand, the ICP results scattered at rather concentrated solutions, and their sensitivity strongly depended on the viscosity of the sample.

CONCLUSIONS

The merits of XAES are demonstrated by two systems: cadmium in silver and zinc in copper. XAES can be applied

for wide concentration range without any working curves. Furthermore, there is no matrix effect and little interferences. Therefore it can be used as an analytical method complimentary with X-ray fluorescence. Application of this method is not restricted to the liquid phase; it can be applied to any phase if a fairly uniform sample is prepared. This method will be powerful for the quantitative analysis of rare earths.

ACKNOWLEDGMENT

The author wishes to express his thanks to Masami Taira of the Radiation and Safety Control Center and Hiroshi Nishiooji of the Toray Research Center for their ICP analysis.

RECEIVED for review January 21, 1992. Accepted July 31, 1992.

Improvement in Fingerprinting Capability of Surface-Enhanced Raman Spectrometry by Simultaneous Measurement of Scattering Signal and Transmitted Light

R. Montes, C. Contreras, A. Rupérez, and J. J. Laserna*

Department of Analytical Chemistry, Faculty of Sciences, University of Málaga, 29701 Málaga, Spain

A method for simultaneous measurement of surface-enhanced Raman spectra (SERS) and absorbance changes occurring in colloid substrates is reported. The method provides information on the aggregation state of the colloid while the SERS spectrum is recorded. The relationship between colloid aggregation and SERS intensity is thus readily established, allowing recording of SERS spectra under the most favorable circumstances. Anomalous bands, which appear and disappear mainly at low concentration, are detected and studied.

INTRODUCTION

Since the discovery[1] of surface-enhanced Raman spectrometry (SERS) most theoretical and practical work has been directed to the elucidation of enhancement mechanisms and description of applicable substrates.[2-5] Most recently, novel aspects of the technique have been investigated, including the relationships between the SERS activity and surface morphology of the substrate[6,7] or chemical structure of the aggregating substance,[8] attenuation of SERS spectra by protein adsorption,[9] and effects of formation of silver clusters and changes in optical properties of silver colloid.[10] The results reported allowed the development of qualitative methods of analysis by SERS.[11-15] However, it has been difficult to obtain reproducible enhancements (signals) mostly when hydrosols are used. Although semiautomatic processing of samples and colloid substrates in flow injection systems[16] could improve precision up to levels of ca. 5%, the poor reproducibility observed in batch systems hinders acceptation of SERS as a practical technique for quantitative trace analysis. In addition, poor reproducibility makes difficult interpretation of SERS spectra.

Silver hydrosols are easy to characterize in terms of particle size by electronic absorption spectroscopy. This issue is of relevance in SERS studies since the enhancement factor for a given adsorbate is closely related to the particle size.[17] The use of absorption spectroscopy as a diagnostic tool in characterization of colloids is of limited scope, however. Crystal growth in colloidal systems depends on a variety of experimental parameters and it is inherently a dynamic process. As a result the colloid examined spectrophotometrically is usually at a different aggregation degree than that used for the SERS measurement.

In this work a method for simultaneous measurement of SERS spectra and absorbance changes occurring in colloid substrates is reported. The method employs a medium-power He–Ne laser for excitation and a low-power He–Ne laser for probing the scattering volume. The lasers are used in a crossed-beam configuration. The intensity of the transmitted probe beam is detected with a silicon photodiode. The method provides information on the aggregation state of the colloid while the SERS spectrum is being recorded. The relationship between colloid aggregation and SERS intensity is thus readily established, allowing recording of SERS spectra under the most favorable circumstances.

EXPERIMENTAL SECTION

Instrumentation. The excitation source consisted of a He–Ne laser (Siemens, Model LGK 7626S), tuned at 632.8 nm, releasing about 30 mW at the sample. The sample was placed in a standard 1-cm square cell (four optical faces). In order to match illumination–collection geometries, the excitation beam illuminated the sample in a vertical configuration. This method allows a 9-fold improvement in signal-to-noise ratio regarding the standard horizontal illumination geometry.[18,19] A 0.5-mW He–Ne laser, also at 632.8 nm, crossed the excitation beam at the center of the scattering volume, in such a way that the excitation, probing, and collection axes were at 90° (ortho configuration). Both lasers were collimated (unfocused). The Raman scatter was dispersed with a 0.22-m double-grating spectrometer (Spex Industries, Model 1680B), and detected with a thermoelectrically cooled photomultiplier tube (Hamamatsu, Model R928) and a photon-counting system (Stanford Research Systems, Model SR400). Data acquisition, storage, processing, and plotting were controlled by an IBM AT compatible microcomputer using the Stanford Research SR465 software. Spectral data were generated in binary code and converted to ASCII for processing in standard graphics software. The intensity of the transmitted probe laser was attenuated with a neutral-density filter and detected with a silicon photodiode. A voltage mode preamplifier was utilized to convert the photocurrent to voltage. A standard chart recorder was used to acquire the transmitted signal. Absorption spectra were recorded in a Hewlett Packard, Model 8452A, diode array spectrophotometer.

(1) Fleischmann, M.; Hendra, P. J.; McQuillan, A. *Chem. Phys. Lett.* **1974**, *26*, 163–166.
(2) Laserna, J. J.; Campiglia, A. D.; Winefordner, J. D. *Anal. Chim. Acta* **1988**, *208*, 21–30.
(3) Alak, A. M.; Vo-Dinh, T. *Anal. Chem.* **1989**, *61*, 656–660.
(4) Ni, F.; Cotton, T. M. *Anal. Chem.* **1986**, *58*, 3159–3163.
(5) Davies, J. P.; Pachuta, S. J.; Cooks, R. G.; Weaver, M. J. *Anal. Chem.* **1986**, *58*, 1290–1294.
(6) Laserna, J. J.; Sutherland, W. S.; Winefordner, J. D. *Anal. Chim. Acta* **1990**, *237*, 439–450.
(7) Sutherland, W. S.; Laserna, J. J.; Winefordner, J. D. *Spectrochim. Acta* **1991**, *47A*, 329–337.
(8) Montes, R.; Laserna, J. J. *Analyst* **1990**, *115*, 1601–1605.
(9) McGlashen, M. L.; Davis, K. L.; Morris, M. D. *Anal. Chem.* **1990**, *62*, 846–849.
(10) Xu, Y.; Zheng, Y. *Anal. Chim. Acta* **1989**, *225*, 227–232.
(11) Laserna, J. J.; Campiglia, A. D.; Winefordner, J. D. *Anal. Chem.* **1989**, *61*, 1697–1701.
(12) Enlow, P. D.; Buncick, M.; Warmack, R. J.; Vo-Dinh, T. *Anal. Chem.* **1986**, *58*, 1119-1123.
(13) Sutherland, W. S.; Laserna, J. J.; Angebranndt, M. J.; Winefordner, J. D. *Anal. Chem.* **1990**, *62*, 689–693.
(14) Vo-Dinh, T.; Hiromoto, M. Y. K.; Begun, G. M.; Moody, R. L. *Anal. Chem.* **1984**, *56*, 1667–1670.
(15) Rupérez, A.; Montes, R.; Laserna, J. J. *Vibr. Spectrosc.* **1991**, *2*, 145–153.
(16) Laserna, J. J.; Berthod, A.; Winefordner, J. D. *Talanta* **1987**, *34*, 745–747.
(17) Creighton, J. A. In *Surface Enhanced Raman Scattering*; Chang, R. K., Furtak, T. E., Eds.; Plenum Press: New York, 1982; pp 315–337.
(18) Laserna, J. J.; Montes, R. *Spectroscopy* (Ottawa) **1991**, *4*, 32–36; *Spectroscopy (Eugene, Oreg.)* **1991**, *6*, 34–38.
(19) Laserna, J. J.; Cabelín, L. M.; Montes, R. *Anal. Chem.* **1992**, *64*, 2006–2009.

0003-2700/92/0364-2715$03.00/0

Chemicals and Procedure. Analytical reagent-grade chemicals and distilled, deionized water were used throughout the study. 9-Aminoacridine, sulfanilamide, and furosemide were from Sigma and used as methanolic solutions. Silver colloids were prepared at room temperature by adding 1 mL of 1×10^{-3} M silver nitrate to 3 mL of 2×10^{-3} M sodium tetrahydroborate. After mixing, 0.1 mL of the analyte solution was added. The SERS signal was measured at the most prominent peak of each compound, i.e., 1370 cm^{-1} for aminoacridine and 948 cm^{-1} for sulfanilamide. The intensity of the transmitted probe beam was monitored simultaneously vs the baseline corresponding to the stopped beam.

RESULTS AND DISCUSSION

The characteristics, stability, and ability to promote intense SERS signals of silver colloids depend on a variety of experimental factors including relative concentrations of reactants, their volume ratio, reagent temperature, and speed of mixing and stirring of the solutions.[20] In addition, the incorporation of the sample to the hydrosols is affected almost equally by the same factors. So it is not surprising that the precision of such Raman measurements is rather poor. Additionally, vibrational modes in SERS spectra change with the evolution of the colloid during the aggregation process.[21,22] Specific bands appear and disappear depending on the aggregation state of the colloid which is being recorded. Figure 1 shows the changes in the SERS spectrum of furosemide on colloidal silver at three different stages of aggregation. A band centered at about 1120 cm^{-1} is observed at 10 min, the band disappearing after 20 min. The initial band at about 840 cm^{-1} disappears after 10 min. It should be noted that for this particular sample the intensity of a band at about 1000 cm^{-1} remains unchanged. The situation depicted in Figure 1 is often encountered when a SERS spectrum is obtained and causes difficulties in spectral interpretation. Measurement of the intensity of the probe beam transmitted by the silver colloid simultaneously recorded as the SERS signal is being obtained provides data on this incident.

Metal particles in aqueous colloidal dispersion carry a negative charge due to adsorbed anions. Repulsive electrostatic forces between the particles hinder aggregation and under these circumstances the colloid is stable. Adsorbate molecules added to the stable colloid displace the adsorbed ions from the surface, decrease the charge of the particles, and result in particle collisions by diffusional movement. Particle growth and aggregation now take place. It has been shown that large enhancement factors on metal colloids are observed when the exciting laser line overlaps the longitudinal surface plasma resonance of the metal.[17] Since the excitation wavelength employed here was in the red (632.8 nm), high aggregation was required to obtain large SERS intensity. Aggregation can be achieved by altering the composition and conditions of preparation of the colloid or by increasing the adsorbate concentration. However, it should be stressed that the aggregation kinetics depends to a large extent on the chemical structure of the adsorbate under study.[8] Compounds with large SERS activity produce large aggregation rates at low concentrations, while inactive compounds cause no aggregation at all even at large concentrations. In this work two model compounds (sulfanilamide and 9-aminoacridine) with SERS activity in between both extremes permitted the study of colloid aggregation by comparing the SERS intensity with the intensity of the probe beam transmitted through the colloid.

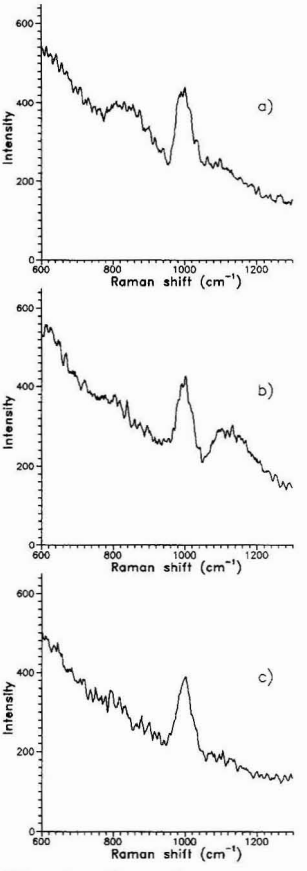

Figure 1. SERS spectrum of furosemide on colloidal silver: (a) initial; (b) after 10 min; (c) after 20 min.

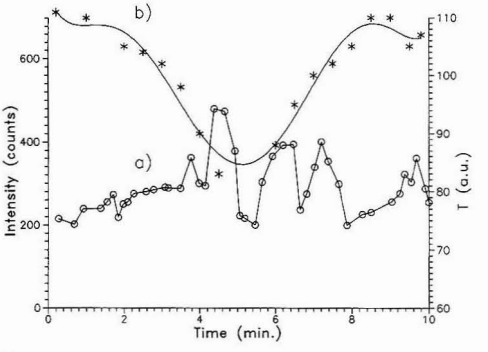

Figure 2. (a) SERS intensity and (b) transmitted light of the aggregation kinetics of a silver hydrosol with 12.5 μg/mL sulfanilamide.

Figure 2 shows the kinetics of aggregation of a silver hydrosol in the presence of 12.5 μg/mL sulfanilamide. Curve a represents the scattering Raman signal at 948 cm^{-1} while curve b corresponds to the signal of the probe beam, both vs time. The sample was placed in the holder when the

(20) Torres, E. L.; Winefordner, J. D. *Anal. Chem.* **1987**, *59*, 1626–1632.
(21) Sun, K.; Wan, C.; Xu, G. *J. Raman Spectrosc.* **1989**, *20*, 267–271.
(22) Yu, F.; Zhang, C.; Zhang, G. *J. Raman Spectrosc.* **1989**, *20*, 435–438.

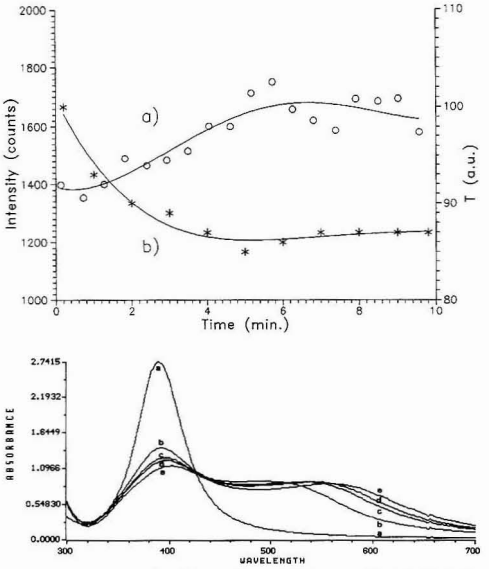

Figure 3. (Top) (a) SERS intensity and (b) transmitted light of the aggregation kinetics of a silver hydrosol with 12.5 μg/mL sulfanilamide stirred manually. (Bottom) absorption spectra of a silver hydrosol following the addition of 12.5 μg/mL sulfanilamide: (a) immediate; (b) 0.5 min; (c) 1 min; (d) 1.5 min; (e) 6 min.

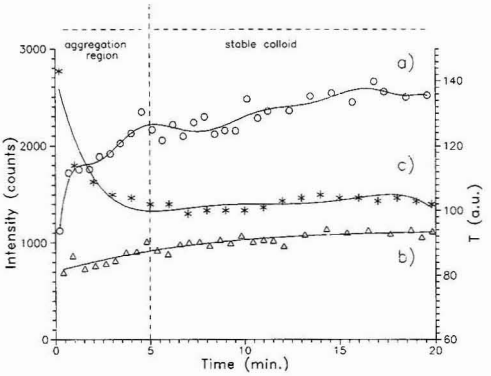

Figure 4. (a) SERS intensity, (b) background intensity, and (c) transmitted light of the aggregation kinetics of a silver hydrosol with 25 μg/mL sulfanilamide.

aggregation had not yet started, the colloid showing a homogeneous yellow color. After a few minutes, a simple visual inspection of the sample cuvette revealed the presence of dark blue color zones forming on the top of the cuvette, indicating that aggregation is taking place. In the absence of stirring, these colored zones diffuse slowly from top to bottom in an irregular fashion (heterogeneous aggregation) and they can be readily detected by the probe beam, as shown in Figure 2b. This curve shows a minimum at about 5 min, indicating that large particle aggregates are blocking partially the probe beam. After 5 min the transmitted light increased to recover the original level, since the zones of inhomogeneous aggregation diffused to the sample. SERS intensity follows the pattern of the transmitted light, as depicted in Figure 2a. Particle aggregates passing through the exciting beam raise the SERS intensity at about 5 min. However, the observed

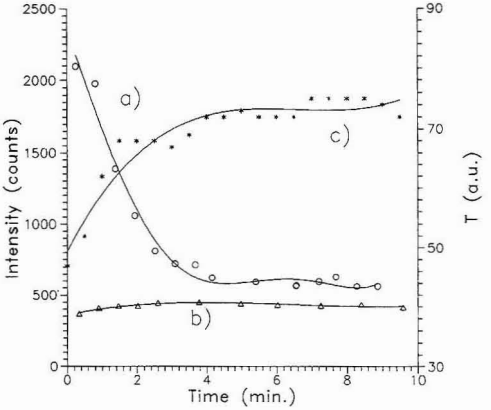

Figure 5. (a) SERS intensity, (b) background of SERS intensity, and (c) transmitted light of the aggregation kinetics of a silver hydrosol with 1.25 μg/mL 9-aminoacridine.

intensity is unstable since the colloid is not homogeneous. Because of the optical configuration used, the degree of heterogeneity detected by the probe beam could be different than that detected by the SERS excitation beam. This fact causes small deviations in the behavior of curves a and b in Figure 2 between 4 and 8 min.

Figure 3 (top) shows the kinetics of aggregation of a sample (12.5 μg/mL sulfanilamide) stirred manually prior to spectral observation. The SERS signal was larger than that in Figure 2a since stirring favored collisions between small particles. Nevertheless, aggregation is still proceeding as manifested by both an increase in SERS intensity and a decrease in the transmitted light. Figure 3 (bottom) shows time-dependent absorption spectra of a sample prepared under the same experimental conditions as that monitored in Figure 3 (top). The correlation between the increase in absorbance at 632.8 nm and the decrease in transmission of the probe laser is evident. The stability of the SERS signal is much improved regarding that in Figure 2a since the observed sample is homogeneous.

For concentrations of adsorbate molecules larger than 50 μg/mL aggregation was rapid and leads to complete precipitation. At intermediate concentrations, new insights into the process taking place in the colloid can be observed. Figure 4 shows the kinetics of aggregation of a silver hydrosol with 25 μg/mL sulfanilamide. The cuvette was stirred and placed in the holder when the color changed from yellow to wine red. Curve a corresponds to absolute counts of the peak at 948 cm^{-1}, curve b corresponds to the background of SERS signal where no peak occurs, and curve c corresponds to the transmitted light. During the first 5 min absolute SERS intensity increased while transmitted light intensity decreased as expected. After 5 min the difference between the SERS signal at 948 cm^{-1} and the background remained stable and the colloid transmittance showed no significant changes (curve c). It should be noted that only the net peak signal remains stable after constant transmitted light (5 min on), while both the absolute peak signal and the background keep growing. This fact is probably due to Rayleigh scattering by very large silver particles unable to cause enhancement of Raman signals because of their large size. For this concentration the stability of the SERS signal is improved regarding that at lower concentrations (Figure 3). The stability of the transmitted signal confirmed the absence of inhomogeneous zones in the sample.

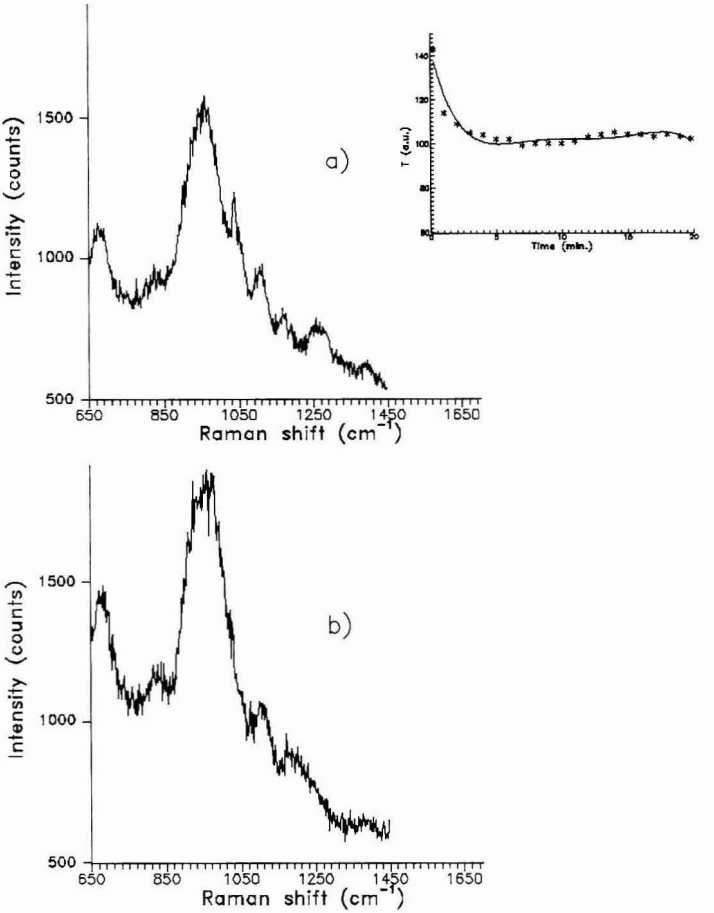

Figure 6. SERS spectra of sulfanilamide (25 μg/mL) on colloidal silver. Scan started (a) immediately after mixing colloid and adsorbate and (b) after 5 min later. The inset shows the variation of the transmitted light with time.

Applications. The extent of the aggregation process and, consequently, the SERS intensity depends on the chemical structure of the adsorbate. So, adsorbates with different SERS-active functional groups show particular aggregation kinetics which are difficult to predict on the sole basis of chemical structure. Figure 5 shows a practical example of how a rapid aggregation leading to useless spectral data can be readily detected with the system proposed here. With 1.25 μg/mL 9-aminoacridine (a compound with large SERS activity), the SERS intensity decreases rapidly (Figure 5a) to levels similar to the background signal (Figure 5b). No spectral information can be obtained from this sample after 4 min. The evident rise in transmitted light (Figure 5c) clearly indicates that spectral data would be recorded under nonoptimal experimental conditions.

The use of monochannel spectrometers for spectral data acquisition in dynamic samples such as those generally found in colloid SERS may cause spectral misinterpretation. At aggregation rates in the same time frame as the spectrometer scan speed what one observes in the abscissa axis is a convolution of time and Raman shift. In SERS, the relative intensity of certain vibrational modes changes in the course of colloid aggregation in response to reorientation of adsorbate molecules at the silver surface. Thus to avoid the dependence of spectral features on data acquisition conditions one should be able to scan the spectral zone of interest at least during the time the colloid is stationary. Figure 6 shows two SERS spectra from the same sample (sulfanilamide at 25 μg/mL). The inset shows the variation of the transmitted intensity with time. Spectrum a, whose scan started immediately after mixing the colloid and adsorbate, shows peaks at 1050 and 1260 cm^{-1}. These peaks do not appear in spectrum b, obtained 5 min later. These peaks could correspond to transient vibrational modes, evolving in the same time frame as the spectral acquisition. The intensity of the transmitted light reveals the dynamic character of the system during the first 5 min and shows that data collected during this time period may be affected by dynamic components. After constant transmitted light, spectral features and intensities are reproducible.

In conclusion, inhomogeneous aggregation and slow adsorption kinetics in colloidal systems may cause severe distortions in SERS intensities. These effects are more prone to occur for low adsorbate concentrations. The measurement

of the transmitted light as proposed here provides information in real time on the aggregation status of the sample being examined and it can be used as a diagnostic tool for unstable and transient situations. This approach is conceptually simple and it is easy to implement in any spectrometer.

ACKNOWLEDGMENT

Research was supported by the Dirección General de Investigación Científica y Técnica (Ministerio de Educación y Ciencia, Madrid, Project PB87-0715) and the Dirección General de Universidades e Investigación (Consejería de Educación y Ciencia, Junta de Andalucía, Sevilla), Spain.

RECEIVED for review February 12, 1992. Accepted August 6, 1992.

Registry No. Ag, 7440-22-4; 9-aminoacridine, 90-45-9; sulfanilamide, 63-74-1; furosemide, 54-31-9.

Spectrophotometric Determination of pH and Its Application to Determination of Thermodynamic Equilibrium Constants

Hideo Yamazaki,† R. P. Sperline, and Henry Freiser*

Strategic Metals Recovery Research Facility, Department of Chemistry, University of Arizona, Tucson, Arizona 85712

Highly accurate pH estimations are conveniently made by evaluation of the spectra of an acid–base indicator suitable for the pH range of interest, if the $pK_{a,ind}$ is accurately known. Stoichiometric pH values were to determine $pK_{a,ind}$ to an accuracy of ±0.008 or better, utilizing a neutralization titration of a reference standard weak acid or base. When acetic acid (HOAc) and aqueous ammonia are adopted as reference substances and the best literature values are taken for their pK_a values and activity coefficients as arbitrary constants, the calculated pH values are more accurate than those given by a glass electrode/pH meter combination. In turn, those pH values can be used for calibration of the glass electrode/pH meter combination. Thus, the pK_a for thymol blue was determined at 25–65 °C and ionic strength = 0–3.2 M, at 20–30 pH values for each set of conditions with an overall error of ±0.002 log unit. Similarly, the pK_a of bromocresol green was determined at 20–30 pH points during titration, at 25 °C, and at ionic strength = 0–0.4 M, with an overall error of ±0.008 log unit. The use of a diode array spectrophotometer and computer statistical calculations made possible analyses of photometric errors at all useful UV–vis wavelengths. Statistical analyses of such measurements permit the measurement of pK_a values of unusually high reliability, limited by errors in pH evaluation, not by those of spectrophotometric measurements.

INTRODUCTION

Great improvements in analytical methodology have accompanied recent advances in spectrophotometric instrumentation, yet their potential for improving classical methods of simple, everyday measurements such as pH, have not been exploited. With the diode array spectrophotometer, absorbance readings with errors on the order of ±0.0002A can be taken every 0.25 nm over the entire UV–vis range. In the past, most of this information was discarded. With the aid of computer spreadsheet analyses, nearly all the information can be employed, resulting in a convenient avenue to significantly improved experimental reliability.

By this means, the spectrophotometric method of pH measurement can challenge the usual pH meter technique[1] in both reliability and convenience. The question of standards can be solved without recourse to potentiometric methods by the expedient of using a small number of highly characterized, highly purified, readily available substances as primary acid–base standards. The best available literature values of their thermodynamic acid dissociation constants, $*K_a$, will be used as arbitrary standards. As a specific example, the $*K_a$ for HOAc is well determined, as are the relevant activity constants. pH values calculated for the titrations, therefore, contain only stoichiometric error. It is significant that when improved values for K_a and the activities for, e.g., HOAc, are determined, then well-defined changes to all derived values can be applied in a simple manner.

The careful titration of a standard, e.g., HOAc vs NaOH, in the presence of a purified colorimetric acid–base indicator can serve to calculate the $*K_a$ of the indicator. The [H^+] at any point along the titration can be calculated to a precision dependent only on the normal titration errors (±0.0006 pH unit). Activity coefficients (γ) appropriate to the ionic strength (I) and temperature (T) are available in the literature for simple buffers, to ±0.001.[2] These values are taken as constants. Application of γ corrections leads to calculated pH values, but with errors only slightly greater (±0.001 pH) than ±0.0006 pH unit due to stoichiometric errors. In any event, pH values can be calculated more precisely than they can be measured by a pH meter, particularly at elevated T and I.

Three strides in analytical precision result. First, calculation of pH with full activity corrections allows a very accurate calibration of a pH meter/electrode pair (over some small range). Accurate calculated pH values are also essential for other equilibrium and kinetic analyses. Second, when pK values for the primary standards are taken as absolute and pH values are calculated during spectrophotometric titration of an indicator, values of p$*K$ may be derived which are accurate enough to be used as secondary standards for spectrophotometric determination of pH, to previously unattainable accuracy and precision. Third, by use of secondary standard indicators to determine pH, activity coefficient ratios for other buffers may be determined over wide ranges of T and I.

This paper reports the adaptation of this approach to systems involving HOAc and NH_3 as primary standards and bromocresol green (BCG) and thymol blue (TB) as indicators. The equilibrium constants of HOAc and NH_3 are among the most carefully determined in the literature and, as will be demonstrated, are as useful as standards as any of the "weighable" primary standards. Subsequent papers will describe our current work in metallochromic and redox systems.

EXPERIMENTAL SECTION

Apparatus. A Perkin Elmer Lambda Array 3840 UV–vis spectrophotometer equipped with a Perkin Elmer 7500 computer was used for measurement of the absorption spectra and data storage. An IBM-PC compatible computer was linked to the Perkin Elmer computer using RS-232 serial interfaces and data transmission/conversion software.[3]

An Orion 801 pH meter equipped with a Corning, Inc. 476560 rugged bulb combination glass electrode (all Ag/AgCl internals) was used for pH measurement. The pH meter was calibrated over the appropriated ranges using pH buffer solutions prepared

* To whom correspondence should be addressed.
† Present address: Department of Nuclear Reactor Engineering, Kinki University, Kowakae, Higashiosaka 577, Japan.

(1) Bates, R. G. *Determination of pH. Theory and Practices*; Wiley: New York, 1964.

(2) (a) Harned, H. S.; Owen, B. B. *The Physical Chemistry of Electrolytic Solutions*, 3rd ed.; Reinhold: New York, 1958; pp 732–736. (b) *Ibid.*, pp 504–508. (c) *Ibid.*, p 709. (d) *Ibid.*, p 733. (e) *Ibid.*, p 557.

(3) Sperline, R. P. *Appl. Spectrosc.* **1991**, *45*, 3886.

0003-2700/92/0364-2720$03.00/0

and used according to compositions of standard reference buffers described by IUPAC.[4]

The pH meter/electrode pair was calibrated in a preliminary fashion using a two-point calibration. The first point, also used to set the isopotential point, was carried out on pH 7 buffer solution (0.025 M Na_2HPO_4 + 0.025 M KH_2PO_4, 1:1). The second point, for slope adjustment, was made with a pH 4 buffer solution (0.05 M potassium hydrogen phthalate) or the pH 10 buffer solution (0.025 M $NaHCO_3$ + 0.025 M $NaCO_3$, 1:1) at the desired T using a constant-temperature bath.

The reaction vessel, a 500-mL three-neck flask, was fitted with a mechanical stirrer and two rubber septa. The analyte solution was magnetically stirred and was circulated through the water-jacketted, flow-through cuvette by a Fluid Metering Inc. aluminum oxide lined Model RHSY lab pump and Teflon tubing.

The titration procedure was carried out using a Mettler V10 digital buret connected to the reaction vessel with Teflon tubing. The temperature of the reaction vessel and absorption cell was controlled to within ±0.1 °C of the desired value using a VWR Scientific 1155 constant-temperature water bath.

Reagents. Bromocresol green (BCG) and thymol blue (TB) (Aldrich Chemical Co., Inc.) were purified by repeated (2×) recrystallization from acetic acid solution. The purities of these chemicals were estimated as 95.1% and 96.0%, respectively, from spectrophotometric absorbance measurements. UV–visible spectra of the solutions, taken before and after recrystallization showed the impurities to be nearly colorless; the extent of their removal has an insignificant effect on subsequent spectra. The stock solution of BCG (8.02×10^{-4} M) was prepared in a 3.4930 M acetic acid solution, and the stock solution of TB (1.21×10^{-4} M) was prepared in water; both solutions were stored in glass bottles shielded from light.

Working solutions of acetic acid, hydrochloric acid, and ammonia (analytical reagent grade, J. T. Baker Inc.) were prepared by dissolution of these reagents in distilled deionized water. Potassium nitrate (AR grade, Mallinckrodt Inc.) was used for controlling I in solutions.

The sodium hydroxide solution, used to standardize the acids, was prepared by dissolution of sodium hydroxide from a freshly opened bottle (Mallinckrodt Inc.) in carbonate-free water and was stored in a polyethylene bottle under nitrogen. The solution was standardized by titration against primary standard potassium hydrogen phthalate (Aldrich, Inc.).

Procedures. *Determination of the pK Value of Bromocresol Green (BCG).* The sample solution (250 mL) was prepared by diluting stock solutions with water to give initial concentrations of 0.18987 M for acetic acid and 2.01×10^{-5} M for BCG. The combination glass electrode and the Teflon tubes were inserted into the flask which was then placed in the water bath. The flow-through cuvette was connected to the flask via the pump. The solution was stirred and circulated until achievement of thermal equilibrium (ca. 10 min). At this point, all circulation was stopped and the pH and absorption spectra of the solution were measured. Subsequent pH adjustments were made by incremental additions of sodium hyroxide solution using the digital buret. After each addition the analyte was stirred and circulated for 2 min, or until the pH meter readings were stable to ≤±0.002, preceding the next measurements of pH and absorption spectra. These procedures were repeated throughout the titration range.

Determination of pK of Thymol Blue (TB). The procedure used was similar to that employed for BCG. The sample solution (380 mL) was prepared by dilution of stock solutions to give initial concentrations of 2.1072 M ammonia and 1.90×10^{-5} M TB. The flask was sealed with rubber septa to prevent evaporation of ammonia during the titration. The losses of ammonia from the analyte solution were estimated, from final titration end points, as less than 0.08% for 90 min at 65 °C and were correspondingly lower at lower T.

The Gran method for location of titration end points[5] was applied using the spreadsheet software "Quattro" (Borland International, Inc.). Reproducibility for the calibration procedure, expressed as the standard deviation for titrations in triplicate, was estimated to be smaller than ±0.05%.

Method of Calculation. The spectroscopic determination of the indicator dissociation constant, K_a, involves the following relationships (eqs 1–4). The absorbance A of a solution containing both forms of an indicator can be expressed as

$$A = \epsilon_0\alpha_0 C_a + \epsilon_1\alpha_1 C_a \quad (1)$$

or

$$A = A_0\alpha_0 + A_1\alpha_1 \quad (2)$$

where ϵ_0 and ϵ_1 are the molar absorptivities (cm^{-1}) for the acid and conjugate base forms of the indicator, C_a is the total analytical concentration of the indicator, and α_0 and α_i are the respective dissociation fractions, as defined in

$$\alpha_0 = [H^+]/([H^+] + K_a) \quad \text{and} \quad \alpha_1 = K_a/([H^+] + K_a) \quad (3)$$

Combining eqs 2 and 3 yields an expression for K_a which is independent of molar absorptivity:

$$K_a = ((A_0 - A)/(A - A_1))[H^+] = \rho[H^+] \quad (4)$$

where ρ (absorbance ratio), as defined in eq 4, is the ratio of absorbance differences between the partially neutralized solution absorbance and the protonated and unprotonated solution absorbances. Equation 4 provides the basis for the determination of the dissociation constant at each wavelength for which absorbance measurements have been made. The weighting scheme described here gives greater weights to spectra taken for solutions at pH values near pK_a.

The method of least squares was employed to obtain the best ρ value at each pH. Advantage was taken of the redundant data available by use of all spectral wavelength data. At each pH, the 1360 absorbance points collected at 0.25-nm intervals from 340 to 680 nm were imported into the spreadsheet for statistical (and other) analyses. These points represent 1360 simultaneous determinations of ρ for this pH from which a weighted average $\bar{\rho}(H)$ and a standard deviation of the mean $\sigma_{\bar{\rho}(H)}$ were calculated (see Appendix).

As an integral part of this approach, HOAc and NH_3 were used as primary standards. The p*K_a (thermodynamic) values of these species have been accurately determined (to ±0.001) and values are available in the literature for several T and I.

The pH value of the analyte solution was calculated by the following method. In this study, the experiments were carried out by titrating acetic acid with sodium hydroxide in the presence of BCG and by titrating ammonia with hydrochloric acid in the presence of TB. The pH in these titration systems, whether weak acid–strong base or weak base–strong acid, can be calculated from the proton balance equation, the dissociation constant of weak acid or weak base, and the dissociation of water in the solution. For the HOAc–NaOH system

$$K = [H^+]\left(\frac{[Na^+] + [H^+] - [OH^-]}{C_a - ([Na^+] + [H^+] - [OH^-])}\right) \quad (5)$$

and for the NH_3–HCl system

$$K = [H^+]\left(\frac{C_b - (*K_w/[H^+] + [Cl^-] - [H^+])}{*K_w/[H^+] + [Cl^-] - [H^+]}\right) \quad (6)$$

where K is the acid dissociation constant of acetic acid or ammonia, $*K_w$ is ion product of water, and C_a and C_b are the total analytical concentrations of weak acid or weak base, respectively. The pH in these systems, therefore, was calculated by using the K value, $*K_w$,[6] and the reagent concentrations. Activity corrections made to $*K_w$ had almost no effect on the results. In practice it was necessary to correct for the volume change effects on the concentrations of reagents and for the effects of I changes on the activity coefficients (except for $*K_w$).

(4) *Manual of Symbols and Terminology for Physicochemical Quantities and Units*; IUPAC Additional Publication; Butterworths: London, 1975; p 30.

(5) Meloun, M.; Havel, J.; Högfeldt, E. *Computation of Solution Equilibria*; Wiley: New York, 1990; pp 37–42.

(6) *CRC Handbook of Chemistry and Physics*, 61st ed.; Weast, R. C., Ed.; CRC Press: Boca Raton, FL, 1981; pp D-168.

RESULTS AND DISCUSSION

For comparison purposes, the pH of analyte solutions during titrations was both measured by pH meter and calculated stoichiometrically. The calculated pH values are predicated on the values 4.756 for HOAc and 9.244 for NH_3,[7-9] as the (perhaps not too) arbitrary reference standard values of p*K at 25 °C and zero I, along with a specified set of published activity coefficients. From these calculations, and the known variance in analytical glassware, variances in pH_{calc} were calculated for use in determination of the variances in calculated pK values of the indicators. The results will be discussed in comparison with those found by using the pH meter and the variances of its readings.

pH of Analyte Solution. The accuracy of a glass electrode/pH meter pH measurement is usually regarded as ±0.02 pH or, with painstaking effort, ±0.01 units.[10] In order to obtain more accurate pH values, attempts were made to calculate the pH of analyte solutions (pH_{calc}). The accuracy of pH_{calc} for a titration system depends upon the accuracies of the concentrations of reagents, the volume of titration, and the activity coefficients.

The experimental error in the concentrations of reagents and volume of titration were estimated to be ±0.05% and a maximum of ±0.04%, respectively. The magnitudes of these experimental errors corresponded to an error in pH_{calc} of ±0.0006 units. This value is far smaller than the expected experimental error in the glass electrode/pH meter measurements (accuracy ±0.02 pH). The dissociation constants of acetic acid and ammonia were taken from published values.[7-9] Activity coefficients for acetic acid and ammonia were also taken from published values.[2a] The results of these calculations at 25 °C and a comparison with pH_{meas} are shown in Table I. The accuracies of these results are, of course, relative to that of our accepted standards.

One value of K_a for each of the standards is selected as an absolute standard, with zero variance. Errors in pH_{calc} at zero I are due mainly to volumetric errors, and the pH_{calc} values are more accurate than pH values measured by a pH meter. Certainly, the precision of pH_{calc} is better than that of pH_{meas}. At other I values, however, corrections to analyte ion activities are necessary to give accurate values of pH_{calc}, and uncertainties in the activity corrections affect the final errors in pH_{calc}.

Corrections to the activity coefficients for T and I were required. Two methods for determination of the activity coefficients at various T were compared. In the first method, activity coefficients were calculated using the following equation[2b]

$$\log \gamma_{\pm} = \log \gamma_{\pm}(25\ °C) + \frac{y}{\nu}\bar{L}_2(25\ °C) - \frac{Z}{\nu}\bar{J}_2(25\ °C) \quad (7)$$

where

$$y = \frac{298.15 - T}{2.303R298.15T} \quad \text{and} \quad Z = 298.15y - \frac{1}{R}\log(298.15/T)$$

and where $\gamma_{\pm}(25\ °C)$, $\bar{L}_2(25\ °C)$, and $\bar{J}_2(25\ °C)$ are the activity coefficient, relative partial molal heat content, and relative partial molal heat capacity, respectively, at 25 °C, and ν is the total number of ions (cations plus anions) produced by the dissociation of one molecule. The $\bar{L}_2(25\ °C)$ of ammonium chloride may be used for I between 0.0001 and 0.10.[2c]

(7) Christensen, J. J.; Hansen, L. D.; Izatt, R. M. *Handbook of Proton Ionization Heats*; Wiley: New York, 1976; pp 17–18.
(8) Olofsson, G. J. *Chem. Thermodyn.* **1975**, *7*, 507–514.
(9) Martell, A. E.; Smith, R. M. *Critical Stability Constants*; Plenum Press: New York, 1982; Vol. 5, pg 284.
(10) Westcott, C. C. *pH Measurements*; Academic Press: New York, 1978; pp 95–108.

Table I. Results of Measurement and Calculation of pH during Titration at 25 °C

ionic strength	meas[a] pH	calc[b] pH	ΔpH
	NH_3–HCl System[c]		
0.0191	10.000	9.9809	−0.0191
0.0275	9.804	9.7880	−0.0160
0.0382	9.602	9.5905	−0.0115
0.0498	9.405	9.3980	−0.0070
0.0560	9.305	9.2984	−0.0066
0.0617	9.209	9.2037	−0.0053
0.0674	9.109	9.1049	−0.0040
0.0727	9.008	9.0063	−0.0017
0.0775	8.906	8.9057	−0.0003
0.0820	8.800	8.8012	0.0012
0.0853	8.709	8.7119	0.0029
0.0886	8.605	8.6087	0.0037
0.0911	8.509	8.5141	0.0051
0.0937	8.393	8.4005	0.0075
0.0970	8.196	8.2055	0.0095
	HOAc–NaOH System[d]		
0.0088	3.411	3.4117	0.0007
0.0140	3.604	3.6149	0.0109
0.0218	3.806	3.8204	0.0144
0.0326	4.003	4.0192	0.0162
0.0468	4.201	4.2184	0.0174
0.0830	4.602	4.6194	0.0174
0.1011	4.801	4.8161	0.0151
0.1298	5.199	5.2075	0.0085
0.1395	5.403	5.4068	0.0038
0.1461	5.599	5.5950	−0.0040
0.1508	5.804	5.7900	−0.0140
0.1538	5.995	5.9671	−0.0279

[a] Glass electrode pH meter was used. [b] Calculated using HOAc and NH_3 concentrations. [c] Initial volume, 380 mL; initial ammonia concentration, 0.1106 M; titrated with 1.561 M HCl solution. [d] Initial volume, 250 mL; initial acetic acid concentration, 0.1899 M; titrated with 1.014 M NaOH solution.

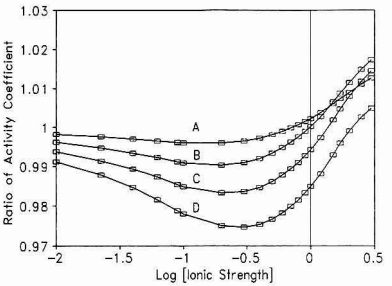

Figure 1. Ratio of NH_4Cl activity coefficient ($\gamma_{\pm}(T)/\gamma_{\pm}(25\ °C)$) vs ionic strength at various temperatures: (A) 35 °C; (B) 45 °C; (C) 55 °C; (D) 65 °C.

Literature values could not be found for $\bar{L}_2(25\ °C)$ of NH_4Cl at higher I, but because the values for KCl were nearly identical with those of NH_4Cl in the lower I range, it was assumed that the available $\bar{L}_2$ values for KCl would approximate those of NH_4Cl in the higher I ranges. The results of these calculations of the activity coefficient of ammonium chloride are shown in Figure 1, which shows the ratios between the activity coefficients at several T and those at 25 °C.

In the second method, multiple linear regression fitting of the available activity coefficients for NaCl gave linear expressions for activity coefficient as a function of I, at each T, of the form $\gamma = A + BI + C(\sqrt{I}/(1 + \sqrt{I}))$.[2e] This approach is far simpler to implement than eq 7 and yields results within 0.01 pH of those obtained by the first method, at the highest T and I examined.

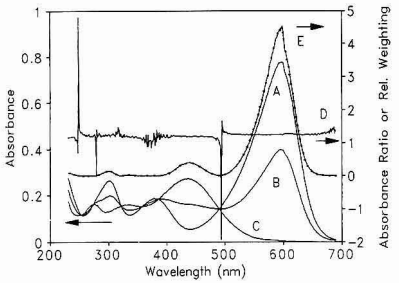

Figure 2. Absorption spectra and absorbance ratio of thymol blue: (A) pH 11.131; (B) pH 9.001; (C) pH 6.447; (D) absorbance ratio (ρ); (E) relative weighting for K_a average.

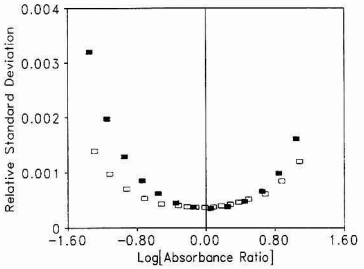

Figure 3. Relative standard deviation of photometric error in determination of p_{K_a} values (σ_{pK_a}/pK_a) vs log ρ: (□) thymol blue; (■) bromocresol green.

The accuracy of pH measurement with a glass electrode/pH meter depends on the composition of analyte solutions and its temperature. Junction potentials, membrane resistivity, sodium ion correction, and meter impedance strongly affect accuracy. The overall accuracy and precision of the pH meter measurements are estimated to be ±0.02 and ±0.001 pH, respectively. On the other hand, the accuracy of the present method is independent of those parameters. In this method, both the stoichiometric and spectrophotometric errors were very small compared with that of a glass electrode/pH meter; hypothetically, if the stoichiometric and spectrophotometric errors had both been zero, a backward calculation shows that pH deviation would have been less than ±0.000 65 pH units—far smaller than expected for the glass electrode/pH meter.

Photometric Error. Figure 2 shows the absorption spectra of solutions of protonated, unprotonated, and partially neutralized TB. By repetition of each acquisition 30 times, the standard deviations for the absorption measurements, σ_{A_0}, σ_{A_1}, and σ_A, were estimated to be ±0.000 68 AU at pH 2.730, ±0.000 39 AU at pH 7.018, and ±0.000 53 AU at pH 4.601, respectively, at all wavelengths between 340 and 680 nm. Corresponding values for BCG were very similar to those for TB, in part because the absorption spectra had similar intensities.

These individual σ's were used to calculate $\sigma_{\bar{\rho}(H)}$ photometric errors (Appendix, eq A1) for use in calculation of σ_K (Appendix, eq A2). Figure 3 shows typical values of $\sigma_{\bar{\rho}(H)}$ vs $\bar{\rho}(H)$. As expected, the most reliable (lowest σ) values occur at pHs giving half-neutralization ($\rho = 1.0$), but for ρ between 0.1 and 10, $\sigma_{\bar{\rho}(H)}$ (typically ca. 0.05% relative) is small compared with other sources of error, e.g., $\sigma_{[H^+]}$. No special consideration of points near or at isosbestic points need be taken, because the weighted averaging process automatically removes erratic ρ points, assuring large variances and small weights for these points. First, for a single-pH spectrum, the absorbance ratio

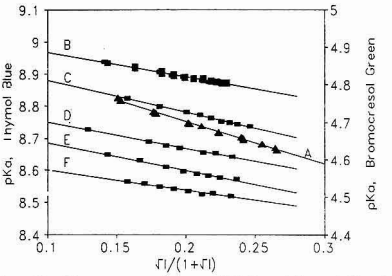

Figure 4. pK_a of bromocresol green (BCG) and thymol blue (TB) vs $\sqrt{I}/(1+\sqrt{I})$ (Debye's function) with linear regression lines: (A) BCG, 25 °C; (B) TB, 25 °C; (C) TB, 35 °C; (D) TB, 45 °C; (E) TB, 55 °C; (F) TB, 65 °C.

was calculated at all wavelengths and a variation of Chauvenet's criterion was used to assign zero weight to data points having absorbance ratios varying from the mean ratio by more than 3 times the standard deviation of the points. (Chauvenet suggested 1.96σ.[11]) This usually occurred only for points within 2–5 nm of an isosbestic point. Second, near the 493-nm isosbestic point for TB, the $(A_1 - A)^4$ denominator assures that the relative weights of points within 10 nm of the isosbestic point fall to less than 1% of the maximum weight.

Figure 2 also shows the relative weighting $\omega_{\rho(H,\lambda)}$ (Appendix, eq A2) for the three spectra presented. As expected, spectral regions having low net absorbance ranges, e.g., below 400 nm, have low weighing factors. For the one pH value represented in Figure 2, using all wavelengths gave $pK_a = 8.9038 \pm 0.000\,20$, while rejection of all wavelengths below 380 nm gave 8.9037 ± 0.000 20 and rejection of all wavelengths below 495 nm gave 8.9025 ± 0.000 21. The automatic rejection of the lower wavelength and isobestic point data by assignment of low weights is convenient. The calculations do not need to be tailored to different indicators. Allowing automatic weighting of the various spectral regions and pH values also removes analyst bias.

Dissociation Constants of Indicators. *pK Value of Bromocresol Green (BCG).* The pK_a of BCG was first determined using pH_{calc}. Figure 4 shows the combined results of triplicate titrations for the determination of the pK for BCG, plotted as Debye's function ($\sqrt{I}/(1+\sqrt{I})$) of I. The pK is strongly correlated with I through Debye's equation, $pK^* = pK_0 + A\sqrt{I}/(1 + aB\sqrt{I})$, up to $I = 0.12$ M. The parameter a is the ionic radius, and A and B are empirical constants, having values of 0.51 and 3.3×10^7 at 25 °C, respectively. By linear regression, the pK of BCG was calculated to be 4.9285 ± 0.0030 at $I = 0$ and 25 °C and decreased with increasing I. This tendency indicates that the formation of ionic species of BCG occurs by its dissociation, and if the activity coefficient for these species can be obtained, the pK value can be corrected directly. The pK value is in close agreement with the published value,[12,13] and the deviation agreed well with the expected experimental error.

The pK values of BCG, corrected for I between 0 and 1.0 at 25 °C, by two different means, are shown in Table II. The activity coefficient of *p*-toluenesulfonate was used as a stand-in for the unavailable BCG anion activity coefficient.[2d] This seems reasonable as they are both aromatic sulfonates. After this correction, the pK became nearly constant between I values of 0 and 1.0; the average value was 4.7838 ± 0.0024.

(11) Young, Hugh D. *Statistical Treatment of Experimental Data*; McGraw-Hill: New York, 1962; Sections 10 and 13.
(12) Chase, E. F.; Kilpatrick, M., Jr. *J. Am. Chem. Soc.* **1932**, *54*, 2284–2292.
(13) Kilpatrick, M. *J. Am. Chem. Soc.* **1941**, *63*, 2667–2668.

Table II. Dissociation Constants of Bromocresol Green at 25 °C

ionic strength	pK_a of bromocresol green	
	obs	corrected[a]
0	4.9285 ± 0.0030	4.8308 ± 0.0068
0.02	4.7887 ± 0.0029	4.7950 ± 0.0067
0.05	4.7223 ± 0.0029	4.7780 ± 0.0067
0.1	4.6525 ± 0.0028	4.7602 ± 0.0067
0.2	4.6284 ± 0.0038	4.7655 ± 0.0081
0.5	4.5988 ± 0.0039	4.7751 ± 0.0081
1.0	4.5725 ± 0.0039	4.7809 ± 0.0081

[a] Activity coefficient of *p*-toluenesulfonate was used.

Table III. Dissociation Constants of Thymol Blue

temp (°C)	ionic strength	pK_a	temp (°C)	ionic strength	pK_a
25	0	9.0493 ± 0.0022	25	0.5	8.7926 ± 0.0032
	0.02	8.9510 ± 0.0022		1.0	8.7557 ± 0.0032
	0.05	8.8992 ± 0.0021		2.0	8.7181 ± 0.0031
	0.1	8.8637 ± 0.0032		3.0	8.6954 ± 0.0031
	0.2	8.8383 ± 0.0032			
35	0	8.9588 ± 0.0031	35	0.5	8.6724 ± 0.0025
	0.02	8.8598 ± 0.0030		1.0	8.6305 ± 0.0025
	0.05	8.8000 ± 0.0030		2.0	8.5882 ± 0.0024
	0.1	8.7627 ± 0.0030		3.0	8.5626 ± 0.0024
	0.2	8.7242 ± 0.0025			
45	0	8.8524 ± 0.0033	45	0.5	8.5613 ± 0.0026
	0.02	8.7377 ± 0.0033		1.0	8.5191 ± 0.0026
	0.05	8.6802 ± 0.0033		2.0	8.4764 ± 0.0025
	0.1	8.6392 ± 0.0033		3.0	8.4508 ± 0.0025
	0.2	8.6136 ± 0.0026			
55	0	8.7633 ± 0.0017	55	0.5	8.4778 ± 0.0026
	0.02	8.6700 ± 0.0017		1.0	8.4355 ± 0.0026
	0.05	8.6259 ± 0.0017		2.0	8.4016 ± 0.0025
	0.1	8.5719 ± 0.0027		3.0	8.3670 ± 0.0025
	0.2	8.5303 ± 0.0026			
65	0	8.6623 ± 0.0016	65	0.5	8.4159 ± 0.0027
	0.02	8.5851 ± 0.0016		1.0	8.3685 ± 0.0018
	0.05	8.5486 ± 0.0016		2.0	8.3722 ± 0.0018
	0.1	8.5120 ± 0.0015		3.0	8.3741 ± 0.0018
	0.2	8.4700 ± 0.0027			

pK Value of Thymol Blue (TB). The pK_a of BCG was also determined using pH_{calc}. The pK values for TB in the I range 0.02–3 were determined at T between 25 and 65 °C. The results are summarized in Table III. These values are in good agreement with the published values.[14] As shown in Figure 4, the pK values decreased both with increasing I and with increasing T, up to ca. 55 °C. At 65 °C, the values became nearly constant for I between 1 and 3. At I less than 0.12, Debye's relationship between pK^* and I (pK proportional to $\sqrt{I}/(1 + \sqrt{I})$) was observed at each T, in a manner similar to that of BCG. The pK values of TB at zero I (9.0493 ± 0.0022) were calculated by the extrapolation of the regression lines. The results are shown in Table III.

The relationship between pK values of TB and temperature is shown in Figure 5. From these results, the free energies ($\Delta G°$) of TB at several T were estimated by use of these pK values and are shown in Table IV. The standard enthalpy change of TB, $\Delta H°$, calculated from the free energy, was 18.70 ± 0.51 kJ/mol.

Application to the Determination of pH. The reduced photometric error, along with the reduced error in pK_a for indicators, can be used to advantage in a pH-meter-free method for the determination of pH. Briefly then, the absorption ratio ρ can be found from spectrophotometric measurements for a solution containing a pH indicator and the pH of the solution can be calculated from eq 5 or 6 using the pK value of the indicator.

(14) Bishop, E. *Indicators*; Pergamon: New York, 1972; pp 115–119.

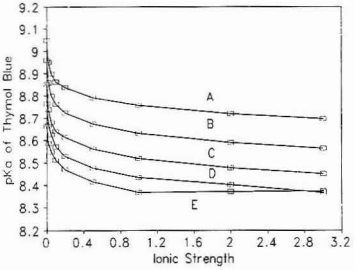

Figure 5. PK_a of thymol blue vs ionic strength and temperature: (A) 25 °C; (B) 35 °C; (C) 45 °C; (D) 55 °C; (E) 65 °C.

Table IV. Free Energy of Thymol Blue

temp (K)	pK_a of thymol blue	$\Delta G°$ (kJ/mol)
298.15	9.0493 ± 0.0022	51.653 ± 0.013
308.15	8.9588 ± 0.0061	52.852 ± 0.038
318.15	8.8524 ± 0.0067	53.919 ± 0.042
328.15	8.7633 ± 0.0033	55.054 ± 0.021
338.15	8.6623 ± 0.0016	56.078 ± 0.013

Table V. Results of the Determination of pH by This Method (NH_3–HCl–Thymol Blue System)

temp (°C)	points	ionic strength	meas pH	(calc pH) − (meas pH)
25	10	0.019–0.101	10.000–7.807	−0.0016 ± 0.0051
25	10	0.285–0.355	10.208–7.806	−0.0115 ± 0.0093
25	10	1.007–1.019	9.259–7.961	−0.0380 ± 0.0092
25	10	2.067–2.077	9.292–7.991	−0.1260 ± 0.0109
25	10	2.933–2.998	10.008–7.800	−0.1278 ± 0.0147
35	10	0.049–0.118	9.303–8.004	−0.0056 ± 0.0052
45	10	0.032–0.111	9.279–7.981	−0.0276 ± 0.0079
55	10	0.028–0.105	9.103–7.903	−0.0320 ± 0.0093
65	10	0.012–0.092	9.288–7.932	−0.0461 ± 0.0074
65	10	1.045–1.082	9.119–7.893	−0.0688 ± 0.0171
65	10	2.950–2.984	9.039–7.973	−0.1252 ± 0.0045

This method was applied to a redetermination of pH for the NH_3–HCl titration system. The sample contained 2×10^{-5} M TB and ca. 0.1 M ammonia, and the pH of the solution was adjusted to between 11 and 6 by the addition of hydrochloric acid. The absorbances A_0, A_i, and A of protonated, deprotonated, and partially neutralized TB were measured at pH 6.5, 11.2, and intermediate values, respectively, between 350 and 690 nm. The results are shown in Table V, along with a comparison with results measured with a glass electrode and pH meter.

The pH_{calc} values found by this method agreed well with those found by pH meter, to within the measurement error of a glass electrode/pH meter, at the lower ionic strengths examined. Across each of the ranges of I and T indicated in Table V, the differences in pH_{calc} and pH_{meas} were consistent. It is also seen that the differences are correlated more with high I than with high T. One possible cause for this difference is that the pH electrode/meter was calibrated in a low I buffer (0.05 M) so that the liquid junction potential changed significantly in the higher I samples.

CONCLUSIONS

Adoption of reference standards has led to a method for determination of pH with greater accuracy than is achievable using a glass electrode and pH meter, and in fact, a pH meter is not required. While it is difficult to reproducibly recalibrate a pH meter with buffers to an accuracy of ±0.01 pH unit, careful titration can, with activity coefficient corrections, provide reproducibility of ±0.001 pH unit or better. The use

of HOAc and NH_3 as primary reference standard materials is justified by the existence of well-determined pK_a and activity constant values and by their availability, purity, and stability. As improved pK_a values and activity coefficients for the reference standard materials become available, it is a simple matter to incorporate those values into the calculations.

With the diode array spectrophotometer and tables of activity coefficients, the dissociation constants of pH indicators can be very accurately determined (±0.002 pK unit for thymol blue and ±0.008 pK unit for bromocresol green) by spectrophotometric measurements taken during careful titrations of standard reference weak acids or bases. Any stable compound with a pH-sensitive chromophore will suffice, not only those compounds having extremely intense visible colors. In turn, these $pK_{a,ind}$ values can be applied to the determination of pH in an unknown solution from spectra to an accuracy of ±0.002 in the case of TB, without use of a pH meter. For standardization, it is only necessary add some indicator to aliquots of the unknown and to adjust the pH of the aliquots to values much higher and much lower than the $pK_{a,ind}$ of the indicator being used. While the method was implemented on one diode array spectrometer, it is applicable to any spectrometer/computer system capable of providing digitized data of high precision.

One aspect of pH determination often ignored is the low reliability of glass electrode pH readings at elevated temperature, in high $[Na^+]$ solutions, and with adsorption occurring on the glass membrane particularly in the presence of protein solutions. In addition, conditions of high humidity can cause electrical leakage in the meter itself, leading to unstable measurements. The use of spectral methods can circumvent some of these difficulties, and it may not be necessary to work at the precision described to obtain useful pH results.

There are other uses for the method. It should be possible to study the junction potentials of glass/references electrode pairs and to determine activity coefficients to a new standard of accuracy. In addition, the pK_a values for extremely acidic solutions are based on sequential comparisons of progressively less acidic indicators; this method could improve the accuracy of the pK_a values throughout this type of indicator series, especially where the ionic strengths become large. Currently, we are extending this approach to analyses of metallochromic and redox indicator systems at elevated temperatures and ionic strengths.

ACKNOWLEDGMENT

The authors wish to thank the Magma Power Co. for a Grant in support of this work.

APPENDIX. WEIGHTED AVERAGE K_A

The Propagation of Errors formula for derived standard deviations,[11] gives $\sigma_{\rho(H,\lambda)}$:

$$(\sigma_{\rho(H,\lambda)})^2 = \left(\frac{\partial\rho}{\partial A}\sigma_{A(H,\lambda)}\right)^2 + \left(\frac{\partial\rho}{\partial A_0}\sigma_{A_0(\lambda)}\right)^2 + \left(\frac{\partial\rho}{\partial A_1}\sigma_{A_1(\lambda)}\right)^2$$

$$\sigma_{\rho(H,\lambda)} = \{[[(A_0(\lambda) - A_1(\lambda))\sigma_{A(H,\lambda)}]^2 + [(A(H,\lambda) - A_1(\lambda))\sigma_{A_0(\lambda)}]^2 + [(A_0(\lambda) - A(H,\lambda))\sigma_{A_1(\lambda)}]^2]/[A_1(\lambda) - A(H,\lambda)]^4\}^{1/2} \quad (A1)$$

where $\sigma_{A_0}(\lambda)$, $\sigma_{A_1}(\lambda)$, and $\sigma_A(H,\lambda)$ are the standard deviations of the absorbances for the protonated species, the deprotonated species, and the mixture of both species, respectively, at a given wavelength. To simplify matters, a single, wavelength-averaged σ_{A_x} could be used in each numerator term, for each pH. The values of $\sigma_{A_0}(\lambda)$, $\sigma_{A_1}(\lambda)$ and $\sigma_A(H,\lambda)$ were estimated at each wavelength from repetitive measurements of single spectra.

To calculate the weighted average $\bar{\rho}(H)$ and the standard deviation of the mean $\sigma_{\bar{\rho}(H)}$ for each pH, weights equal to the reciprocal of the variance of each $\rho(H,\lambda)$ were used:

$$\omega_{\rho(H,\lambda_i)} = \frac{1}{(\sigma_{\rho(H,\lambda_i)})^2} \qquad \bar{\rho}(H) = \frac{\sum \omega_{\rho(H,\lambda_i)}\rho(H,\lambda_i)}{\sum \omega_{\rho(H,\lambda_i)}}$$

$$(\sigma_{\bar{\rho}(H)})^2 = \frac{1}{\sum \omega_{\rho(H,\lambda_i)}} \quad (A2)$$

Finally, an overall weighted average $\bar{K}_a$ could be calculated using weights equal to the reciprocals of the individual variances in $K_{ai}(H)$. The variances are again calculated by the propagation of errors formula:

$$(\sigma_{K_{ai}})^2 = \left(\frac{\partial K_a}{\partial \rho}\sigma_{\rho i}\right)^2 + \left(\frac{\partial K_a}{\partial H}\sigma_{Hi}\right)^2 \approx (H_i\sigma_{\rho i})^2 + (\bar{\rho}_i \ln 10 H_i \sigma_{pHi})^2 \quad (A3)$$

and the final weighted average $\bar{K}_a$ is given by

$$\omega_{K_{ai}} = \frac{1}{(\sigma_{K_{ai}})^2} \qquad \bar{K}_a = \frac{\sum \omega_{K_{ai}} K_{ai}}{\sum \omega_{K_{ai}}}$$

$$(\sigma_{\bar{K}_a})^2 = \frac{1}{\sum \omega_{K_{ai}}} \quad (A4)$$

This result takes into account all the variations in spectrometer noise and all variations in pH measurement, including meter noise, junction and streaming potentials, and small T fluctuations. The same averaging method is also applicable to results where $[H^+]$ and σ_H are calculated stoichiometrically from the titrations.

RECEIVED for review March 4, 1992. Accepted August 12, 1992.

Analytical Spectroscopy and Structure of Biomolecules Using an ab Initio Computational Method

Yeong Choi and David M. Lubman*

Department of Chemistry, The University of Michigan, Ann Arbor, Michigan 48109

An ab initio computational method has been applied to the study of biologically and pharmaceutically important phenethylamine and its derivatives (tyramine, dopamine, and tyrosine) in order to predict the structure of some of their stable conformers and consequently their spectroscopic properties. The structures were optimized at the HF/3-21G level and their stabilities were determined by performing vibrational frequency calculations on the optimized structures. In the case of phenethylamine and tyramine, three stable conformers were found, two of which have an ethylamine-folded structure and the other has an ethylamine-extended structure with the former two lying about 0.01 eV higher in energy than the latter. The stable conformers of phenethylamine found in the present study are compared with the results obtained by experiments and other theoretical methods. From the resulting structural calculations, IR and Raman vibrational frequencies of phenethylamine and tyramine were predicted which are particularly useful for the analyses of the experimental spectra when available. In particular, the capability to visualize the vibrational motion responsible for a particular peak enhances its usefulness in the assignment of the features in the IR spectra. Ionization potentials, electron affinities, and the charge density distribution of phenethylamine and its derivatives were predicted, and their utility in the interpretation of the experimental spectroscopic data is demonstrated.

INTRODUCTION

There has recently been a great deal of interest in the study of biological molecules by a variety of spectroscopic techniques. These have ranged from studies of the trace detection of biological species[1-6] to studies of their structure, function, and reactivity.[7-12] The former are important for analytical purposes while the latter have been particularly important in understanding the properties of molecules for drug design and pharmacological activity. The various studies used to probe these molecules have involved different spectroscopic techniques in many different environments ranging from gas-phase jet studies[12-18] to in vitro studies in the liquid phase at physiological pH.[19-21] However, any particular spectroscopic method can only provide a limited amount of information on any system and the experimental spectra of these molecules may not be easily interpretable by themselves. In particular, many of these biomolecules are thermally labile and spectroscopic measurements of these molecules are often plagued by artifacts due to thermal decomposition or other background impurities that may not be easily distinguishable in these experiments. Thus, there has been a motivation toward developing computational methods that can be used to predict a priori a broad range of spectroscopic properties.[22-24] Such calculations can be used to study the properties of various biological substances which are difficult to measure accurately by present experimental methods. Such computational methods can be extremely valuable for developing an accurate analytical data base for spectral properties of molecules in combination with experimental methods. In addition, computational methods have found an increasingly important role in analytical chemistry more generally.[25-27]

There are several classes of molecules that are being studied rather extensively because of their potent biological activity and pharmaceutical importance. These include various derivatives of catechol, indole and phenyl compounds. In particular, phenethylamine is a precursor for molecules such as tyramine (adrenergic), tyrosine (amino acid), and dopamine (neurotransmitter) and is structurally related to amphetamine (stimulant) and various other important hallucinogens. The indole group of compounds includes derivatives of tryptamine, such as serotonin (neurotransmitter) and *N,N*-dimethyl-

(1) Lubman, D. M.; Li, L. In *Lasers and Mass Spectrometry*; Lubman D. M., Ed.; Oxford University Press: Oxford, U.K., 1990; pp 353–381.
(2) Li, L.; Lubman, D. M. *Anal. Chem.* **1988**, *60*, 2591–2598.
(3) Wehry, E. L.; Gore, R. R.; Dickinson, R. B. In *Lasers in Chemical Analysis*; Hieftje, G. M., et al., Eds.; The Humana Press: Clifton, NJ, 1981; Chapter 10.
(4) Strojny, N.; deSilva, J. A. In *Lasers in Chemical Analysis*; Hieftje, G. M., et al., Eds.; The Humana Press: Clifton, NJ, 1981, Chapter 11.
(5) See: *Analytical Laser Spectroscopy*; Omenetto, N. Ed.; Chemical Analysis Series, Vol. 50; John Wiley & Sons, Inc.: New York, 1979.
(6) See: *Detectors for Liquid Chromatography*; Yeung, E. S., Ed.; John Wiley & Sons, Inc.: New York, 1986.
(7) Pullman, B.; Coubelis, J.-L.; Courriere, Ph.; Gervois, J.-P. *J. Med. Chem.* **1972**, *15*, 17–23.
(8) Pauling, P. In *Conformation of Biological molecules and polymers*; Bergman, E. D., et al., Eds.; The Jerusalem symposia on Quantum Chemistry and Biochemistry V; Academic Press Inc.: New York, 1973; pp 505–516.
(9) Pullman, B.; Courrier, P. In *Conformation of Biological molecules and polymers*; Bergman, E. D., et al., Eds.; The Jerusalem symposia on Quantum Chemistry and Biochemistry V; Academic Press Inc.: New York, 1973; pp 547–570.
(10) Pullman, B.; Berthod, H.; Courriere, Ph. *Int. J. Quantum Chem., Quantum Biol. Symp.* **1974**, *1*, 93–108.
(11) Martin, M.; Carbo, R.; Petrongolo, C.; Tomasi, J. *J. Am. Chem. Soc.* **1975**, *97*, 1338–1347.
(12) Mazurek, A. P.; Weinstein, H.; Osman, R.; Topiol, S.; Ebersole, B. J. *Int. J. Quantum Chem., Quantum Biol. Symp.* **1984**, *11*, 183–194.
(13) Cable, J. R.; Tubergen, M. J.; Levy, D. H. *J. Am. Chem. Soc.* **1988**, *110*, 7349–7355.
(14) Cable, J. R.; Tubergen, M. J.; Levy, D. H. *J. Am. Chem. Soc.* **1989**, *111*, 9032–9039.
(15) Breen, P. J.; Warren, J. A.; Bernstein, E. R.; Seeman, J. I. *J. Am. Chem. Soc.* **1987**, 109, 3453-3455.
(16) Seeman, J. I.; Secor, H. V.; Breen, P. J.; Grassian, V. H.; Bernstein, E. R. *J. Am. Chem. Soc.* **1989**, *111*, 3140–3150.
(17) Hager, J.; Ivanco, M.; Smith, M. A.; Wallace, S. C. *Chem. Phys.* **1986**, *105*, 397–416.
(18) Bickle, G. A.; Leach, G. W.; Demmer, D. R.; Hager, J. W.; Wallace, S. C. *J. Chem. Phys.* **1988**, *88*, 1–8.
(19) Spiro, T. G. In *Chemical and Biochemical Applications of Lasers*; Moore, C. B., Ed.; Academic Press: New York, 1974; Chapter 2.
(20) See: *Spectroscopy in Biochemistry*; Bell, S. E., Ed.; CRC Press, Inc.: Boca Raton, FL, 1981; Vol. 1.
(21) See: Carey, P. R. *Biochemical Applications of Raman and Resonance Raman Spectroscopies*; Academic Press: New York, 1982.
(22) Stanton, D. T.; Jurs, P. C. *Anal. Chem.* **1990**, *62*, 2323–2329.
(23) Stuper, A. J.; Brügger, W. E., Jurs, P. C. *Computer Assisted Studies of Chemical Structure and Biological Function*; Wiley-Interscience: New York, 1979.
(24) Barber, A. S.; Small, G. W. *Anal. Chem.* **1989**, *61*, 2658–2664.
(25) Rogers, L. B. *Anal. Chem.* **1990**, *62*, 703A–711A.
(26) Small, G. W.; Jurs, P. C. *Anal. Chem.* **1984**, *56*, 1214–1323.
(27) Morrow, J. C.; Baer, T. *J. Phys. Chem.* **1988**, *92*, 6567–6571.

0003-2700/92/0364-2726$03.00/0

tryptamines (hallucinogens). Thus, it is important to develop an analytical data base for spectroscopic detection and study of the basic structure of these molecules. Some of these species have been studied in gas-phase ultraviolet absorption spectroscopy[2,28] and in the condensed phase in the ultraviolet, visible, and infrared regions of the spectrum.[29-32] However, the information available on many of these important species is clearly rather limited or nonexistent. Here, computational methods can, in principle, be used to predict many of the properties and spectra of these molecules.

Traditionally, theoretical predictions on the structure and electronic properties of these classes of compounds have been performed by using semiempirical methods such as CNDO (complete neglect of differential overlap), INDO (intermediate neglect of differential overlap), PCILO (perturbative configuration interaction using localized orbitals), and EHT (extended Hückel theory).[7-12] However, the accuracy of the predictions by these semiempirical methods is often limited, in part, due to crude approximations inherent in these methods. Ab initio computational methods can be expected to yield much more accurate information than the semiempirical methods. However, general application of ab initio methods has been limited to considerably smaller molecules and biomolecules have been considered as too large to be studied by these methods. For molecules of this size, most of which are of low symmetry, such computations have been prohibitively expensive and time-consuming, and it is only recently that the application of ab initio calculations to these biomolecules has become reasonably feasible. This is due to (a) improved algorithms in computational methodology and (b) easier access to supercomputers, such as CRAY Y/MP, as a result of rapid advances in computer technology. Thus, ab initio methods have the potential for wider use beyond the tool of theoretical and computational chemists. In principle, such calculations can be used by a broad range of analytical and structural chemists for its accurate predictive power on structural, electronic, and spectroscopic properties of various atoms, radicals, ions, solids, and now larger polyatomics.

In the present study, phenethylamine, tyramine, dopamine, and tyrosine, shown in Figure 1, are examined using the ab initio method. Even with the capability of the present supercomputer, calculations on biologically and pharmaceutically interesting molecules that are significantly larger would still be difficult. However, it is expected that as computer software and hardware improve significantly over the next decade, these methods will be extended to even larger systems. Nonetheless, accurately determined parameters of these biomolecules provide an excellent building block for semiempirical calculations on larger biological systems. More significantly, ab initio methods can provide a broad range of information on biologically interesting systems.

In this work, ab initio computational methods are used to obtain several stable conformers by optimizing the structure of biomolecules and calculating the corresponding vibrational frequencies. Vibrational frequency calculations are shown to provide relatively accurate predictions of the IR and Raman spectra of these molecules where experimental data are available, and visualization of particular vibrational modes

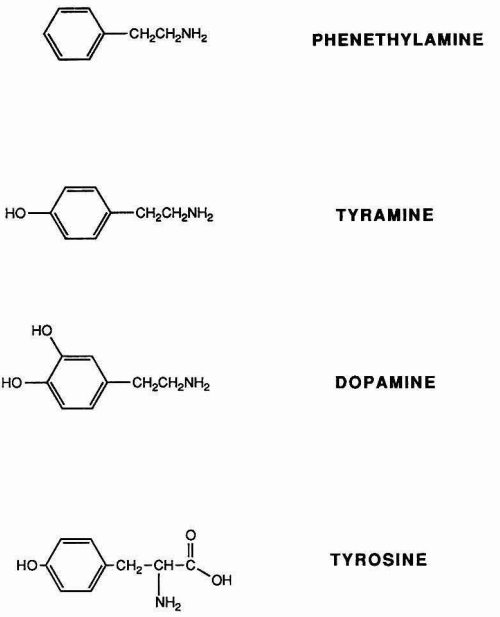

Figure 1. Phenethylamine and substituted phenethylamines.

using a software program, Molecular Editor,[33,34] helps the assignment of the features observed in the IR spectra. In addition, the vibrational frequency calculations are also used to differentiate stable conformers (local minima in the potential energy surface) from transition states. Ab initio calculations can also provide a variety of information on electronic properties of these molecules. Within the context of Koopmans' theorem, ionization potentials (IP's) and electron affinities (EA's) are predicted which will be very useful for studies of biomolecules by laser-induced fluorescence[13,14] or multiphoton ionization spectroscopic techniques.[2,3,13-18]

COMPUTATIONAL DETAILS

The calculations for the present study have been performed using the Gaussian 90 program [35,36] available on CRAY Y/MP at the San Diego Supercomputer Center. A 3-21G split-valence basis set was used for all the calculations. Although it is the smallest basis set required for freqency calculations, the predictive power of the calculations using this basis set is well documented[37] and using a 6-31G basis set does not seem to change the results significantly. Calculations on phenethylamine and its derivatives using a basis set larger than 3-21G would be much too expensive and time-consuming even for the CRAY Y/MP. For the readers who are not familiar with ab initio methods, there are many excellent books and review articles available.[37,39-41]

(28) Li, L.; Lubman, D. M. *Anal. Chem.* **1987**, *59*, 2538–2541.
(29) Johnson, C. R.; Ludwig, M.; Asher, S. A. *J. Am. Chem. Soc.* **1986**, *108*, 905–912.
(30) Ludwig, M.; Asher, S. A. *J. Am. Chem. Soc.* **1988**, *110*, 1005–1011.
(31) Lee, N.-S.; Hsieh, Y.-Z.; Paisley, R. F.; Morris, M. D. *Anal. Chem.* **1988**, *60*, 442–446.
(32) McGlashen, M. L.; Davis, K. L.; Morris, M. D. *Anal. Chem.* **1990**, *62*, 846–849.
(33) Smith, A. *Molecular Editor, software package for Apple Macintosh*; Intellimation: Santa Barbara, CA.
(34) Allan, D. S.; Seeger, D. M.; Korzeniewski, C. *Appl. Spectrosc.* **1990**, *44*, 1579–1581.
(35) Frisch, M. J.; Head-Gordon, M.; Trucks, G. W.; Foresman, J. B.; Schlegel, H. B.; Raghavachari, K.; Robb, M.; Binkley, J. S.; Gonzalez, C.; Defrees, D. J.; Fox, D. J.; Whiteside, R. A.; Seeger, R.; Melius, C. F.; Baker, J.; Martin, R. L.; Kahn, L. R.; Stewart, J. J. P.; Topiol, S.; Pople, J. A. *Gaussian 90*, revision F; Gaussian, Inc.: Pittsburgh, PA, 1990.
(36) Frisch, M. *Gaussian 90 User's Guide and Programmer's Reference*, revision I version; Gaussian, Inc.: Pittsburgh, PA, 1991.
(37) Hehre, W. J.; Radom, L.; Schleyer, P.v.R.; Pople, J. A. *Ab Initio Molecular Orbital Theory*; John Wiley & Sons, Inc.: New York, 1986 (see also references therein).
(38) For example, see: Pulay, P.; Lee, J.-G.; Boggs, J. E. *J. Chem. Phys.* **1983**, *79*, 3382–3391.
(39) Simons, J. *J. Phys. Chem.* **1991**, *95*, 1017–1029.
(40) Szabo, A.; Ostlund, N. S. *Modern Quantum Chemistry*, revised 1st ed.; McGraw-Hill Co.: New York, 1989.

Table I. Relative Computational Time vs Basis Set for Phenethylamine Calculation

basis set	no. basis functions	rel computational time
STO-3G	56	1
3-21G	103	11
6-31G*	157	62
6-31+G*	204	176

(A) Geometry Optimization. Most initial parameters of phenyethylamine were obtained from the experimental geometries of benzene and ethylamine. The two dihedral angles of phenethylamine which are responsible for the stability of the molecules were semiempirically determined values which were reported in the literature.[7-9] For the optimization of the subsequent molecules (tyramine, dopamine, and tyrosine), the 3-21G optimized parameters of phenethylamine were adopted as the starting geometries and the additional parameters were approximated by using a reasonable guess obtained from other related molecules.

All the optimization calculations were carried out using a Murtaugh-Sargent optimization algorithm instead of the default Berny algorithm.[36] The Murtaugh-Sargent method usually converges more slowly than the Berny method and thus takes a longer computational time, but occasionally, it performs more reliably, especially in the cases where the dihedral angles to be optimized are close to 180°.[36] Due to computer time constraint, neither an exhaustive search for all the stable conformers nor the global search of the conformational surface for the most stable conformer have been attempted in the present study.

(B) Vibrational Frequency. Calculated normal-mode vibrational frequencies provide two important pieces of information;[37] first, they may be used to characterize stationary points on the potential energy surface, i.e., to distinguish local minima which have all real frequencies from saddle points which have a single imaginary frequency, and second, they may be used as an aid in assigning fundamental vibrational modes observed in the IR and Raman spectra. Vibrational frequency calculations were performed at the HF/3-21G level using the 3-21G optimized parameters. A total of $3n-6$ normal-mode vibrational frequencies are predicted which are typically about 8–15% larger than the experimental values.[37] This offset is due to the effects of anharmonicity of the potential energy surface near the local minimum and the deficiencies of the HF procedure. The latter deficiencies can be removed by including polarization functions to the basis set and by including electron correlation.[38] Therefore, when comparing the calculated and experimental frequencies, it is necessary to "scale down" the calculated values by about 10%.[37] A checkpoint file saved from the optimization procedure was used as a starting point for the frequency calculation in order to save some computational time.

(C) Computational Time. When the electronic Schrödinger equation is actually solved, evaluation of two-electron integrals is the most time-consuming step. The computational time required for a single cycle of HF energy calculation is approximately proportional to n^4, where n is the number of basis functions used in the calculation.[36,37] The computational time for this step can be significantly reduced if the chemcial species under consideration is highly symmetrical since the number of two-electron integrals to be evaluated is reduced. Table I shows the number of basis functions and the approximate relative computational time for single-point HF calculations of phenethylamine in which several basis sets were used. It is estimated that the computational time for single-point HF calculations on phenethylamine using 3-21G, 6-31G*, and 6-31+G* basis sets is 11, 62, 176 times longer, respectively, than that using the minimum STO-3G basis set. A single-point HF calculation on phenethylamine using the 3-21G basis set takes slightly less than 10 min of CRAY Y/MP CPU time, thus showing that the calculations, particularly optimization calculations, using a basis set larger than 3-21G quickly become excessively expensive and time-consuming. A 3-21G vibrational frequency calculation on phenethylamine using the Gaussian 90 program on CRAY Y/MP required approximately 30 CPU min.

(41) Schaefer, H. F. *Quantum Chemistry: the development of ab initio methods in molecular electronic structure theory*; Oxford University Press: New York, 1984.

Table II. Stable Conformers, Their Dihedral Angles, and the Total Energies

compd	$d1$	$d2$	E_T (Hartree)	ΔE (eV)
Phenethylamine				
folded	90.0	−63.3	−361.7716	
folded	90.0	63.3	−361.7716	
extended	90.0	180.0	−361.7713	0.01
TS	180.0	180.0	−361.7685	0.11
Tyramine				
folded	90.0	−62.7	−436.2117	
folded	90.0	62.7	−463.2117	
extended	90.0	179.9	−436.2113	0.01
TS	0.0	61.3	−436.2073	0.20
Dopamine				
folded(a)[a]	90.0	−63.3	−510.6559	
folded(a)[a]	90.0	63.3	−510.6559	
extended(a)[a]	90.0	179.8	−510.6555	0.01
folded(b)[a]			−510.6556	<0.01
folded(c)[a]			−510.6444	0.31
Tyrosine				
folded	90.0	−69.3	−622.7777	

[a] (a), (b), and (c) refer to the orientations of the two hydroxy groups in dopamine. See Figure 5a–c, respectively, for the corresponding configurations.

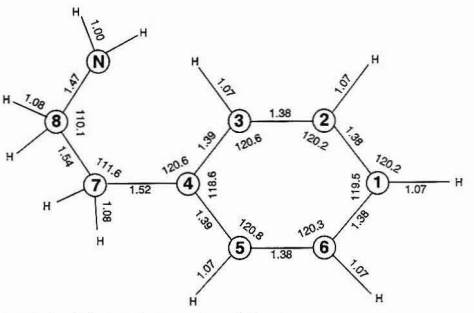

Figure 2. 3-21G optimized phenethylamine.

RESULTS AND DISCUSSION

(A) Structures of Stable Conformers. Table II summarizes the results of the optimization calculations performed to identify some of the stable conformers and the transition states of phenethylamine, tyramine, dopamine, and tyrosine. Three stable conformers each were found for phenethylamine and tyramine whereas five stable conformers were found for dopamine. Only one stable conformer was located for tyrosine via these computational methods. As mentioned in the previous section, no attempts have been made to locate the global minimum for all the molecules studied here. The two relevant dihedral angles which are mainly responsible for the stability of the molecule and the total energy of each of the conformers are also presented in Table II, as well as the energy difference with respect to the most stable conformer identified in the present study. In the following discussion, the structure and atomic positions in each molecule are described by referring to the phenethylamine structure shown in Figure 2 which forms the basic structure for all the molecules considered in the present study.

(i) Phenethylamine. Three stable conformers have been found for phenethylamine, two of which are equivalent and mirror image to each other. Figure 2 shows the 3-21G optimized structure of one of the two more stable pheneth-

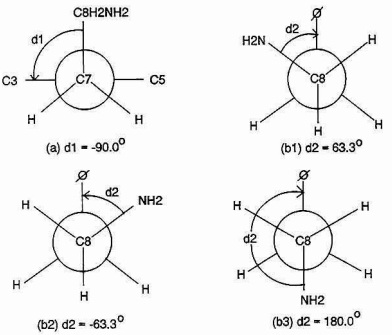

Figure 3. Newman projections of phenethylamine conformers along the (a) C7–C4 and (b) C8–C7 axes.

ylamine conformers found. Carbon atoms are arbitrarily numbered 1 through 8 and the nitrogen and hydrogen atoms are represented by N and H's, respectively. The bond angles and distances are represented in degrees and angstroms, respectively. The parameters of the benzene ring do not seem to change significantly from one conformer to another and the stability of the structure depends strongly on how the ethylamine chain is arranged. This can be more clearly elucidated by referring to Figure 3 where the two relevant dihedral angles, $d1$ and $d2$, are shown in Newman projections along (a) C7–C4 and (b1–3) C8–C7 axes, respectively. The dihedral angles $d1$ and $d2$ correspond to the angles C8C7C4C3 and NC8C7C4, respectively. Parts b1 and b2 of Figure 3 correspond to the two most stable conformers found with $d2$ = +63.3 and −63.3°, respectively. The sign of the dihedral angle depends on whether the front axis (N–C8) is rotated clockwise (+) or counterclockwise (−) in order to superimpose it to the back-axis (C7–C4), as indicated in the figure by the arrows. Figure 3b3 represents another stable conformer with $d2$ = 180.0°, which is slightly less stable (about 0.01 eV) with respect to the other two conformers. The ethylamine chain in the first two more stable conformers is *folded* whereas the one in the third conformer is *extended*. Figure 4 shows a snapshot of the more stable conformer of phenethylamine with the ethylamine chain folded.

Previous studies on phenethylamine show contradicting results on the structure of its most stable conformer.[11] Whereas the calculations using the semiempirical methods (CNDO, INDO, and PCILO) identified the ethylamine-folded form as the most stable conformer for phenethylamine, the EHT calculations showed the ethylamine-extended form as the most stable conformer, which is in agreement with the NMR experimental results where amphetamine in D_2O was shown to be in the ethylamine-extended form.[11]

Carbo et al.[11] performed ab initio calculations on phenethylamine at the Hartree–Fock level using the minimum STO-3G basis set and, on the basis of their results, concluded that the most stable conformer was the ethylamine-extended form, in agreement with the results of the EHT calculations. This is in constrast with the results obtained in the present study where the ethylamine-folded form is shown to be slightly more stable than the ethylamine-extended form. There are several reasons to believe that our results are more reliable than Carbo's: (1) the calculations in the present study used the split-valence 3-21G basis set which describes the nonspherical anisotropic aspects of molecular charge distribution more adequately than the minimum STO-3G basis set which Carbo et al. used in their calculations, (2) for all the optimized structures considered in the present study, the stability of the conformer was verified by performing vibrational frequency calculations whereas Carbo et al. performed single-point ab initio calculations on the possible conformers as determined by semiempirical methods, and (3) the NMR experimental results of amphetamine in D_2O cannot be used to support the results of ab initio calculations because phenethylamine is present in different chemical environments. More specifically, the ab initio calculations were performed on free phenethylamine whereas the NMR experiment was performed on amphetamine in D_2O where solvation effects may be important. In the crystal form of phenethylamine, only the ethylamine-extended form seems to dominate, possibly because it leads to more efficient crystal-packing forces.[9,42] However, in solution, both the ethylamine-extended and -folded forms coexist.[9]

The results of the present study are in agreement with those of the previous study using PCILO in which three stable conformers were found.[7,8,11] The present study determines the $d2$ dihedral angle more precisely and indicates that there is a small energy difference (about 0.01 eV) between the ethylamine-folded and ethylamine-extended conformers. Whether this represents the real situation or the consequence of using a relatively small 3-21G basis set cannot be determined by the present study. To clarify this point, more extensive calculations with basis sets more flexible than 3-21G and perhaps the inclusion of a correlation effect will be required.

In addition to the three stable conformers described above, a transition state was located for phenethylamine which yields one imaginary frequency in the vibrational frequency calculation. In this structure, $d1$ = $d2$ = 180.0°, which is equivalent to having all the carbon and nitrogen atoms on the same plane as the benzene ring. This transition state lies 0.11 eV (about 2.8 kcal/mol) in energy above the two most stable ethylamine-folded conformers.

(ii) Tyramine, Dopamine, and Tyrosine. Tyramine is a substituted phenethylamine where a hydroxy group on the benzene ring is in the para position (C1) to the ethylamine chain. As in the case of phenethylamine, three stable conformers have been identified for tyramine. Figure 4 shows a snapshot of the most stable conformer of tyramine found in the present study with the ethylamine chain folded. All 3-21G optimized parameters of tyramine do not differ significantly (less than 0.2 Å and 1.0° for bond distance and angle, respectively) from those of phenethylamine. Using the same definition of dihedral angles as in phenethylamine, the two equivalent mirror-image conformers have $d1$ = 90.0° in common and $d2$ = +62.7 and −62.7°. These conformers are slightly more stable by 0.01 eV than the conformer with $d1$ = 90.0° and $d2$ = 179.9°. The first two conformers correspond to the ethylamine-folded form while the third conformer corresponds to the ethylamine-extended form. The semiempirical calculations on tyramine using the PCILO method found two ethylamine-folded conformers at the two dihedral angles, $d1$ = 90° and $d2$ = +60 and =60°, approximately in agreement with the result of the present study.[7] But for the ethylamine-extended conformer, the PCILO method found $d1$ and $d2$ to be 120 and 180°, respectively, as compared to 90 and 179.9° observed in the present study. Other optimized parameters specific to tyramine are OC1 = 1.38 Å, HO = 0.96 Å, OC1C2 = 117.3°, and HOC1 = 112.8°. A transition state has been located at $d1$ = 0° and $d2$ = 61.3°, which is equivalent to rotating the ethylamine chain of a stable conformer along the C7–C4 axis by 90° counterclockwise. The energy difference between the most stable conformers found and this transition state is 0.20 eV (about 4.6 kcal/mol).

Dopamine is a substituted phenethylamine where two hydroxy groups are in the para (C1) and meta (C6) positions

(42) Tsoucaris, P. G. *Acta Crystallogr.* **1961**, *14*, 909–914.

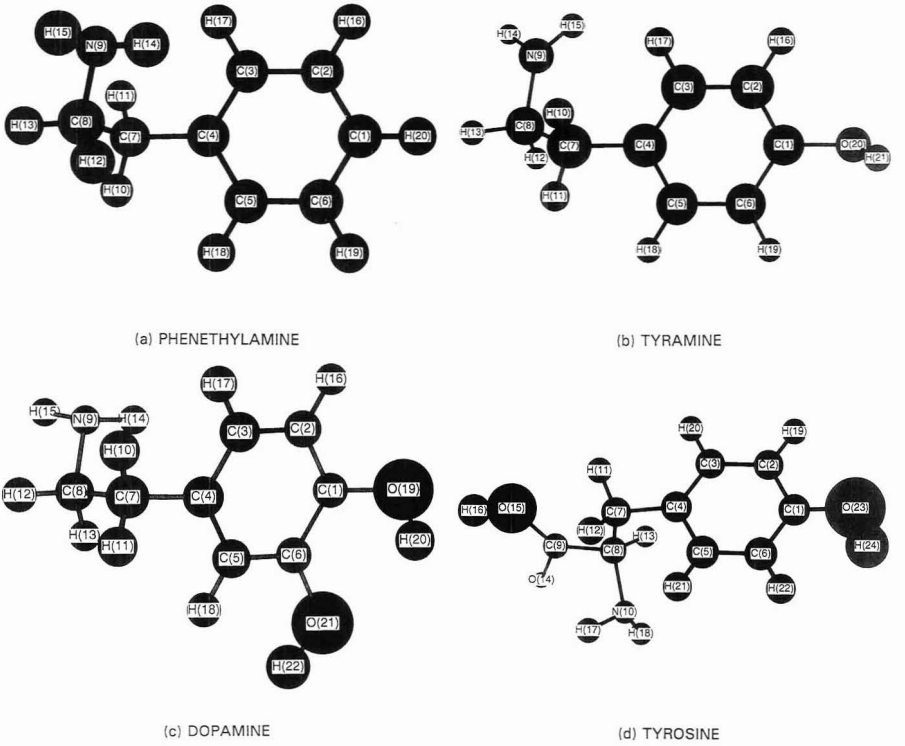

Figure 4. Snapshots of the stable conformer of (a) phenethylamine, (b) tyramine, (c) dopamine, and (d) tyrosine.

to the ethylamine chain on the benzene ring. A total of five stable conformers were identified for dopamine. As shown in Figure 5, there are three possible configurations for the two hydroxy groups in dopamine. Optimization of the two dihedral angles have been performed on the configuration of Figure 5a which has the lowest energy of the three possible configurations.

In accord with the cases of phenethylamine and tyramine, the dopamine with the configuration of Figure 5a has two stable conformers which are isoenergetic and mirror image to each other. These two conformers correspond to the ethylamine-folded structure with $d1 = 90.0°$ in common and $d2 = +63.3$ and $-63.3°$. Other optimized parameters specific to this stable conformer are OC1 = 1.39 Å, HO1 = 0.96 Å, OC6 = 1.37 Å, HO2 = 0.97 Å, OC1C6 = 114.3°, OC6C5 = 120.6°, HO1C1 = 113.5°, and HO2C6 = 110.1°. As in the cases of phenethylamine and tyramine, all 3-21G optimized parameters common to both tyramine and dopamine do not change significantly (less than 0.1 Å and 1.0° for bond distance and angle, respectively). Another stable conformer of dopamine with Figure 5a configuration was found with $d1 = 90.0°$ and $d2 = 179.8°$, corresponding to the ethylamine-extended structure. This conformer is slightly higher in energy (about 0.01 eV) than the other two conformers.

Using the optimized ethylamine-folded structure as a starting geometry, optimization calculations were performed on dopamine with the configurations of Figure 5b,c. There is almost no energy difference between the optimized Figure 5a,b (less than 0.01 eV) whereas optimized Figure 5c is about 0.31 eV (7.1 kcal/mol) higher in energy than the optimized Figure 5a. From the symmetry consideration, it is reasonable

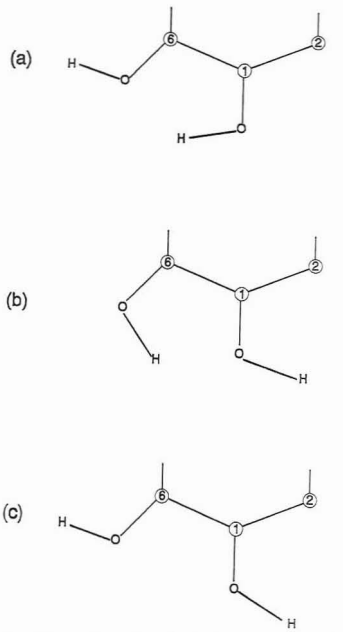

Figure 5. Possible configurations for hydroxy groups in dopamine.

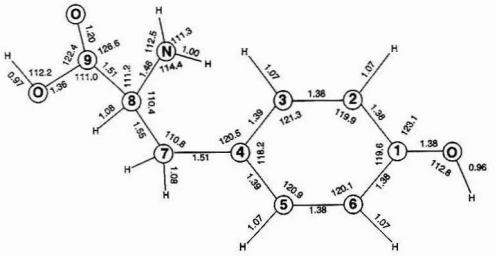

Figure 6. 3-21G optimized tyrosine.

Table III. Predicted Vibrational Frequencies, IR Intensities, and Raman Activities of Phenethylamine

ν_N	freq (cm^{-1})	IR inten	Raman act.	ν_N	freq (cm^{-1})	IR inten	Raman act.
1	3397	1	29	28	1117	1	1
2	3309	0	52	29	1076	3	0
3	3044	7	100	30	1067	0	0
4	3032	15	3	31	1041	6	3
5	3025	8	32	32	1039	3	2
6	3015	0	39	33	1029	1	0
7	3010	2	8	34	1004	1	1
8	2941	10	20	35	995	0	14
9	2903	27	48	36	973	0	1
10	2885	9	37	37	894	0	2
11	2851	29	32	38	875	0	2
12	1659	16	4	39	842	0	3
13	1597	2	10	40	790	16	1
14	1577	1	4	41	746	4	6
15	1512	1	7	42	733	22	0
16	1504	7	1	43	711	100	2
17	1484	3	5	44	642	0	2
18	1464	6	0	45	584	6	1
19	1397	6	1	46	495	4	2
20	1369	1	1	47	424	0	0
21	1342	3	6	48	417	4	1
22	1318	2	6	49	340	0	0
23	1244	1	1	50	266	15	6
24	1199	0	3	51	256	34	2
25	1192	1	4	52	148	3	1
26	1189	0	1	53	98	1	1
27	1145	0	2	54	45	2	3

to speculate that there are more stable conformers for dopamine with the hydroxy groups in either Figure 5b or 5c configuration. Figure 4 shows a snapshot of the most stable conformer of dopamine found with the ethylamine chain folded.

Tyrosine is a substituted tyramine where the –COOH group is attached to the ethylamine chain at the C8 position. Structural optimization of tyrosine was a nontrivial matter due to the increased number of parameters compared with the other molecules in the present study. The 3-21G optimized stable conformer is shown in Figure 6 and a snapshot of this conformer in Figure 4. Using the same definition of dihedral angles as in phenethylamine, $d1$ = C8C7C4C3 = 90.0° AND $d2$ = NC8C7C4 = 69.3°, which correspond to the ethylamine-folded structure. Other dihedral angles specific to tyrosine are O=C9C8C7 = –114.7° and OC9C8C7 = 63.9°. By symmetry, there should be another stable conformer with $d2$ = –63.9°, as well as other stable conformers, which have not been explored due to the computer time constraint.

(B) Vibrational Frequencies. Tables III and IV show the predicted vibrational frequencies, their relative IR intensities, and Raman activities for phenethylamine and tyramine, respectively. The IR intensities and Raman activities are normalized to ν_{43} at 711 cm^{-1} and ν_3 at 3044 cm^{-1}, respectively, for the vibrational frequencies of phenethylamine in Table III, and to ν_{42} at 718 cm^{-1} and ν_4 at 3045 cm^{-1}, respectively, for the vibrational frequencies of tyramine in Table IV. Although frequency calculations predict only the fundamentals ($3n - 6$ in the case of nonlinear molecules with n atoms), it is quite useful for the assignments of the experimental spectra which include not only fundamentals but also overtone and combination bands. It is well-known that simple vibrational frequency calculations such as the ones used in the present study predict the in-plane vibrational modes more accurately than the out-of-plane vibrational modes which are extremely sensitive to the basis set used in the calculation.[43] Inclusion of electron correlation effects may improve the prediction significantly, particularly for the out-of-plane vibrational mode calculations. Figure 7 shows a simulated IR spectrum of phenethylamine which includes only the fundamental vibrational modes. In this figure, the locations of the experimental vibrational frequencies are indicated with the dotted lines in the middle of the spectrum

Table IV. Predicted Vibrational Frequencies, IR Intensities, and Raman Activities of Tyramine

ν_N	freq (cm^{-1})	IR inten	Raman act.	ν_N	freq (cm^{-1})	IR inten	Raman act.
1	3523	28	87	30	1101	66	1
2	3395	1	46	31	1045	2	5
3	3308	0	81	32	1041	5	2
4	3045	2	100	33	1024	7	1
5	3038	6	43	34	1020	1	0
6	3020	5	36	35	1004	5	2
7	3020	7	26	36	901	31	0
8	2938	11	32	37	897	1	3
9	2901	32	83	38	870	8	4
10	2885	13	56	39	833	12	4
11	2851	31	50	40	812	9	18
12	1658	17	6	41	770	1	0
13	1615	18	19	42	718	100	3
14	1579	7	5	43	694	4	1
15	1523	36	1	44	661	1	3
16	1511	2	10	45	574	11	0
17	1485	3	10	46	493	2	1
18	1438	12	0	47	438	1	0
19	1397	8	1	48	424	4	3
20	1360	6	1	49	409	8	1
21	1343	4	10	50	362	3	2
22	1319	4	10	51	291	6	1
23	1261	2	2	52	271	97	3
24	1238	29	2	53	257	45	3
25	1193	1	4	54	212	2	0
26	1189	3	1	55	128	3	0
27	1177	72	9	56	82	1	1
28	1145	3	3	57	41	3	4
29	1103	11	0				

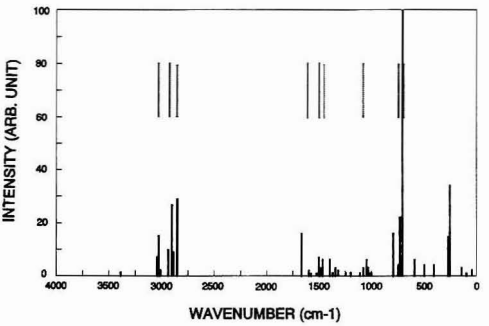

Figure 7. Predicted IR spectrum of phenethylamine. Dotted lines indicate the locations of the experimental peaks.

(43) Barstis, T.; Lubman, D. M. Unpublished results, University of Michigan, 1992.

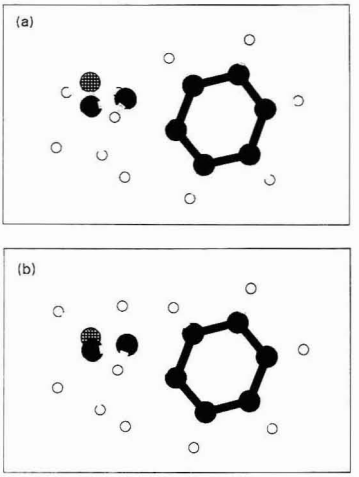

Figure 8. Visualization of a vibrational mode of phenethylamine obtained by using the Molecular Editor program.[33]

for comparison purposes. (The relative intensities are not included). Although not exactly identical, mostly due to the presence of the overtone and combination peaks, the approximate regions where major fundamental peaks appear are quite well predicted.

The experimental IR spectrum of phenethylamine in the vapor phase contains nine major peaks at ν = 3037 (m), 2943 (s), 2860 (m), 1613 (m), 1500 (m), 1454 (m), 1075 (m), 744 (s), and 699 (s) cm^{-1},[44] as indicated in the simulated IR spectrum by the dotted lines in Figure 7. By comparing the experimental and theoretical frequencies and intensities of the peaks, it is possible to speculate on the tentative assignment of the peaks in the experimental IR spectrum. For example, the most intense peak in the experimental IR spectrum of phenethylamine at ν = 743 cm^{-1} is most likely the fundamental ν_{43} which is predicted at ν = 711 cm^{-1} as the most intense peak. Also, the three closely spaced peaks at ν = 3037, 2943, and 2860 cm^{-1} observed in the 3050–2850-cm^{-1} region of the experimental IR spectrum probably correspond to the three peaks predicted at ν_3 = 3032 cm^{-1}, ν_9 = 2903 cm^{-1}, and ν_{11} = 2851 cm^{-1}, respectively, as can be deduced from the spacings and the intensities of these peaks.

In order to make a more definitive assignment of the features in these spectra, it is often quite useful to be able to actually visualize a specific vibrational mode that is responsible for a particular peak. Theoretical vibrational modes can be visualized by using the Molecular Editor software program[33,34] which graphically represents a mode by oscillating between the two extremes of vibrational motion. The two extremes of a particular vibrational mode are calculated by adding and subtracting the nuclear displacements from the equilibrium nuclear positions, all of which is available from the Gaussian output. This capability is especially useful when there are ambiguities in assigning the peaks that are closely spaced. Figure 8, for example, shows the vibrational mode ν_{43} predicted to be the most intense peak at 711 cm^{-1}. As can be seen from Figure 8a,b, which represent the two extremes of vibrational motion, the peak at ν_{43} = 711 cm^{-1} is mainly due to the rocking motion of the $-NH_2$ group. On a computer, the molecule can be rotated in three dimensions which enhances the visualization of the vibrational mode responsible for a particular peak in the spectrum.

Due to experimental difficulties, the Raman spectra of phenethylamine and substituted phenethylamines in the gas phase are not found in the literature. When the experimental Raman spectra of these compounds become available in the future, the predicted vibrational frequencies and Raman activities presented in Tables III and IV will be particularly useful for the analyses of the experimental data. For phenethylamine and tyramine, the most intense peaks are predicted to be at ν = 3044 and 3045 cm^{-1}, respectively, when scaled down by 10% from the calculated values.

Table V. Calculated Molecular Orbital Energies (eV) of Phenethylamines

compd	SHOMO	HOMO	LUMO	SLUMO
phenethylamine	−9.16 (9.35)[a]	−8.84 (8.99)[a]	4.21	4.15
tyramine	−9.39 (9.35)[a]	−8.32 (8.41)[a]	3.95	4.48
dopamine	−9.09 (8.90)[a]	−8.18 (8.18)[a]	4.08	4.50
tyrosine	−9.30	−8.33	4.01	4.37

[a] The experimental IP's are in the parentheses. From refs 46 and 47.

(C) Ionization Potentials and Electron Affinities. Ionization potentials (IP's) and electron affinities (EA's) are two of the most fundamental properties of chemical species which are the key to understanding oxidation and reduction processes as well as for estimating their electronegativities. The ionization potential is particularly important for experiments in photoionization or multiphoton ionization spectroscopies.[1,2] The simplest way to estimate these properties is by invoking Koopmans' theorem[45] in which the IP and EA are associated with the negatives of the energies of the orbitals the electron is ejected from and captured into, respectively. Since the orbital energies are obtained from a Hartree–Fock calculation on the neutral species, the Koopmans' theorem approximation includes neither the relaxation of the rest of the electrons upon gain or loss of an electron nor the difference in correlation energies between the neutral and ionic species.

IP's are predicted much better than EA's by invoking Koopmans' theorem in the HF calculations. The fact that IP's are accurately predicted, often within a few tenths of an electronvolt, is actually quite fortuitous due to the relative magnitudes and sign of relaxation and correlation effects in neutrals and the corresponding cations. Table V shows the energies of the SHOMO (second highest occupied molecular orbital), HOMO (highest occupied molecular orbital), LUMO (lowest unoccupied molecular orbital), and SLUMO (second lowest unoccupied molecular orbital) of the most stable conformers of phenethylamine, tyramine, dopamine, and tyrosine. These energies, expressed in electronvolts (eV), were calculated at the HF/3-21G level and obtained by invoking the Koopmans' theorem. The negatives of the energies of the SHOMO, HOMO, LUMO, and SLUMO correspond to the second IP (ionization potential), first IP, first EA (electron affinity), and the second EA of the molecules, respectively.

The experimental ionization potentials of the compounds obtained by photoelectron spectroscopy[46,47] are also included in Table V in parentheses. Considering the fact that the experimental deviations in the photoelectron spectra are typically 0.12–0.20 eV,[46,47] the ionization potentials of phenethylamine, tyramine, and dopamine are quite accurately predicted within the margin of the experimental deviation at

(44) Pouchert, C. J. *The Aldrich Library of FT-IR Spectra Vapor Phase*, ed. I; Aldrich Chemical Co., Inc.: Milwaukee, WI, 1989; Vol. 3, p 1164.

(45) Koopmans, T. *Physica* **1934**, *1*, 104–113.

(46) Domelsmith, L. N.; Munchausen, L. L.; Houk, K. N. *J. Am. Chem. Soc.* **1977**, *99*, 4311–4321.

(47) Domelsmith, L. N.; Houk, K. N. *Int. J. Quantum Chem., Quantum Biol. Symp.* **1978**, *5*, 257–268.

this level of calculation. It appears from Table V that the first ionization potentials are somewhat more accurately predicted by the calculation than the second ionization potentials. Although not available in the literature, the first and second ionization potentials of tyrosine are predicted to be 8.33 and 9.30 eV, with its first ionization potential quite close to that of tyramine.

In contrast to the accurate prediction of the ionization potentials, the prediction of electron affinities of these molecules is not expected to be quantitatively accurate due to the additiveness of relaxation and correlation effects in neutrals and corresponding anions. However, it is well-known that among the related molecules, relaxation and correlation effects often remain nearly constant so that the HF calculations invoking Koopmans' theorem approximation can predict the *relative* electron affinities quite well when adjusted with a constant scaling factor.[48] Nevertheless, one has to be cautious when applying Koopmans' theorem to predict the electron affinities of the molecules since there are complications associated with the fact that the unfilled orbitals corresponding to electron affinities are usually buried in the continuum region. Therefore, as more diffuse basis sets are used for calculations, the low-lying unoccupied orbitals may actually correspond to discretized continuum states, not the anion states.[49-51] Since extensive discussion on this subject is beyond the scope of this paper, interested readers are referred to the references for detail.[49-52]

Although no experimental data are available at the present time for phenethylamine and its derivatives considered in the present study, it can be predicted that the magnitude of the first electron affinities will be in the order phenethylamine > dopamine > tyrosine > tyramine, as shown in Table V. Once the electron affinity of one of these molecules is determined experimentally, for example by using electron transmission spectroscopy,[52] then on the basis of the scaling factor between the calculated and experimental values, the electron affinities of the rest of the related molecules may be predicted quantitatively.

(D) Total Atomic Charges. Parts a and b of Figure 9 show the total atomic charges of phenethylamine and tyrosine, respectively, which were obtained from the Mulliken population analyses of the HF/3-21G calculations.[35-37] Figure 9a also includes the atomic charges obtained from the HF/STO-3G calculations in parentheses.[11] When relative atomic charges are compared, there is little difference between the two calculations except for the carbon atom, C4, which is predicted to be negatively and positively charged according to the 3-21G and STO-3G calculations, respectively.[11] Other carbon atoms on the benzene ring (C1–C4, C5, and C6) are all negatively charged with similar magnitudes. A carbon atom on the ethylamine group, C7, is negatively charged and the other carbon atom, C8, is less negatively charged due to a larger electronegativity of the neighboring nitrogen atom which is the most negatively charged atom of the compound. In tyrosine, shown in Figure 9b, C1 is positively charged due to the neighboring oxygen atom and the carbon atom C9 is also positively charged due to the two neighboring oxygen atoms in the carbonyl group. Since the nitrogen atom is more negatively charged than the three oxygen atoms present in the compound, other conditions being considered equal, the nitrogen is the most likely atom predicted to be protonated.

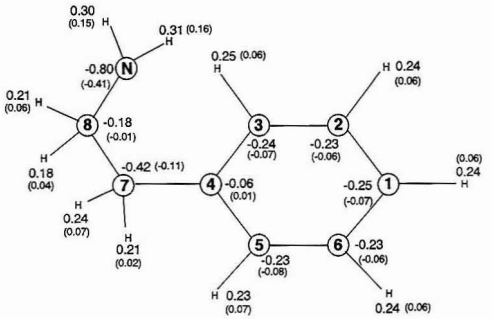

(a) TOTAL ATOMIC CHARGES OF PHENETHYLAMINE

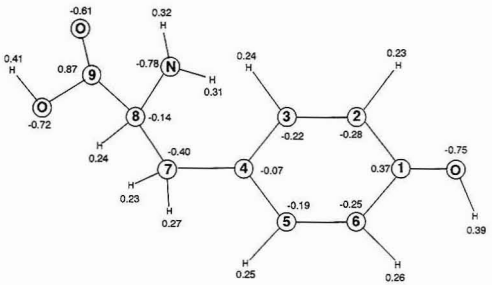

(b) TOTAL ATOMIC CHARGES OF TYROSINE

Figure 9. Total atomic charges of (a) phenethylamine and (b) tyrosine.

It is very important to obtain information concerning the protonated form of a molecule in order to understand the structure–activity relationship. In addition to being the most abundant form at the physiological value of pH = 7.4, the protonated form is the main form of a molecule responsible for its pharmacological responses by means of ionic interaction between the cationic head and some anionic receptor site.[11] In order to further investigate these problems, studies on protonated forms of phenethylamine and substituted phenethylamines are in progress.

CONCLUSIONS

The present study demonstrates the utility of the ab initio computational method to study the structural and spectroscopic properties of biomolecules which are frequently difficult to determine experimentally. Specifically, phenethylamine and its derivatives are pharmaceutically and biologically interesting molecules which have been studied by various semiempirical methods. Using the ab initio method, structural and spectroscopic properties of these biomolecules have been predicted and compared with those obtained by semiempirical methods. Several stable conformers were identified for phenethylamine, tyramine, and dopamine, and their relative energies were predicted. In the case of phenethylamine and tyramine, transition states were also identified.

In particular, two ethylamine-folded ($d1 = 90.0°$ and $d2 \simeq 60.0°$) and one ethylamine-extended ($d1 = 90.0°$ and $d2 \simeq 180.0°$) stable conformers were found for both phenethylamine and tyramine, with the first two about 0.01 eV lower in energy than the last one. While there is general agreement between the results of ab initio calculations presented in this study and those by several semiempirical methods, the ab initio calculations yield more precise values for the two dihedral angles that are responsible for the stability of the conformers.

(48) For example, see: Balaji, V.; Ng, L.; Jordan, K. D.; Paddon-Row, M. N.; Patney, H. K. *J. Am. Chem. Soc.* **1987**, *109*, 6957–6969.
(49) Chao, J. S.-Y.; Falcetta, M. F.; Jordan, K. D. *J. Chem. Phys.* **1990**, *93*, 1125–1135.
(50) Falcetta, M. F.; Jordan, K. D. *J. Phys. Chem.* **1990**, *94*, 5666–5669.
(51) Falcetta, M. F.; Jordan, K. D. *J. Am. Chem. Soc.* **1991**, *113*, 2903–2909.
(52) Jordan, K. D.; Burrow, P. D. *Acc. Chem. Res.* **1978**, *11*, 341–348.

IR vibrational frequencies were reasonably well predicted when the calculated frequencies were scaled down by 10% to compensate for the deficiencies of the computational method used in the present study. The capability to visualize a vibrational mode responsible for a particular peak enhances its usefulness for the assignment of the features in the IR spectra. Invoking Koopmans' theorem, the experimental ionization potentials were quite accurately predicted whereas calculated electron affinities need to be scaled in order to predict the experimental values.

It is important to remember that, when comparing theoretical predictions with the experimental data, one has to take into consideration the environment of the molecule. For example, whereas the calculations are performed on molecules in their free forms, approximately equivalent to their being in the gas phase, molecules studied experimentally are often present in highly perturbed condensed-phase environments in which solvation effects (NMR) or crystal-packing efficiency (X-ray crystallography) may be important. In these cases, direct comparisons between the experimental data and the theoretical predictions are not possible. In order to further investigate some of these problems, studies on protonated phenethylamine and substituted phenethylamines are in progress.

ACKNOWLEDGMENT

We would like to thank C. Korzeniewski for helpful suggestions regarding the Molecular Editor program. We acknowledge financial support of this work under NSF Grant No. CHE 9022610. Most of the computations in the present study were performed on CRAY Y/MP at the San Diego Supercomputer Center.

RECEIVED for review March 17, 1992. Accepted August 6, 1992.

Self-Modeling Mixture Analysis of Second-Derivative Near-Infrared Spectral Data Using the Simplisma Approach

W. Windig* and D. A. Stephenson

Analytical Technology Division, Eastman Kodak Company, Rochester, New York 14652-3712

One of the major methods used to resolve spectral data by self-modeling techniques requires the presence of pure variables. A pure variable is a variable that has an intensity contribution from only one of the components in the data set. For spectral data obtained in the near-infrared (near-IR) region (ca. 1–2.5 μm), pure variables are often not available, due to the width of the spectral peaks and the presence of a baseline. The application of self-modeling mixture analysis techniques has to be used with caution for these data. In this paper, it will be shown that, despite the absence of pure variables in near-IR data, it is possible to resolve the data properly by using the second-derivative spectra as an intermediate step. The basic technique will be demonstrated with the recently developed SIMPLISMA (SIMPLe-to-use Interactive Self-modeling Mixture Analysis) approach using a simulated data set. A complete example is given for a five-component solvent mixture using near-IR data.

INTRODUCTION

An important part of the methods used to resolve mixtures by self-modeling methods is based on the presence of pure variables for each of the components. A pure variable (e.g., a wavelength for near-infrared (near-IR) data is a variable that has intensity contributions from only one of the components in the mixture. The pure variable concept is based on the work of Lawton and Sylvestre,[1] Knorr and Futrell,[2] and Malinowski.[3,4] Gemperline et al.[5,6] gave an excellent review of these and related types of methods. To facilitate the resolution of complex mixtures by a user-friendly, interactive approach for a pure variable selection, the SIMPLISMA (SIMPle-to-use Interactive Self-modeling Mixture Analysis) approach was developed.[7,8]

In cases where a data set does not contain pure variables, resolution of the data results in pure component spectra that show characteristic spectral features in an exaggerated way.[9] This can be rationalized as follows: when pure variables are not present, the individual calculated concentrations, which are based on pure variables, contain contributions from other components. In other words, the concentrations are "under-resolved". Using these under-resolved concentrations to calculate the pure spectra from the original data results in a compensation for the incomplete resolution giving "over-resolved" spectra. The reasons for the absence of pure variables are a high degree of spectral overlap, the presence of a nonzero baseline, and commonly both. The purity of a variable is not an absolute requirement, though, as minor under-resolution in the resolved concentrations and over-resolution in the resolved spectra are acceptable for an interpretation tool such as SIMPLISMA.

It has been shown that the use of first- and second-derivative spectra can minimize the problems due to overlap and baselines.[10,11] Applications of derivative spectrometry in combination with multivariate mixture analysis have been described for least squares techniques,[12] the adaptative Kalman filter,[13] and multivariate prediction and background correction.[14]

This paper shows that second-derivative spectra can be used as an intermediate step to resolve highly overlapping components with a baseline problem. The principles will be first demonstrated using a simulated data set. Then, a near-IR data set of mixtures of five solvents, methanol, butanol, acetone, methylene chloride, and dichloropropane will be resolved.

MATERIALS AND METHODS

The following solvents were used to prepare the mixtures: 2-butanol, Aldrich Catalog No. 29,481-0; methylene chloride, Aldrich Catalog No. 27,099-7; methanol, Aldrich Catalog No. 32,241-5; dichloropropane, Aldrich Catalog No. D7,218-2; Acetone, Aldrich Catalog No. 27,072-5.

An orthogonal mixture design was used for the first of the four components listed above. All possible combinations of the fractional concentrations 10, 22.5, 35, 47.5, and 60% were used, resulting in 70 different mixture samples. Every sample was analyzed in duplicate, resulting in 140 spectra. The fractional concentration of the fifth component is the amount to make the fractional concentrations add up to 100%.

Care was taken to obtain anhydrous mixtures. Each of the five component samples weighed a nominal 100 g. Samples were weighed in a tared 250-mL amber bottle on a Sartorius Model 1409-C-MP7-2 balance. Weights were recorded to the nearest 0.01 g. The balance was tared between each component weighed. The bottle was capped after each component was added.

The instrument was a Pacific Scientific Model 6250 near-infrared spectrophotometer. The wavelength range was from 1100 to 2500 nm with an increment of 2 nm, resulting in 700 intensities per spectrum. The cuvette path length was 1.0 mm. Each sample was scanned 32 times. The raw spectra were smoothed using an five-point moving average. This is done by default in the manufacturers software. Second-derivatives were calculated using the Pacific Sciencific software. The parameters used for this procedure were segment = 10 and gap = 0. These settings are recommended by the instrument manufacturer as the minimum smoothing needed to avoid noise in the second-derivative spectra. This was experimentally verified. Furthermore, independent partial least squares studies on the second-derivative data set (not shown) gave excellent correlations (r = 0.999) and predictions of (known) concentrations of an independent data set, which also confirms the integrity of the second-derivative data set.

(1) Lawton, W. H.; Sylvestre, E. A. *Technometrics* **1971**, *13*, 617–632.
(2) Knorr, F. J.; Futrell, J. H. *Anal. Chem.* **1979**, *51*, 1236–1241.
(3) Malinowski, E. R. *Anal. Chim. Acta* **1982**, *134*, 129–137.
(4) Schostack, K. J.; Malinowski, E. R. *Chemom. Intell. Lab. Syst.* **1989**, *6*, 21–29.
(5) Gemperline, P. J. *J. Chemom.* **1989**, *3*, 549–568.
(6) Hamilton, J. C.; Gemperline, P. J. *J. Chemom.* **1990**, *4*, 1–13.
(7) Windig, W.; Guilment, J. *Anal. Chem.* **1991**, *63*, 1425–1432.
(8) Windig, W.; Heckler, C. E.; Agblevor, F. A.; Evans, R. J. *Chemom. Intell. Lab. Syst.* **1992**, *14*, 195–207.
(9) Meister, A. *Anal. Chim. Acta* **1984**, *161*, 149–161.
(10) O'Haver, T. C.; Green, G. L. *Anal. Chem.* **1976**, *48*, 312–318.
(11) O'Haver, T. C. *Anal. Chem.* **1979**, *51*, 91A–100A.
(12) Tahboub, Y. R.; Pardue, H. L. *Anal. Chem.* **1985**, *57*, 38–41.
(13) Gerow, D. D.; Rutan, S. C. *Anal. Chim. Acta* **1986**, *184*, 53–64.
(14) Karstang, T. V.; Kvalheim, O. M. *Anal. Chem.* **1991**, *63*, 767–772.

0003-2700/92/0364-2735$03.00/0

The stored spectra was transferred into a Lotus spreadsheet (Lotus Development Corp., Cambridge, MA), from which SIMPLISMA files were created.

THEORY

As was shown before,[7] a pure variable is based on the variable with the maximum ratio of the standard deviation to the mean. This ratio is called the purity and is given by the expression

$$p_{ij} = w_{ij}\frac{\hat{\sigma}_i}{\hat{\mu}_i + \alpha} \quad (1)$$

In this expression, p_{ij} is the purity value of the variable (i is the variable index), from which the jth pure variable will be selected. $\hat{\mu}_i$ and $\hat{\sigma}_i$ represent the mean and standard deviation of variable i. The constant α is added to the denominator of eq 1 to give variables with a low mean value (i.e., in the noise range) a lower purity value p_{ij}. Typical values for α range from 1 to 5% of the maximum of $\hat{\mu}_i$. The weight factor w_{ij} is a determinant-based function that corrects for previously chosen pure variables. The values of w_{ij} depend also on the value of α. For more details about this function, see refs 7 and 8.

The purity values as given in eq 1 are represented in the SIMPLISMA approach in the form of spectra. Along with the purity spectrum, the standard deviation spectrum is available, described by the following equation:

$$s_{ij} = w_{ij}\hat{\sigma}_i \quad (2)$$

This spectrum has more similarities with the original spectra, has a well-defined relationship to the purity spectra, and is used to facilitate the valiation of the pure variables. The interactive process makes it possible to guide the pure variable selection by changing the value for α (eq 1) in combination with the option to exclude certain spectral ranges for the selection of pure variables. This is especially useful since pure variables may describe unwanted features in the data set.[2,7,8,15]

Once the pure variables have been determined, the data set can be resolved into the pure components and their contributions in the original spectra.[8] The principle for the resolution of the spectra is as follows. The task of mixture analysis is to express a data set as a product of a matrix containing the concentrations and a matrix containing the spectra of the pure components.

$$\mathbf{D} = \mathbf{CR} \quad (3)$$

D is the matrix with the original data, its size is cv, where c is the number of cases (spectra) and v is the number of variables (wavelengths). The matrix **C** (size cn, where n is the number of pure components) contains the concentrations of the pure components in the mixtures. The matrix **R** (size nv) contains the resolved spectra.

Because pure variables are directly proportional to the concentrations of the pure components, their intensities can be used in the matrix **C**, and since the matrix **D** is known, the matrix **R** of the pure components can be calculated. Although the pure variable intensities can be used directly (after a normalization step) to calculate the concentrations, it is better to use the newly calculated **R** in combination with **D** to calculate **C**. In the latter case, a least squares approximation of the concentrations can be obtained with the inherent noise reduction. The thus obtained concentrations are in fact a projection of the second-derivative pure variable intensities on the original data set. For details about the procedure to calculate the spectra and concentrations, see ref 7. Where replicate analyses of samples are available, this information can be used for an additional noise reduction in the results.[8]

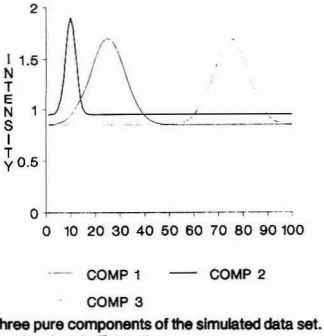

Figure 1. Three pure components of the simulated data set. Mixtures are based on the data in Table I.

Table I. Composition of the Mixtures of the Components Given in Figure 1

	fractional concentrations		
mixture no.	comp 1	comp 2	comp 3
1	0.34	0.34	0.32
2	0.44	0.23	0.33
3	0.48	0.25	0.27
4	0.20	0.35	0.45
5	0.21	0.51	0.28
6	0.22	0.54	0.24
7	0.44	0.37	0.19
8	0.17	0.54	0.29
9	0.33	0.05	0.62
10	0.19	0.37	0.44

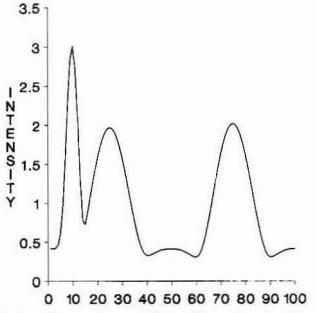

Figure 2. First purity spectrum obtained from the simulated data set.

RESULTS AND DISCUSSION

Simulated Data Set. To demonstrate the effect of the absence of pure variables and the subsequent use of derivative spectra, a simulated data set was created from the spectra shown in Figure 1. Mixtures were created from these spectra using the fractional concentrations listed in Table I. This data set serves as a model for near-IR data that typically contain peaks of varying width and substantial baseline shifts. The first purity spectrum is shown in Figure 2. Since no noise is present, the value of 0 was used for α in eq 1. The pure variables for this data set are at 10, 75, and 25,

(15) Windig, W.; Lippert, J. L.; Robbins, M. J.; Kresinske, K. R. *Chemom. Intell. Lab. Syst.* **1990**, *9*, 7–30.

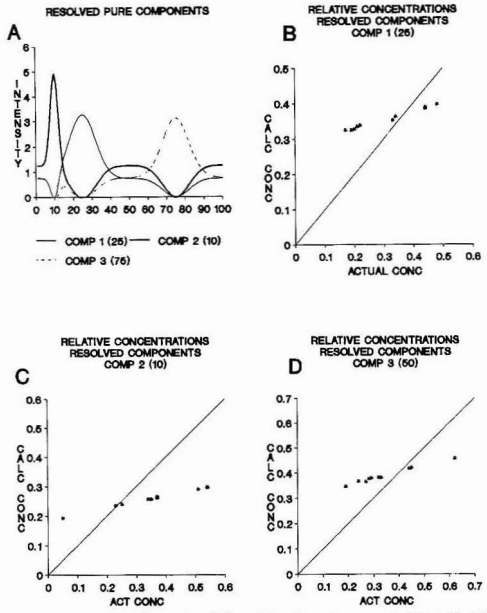

Figure 3. Resolved spectra (A) and fractional concentrations (B–D) obtained on the simulated data set. The spectra show the typical features of over-resolution. The fractional concentrations are clearly under-resolved.

Table II. Relative Purities of the Pure Variables

component	pure variable	rel purity
	Original Data Set	
1	25	0.49
2	10	0.51
3	75	0.49
	Second-Derivative Data Set	
1	25	1.00
2	11	0.97
3	76	1.00

respectively. The resolved spectra are shown in Figure 3. The characteristic patterns of over-resolved spectra are evident, that is, the typical feature of that component are present, but other regions are under-represented. The under-represented regions are especially clear at the pure wavelengths. Recall that a pure wavenumber of a certain component results by definition in a 0 intensity at that wavenumber for the other resolved components. This requirement is obviously not met for this data set.

The concentration plots of the resolved components are shown in Figure 3B–D. The calculated values are plotted against the values listed in Table I. There is a clear offset present in all these curves, mainly due to the overlap caused by the baselines of the other components. Clearly, the concentration profiles are under-resolved.

The baseline problem and the overlap of the peaks can be minimized by using derivative spectra. Although first- or second-derivative or higher derivative spectra can be used,[10-14] the second derivative was chosen for the approach described in this paper. The reason is that SIMPLISMA is meant to be an interactive tool for spectroscopists. As a consequence, the transformed spectra should have recognizable spectral features. As will be shown below, this is the case for second-derivative spectra.

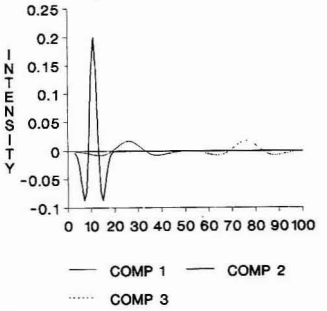

Figure 4. Three pure components of the inverted second-derivative simulated data set. Mixtures created are based on Table I.

The second derivatives of the spectra in Figure 1 are shown in Figure 4. The sign of the second-derivative spectra in this figure has been changed. This is done because it results in positive peaks in the same locations where the original spectra had their peaks, and it is therefore suitable for the interactive SIMPLISMA approach. In order to avoid confusion with the sign of the second-derivative spectra, the presentation of the second-derivative spectra as given in Figure 4 will be referred to as the inverted second-derivative spectra. As a consequence, the positive regions of the inverted second-derivative spectra are based on the negative regions of the second-derivative spectra.

A comparison of Figures 1 and 4 shows that the baseline is eliminated and that the peaks of the components are considerably narrowed, resulting in an almost complete elimination of the overlap. To obtain a quantitative measure of the "relative purity" of the peaks, the intensity of each of the pure variables was expressed as a fraction of the sum of the (absolute) intensities of all three components (see Table II). The determination of the pure variables of the inverted derivative data is discussed below. From Table II it is clear that there is a significant increase in the purity of the variables.

An inverted second-derivative mixture data set of the three-component model was created in the same way as the original data set discussed above, i.e., by using the numbers of Table I in combination with the spectra in Figure 4. It is important to realize that derivatives behave in a linear manner. In other words, the derivative of a mixture spectrum is the same as the sum of the derivative spectra of the pure components. As a consequence, the spectra obtained as described above are identical to those obtained by calculating the inverted second derivative of the mixture spectra of the original data set.

The inverted second-derivative spectra of the pure components (see Figure 4) and the mixture spectra to be analyzed by the SIMPLISMA approach (not shown) obviously have both positive and negative regions. The pure variable approach inherently assumes positive spectra and concentrations. Furthermore, to obtain data with "normal" spectral features, positive intensities are highly desirable. One way to deal with inverted second-derivative spectra is then to simply ignore the negative regions of the spectra as given in Figure 4. Before that is done, the implications of this procedure need to be discussed. As can be seen in Figure 4, the second component with a maximum at variable 11 contains a negative contribution of the first component with a peak at variable 25. This is entirely different from the original data, where the overlap of components 1 and 2 results in a positive contribution of component 1 to component 2, resulting in under-resolved concentrations. Because of the negative contribution of component 1 to component 2 in the inverted second-derivative data set, the concentrations will be over-

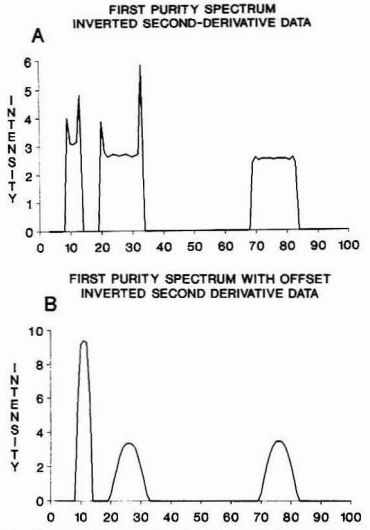

Figure 5. First purity spectrum with (A) $\alpha = 0$ and with (B) $\alpha = 3$.

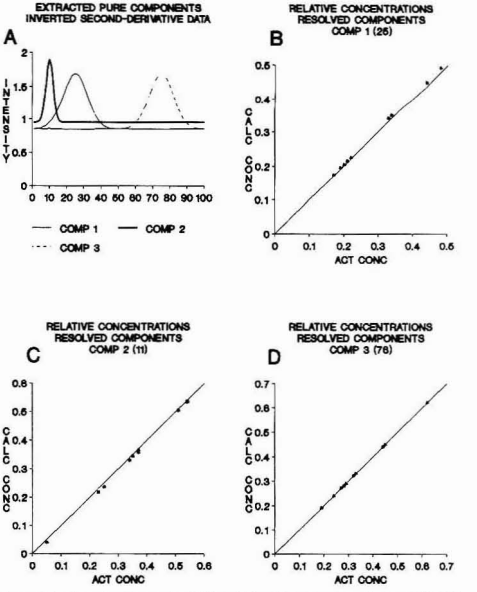

Figure 6. Resolved spectra (A) and fractional concentrations (B–D) based on the original data set in combination with pure variables obtained on the inverted second-derivative simulated data set. The spectra and fractional concentrations are very close to the ideal values.

resolved. It will be clear, however, that inverted second-derivative data exhibit significantly less overlap.

When we consider only the second component (peak at variable 11), it is clear that, when there is a relatively high amount of the second component and a relatively low amount of the first component, the intensity at pure variable 11 of the second component will be relatively accurate. Conversely, when there is a relatively high amount of component 1 and a relatively low amount of component 2, the intensity at pure variable 11 will be heavily influenced by the first component. This influence is a negative one and can result in a negative intensity for that pure variable. However, since a negative intensity at pure variable 11 is bound to be caused by an overlap with the first component, setting negative values to 0 will give a better estimate of the concentration of component 2. This implies that ignoring the negative regions of the inverted second-derivative spectrum for self-modeling mixture analysis is a valid approach. One has to realize it is possible that, due to the interaction of positive and negative contributions, a certain component could have contributions only in a negative region of the spectrum. Ignoring the negative regions will then cause the loss of that component. In practice, however, there is generally more than one peak for a component, and it is unlikely that all these peaks will become negative in the inverted second-derivative spectrum. Furthermore, the components with only negative intensities in the inverted second-derivative are far from pure and cannot be properly calculated for just this reason.

It should be mentioned that there are several approaches to obtain quantitative information from derivative spectra.[10] It is possible to include both parts of the spectrum by using a baseline measurement. This, however, would basically involve a baseline correction of the data. Because second-derivative spectra are used to minimize baseline problems, this is not an acceptable approach for complex data sets. Furthermore, when there are baseline corrections which are different for each spectrum, it generally causes more problems than it solves for multivariate data analysis.

As a next step, the SIMPLISMA approach was applied to the positive regions of the inverted second-derivative simulated mixture spectra. The first purity spectrum, with a value of 0 for α is given in Figure 5A. It is obvious that there is a problem at the flanks of the peaks. The high purities at the flanks are simply caused by round-off errors. The peak centered around variable 25 does not have any contributions fromany other component. As a consequence, all the variables associated with that component should have exactly the same purity value. Problems arise, though, for the very low intensity variables at the flanks, which suffer from round-off errors, resulting in high purity values and the ripple in the centers of the peaks. There is another reason for high purity values at the flanks, which is not very prominent for this data set, but which plays an important part in the near-IR data set that will be discussed in the next section. The reason is the interaction of positive and negative contributions to the variables. Because of this, peaks may have different widths at the baseline (zero) level. This varying width also contributes to high purity values at the flanks of the peaks. The problem caused by low-intensity variables at the flanks of the peaks can be solved by adjusting α in eq. 1. The effect of using a value of 3% of the maximum mean value of the variables for α results in the purity spectrum shown in Figure 5B, which clearly demonstrates the elimination of the high purities at the flanks of the peaks. On the basis of this purity spectrum, the pure variables 11, 76, and 25 were found for the second, third, and first pure component, respectively.

The pure variable intensities established as described above give a good estimate of the concentrations of the components in the mixture spectra. To calculate the spectra of the pure components, the pure variables (based on the inverted second-derivative spectra) are now used in matrix **C** in eq 3. For the matrix **D**, however, the original (i.e., no derivative) data are used. The use of the original data set is an important aspect of this approach and gives it a certain robustness: possible artifacts in the second-derivative pure variable intensities will be minimized by the series of least squares calculations used to calculate the spectra and the concentrations. This results in the spectra shown in Figure 6A. These extracted

Table III. Diagnostic Values[a]

pure variable	rel int st dev spec	successive ratios
	Original Data	
2240	100.0000	12.6631
2080	7.8969	45.7261
2408	0.1727	110.9451
1716	0.0016	69.1147
2276	0.0000	2142.6738
	0.0000	
	Second-Derivative Data	
2242	100.0000	2.1399
2302	46.7321	2.0782
2276	22.4873	2.1915
2250	10.2613	2.8786
2410	3.5646	7.9666
	0.4474	

[a] The first column indicates the pure variable. The second column represents the total intensity of the standard deviation spectra, which decreases when a component is eliminated by accepting a pure variable. The values have been made relative by scaling the first value to be 100. The third column lists the successive ratios of the values; e.g., the first value is the ratio of the first and second number in the second column. After all components all selected, the residual standard deviation spectrum should have a total intensity of 0 (because of noise it will always be higher). This results in a high ratio, since one basically divides by 0. As a consequence, a high ratio is an indication of the number of components in the data set.

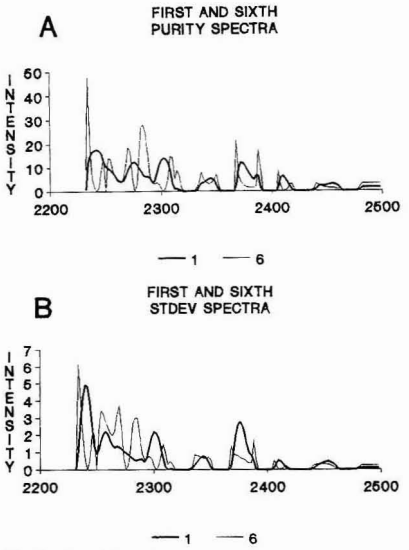

Figure 7. Overlay plot of the first and sixth purity (A) and standard deviation (B) spectra. The sixth purity and standard deviation spectra are dominated by high purities in the flanks of the peaks, which indicated that no more useful information was present.

spectra are almost identical to the original pure-component spectra given in Figure 1. Comparison with the extracted spectra using the original data set in Figure 3A shows that the improvement is significant.

In Figure 6B–D, the calculated concentrations of the components are plotted against the values listed in Table I. The improvement compared with the results obtained on the original data set shown given in Figure 3B–D is again significant.

It is important to note that the concentrations of the second component (Figure 6B) are systemically too low when compared to the line on which the data points should lie in the case of no error. This is because the pure variable of the second component (variable 11) has negative contributions from the first component. This problem is also expressed in the relative purities given in Table II. As discussed above, this results in over-resolved concentrations. Although the other two components are 100% pure in the inverted second-derivative spectra, minor deviations from ideal behavior are observed. The reason is that the deviation from the ideal behavior of the pure variable for the second component (under-resolved) is reflected in the other components through the combination of normalization and least squares procedures used to calculate the results.[7,8]

In summary, it was shown that the inverted second-derivative spectra of mixtures eliminate baseline problems and show significantly less overlap of the components. As a result, the use of pure variables based on the positive regions of the inverted second-derivative spectra to resolve the original data is significantly better than using pure variables of the original data set.

Near-IR Data Set. By definition, self-modeling mixture analysis approaches do not require reference spectra. To show the feasibility of the approach discussed here, reference spectra of the pure components are available to evaluate the results but are not used in any way for the data analysis. The original near-IR data set was analyzed by the SIMPLISMA approach, using a value for α of 5% of the maximum mean value. It was not trivial to analyze this data set, probably due to the large baseline shifts. Low-intensity peak areas consistently produced high-purity values, despite the use of high values for α in eq 1. The diagnostic values listed in Table III for the original data also reflect a nontrivial behavior. Although the high ratio after selecting three pure variables (110.9451) seems like a clear indication of only three components in the data set, the purity spectrum clearly showed that more information is present. After five components no significant information seemed to be present, which is clearly confirmed by the exceptional high ratio of 2142.6738. The resulting spectra and concentrations will be discussed along with the results using inverted second-derivative spectra.

As a next step, the positive regions of the inverted second-derivative spectra were used for SIMPLISMA analysis. Similar to the simulated data set, there were high purities at the flanks of the peaks. In addition to the round-off problems, there was a significant contribution to the high purities of the flanks because of varying peak widths caused by interaction of positive and negative contributions in the second-derivative spectra of the components. An offset value of 10 for α eliminated the flank problem, similar to Figure 5A,B. This is a higher value than used previously.[7,8] A high α may cause problems for severely overlapped peaks, but with the use of derivative data, the chance for highly overlapping peaks is small. As with every data analysis technique, it is important to check the validity of the results, with the assumptions of the technique in mind.

After the determination of the proper value for α, the procedure did not give any problems; i.e. no user interaction was necessary to eliminate (inactivate) spectral regions for the search of pure variables. It is important, however, to realize the utility of the interactive approach for the determination of the proper value of α. The first five purity and standard deviation spectra (not shown) clearly showed spectral features easily recognizable by a spectroscopist. The sixth purity spectrum, however, is heavily dominated by high values at the flanks. In order to illustrate this, the first and sixth purity and standard deviation spectra with an extended wavelength scale are shown for comparison in Figure 7. At this point, it was not possible to extract more information from the data set. In addition, the diagnostic values in Table III for the second-derivative data show a sudden increase in

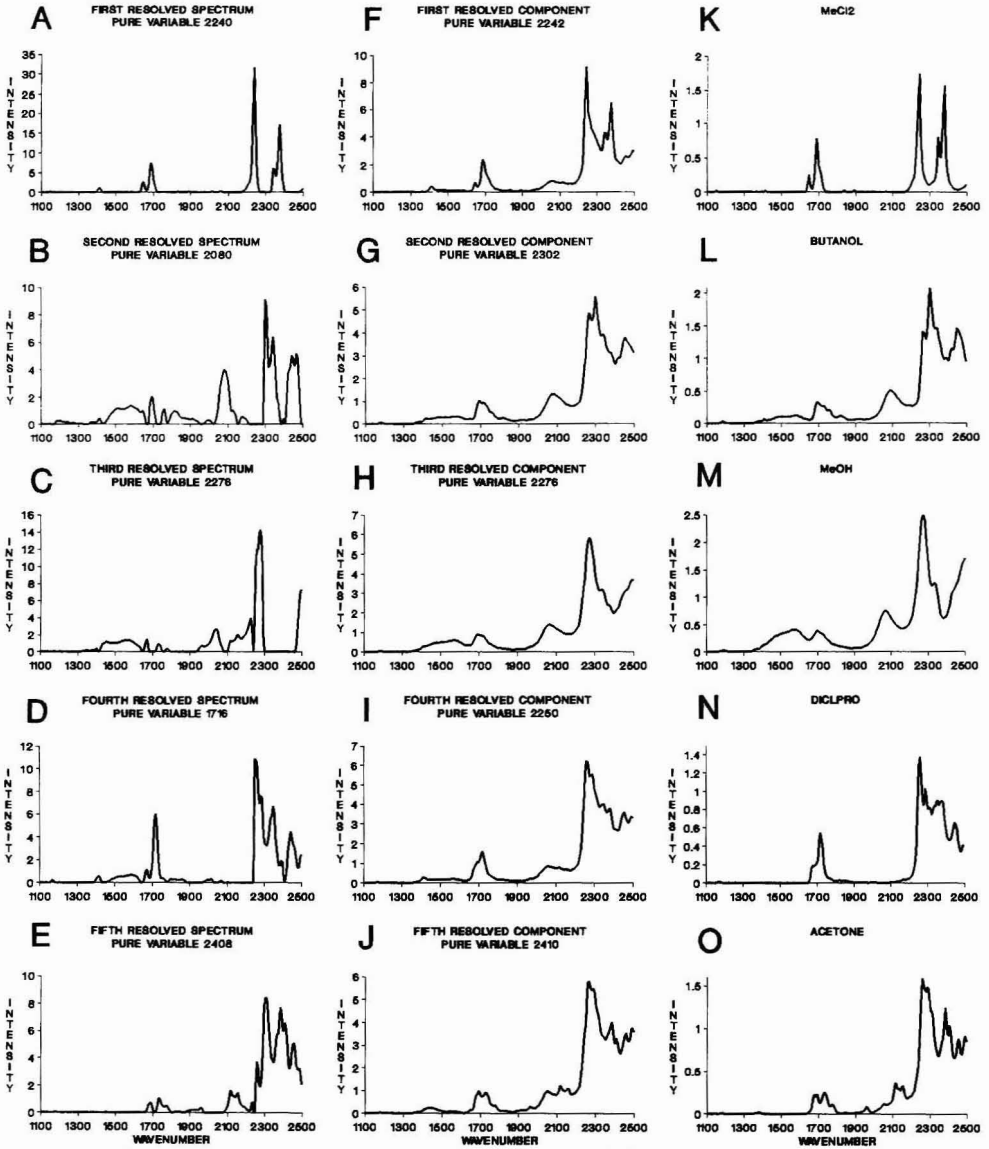

Figure 8. Resolved spectra obtained when pure variables of the original data set are used (A–E), the pure variables of the inverted second-derivative data are used (F–J) and model compounds are used (K–N). The order of these spectra is based on the order in which the pure variables of the inverted second-derivative data were determined.

the ratios of the standard deviation values, which is another indication that the number of the components in the mixture data set is 5.

After the original data set is resolved using the pure variable intensities of the inverted second-derivative data, the spectra shown in Figure 8 are obtained. Spectra 8A–E, produced from the pure variable intensities in the original data set, show the typical pattern of over-resolved spectra. Various spectral regions are missing. There were significant negative contributions in these resolved spectra that are not shown which may also be an indication of over-resolution. Comparison with spectra of the model compounds (Figure 8K–O) shows some similarities, but the similarities are not always clear. The spectra obtained by using the pure variables derived from the inverted second-derivative spectra (in combination with the original data set) are given in Figure 8F–J). The similarities with the pure compounds in Figure 8K–O are clearly superior to the results obtained using the original data set. It is clear, though, that the spectrum of $MeCl_2$ obtained using the original data (Figure 8A) is

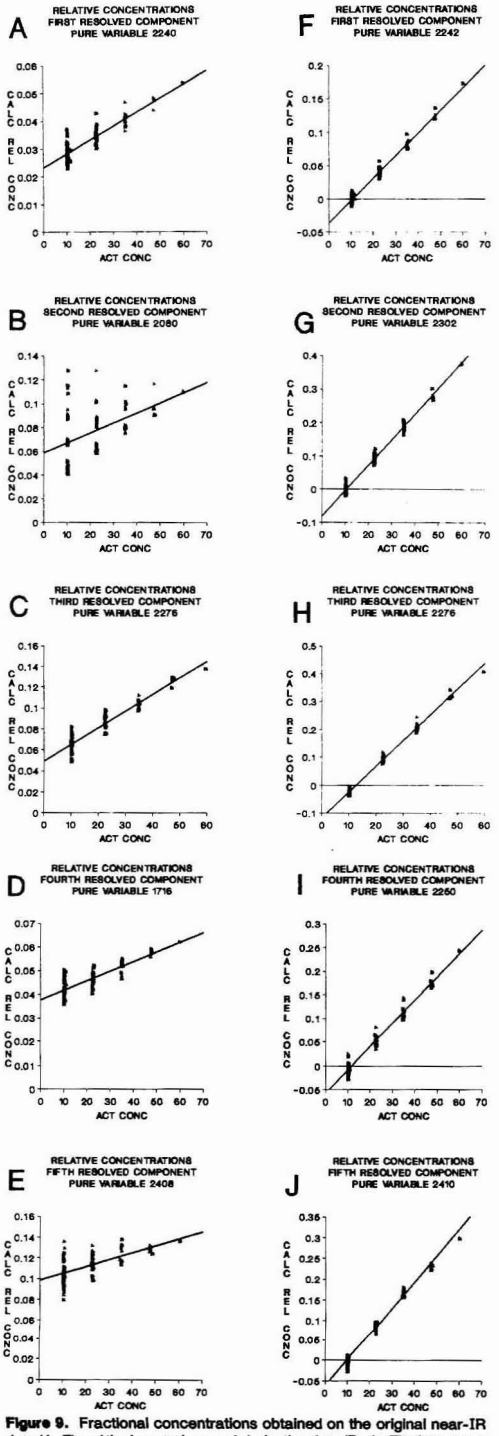

Figure 9. Fractional concentrations obtained on the original near-IR data (A–E) and the inverted second-derivative data (F–J). The intercepts of the least squares line with the *x*-axis are given in Table IV.

Table IV. Intercept of the Least Squares Lines in Figure 9 with the Actual Concentration Axis

component	original data	derivative data
$MeCl_2$	−46	10
butanol	−70	11
MeOH	−31	13
DiCl	−94	12
acetone	−150	10

comparable in its visual similarity with the spectrum of this same component obtained using the inverted second-derivative data (Figure 8F), although the "gap" at about 2300 nm between the two main peaks is a clear sign of over-resolution.

As the relative concentrations will show, there is still some overlap in the inverted second-derivative data. As a consequence, the spectra obtained using inverted second-derivative data are under-resolved, which is the likely reason why the resolved $MeCl_2$ spectrum in Figure 8F has a baseline. Some possible under-resolution effects can also be observed since there are intensities around 2100 nm in Figure 8F,I, which are not present in the spectra of the pure components.

The extracted relative concentrations of these components in the two data sets are shown in Figure 9. The plots of these values against the known values show a clear under-resolution for the results obtained using the inverted second-derivative data (Figure 9A–E), since the values are too high. The relative concentrations of butanol show clear deviations from the expected relation. The extracted concentrations based on the inverted second-derivative data show a much better relationship with the known concentrations. The correlation coefficients are all better than 0.98. Furthermore, the concentration profiles do not show any significant deviation from a nonlinear behavior. It is obvious, though, that these results are under-resolved, because the least squares line through these data has a negative intercept. This was to be expected, since all the pure variables had negative values, indicating an overlap. As explained above, these negative values were set to 0. Comparing the intercepts of the results in Figure 9A–E with 9F–J shows that the variables of the inverted second-derivative spectra are clearly much more pure than the pure variables obtained from the original data set. To give a concentration-based value to compare the purity of the results, the intercept with the concentration axis is listed in Table IV.

As can be seen, there are some negative intensities in the relative concentrations obtained using inverted second-derivative data (see Figure 9). Although it is possible to make the values positive in an iterative approach similar to those of Gemperline[16] and Vandeginste,[17] there is no guarantee that forcing the minor negative values of the data to 0 results in a better estimate of the relative concentrations of the components. Therefore, this approach was not further pursued.

CONCLUDING REMARKS

It was shown that the positive regions of inverted second-derivative spectra are useful for resolving highly overlapping data with baseline problems. The results of using the second-derivative data yield resolved spectra that are very similar to pure component spectra and are clearly better than those obtained using the original data. Similary, the concentrations derived using derivative spectra also show a clear improvement over those obtained with the original data.

There are some possible problems with the approach discussed above. Components may be lost using only the

(16) Gemperline, P. J. *J. Chem. Inf. Comput. Sci.* **1984**, *34*, 206–212.
(17) Vandeginste, B. G. M., Derks, W.; Kateman, G. *Anal. Chim. Acta* **1985**, *173*, 253–264.

positive regions of the inverted second-derivative data. Another problem that may arise using derivative spectra is that information can be lost about very broad peaks. Noise sensitivity of derivative spectra is also well-known. Therefore, some sort of data smoothing, as was used for the data set described above, is often applied before or during calculation of the derivative spectra. Since smoothing results in increasing the overlap of the peaks, minimal smoothing is required. Further research will investigate how different methods for calculating and smoothing second-derivative spectra affect the self-modeling mixture analysis process.

The limited research that was done until now shows that the method is rather robust with respect to variations in the calculation of the second derivative spectra. This is very likely due to the fact that, although the pure variable intensities were obtained on the *second-derivative* data, the *original* data set was resolved using a series of least squares approximations. This results in a certain robustness of the approach with respect to possible artifacts in the second-derivative data.

ACKNOWLEDGMENT

Charles Appell is gratefully acknowledged for discussions concerning the application of derivative spectra to mixture analysis. Tom Kaltenbach provided supporting data analysis and discussions. John Paul Twist provided the solvent mixture design, and Neil Redden performed all experimental work.

RECEIVED for review March 23, 1992. Accepted August 7, 1992.

Simultaneous Measurement of the Atomic and Molecular Absorption of Aluminum, Copper, and Lead Nitrate in an Electrothermal Atomizer

Judy Ratliff and Vahid Majidi*

Department of Chemistry, University of Kentucky, Lexington, Kentucky 40506

The transient molecular and atomic species produced in an electrothermal atomizer are probed by back-lighting a graphite furnace with continuum emission from laser-induced plasmas. The atomic absorption is measured simultaneously along with the molecular absorption by passing the emission from a hollow cathode lamp through the furnace in the opposite direction from the continuum propagation. Laser plasma sources exhibit a substantial improvement in UV emission intensities over more conventional sources, permitting good time resolution for monitoring transient molecular species. The simultaneous atomic and molecular absorption spectra obtained from the atomization of $Al(NO_3)_3$, $Cu(NO_3)_2$, and $Pb(NO_3)_2$ in both tantalum-lined and unlined furnaces are illustrated. The molecular species produced in a heating cycle and their relationship to the appearance of the atomic species is presented. By monitoring the atomic and molecular species formed during the atomization cycle, we have observed a more complete thermal history of the formation and dissociation of transient species in electrothermal atomizers.

INTRODUCTION

Graphite furnace atomic absorption spectroscopy (GFAAS) has a primary analytical advantage in that its detection limits are typically 2 orders of magnitude better than either flame atomic absorption spectroscopy or inductively coupled plasma atomic emission spectroscopy. The disadvantages arise mainly from interference by refractory compounds and matrix molecular absorption.[1] There are numerous atomization mechanisms proposed for GFAAS; however, data collected nonintrusively which identify the molecular species generated during a heating cycle are scarce.

GFAAS is used because of its sensitivity, but some of the elements of interest are prone to interferences. These interferences arise because many gas-phase chemical reactions can occur during the heating cycle which changes the free atom density within the furnace. These vapor-phase interferences occur when analyte atoms combine with interferents after entering the vapor phase.[2] This may tie up the analyte, making it undetectable at the sampled wavelength, or the interferents may have a molecular band which contributes to an increase in the absorption signal seen for the analyte. More information on the species generated in a furnace is needed in order to develop a better understanding of the mechanisms by which atomization proceeds. The gas-phase molecular species that evolve with the free atomic species should be identified by nonintrusive techniques. The identification of gas-phase intermediates involved in the atomization/vaporization process may lead to enhanced detection limits in GFAAS. Many studies have been carried out to identify the gas-phase reactions which occur during electrothermal atomization. These include molecular absorption,[3-5] mass spectrometry,[6-13] and mathematical modeling concerning reaction mechanisms involved in desorption processes.[14-18]

One proposed mechanism suggests that gas-phase species, such as oxygen and carbon monoxide, influence the process of analyte atom formation in a high-temperature furnace.[19] It has been postulated that oxygen and carbon monoxide play a role in the reduction of an analyte according to oxide dissociation and carbothermal reduction mechanisms.[19] This gaseous carbide mechanism for the reduction of oxides by carbon (ROC) is based on two concurrent reactions:[19]

$$M(g) + zC(s) \leftrightarrow MC_z(g)$$

$$MC_z(g) + (z/y)M_xO_y(s/l) \leftrightarrow (1 + z/y)M(g) + zCO(g)$$

In this proposed mechanism the first reaction occurs on the surface of graphite and the second on that of the oxide.[19] Holcombe suggested that this may not be the most probable mechanism.[6]

By simultaneous monitoring of the atomic and molecular absorption within a graphite tube the problems associated with varying tube conditions from one firing to another such as deterioration of the tube, variations in the heating rate, or different day-to-day conditions can be overcome. The amount of information collected with a diode array detection system, such as the one used for these studies, improves the confidence level of unknown measurements while increasing the precision of the technique, as explained by Jones et al.[20]

* To whom correspondence should be addressed.

(1) Slavin, W. *Spectroscopy* **1991**, *6*, 16–21.
(2) Tsunoda, K.; Haraguchi, H.; Fuwa, K. *Spectrochim. Acta, Part B* **1985**, *40B*, 1651–1661.
(3) Sedykh, É. M.; Belyaev, Y. I.; Ozhegov, P. I. *Zh. Anal. Khim.* **1979**, *34*, 1984–1992.
(4) Vago, E. E. V.; Barrow, R. F. *Proc. Phys. Soc.* **1947**, *59*, 449–457.
(5) Majidi, V.; Ratliff, J.; Owens, M. *Appl. Spectrosc.* **1991**, *45*, 473–476.
(6) Holcombe, J. A.; Styris, D. L.; Harris, J. D. *Spectrochim. Acta Part B* **1991**, *46B*, 629–639.
(7) Wang, P.; Majidi, V.; Holcombe, J. A. *Anal. Chem.* **1989**, *61*, 2652–2658.
(8) Bass, D. A.; Holcombe, J. A. *Anal. Chem.* **1988**, *60*, 578–582.
(9) Styris, D. L.; Redfield, D. A. *Anal. Chem.* **1987**, *59*, 2891–2897.
(10) Styris, D. L.; Kaye, J. H. *Spectrochim. Acta, Part B* **1981**, *36B*, 41–47.
(11) Bass, D. A.; Holcombe, J. A. *Anal. Chem.* **1987**, *59*, 974–980.
(12) Prell, L. J.; Styris, D. L.; Redfield, D. A. *J. Anal. At. Spectrom.* **1991**, *6*, 25–32.
(13) Sturgeon, R. E.; Mitchell, D. F.; Berman, S. S. *Anal. Chem.* **1983**, *55*, 1059–1064.
(14) Güell, O. A.; Holcombe, J. A. *Anal. Chem.* **1990**, *62*, 529A–542A.
(15) Güell, O. A.; Holcombe, J. A. *Spectrochim. Acta, Part B* **1989**, *44B*, 185–196.
(16) Cathum, S. J.; Chakrabarti, C. L.; Hutton, J. C. *Spectrochim. Acta* **1991**, *46*, 35–44.
(17) Genç, Ö.; Akman, S.; Özdural, A. R.; Ates, S.; Balkis, T. *Spectrochim. Acta, Part B* **1981**, *36B*, 163–168.
(18) Bauschlicher, C. W.; Langhoff, S. R.; Pettersson, L. G. M. *J. Chem. Phys.* **1988**, *89*, 5747–5752.
(19) L'vov, B. V. *Spectrochim. Acta, Part B* **1989**, *44B*, 1257–1271.
(20) Jones, B. T.; Smith, B. W. Winefordner, J. D. *Anal. Chem.* **1989**, *61*, 1670–1674.

0003-2700/92/0364-2743$03.00/0

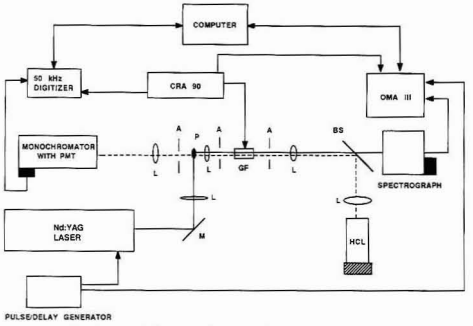

Figure 1. Instrument diagram/setup: focusing lens (L); aperture (A); beam splitter (BS); mirror (M); graphite furnace (GF); hollow cathode lamp (HCL); carbon rod atomizer (CRA); optical multichannel analyzer (OMA); plasma (P).

EXPERIMENTAL SECTION

Apparatus. A block diagram of the setup is shown in Figure 1. Molecular absorption was monitored by focusing the output of a pulsed Nd:YAG laser (Model GCR-3, Spectra-Physics, Mountain View, CA) at 1064 nm, approximately 100 mJ (7-ns duration), with a quartz lens (f = 127 mm) to form a plasma. The plasma emission was then focused inside the graphite furnace with a second quartz lens (f = 58 mm). The contents of the furnace were subsequently focused by another quartz lens (f = 127 mm) onto the entrance slit of the spectrograph (Model 1234, Jarrell-Ash, Franklin, MA). An iris was placed between the lens and the furnace to block residual plasma emission and to reduce interference from furnace emission. The spectrograph was equipped with three gratings and an intensified photodiode array detector (Model 1421BR-1024-G, EG&G Princeton Applied Research, Princeton, NJ). The data acquisition and gating of the photodiode array were accomplished through an OMA III system (Model 1460, EG&G Princeton Applied Research, Princeton, NJ) and a pulse amplifier (Model 1304, EG&G Princeton Applied Research, Princeton, NJ). For these studies the pulse window of the photodiode array was set to 10 μs.

The atomic absorption was monitored by focusing the output of an appropriate hollow cathode lamp into the center of the furnace with a quartz lens (f = 65 mm). This point was subsequently focused by a pair of lenses (f = 58 mm and f = 72 mm) onto the entrance slit of a monochromator (AA6 Varian Techtron, Ltd., Springvale, Australia). The selected wavelength was monitored with a photomultiplier tube (Type 1P28; Hamamatsu Photonics K. K., Japan) and digitized by a 556-series Keithley measurement and control system (Keithley Instruments, Inc., Cleveland, OH).

The molecular and atomic species were generated in a tubular graphite furnace (Model CRA-90, Varian Techtron, Ltd., Springvale, Australia). The furnace was purged with argon flowing at 6 L/min to prevent oxidation of the graphite during the heating cycle. Due to the open atomization configuration, the synchronization of the atomization, plasma generation, and data collection were achieved by a delay/pulse generator (Model DG535, Stanford Research Systems, Sunnyvale, CA). The delay generator produced a 10-Hz TTL pulse train synchronizing the laser pulse and the OMA. The data collection was initiated at the onset of the atomization cycle.

All instruments were controlled by an IBM PC, and after data collection by the OMA and Keithley, information was transferred through a GPIB bus to the IBM and stored on disks. Absorption profiles were internally corrected, as suggested by Harnly and Holcombe.[21-23]

(21) Harnly, J. M.; Holcombe, J. A. *J. Anal. At. Spectrom.* **1987**, *2*, 105–113.
(22) Holcombe, J. A.; Harnly, J. M. *Anal. Chem.* **1986**, *58*, 2606–2611.
(23) Harnly, J. M.; Holcombe, J. A. *Anal. Chem.* **1985**, *57*, 1983–1986.

Table I. Operating Parameters for Experiments

element	dry temp (°C)	time (s)	ash temp (°C)	time (s)	atomize temp (°C)	line (nm)	temp ramp (°C/s)
Na	100	60	0–500	0–20	2500	589	700
Pb	100	60	0–500	0–20	2100	217	700
Al	100	60	0–500	0–20	2500	309	700
Cu	100	60	0–500	0–20	2100	324	700

Reagents. Test solutions were prepared from appropriate dilutions of a 5×10^3 mg/L stock solution of the nitrate salt of the element of interest in deionized water.

Procedure. New furnaces were cleaned by heating to 3300 K in a 6 L/min flow of argon at least twice prior to collecting data. After cleaning, they were water-cooled to room temperature before samples were introduced. Furnace emission profiles were obtained daily and each time a new furnace was used. Furnaces were also cleaned between sample runs. A 5-mL aliquot of the desired sample was placed in the graphite furnace, and the heating cycle outlined for each element in Table I was followed. At the onset of the atomization cycle, the CRA-90 triggered the OMA and the Keithley to collect data simultaneously. For each heating cycle 40 wavelength-resolved spectra were collected during the atomization cycle by the OMA and a 1000-point, time-resolved, atomic absorption spectrum was recorded by the Keithley. At least three separate sets of spectra were collected for each different sample, concentration, and instrument setting used. The time resolution for the OMA in these studies was 100 ms (dictated by the 10-Hz repetition rate of the laser) and the wavelength resolution 0.2 nm. A new furnace was used each time a different element was examined. For the studies which utilized a tantalum lining, a 0.05-mm-thick piece of foil (99.9+%, Aldrich) was cut and molded to the shape of the furnace.

The atomic absorption profiles were corrected for the 10-Hz noise superimposed on them by the emission from the laser. This was accomplished by calculating the Fourier transform and filtering out anything which occurs at 10 Hz. This sometimes produced some artifacts which can be seen in the baseline of the resulting spectra. A signal before and after this correction is illustrated in Figure 2. This atomization cycle was collected at a different ramp rate than the other cycles shown.

RESULTS AND DISCUSSION

Atomization mechanisms within a graphite furnace are not clearly understood. To develop a better understanding of the processes taking place in electrothermal atomization, a reliable method of monitoring gas-phase species is needed. The system used in these studies does this and has been described in an earlier publication.[5] Larger sample sizes than those typically used in atomic absorption were used in these studies. Atomization mechanisms observed for large samples may differ from those seen for smaller samples. Three cases would be expected to be seen in these studies: first, direct and clean atomization of an analyte from the surface of the furnace producing atomic absorption lines with no broad band absorption; second, the desorption of the analyte from the surface and subsequent gas-phase reactions which would produce molecular species (in this case our system should show an atomic species appearing first then molecular species developing); third, appearance of a molecular species prior to an atomic species which would then dissociate to form atomic species. As a test of the features added to the original system design, simultaneous molecular and atomic absorption spectra of sodium iodide were collected (Figure 3). NaI is a much-studied molecule with a UV spectrum readily available.[2,5,24-27] From this test, it was apparent that reliable and

(24) Güçer, S.; Massmann, H.; Gohary, Z. E. *Chim. Acta Turc.* **1976**, *4*, 1–6.
(25) Culver, B. R.; Surles, T. *Anal. Chem.* **1975**, *47*, 920–921.
(26) Shekiro, J. M., Jr.; Skogerboe, R. K.; Taylor, H. E. *Anal. Chem.* **1988**, *60*, 2578–2582.
(27) Niemczyk, T. M.; Yin, I. H. *Appl. Spectrosc.* **1985**, *39*, 882–883.

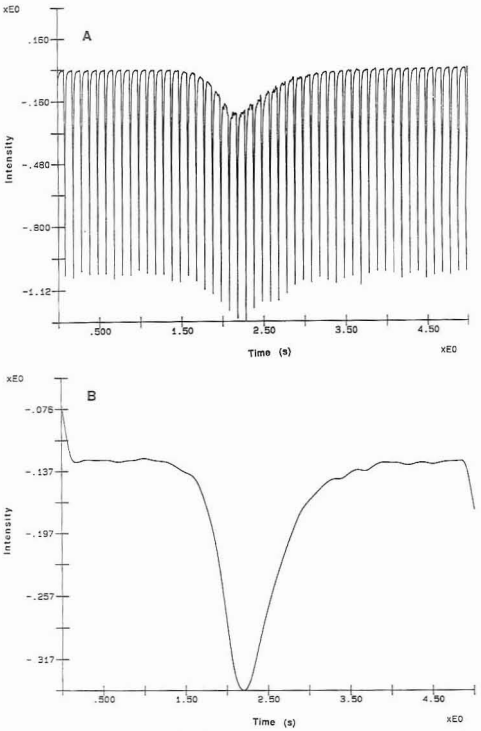

Figure 2. (A) Raw data collected with the photomultiplier tube showing the emission of the laser superimposed on the furnace radiation. (B) Photomultiplier data corrected by filtering out the 10-Hz emission of the laser using Fourier transformation.

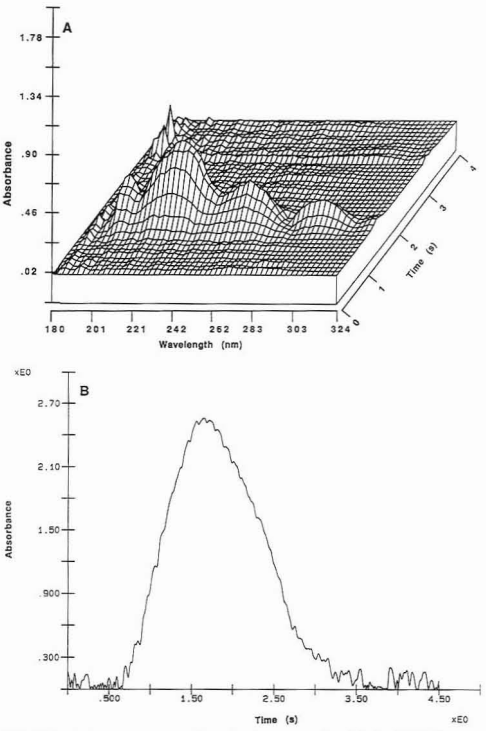

Figure 3. Plot of the absorption of a 5-μg sample of NaI. (A) Molecular absorption as a function of time and wavelength for NaI. (B) Atomic absorption of Na collected at 589 nm simultaneously with (A).

correct spectra of the transient gas-phase species, both atomic (B) and molecular (A), present in the graphite furnace heating cycle were being obtained. From Figure 3 molecular sodium iodide can be seen appearing and disappearing concurrently with atomic sodium. This indicates that the atomic sodium observed is due to the dissociation of gas-phase NaI molecules.

All studies were performed using both an unlined tubular graphite furnace and fully tantalum-lined graphite furnace. The use of a tantalum lining did not appear to significantly alter the gas-phase species observed as had been noted by other researchers.[28,29] L'vov et al. noted a difference in the shape of signals observed in analyte vaporization from graphite and tantalum platforms. Their studies showed a signal decay rate for the Ta platform to be several times faster than for the graphite platform. The data collected from lined and unlined tubes is due mostly to the difference in the heating rates of the two tubes. The tantalum-lined furnaces in our studies did exhibit larger atomic and molecular absorption signals than the unlined furnaces using the same amount of analyte. This increase in signal intensity could be due to the decrease in furnace cross-sectional area caused by the addition of the tantalum liner.[30] An advantage in using the tantalum lining might therefore be in enhancing the detection of elements, including those that vaporize well from graphite surfaces. This has been pointed out previously by L'vov and co-workers.[29]

Copper. Studies performed by Wang et al. indicate that copper oxide molecules are produced prior to atomic copper in the atomization cycle of aqueous solutions of $Cu(NO_3)_2$.[7] The reaction mechanism suggested by their studies of the copper atomization cycle is

$$Cu(NO_3)_2(s) \rightarrow CuO(ads) \rightarrow Cu(ads) \rightarrow Cu(g)$$

It was also suggested that at higher concentrations than those used in their studies a Cu dimer could possibly form in the gas phase though their system did not allow for such an interaction of the gas-phase copper. In monitoring the atomization of copper using mass spectrometry, Wang et al. observed a CuO^+ peak early in time (about 700 K).[7] Coincident with that peak were signals from NO_2^+ and O_2^+ which suggested that the $Cu(NO_3)_2$ being used was decomposing at this temperature, releasing the oxide. Their system was unlike the tube-type graphite furnace atomizers, so gas-phase collisions and readsorption of gasses onto the graphite surface were minimal. Their studies indicate that the Cu was adsorbed on the graphite rather than present as a copper carbide since no CuC^+ or Cu_2C above noise level was found. Cu_2^+ and Cu_2O^+ were observed early in time with nearly identical peak shapes and coincident appearance times, suggesting that they originated from the same source. Several papers have supported the reduction of the oxide to elemental

(28) Zatka, V. J. *Anal. Chem.* **1978**, *50*, 538–541.
(29) L'vov, B. V.; Nikolaev, V. G.; Novichikhin, A. V.; Polzik, L. K. *Spectrochim. Acta* **1988**, *43B*, 1141–1146.
(30) Fonseca, R. W.; Güell, O. A.; Holcombe, J. A. *Spectrochim. Acta* **1990**, *45B*, 1257–1264.

copper prior to atomization.[31-32] Mass spectrometric studies suggest that surface-adsorbed copper is the precursor to atomic Cu in the gas phase.[10] Since CuO, NO_2, and O_2 have bands which appear in the areas being monitored, our system should have detected them had they been present in the gas phase.[33] However, no molecular species were observed as being present in the gas phase prior to the appearance of atomic Cu. After atomic Cu had appeared and disappeared, some molecular absorption was noted in the higher wavelength region monitored.

Figure 4 shows the spectra collected during the atomization of $Cu(NO_3)_2$. In Figure 4A the molecular absorption spectrum collected in the lower wavelength ranges in an unlined furnace is shown with the atomic absorption profiles for the unlined (solid line) and a tantalum-lined (dotted line) furnace shown in Figure 4B. The molecular spectrum obtained for copper was relatively clean in the lower wavelength regions, showing no observable molecular absorption. A weak atomic absorption line appeared in the molecular spectrum only when $Cu(NO_3)_2$ crystals were used as the sample. No molecular absorption was noted in this region regardless of the sample sizes used. CuO has band maxima between 400 and 500 nm.[33] In Figure 4C the spectrum collected in this wavelength range can be seen. Strong molecular species do appear in this area but not until around 1400 K. It is unlikely that this species is the CuO observed by Wang et al. because of its high appearance temperature and the fact that it occurs after atomic copper has disappeared. These molecular species appear immediately after the atomic absorption signal for Cu has disappeared. These species were also observed in a Ta-lined furnace and appeared after the atomic species disappeared, as had been noted for the tantalum-unlined system.

Katskov detected the presence of Cu_2C_2 during the atomization of copper from a graphite substrate using a colorimetric technique for the detection of acetylides.[34] The carbide, Cu_2C_2, is only stable at high temperatures and instantaneously decomposes in air.[34] This species arises in the gas phase, according to Katskov's research, and appears at 1400 K or greater temperatures. The absorption at higher wavelengths suggests that this species may be present; yet, it could not be confirmed by another source. Weak copper molecular absorption systems may be present at the lower wavelengths. However, no molecular absorption above background level was noted.

A persistent interference around 464 nm appears throughout the studies carried out in the higher wavelength range, as can be seen in Figure 4C. This spectrum was collected in a furnace which had been precleaned and had had no contact with any other analyte. Furthermore, the concentration of analytes required for them to be seen in these spectra is quite high, around 1000 mg/L, and a contaminant of this magnitude is unlikely to be present in the sample. This band was found to correspond to an emission maximum on the plasma emission profile, as seen in Figure 5. It is the fluctuations in the plasma intensity over this region that are responsible for this absorption artifact at 464 nm.

Lead. Several researchers have reported the appearance of PbO early in time in relation to that of Pb when the thermal desorption of $Pb(NO_3)_2$ is monitored using mass spectrometry.[8,11,13] Sedykh et al. monitored this process optically and reported a second molecular species, in addition to the PbO they observed, which they attributed to Pb_2.[3] Their assignment of this species was confirmed by Huber and Herzberg.[3,35] This second species which they observed appeared coincident with atomic Pb in their studies.[3] In investigating the $Pb(NO_3)_2$ vaporization mechanism, Bass and Holcombe found evidence that $Pb(NO_3)_2$ decomposes at 550 K to form a surface-bound PbO.[11] This PbO was subsequently reduced to form atomic Pb.[8,11]

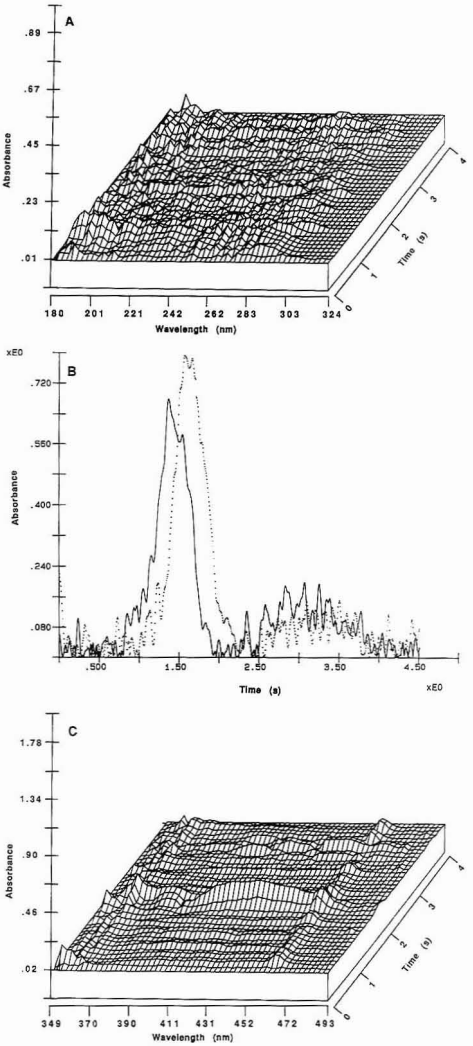

Figure 4. Plots of the absorption of a 5-μg sample of $Cu(NO_3)_2$. (A) Molecular absorption as a function of time and wavelength for $Cu(NO_3)_2$ between 180 and 324 nm. (B) Atomic absorption profiles for Cu collected at 324 nm from an unlined (solid line) and a tantalum-lined (dotted line) furnace. The solid line is the atomic absorption spectrum collected simultaneous with (A). (C) Molecular absorption as a function of time and wavelength for $Cu(NO_3)_2$ between 349 and 493 nm.

(31) Sturgeon, R. E.; Chakrabarti, C. L.; Langford, C. H. *Anal. Chem.* **1976**, *48*, 1792–1807.
(32) Smets, B. *Spectrochim. Acta, Part B* **1980**, *35B*, 33–42.
(33) Pearse, R. W. B.; Gaydon, A. G. *The Identification of Molecular Spectra*, 3rd ed.; John Wiley and Sons Inc.: New York, 1963.
(34) Katskov, D. A.; Grinshtein, I. L. *Zh. Prikl. Spektrosk.* **1981**, *36*, 181–185.
(35) Huber, K. P.; Herzberg, G. *Molecular Spectra and Molecular Structure-Constants of Diatomic Molecules*; Van Nostrand Reinhold Company: New York, 1979.

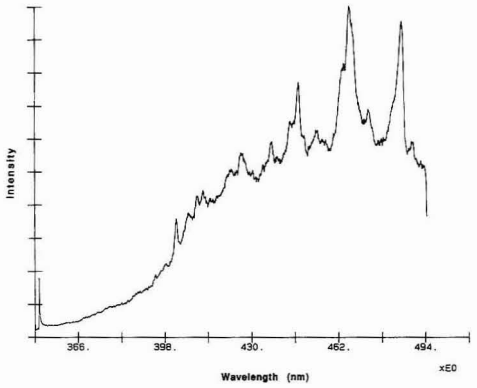

Figure 5. Plot of the laser emission profile used as the continuum source for collecting spectra in higher wavelength regions.

It is well-known that in GFAAS Pb is not lost as PbO during nitrate decomposition because the lead recondenses on the graphite surface as a result of multiple surface collisions with the wall. Bass and Holcombe's mass spectrometric data contained two peaks for Pb^+ in the vacuum vaporization of $Pb(NO_3)_2$.[8] It is hypothesized that the first peak was produced by the shattering of the nitrate salt deposited on the graphite substrate, and the second peak, from the reduction of PbO which was adsorbed on the graphite surface.[8] PbO was further believed to recondense on the graphite surface during the nitrate decomposition and then be reduced to form Pb(g) around 800 K.[8] Since their studies did not detect Pb_2^+, it is possible that Pb_2 could be produced in a gas-phase reaction since it has not been detected in studies which minimize gas-phase reactions but does appear in studies which are performed at atmospheric pressure.

Our lead studies yielded very interesting results. As seen in Figure 6A, early in the atomization cycle of lead, four band heads were observed. This species was present in both lined and unlined furnaces and with ashing at 800 K or without ashing. These band heads appear around 194, 204, 214, and 225 nm. This species appears at about 1.3 s in the unlined furnaces and around 1.5 s in the tantalum-lined furnaces, as seen in Figure 7A,B, respectively. This quartet disappears at the same time for both the unlined and lined furnaces, around 2.1 s. As shown in Figure 7C, no atomic absorption is apparent at this time and does not appear until 2.3 s into the atomization cycle. Around 2.3 s into the atomization cycle of $Pb(NO_3)_2$, Pb atomic absorption lines are prominent in their appearance (Figures 6B and 7A,B). A second molecular species was observed to appear concurrently with the atomic Pb lines.

The molecular spectra in Figure 7A,B show the evolution of a molecular species prior to the appearance of the atomic species and a subsequent molecular species which appears with the atomic species. The first molecular species appears early in time in the wavelength range given by Herzberg and monitored by Sedykh and Vago for PbO.[3,4,35,36] The absorption observed for the earlier molecular species in our studies was not coincident with the atomic absorption signals which were collected simultaneously (Figure 7C). All of this indicates that this species is PbO.

We do not believe that the quartet band observed early in the atomization cycle for $Pb(NO_3)_2$ belongs to NO molecules,

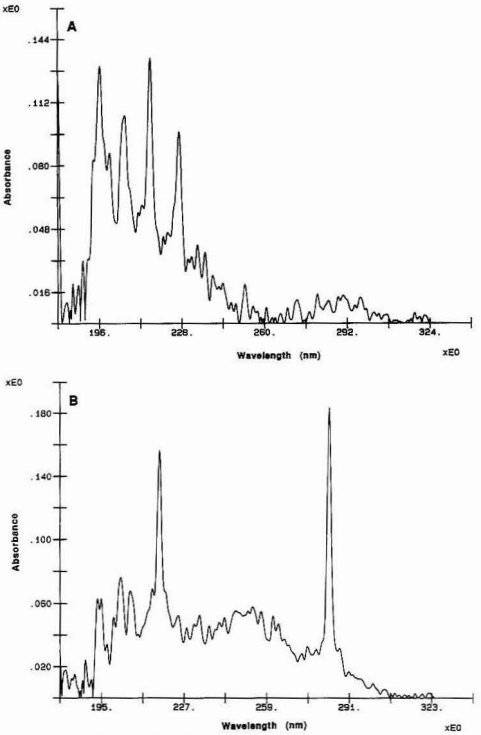

Figure 6. (A) Quartet band observed for a 5-μg sample of $Pb(NO_3)_2$ at 900 K into the heating cycle. The band heads appear at 194, 204, 214, and 225 nm, respectively. (B) Second molecular species observed during the atomization of $Pb(NO_3)_2$ with atomic absorption lines for Pb superimposed on it. This cross section is from around 1700 K into the atomization cycle of $Pb(NO_3)_2$. The two atomic lead lines appear at 217 and 283 nm.

as suggested by L'vov et al.[37] This is because it is absent in the atomization cycles of the other nitrate salts sampled and because PbO has been detected at this time and temperature by mass spectrometric and emission studies performed by other researchers.[11,13,36]

The second molecular species arises concurrently with the lead atomic absorption lines and could be due to the formation of Pb_2. This species observed coincides with the wavelength range observed by others for Pb_2 and could be the product of gas-phase reactions within the graphite furnace which produce the lead dimer.[3,35] This molecular species appears when the atomic lead appears and disappears when the atomic lead disappears from the gas phase, suggesting more strongly that this species might indeed be Pb_2 and be the result of a gas-phase reaction of the lead.

The only difference noted when the atomizations of $Pb(NO_3)_2$ from lined and unlined furnaces are compared appears to be that the tantalum lining causes the appearance of molecular and atomic species to shift to later times. Also, the absorbances noted in the tantalum-lined furnaces appear to be larger than those for unlined furnaces. The atomization mechanism for $Pb(NO_3)_2$ appears to be the same whether a tantalum lining is used in the furnace or not. The observations presented thus far indicate the following mechanism for the atomization of lead from a graphite substrate. This mech-

(36) Sturgeon, R. E.; Willie, S. N. *J. Anal. At. Spectrom.* **1992**, *7*, 339–342.

(37) L'vov, B. V.; Ryabchuk, G. N. *Zh. Prikl. Spektrosk.* **1980**, *33*, 1292.

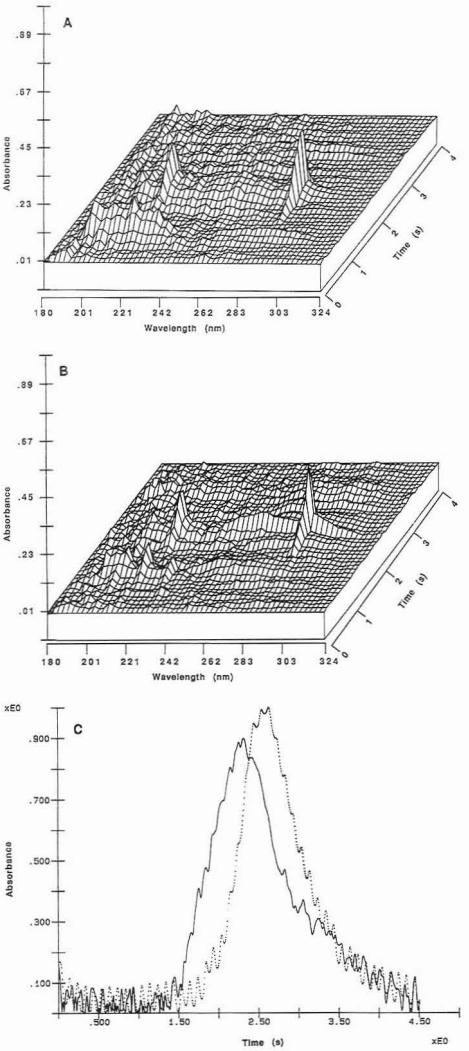

Figure 7. Plots of the absorption of a 5-μg sample of $Pb(NO_3)_2$ with and without a Ta lining in the furnace showing a molecular species arising around 900 K with band heads at 194, 204, 214, and 225 nm. A second molecular species appears coincident with two atomic lead lines. The atomic lead lines are at 217 and 283 nm. (A) Molecular absorption as a function of time and wavelength for $Pb(NO_3)_2$ in an unlined furnace. (B) Molecular absorption of $Pb(NO_3)_2$ as a function of time and wavelength in a completely Ta-lined furnace. (C) Atomic absorption signals of Pb collected at 217 nm simultaneously with (A) (solid line) and (B) (dotted line).

anism is one which has been suggested previously by other researchers:[8,11,13]

$$Pb(NO_3)_2(s) \rightarrow PbO(ads), PbO(g) \rightarrow Pb(ads) \rightarrow Pb(g) \rightarrow Pb_2(g)$$

Aluminum. In studying the atomization mechanism of aluminum, L'vov and co-workers observed a band maxima at 255 nm and a 233-nm band minimum (between 214- and 255-nm bands) which were not present when samples were vaporized from a Ta-foil-lined surface. They assigned the band that appeared around 255 nm to absorption by Al_2C_2 but did not confirm the absorbance band they observed with another source.[38] L'vov et al. explain spike formation in absorption signals, from the slow vaporization of Al, as gas-phase reductions of oxides by carbides (ROC).[39] They support this hypothesis by the absence of such spikes in experiments performed with tantalum linings. The atomization mechanism proposed by these researchers is[39]

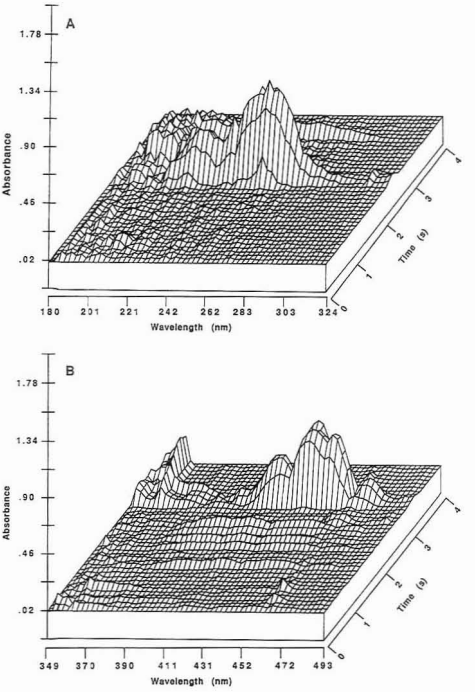

Figure 8. Plots of the absorption of a 5-μg sample of $Al(NO_3)_3$. (A) Molecular absorption as a function of time and wavelength for $Al(NO_3)_3$ between 180 and 324 nm. Atomic aluminum lines appear alone and superimposed on the molecular species at 237, 256, and 309 nm. (B) Molecular absorption as a function of time and wavelength for $Al(NO_3)_3$ between 349 and 493 nm.

$$Al(g) + 2C(s) \rightarrow AlC_2(g)$$

$$1.5AlC_2(g) + Al_2O_3(s) \rightarrow 3.5Al(g) \rightarrow 3CO(g)$$

The observations of Holcombe et al. using mass spectrometry did not support such a mechanism.[6] According to their mass spectral data, the assumptions and experimental results used indicated the possibility of ROC involvement but were insufficient to prove the mechanism. In their studies atomization was performed in vacuum (5×10^{-7} Pa) using aluminum nitrate samples. They found that the greater abundance of an aluminum monocarbide appeared prior to atomization and was the more abundant species present when high heating rates were used. Less intense signals from Al_2C^+ were

(38) L'vov, B. V.; Romanova, N. P.; Polzik, L. K. *Spectrochim. Acta, Part B* **1991**, *46B*, 1001–1008.
(39) L'vov, B. V.; Polzik, L. K.; Romanova, N. P.; Yuzefovskii, A. I. *J. Anal. At. Spectrom.* **1990**, *5*, 163–169.

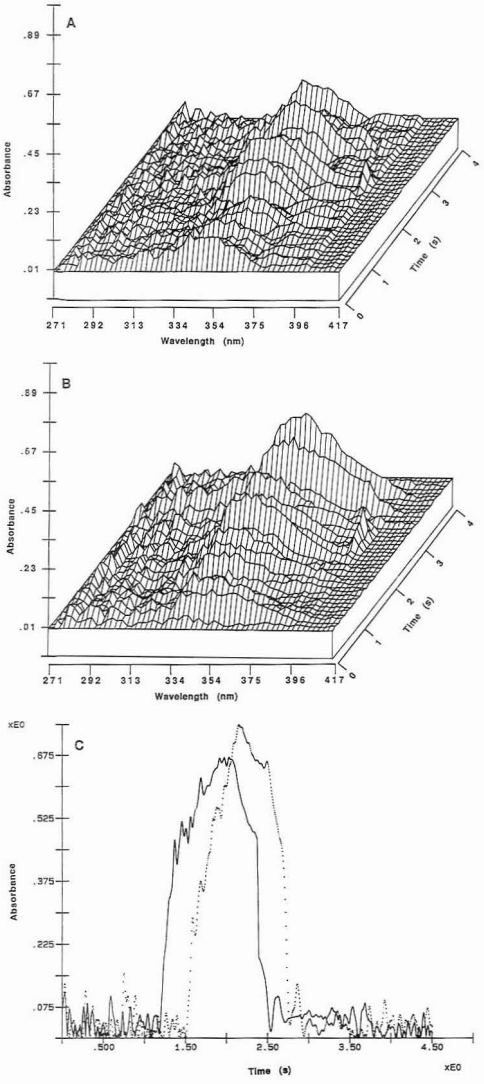

Figure 9. Plots of the absorption of a 5-μg sample of $Al(NO_3)_3$ with and without a Ta lining in the furnace. Atomic aluminum lines at 394.5 and 396 nm appear as one peak. (A) Molecular absorption as a function of time and wavelength for $Al(NO_3)_3$ in an unlined furnace. (B) Molecular absorption of $Al(NO_3)_3$ as a function of time and wavelength in a completely Ta-lined furnace. (C) Atomic absorption profiles of Al collected simultaneously with (A) (solid line) and (B) (dotted line).

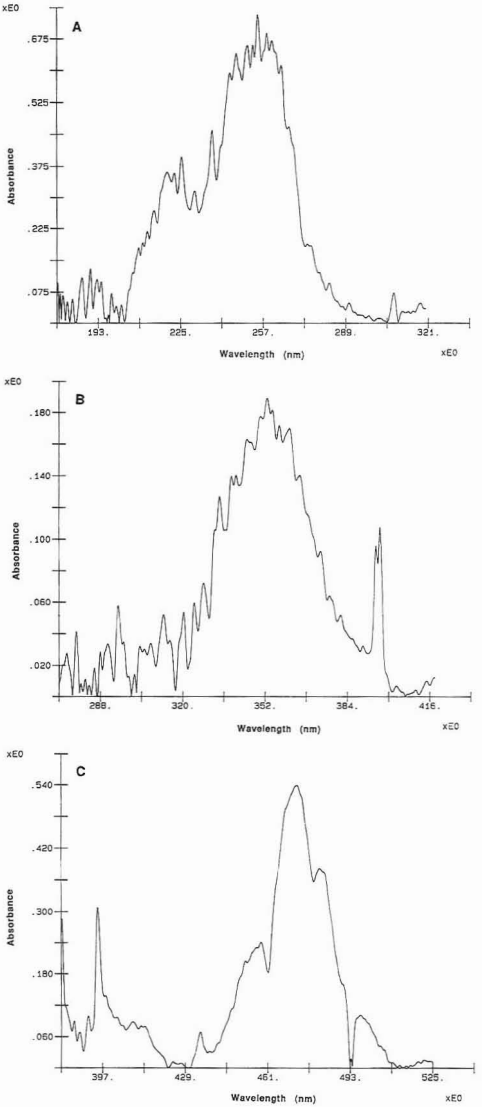

Figure 10. Cross sections from each of the wavelength ranges monitored for the atomization of a 5-μg sample of $Al(NO_3)_3$ taken at the same point in time, around 2500 K into the atomization cycle of the sample. (A) Cross section between 180 and 337 nm. An atomic Al line at 309 nm can be seen coincident with a much larger molecular absorption. (B) Cross section between 272 and 432 nm. Atomic aluminum lines at 394.5 and 396 nm appear as a doublet. (C) Cross section between 381 and 541 nm. Atomic aluminum lines at 394.5 and 396 nm appear again, but the line at 394.5 nm has diminished in size because of its placement on the photodiode array detector.

observed in conicidence with the free Al peak intensity near 2600 K. Holcombe et al. observed a weak $Al_2C_2^+$ mass spectrometric signal that was about 3 orders of magnitude smaller than that for Al when both species were ionized.[6] Intense Al_2 and Al_2O signals were observed coincident with free Al. Their studies indicate that ionizer-induced fragmentation of Al_2O was not responsible for the Al_2 signal, since a strong dimer signal occurred even when the ionization electron energy was reduced to above the oxides' appearance potential. Species absent during the vaporization in their studies include AlC, Al_2O_2, AlO, and AlO_2.[6]

Our results show molecular absorption by multiple species when monitoring the atomization of $Al(NO_3)_3$, as seen in Figures 8 and 9. Aluminum atomic absorption lines at 237, 256, and 309 nm appear in the molecular spectrum around 2700 K, as can be seen in the cross sections of each wavelength area studied in Figure 10A–C. Similar spectra were collected for the atomization of aluminum from a tantalum-unlined and completely tantalum-lined furnace (Figure 9A,B). The

difference in the spectra collected from the unlined furnace and the lined furnace appears to be the same difference observed for lead. The atomic and molecular species in the lined furnace appear at later times than those in the unlined furnace. This difference is easier to see when the atomic absorption spectra in Figure 9C are compared. The atomic absorption observed for aluminum in an unlined furnace (solid line) appears earlier and gives a lower absorption signal than the same amount of analyte in a tantalum-lined furnace (dotted line). The atomic absorption lines prominent in the molecular spectrum appear around 2200 K and disappear around 2700 K.

The aluminum lines observed appeared by themselves and superimposed on molecular species. Multiple aluminum atomic absorption lines were detected; from Figure 8A peaks around 237, 256, and 309 nm can be seen. All of these peaks appeared in the same temperature range. All atomic absorption lines in the molecular spectrum appeared at the same time and disappeared at the same time.

Our studies suggest that, more or less, the same molecular species are present (i.e. the same mechanism occurs) with and without a tantalum lining. The only difference between the absorption profiles shown in Figure 9 is that the tantalum-lined furnace appears to lag the atomization from the unlined furnace. The difference in atomization cycles could be explained by the difference in heating rates between the graphite furnace and the fully tantalum-lined graphite furnace.

Our studies show absorption by several molecular species, which are likely oxides in Figures 7 and 8. Because of the similarity in appearance temperatures and the overlap of wavelengths, we have not been able to identify them. The strong molecular species which appear in the lower wavelength range has been attributed to Al_2C_2 by L'vov et al. and Tittarelli et al.[38-40] This assignment is made because the species they saw in this area during the atomization cycle of $Al(NO_3)_3$ from a graphite furnace was not observed by them with atomization from a tantalum-lined furnace. Our results did not indicate this. The species we observed in the area monitored by other researchers for Al_2C_2 did yield a strong molecular absorption.[38-40] This species appeared when an unlined furnace or a tantalum-lined furnace was used, leading us to believe what we were observing was not a carbide. Huber and Herzberg and Pearce and Gaydon show that AlO absorbs in this area.[33,35] Therefore, a more probable mechanism for the atomization of aluminum nitrate in an electrothermal atomizer appears to be

$$Al(NO_3)_3 \rightarrow Al_{x-n}O_{y-m}(ads), Al_{x-n}O_{y-m}(g) \rightarrow Al(ads), Al(g)$$

where n and m can take any integer value.

CONCLUSIONS

The atomization cycle of copper was not followed effectively with this system. The species expected to be seen were not observed. The copper was also different than the lead and aluminum examined in that no atomic absorption lines could be seen in its molecular spectrum without using copious amounts of sample. The lead samples show strong absorption by two molecular species; the first appears to be PbO, and the second, Pb_2. The identity of the molecular species which appeared in the lead studies was confirmed by literature values. In monitoring aluminum atomization cycles, our results show many molecular species appearing in both a lined and unlined furnace which we have not yet identified. However, since several different species appear which are dynamically changing, this indicates that there are extensive gas-phase reactions occurring within the graphite furnace. Aluminum atomic absorption lines could be seen coincident with molecular species; however, molecular species were present prior to and after the appearance of the aluminum. Clearly, the atomization mechanism for aluminum is more complicated than those of the lead and copper nitrates examined and requires further study.

Received for review April 1, 1992. Accepted August 14, 1992.

Registry No. PbO, 1317-36-8; Pb_2, 12596-92-8; AlO, 14457-64-8; aluminum, 7429-90-5; copper, 7440-50-8; lead, 7439-92-1; lead nitrate, 10099-74-8; copper nitrate, 3251-23-8; aluminum nitrate, 13473-90-0.

(40) Tittarelli, P.; Biffi, C. *J. Anal. At. Spectrom.* **1992**, *7*, 409–415.

Axial Evolution of the Negative Glow in a Hollow Cathode Discharge

Robert B. Bartlow and Steven T. Griffin

Department of Electrical Engineering, Memphis State University, Memphis, Tennessee 38152

J. C. Williams*

Department of Chemistry, Memphis State University, Memphis, Tennessee 38152

The purpose of these studies was to examine the axial evolution of the negative glow in a hollow cathode discharge. The time-average negative glow profiles along the central axis of a hollow cathode were recorded for 81 pulse widths over the range of 5–25 μs in increments of 0.25 μs at a constant interpulse delay of 206.4 μs. Subsequent numerical processing yielded the instantaneous negative glow profile. The negative glow was viewed through a mesh-covered slot along the length of the hollow cathode. The negative flow profiles were imaged using a vidicon video camera. A PC-based frame grabber digitized the video images and stored them for subsequent processing.

INTRODUCTION

The hollow cathode discharge (HCD) is a significant excitation source for atomic emission spectroscopy. Although the hollow cathode effect was recognized in 1916 by Paschen,[1] its application as an emission source for the analysis of solution residues has been minimal at best. In the HCD, the sample is sputtered into the plasma where it is excited. The sputtering process for such samples is poorly understood; as a result, the precision has been unacceptable at the 10–30% range. On the other hand, sputtering as related to the development and operation of vacuum tubes was studied extensively and understood sufficiently for the development of these devices in the 1930s. The production of certain semiconductors also required the development of sputtering technology for their production. The required technology was developed under the pressure of the need and advantages of semiconductors over tube electronic devices. Such is the case for the HCD as an emission source. The role of sputtering in the analytical HCD must be understood if it is to realize its capabilities.

Recent work in this laboratory has focused on improving the HCD as a dc analytical source.[2-4] In these efforts, the analytical sample is typically sputtered from the hollow cathode within a second with the majority of the analytical signal occurring in the first few milliseconds. Advantages of operating the HCD in the pulsed mode have been recognized for some time, and analytically optimal parameters have been empirically determined for some hollow sizes.[5-7] Optimal pulse widths within a narrow range of 7–11 μs and an optimal pulse frequency of 5 kHz have been reported.[8] Pulses this short in duration may not allow the normal steady-state dc discharge to be established due to the inductive character of the discharge. Thus, proper application of a pulsed discharge to the analysis of solution residues requires a deeper understanding of the early evolution of the HCD for both the dc and pulsed modes.

Although the evolution of the negative glow in a hollow cathode discharge has been determined from the frontal view,[9,10] no such work examining the axial evolution of the negative glow in a hollow cathode discharge is known to the authors. In the standard deposition techniques for the micro-HCD the sample is deposited in the very bottom of the hollow cathode.[2-4] Based on oscillographs presented here, the discharge in the pulsed micro-HCD begins as a planar discharge on the unshielded face of the hollow cathode and subsequently evolves into the hollow. This is an axial motion whose exact nature and time of arrival at the sample is of significant analytical interest. Therefore, the efforts reported here concentrate on the axial evolution of the HCD in a time frame compatible with the previously determined analytically optimum pulse widths of 10's of microseconds. As with other temporal studies,[9] the axial evolution of the discharge inside the hollow was observed by monitoring optical emission signals. Thus, results should be directly comparable.

This experiment determined the spatial emission intensity along the major axis of the HCD versus time. This was accomplished by cutting an axial slot in the hollow cathode and covering it with a very fine metal mesh. This mesh prevented disturbance of the discharge by the slot but allowed a significantly attenuated optical signal to pass through. Time-averaged axial temporal profiles of the negative glow were recorded with an imaging system which consisted of a video camera, collecting optics, a frame grabber, and a PC for control and data processing. The slot was imaged from a distance with a narrow field of view so that only light directly behind the slot was viewed by the camera.

The discharge was pulsed with a fast current controlled switch recently described.[4] The length of the pulse is referred to here as t_{PW}. The period between pulses is referred to as t_{PD}. As shown in a section below this serves as an effective gate of period t_{PW} for the discharge emission. Thus, the imaging system recorded the emission intensity time integrated over the gate width t_{PW} at each point along the HCD axis. By recording incremental gate widths and numerically differentiating the results the time evolution of the discharge emission intensity at each point on the HCD was determined.

(1) Paschen, F. *Ann. Phys.* **1916**, *50*, 901.
(2) Ryu, J. Y.; Davis, R. L.; Williams, J. C.; Williams, J. C., Jr. *Appl. Spectrosc.* **1988**, *42*, 1379–1387.
(3) Chen, Fu-yih; Williams, J. C. *Anal. Chem.* **1990**, *62*, 489–495.
(4) Tseng, J. L.; Williams, J. C.; Bartlow, R. B.; Griffin, S. T.; Williams, J. C., Jr. *Anal. Chem.* **1991**, *63*, 1933–1942.
(5) Dawson, J. B.; Ellis, D. J. *Spectrochim. Acta* **1967**, *23A*, 565–569.
(6) Caroli, S. *Improved Hollow Cathode Lamps for Atomic Spectroscopy*; Ellis Horwood Ltd.: Chichester, 1985; pp 52–73.
(7) Borkowska-Burnecka, J., Zyrnicki, W. *Spectrosc. Lett.* **1987**, *20*, 795–803.
(8) Caroli, S. *Improved Hollow Cathode Lamps for Atomic Spectroscopy*; Ellis Horwood Ltd.: England, 1985; pp 63–65.
(9) Hebner, G. A.; Verdeyen, J. T. The Spatial and Temporal Evolution of the Glow in an RF Discharge. *IEEE Trans. Plasma Sci.* **1986**, *PS-14*, 132–136.
(10) De Jong, G. J.; Piepmeier, E. H. *Spectrochim. Acta* **1974**, *29B*, 159–177.

0003-2700/92/0364-2751$03.00/0

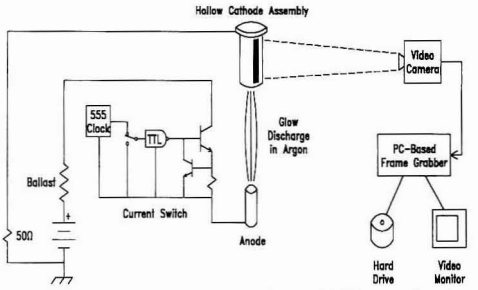

Figure 1. An overview of the apparatus used in this experiment.

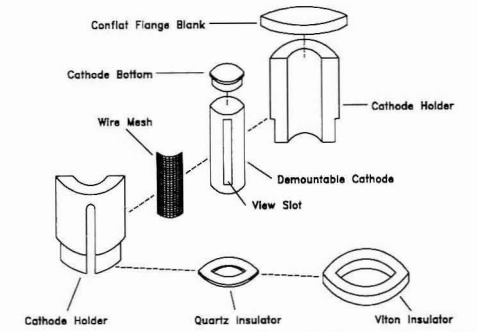

Figure 2. An exploded view of the hollow cathode assembly used in this experiment.

Since differentiation is a noise-enhancing process high signal-to-noise ratios were required and obtained. System linearity required for quantitative results is developed and demonstrated below.

EXPERIMENTAL SECTION

The initial experimental efforts concentrated on the construction and validation of the instrument, which was custom built using a mix of commercial and custom components.

A. Instrumentation Details. A schematic diagram of the experimental apparatus used to examine the evolution of the negative glow is shown in Figure 1. The hollow cathode and the anode were enclosed in a vacuum-tight enclosure consisting of a $^1/_4$-in.-o.d. borosilicate tube with the ends sealed by rotatable flanges ($2\ ^1/_8$-in. Conflat, 304 stainless steel) and Viton gaskets. The vacuum/gas system consisted of a two-stage vacuum pump capable of a minimum pressure of 0.1 Torr, a tank of zero-grade argon, and a needle valve to set the gas inflow rate. A gas filter (Millipore Wafer-Gard, Bedford MA) cleaned the gas coming from the tank. Pressure was measured with a thermocouple vacuum gauge (Varian Associates 871, Lexington MA) attached to a static port on the discharge chamber.

Hollow Cathode. Figure 2 depicts an exploded view of the hollow cathode assembly. The view slot permits an axial view of the negative glow inside the hollow cathode. The range of visibility extends from the base of the hollow to near the mouth of the hollow where it is blocked by the Viton insulator. The discharge was prevented from escaping through the view slot by a wire mesh (250 × 250 wires/in., 304 stainless steel, 36% open area) cover held between the demountable cathode and the cathode holder. The demountable cathode was a section of $^1/_2$-in.-o.d. tubing (304 stainless steel, 1.1-cm i.d.) with a slot milled along most of its length. This assembly was attached to the rotatable blank of the Conflat flange.

The insulators ensured that the discharge was confined to inside the hollow. The Viton insulator was press-fitted around the end of the cathode holder. It fit snugly against the borosilicate tube and formed a discharge barrier. The quartz insulator was held against the face of the cathode holder by radial pressure from the Viton insulator. This insulator prevents discharge to the cathode surface it covers. However, the diameter of the opening in the quartz is slightly larger than the hollow diameter, leaving a small band of planar cathode surface open to the discharge. The bottom surface of the hollow could be viewed directly through the slot. The hollow was 24 mm deep. However, the top 5 mm showing the cathode mouth was obscured by the Viton insulator.

Discharge Electronics. The two transistors and unlabeled resistor in Figure 1 symbolize a regulated current switch. The operation of this circuit has been described previously in detail.[4] It was shown there that the rise time of the resistive load current of 3 μs was 1 order of magnitude shorter than the approximately 30-μs rise time of a discharge load. The time constants of the exponential current decay observed at turn-off were 0.7 and 16 μs, respectively, for resistive and discharge loads. Therefore, the discharge rise time of this electrical construction is limited by the discharge characteristics and not the electronic behavior. The rise time and decay constant of the discharge dominate the spectral transient response such that speed limitations of the switch can be ignored. Hence, this switch is useful as a shutter in temporal evolution studies.

The dc power supply (Sorenson DCR600-.75B, Sorenson is a Division of Switchcraft, Chicago, IL) was set at 640 V. A ballast resistor (1 kΩ at 225 W) was used with a current-regulated switch to reduce the power dissipation of the main switch transistor. This further reduced temperature-induced regulated current drift. A 50-Ω shunt resistor from the cathode to ground was added to monitor the discharge current on an oscilloscope (Tektronix 7104). All high-voltage connections used RG-61/U coaxial cable and MHV-BNC connectors for noise suppression.

Video Camera. The image detector was a vidicon-based video camera. The time constant of the imaging tube, $1/a$, can be calculated from the third-field lag. A typical antimony sulfide (Sb_2S_3) vidicon has a third-field lag of 18%[11] which corresponds to a time constant of 86 ms. Since the length of one discharge cycle ($t_{PW} + t_{PD}$) in this project is no greater than 0.3 ms, this camera can serve as a time-integrating detector provided that a train of pulses ≫86 ms is observed. A handbook by Wolf and Zissis[12] is a good reference source for imaging devices of this sort.

Collecting Optics. The collecting optics consisted of a zoom lens (Sony by Tamron, TV Zoom Lens, f = 12.5–75 mm at f/1.8, f/1.8–16) mounted on the video camera body. The video camera was mounted such that the distance from the vidicon surface to center of the hollow cathode (92 cm) was equal to the minimum distance at which the hollow cathode was in focus at maximum zoom. The extent of the visible axial negative glow (19.1 mm) corresponded to approximately 105 pixels on the frame grabber or 0.18 mm/pixel. Pixel 0 was below the cathode bottom. Thus the cathode bottom corresponded to approximately pixel 3 and pixel 105 corresponded to a depth in the hollow of approximately 5 mm from the cathode mouth. The wire mesh had an interwire spacing of 0.10 mm. Thus the camera at maximum zoom exhibited no adverse interference effects from the mesh.

Frame Grabber. The video information from the camera was digitized by a PC-based frame grabber (Imaging Technology Inc. PCVision*plus*, Woburn MA) for storage and processing. The gain and offset settings of the video amplifier of the frame grabber were set to 0 (maximum) and 43, respectively. This allowed the entire dynamic range of the video camera to be within the dynamic range of the frame grabber with no offset.

Computer programs written in C (Microsoft Corp. v 5.1, Redmond WA) using run-time libraries purchased with the frame grabber (Imaging Technologies Inc. ITEX PC*plus*) assisted in the acquisition and processing of video data. Separate programs were written to run the frame grabber for general and serial data-taking, to combine a series (set) of images into a single image,

(11) *Electro-Optics Handbook*; Burle Industries: Lancaster, PA, 1974; pp 189–193.

(12) Wolfe, W. L.; Zissis, G. J. *The Infrared Handbook*; Office of Naval Research, Department of the Navy: Washington, DC, 1978; Chapters 12 and 13.

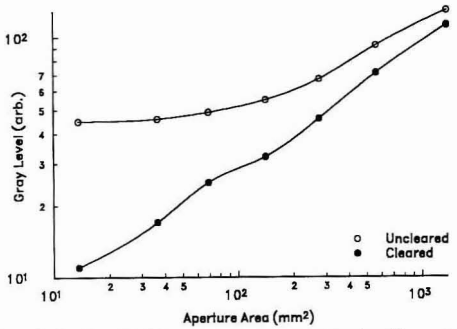

Figure 3. log–log plot of the aperture area versus gray level for a pulse width of 5 μs and an interpulse delay of 100 μs without and with previous clearing of the vidicon tube by a bright light source.

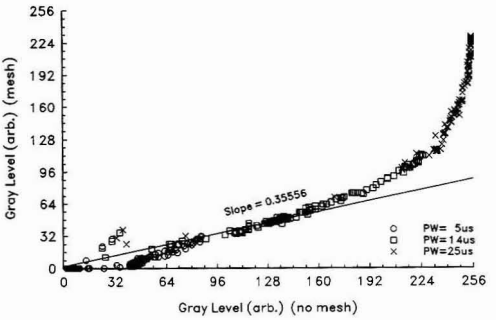

Figure 4. Nonlinearity of the imaging system response.

and to compensate and convert images to ASCII files for importation into a spreadsheet.

B. Instrument Validation. *Imaging System Operation.* Two difficulties were overcome to obtain quantitative data from the imaging system. The first encountered was a slight noise in the signal which caused the pixel values obtained from two successive frames to be subject to noise variation caused by the rf power radiated from a discharge. Since the pixel values for a series of frames are independent, the variance of a particular pixel value is reduced by a factor of n by averaging over n frames.[13,14] Sixteen frames were averaged for this work.

The second problem occurred as the imaging system initially exhibited a highly nonlinear transfer characteristic with poor dynamic range. It is believed that this problem resulted from electrons residing in trapped states in the bandgap of the photo conductor surface of the vidicon tube. These electrons are easily excited at low light levels producing excess conductivity at low illumination. This manifests itself as high dark signals. Investigation showed that this was temporarily resolved by exposing the vidicon tube surface to a bright light source just before taking data.

Figure 3 illustrates the effect of this technique. The vertical axis represents levels of gray as recorded by the image acquisition system. The horizontal axis is the vidicon aperture stop area. Since these data were taken with constant irradiance, the aperture stop area is directly proportional to the irradiance on the vidicon photo surface. Thus, the horizontal axis represents signal strength at the photo surface to within an arbitrary constant. By comparison of the two curves in Figure 3, it is seen that the linearity and dynamic range is improved by a lowering of the dark current. Bright light appears to empty the trapped states either by photoexcitation or thermal excitation. After a period of time (minutes) room temperature thermal excitation appears to refill the trapped states as the photo surface returns to its normal state. All data for this work were taken in the interval where the lower curve in Figure 3 was valid. In the actual experiment the clearing was accomplished by using the switch in Figure 1. It disconnects the current switch input from the clock output and connects it to ground. The resulting dc discharge provided the necessary light intensity without requiring changes to the clock settings.

Calibration of Imaging System. This imaging system was calibrated to yield intensity numbers that were quantitative to within a normalization constant. This required an instrument linear in its response over a known dynamic range with zero offset. A calibration test to verify this required a comparison of the instrument reading for a standard input and an input attenuated by a precisely known amount. In this test the readings for the attenuated input were plotted versus the readings for the standard input. A functional measurement system would exhibit a characteristic curve with a linear lower and central section. Such a system gives stochastic behavior at low signal/noise (i.e. low signal levels) and some type of nonlinear behavior at high signal levels. The linear calibration range of any instrument is defined as the region between stochastic low signal behavior and high signal nonlinearity. The difference between these limits defines dynamic range. The difference between the measured and actual slope within this range determines accuracy. The data scatter within this range determines precision.

Figure 4 depicts data for calibration of this imaging system. The horizontal axis is the pixel gray levels recorded for a pulsed discharge (with an interpulse delay of 136 μs) for three pulse widths (5 μs, 14.3 μs, and 25 μs). The vertical axis is the corresponding pixel gray values with a wire mesh attenuator blocking the view of the discharge. The wire mesh is a reliable absolute attenuator which reduces the intensity of the calibration source by a known value of 0.36. As previously calculated, the detailed structure of the mesh is too fine for resolution by the optics of the imaging system.

Although the linear region extends from 0 to 150 pixels on the abscissa, the small signal-to-noise ratio in the region from 0 to ~80 pixels (the stochastic region) limits the usefulness of these data. Within the central deterministic region, which extends from ~81 to ~150 pixels, the precision can approach the 1% limit set by quantization noise. The slope of the linear portion of the curve in Figure 4 is 0.3556 which agrees with the theoretical value to within 1%. Without the mesh in place the slope returns to one.

The points at the right of Figure 4 which deviate from the linear approximation are due to intentional manufacturer compression of the imaging system response for the purpose of increasing the dynamic range. The behavior of the instrument in this region is deterministic to within the specification of its components subsystems. Noise contributions dominate in the low signal portion at the left of Figure 4, and the standard deviation increases dramatically. Since data will not be utilized in this region, no statistical analysis was undertaken of it.

Preliminary data demonstrated the need to increase the calibrated dynamic range of the instrument. This could be accomplished by extending the linear deterministic portion of Figure 4 either into the high or low signal region. The deterministic behavior over the high region makes it possible to "decompress" this portion of the scale within the instrument software and extend the calibrated range. The extension into the stochastic low signal region can also be accomplished by the use standard statistical methods. The degree of extension required is slight, and therefore the faster approach of decompression was chosen.

This decompression was accomplished using a look-up table generated from Figure 4. The results of the decompression are depicted in Figure 5 where the linear dynamic range is extended. At the right of Figure 5 the high slope from Figure 4 has amplified the data scatter. To eliminate this from the instrument an artificial saturation point at a decompressed gray level value of 511 was instituted in the system software.

In summary, this instrument exhibits a precision of 1% within its central region. In the compensated gray ranges of 0–80 and

(13) Gonzalez, R. C.; Wintz, P. *Digital Image Processing*; Addison-Wesley: Reading, MA, 1987; pp 173–175.

(14) Papoulis, A. *Probability, Random Variables, and Stochastic Processes*; McGraw-Hill: New York, 1984; p 178.

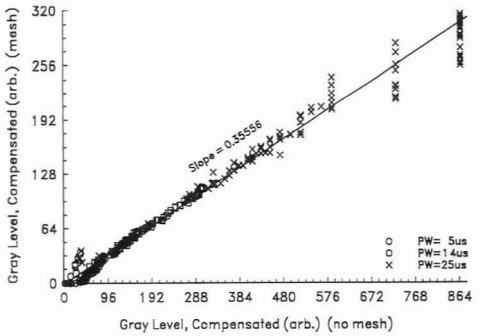

Figure 5. Linearity of the imaging system response after compensation.

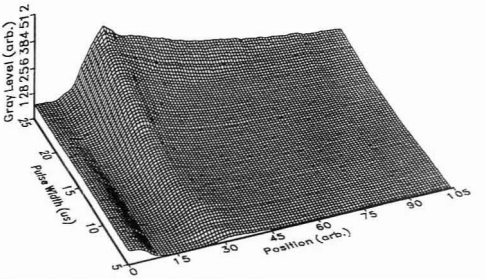

Figure 6. Time-integrated axial negative glow profiles for pulse widths of 5–25 μs with (0.25-μs intervals) a fixed interpulse delay of 206.4 μs on the position axis.

300–511 the instrument exhibits reduced precision. The relative accuracy was determined from the slope to be one percent. During the experimental runs the aperture stop on the vidicon optics was adjusted to optimize the collection of data in the calibrated central portion of the curve where a precision of 1% was expected.

RESULTS AND DISCUSSION

A. Data Acquisition. A series of preliminary experiments were run prior to recording data in order to determine appropriate operating conditions for pressure, electrical, and optical parameters.

Choice of Operating Pressure. Since the nonlinear nature of a discharge tends to amplify small parametric variations into significant variations in output, it is desirable to choose values for critical parameters that produce low sensitivity. Thus, an operating pressure which minimizes the effects of small pressure changes on the discharge is desired. The discharge voltage for two different discharge currents and four different pressures was measured while the diameter of the hollow cathode was held constant at 1.1 cm. A local extremum of zero sensitivity was found for both currents near a pressure of 1.5 Torr. The pressure–diameter product, pd, of the 1.5-mm microcavity used here in recent work is 1.65 Torr cm.[4] The same pd product gives approximately the same excitation conditions in the hollow.[15] An operating pressure of 1.5 Torr in the 1.1-cm-diameter hollow used in this report gives the same pd value. Therefore, 1.5 Torr was chosen as the operating pressure for this study.

Choice of Interpulse Delay and Pulse Width. The interpulse delay of 206.4 μs was chosen as the minimum value for which no distortion of the leading edge of the discharge current wave form was observed. Thus, each discharge pulse acts as an isolated event due to this long interpulse delay. The minimum pulse width used was 5 μs. The maximum pulse width (25 μs) allowed the discharge current to reach its steady-state value of 30 mA.

Argon Ion Glow versus Overall Negative Glow. An argon-ion line filter (Oriel 52640, Stratford CT, 488 nm ± 3 nm) was initially used to filter the discharge. The intent was to avoid inference from stray light and to limit the imaging system response to the spontaneous emission from argon ions. Since the spontaneous emission depends directly on upper state population density, the evolution of the argon ion density could be tracked. The argon ion density is believed to be a measure of the sample particle density in the negative glow.[16]

In preliminary work the output of the discharge with and without the filter was compared under a variety of conditions using an oscilloscope. The two signals were identical in temporal characteristics and response to parametric changes. The lone exception was that the filtered intensity was significantly less. In the experiment reported here difficulties were encountered due to the low transmittance of the argon ion line filter across the visible spectrum. The amount of light available was greatly reduced in the experimentation due to the low duty cycle of 2.4–11% used in the experiments. Given the similarity in the filtered and unfiltered emission it was decided to utilize the unfiltered version so that the dynamic range of the data was improved. Since the time signals were the same, the total intensity is as valid as the filtered intensity as a sample particle density indicator.

Procedure. Data were acquired after preliminary experiments and apparatus checks were completed. Axial negative glow profiles were recorded by the imaging system for 81 pulse widths over the 5–25-μs range in 0.25-μs intervals. The series of axial negative glow profile images was combined into a single image. The image was then converted to an ASCII file and compensated as previously described (see Figure 5). Figure 6 is a 3D plot made using Axum v1.0 (Seattle, WA) which depicts the time-integrated axial negative glow for an interpulse delay of 206.4 μs.

B. Data Analysis. To clearly demonstrate the results from these data it was necessary to recover the instantaneous intensity information from the raw data. This was accomplished via digital differentiation. The validity of the algorithm used is demonstrated in the Appendix. The time constant of the video camera and the decay constant of the discharge can have values which would invalidate the determination of the instantaneous negative glow by simple differencing. The mathematical analysis in the Appendix proves that the time constant of the video camera used and the decay constant of the discharge are such that simple differencing is in fact valid. The reader may avoid the Appendix by accepting that simple differencing of data from adjacent pulse widths yields the instantaneous intensity of the negative glow as given in eq 12.

Instantaneous Axial Negative Glow Profile. Figure 7 is a plot of the instantaneous axial negative glow derived using eq 12. As expected the numerical differentiation accentuated the residual noise. A convolution mask filter was implemented to attenuate this noise. The mask implemented the function given as eq 1. Note that the central point dominates the

$$f_{x,y} = \frac{1}{40}[f_{x-2,y} + f_{x+2,y} + f_{x,y-2} + f_{x,y+2} + 5(f_{x-1,y} + f_{x+1,y} + f_{x,y-1} + f_{x,y+1}) + 16f_{x,y}] \quad (1)$$

smoothing function of eq 1 to help retain the detail of the original data which is partially occluded by noise.

(15) Cobine, J. D. *Gaseous Conductors*; Dover Publication: New York, 1958; Chapters 7–8.
(16) Pillow, M. E. *Spectrochim. Acta* **1981**, *36B*, 821–843.

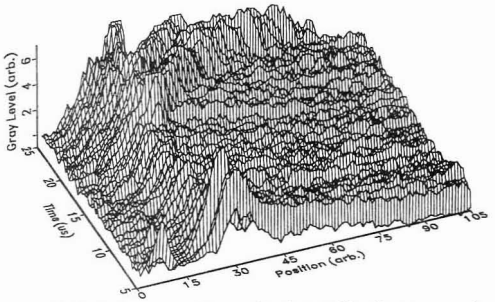

Figure 7. Instantaneous axial negative glow profile. Zero represents the cathode bottom on the position axis.

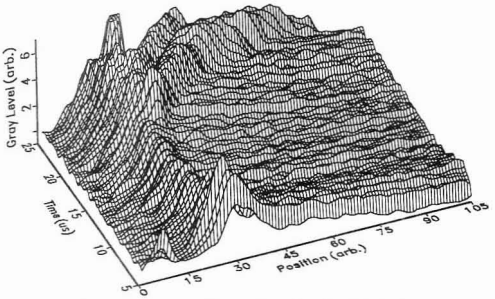

Figure 8. Instantaneous axial negative glow profile after smoothing. The cathode bottom is located approximately at pixel 3, and pixel 105 represents a point approximately 5 mm into the hollow which is 24 mm deep. The top 5 mm of the axial view of the hollow is obscured by the Viton insulator used to hole the quartz insulator.

Figure 8 is the result of smoothing Figure 7. Insight into the structure of Figure 8 is aided by representing the same data on a gray scale. Figure 9 is a 2D gray-scale representation of the smoothed instantaneous axial negative glow data depicted in Figure 8.

C. Validation. The validity of the data reduction techniques was checked by comparing the intensities of the processed images with visual observation. Visual observation of the discharge in operation confirmed the major salient features including the presence of the more intense region at the cathode base and the presence of striations in the hollow.

D. Planar Discharge. The axial view of the planar surface of the cathode at its mouth was obscured by the Viton insulator, and there was no port available for viewing the cathode mouth from the front. Thus, other evidence of the evolution of the discharge in this region was needed. The hollow cathode used in this report has the same pd product as the 1.5-mm-diameter mini hollow cathode[4] used in this laboratory for several years. Frontal observation of the discharge evolution at the 1.5-mm mini hollow cathode was used to characterize the early stages of the discharge which could not be seen from the axial view in the present HCD.

Figures 10–12 are front-view oscillographs of the 1.5-mm mini hollow cathode operated at 11 Torr which gives the same pd product as that of the hollow used here. The oscillographs are not of single pulses but are the integrated image of a relative long train of pulses. Figure 10 shows the current wave form with a rise time of ~ 1 μs which is characteristic of the electronic system when driving a resistive load with a 5-μs pulse. The top portion of Figure 11 shows the current wave form when the inductive HCD is driven with the same 5-μs pulse. Although two pulse forms are evident, a discontinuity or hump on the leading edge of the current pulse in

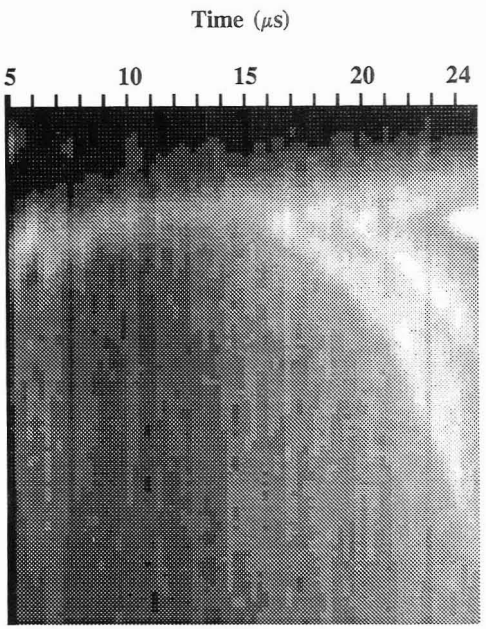

Figure 9. Gray scale plot of the instantaneous axial negative glow profile. The top of the figure is pixel 0 and the bottom is pixel 105. The bottom of the hollow appears just below the top of the figure. The bottom of the figure represents the gray scale for the location 5 mm deep in the hollow from the hollow mouth.

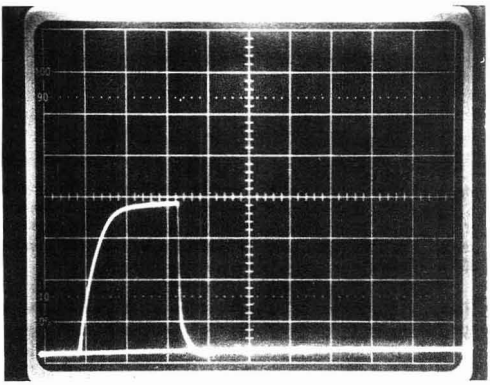

Figure 10. Oscillograph of the current wave form as a resistive load is driven with a 5-μs pulse with a repetition rate of 5 kHz. The vertical scale is 2 V/div. The horizontal scale is 2 μs/div.

Figure 10 can be seen clearly. The current wave forms of resistive and discharge loads are clearly different.

The bottom portion of Figure 11 gives the current wave form obtained from the discharge driven by the same 5-μs pulse when the hollow was replaced with a plane cathode. There was no hole drilled in the stainless steel rod used as the cathode. A current pulse ~ 2 μs wide occurs first then collapses into a much lower and relatively constant sustain current.

The upper portion of Figure 12 shows the current wave form of the discharge when driven with a 10-μs pulse and using a 1.5-mm Al hollow cathode. The leading edge of the current pulse is the same as observed for the 5-μs pulse.

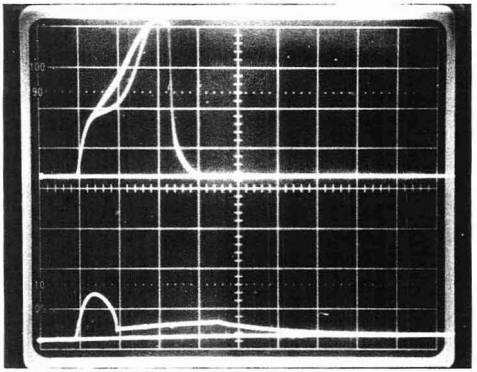

Figure 11. Oscillograph of the current wave forms as the discharge is driven by a 5-μs pulse with a repetition rate of 5 kHz. The vertical scale is 2 V/div. The horizontal scale is 2 μs/div. The upper half shows the current during the 5-μs discharge at a hollow cathode. The lower half shows the current when the discharge is conducted at a planar cathode.

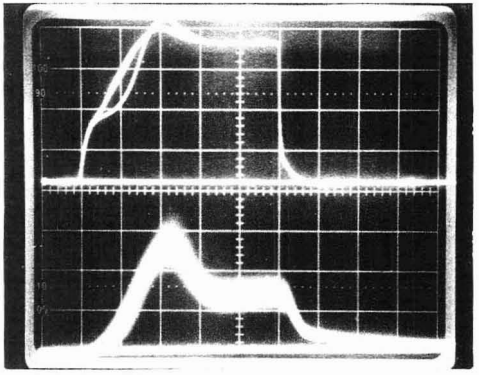

Figure 12. The upper half of the figure is an oscillograph of the current in an Al HCD as produced by a 10-μs discharge with a repetition rate of 5 kHz. The vertical scale is 2 V/div. The horizontal scale is 2 μs/div. The lower half shows the associated photocurrent from the 309.2 Al line.

However, the discharge current settles to a much lower value for the remainder of the pulse. The lower portion of Figure 12 shows the photocurrent for the emission profile of the Al 309.2-nm line. There is little photocurrent in the first 2 μs. In a manner similar to the current, the photocurrent peaks between 4 and 5 μs then collapses to a lower constant value for the remainder of the 10-μs pulse. Little light is seen during the 2 μs of the planar discharge.

CONCLUSIONS

Based on the data taken, a number of conclusions can be drawn regarding the early evolution of the HCD and its implications for pulsed analytical applications.

The first of these conclusions regards the presence of transient ionization waves early in the negative glow formation. These are indicated by the traveling intensity waves seen in Figures 7–9. This phenomena is somewhat unexpected since the dc negative glow is without structure. Ionization waves have been observed in the positive column of planar glow discharges. Such waves in the negative glow have not been reported in the literature nor have they been seen here previously. Since the negative glow is normally a constant voltage region, classic positive column style striations are not expected. Therefore the presence of the excitation waves in the negative glow transient is significant. For more information Garscadden provides an effective summary of prior positive column efforts which examine standing and traveling ionization waves using streak photography and synchronous shuttering.[17]

The second conclusion is that the early evolution of the HCD occurs in a number of distinct stages. Combining information from Figures 8, 11, and 12 reveals the very early stages of the evolution of the discharge in the hollow cathode. Figure 11 shows that the discharge starts as a planar discharge near the open end of the hollow cathode. This planar discharge lasts for approximately 2 μs. The discharge then moves rapidly down the hollow and arrives at the hollow bottom approximately 6 μs after discharge initiation. The latter stage of this early peak at the hollow bottom is clearly evident in Figure 8. Shortly after 6 μs, the discharge moves quickly approximately 6 mm (33 pixel units) up the hollow from the bottom. From this position 6 mm from the hollow bottom, the discharge moves slowly toward the base until the region of negative glow reaches a temporary equilibrium position after about 10 μs from discharge initiation. For the next 4 μs (10–14 μs), the glow along the axis spreads axially in both directions with a net motion towards the open end of the hollow and toward the anode. At 16.5 μs, an ionization "spike" is evident. This spike is followed by bidirectionally traveling ionization waves. The anode-bound ionization wave travels at an estimated (nonconstant) velocity of 700–900 m/s. Limited cathode-bound wave motion is also evident. Additional spikes occur at 20 and 24 μs. It is expected that this transient is, after sufficient time, damped to the uniform dc values previously demonstrated both in the literature and at this site.

The third set of implications pertains to the use of pulsed HCD for analytical purposes. Prior work (referred to in the Introduction) indicates that the range of optimal pulse widths is 7–11 μs. Examining Figure 9 determines that this pulse width range is large enough to allow the negative glow to approach the base of the hollow and short enough to prevent ionization waves from forming. The lack of negative glow at the base of the hollow for very short pulses (<6 μs) implies that little sample excitation will occur in the HCD source for extremely short pulses. Pulses much longer than ~ 11 μs will likely demonstrate reduced precision as a result of the chaotic nature of the ionization waves. Thus it is believed that pulsed HCD should be operated within the range of pulse widths from 7 to 11 μs. Increasing pulse widths beyond this range may lead to reduced precision long before self absorption becomes severe.

ACKNOWLEDGMENT

The authors would like to extend their personal thanks to John Coltart for machining the discharge enclosure. This work supported by The Memphis State University Foundation, the National Institutes of Health, and the Departments of Chemistry and Electrical Engineering of Memphis State University.

APPENDIX

Differentiation of Time-Integrated Data To Yield Instantaneous Data. Since the imaging system serves as

(17) Garscadden, A. Ionization Waves in Glow Discharges. In *Gaseous Electronics Vol. I*; Hirsh, M. N., Oskam, H. T., Eds.; Academic Press: New York, 1978; pp 65–108.

an integrating detector it was necessary to develop software algorithms to recover the spatial intensity information from the raw data. An analysis of the imaging system's signal processing characteristics was undertaken to determine the required software processing and to estimate any contribution the software made to the total error.

The negative glow $f(t)$ at a particular pixel and integrated along the field-of-view at a particular time $t = t_{PW}$ (referred to, herein, as the glow function) is related to the integral of the glow function by the identity stated as eq 2.[18]

$$f(t_{PW}) \equiv \frac{d}{dt_{PW}}\left[\int_0^{t_{PW}} f(t)\,dt\right] \tag{2}$$

The output of the video camera when averaged over N cycles is described by eq 3.

$$F(t) = k\sum_{n=-n/2}^{N/2}\left[\int_{(n-1)t}^{nt} f(t)e^{-a(nt-1)}\,dt\right] \tag{3}$$

$$F(\tau) = kNe^{-a\tau}\int_0^{\tau} f(t)e^{-at}\,dt$$

Where a, the decay constant of the video camera detector, is on the order of $^1/_{86}$ ms^{-1} as calculated from the third-field lag and $\tau = t_{PW} + t_{PD}$ is the period of the signal.

An additional factor to consider is the behavior of the emission after the discharge pulse. It is characterized by an exponential decay with a decay constant b (on the order of $^1/_{10}$ ns^{-1}) acting upon the value of the glow function at $t = t_{PW}$. This allows the integrated signal $F(t_{PW})$ measured at $t = t_{PW}$ to be calculated in eq 4.

$$F(t_{PW}) = kNe^{-a\tau}\left[\int_0^{t_{PW}} f(t)e^{at}\,dt + \int_{t_{PW}}^{\tau} f(t_{PW})e^{-b(t-t_{PW})}e^{at}\,dt\right] \tag{4}$$

$$F(t_{PW}) = kNe^{-a\tau}\left[\int_0^{t_{PW}} f(t)e^{at}\,dt + e^{at_{PW}}\int_0^{t_{PW}} f(t_{PW})e^{-(b-a)t}\,dt\right] \tag{4a}$$

Since $(b - a)t_{PD}$ is greater than 8.4, the approximation in eq 5 is obtained after integration. Each approximation in this derivation yields no more than 1% error individually.

$$F(t_{PW}) \approx kNe^{-a\tau}\left[\int_0^{t_{PW}} f(t)e^{at}\,dt + e^{at_{PW}}\frac{f(t_{PW})}{(b-a)}\right] \tag{5}$$

Further approximations where a/b and at_{PW} are less than 0.01 yield eq 6.

$$F(t_{PW}) \approx kNe^{-a\tau}\left[\int_0^{t_{PW}} f(t)\,dt + \frac{f(t_{PW})}{b}\right] \tag{6}$$

(18) *CRC Standard Mathematical Tables*; Beyer, W. H., Ed.; CRC Press: Boca Raton, FL, 1981; p 282.

Solving eq 6 for the integral of the glow function yields eq 7.

$$\int_0^{t_{PW}} f(t)\,dt \approx \frac{F(t_{PW})}{kN}e^{a\tau} - \frac{f(t_{PW})}{b} \tag{7}$$

Substituting eq 7 into eq 2 yields eq 8 as an approximationof the glow function .

$$f(t_{PW}) \approx \frac{d}{dt_{PW}}\left(\frac{F(t_{PW})}{kN}e^{a\tau}\right) - \frac{1}{b}\frac{d}{dt_{PW}}(f(t_{PW}))$$

$$f(t_{PW}) \approx \frac{e^{at_{PW}}}{kN}\frac{d}{dt_{PW}}\left(\frac{F(t_{PW})}{kN}e^{a\tau}\right) - \frac{1}{b}\frac{d}{dt_{PW}}(f(t_{PW})) \tag{8}$$

$$f(t_{PW}) \approx \frac{e^{at_{PW}}}{kN}\left(\frac{F(t_{PW})}{kN}e^{a\tau} + aF(t_{PW})\right) - \frac{1}{b}\frac{d}{dt_{PW}}(f(t_{PW}))$$

When $a\Delta t < 0.01$, the quantity in parentheses in eq 7 can be approximated as shown in eq 9.

$$\left(\frac{dF(t_{PW})}{dt_{PW}} + aF(t_{PW})\right) \approx \frac{F(t_{PW+1}) - F(t_{PW})}{\Delta t} + aF(t_{PW})$$

$$\left(\frac{dF(t_{PW})}{dt_{PW}} + aF(t_{PW})\right) \approx \frac{F(t_{PW+1}) - (1 - a\delta t)F(t_{PW})}{\Delta t} \tag{9}$$

$$\left(\frac{dF(t_{PW})}{dt_{PW}} + aF(t_{PW})\right) \approx \frac{F(t_{PW+1}) - F(t_{PW})}{\Delta t}$$

The approximation derived as eq 9 yields eq 10 when substituted into eq 7.

$$f(t_{PW}) \approx De^{a\tau}[F(t_{PW+1}) - F(t_{PW})] - \frac{1}{b}\frac{d}{dt_{PW}}(f(t_{PW})) \tag{10}$$

In eq 10, k, N, and Δt have been absorbed into a new constant D. An additional approximation where $a\tau < 0.01$ allows the exponential to be considered equal to one, yielding eq 11.

$$f(t_{PW}) \gg \frac{1}{b}\frac{d}{dt_{PW}}(f(t_{PW})) \tag{11}$$

Recognizing that $b \gg \Delta t$ yields eq 12 as the final approximation for the glow function at $t = t_{PW}$.

$$f(t_{PW}) \approx D[F((t_{PW+1}) - F(t_{PW}))] \tag{12}$$

This final equation establishes that, for the time constants relevant to this instrument, simple difference between successive integrated pulse intensities yields the instantaneous intensities to within an arbitrary constant.

RECEIVED for review April 6, 1992. Accepted August 20, 1992.

Registry No. Argon, 7440-37-1.

Acridinium Chemiluminescence Detection with Capillary Electrophoresis

Michael A. Ruberto and Mary Lynn Grayeski*

Department of Chemistry, Seton Hall University, South Orange, New Jersey 07079

A detection interface has been designed to allow for the addition of postcolumn reagents to evaluate chemiluminescence as a method of detection for capillary electrophoresis. The interface utilizes a reactor that introduces reagents into the electrophoretic system in a sheathing flow profile. The reaction conditions including pH, concentration, and flow rates of the reagents for acridinium chemiluminescence have been studied to evaluate the effect on the detector response. The detection limit for the interface was found to be in the low femtomole to upper attomole range for acridiniums. The interface was evaluated as a potential source of zone dispersion by investigating its effects on band width. "Chemical band narrowing" was observed due to the fast kinetics of the chemiluminescence reaction.

INTRODUCTION

Capillary electrophoresis (CE) has been well documented as a rapid, highly efficient means of separation with tremendous resolving power.[1-3] Ever since the initial work on CE was reported in the seventies,[4,5] there has been a movement toward smaller diameter capillaries and research with an emphasis on biotechnology. With this trend has come the need for detection of trace amounts of analytes in extremely small volumes. Therefore, detection is conventionally done on-column without the use of flow cells so as not to introduce zone dispersion. On-column UV[6-8] and fluorescence detection, with either arc lamp[9,10] or laser sources,[11,12] are most commonly used; however, alternative methods of detection such as electrochemical,[13] thermal lensing,[14] and chemiluminescence using the luminol reaction[15] are beginning to emerge.

Chemiluminescence (CL) is a sensitive measurement uniquely suited to low-volume, on-line detection because of the nature of the kinetic measurement, which allows for rapid detection in a larger volume flow cell with minimal band broadening.[16] Acridinium CL has been chosen as the reaction scheme to be evaluated since it has many qualities that make it particularly advantageous for use with CE. This CL reaction (Figure 1) of the oxidation of an acridinium ester by hydrogen peroxide in the presence of a base[17] is characterized by several features that make it suitable for use as a derivatizing agent for CE. The acridinium reaction has a high CL efficiency for improved detectability. The rate can be adjusted for measurements in flowing systems, which require reaction completion in a few seconds to minimize overlapping bands. Acridiniums have been modified to include functional groups suitable for derivatizing biomolecules.[18,19] Furthermore, the positive charge provides greater mobility in an applied electric field.

This report describes the design and fabrication of an interface that will allow for the evaluation of acridinium CL as a detection method for CE. The effect of various reaction conditions on the detector response are reported as well as the effect of the interface and the mixing profile on zone dispersion. The sensitivity and detection limits are also reported.

EXPERIMENTAL SECTION

CE and Detection Interface. The apparatus used for capillary electrophoresis is pictured in Figure 2. A Spellman (Plainview, NY) dc power supply was used to provide the high voltage for the electrophoresis. The electrodes were platinum wire, and the high voltage end was operated in a Plexiglas box for safety. Two sizes of fused silica capillary (Polymicro Technologies, Inc., Phoenix, AZ) were used for the separation and detection. The electrophoretic capillary, which provided the means for separation, had an inner diameter of 50 μm and an outer diameter of 350 μm, while the reaction capillary, which housed the CL reaction, had an inner diameter of 400 μm. The two fused silica capillaries were coupled together with a Parker-Hannafin stainless steel tee which served as the reaction tee. Injections were performed by electromigration at 15 kV for various time intervals. The reagents needed to produce the CL reaction were delivered from Gastight syringes (Hamilton Co., Reno, NV) by Sage (White Plains, NY) Model 351 syringe pumps. The hydrogen peroxide from pump 1 was combined with the base from pump 2 by an SSI mixing tee, the outlet of which led to the reaction tee of the detection interface. The light generated by the CL reaction was detected by a Kratos (now ABI, Foster City, CA) Model 950 Fluoromat, which was operated with its source turned off. The PMT of the detector was operated at 900 V, and its output was monitored by a Spectra Physics (San Jose, CA) SP 4290 integrator. The only ground in the system was the grounding electrode which was dipped in a buffer reservoir.

The detection interface (Figure 3) utilizes a coaxial reactor, similar to that used by Weber and Grayeski for CL detection in capillary LC[16] and Rose and Jorgenson for fluorescence derivatization in CE,[20] in which the smaller diameter 50-cm-long electrophoretic capillary is inserted into the larger diameter 35-cm-long reaction capillary. The CL reagents enter the reaction

(1) Joregenson, J. W.; Luckacs, K. D. *Anal. Chem.* **1981**, *53*, 1298–1302.
(2) Tsuda, A.; Kazuhiro, N.; Nakagawa, G. *J. Chromatogr.* **1983**, *264*, 385–392.
(3) Lauer, H. H.; McManigill, D. *Anal. Chem.* **1986**, *58*, 165–170.
(4) Viratanen, R. *Acta Polytech. Scand.* **1974**, *123*, 1–67.
(5) Mikkers, F. E. P.; Everaerts, F. M.; Verheggen, Th. P. E. M. *J. Chromatogr.* **1979**, *169*, 11–20.
(6) Terabe, S.; Otsuka, K.; Ichikawa, K.; Tsuchiya, A.; Ando, T. *Anal. Chem.* **1984**, *56*, 113–116.
(7) Walbroehl, Y.; Jorgenson, J. W. *Anal. Chem.* **1986**, *58*, 479–481.
(8) Terabe, S.; Otsuka, K.; Ando, T. *Anal. Chem.* **1985**, *57*, 834–841.
(9) Jorgenson, J. W.; Luckacs, K. D. *J. Chromatogr.* **1981**, *218*, 209–216.
(10) Jorgenson, J. W.; Luckacs, K. D. *Science* **1983**, *222*, 266–272.
(11) Pentoney, S. L., Jr.; Huang, X.; Burgi, D. S.; Zare, R. N. *Anal. Chem.* **1988**, *60*, 2625–2629.
(12) Cheng, Y. F.; Dovichi, N. J. *Science* **1988**, *242*, 562–564.
(13) Wallingford, R. A.; Ewing, A. G. *Anal. Chem.* **1987**, *59*, 1762–1766.
(14) Waldron, K. C.; Dovichi, N. J. *Anal. Chem.* **1992**, *64*, 1396–1399.
(15) Dadoo, R.; Colon, L. A.; Zare, R. N. *J. High Res. Chromatogr.* **1992**, *15*, 133–135.
(16) Weber, A. J.; Grayeski, M. L. *Anal. Chem.* **1987**, *52*, 1452–1457.
(17) McCapra, F. *Pure Appl. Chem.* **1970**, *24*, 611–629.
(18) Weeks, I.; Beheshti, I.; McCapra, F.; Campbell, A. K.; Woodhead, J. S. *Clin. Chem.* **1983**, *29* (8), 1474–1479.
(19) Zomer, G.; van den Berg, R. H.; Jansen, E. H. J. M. *Anal. Chim. Acta* **1988**, *205*, 267–271.
(20) Rose, D. J., Jr.; Jorgenson, J. W. *J. Chromatogr.* **1988**, *447*, 117–131.

0003-2700/92/0364-2758$03.00/0

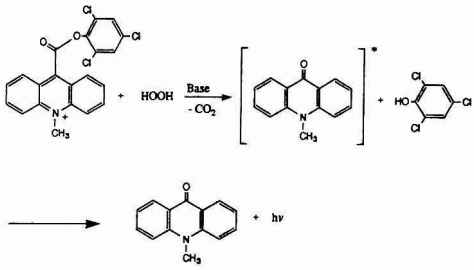

Figure 1. Acridinium chemiluminescence reaction.

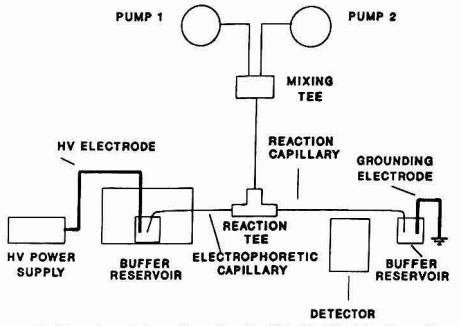

Figure 2. Experimental configuration for CE with CL detection. Pump 1 introduces the hydrogen peroxide to the detection interface while the base flows from pump 2.

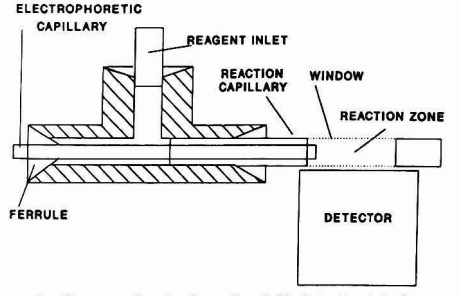

Figure 3. Cross-sectional schematic of CL detection interface.

tee and flow in a sheathing profile around the electrophoretic capillary and its effluent. Mixing of the reagents with the acridinium ester occurs through diffusion as well as radial migration of the analyte and electrophoretic buffer which is necessary to distribute current over the full cross-sectional area of the reaction capillary.[20] This mixing of the reagents and the acridinium ester takes place in a designated section of the reaction capillary called the reaction zone. The reaction zone is placed in front of the detector PMT at a distance of 1 cm with its protective polyimide coating removed. The photons emitted from the CL reaction are then detected by the PMT. The end portion of the reaction capillary exits the detector and enters a buffer reservoir to complete the circuit.

Chemicals. The acridinium esters were synthesized in our lab.[21] A 10^{-3} M stock solution of each acridinium was made using HPLC-grade acetonitrile (Fisher, Fairlawn, NJ), and all dilutions were performed using the electrophoretic buffer.

The electrophoretic buffer was a 50 mM tartrate buffer prepared by dissolving sodium tartrate (Mallinckrodt, St. Louis, MO) in distilled water and adjusting the pH to 2.8 with 6 M hydrochloric acid. The postcolumn reagents consisted of a base and hydrogen peroxide. The base was a 100 mM phosphate buffer prepared by dissolving potassium phosphate (Fisher) in distilled water and varying the pH with either hydrochloric acid or sodium hydroxide. The hydrogen peroxide solution was prepared by diluting a 30% reagent (Sigma, St. Louis, MO) to various concentrations with 3 mM nitric acid solution. The acidic conditions were used to stabilize the hydrogen peroxide solution. These solutions were filtered through 0.45-μm filters (Millipore Corp., Milford, MA) and degassed prior to use.

CE with UV Detection. A Waters variable-wavelength UV detector was modified for use with CE. A single 85-cm × 50-μm-i.d. fused silica capillary was used for these experiments. The distance from the injection end to the detector was 50 cm. A 50 mM sodium tartrate pH 2.8 buffer was used. UV detection was at 265 nm.

RESULTS AND DISCUSSION

Reagents. Because acridinium esters are very susceptible to hydrolysis above pH 3, the pH of the electrophoretic buffer used in these experiments was 2.8.[17] When the pH of the electrophoretic buffer was increased to 4, the CL signal decreased by more than 99%. This hydrolysis is one of the competing dark reactions to the photon-generating mechanism and can be avoided by maintaining acidic conditions until the point of detection. At pH 2.8, most of the sites on the capillary wall were protonated so there was virtually no electroosmotic flow. Therefore, the migration of the acridinium ester was primarily due to the electrophoretic mobility of the molecule under the induced electric field. The acridinium used had a quaternary nitrogen atom as part of the ring structure, so the positive charge provided adequate mobility at the applied potential.

The kinetics of a CL reaction can be controlled by varying the concentration and pH of the reagents. For use in flowing systems, reaction conditions must be modified so that maximum emission occurs in a short time frame to coincide with the passage of the analyte in front of the PMT. In this research, the flowing system consisted of a nanoliter per minute dropwise flow of the electrophoretic capillary which was combined with the CL reagents so that mixing occurred directly in front of the PMT. The reaction conditions for acridinium CL in the CE interface were analyzed using 9-[(2,4,6-trichlorophenoxy)carbonyl]-10-methylacridinium trifluorosulfonate as the test compound.

A study of the effects of pH on the detector response was performed (Figure 4) by using various basic catalysts which consisted of several solutions of 100 mM phosphate buffer each adjusted to different pH values. The concentration was chosen because it was adequate enough to maintain the pH of the solution in the presence of the acidic hydrogen peroxide reagent and the electrophoretic buffer. The maximum light output was observed with the pH 8.0 phosphate buffer as expected for the base-catalyzed reaction. Further increases in the pH lowered the measured light production primarily because of increased competition of the dark mechanism of base hydrolysis of the ester.

The effects of hydrogen peroxide concentration were also studied (Figure 5). The amount of light detected increased with hydrogen peroxide concentration; however, a concentration greater than 20 mM could not be used due to bubble formation from the breakdown of the peroxide in the presence of the base. When operating above 20 mM, this bubble formation caused problems with maintaining a uniform current throughout the electrophoretic system.

The combined flow rate of the post column reagents was also found to influence the detector response (Figure 6). The measured signal reached a maximum at 11 μL/min. Generally, when utilizing a flow system to detect a CL reaction with fast

(21) Grayeski, M. L.; Novak, T. J.; Mohan, A. G. *Bioluminescence and Chemiluminescence Current Status*; John Wiley and Sons: New York, 1991; Session 2.

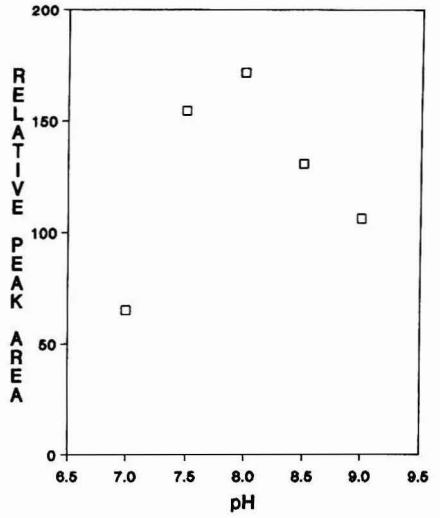

Figure 4. Effect of pH on detector response. Acridinium concentration is 5×10^{-6} M; injection is for 20 s at 15 kV; operating voltage is 15 kV; operating buffer is 50 mM tartrate buffer, pH 2.8.

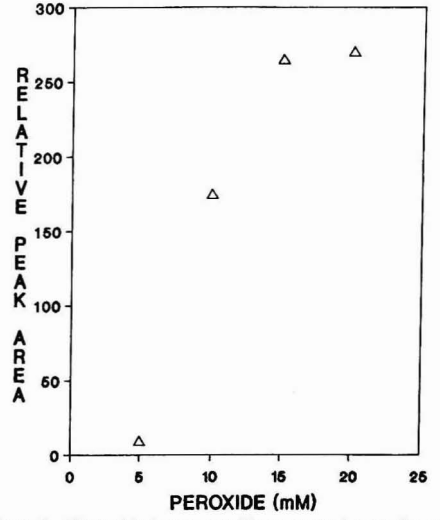

Figure 5. Effect of hydrogen peroxide concentration on detector response. Acridinium concentration is 5×10^{-6} M. Conditions are the same as in Figure 4.

kinetics, as is the case for many acridinium esters, a response such as that in Figure 6 is obtained.[22] Faster flow rates apparently push the analyte past the detector before the reaction is completed, while slower flow rates produce inadequate mixing of the reagents in the period of time the analyte is in the proximity of the detector. Each reagent was pumped at the same rate.

Analytical Figures of Merit. Using the experimental conditions for the postcolumn reagents determined above, 20 mM hydrogen peroxide and 100 mM phosphate buffer at

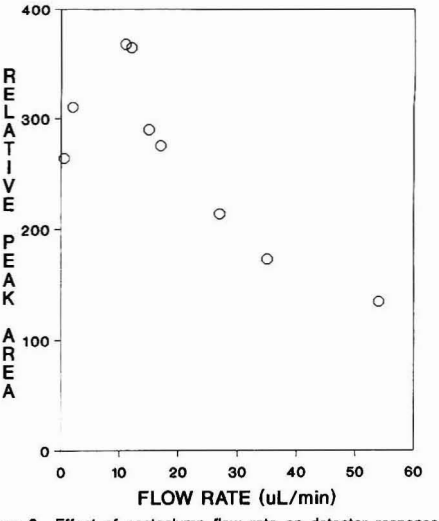

Figure 6. Effect of postcolumn flow rate on detector response. Acridinium concentration is 10^{-5} M. Conditions are the same as in Figure 4.

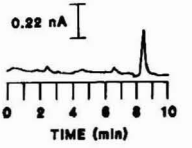

Figure 7. Electropherogram of 9-[(2,4,6-trichlorophenoxy)carbonyl]-10-methylacridinium trifluorosulfonate. Peak represents a 10^{-7} M solution or 6 fmol injected. Operating buffer is 50 mM tartrate buffer, pH 2.8; injection is for 20 s at 15 kV; operating voltage is 15 kV.

pH 8.0, the linearity of the detector interface was determined from a log–log plot of peak area as a function of sample concentration. The detection interface is linear over 2.5 orders of magnitude, with a slope of 0.9044 ± 0.0485 at the 95% confidence limit. The standard deviation of injections of 5×10^{-4} M acridinium is 8% at 95% confidence limit. When compared to the standard deviation of 10% obtained for the same concentration of analyte detected by UV without the interface, it can be concluded that the inflated injection variance is a function of the manual injection system employed and not a result of the interface or CL detection.

Figure 7 shows an electropherogram of 10^{-7} M 9-[(2,4,6-trichlorophenoxy)carbonyl]-10-methylacridinium trifluorosulfonate obtained using the interface for CL detection. The peak represents a 10^{-7} M solution or 3.4 pg or 6 fmol injected as determined by the equation

$$Q = (v + \mu)C\pi r^2 t \qquad (1)$$

where Q is the quantity injected, v is the electrophoretic mobility of the analyte, μ is the electroosmotic flow, C is the concentration, r is the radius of the capillary, and t is the injection time.[23] The signal is approximately 20 times the RMS noise, with an extrapolated detection limit of 640 amol at 3 times the RMS noise. Under the conditions evaluated, detectability is limited by detector optics and electronics with a maximum obtainable voltage of 900 V for the PMT. Although other detectors are more sensitive, the model

(22) Rule, G.; Seitz, W. R. *Clin. Chem.* **1979**, *25* (9), 1635–1638.

(23) Wallingford, R.; Ewing, A. *Adv. Chromatogr.* **1989**, *29*, 1–76.

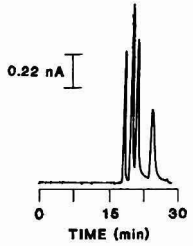

Figure 8. Separation of 5 × 10^{-6} M solution of related acridiniums, 9-(phenoxycarbonyl), 9-[(2-chlorophenoxy)carbonyl], 9-[(2,4-dichlorophenoxy)carbonyl], and 9-[(2,4,6-trichlorophenoxy)carbonyl], respectively. Electrophoretic capillary length is 1 m; operating buffer is 50 mM tartrate/10 mM γ-cyclodextrin, pH 2.8; postcolumn reagents 20 mM peroxide, 100 mM phosphate buffer, pH 9; injection is for 3 s at 25 kV; operating voltage is 25 kV.

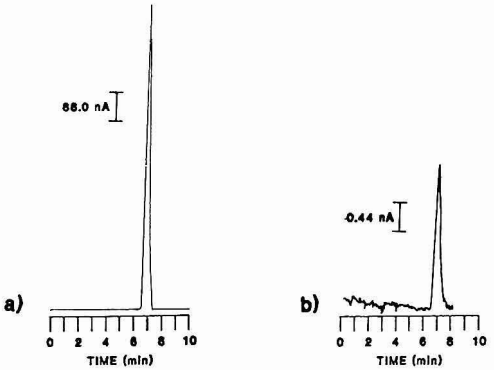

Figure 9. Electropherogram of 10^{-4} M injections of 9-[(2,4,6-trichlorophenoxy)carbonyl]-10-methylacridinium trifluorosulfonate with (a) CL detection and (b) UV detection. Conditions are the same as in Figure 7 except the injection which was 3 s at 15 kV.

reported here was chosen because of the mechanical advantages of its geometrical design for incorporating the interface close to the PMT and for ease of modification for exploratory experiments. Because of the extremely low background associated with acridinium CL, it is quite possible to achieve better detection limits with a more sensitive detector by operating the PMT at higher voltages without an intolerable increase in background.[24]

A separation of several related acridinium esters has been performed (Figure 8). The base used in the detection of these acridinium esters had a pH of 9. Each of the acridinium esters exhibits different reaction kinetics depending on the pH in the detector. At pH 9 all of the acridiniums could be detected at an appreciable amount.

Effect of the Interface on Band Broadening. Band broadening can be predicted by calculating the variance of a sample zone as it migrates through a CE capillary. The total variance of an electrophoretic peak is the sum of the variance contributions of each of the instrumental components or chemical interactions present in the system. The variance can be expressed as[25]

$$\sigma^2_{tot} = \sigma^2_{diff} + \sigma^2_{inj} + \sigma^2_{int} \quad (2)$$

where σ^2_{diff} is the variance due to diffusion, σ^2_{inj} is the variance due to the injection plug length, and σ^2_{int} represents zone broadening variance arising from interactions between the analyte and the walls of the capillary.

With CE, detection is usually performed in the electrophoretic capillary, so there is no need for a flow cell and, therefore, no variance term for a detector. However, the detection interface presented in this paper employs a reaction capillary of larger volume than the electrophoretic capillary. The mixing that takes place in this reaction capillary is a potential source of band broadening and must be evaluated. The equation for the variance of the CE system with the interface would then be

$$\sigma^2_{tot} = \sigma^2_{diff} + \sigma^2_{inj} + \sigma^2_{int} + \sigma^2_{det} \quad (3)$$

where the theoretical contribution to the band dispersion in the detector is represented as σ^2_{det}. This term is defined as

$$\sigma^2_{det} = V^2_{det}/K \quad (4)$$

where V is the reaction zone volume and the constant K can be assumed to be equal to 12 for a plug flow profile in a cylindrical cell geometry.[26] The volume of the detector interface is 2.51 μL which yields a calculated σ^2_{det} equal to 0.525 μL^2.

The actual band broadening due to the interface was determined experimentally by comparing the widths of peaks obtained from CL detection with those obtained by CE without the interface using UV detection. The amount of acridinium injected and the conditions for both experiments were identical. The result of the comparison was an actual decrease in the peak width when the interface and CL detection was used (Figure 9). Note that equal concentrations were used for comparison even though 5 × 10^{-4} M was much higher than would typically be used for a chemiluminescence measurement. A peak width at half height of 0.22 min was obtained with the interface and CL detection compared to 0.32 min for conventional UV detection. The decrease in peak width has been previously observed and can be explained in terms of the "chemical band narrowing" effect.[22,27,28] The CL reaction kinetics allow for an intense, rapidly decaying signal to be produced when the acridinium enters the reaction zone of the interface. Unlike conventional photometric detectors, a signal is only produced when the analyte is in contact with "fresh" reagents. Once the reagents are spent, the signal stops, thus reducing the effective volume of the flow cell to a smaller reaction zone because a signal is not recorded for the entire residence time in the flow cell.

CONCLUSION

Chemiluminescence detection offers several advantages as a method of detection for capillary electrophoresis. Increased sensitivity can be achieved due to the larger detection volumes provided by the interface without the band broadening expected from these volumes. If the kinetics of the CL reaction are fast, light production ceases before any significant diffusion occurs into the spent reagents that encompass the extra volume of the interface resulting in relatively narrow bands. Low detection limits can be attained with acridinium CL due to the reduced background present from chemical excitation.

(24) Weinberger, R.; Mannan, C.; Cerchio, M.; Grayeski, M. L. *J. Chromatogr.* **1984**, *288*, 445–450.
(25) Huang, X.; Coleman, W. F.; Zare, R. N. *J. Chromatogr.* **1989**, *480*, 95–110.
(26) Gluckman, J. C.; Hirose, A.; McGuffin, V. L.; Novotny, M. *Chromatographia* **1983**, *17*, 303–309.
(27) Grayeski, M. L.; Weber, A. J. *Anal. Lett.* **1984**, *17* (A13), 1539–1552.
(28) DeJong, G. J.; Lammers, N.; Sprint, F. J.; Brinkman, U. A. Th.; Frei, R. W. *Chromatographia* **1984**, *18*, 129–133.
(29) McCormick, R. *Anal. Chem.* **1988**, *60*, 2322–2328.
(30) Bruin, G.; Chang, J.; Kuhlman, R.; Zegers, K.; Kraak, J.; Poppe, H. *J. Chromatogr.* **1989**, *471*, 429–436.

Acridiniums can be used as "tags" to label analytes for separation and sensitive detection with CE. The pH under which the separation is performed is restricted to below 3, but several types of analytes, such as amino acids and proteins,[29-31] can be separated under such conditions. Acridinium esters have been used to label amino acids as well as proteins in immunoassays.[18,19] Future work will include the synthesis of acridinium esters that can be utilized to label amino acids and peptides.

RECEIVED for review May 5, 1992. Accepted August 12, 1992.

Registry No. Acridinium, 22559-71-3; hydrogen peroxide, 7722-84-1.

(31) Bruin, G.; Huisden, R.; Kraak, J.; Poppe, H. *J. Chromatogr.* **1989**, *480*, 339–350.

Pyrrole Copolymerization and Polymer Derivatization Studied by X-ray Photoelectron Spectroscopy

Stephen J. Vigmond, Krishna M. R. Kallury, and Michael Thompson*

Department of Chemistry, University of Toronto, 80 St. George Street, Toronto, Ontario, Canada M5S 1A1

Nitro-functionalized polypyrrole films have been deposited on gold surfaces by copolymerization with pyrrole or by derivatization of the polymer. Electrochemical copolymerization of 2- and 4-nitrostyrenes or 2- and 4-nitrobenzaldehydes with pyrrole indicates that lower polymerization yields result from the 2-nitro aromatics due to steric factors. Copolymerization of pyrrole in the presence of 2- or 4-nitrotoluene or isomeric chloronitrotoluenes does not incorporate the nitroaromatics into the polypyrrole matrix, but does affect the oxidation state of the resulting polymer. N-Arylation or N-acylation of preformed polypyrrole films were performed using 2,4-dinitrofluorobenzene, 4-nitrobenzoyl chloride, or 5-nitro-2-furoyl chloride. Electropolymerization of (2,2′-dipyrrolyl)(nitrophenyl)methanes were also performed for comparison purposes. X-ray photoelectron spectroscopic analysis of the derivatized polymers shows that the nitro substituents exhibit varying degrees of stability toward oxidation, reduction, and aging.

INTRODUCTION

The unique characteristics of conducting organic polymers have spurred a range of studies in an effort to develop materials suitable for diverse applications. The conductivity of these materials can be switched between approximately 10 orders of magnitude by applying an appropriate potential, while also displaying electrochromic changes.[1,2] Other desirable characteristics include stability, light weight (with respect to other conducting materials), ease of formation, and often the presence of functional groups to allow derivatization of the polymer. With a view to utilize these properties, research has been undertaken to incorporate organic polymers into switching devices,[3] protective coatings,[4] rechargeable batteries,[2] and chemical sensors.[5]

Many studies have been carried out documenting the effect of reaction conditions on electrochemically-prepared polymers.[6-9] The nature of the synthesized material has been found to depend on solvent, temperature, applied potential, choice of counteranion, and concentration of reactants. In addition to controlling the characteristics of the polymer through these means, it is the goal of many researchers to prepare interfaces with various functionalities in an attempt to produce chemical sensors with greater selectivity. Of particular significance is the conducting polymer polypyrrole which finds increasing utility in the area of chemical sensors due to its capability of ready transformation between oxidized and neutral states. Furthermore, the pyrrole nucleus is amenable to a variety of derivatization reactions. The common procedure to form derivatized polypyrrole consists of polymerizing an appropriately derivatized pyrrole monomer. These polymerizations are usually carried out in the presence of pyrrole since N-substituted pyrroles do not normally produce even coatings by themselves. Ferrocene,[10] alkyl and aromatic groups,[11] phenothiazine,[12] sulfopropane,[13] glucose oxidase,[14] and amino ligands[15] have all been reacted with pyrrole before polymerization in an effort to obtain polymers incorporating electroactive agents,[16] active enzymes, and ionic sites. Functionalization at the 3-position, which requires extra synthetic steps in order to avoid reaction at the 2-position, has been performed in order to produce polymers with unique properties such as solubility,[17] self-doping,[18] ionic sites,[19] and amphiphilicity.[20]

An alternate approach used to form polypyrrole derivatives is through copolymerization with organic compounds. Josowicz et al.[21] have reported coating polypyrrole derivatives on the gate of a suspended-gate field effect transistor and obtained chemical selectivity to adsorption of various chemical species from these films. Copolymerization of pyrrole with either 2-nitrotoluene or 4-nitrotoluene resulted in films that behaved oppositely to toluene vapor; the pyrrole/4-nitrotoluene copolymer underwent a work function decrease upon exposure to toluene vapor while the pyrrole/2-nitrotoluene copolymer experienced a work function increase. The products of the copolymerizations were proposed to be as shown for the para isomer in Figure 1 and the work function changes were attributed to N–π interactions between toluene and the nitroarene moiety in the copolymer.

One of the limitations of polymerization involving pyrrole is that copolymerization reagents may not contain a nucleophilic species as this will react with pyrrole radicals and prevent polymer propagation. An alternative scheme for incorporating functionalities into the polypyrrole matrix is to react the preformed polymer with appropriate reagents. As the polymerization occurs through the 2- and 5-positions,

(1) Billingham, N. C.; Calvert, P. D. *Adv. Polym. Sci.* **1989**, *90*, 1.
(2) Heinze, J. In *Topics in Current Chemistry*; Steckhan, E., Ed.; Springer-Verlag: Berlin, 1990; pp 1–48.
(3) Osaka, T.; Ouchi, K.; Fukuda, T. *Chem. Lett.* **1990**, 1535.
(4) Noufi, R.; Nozik, A. J.; White, J.; Warren, L. F. *J. Electrochem. Soc.* **1982**, *129*, 2261.
(5) Potember, R. S.; Hoffman, R. C.; Hu, H. S.; Cocchiaro, J. E.; Viands, C. A.; Murphy, R. A.; Poehler, T. O. *Polymer* **1987**, *28*, 574.
(6) Olmedo, L.; Chanteloube, I.; Germain, A.; Petit, M.; Genies, E. M. *Synth. Met.* **1989**, *30*, 159.
(7) Vork, F. T. A.; Schuermans, B. C. A. M.; Barendrecht, E. *Electrochim. Acta* **1990**, *35*, 567.
(8) Satoh, M.; Kaneto, K.; Yoshino, K. *Synth. Met.* **1986**, *14*, 289.
(9) Machida, S.; Miyata, S.; Techagumpuch, A. *Synth. Met.* **1989**, *31*, 311.
(10) Eaves, J. G.; Mirrazaei, R.; Parker, D.; Munro, H. S. *J. Chem. Soc., Perkin Trans. 2* **1989**, 373.
(11) Reynolds, J. R.; Poropatic, P. A.; Toyook, R. L. *Macromolecules* **1987**, *20*, 958.
(12) Deronzier, A.; Essakalli, M., Moutet, J.-C. *J. Chem. Soc., Chem. Commun.* **1987**, 773.
(13) Zhong, C.; Storck, W.; Dohlhofer, K. *Ber. Bunsenges. Phys. Chem.* **1990**, *94*, 1149.
(14) Evans, S. E.; Yon Hin, B. F. V.; Lowe, C. R. *Third Int. Meet. Chem. Sen. Cleveland, Ohio* **1990**, 115.
(15) Bartlett, P. N.; Chung, L.-Y.; Moore, P. *Electrochim. Acta* **1990**, *35*, 1273.
(16) Curran, D.; Grimshaw, J.; Perera, D. *Chem. Soc. Rev.* **1991**, *20*, 391.
(17) Masuda, H.; Tanaka, S.; Kaeriyama, K. *J. Chem. Soc., Chem. Commun.* **1990**, 725.
(18) Delabouglise, D.; Garnier, F. *New J. Chem.* **1991**, *15*, 233.
(19) Iyoda, T.; Aiba, M.; Saika, T.; Honda, K.; Shimidzu, T. *J. Chem. Soc., Faraday Trans. 2* **1991**, *87*, 1765.
(20) Collard, D. M.; Fox, M. A. *J. Am. Chem. Soc.* **1991**, *113*, 9414.
(21) Josowicz, M.; Janata, J.; Ashley, K.; Pons, S. *Anal. Chem.* **1987**, *59*, 253.

0003-2700/92/0364-2763$03.00/0

derivatization could be affected through the amine or by electrophilic substitution at the 3-position. Reaction at the 3-position is typically initiated by nitration and followed by conversion to an amine. Early work by Diaz et al.[22] covalently bound an electroactive derivative, tetrathiafulvalene, to polypyrrole and observed oxidation peaks in cyclic voltammograms from the attached molecule. Schuhmann and co-workers[23-25] have recently published several papers describing the immobilization of glucose oxidase by this route and report that the size-exclusion properties of the polypyrrole matrix allows more reliable glucose measurements of real samples to be made in comparison to other existing electrodes. This group has also bound chloranil and 2,3-dichloro-1,4-naphthoquinone to polypyrrole utilizing the 3-amino group and obtained a polymer which exhibited electrocatalytic properties for the oxidation of NADH.[26]

Fewer attempts have been made to functionalize polypyrrole through its amino site. O'Riordan and Wallace[27] have incorporated a carbodithioate in an effort to produce a modified electrode capable of complexing metal ions in solution, while Rosenthal et al.[28] have attached ferrocene to the surface and noted that this molecule retains its electroactivity. Although the latter work considers the degree of reaction to be a function of reaction temperature and steric factors, neither report has quantitated the reactivity of the amino group.

The current investigation involves the generation of nitrofunctionalized polypyrrole matrices either through copolymerization of pyrrole with nitroarenes or the derivatization of polypyrrole with nitro aromatic compounds and their characterization by XPS. The nitro groups were expected to provide highly polar surfaces capable of undergoing facile reduction to the corresponding amino derivative to permit the covalent binding of large receptors and other biomolecules. Quantitation of the nitro groups is straightforward since the chemical shifts of the two nitrogen types are readily distinguishable (about 400 eV for an amino group and 406 eV for the nitro group). Therefore, this spectroscopic study will facilitate the monitoring of the degree of derivatization and the stability of these surfaces to reaction conditions, such as the application of various electrochemical potentials.

EXPERIMENTAL SECTION

Materials and Reagents. The 9-MHz gold-plated piezoelectric quartz crystals were obtained from International Crystal Manufacturing Co.

Quinoline, pyrrole, furan, 3-methylthiophene, triethylamine, dimethylformamide, thionyl chloride, copper chromite, zinc dust, and all the nitro aromatic compounds used in the current work were purchased from Aldrich (Milwaukee, WI) and used as received with the exception of pyrrole and quinoline which were distilled prior to use. Tetrabutylammonium perchlorate was supplied by Fluka (Switzerland) and was of electrochemical grade. All the solvents utilized were of reagent grade procured from BDH (Toronto, Ontario).

Instrumentation. X-ray photoelectron spectra reported were recorded on a Leybold MAX-200 ESCA spectrometer using an unmonochromated Mg Kα source operated at 12 kV and 25 mA. The shape of the spectra indicated that no compensation for differential surface charging was needed. The binding energy scale was calibrated to 285.0 eV for the main C(1s) (C–C) feature. Spectra were run in both low-resolution (pass energy = 192 eV) and high-resolution (pass energy = 48 eV) modes for the C(1s), N(1s), and O(1s) regions. Each sample was analyzed at a 90° angle relative to the electron detector. An analysis area of 2 × 4 mm^2 was used for rapid data collection (typically 5 min for the C(1s) high-resolution spectrum).

Elemental compositions were calculated from the satellite-subtracted low resolution spectra normalized for constant transmission using the software supplied by the manufacturer.[29] The sensitivity factors employed in these computations, C(1s) = 0.34, N(1s) = 0.54, O(1s) = 0.78, and Cl (2p) = 1.08, were empirically derived for the MAX-200 spectrometer by Leybold.

Electrochemical oxidations and reductions were performed with a polarographic analyzer (Model 473) from ECO Instruments (Cambridge, MA).

Piezoelectric frequency measurements were made on a Universal frequency counter (Hewlett-Packard Model 5334B).

2- and 4-nitrostyrenes were synthesized by the decarboxylation of the corresponding nitrocinnamic acids (Aldrich), following the procedure reported by Wiley and Smith.[30] They were characterized by ^{1}H NMR spectroscopy. 5-Nitrofuroyl chloride was prepared by treatment of 5-nitrofuroic acid (Aldrich) with thionyl chloride under standard conditions.

Synthesis of the Di(2,2′-pyrrolyl)(2- or 4-nitro-1-phenyl)-methane. A solution of pyrrole (5 g) in acetic acid (20 mL) was cooled in an ice bath and treated by dropwise addition with the appropriate nitrobenzaldehyde (0.5 molar equiv) dissolved in a mixture of acetic acid and DMF (9:1, 50 mL). After completion of the addition (20 min), the mixture was stirred for a further 30 min with continued cooling in the ice bath and then at room temperature for an additional 2 h. The mixture was poured into ice–water (250 mL) with stirring and extracted with toluene (100 mL). The extract was filtered through Celite to remove the emulsion formed, and the organic layer was separated, washed with water (2 × 25 mL), dried (Na_2SO_4), and concentrated on a rotary evaporator to yield a crude solid product (3 g). A purity check of this material by TLC in toluene–ethyl acetate (9:1) indicated three main spots, the lower two probably due to higher molecular weight impurities (these lower spots were more intense with the 4-nitrophenyl isomer than the 2-nitro compound). Purification of the crude product was carried out by column chromatography with silica gel stationary phase and toluene as the eluent. The pure material was recovered from the first fraction.

The products were characterized by ^{1}H NMR, and mass spectrometry confirmed the products by recording a molecular ion peak for both.

2-Nitro Isomer (I). ^{1}H NMR ($CDCl_3$): δ 8.3–7.2 (m, 4 H, aromatic ring/heterocyclic ring protons), 6.9–6.6 (m, 2 H, pyrrole ring), and 6.4–5.7 (m, 5 H, CH, pyrrole ring).

4-Nitro Isomer (II). ^{1}H NMR ($CDCl_3$): δ 7.9 (d, 2 H), 7.1 (d, 2 H) (aromatic protons), 6.7–6.4 (m, 2 H), 6.0 (q, 2 H), 5.7 (m, 2 H, pyrrole protons), and 5.4 (s, 1 H, CH).

Electropolymerization. All the electrochemical polymerization reactions as well as the oxidation-state modification experiments were performed utilizing a cell configuration described previously,[31] which prevents the electrolyte solution from wetting the electrical contacts of the piezoelectric crystals. Deposition of polypyrrole on the gold-coated crystal surface was effected by the electropolymerization of a solution of pyrrole and tetrabutylammonium perchlorate (0.1 M) in acetonitrile. The solution was deoxygenated prior to the electrodeposition by bubbling nitrogen through for about 15 min. The copolymerization reactions of pyrrole with the appropriate nitroaromatic compounds were carried out under the same conditions as above, employing molar quantities (1 M) of the latter. A duration of 1 min per side at 1.0 V was uniformly used in all these experiments

(22) Diaz, A. F.; Lee, W.-Y.; Logan, A.; Green, D. C. *J. Electroanal. Chem. Interfacial Electrochem.* **1980**, *108*, 377.
(23) Schuhmann, W.; Kittsteiner-Eberle, R. *Biosens. Bioelectron.* **1991**, *6*, 263.
(24) Schuhmann, W. *Synth. Met.* **1991**, *41–43*, 429.
(25) Schuhmann, W.; Lammert, R.; Uhe, B.; Schmidt, H.-L. *Sens. Act.* **1990**, *B1*, 537.
(26) Schuhmann, W.; Lammert, R.; Hammerle, M.; Schmidt, H.-L. *Biosens. Bioelectron.* **1991**, *6*, 689.
(27) O'Riordan, D. M. T.; Wallace, G. G. *Anal. Chem.* **1986**, *58*, 128.
(28) Rosenthal, M. V.; Skotheim, T.; Warren, J. *J. Chem. Soc., Chem. Commun.* **1985**, 342.
(29) Berresheim, K.; Mattern-Klosson, M.; Wilmers, M. *Fresenius J. Anal. Chem.* **1991**, *341*, 121.
(30) Wiley, R. H.; Smith, N. R. *J. Am. Chem. Soc.* **1950**, *72*, 5198.
(31) Vigmond, S. J.; Kallury, K. M. R.; Ghaemmaghami, V.; Thompson, M. *Talanta* **1991**, *39*, 449.

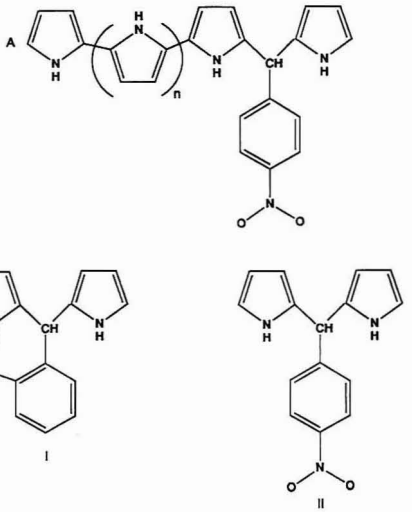

Figure 1. (A) Pyrrole/4-nitrotoluene copolymerization product proposed by Josowicz et al. *o*- (I) and *p*-nitrophenyl (II) monomers used to prepare analogs of A.

and produced a film of approximately 0.5-μm thickness as determined by SEM.

Polymerizations involving the dipyrrolyl(nitrophenyl)methanes (I and II) were carried out in an analogous manner, except that concentrations of 0.7 g per 100 mL were utilized (i.e. the same mass/volume used in the pyrrole polymerizations), and the depositions were performed for 3 min.

Chemical Reduction of the Polypyrrole Films. The polypyrrole-coated crystals were suspended in a solution of acetic acid (30 mL, 1:1 aqueous) and treated with zinc dust in portions (10 × 10 mg) over a period of 2 h. The crystals were then washed thoroughly with distilled water and rinsed with acetone prior to XPS measurements.

N-Acylation/Arylation of the Polypyrrole Films. These derivatization reactions were carried out under conditions similar to those reported for pyrrole itself in literature,[32,33] with slight modifications. The polymer-coated crystals were treated with a solution of the appropriate derivatizing agent (4-nitrobenzoyl chloride, 5-nitro-2-furoyl chloride, or 2,4-dinitrofluorobenzene) in dichloromethane (2% w/v, 30 mL) and triethylamine (2 mL). The mixture was refluxed for 20 h, and the crystals were subjected to extraction with acetonitrile in a Soxhlet apparatus for 5 h.

RESULTS AND DISCUSSION

XPS Analysis of Polypyrrole in Different Oxidation States. The high-resolution XP spectra of polypyrrole in various oxidation states are presented in Figure 2, and the data computed for the C(1s) region are included in Table I. In the N(1s) region, the neutral amino group exhibits a binding energy peak at 400 eV while the positive sites along the backbone in the oxidized polymer appear around 402.5 eV, the latter approximately corresponding to the extent of counteranion inclusion. These assignments are in agreement with those reported earlier.[34,35] This higher binding energy peak has also been assigned to either a quarternary nitrogen[36]

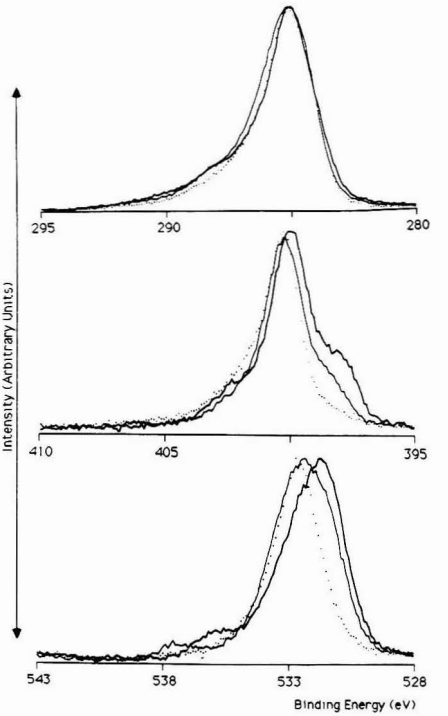

Figure 2. C(1s), N(1s), and O(1s) XPS, respectively, of polypyrrole in as-prepared (dots), neutral (thick line) and oxidized (thin line) states.

Table I. Relative Peak Intensities in C(1s) Region of Polypyrrole (±2%)

	peak positions		
state of polymer	285.0	286.5	288.0
as prepared	72	19	9
reduced at −1.5 V	77	16	7
oxidized at +1.0 V	62	25	13

or a Doniach–Sunjic type of surface electron excitation.[37] In the neutral form a third peak around 398.5 eV, which is usually accompanied on the higher binding energy side by a peak of similar intensity, is ascribable to a hydrogen bonded network with the pyrrolic nitrogens involved in electron donation and acceptance, as postulated by us earlier.[31]

The C(1s) spectra have been deconvoluted into three peaks around 285.0, 286.5, and 288.0 eV. While the former two have been assigned by earlier workers[34] to the α and β carbons of the pyrrole skeleton, it is conceivable that the resolution of the instrument will not be good enough to completely resolve these two species, if the conclusions drawn from the XPS studies on polythiophene are any indication.[38] In view of the fact that these polymers contain several types of structures which present various environments to functionalities (for example, the quinonoid regions over which the bipolarons are distributed in the oxidized form), peak overlap/broadening occurs making specific assignments difficult. Therefore, it is likely that the 285.0-eV peak includes both types of ring carbons. The second peak near 286.5 eV results from carbons subjected to electron abstraction caused by oxidation, in-

(32) Cipiciani, A.; Linda, P.; Savelli, G. *J. Heterocycl. Chem.* **1979**, *16*, 673.
(33) Gilman, N. W.; Holland, B. C.; Walsh, G. R.; Fryer, R. J. *J. Heterocycl. Chem.* **1977**, *14*, 1157.
(34) Pfluger, P.; Street, G. B. *J. Chem. Phys.* **1984**, *80*, 544.
(35) Eaves, J. G.; Munro, H. S.; Parker, D. *Polym. Commun.* **1987**, *28*, 38.
(36) McLeod, G. G.; Jeffreys, K.; MacAllister, J. M. R.; Mundell, J.; Affrossman, S.; Petherick, R. A. *J. Phys. Chem. Solids* **1987**, *48*, 921.
(37) Hino, S.; Iwasaki, K.; Tatematsu, H.; Matsumoto, K. *Bull. Chem. Soc. Jpn.* **1990**, *63*, 2199.
(38) Tourillon, G.; Jugnet, Y. *J. Chem. Phys.* **1988**, *89*, 1905.

teraction with counterions present, and from the formation of C–O (by the oxidation of the polymer) or C–Cl bonds (obtained by the electrophilic attack of chlorine initially present as perchlorate). The peak near 288 eV could result from carbonyl moieties (e.g. amides) produced by the oxidation of the polymer and residual acetonitrile, which is known to be retained even under vacuum conditions.[39] Both of the higher binding energy peaks have also been attributed to satellite[38] or shake-up[37] peaks.

In spite of the fact that specific assignments cannot be made to the C(1s) peaks observed, the data in Table I clearly shows that the oxidized form of the polymer exhibits enhancement in the relative intensities of the higher binding energy peaks. Such behavior has been noted previously,[38] although not quantitated. Thus, reduction over a duration of 10 min increases the abundance of the 285.0 eV peak by 5% while oxidation at +1.0 V for 10 min caused a 10% decrease. Furthermore, despite the fact that some changes in the spectra are permanent, such as the covalent attachment of chlorine upon oxidation, shifts between the 285.0-eV peak and the two higher ones are reversible and, therefore, indicative of the oxidation state of the polymer. Our studies also indicate that the polymer shows analogous increases in the higher binding energy peaks upon aging.

Assuming 25% perchlorate counteranion incorporation, the oxygen content of the as-prepared polymer is calculated to be 16%, and a value close to this figure is generally obtained (20 ± 3%). While the broad peaks usually observed in the O(1s) spectra make assignments difficult, the oxidized polymer has peaks at 532.5 ± 0.2 eV, attributable to the perchlorate oxygen, and 534 ± 0.5 eV due to organic oxygenated functionalities. However, although all the perchlorate has been removed consequent to neutralization, as evidenced by the absence of any chlorine in the spectrum, the oxygen content only decreases by about 5%. The more abundant O(1s) component moves down to 531.5 ± 0.2 eV and the other peak to 533 ± 0.5 eV. Some contribution from water in the solvent which can hydrogen bond to the pyrrole units can be expected. In a previous paper,[31] we have observed that the degree of solvation of polypyrrole is a function of its oxidation state. Upon electrochemical reoxidation, the two peaks shift back to the higher energy side by 1 eV, and the total relative oxygen content of the polymer goes back close to its initial value.

Copolymerization with Pyrrole. Two types of nitro aromatics were copolymerized in 10-fold molar excesses with pyrrole. One set comprised 2- and 4-nitrostyrenes and 2- and 4-nitrobenzaldehyde, which have either a reactive double bond or an aldehyde moiety capable of interacting with pyrrole through a nucleophilic addition mechanism. The second series consisted of nitrobenzenes with methyl and/or chloro substituents on the aromatic ring. With the former set, analysis of the N(1s) regions of the XP spectra revealed 10% incorporation of 4-nitrostyrene in the copolymerization product while no reaction was detected with the ortho isomer. In the case of the nitro aldehydes, the polymeric product consisted of equal amounts of the pyrrole and nitrophenyl moieties for the 4-nitro derivative, but only a 15% reaction was observed with the ortho isomer. A steric effect is thus obvious with both 2-nitro derivatives.

The nitro group was absent in the high-resolution N(1s) spectra of polymer films resulting from copolymerizations of pyrrole with 2- and 4-nitrotoluenes, 2-chloro-4-nitrotoluene, or 2,4-dichloronitrobenzene. However, the 60:25:15 distribution of the C(1s) components observed with these reagents indicates that the oxidation state of the resulting polymer is altered. This distribution is quite similar to that obtained from polypyrrole subjected to a +1.0-V potential (see Table I). The as-prepared copolymerization products contain about 30 mol % of perchlorate (computed from Cl(2p) vs N(1s) signal intensities), and the O(1s) region showed two peaks at 532.5 and 534.0 eV. Upon reduction to the neutral form, enhancement of the 285.0 eV C(1s) peak and a shift of the O(1s) peak to 531.5 eV were observed, characteristics exhibited by polypyrrole itself (see earlier discussion). A feature of note is that no covalently bound chlorine is detectable with these copolymerization products, while covalently bound chlorine is present in polypyrrole subjected to the extra oxidation step.

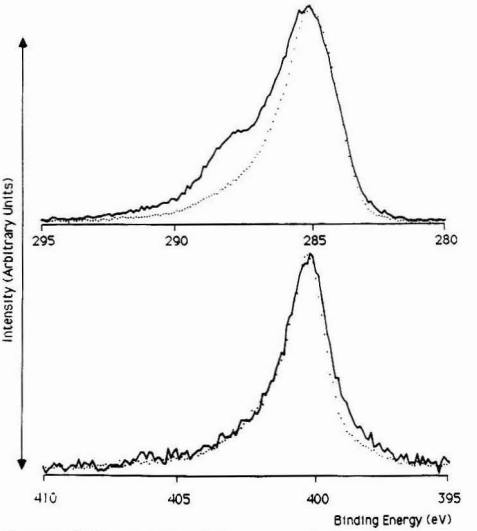

Figure 3. C(1s) and N(1s) XPS of as-prepared polypyrrole (dots) and pyrrole/4-nitrotoluene copolymer (line).

When copolymerization of pyrrole was performed with either 4-nitrophenol or 4-chloro-2-nitrotoluene, no such oxidative effect was observed. The behavior of the latter compound could be due to steric factors. The former perhaps reacts with the pyrrole skeleton through a weak acid–base interaction rather than through the nitro moiety.

As it has been postulated that nitrotoluenes become covalently attached to polypyrrole,[21] copolymerizations with furan and 3-methylthiophene were performed in order to ascertain whether these nitro aromatics become incorporated into non-nitrogenous polymer skeletons through reactions involving the nitro group. However, only 1–3% of nitrogen was observed in the spectra of the products, and this was determined to be from the solvent, acetonitrile, as equal amounts were also found in plain polyfuran and poly(3-methylthiophene) samples. The chemical shifts are also consistent with this interpretation. The low affinity of the nitrotoluenes toward polypyrrole was verified by soaking the polymer in a 4-nitrotoluene/acetonitrile solution overnight and examining the sample with XPS. The absence of a nitro signal indicates that any adsorption that does occur cannot survive ultra-high vacuum conditions. The rapid loss (over 30 min) of nitrotoluenes deposited on polypyrrole-coated 9-MHz gold piezoelectric crystals under atmospheric conditions further supports the low level of interaction between the compounds and polypyrrole.

The formation of polypyrrole with a higher degree of oxidation during the copolymerization of pyrrole with nitro

(39) Vork, F. T. A.; Janssen, L. J. J. *Electrochim. Acta* **1988**, *33*, 1513.

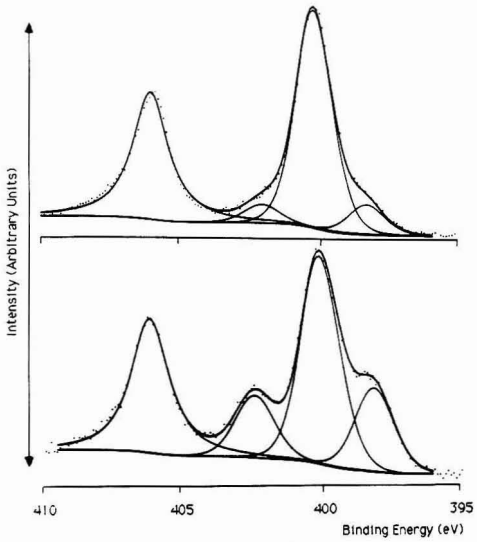

Figure 4. N(1s) spectrum of poly(bis(2,2′-pyrrolyl)(4-nitro-1-phenyl)-methane) as-prepared (top) and after reduction at −1.5 V (bottom).

aromatics may be attributed to either an increase in the polarity of the electrochemical reaction medium caused by the polar nitro compounds or an interaction between the nitro group and pyrrole (or its oligomers), in a manner analogous to that proposed for *N*-methylphenothiazine.[40] By complexing with pyrrole, the *N*-methylphenothiazine dication produces a species with a lower ionization potential than free pyrrole, and hence the polymerization is catalyzed. Although the nitrotoluene copolymerization reactions show no evidence of catalysis or incorporation of nitro compounds, a weak complex may form in solution and produce a polarization of pyrrole which will alter the ionization of the monomer or the growing oligomers.

Polymerization of Dipyrrolyl(nitrophenyl)methanes. In order to study the characteristics of a product structurally similar to that proposed by Josowicz et al.,[21] pyrrole was reacted with 2- and 4-nitrobenzaldehydes to furnish the dipyrrolyl(nitrophenyl)methanes (DPMs, see Figure 1). The polymers obtained from these DPMs possess spectral characteristics quite similar to polypyrrole, although they do not appear to achieve as high an oxidation level. The lower oxidation level can be inferred from a much lower level of anion incorporation, the perchlorate contribution being only 5% relative to the pyrrole nitrogens. The nitrogen spectra (Figure 4) clearly show nitro N(1s) binding energy peaks with intensities comprising up to 40% of the total intensity of the N(1s) region. The value appears to be higher than that expected from this structure (two pyrrolylimino moieties per nitro group) and may be the result of an enrichment of the nitro group at the surface, contributions from shake-up peaks overlapping the nitro region or the inclusion of some higher molecular weight products in the polymerization solution. Both isomeric polymers show larger enhancements on the lower binding energy side of the amino peaks (near 398 eV) than seen with polypyrrole. This may be an indication of hydrogen bonding between the oxygen of the nitro groups and the amino protons.

The C(1s) spectra of the two isomeric polymers are comprised of a relatively larger 285.0-eV component (about 78% for the as-prepared polymers) which arises from the additional carbons from the phenyl ring. While the relative intensities of the carbon peaks still change upon oxidation and reduction, the changes are only about half as large as those seen with polypyrrole. Likewise, the O(1s) spectra show a shift to lower binding energies upon reduction, which is reversible with subsequent oxidation, but it is not as pronounced as that observed with polypyrrole. The ortho isomer is particularly insensitive to oxidation and reduction and only shows shifts of a few tenths of an eV. These polymers obviously contain stable nitro oxygens which moderate the extent of changes observed in total oxygen content with oxidation and reduction.

The stability of the nitro group in the above polymers to electrochemical reducing conditions can be monitored through the N(1s) spectra. While it has been reported that reduction of a nitro group at the 3-position of pyrrole to an amino functionality requires a reducing potential of more than −2.0 V[25] (with respect to the Ag/AgCl reference electrode), the application of lower potentials to these polymers does cause some reduction, possibly to a nitroso, which is detected by a decrease in the intensity of the peak at 406 eV. Reductions at −1.5 V decrease the amount of surface nitro groups present, but this effect appears to be limited. A 10-min reduction at this potential lowers the nitro component by about 5% in the N(1s) spectrum but does not result in lowering the nitro component to less than 25% of the total nitrogen content (about 30% less than the initial value) even after several reduction cycles. The reduction also produces large enhancements on both sides of the 400-eV peak, a result of hydrogen bonding.

Lowering the nitro content to 15–20% (50% of the original level) could be observed by the application of a potential of −2.5 V. After 10 min, this higher negative potential causes severe degradation as evidenced by much broader peaks and a loss in resolution of the components. While reduction potentials of −1.5 V or lower increase the 285.0-eV component in the C(1s) spectrum with respect to the 286.5- and 288-eV components for polypyrrole and these DPM polymers, the −2.5-V potential produces carbon species with greater contributions from the higher oxidation states. This suggests that the polymers undergo some type of reaction with reagents in solution.

The effect of aging appears to be as significant as the application of reduction potentials. The nitro component decreases by about 10% of the total N(1s) signal over a period of a few months and then remains essentially stable for up to 1 year. This phenomenon also appears to be limited to eliminating the surface nitro groups to no less than 15% of the N(1s) signal, similar to the −2.5-V reduction. The relative areas of the higher binding energy components in the C(1s) spectra increase with respect to the 285-eV peak by about 10% for the para isomer and 5% for the ortho. To reduce the nitro group to insignificant levels typically requires a chemical reduction with zinc in aqueous acetic acid. The loss of the nitro signal from aging is at least partially ascribable to a restructuring of the polymer surface to reduce the interfacial energy while it is in contact with a nonpolar environment, viz. air. However, upon either oxidation or reduction after standing for several months, an increase of the nitro signal is normally obtained. A typical set of results from a series of oxidation and reduction potentials for the 4-isomer is presented in Table II, but similar behavior is also observed for the ortho case. The nitro signal appears to be stable to initial oxidation but decreases by one-fourth upon reduction and then by about one-third after standing for 1

(40) Mendes Viegas, M. F.; Genies, E. M.; Fouletier, M.; Vieil, E. *Electrochim. Acta* **1992**, *37*, 513.

Table II. Stability of Surface Nitro Groups for a Poly(*p*-trimer) Sample

conditions	% nitro of N(1s) region (±3%)	fwhm of nitro signal (eV)	fwhm of amino signal (eV)
as prepared	40	1.51	1.53
oxidized at +1.0 V[a]	40	1.62	1.62
reduced at −1.5 V[a]	30	1.74	1.68
two oxidations at +1.0 V[a]	31	1.51	1.76
2 months after oxidations	18	1.54	1.72
12 months after oxidations	16	1.36	1.68
reduced at −1.5 V[a]	23	1.66	1.77
oxidized at +1.0 V[a]	26	1.55	1.81

[a] Oxidations/Reductions performed for 10 min.

year. The partial regeneration of the surface nitro groups seems to be possible upon either oxidation or reduction and is most likely the result of restructuring induced in a polar electrolytic environment.

Reduction and aging both decrease the amount of the nitro signal measured but the values in Table II show a difference in the width of the nitro peaks resulting from the two sets of conditions. The reduction usually causes a broadening of the nitro peak, although it is reversible with oxidation, while aging normally produces only small, random changes in the widths of the peaks. As with the N(1s) spectrum of the neutral polypyrrole, this phenomenon is related to the strong hydrogen-bonding capabilities of the pyrrole units. In the neutral state, many pyrrole units in the DPMs hydrogen bond to the highly electronegative nitro group, producing a new environment for some of the moieties, which is manifested in a broader peak. The aging effect arises predominantly from surface reorientation and is partially reversed when it is subjected to the polarizing conditions of either oxidation or reduction with only minor changes in the oxidation level of the polymer such that hydrogen-bonding capabilities remain about the same. The broadening of the amino signals are independent of the electrochemical conditions although there does appear to be a general increase in fwhm values with time which probably results from greater irreversible oxidation of the polymer.

Derivatization of Polypyrrole through Reactions Involving the Amino Groups. The third method utilized to functionalize polypyrrole was through the reaction of the thin film polymers with 4-nitrobenzoyl chloride, 2,4-dinitrofluorobenzene, and 5-nitro-2-furoyl chloride. The synthetic routes are depicted in Figure 5, and the yields of the reactions under various conditions are presented in Table III. The reaction with 4-nitrobenzoyl chloride proceeds faster at elevated temperatures, and the yields could be higher than those presented, given appropriate conditions. Doubling the reflux time to ca. 40 h with 4-nitrobenzoyl chloride allows the reaction to proceed to 70%. Reaction of neutral polypyrrole with all the reagents was more facile than with the oxidized form due to its greater nucleophilic character. The dicationic bipolaron segments in the polymer must limit the available regions where the S_N2 reactions may occur. Better yields are obtained from polymers which have been reduced with zinc than those which are electrochemically reduced.

Of the three reagents studied, the reaction with 4-nitrobenzoyl chloride was the most facile. The resulting functionalized polymer surface appears to be composed of the calculated amount of carbon (72%), but the oxygen content is high (17%) and the nitrogen is low (11%) [assuming a 50% reaction, the calculated values are carbon 71%, oxygen 14% and nitrogen 14%]. The increased oxygen level results from adsorbed water or oxidation of the polymer. The oxygen level is seen to increase to about 25% over several months, and

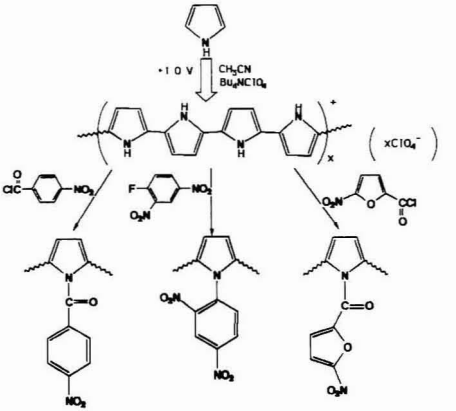

Figure 5. Reaction schemes used for the derivatization of polypyrrole.

Table III. Reaction Yields with Polypyrrole

polymer state	reactant	reaction temp, °C	% completion
neutral	4-nitrobenzoyl chloride	22	43
oxidized	4-nitrobenzoyl chloride	22	24
neutral	4-nitrobenzoyl chloride	40	69
oxidized	4-nitrobenzoyl chloride	40	56
neutral	2,4-dinitrofluorobenzene	40	28
oxidized	2,4-dinitrofluorobenzene	40	24
neutral	5-nitro-2-furoyl chloride	40	40
oxidized	5-nitro-2-furoyl chloride	40	38

Table IV. Stability of Surface Nitro Groups of Polypyrrole Reacted with *p*-Nitrobenzoyl Chloride

conditions	% nitro of N(1s) region (±3%)	fwhm of nitro signal (eV)	fwhm of amino signal (eV)
after reaction of zinc-reduced polypyrrole	33	1.45	1.91
1 min at −1.5 V	19	1.51	1.85
+15 min at −1.5 V	10	1.57	1.79
19 months later	–[a]		1.84

[a] A 4% signal at 406 eV did appear, but upon inspection of C(1s) and O(1s) regions, it was determined to be a shake-up peak.

this is probably due to oxidation of the polymer. Similar to the parent polypyrrole, the O(1s) spectrum is deconvoluted into two peaks at 531.7 and 533.0 eV which shift to higher binding energy upon oxidation to 532.4 and 534.0 eV. However, the regular shifts in the C(1s) components are no longer observed with oxidation and reduction. The shifts appear to be more random, and in fact there is a tendency for some reductions to actually decrease the 285-eV component, which indicates a much greater sensitivity to experimental conditions than is observed with the underivatized polymer.

Table IV lists the relative abundance of the nitro group for a typical sample subjected to some reducing potentials and aging. This derivative is more electrochemically-labile than the poly-DPMs, although repeated reductions seem to be limited to decreasing the nitro level to 5%. In this case, though, the reduction does not produce the broader nitro peaks recorded with the poly-DPMs; the nitro peak tended to broaden with age, but no obvious reversal of peak widths was observed upon oxidation of the reduced polymers. Aging of the samples seems to bring about complete elimination of the nitro groups from the surface.

Table V. Stability of Surface Nitro Groups of Polypyrrole Reacted with 5-Nitro-2-furanoyl Chloride

conditions	% nitro of N(1s) region (±3%)	fwhm of nitro signal (eV)	fwhm of amino signal (eV)
after reaction of electrochemically-reduced polypyrrole	30	1.75	2.11
1 min at −1.5 V	5	1.51	1.87
+5 min at −1.5 V			1.73

Reaction of oxidized polypyrrole with subsequent Soxhlet washing with acetonitrile yields a product in the neutral state. Therefore, regardless of the state of the starting polypyrrole, the modified polymer requires an additional oxidation step in order to synthesize the cationic polymer backbone. Application of a +1.0-V potential in an acetonitrile solution containing tetrabutylammonium perchlorate has a similar effect to that observed with polypyrrole itself; the level of chlorine increases to near 35% of the nitrogen level (or about 50% of the pyrrolic amines, very similar to the value obtained with polypyrrole) which is approximately evenly divided between perchlorate counteranions and the covalently-incorporated form. The neutral form of the modified polypyrrole was the one predominantly studied, and a major difference in the distribution of the anionic components was observed for this material compared to the other polymers thus far. While the other polymers were able to form hydrogen-bonded networks that were detected by large enhancements on both sides of the amino signal at 400 eV, this is not seen after reaction with nitrobenzoyl chloride. While some combinations of reductions and standing for periods of time did cause large enhancements, the 400-eV peak is generally more prominent in the spectrum (80% of the amino region versus 65% for polypyrrole itself), and this was most likely the result of steric factors from the attached nitrobenzoyl substituent preventing hydrogen bond interactions.

The next most reactive species was 5-nitro-2-furoyl chloride. The values from Table V indicate the much greater sensitivity of the nitro group to reduction; complete elimination of the nitro group is observed within 10 min at −1.5 V. While no conclusions can be drawn from the breadth of the nitro signal since it is eliminated so easily, the fwhm of the amino components decreases somewhat, indicating a more uniform environment within the polymer. However, a major difference with this more labile derivative is observed upon oxidation. While the nitro groups of all the polymers discussed so far are stable to oxidation, 10 min at +1.0 V decreases the nitro signal by about 50% in the spectrum of the 5-nitrofuroyl derivative, and further oxidation is seen to essentially eliminate the nitro signal entirely.

The third reagent utilized was 2,4-dinitrofluorobenzene, and while only about 50% as much reacted with the surface compared to the other two compounds, similar levels of nitro groups are present as this molecule obviously contains two nitro substituents. While some of the reduced yield may be attributed to the different nucleophile involved in this case, part of the reason for this behavior may be from steric hindrance resulting from the additional functionality. Reduction of this surface does decrease the nitro signal, but typically by no more than about two-thirds. This is similar to the stability exhibited by the 4-nitrophenyl derivative (see Table VI). However, an additional artefact of the electrochemical reductions is the broadening of the nitro signal. Subsequent reductions increase the peak width in the example shown from 1.96 to 2.75 eV, and this is probably also due to hydrogen bonding between the nitro groups and amino moieties. This may infuse some stability to the nitro groups and be a factor in their resistance to further reduction. There does not appear to be any correlation to the width of the amino components.

Table VI. Stability of Surface Nitro Groups of Polypyrrole Reacted with 2,4-Dinitrofluorobenzene

conditions	% nitro of N(1s) region (±3%)	fwhm of nitro signal (eV)	fwhm of amino signal (eV)
after reaction of electrochemically-reduced polypyrrole	31	1.96	1.92
3.75 min at −1.5 V	23	2.18	1.86
+3.75 min at −1.5 V	17	2.30	1.96
+15 min at −1.5 V	17	2.75	1.86

This derivatized product also shows susceptibility to oxidizing potentials. Applying a potential of +1.0 V for 10 min also eliminates about 50% of the nitro signal. These last two derivatizing agents both show a loss of the nitro group upon oxidation, but as nitro groups are normally stable to oxidizing potentials, this loss must be a result of elimination of the whole derivatized segments. Although the two species are covalently attached through different bonds, one an amide and the other a nitrogen–aryl carbon linkage, both molecules are lost at approximately the same rate. Therefore, the lability of certain species bound to polypyrrole through the nitrogen atom must arise from a property within the attached-species, and this characteristic will need to be further examined in future work.

CONCLUSIONS

The current study demonstrates that X-ray photoelectron spectroscopy can serve to distinguish between various oxidation states of polypyrrole. In addition, this technique can provide information on structural features such as inter/intramolecular hydrogen bonding and degree of surface modification, besides enabling one to follow the effects of aging and behavior of unique functionalities under different electrochemical conditions.

The results also indicate that nitro-functionalized polypyrrole surfaces could be generated either by copolymerization of pyrrole with reactive molecules like nitrobenzaldehydes or nitroethenylbenzenes (styrenes) or by derivatization of a preformed polypyrrole with nitro aromatic acid chlorides or halodinitrobenzenes through the neutral imino moieties of the polymer. A strong steric effect is observed with copolymerizations involving *o*-nitro aromatics which retards the functionalization process severely. The stability of the nitro group in *N*-(nitroaroyl)- and *N*-(nitroaryl)polypyrroles has also been shown to be dependent upon the electrochemical conditions. A third route for nitro functionalization consists of the electropolymerization of dipyrrolyl(nitroaryl)methanes, which could be synthesized by treating pyrrole with nitrobenzaldehydes. The polymers thus obtained show a limited degree of reduction under electrochemical conditions as well as aging effects.

An interesting feature in the present study is the production of a polypyrrole with a higher oxidation state when pyrrole is electropolymerized in the presence of nitrotoluenes and nitrohalobenzenes. Subsequent oxidations and reductions follow the trend noted for polypyrrole formed in the absence of any coreagents.

ACKNOWLEDGMENT

Support for this work from the Natural Sciences and Engineering Research Council of Canada is gratefully acknowledged.

RECEIVED for review May 11, 1992. Accepted August 28, 1992.

Application of Linear Prediction to Fourier Transform Ion Cyclotron Resonance Signals for Accurate Relative Ion Abundance Measurements

Thomas C. Farrar,* John W. Elling, and Mark D. Krahling

Department of Chemistry, University of Wisconsin, Madison, Wisconsin 53706

Pulse ion cyclotron resonance (ICR) time domain signals arising from a mixture of ion species typically do not exhibit the smooth exponential decay one normally observes in FTIR and pulse nuclear magnetic resonance (NMR) time domain signals. This nonexponential decay is caused by a number of factors which leads to a time variation in the relative ion intensities of the species present and to large errors in the accurate experimental measurement of those relative abundances. If pulse ICR signals of short time duration are used (e.g. the first 1K data points out of a total of 64K data points), the accuracy of the ion abundance measurements is greatly improved. It is shown that the linear prediction (LP) method gives more accurate intensity values for each frequency component of the time domain signal than those obtained from the more standard Fourier transform (FT) method, and for short acquisition times the resolution obtained with LP methods is much greater than for FT. In addition, the intensities determined by LP are much less sensitive to instrument operating conditions. The advantages of LP methods are particularly relevant to laser desorption ICR spectroscopy.

INTRODUCTION

Fourier transform ion cyclotron resonance mass spectroscopy (FTICR MS or FTMS) is now a widely used analytical tool for making mass measurements with very high resolution and mass accuracy. This work and other applications have been reviewed in the literature.[1-3] The accurate measurement of ion abundances with FTICR has, however, proven to be particularly difficult. These difficulties have limited the utility of FTICR for quantitative measurements. Several articles addressing the problem of the accuracy and precision in ion abundance measurements have recently appeared in the literature.[4-8] In this work, the difficulty in obtaining accurate relative abundance information is attributed to the averaging process of the Fourier transform methods conventionally used to convert the observed time domain signal into a frequency, or mass, spectrum. The use of linear prediction rather than a Fourier transform allows one to use time domain signals of very short duration and avoids the time-dependent distortions. This leads to much more accurate ion abundance information.

FTICR spectroscopy is typically done with ions trapped with parallel electric and magnetic fields in an analyzer cell. Ions undergo characteristic cyclotron motion in the plane perpendicular to the magnetic field. Ideally, the frequency of the ion cyclotron motion is related only to the strength of the magnetic field and the mass to charge ratio of the ion. The cyclotron motion of the trapped ions is excited with a sinusoidal excitation voltage applied across the magnetic field. Each species of ions in the cell is excited as a coherent ion packet that cyclotrons in the cell at the characteristic cyclotron frequency. The excited cyclotroning packets of ions induce a sinusoidal signal on the cell detection plates, with a characteristic frequency which is dependent upon the mass to charge ratio, m/z.

In FTICR, the digitized time domain signal is converted to the frequency domain by means of the Fourier transform.[9a,10] The Fourier transformation produces the familiar mass (or frequency) spectrum in the frequency domain, $F(\omega)$

$$F(\omega) = \int_{-\infty}^{+\infty} x(t)e^{-i\omega t}\,dt \qquad (1)$$

where ω is the cyclotron frequency of the different ion species. In practice, the integral in eq 1 is replaced by a summation over a discrete number of data points and one obtains

$$F(\omega_j) = \sum_{k=0}^{N-1} g(t_k)\,\exp(-i\omega_j t_k/N) \qquad j = 0, 1, ..., N-1 \quad (2)$$

where $F(\omega_j)$ is the intensity of the jth element in the frequency domain, $g(t_k)$ is the amplitude of the kth element in the time domain, and N is the number of data points. The discrete Fourier transform (DFT) given by eq 2 is mathematically not very efficient (it requires N^2 mathematical operations) and has been superceded by the much more efficient fast Fourier transform (FFT) developed by Cooley and Tukey.[9b]

Because the phase of the signal for each of the ion species is a complex function of ion mass and experiment timing, phase corrections for the Fourier transformation are neither linear nor simple. Consequently, the mass spectra are conventionally displayed as magnitude-mode frequency domain spectra. Since magnitude-mode peaks do not have finite integrals, the frequency domain spectra do not accurately represent the ion abundance. In most of the FTICR spectrometers currently in use the peaks are digitally integrated over a fixed frequency range. The resulting area depends on both the initial time domain amplitude, A_j, of the jth component of the time domain signal and the time domain

* To whom communications should be sent.

(1) Wilkins, C. L.; Chowdhury, A. K.; Nuwaysir, L. M.; Coates, M. L. *Mass Spectrom. Rev.* **1989**, *8*, 67–92.

(2) Asamoto, B. *Spectroscopy* **1989**, *3*, 38–46. See also: Asamoto, B.; Dunbar, R. C. *Analytical Applications of Fourier Transform Ion Cyclotron Resonance Mass Spectrometry*; VCH: New York, 1991.

(3) Laude, D. A.; Johlman, C. L.; Brown, R. S.; Weil, D. A.; Wilkins, C. L. *Mass Spectrom. Rev.* **1986**, *5*, 107–166.

(4) Huang, S. K.; Rempel, D. L.; Gross, M. L. *Am. Soc. Mass Spectrom.* **1984**, 596.

(5) Poretti, M.; Rapin, J.; Gaumann, T. *Int. J. Mass Spectrom. Ion Processes* **1986**, *72*, 187–194. Rapin, J.; Poretti, M.; Gaumann, T. *Spectrosc. Int. J.* **1984**, *3*, 124–128.

(6) Liang, Z.; Marshall, A. G. *Anal. Chem.* **1990**, *62*, 70–75.

(7) de Koning, L. J.; Kort, C. W. F.; Pinkse, F. A.; Nibbering, N. M. M. *Int. J. Mass Spectrom. Ion Processes* **1989**, *95*, 71–92.

(8) Mitchell, D. W.; DeLong, S. E. *Int. J. Mass Spectrom. Ion Processes* **1990**, *96*, 1–16.

(9) (a) Fourier, J. B. *Theorie Anal. Chaleur* **1822**. (b) Cooley, J. W.; Tukey, J. W. *Math Comput.* **1975**, *19*, 9.

(10) Marshall, A. G.; Comisarow, M. B.; Parisod, G. *J. Chem. Phys.* **1979**, *71*, No. 11, 4434–4444. See also: Marshall, A. G.; Grosshans, P. B. *Anal. Chem.* **1990**, *63*, 215A–229A.

0003-2700/92/0364-2770$03.00/0

decay rate, τ_j, of that same jth component of the time domain signal (see eq 3 below). Using the magnitude-mode peak heights to represent A_j requires that each peak have an identical line width. Since the magnitude mode peak shapes are determined by τ_j, this implies that the τ_j values for each signal component must be identical and A_j must depend only on the number of ions of each species trapped in the cell. Since neither of these two basic requirements is met, inaccuracies in ion abundance measurements made with FTICR arise.

The initial amplitude of each ion signal depends not only on the number of ions in the cell but also on the radius of its cyclotron orbit. For the mass spectrum to accurately reflect ion abundance, all the ions must be excited to the same cyclotron radius. This is difficult to achieve. The distribution of excitation power in "burst", "chirp", and tailored waveform excitation techniques is not uniform over the excited frequency range.[11-14] The uneven frequency distribution of the excitation power and the mass dependence of the excited radius results in the excitation of ions of different masses to different radii and reduces the correlation between peak area and ion abundance.

Further distortions in the relation between peak area or peak height to ion abundance arise from the unique τ_j value associated with each frequency component in the composite signal (see eq 3). The frequency domain peak shape and, consequently, the peak area, depends on the τ_j of each frequency component.[11] The τ_j value of each component depends on ion mass, relative ion abundance, charge density, and the mass distribution of the neutral background and varies in time during a transient.[7,15-17] For magnitude-mode spectra, the differences in τ_j among components of the same signal reduce the correlation between peak height or peak areas and relative ion abundance. The nonexponential decay of the signal further reduces the correlation between peak shape and the time domain signal intensity.

Various techniques have been developed to correct for the variations in τ_j between components of the same signal.[7,8] In these techniques, information about the time dependence of the power in the signal is retained by transforming parts of the time domain signal separately. Comparison of the transformed segments yields information about how the intensity of each signal changes as a function of time. For example, a time domain signal consisting of 64K (1K = 1024) data points may be divided into eight 8K segments.[8] Each segment is Fourier-transformed, and the amplitudes of the resulting low-resolution lines are obtained. The eight amplitudes of each of the signals in each 8K segment are plotted as a function of time and extrapolated to zero time. This zero-time amplitude has been found to be a much more accurate representation of the true amplitude than any of the amplitudes in the various 8K segments.

We have analyzed time domain signals using linear prediction (LP) methods rather than the more conventional Fourier transformation methods.[26] As seen below, the LP method avoids some of the problems associated with Fourier transformation of long, time domain signals.[18,19] Linear prediction is an autoregressive technique and is based on the important assumption that the time domain signal is a composite of a number of different, damped cosine signals. If this is true then a faithful representation of the time domain signal is given by the expression

$$x(t) = \sum_{j=1}^{n} A_j \exp(-t/\tau_j) \cos(\omega_j t + \phi_j) \qquad (3)$$

where $x(t)$ is the amplitude of the time domain signal at time, t, n is the number of signal components present, A_j is the initial amplitude of the jth signal component, τ_j is the decay time, ω_j is the frequency, and ϕ_j is the initial phase. As can be seen here, for each signal present, there are four degrees of freedom, an amplitude, a decay time (or line width), a frequency, and a phase. In other words, the time domain signal defined by eq 3 above is a superposition of Lorentzians. The linear prediction method is simply a way of obtaining the least squares best-fit values for the four parameters associated with each frequency component.

One popular implementation of the linear prediction method, linear prediction with singular valued decomposition (LPSVD), was introduced by Kumaresan and Tufts.[20] This method and other recently developed more efficient ones have been applied with great success to NMR spectroscopy.[21-23] All of these procedures involve the use of an autoregressive algorithm used to fit the observed transient to a known mathematical model of the signal. The ideal model of the pulse-mode ICR time domain signal is presented by eq 3 given above.

In autoregressive methods one attempts to reconstruct the entire time response from a small fraction of the total number of data points, thus the amplitude, x_n of the nth data point may be obtained from a knowledge of the preceding k data points

$$X_n = \sum_{k=1}^{M} a_k X_{N-k} + Z_n \qquad (4)$$

Note that each data point, X_n, is represented as a combination of the M previous data points, weighted by a AR coefficient, a_j, plus a residual Z_n. Equation 3 is solved by determining the AR coefficients needed to model the known data with minimum residuals. The solution technique developed by Kumaresan and Tufts[20] uses the singular value decomposition (SVD) linear least squares procedure to solve eq 4 in matrix form by minimizing the residuals of the fit of the data matrix to the predicted values.

The LPSVD technique yields a vector of AR coefficients. Without noise in the data, only two AR coefficients are needed to describe each of the K sinusoidal components. To model real data sets that include noise, as many as $0.75N$ AR coefficients are used.[20] In the case of transients with a high signal to noise ratio, the signal-related AR coefficients can be distinguished from the coefficients describing noise by their

(11) Comisarow, M. B.; Marshall, A. G. *Chem. Phys. Lett.* **1974**, *26*, No. 4, 489–491.
(12) Noest, A. J.; Kort, C. W. F. *Comput. Chem.* **1983**, *7*, No. 2, 81–86.
(13) Chen, L.; Wang, T. C.; Ricca, T. L.; Marshall, A. G. *Anal. Chem.* **1987**, *59*, 449–445.
(14) (a) Tomlinson, B. L.; Hill, H. D. W. *J. Chem. Phys.* **1973**, *59*, 2775. (b) Marshall, A. G.; Wang, T. C.; Chen, L.; Ricca, T. L. In *Fourier Transform Mass Spectrometry*; Buchanan, M. V., Ed.; ACS Symposium Series No. 359; American Chemical Society: Washington, DC, 1987; pp 21–33.
(15) Dunbar, R. C. *Int. J. Mass Spectrom. Ion Processes* **1984**, *56*, 1.
(16) Comisarow, M. B. *Lect. Notes Chem.* **1982**, *31*, 484.
(17) Laukien, F. H. *Int. J. Mass Spectrom. Ion Processes* **1986**, *73*, 81.
(18) Loo, J. F. Thesis, University of Wisconsin-Madison, Madison, Wisconsin, 1989.
(19) Loo, J. F.; Krahling, M. D.; Farrar, T. C. *Rapid Commun. Mass Spectrom.* **1990**, *4*, 297–299.
(20) Kumaresan, R.; Tufts, D. W. *IEEE Trans.* **1982**, *ASSP-30*, 671–675.
(21) Barkhuijsen, H.; de Beer, R.; Bovee, W. M. M. J.; van Ormondt, D. *J. Mag. Reson.* **1985**, *61*, 465–481.
(22) Tirendi, C. F.; Martin, J. F. *J. Mag. Reson.* **1989**, *85*, 162–169.
(23) Tang, J.; Norris, J. R. *J. Mag. Reson.* **1988**, *79*, 190–196.
(24) McLafferty, F. W.; Stauffer, D. B.; Loh, S. W.; Williams, E. R. *Anal. Chem.* **1987**, *59*, 2213–2216.
(25) Cody, R. B.; Bjarnason, A.; Weil, D. A. In *Lasers in Mass Spectrometry*; Lubman, D. M., Ed.; Oxford University: New York, 1990; pp 316–340.
(26) Farrar, T. C.; Loo, J. F.; Krahling, M. D.; Elling, J. W. U.S. Pat. No. P89083US.

magnitude. The AR coefficients describing sinusoids form a polynomial whose roots represent the frequencies and decay constants of the sinusoids making up the signal. The amplitude and phase of the sinusoids are calculated by substituting the frequency and decay constants into the model equation and doing another least squares fit to the data. Altogether then, a total of four parameters is required to define each sinusoid. The resolution is not limited by the total sampling time; this is the strength of the linear prediction method. The price one pays for this advantage is that the LPSVD procedure is computationally intensive, requiring up to N^2 calculations compared to only $N \log_2 N$ calculations for an FFT.

The advantage of using LPSVD is that the calculations may be carried out on very small data sets (64–1024 points). These data sets can be collected over a very short period of time, minimizing the effect of differences in τ_j for the various signal components and for the variation of the different τ_j as a function of time. The signal amplitudes calculated with LPSVD are therefore less susceptible to the time-dependent processes that distort the signal-to-abundance relationship when the FFT is used to analyze long transients.

EXPERIMENTAL SECTION

Experiments were performed with an Extrel FTMS 2001 Fourier transform ion cyclotron resonance mass spectrometer equipped with a 3.0 T superconducting magnet and used in the single-cell configuration.[24] A pulsed TEA CO_2 laser was used for laser desorption.[25]

Krypton gas was introduced to the vacuum system through the batch inlet at varying pressures and ionized with 70-eV electrons. Krypton of 99.999% purity was purchased from Spectra Gasses, Inc. A highly frequency-selective, tailored excitation waveform was used to apply excitation power such that only ions in the mass range from m/z 70 to m/z 90 were excited.[13,14] The time domain signal resulting from the krypton ions was mixed with a 615-kHz reference signal and digitized at a rate of 175.7 kHz for a period of 1.49 s. The signal to noise ratio (S/N) was increased by averaging (coadding) 500 time domain signals.

Laser desorption experiments were carried out using a lead sample. The lead standard reference material was obtained from the National Institute of Standards and Technology (SRM No. 981). The lead ions were excited with a rapid frequency sweep chirp excitation from 0 Hz to 2.6 MHz at 1.0 kHz/μs. The excited signal was mixed with a 244-kHz reference signal and digitized at a rate of 66.6 kHz for 0.98 s. Ions generated by a single laser desorption experiment were excited and detected without signal averaging. The LPSVD software was received from Drs. Barkhuijsen and de Beer, from the Technische Hogeschool Delft, to whom requests for copies of the program should be sent.[20]

RESULTS AND DISCUSSION

The magnitude of time-dependent variations in the signal decay rate was investigated. To this end, krypton gas at 0.7×10^{-8} Torr was ionized and approximately 6000 ions were trapped to minimize the effects of space charge on the ion signal. The time-dependent charge in intensity during the 1.49-s signal from the krypton ions was assessed by performing an FFT on sequential 8K segments of the 256K points acquired. The magnitude-mode FFT of each 8K (47 ms) segment yielded the intensity of each frequency component in that segment of the total signal. Prior to transformation, each 8K segment was zero-filled four times to minimize "picket fence" errors. The frequency resolution produced by an FFT of 8K points was sufficient to provide baseline resolution of the Kr isotope peaks.

In Figure 1 the natural log of the heights of the five major Kr isotope peaks is plotted as a function of the time between the beginning of the signal acquistion and the middle of the

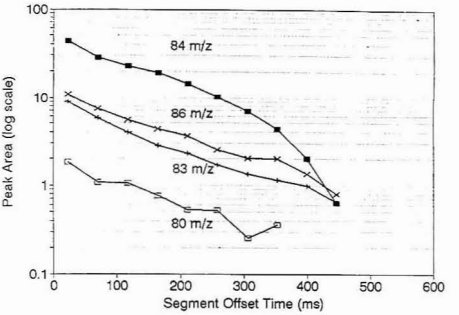

Figure 1. Natural log of the peak areas in each sequential 8K segment of the time domain signal versus the time between the start of the signal and the center of the segment. The line corresponding to the $^{82}Kr^+$ isotope signal overlies the line for the $^{83}Kr^+$ isotope and is omitted for clarity.

8K segment. On the logarithmic scale in Figure 1, a purely exponential decay would result in a linear drop in the intensity in time. Figure 1 illustrates that the variations in signal intensity from this ideal linear relationship are severe and grow with time. Similar experiments on signals generated at higher background pressures were conducted. At higher pressures the signals decay faster but in a more exponential fashion.

Techniques that perform segmented transformations of the transient[7,8] assume a constant signal decay rate in the models that extrapolate signal intensity back to the time of signal excitation. The accuracy of these techniques are limited by the nonideal behavior illustrated in Figure 1 at the low pressures needed to obtain high signal resolution.

In order to evaluate the performance of LPSVD on ICR transients, three different procedures were used to determine the relative abundance of the five most abundant Kr isotopes from a series of time domain signals generated at low Kr background pressures.

(1) The LPSVD procedure was applied to the first 512 points in the 256K point signal. The calculated amplitudes of each frequency component were used to represent relative ion abundance.

(2) The entire 1.49-s transient was Fourier-transformed without apodization. The peak areas were used to represent relative ion abundance.

(3) The first 64K points of the time domain signal were transformed in 8K segments (see Figure 1). A line was fit to the natural log of the intensity of each peak versus the segment offset time from the beginning of the signal.[8] The linear equation describing the signal decay in time was used to extrapolate each signal amplitude to the time the ICR frequency was excited. The extrapolated intensities were used to represent ion abundances.

The results in Table I illustrate the accuracy of the relative ion abundances determined with each of these methods. The data in Table I were generated from analysis of seven Kr^+ signals generated under identical conditions. The error in isotopic abundance is reported as the average error in the normalized signal intensities

$$\text{err} = \frac{\sum_{i=1}^{n} |Q_i - E_i|/E_i}{n} \qquad (5)$$

where E_i is the natural abundance of the ^{80}Kr, ^{82}Kr, ^{83}Kr, ^{84}Kr, or ^{86}Kr ions and O_i is the observed normalized intensity of each signal. The average error in all the signal intensities

(27) *CRC Handbook*, 59th ed.; CRC Press: Boca Raton, FL.

Table I. Normalized Signal Intensity of the Krypton Isotopes and the MSE from Various Treatments of the Same Seven Time Domain Signals

	normalized % intensity (std dev)					
method[a]	*m/z* 80	*m/z* 82	*m/z* 83	*m/z* 84	*m/z* 86	av error
LPSVD	2.24 (0.40)	11.98 (0.70)	11.36 (0.85)	57.88 (0.91)	16.54 (0.71)	0.044
128K FFT	2.88 (0.31)	9.61 (0.79)	9.63 (0.63)	60.84 (1.25)	14.64 (0.48)	0.166
						0.166
segmented FFT	2.18 (0.21)	10.65 (0.37)	10.80 (0.33)	60.15 (0.38)	16.21 (0.28)	0.102
						0.102
NIST[b]	2.27	11.56	11.55	56.90	17.37	

[a] See Results and Discussion. [b] See ref 27.

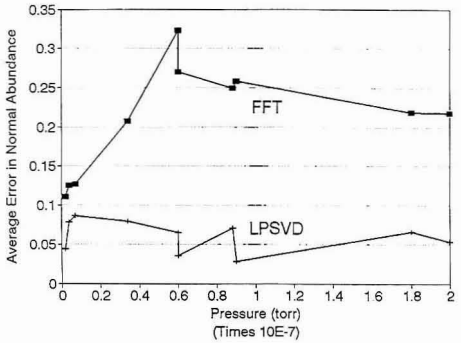

Figure 2. Effect of pressure and space charge on relative ion abundances in the magnitude-mode krypton mass spectra. The upper line is the average error in the relative abundance of the five krypton isotopes determined from the peak areas in the mass spectra obtained with an FFT. The lower line is the average error in relative abundance determined from the intensities reported by the LPSVD calculations on the same signals.

determined by LPSVD is 0.044. The average error of all the relative peak areas in the seven mass spectra is 0.166. The segmented FFT procedure produced an error of 0.102. The failure of the segmented FFT technique to produce accurate isotope abundances is expected, given the nonideal behavior shown in Figure 1. This experiment illustrates that the initial intensities of the signals are a better representation of ion abundance than the average intensity obtained by Fourier transformation of the entire signal.

High background pressure of neutrals and high space charge during the FTICR experiment increases the error in relating signal power to ion abundance. The increased error results from the increased collisional dampening which increases the mass-dependent differences in τ_j.[16] Rapid damping also limits the mass resolution, causing peak overlap in the transformed spectrum. With constant ionization conditions, increased neutral pressure also leads to the generation of a large number of ions, the space charge from which can both further increase damping and cause peak distortions.[17]

The effect of pressure and space charge on the error in Kr isotopic abundance determination is illustrated in Figure 2. In all cases the ionization conditions remained constant while the background pressure of Kr neutrals was varied. Procedures 1 and 2 described above were used to analyze each time domain signal collected at each different background pressure. Figure 2 illustrates both the superior accuracy of the LPSVD-determined signal intensities and the resistance of the LPSVD technique to changes in peak ratios with changing experimental conditions. At krypton background pressures higher than those shown in Figure 2, distortions in peak shapes became severe and the areas could not be integrated for procedure 2. Even when the peaks resulting from Fourier transformation were split, the LPSVD technique was able to produce accurate abundance information from the signal intensities.

Table II. Three LD/ICR Experiments on Lead Standard Reference Material No. 981[a]

	exp	normalized % intensity				av %
method[a]	no.	^{208}Pb	^{207}Pb	^{206}Pb	^{204}Pb	error
apodized[a]	1	57.17	17.4	23.03	2.43	24.7
128K FFT	2	64.83	9.50	20.14	5.52	96.2
	3	39.14	29.54	26.27	5.04	80.5
1K LPSVD	1	54.05	20.05	24.82	1.07	10.0
	2	53.3	21.16	23.63	1.91	10.5
	3	54.79	21.94	22.34	0.93	11.9
NIST[b]		52.3470	22.0833	24.1142	1.4255	

[a] The isotopic abundances determined by apodized FFT and LPSVD on the time domain signal are compared. [b] A three-term Blackman Harris apodization function. [c] See ref 27.

The accuracy of the LPSVD technique and resistance of the LPSVD calculations to changes in pressure and number of ions is especially valuable in laser desorption experiments. The large, irreproducible pressure bursts and variable ionization resulting from laser impact with a sample result in widely varying relative peak ratios for repeated LD/FTICR experiments. In contrast, the signal intensities that are calculated with the LPSVD method are not strongly dependent on the variable pressure and ionization that characterize the laser desorption experiment.

Several laser desorption FTICR experiments were carried out on a lead standard reference material. In Table II, the MSE in intensity ratio calculated for the ^{204}Pb, ^{206}Pb, ^{207}Pb, and ^{208}Pb peaks are shown for spectra resulting from a full 64K apodized transformation of the signal and a LPSVD performed on the first 1024 points. Of particular interest in Table II is the tremendous variation of relative peak area between LD-FTICR experiments. It is clear from the LPSVD results that these variations do not arise from variations in ion abundances and so must represent extremes in pressure and space charge distortions.

CONCLUSIONS

The use of LPSVD instead of the standard Fourier transform to evaluate ICR transients can produce significantly more accurate relative ion abundance measurements. The superior performance is especially critical when LPSVD is applied to transients collected under nonideal operating conditions such as high background pressure and large numbers of ions. The LPSVD results are more accurate than the peak areas in spectra produced by Fourier transforms and the accuracy is available over a wider range of instrument operating parameters. The LPSVD results are also resistant to variation in the relative peak areas with changes in operating conditions. The later advantage is particularly valuable when the signal-to-signal variations are uncontrollable, as in laser desorption ionization.

The advantages of LPSVD in ion abundance determination outweigh the computational disadvantage of autoregressive techniques. As refinements are made to the LPSVD algorithm and the power of the data acquisition computers increase, it will be possible to add LPSVD as an option for routine evaluation of transients.

ACKNOWLEDGMENT

The authors would like to thank Dave Weil, Extrel FTMS, for carrying out the laser desorption experiments. Susan J. Zirbel was a great help with some of the mathematics. J.W.E. is grateful to Nicolet Instruments and Extrel FTMS for a graduate fellowship. This work was supported in part by a grant from the National Science Foundation, Grant No. 8802373, and by the Wisconsin Alumni Research Foundation.

RECEIVED for review May 18, 1992. Accepted August 24, 1992.

Acousto-Optic Tunable Filter as a Polychromator and Its Application in Multidimensional Fluorescence Spectrometry

Chieu D. Tran* and Ricardo J. Furlan

Department of Chemistry, Marquette University, Milwaukee, Wisconsin 53233

Acousto-optic tunable filter (AOTF) is an electronically driven dispersive device which operates on the principle of acousto-optic interaction in an anisotropic medium. Incident white light will be diffracted by the AOTF into a specific wavelength when a specific rf is applied to it. The diffracted light needs not be a monochromatic light. Multiwavelength light can be diffracted from the AOTF when several rf signals are simultaneously applied into the filter. Compared to conventional polychromators, advantages of this electronic AOTF polychromator include its ability to individually amplitude-modulate each wavelength of the diffracted multiwavelength light at different frequency. This is accomplished by individually and sinusoidally modulating each applied rf signal at the desired frequency. This feature makes it possible to develop a novel AOTF-based multidimensional fluorimeter in which the sample was simultaneously excited by two different wavelengths (514.5 and 488.0 nm) whose amplitudes were sinusoidally modulated at two different frequencies (100 and 66 Hz). Multicomponent samples, e.g., mixtures of rhodamine 6G and rhodamine B, were successfully analyzed using this novel fluorimeter and the developed data analysis.

INTRODUCTION

Fluorescence technique has been demonstrated to be a sensitive method for trace characterization. Since realtime samples are generally present in multicomponent form, their analyses usually require measurements of the fluorescence spectra at different excitation wavelengths. This time-consuming process was alleviated with the use of the videofluorimeter.[1-5] In this instrument, the monochromators (excitation and emission) are replaced with polychromators. By appropriately configurating the two polychromators and by using a two-dimensional detector such as silicone-intensified target vidicon, emission spectra of the sample produced by the multiwavelength excitation can be simultaneously measured.[1-5] The two-dimensional spectra obtained are then analyzed with the linear algebra techniques.[6,7] The technique has proven to be a very powerful method for the determination of multicomponent trace chemical species. However, in addition to the relatively low sensitivity, the videofluorimeters normally require elaborate data analysis. Novel two-dimensional detectors such as charge-coupled devices (CCDs) and charge-injection devices (CIDs) may provide improvement in the sensitivity but also undesiredly increase the cost.[4] By use of the recently developed acousto-optic tunable filter, a novel and relatively inexpensive multidimensional fluorimeter which has a high sensitivity and simple data analysis can be developed.

Acousto-optic tunable filter (AOTF) is an electronic dispersive device.[8-17] It is based on the acousto-optic interaction in an anisotropic medium. The filter is generally constructed from such birefringent crystal as TeO_2 onto which an array of piezoelectric transducers are bonded. These transducers will transform the applied rf into acoustic wave.[8-17] The propagating acoustic waves produce a periodic moving grating which will diffract portions of an incident beam. Due to the conservation of momentum, only a very narrow band of optical frequencies can be diffracted. Therefore, the spectral bandpass of the filter can be tuned over large optical regions by simply changing the frequency of the applied rf.[8-17] The AOTF is thus similar to the diffraction grating, but in the former, the grating constant, which in this case is the frequency of the acoustic wave, can be electronically changed. Furthermore, since the scanning speed of the AOTF is controlled by the transit time of an acoustic wave across an optical beam which is on the order of few microseconds, the tuning speed of the filter can be as fast as a few microseconds.[8-17] Taken together, compared to other dispersive devices, the AOTF has such advantages as (1) compact, all solid state, rugged, and contains no moving parts; (2) wide angular field; (3) high throughput (diffraction efficiencies of the filter are generally greater than 85%); (4) wide tuning range (from UV through visible to IR); (5) high spectral resolution (bandwidth of light transmitted by the filter is about 2–6 Å); (6) rapid scanning ability (order of few microseconds); (7) light with adjustable intensity; (8) high-speed random or sequential wavelength access; and (9) imaging capability.[8-11] The AOTF has been called "the new generation" monochromator and has offered unique means to develop scientific instruments for fundamental research as well as industrial, medical, and aerospace applications. In fact, advantages of the AOTF have been exploited recently to develop a wide range of instruments which include the fast scanned multiwavelength thermal lens spectrophotometer,[12] the UV, visible and IR absorption, and circular dichroism spectrophotometers,[13-15] the astronomical photometer,[10] the multigas analyzer,[16] and the fluorescence microscope.[17]

In all applications to date the AOTF is used as a fast scanned electronic grating. That is at any given time, only a single

(1) Warner, I. M.; Callis, J. B.; Davidson, E. R.; Gauyeman, M.; Christian, G. D. *Anal. Lett.* **1975**, *8*, 665.
(2) Warner, I. M.; Patonay, G.; Thomas, M. P. *Anal. Chem.* **1985**, *57*, 463A.
(3) Ndou, T. T.; Warner, I. M. *Chem. Rev.* **1991**, *91*, 493.
(4) Warner, I. M.; McGown, L. B. *Advances in Multidimensional Luminescence*; JAI Press, Inc.: Greenwich, CT, 1991.
(5) Vo-Dinh, T. *Room Temperature Phosphorimetry for Chemical Analysis*; John Wiley: New York, 1986.
(6) Warner, I. M.; Callis, J. B.; Christian, G. D.; Davidson, E. R. *Anal. Chem.* **1977**, *49*, 564.
(7) Rossi, T. M.; Warner, I. M. *Appl. Spectrosc.* **1984**, *38*, 422.
(8) Chang, I. C. *Opt. Eng.* **1981**, *20*, 824.
(9) Sivanayayam, a.; Findley, D. *Appl. Opt.* **1984**, *23*, 4601.
(10) Bates, B.; Halliwell, D. R.; McNoble, S.; Li, Y.; Catney, M. *Appl. Opt.* **1987**, *26*, 4783.
(11) Gottlieb, M.; Feichtner, J. D.; Conroy, J. *SPIE International Optical Computing Conference* **1980**, *232*, 33.
(12) Tran, C. D.; Simianu, V. *Anal. Chem.* **1992**, *64*, 1419.
(13) Shipp, W. S.; Biggins, J.; Wade, C. W. *Rev. Sci. Instrum.* **1976**, *47*, 565.
(14) Kradjel, C. *Fresenius' J. Anal. Chem.* **1991**, *339*, 65.
(15) Hatano, M.; Nozawa, T.; Murakami, T.; Yamamoto, T.; Shigehisa, M.; Kimura, S.; Takakuwa, T.; Sakayanagi, N.; Yano, T.; Watanabe, A. *Rev. Sci. Instrum.* **1981**, *52*, 1311.
(16) Nelson, R. L. *ISA Trans.* **1986**, *25*, 31.
(17) Spring, K. R.; Smith, P. D. *J. Microsc.* **1987**, *147*, 265.

0003-2700/92/0364-2775$03.00/0

rf is applied into the filter thereby providing a diffracted beam with only a single wavelength. It is, however, possible to simultaneously apply several rf signals into the filter. This multifrequency application will enable the AOTF to simultaneously diffract more than one wavelength, thereby serving as a polychromator. Optically, this electronic polychromator is relatively easier to use than the conventional grating polychromator because in the former, the diffracted beam is not deviated by the chromaticity of the light, i.e., light with different wavelengths are diffracted from the filter at the same angle. The AOTF is thus particularly suited for the multidimensional fluorimeter. Furthermore, the diffracted light can be made to amplitude modulate at any specific frequency by simply amplitude modulating the applied rf at that same AM frequency. Thus, by AM modulating each applied rf at different AM frequency, each wavelength of the multiwavelength beam diffracted from the AOTF will be AM modulated at a different frequency. When this multiwavelength beam is used to excite the sample, the fluorescence signal will be modulated at those AM frequencies. Therefore, the data analysis will be much simpler and faster than those used in the existing multidimensional fluorimeter. However, in spite of its potentials, AOTF has not been used as a polychromator, and different AM of the AOTF has not been performed. Such consideration prompted us to investigate these possibilities, to implement the AOTF as an electronic polychromator, and to use it to develop a novel, all solid state, fast scanned multidimensional fluorimeter whose data analysis is relatively faster and simpler. Preliminary results on the instrumentation development and its utilization to characterize multicomponent samples will be reported in this paper.

EXPERIMENTAL SECTION

Experiments were designed to investigate the possibility of simultaneously applying many rf signals into the AOTF, to amplitude modulate each rf signal with a different sine wave, and to characterize the light diffracted by the filter for each case. The schematic diagram for the instrument is shown in Figure 1A. A Spectra-Physics argon ion laser (Model 165) operating in the multiline mode was used as the light source. The acousto-optic tunable filter used in this work was the same as previously. Specifically it is a noncollinear type, fabricated from a single crystal of paratellurite (TeO_2) (Matsushita Electronic Components Co., Ltd., Osaka, Japan, Model EFL-F20) and has a clear aperture of 3.0 mm × 5.0 mm. The filter resolution which is defined as the full width at half maximum, $\Delta\lambda$, is given by[8]

$$\Delta\lambda = \frac{\lambda^2}{2l\Delta n \sin^2\theta_i}$$

where λ is the wavelength of observation, l is the interaction length between the acoustic wave and the light wave, $\Delta n = n_e - n_o$, and θ in the incident angle. The filter is specified to have a resolution of 4 Å at 400 nm.[12] Since Δn, l, and θ are almost constant for the 488.0- and 514.5-nm wavelengths, the resolutions for these two wavelengths were calculated to be 6.0 and 6.6 Å, respectively. However, the difference of 0.6 Å in the resolution at the two wavelengths used should not affect the results of the present work because these two wavelengths, being derived from the argon ion laser, are monochromatic.

Two different oscillators (Osc 1 and Osc 2, MCM Electronics, Centerville, OH, Model TENMAC 72-585) were used to provide two different rf signals. These rf signals were sinusoidally amplitude modulated at two different frequencies (66 and 100 Hz) by two home-built modulators (Mod 1 and Mod 2) whose circuitries are shown in Figure 1B. Essentially, the rf signal provided by the oscillator was amplified by an amplifier (A, Mini-Circuits, Brooklyn, NY, Monolithic Amplifier MAV-11) prior to being modulated by a Mini-Circuits Model CBL-1 mixer. The modulation signal which was provided by a microcomputer (IBM AT compatible with a 386 microprocessor (Northgate Computer

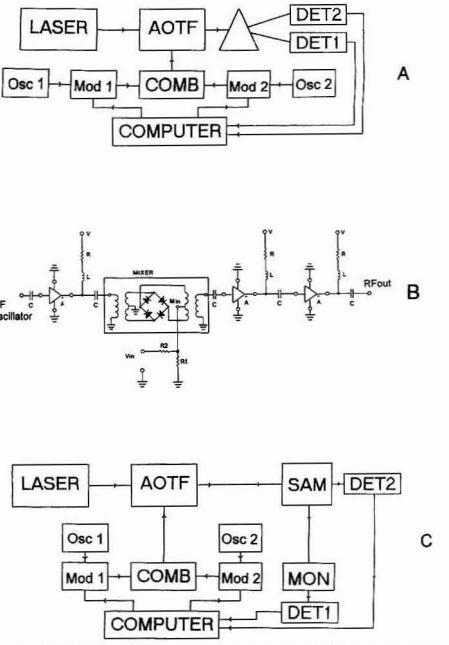

Figure 1. (A) Schematic diagram of the apparatus to characterize the light diffracted by the AOTF: AOTF, acousto-optic tunable filter; DET1 and DET2, PIN photodiode; Osc 1 and Osc 2, oscillator to provide the rf signal; Mod 1 and Mod 2, modulator to sinusoidally amplitude-modulate the rf signals; COMB, rf combiner; SAM, sample. (B) The circuitry to modulate and amplify the rf signal: C, 2200 pF capacitor; L, 1.2 μH inductor; R, R1 and R2, 100-Ω × 1/2-W, 50-Ω × 1/4-W, and 680-Ω × 1/4-W resistors; V, 11.6 V; A, Mini-Circuit MAV-11 monolithic amplifier and MIXER, Mini-Circuit CBL-1 mixer. (C) The apparatus to measure fluorescence: MON, monochromator; DET1, photomultiplier tube; DET2, PIN photodiode; other symbols are the same as in A.

Systems, Eden Prairie, MN)) through the D/A of the 12-bit DAS 16 board (Metra-Byte, Taunton, MA). The power of each modulated rf signal at this point was not adequate to drive the AOTF. Therefore, they were consecutively amplified by two amplifiers (A) to achieve a maximum power level of 20 dBm. Subsequently they were combined by means of a combiner (COMB, Mini-Circuits splitter/combiner Model ZSC-2-1) before being connected to the AOTF.

When the AOTF was applied by the signal which contains two different rf's, the diffracted light had two different wavelengths. This dual-wavelength light was dispersed into individual colors by an equilateral prism (Figure 1A). The intensities of each beam are measured by a PIN photodiode (DET1 and DET2, United Detector Technology Model 10DP).

Subsequent to the confirmation of this multifrequency diffraction and the characterization of the diffracted light, the instrument was modified for the fluorescence measurements. The set up is shown in Figure 1C. As illustrated, the sample (SAM) was excited by the sinusoidally modulated diffracted light. The fluorescence emitted was dispersed by the monochromator (Oriel model 7240) and detected by a photomultiplier tube (DET 1, Hamamatsu Model R446). A PIN photodiode (DET 2, United Detector Technology Model 10 DP) was used to measure the light transmitted through the sample for reference.

A computer program was written to provide sinusoidal amplitude modulations for the rf signals and to acquire and to analyze data. Through one A/D-D/A board (DAS-16), one subroutines of the program was developed to send the sinusoidal signals (through the D/A) to separately amplitude modulate each of the rf signals at a different AM frequency, and to acquire the

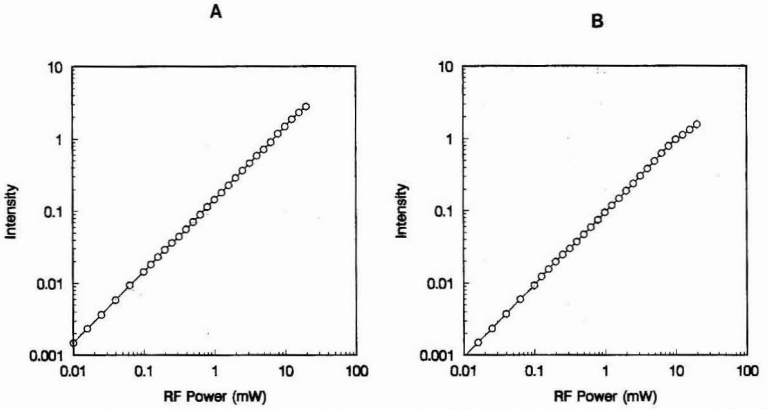

Figure 2. Relationship between the power of the applied rf and the intensity of the diffracted light for 514.5-nm beam (A) and 488.0-nm beam (B).

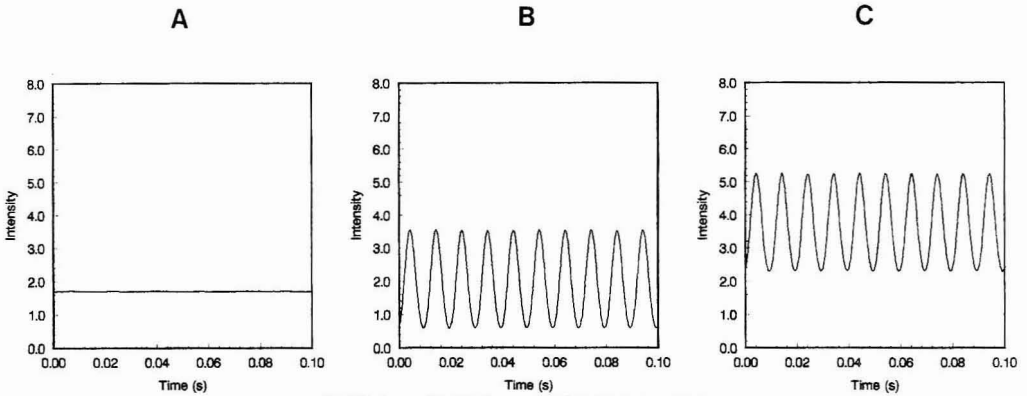

Figure 3. Intensity of the diffracted light at (A) 488.0 nm, (B) 514.5 nm, and (C) 514.5 plus 488.0 nm obtained when the AOTF was applied, respectively, with a constant-amplitude 69.200-MHz rf signal, with a 64.310-MHz rf signal modulated at 100 Hz, and with a constant-amplitude 69.200-MHz rf plus the 64.310-MHz signal modulated at 100 Hz.

data (through the A/D). The data collected was analyzed by a program whose main function is to calculate the averages of the excitation and fluorescence signals (i.e., AV_I and AV_F in eq 17 and 19 of the Appendix). Through signals summation, the program also enables the calculation of the frequency components of the excitation and fluorescence signals (i.e., Q_{I_n} in Q_{F_n} in eqs 18 and 20 of the Appendix).

RESULTS AND DISCUSSION

1. Acousto-Optic Tunable Filter as a Polychromator. The two wavelengths used in this work are 514.5 and 488.0 nm. They were obtained by applying rf frequencies of 64.310 and 69.200 MHz, respectively, to the AOTF. Initial investigation was on the relationship between the power of the applied rf and the intensity of the diffracted light. As shown in Figure 2A,B, the intensities of the 514.5- and 488.0-nm light are linearly proportional to the power of the applied rf for over four decades of power.

It was found that the AOTF will diffract light having two different wavelengths when two different rf signals are simultaneously applied into it. For example the filter will diffract light at 514.5 nm when an rf signal of 64.310 MHz is applied into it. Changing the frequency to 69.200 MHz led to the change in the wavelength to 488.0 nm. When both frequencies, 64.310 and 69.200 MHz, were simultaneously applied into the filter, the intensity of the diffracted light, as measured by the detector 2 (DET2) of the set up shown in Figure 1C, is the sum of the intensities of the 514.5-nm light and of the 488.0-nm light. To further confirm this observation, the diffracted light was dispersed by a prism using the apparatus shown in Figure 1A. It was found that the diffracted light contained two wavelengths, 514.5 and 488.0 nm, whose intensities as measured by DET1 and DET2 (of the instrument shown in Figure 1A) were the same as the intensities obtained when the filter was individually applied at a frequency of 64.310 or 69.200 MHz. It is thus evidently clear that when applied by an rf signal of multifrequencies, the AOTF will diffract multicolor light. Each color component of the diffracted light corresponds to each frequency of the applied rf. There was no interaction between one color component and others.

Subsequently, the response of the AOTF when it is applied by a sinusoidally modulated rf signal was investigated. Figure 3A shows the intensity of the 488.0-nm diffracted light when the AOTF was applied by an rf frequency of 69.200 MHz. Changing the frequency of the applied rf to 64.310 MHz and amplitude modulating it by a sinusoidal signal at 100 Hz resulted in the sinusoidal modulation of the diffracted light at the same frequency of 100 Hz (Figure 3B). When the two rf signals (i.e., the constant-amplitude rf at 69.200 MHz and

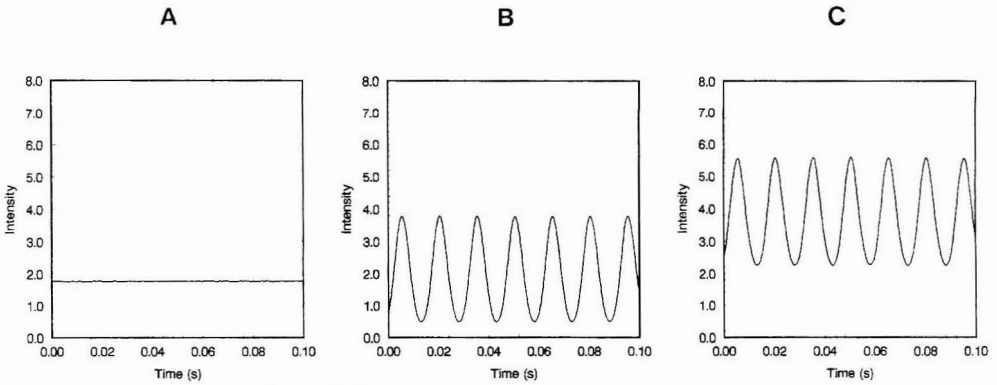

Figure 4. Intensities of the diffracted light at (A) 514.5 nm, (B) 488.0 nm, and (C) 514.5 plus 488.0 nm obtained when the AOTF was applied, respectively, with a constant-amplitude 64.310-MHz signal plus the 69.200-MHz signal modulated at 66 Hz.

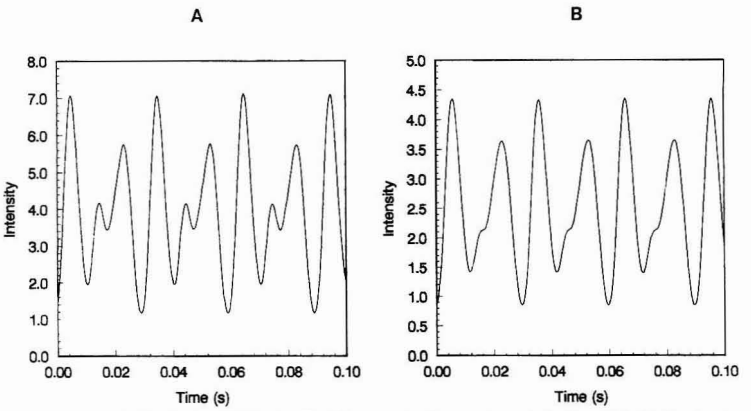

Figure 5. (A) Intensity of the light diffracted by the AOTF when the filter was simultaneously applied with a 64.310-MHz signal modulated at 100 Hz and 69.200-MHz signal modulated at 66 Hz. (B) Fluorescence intensity (at 517 mm) of a 9.88×10^{-8} M solution of fluorescein in methanol when it was excited by the light shown in A.

the sinusoidal-modulated rf at 64.310 MHz) were simultaneously applied into the AOTF, the amplitude of the diffracted light was sinusoidally modulated at 100 Hz (Figure 3C). When spectrally dispersed by a prism using the apparatus shown in Figure 1A, it was found that this diffracted beam contains two different wavelengths, 488.0 and 514.5 nm. As revealed by detectors 1 and 2 (i.e., DET1 and DET2 in Figure 1A), the 488.0-nm beam had a constant amplitude and the same intensity as the one shown in Figure 3A. The amplitude of the 514.5-nm beam was sinusoidally modulated at 100 Hz and was the same as the one previously shown in Figure 3B. Conversely, when the AOTF was simultaneously applied by two rf signals: a constant-amplitude 64.310 MHz and the sinusoidally-modulated (at 66 Hz) 69.200 MHz, the diffracted light (Figure 4C) was a combination of two different wavelengths 514.5 and 488.0 nm. The 514.5-nm beam as shown in Figure 4A had a constant amplitude whereas the 488.0-nm beam was amplitude modulated at 66 Hz (Figure 4B). When the two applied rf signals (69.200 and 64.310 MHz) were sinusoidally modulated (at 100 and 66 Hz, respectively) the diffracted light, as shown in Figure 5A, is a mixture of the two sinusoidally modulated 514.5- and 488.0-nm beams (i.e., Figures 3B and 5B). These results clearly demonstrate that by sinusoidally modulating the amplitude of the applied rf signal, the diffracted light will be sinusoidally modulated at the same frequency. The diffracted light depends only on the nature of the corresponding rf signal. It will be AM modulated at the same frequency of the amplitude modulation of the applied rf. When the applied signal was a mixture of more than one sinusoidally modulated rf's, there was no influence on one wavelength component of the diffracted light by the AM modulations of other rf signals which are not correspondent to this particular wavelength. In other words, there was no interaction or "cross talk" between the AM modulation of one rf and the others.

To illustrate the absence of cross talk and the validity of the theory and data analysis, additional experiments were performed in which different combinations and modulation indices of the sinusoidal amplitude modulations were used. The results are listed in Table I. In all of the cases listed in Table I, the AOTF was simultaneously applied by two different rf's: 64.310 and 69.200 MHz. Using the apparatus shown in Figure 1A, the diffracted light was spectrally resolved into two wavelengths, 514.5 and 488.0, whose intensities were detected by detector 1 and 2 (DET1 and DET2), respectively. The output signals of the detectors were fed into the computer for data analysis using methods described in the theory and experimental section. As listed in Table I, in case 1, the AOTF was simultaneously applied with two rf's, 64.310 and 69.200 MHz. The amplitude of the 69.200-MHz signal was kept

Table I. Types of the Applied rf Signals and Properties of Light Diffracted from the AOTF

	amplitude of sinusoidal modulation		intensity					
			detector 1			detector 2		
				modulated component			modulated component	
case	514.5 nm (100 Hz)	488.0 nm (66 Hz)	average	100 Hz	66 Hz	average	100 Hz	66 Hz
1	1.00	0.00	3.524	1.960	0.000	2.162	0.000	0.000
2	0.75	0.00	3.120	1.484	0.000	2.162	0.000	0.000
3	0.50	0.00	2.822	0.994	0.000	2.159	0.000	0.000
4	0.25	0.00	2.646	0.499	0.000	2.159	0.000	0.000
5	0.00	0.00	2.593	0.000	0.000	2.159	0.000	0.000
6	0.00	1.00	2.583	0.000	0.000	3.011	0.000	1.836
7	0.00	0.75	2.590	0.000	0.000	2.642	0.000	1.391
8	0.00	0.50	2.580	0.000	0.000	2.372	0.000	0.933
9	0.00	0.25	2.587	0.000	0.000	2.215	0.000	0.470
10	0.00	0.00	2.593	0.000	0.000	2.159	0.000	0.000
11	1.00	1.00	3.539	1.969	0.000	3.020	0.000	1.841
12	1.00	0.75	3.538	1.968	0.000	2.652	0.000	1.396
13	0.50	1.00	2.823	0.994	0.000	3.017	0.000	1.839
14	0.25	0.75	2.646	0.499	0.000	2.645	0.000	1.393
15	0.00	0.00	2.593	0.000	0.000	2.159	0.000	0.000

constant while the 64.310-MHz signal was sinusoidally modulated at 100 Hz (at the modulation level of 1.00). The output signal of the detector 1 which detected the 514.5-nm beam was analyzed for the average component of the signal (i.e., AV_I in eq 17 of the Appendix). The modulated components of the signal at 100 and at 66 Hz (i.e., Q_I in eq 18 of the Appendix) were also analyzed. Similarly, the signal output of detector 2 which detected the 488.0-nm beam was analyzed for the average, and the modulated components at 100 and at 66 Hz. As expected, in this case, only the intensity of the light at 514.5 nm was modulated (at 100 Hz) because the sinusoidal modulation was applied to the 64.310-MHz signal. The 488.0-nm light was not detected at the detector 1. At the detector 2, which detected the 488.0-nm beam, only a constant light intensity was detected. No modulation at either 100 or 66 Hz was observed at this detector. As expected from eq 18, decreasing the AM modulation index (i.e., m) by 25% (case 2), 50% (case 3), and 75% (case 4) led to 24.3%, 49.3%, and 74.5% decreases, respectively, in the modulation component of the 514.5-nm beam at 100 Hz. There was no change in the average intensity of the 488.0-nm beam as detected by detector 2. In cases 6–9, the amplitude of the 64.310-MHz signal was kept constant while the 69.200-MHz signal was sinusoidally modulated at 66 Hz (at different magnitudes, i.e., different m values). As expected, detector 1 detected only a constant magnitude signal at 514.5 nm. There were no modulated components at either 100 or 66 Hz at this detector. Conversely, detector 2, which detected the 488.0-nm beam, detected the signal which was modulated at 66 Hz. There was no modulation of this 488.0-nm signal at 100 Hz. The magnitude of the 66-Hz-modulated 488.0-nm signal was decreased to 75.8%, 50.8%, and 25.6% of the 100% modulation value (i.e., 1.836 in case 6) as the modulation index decreased to 75% (case 7), 50% (case 8), and 25% (case 9), respectively. In cases 11–14, both rf signals were sinusoidally modulated. The 64.310-MHz signal was modulated at 100 Hz while the 69.200-MHz signal was modulated at 66 Hz. As expected, the 514.5-nm beam was modulated only at 100 Hz, not at 66 Hz (detector 1) whereas the 488.0-nm beam was modulated only at 66 Hz (detector 2). Decreasing the modulation index of the 514.5- and 488.0-nm beam by 75% and 25%, respectively (case 14), resulted in the decrease in the magnitudes of the modulated signals at 100 Hz (for the 514.5-nm beam) and at 66 Hz (for the 488.0-nm beam) by 74.7% and 24.3%, respectively. Only constant 514.5- and 488.0-nm beams were detected where neither the 64.310- nor the 69.200-MHz signals were sinusoidally modulated (case 15).

Collectively we have successfully demonstrated that the AOTF can be used as a polychromator, i.e., the filter can simultaneously diffract more than one wavelength at the same time. Compared to the conventional gratings, the AOTF, in addition to its inherent advantages such as all solid state, compact, fast scanning capability, and containing no moving parts, can also provide some unique features, namely the multiwavelength beam diffracted from the filter is well collimated (i.e., all wavelengths will be diffracted from the filter at approximately the same angle). Furthermore, by amplitude modulating each applied rf signal at different frequency, each wavelength of the diffracted multiwavelength beam will be modulated at different frequency. It should be noted that in this study the laser was used as a light source. However, the AOTF is not limited to this type of light source. Due to the relatively large acceptance angle, the AOTF can be utilized with other light sources which do not provide well-collimated beams, e.g., incandescent and arc lamp. These features enable the AOTF to serve as a unique means in the development of novel instruments. In the following section, the AOTF is used as a novel polychromator to construct a novel multidimensional fluorescence spectrophotometer. The instrumentation development and preliminary results will be described.

2. Multidimensional Fluorescence Spectrophotometer Based on the AOTF. Fluorescence signals of 9.88×10^{-8} M solution of fluorescein in ethanol were measured at 517 nm using the apparatus shown in Figure 1C. It was found that there was no modulation in the fluorescence signal of the sample when it was excited by a constant-amplitude (no modulation) 514.5-nm beam (i.e., the beam whose intensity was shown previously in Figure 4A). The lack of the modulated component is further confirmed when the fluorescence signal was analyzed, according to the method described in the previous section, to calculate the average (i.e., AV_F) and modulated components (Q_F). The analyzed results were listed in Table II. As listed, the fluorescence signal belongs to case 1 where there was no modulation in the fluorescence signal at either 66 or 100 Hz; the constant (i.e., average) is the only component in the signal. When the sample was excited by the 488.0-nm beam sinusoidally modulated at 66 Hz (whose intensity profile was shown previously in Figure 4B), the fluorescence signal seems to modulate at the same frequency. This is case 5 and as the calculated results illustrate, the fluorescence signal does, in fact, modulate at 66 Hz. When both of these excitation beams were simultaneously applied into the sample, the fluorescence signal obtained is expected to be the combination of the two previous

Table II. Fluorescence Intensities (at 517.0 nm) of a 9.88×10^{-8} M Solution of Fluorescein in Ethanol

	excitation light		fluorescence		
				modulated component	
case	514.5 nm	488.0 nm	average	100 Hz	66 Hz
1	on, no modulation	off	0.835	0.000	0.000
2	off	on, no modulation	1.363	0.000	0.000
3	on, no modulation	on, no modulation	2.228	0.000	0.000
4	on, modulated at 100 Hz	off	0.905	0.294	0.000
5	off	on, modulated at 66 Hz	1.560	0.000	0.616
6	on, modulated at 100 Hz	on, no modulation	2.308	0.306	0.000
7	on, no modulation	on, modulated at 66 Hz	2.391	0.000	0.617
8	on, modulated at 100 Hz	on, modulated at 66 Hz	2.475	0.302	0.616

signals. The analyzed results (case 7) show that this is, in fact, the case. That is the average component of the signal (2.391) is the sum of the average component of 0.835 in case 1 and 1.560 in case 5. The signal is expectedly modulated at 66 Hz and its modulated component at this frequency (0.617) is the same as that of case 5 (0.616). Similar results were obtained when the sample was excited by a constant-amplitude 488.0-nm beam (case 2); by the 514.5-nm beam modulated at 100 Hz (case 4), and by the combination of both of these beams (case 6). Figure 5B and case 8 illustrate the fluorescence signal of the sample when it was simultaneously excited by the modulated (at 100 Hz) 514.5-nm beam and the modulated (at 66 Hz) 488.0-nm beam (the intensity profile of this combined excitation beam was shown in Figure 5A). The calculated signal shows that, as expected, the average component (2.475) is, within experimental error, the sum of the individual cases (i.e., 0.905 in case 4 and 1.560 in case 5). The fluorescence signal is modulated at 100 Hz as well as at 66 Hz. However, the 100-Hz modulation is due to the 100-Hz 514.5-nm excitation beam (i.e., compare the 0.302 in case 8 and 0.306 in case 6) and the 66-Hz 488.0-nm beam is responsible for the 66-Hz modulation component in the signal (0.616 in case 8 and 0.616 in case 5). There was no cross talk between the modulation of one beam and the fluorescence induced by the other beam.

Taken together, the results obtained provide a clear and unequivocal evidence for the fact that the AOTF-based fluorimeter is capable of simultaneously measuring fluorescence signals at two different wavelengths and for the validity of the derived theory and data analysis. Subsequently, the instrument was used for the determination of one- and two-component samples. Three different dyes, namely fluorescein, rhodamine 6G, and rhodamine B, were selected for this preliminary study. For fluorescein, calibration curves at two different wavelengths, 514.5 and 488.0 nm, were constructed from the measured fluorescence signals using the (calculated) modulated components at 514.5 nm (100 Hz) and at 488.0 nm (66 Hz). Linear relationship (not shown) was obtained for both wavelengths (correlation coefficients are 0.9986 and 0.9987, respectively) for the concentrations range from 9.88×10^{-9} to 7.41×10^{-7} M.

Simultaneous determination of concentrations of each component in the two-component mixture was then performed using this AOTF-based fluorimeter. Rhodamine B and rhodamine 6G were the two dyes selected for this determination. Individually, these two dyes exhibit a linear relationship between the concentration and the fluorescence intensity detected at 563 nm and excited at 514.5 and 488.0 nm. Correlation coefficients at 514.5- and 488.0-nm excitation were found to be 0.999 95 and 0.999 97 (for rhodamine 6G) and 0.999 99 and 0.999 99 (for rhodamine B) for the concentration range of 1.02×10^{-8} to 1.02×10^{-6} M. Four different mixtures of the two dyes having different relative concentrations were prepared. Using the method described in the theory section, the concentrations of each component in the mixtures were calculated from the measured fluorescence intensities at 514.5- and 488.0-nm excitation. The obtained concentrations are listed in Table III together with the added concentrations. In all cases and for concentrations of each component ranging from 5.1×10^{-9} to 5.1×10^{-8} M, good agreement was found between the added concentration and the calculated values.

Table III. Simultaneous Determination of Rhodamine B and Rhodamine 6G by AOTF-Based Fluorescence Spectrometry

	added		found	
sample no.	rhodamine B $\times 10^8$ M	rhodamine 6G $\times 10^8$ M	rhodamine B $\times 10^8$ M	rhodamine 6G $\times 10^8$ M
1	0.51	1.30	0.56	1.27
2	1.30	2.55	1.37	2.52
3	3.85	5.10	3.89	4.93
4	5.10	3.85	5.59	3.56

CONCLUSIONS

We have successfully demonstrated that it is possible to diffract light with more than one wavelength from the AOTF by simultaneously applying more than one rf signals into the filter. In this way, the AOTF behaves as a polychromator. This electronic polychromator inherently has more advantages compared to the conventional polychromators. As an example, each wavelength of the diffracted light can be readily and individually amplitude modulated at different frequency by individually and sinusoidally modulating each applied rf signal at the desired frequency. This feature makes this electronic polychromator uniquely suited for the development of a novel multidimension fluorescence spectrophotometer. A novel AOTF-based multidimension fluorimeter was successfully developed in which the sample was simultaneously excited by two different wavelengths whose amplitudes were modulated at two different frequencies. This fluorimeter was used for the determination of a sample having two different components. It should be noted that the objective of the present work is to demonstrate the principle and feasibility of the technique. Therefore, only two different rf signals (and hence two different wavelengths) were used. In principle, the AOTF can have truly multiwavelength capability. This is based on the fact that the total number of wavelengths of the diffracted light is determined by the total power of the applied rf for which the AOTF can tolerate. For this particular AOTF, the maximum rf power is 200 mW. Since each applied rf used in this work has a power of 20 mW, up to 10 different rf signals can be simultaneously applied, and hence, up to 10 different wavelengths can be diffracted from the filter. Higher rf power can be applied to a filter when it is specially constructed to exploit the resonance acoustic feature. In this study, a laser was used as the light source. However, the use of the AOTF is not restricted to this source. This is because the AOTF is known to have a relatively large acceptance angle compared to conventional

acousto-optic deflectors based on Bragg cells. In fact, it has been reported that an acceptance angle as large as 28° was achieved for AOTF.[18] As a consequence, the filter can be used for other light sources which do not provide low-diverging, well-collimated beams, e.g., incandescent and arc lamp. Furthermore, in the present work the AOTF is used only for the selection of the excitation wavelengths. A conventional monochromator was still utilized for the dispersion of the emission wavelengths. Advantages of the AOTF-based multidimension fluorescence spectrophotometer can, therefore, be fully achieved when (1) a continuous light source is used for excitation; (2) the emission monochromator is replaced with an AOTF; and (3) multi-rf signals are applied to both excitation and emission AOTFs. These are the subject of our intense investigation.

ACKNOWLEDGMENT

We are grateful to the National Institutes of Health, National Center for Research Resources, Biomedical Research Technology, for financial support of this work.

APPENDIX

Theory of Modulation and Data Analysis. The AOTF will diffract light with one wavelength when it is applied by a rf signal. The wavelength of the light diffracted from the AOTF is a function of the frequency of the rf signal. Increasing the frequency of the rf signal decreases the wavelength of the diffracted light. The efficiency of the diffraction is proportional to the power of the rf signal (e.g., for powers less than 20 mW for the AOTF used in this work). The wavelength and the intensity of the diffracted light can, therefore, be controlled by controlling the frequency and power of the applied rf signal, i.e.

$$I(\lambda_n) = I_o(\lambda_n)K(\lambda_n)P(\lambda_n) \quad (1)$$

where $I(\lambda_n)$ is the intensity of light of wavelength λ_n diffracted by the AOTF; $I_o(\lambda_n)$ is the intensity of the incident light at wavelength λ_n; $K(\lambda_n)$ is the proportional factor for wavelength λ_n; and $P(\lambda_n)$ is the power of the applied rf signal for wavelength λ_n.

If the applied rf signal is the mixture of different frequencies, i.e.

$$\mathrm{RF}_{\mathrm{signal}} = P_1 + P_2 + P_3 + ... + P_n \quad (2)$$

then the intensity of the light diffracted by the AOTF (I_{out}) is the sum of each individual signals $I_{\lambda_1}, I_{\lambda_2}, I_{\lambda_3}, ..., I_{\lambda_n}$, which correspond to the applied rf power P_1, P_2, P_3, ..., P_n, respectively.

$$I_{\mathrm{out}} = I_{\lambda_1} + I_{\lambda_2} + I_{\lambda_3} + ... + I_{\lambda_n} \quad (3)$$

Furthermore, if the applied rf signal varies with time, the intensity of the diffracted light also varies

$$I_{\mathrm{out}}(t) = I_{\lambda_1}(t) + I_{\lambda_2}(t) + I_{\lambda_3}(t) + ... + I_{\lambda_n}(t) \quad (4)$$

When the light $I_{\lambda_n}(t)$ whose intensity is a function of time (at a time scale much longer than the fluorescence lifetime of the compound) is used to excite a fluorescence sample having concentration c, the fluorescence intensity can be written as

$$F_{\lambda_n}(t) = L_{\lambda_n} I_{\lambda_n}(t) \quad (5)$$

where $L_{\lambda_n}(t)$ is proportional to the sample concentration and is dependent on the fluorescence properties of the sample.

(18) Katzka, P. *Proc. SPIE* **1987**, *752*, 23.

When the compound is simultaneously excited by more than one wavelength ($I_{\lambda_1}, I_{\lambda_2}, I_{\lambda_3}, ..., I_{\lambda_n}$), the fluorescence signal obtained (at one emission wavelength) is the sum of each signal induced by each excitation wavelength, i.e.

$$F(t) = F_{\lambda_1}(t) + F_{\lambda_2}(t) + F_{\lambda_3}(t) + ... + F_{\lambda_n}(t) \quad (6)$$

$$= L_{\lambda_1} I_{\lambda_1}(t) + L_{\lambda_2} I_{\lambda_2}(t) + L_{\lambda_3} I_{\lambda_3}(t) + ... + L_{\lambda_n \lambda_n}(t) \quad (7)$$

It will be demonstrated in the following section that by sinusoidally modulating the applied rf signal, the fluorescence signals, $F_{\lambda_1}(t)$, $F_{\lambda_2}(t)$, $F_{\lambda_3}(t)$, ..., induced by each excitation beam $I_{\lambda_1}(t), I_{\lambda_2}(t), I_{\lambda_3}(t), ...$, can be extracted from the measured total fluorescence $F(t)$.

To enable the AOTF to diffract light at wavelength λ_n, an rf signal with frequency f_n is needed

$$\mathrm{RF}_n(t) = V_{\mathrm{no}} \sin (2\pi f_n t) \quad (8)$$

The amplitude of this rf signal is sinusoidally modulated at frequency ω_n. The modulation sine wave is supplied by the computer and has the form

$$M_n(t) = 1 + m_n \sin (\omega_n t) \quad (9)$$

where m_n is the modulation index and ω_n is the angular frequency.

Upon amplitude modulation by this sine wave, the rf signal becomes

$$V_n(t) = V_{\mathrm{no}} M_n(t) \sin (2\pi f_n t) \quad (10)$$

The diffraction efficiency of the AOTF is known to be proportional not to the intensity of the rf signal (in volts) but rather to the power of the rf signal.

Assuming that the change in the diffraction of the AOTF induced by the frequency of side bands generated by this sinusoidal modulation is very small and when $f_n \gg \omega_n/2\pi$, the averaged rf power in one cycle is approximated as

$$P_n(t) = P_{\mathrm{no}}[M_n(t)]^2 \quad (11)$$

where $P_{\mathrm{no}} = V_{\mathrm{no}}^2/2R$; R is the impedance of the AOTF.

$$P_n(t) = P_{\mathrm{no}}(1 + m_n \sin (\omega_n t))^2 =$$
$$P_{\mathrm{no}}(1 + m_n^2/2) + 2m_n \sin (\omega_n t) - m_n^2/2 \cos (2\omega_n t) \quad (12)$$

When this modulated signal is applied to the AOTF, the diffracted light is modulated and its intensity is described as

$$I_{\lambda_n}(t) = I_{\lambda \mathrm{no}}\{1 + m_n^2/2 + 2m_n \sin (\omega_n t) - m_n^2/2 \cos (2\omega_n t)\} \quad (13)$$

The average of this light intensity is

$$\mathrm{AV} = \frac{1}{T}\int_t^{t+T} I_{\lambda_n}(t)\, dt = I_{\lambda_{\mathrm{no}}}(1 + m_n^2/2) \quad (14)$$

where $T = 2\pi X_n/\omega_n$ and X_n is an integral number greater than 0.

The sinusoidally modulated component of the intensity is

$$Q_n = \frac{1}{T}\int_t^{t+T} I_{\lambda_n}(t) \sin (\omega_n t)\, dt = I_{\lambda_{\mathrm{no}}} m_n \quad (15)$$

It is interesting to point out that there is no modulated component at frequencies other than ω_n and at wavelength other than λ_n. That is the value Q is zero for wavelength different from λ_n and for sinusoidal modulation $\omega \neq \omega_n$.

When more than one rf signal is simultaneously applied to the AOTF, the light intensity becomes

$$I(t) = I_{\lambda_1}(t) + I_{\lambda_2}(t) + ... + I_{\lambda_n}(t) \quad (16)$$

and the averaged component is

$$AV_1 = \frac{1}{T}\int_t^{t+T} I(t)\,dt = I_{\lambda 10}(1 + m_1^2/2) + I_{\lambda_{20}}(1 + m_2^2/2) + \ldots + I_{\lambda_{no}}(1 + m_n^2/2) \quad (17)$$

where

$$T = \frac{2\pi}{\omega_1}X_1 = \frac{2\pi}{\omega_2}X_2 = \ldots = \frac{2\pi}{\omega_n}X_n$$

where X_1, X_2, ..., X_n are lowest integral numbers (greater than 0).

The modulated component is

$$Q_{I_n} = \frac{1}{T}\int_t^{t+T} I(t)\sin(\omega_n t)\,dt = I_{\lambda_{no}} m_{no} \quad (18)$$

When this diffracted light is used to excite the sample, the corresponding averaged component of the fluorescence signal is

$$AV_F = \frac{1}{T}\int_t^{t+T} F(t)\,dt = L_{\lambda_1} I_{\lambda_{10}}(1 + m_1^2/2) + L_{\lambda_2} I_{\lambda_{20}}(1 + m_2^2/2) + \ldots + L_{\lambda_n} I_{\lambda_{no}}(1 + m_n^2/2) \quad (19)$$

and the modulated component is

$$Q_{F_n} = \frac{1}{T}\int_t^{t+T} F(t)\sin(\omega_n t)\,dt = L_{\lambda_n} I_{\lambda_{no}} m_{no} \quad (20)$$

The m_n and $I_{\lambda_{no}}$ values are known from the applied rf signals and the light source. The Q_{F_n} value can be determined by integrating the fluorescence signals as described in eq 20. From Q_{F_n}, $I_{\lambda_{no}}$, and m_n values, an L_{λ_n} value can be obtained. However, because the laser intensity, i.e., $I_{\lambda_{no}}$, can fluctuate with time, it is more accurate to determine L_{λ_n} from

$$L_{\lambda_n} = \frac{Q_{F_n}}{Q_{I_n}} \quad (21)$$

where Q_{F_n} and Q_{I_n} are obtained by integrating the fluorescence and excitation light intensity as described in eqs 20 and 18, respectively.

The L_{λ_n} value is proportional to the sample concentration C and is dependent on the fluorescence properties of the sample excited at wavelength λ_n.

Therefore

$$L_{\lambda_n} = l_{\lambda_n} C \quad (22)$$

where l_{λ_n} is constant which is independent of sample concentration and is dependent on the fluorescence of the sample excited at λ_n. Since each l_{λ_n} can be independently determined from calibration curves, sample concentration can be obtained from Q_{F_n} and Q_{I_n}.

The treatment can be extended for cases where the sample is a mixture of many components whose concentrations are C_1, C_2, ..., C_n. In this case

$$\begin{aligned} L_{\lambda_1} &= l_{\lambda_{11}} C_1 + l_{\lambda_{12}} C_2 + \ldots + l_{\lambda_{1n}} C_n \\ L_{\lambda_2} &= l_{\lambda_{21}} C_1 + l_{\lambda_{22}} C_2 + \ldots + l_{\lambda_{2n}} C_n \\ L_{\lambda_n} &= l_{\lambda_{n1}} C_1 + l_{\lambda_{n2}} C_2 + \ldots + l_{\lambda_{nn}} C_n \end{aligned} \quad (23)$$

Since L_{λ_1}, L_{λ_2}, and L_{λ_n} values are obtained from Q_{F_n} and Q_{I_n}, concentration for each componentcan be calculated.

RECEIVED for review May 20, 1992. Accepted August 20, 1992.

Horizontal Polymerization of Mixed Trifunctional Silanes on Silica: A Potential Chromatographic Stationary Phase

Mary J. Wirth* and Hafeez O. Fatunmbi

Department of Chemistry & Biochemistry, University of Delaware, Newark, Delaware 19716

A new design for surface bonding of monolayers, applicable to chromatographic stationary phases, is reported. This design is shown to combine the superior hydrolytic stability of self-assembled monolayers with the selectivity and reproducibility of monomeric stationary phases. While the new methodology is applicable to any type of functionality, it is demonstrated here for C_{18} on a flat silica surface. The phases are bonded by using horizontal polymerization: a mixture of $CH_3(CH_2)_{17}SiCl_3$ and $CH_3(CH_2)_2SiCl_3$ in anhydrous *n*-hexadecane is reacted with silica. The reagents and silica are dry, except for a surface monolayer of water on the silica, to ensure that the polymerization reaction occurs only at the surface. The C_3 groups act as spacers to control the density of the C_{18} groups. The origin of the higher stability is the higher density near the surface. The C_{18} bonding density can, in principle, be varied from 0 to 7 μmol/m^2 by varying the proportions of the reagents. For a C_{18} density comparable to that of monomeric C_{18} phases used in chromatography, it is shown by FTIR spectroscopy that the horizontally polymerized phase has remarkably better hydrolytic stability than the conventional monomeric phase for both acid and base hydrolysis.

INTRODUCTION

Chromatographic bonded phases undergo hydrolysis at a rate sufficiently high as to hamper chromatographic applications as well as spectroscopic studies of chromatographic surfaces. For example, the C_{18} surface coverage decreases even at neutral pH, as shown by both increased base retention and decreased hydrocarbon signal in FTIR spectroscopy.[1] Hydrolysis is catalyzed both by acid and base.[2]

Improvement in hydrolytic stability at low pH is important to the separation of basic compounds such as pharmaceuticals, agricultural chemicals, and proteins and peptides. Separation of these types of samples at pH < 4 results in better peak shape and retention behavior, presumably because the surface silanols are protonated.[3] Improvement in hydrolytic stability at high pH, which is important in capillary zone electrophoresis and protein chromatography, has been achieved by forming a direct silicon–carbon bond at the surface.[4] Alternatively, polymeric C_{18} phases have improved hydrolytic stabilities at low pH;[5] however, the selectivity differs from that of monomeric phases.[6] Polymeric phases also have the reputation of being irreproducible. A hydrolytically stable monomeric phase of optimal surface coverage would be valuable for chromatographic applications.

To achieve improved stability, a principle can be learned from advances in self-assembled alkyl monolayers. A very dense C_{18} monolayer forms a virtually solid barrier to the substrate upon reacting $CH_3(CH_2)_{17}SiCl_3$ in anhydrous *n*-hexadecane with humidified silica.[7-11] The intrinsic monolayer of water known to be adsorbed to silica[12] provides the reagent water needed for the hydrolysis. The term "horizontal polymerization" has been used to convey the notion that a monolayer film is achieved when anhydrous reagents are used because the reaction is restricted to the surface. Polymeric stationary phases used in chromatography, by contrast, are made by using deliberately wet solvents to allow for some polymerization before the reagents attach to the surface. Since the alkylsiloxane polymers from the solution would likely attach to the surface at only one point as the reaction proceeds, this process is commonly referred to as vertical polymerization. The carbon content of polymeric stationary phases is higher than that of monomeric phases, but one can expect from the synthesis that the density at the surface is much lower than that for the horizontally polymerized monolayer.

For horizontal polymerization, Moaz and Sagiv[7,8] showed by FTIR that a nearly solid layer of alkyl chains in an all-trans conformation quickly forms on silica in contact with $CH_3(CH_2)_{17}SiCl_3$ in anhydrous hexadecane. The Whitesides group has shown by ellipsometry that this dense C_{18} layer on silica has a thickness of 20 Å and, by X-ray reflection,[9] that the density is 21 ± 3 Å^2/chain (7.9 ± 1.1 μmol/m^2).[10] Kessel and Granick confirmed this by showing that the spectra of the C_{18} self-assembled monolayer is virtually identical to that of a cadmium arachidate Langmuir–Blodgett film compressed to a density of approximately 22 Å^2/chain (7.6 μmol/m^2).[11] The Whitesides group also reported that the dense film was only slowly removed by concentrated HNO_3, but the decomposition was nonuniform. The horizontally polymerized C_{18} surface thus achieves excellent hydrolytic stability; however, it is much too dense for chromatographic applications. Typical surface coverages in chromatography are on the order of 55 Å^2/chain (3 μmol/m^2). A modification of the horizontal polymerization scheme is needed to achieve optimal chromatographic retention and hydrolytic stability simultaneously.

The purpose of this work is to investigate whether horizontal polymerization can be applied to the design of a more hydrolytically stable stationary phase. The essential idea is that a mixture of short- and long-chain silanizing reagents, having the Cl_3Si–R functionality, would result in the surface structure schematically illustrated in Figure 1. The high density and multiple bonding immediately near the surface would retard hydrolysis, while the lower density of the remainder of the long chains would allow for analyte retention. Furthermore, Sentell and Dorsey have shown that the

* Corresponding author.

(1) Boudreau, S. P.; Cooper, W. T. *Anal. Chem.* **1989**, *61*, 41.
(2) Unger, K. K. *Porous Silica*; Elsevier: New York, 1979; Chapter 3.
(3) Bennett, H. J. P.; Hudson, A. M.; McMartin, C.; Purdon, G. E. *Biochem. J.* **1977**, *168*, 9.
(4) Cobb, K. A.; Dolnik, V.; Novotny, M. *Anal. Chem.* **1990**, *62*, 2478.
(5) Kirkland, J. J.; Glajch, J. L.; Farlee, R. D. *Anal. Chem.* **1989**, *62*, 2478.
(6) Sanders, L. C.; Wise, S. A. *Anal. Chem.* **1984**, *56*, 504.
(7) Moaz, R.; Sagiv, J. *J. Colloid. Interface Sci.* **1984**, *100*, 465.
(8) Moaz, R.; Sagiv, J. *Langmuir* **1987**, *3*, 1034.
(9) Wasserman, S. R.; Tao, Y.-T.; Whitesides, G. M. *Langmuir* **1989**, *5*, 1074.
(10) Wasserman, S. R.; Whitesides, G. M.; Tidswell, I. M.; Ocko, B. M.; Pershan, P. S.; Axe, J. D. *J. Am. Chem. Soc.* **1989**, *111*, 5852.
(11) Kessel, C. R.; Granick, S. *Langmuir* **1991**, *7*, 532.
(12) Gee, M. L.; Healy, T. W.; White, L. R. *J. Colloid. Interface Sci.* **1990**, *140*, 450.

0003-2700/92/0364-2783$03.00/0

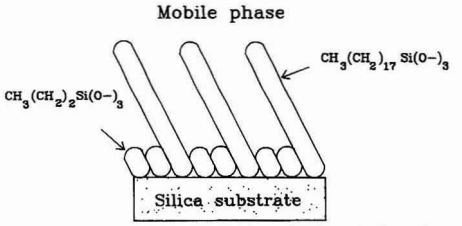

Figure 1. Illustration of mixed, horizontal polymerization scheme, where a mixture of long and short alkyltrichlorosilanes are horizontally polymerized. The high density near the surface provides hydrolytic stability while the lower density away from the surface allows for conventional chromatographic selectivity.

partition coefficient passes through a maximum at this surface coverage and that additional selectivity can be obtained at higher surface coverages.[13] The scheme of Figure 1 potentially allows these higher coverages to be readily achieved. In this work, mixtures of $CH_3(CH_2)_{17}SiCl_3$ and $CH_3(CH_2)_2SiCl_3$ are used to prepare the surface, and the hydrolytic stabilities of these surfaces are tested.

EXPERIMENTAL SECTION

The method of horizontal polymerization differs from previous reports in three ways. First, silica plates are used, rather than the native oxide of silicon. The surface of the silica plates is believed to be the same as the native oxide and silica gel, because it is completely wetted by water. Second, special care was taken to avoid contamination of the silica surface during monolayer self-assembly, as detailed below. Third, mixed monolayers of long and very short chains are prepared. The mixed horizontal polymerization of functional groups of interest along with spacers on silica has not previously been reported.[14]

The silica plates were obtained from Quartz Products (Georgetown, DE). Atomic force microscopy has revealed the surfaces to be flat on the molecular scale.[15] The plates were cleaned in boiling, concentrated nitric acid, rinsed in ultrapure water, and dried under nitrogen. The nitrogen itself was filtered by a silica column. The plates were then allowed to equilibrate with the vapor of ultrapure water for 60 min under the filtered nitrogen atmosphere. (It has since been determined that less than 1 min is required.) It was confirmed that a plate is completely wetted by water after this procedure. The plates were then put in contact with a reagent mixture of 0.59 mole fraction of $CH_3(CH_2)_{17}SiCl_3$ and 0.41 mole fraction of $CH_3(CH_2)_2SiCl_3$ dissolved in anhydrous *n*-hexadecane. The concentrations were in great excess of the expected amount of material needed for complete reaction. These silanizing reagents were obtained from Hüls-America. The *n*-hexadecane (Aldrich) was made to be anhydrous by passage through a column containing a layer of dry alumina followed by a layer of dry silica, in a glovebox. A period of 24 h at room temperature was allowed for the self-assembled monolayer to form. After the self-assembly, the plates were rinsed thoroughly in hexane, acetone, and methanol and were then stored under nitrogen.

Conventional monomeric C_{18} surfaces were prepared by cleaning the silica plates the same way, but then refluxing them for 3 h in a solution of $CH_3(CH_2)_{17}Si(CH_3)_2Cl$ in *n*-hexadecane, with *n*-butylamine as the catalyst. These surfaces were end-capped with trimethylchlorosilane. This was done to make the surface as hydrophobic as possible to retard the hydrolysis of the conventional monomeric phase.

The FTIR spectra were obtained using a BOMEM MB100 at 4-cm^{-1} resolution and 200 scans. The baselines in the spectra were corrected. The plates were oriented at normal incidence with respect to the beam. The thick plates resulted in no apparent interference fringes in the FTIR spectra. The plates were cleaned with acetone and dried with nitrogen before the spectra were obtained.

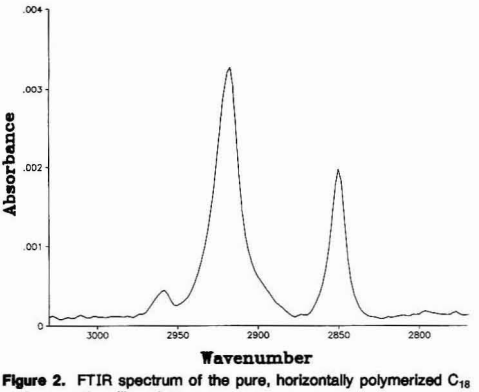

Figure 2. FTIR spectrum of the pure, horizontally polymerized C_{18} surface on the silica plate.

RESULTS AND DISCUSSION

1. Horizontal Polymerization. The FTIR spectrum of a horizontally polymerized, pure C_{18} surface, shown in Figure 2, was obtained to confirm that the experimental procedure provides the same quality of horizontal polymerization as has been reported in the literature. The spectrum is virtually identical in both absorbance (0.003) and spectral width (15 cm^{-1}) to those reported by Moaz and Sagiv[7,8] and Kessel and Granick,[11] indicating a surface coverage on the order of 22–25 $Å^2$/chain (7.6–6.7 $\mu mol/m^2$). The major peaks are the methylene symmetric and asymmetric stretches at 2850 and 2917 cm^{-1}, respectively,[16] and these are narrowed significantly compared to solution-phase spectra. This narrowing has been attributed to significant all-trans conformation due to the high density. The smaller peak at 2959 cm^{-1} is assigned to the asymmetric methyl stretch.[16] Finally, this type of plate was found to bead water uniformly after boiling in concentrated nitric acid for a period of 1 h. The improvement in uniformity is attributed to the clean conditions that reduce large defects. It is concluded that the self-assembly technique employed in this work provides the expected horizontally polymerized monolayer. Comparable horizontal polymerization for the mixed alkyltrichlorosilane reagants is thus expected from the same procedure.

The FTIR spectrum for the horizontally polymerized surface of mixed C_{18} and C_3 composition is shown in Figure 3a, and the FTIR spectrum of the end-capped monomeric surface is shown in Figure 3b. A visual comparison of these spectra shows that the ratio of CH_3 to CH_2 groups is qualitatively similar to that of the monomeric surface. The similarity of the spectra for the monomeric and mixed surfaces corresponds to similar C_{18} coverage. The spectrum for the mixed, horizontally polymerized surface has broader bands than the spectrum for the pure C_{18}, horizontally polymerized surface of Figure 2. This is expected because the density is significantly lower owing to the spacing by the C_3 groups. On the basis of the areas of the asymmetric methyl stretch and under the assumption that the coverage of the pure C_{18} monolayer of Figure 1 is 6.7 $\mu mol/m^2$, the coverages of both the conventional monomeric and the mixed horizontally polymerized monolayers are calculated from the data of Figure

(13) Sentell, K. B.; Dorsey, J. G. *Anal. Chem.* **1989**, *61*, 930.
(14) U.S. Pat. Appl. 900,215, June 17, 1992.
(15) Burbage, J. D.; Wirth, M. J. *J. Phys. Chem.* **1992**, *96*, 5943.
(16) Wiberly, S. E.; Bunce, S. C.; Bauer, W. H. *Anal. Chem.* **1960**, *32*, 217.

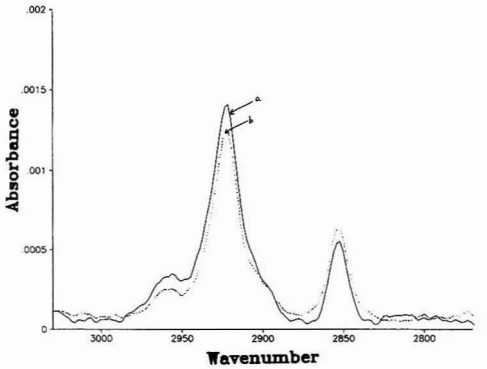

Figure 3. Comparison of FTIR spectra for (a) the mixed, horizontally polymerized surface and (b) the conventional end-capped monomeric surface.

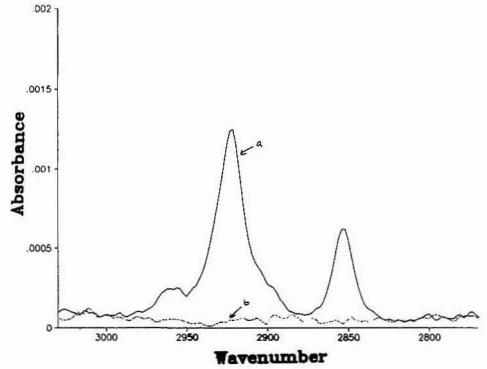

Figure 4. FTIR spectrum of the conventional monomeric end-capped phase before (a) and after (b) boiling in concentrated nitric acid for 10 min.

2 to be 3.2 and 2.8 μmol/m^2, respectively. These are coverages typically used in chromatography.

2. Acid Hydrolysis Studies. The mixed, horizontally polymerized surface and the end-capped, conventional monomeric surface were both boiled in concentrated nitric acid for 10 min. When these two plates were removed from the nitric acid solution, water beaded up on the mixed, horizontally polymerized plate, while a uniform layer of water clung to the monomeric plate. The mixed phase was further boiled in the concentrated nitric acid for an additional 15 min. For the monomeric phase, the FTIR spectrum confirmed that the hydrocarbon monolayer was completely removed, as illustrated in Figure 4. For the mixed horizontally polymerized phase, the FTIR spectrum changed little, as shown in Figure 5: after the 25 min of boiling in concentrated nitric acid, the absorbance decreased negligibly. These results demonstrate that the mixed, horizontally polymerized surface has dramatically improved stability to acid hydrolysis.

3. Base Hydrolysis Studies. An end-capped, mixed, horizontally polymerized surface and an end-capped, conventional monomeric surface were boiled for a period of 3 h in solutions of pH 12, with 5% *n*-propanol added. This solution composition at 100 °C provides a very severe test of stability toward base hydrolysis. When removed from the basic solution, the conventional monomeric surface was completely wetted by water, while the mixed, horizontally polymerized surface beaded water. The FTIR spectra for

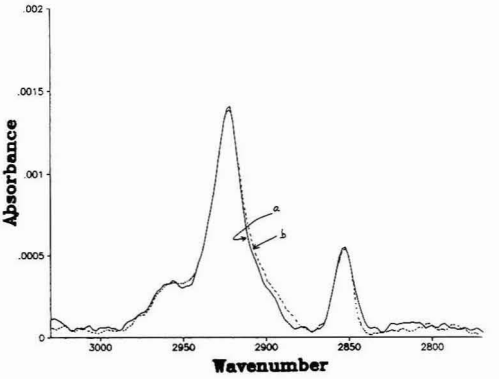

Figure 5. FTIR spectrum of the mixed, horizontally polymerized phase before (a) and after (b) boiling in concentrated nitric acid for 25 min.

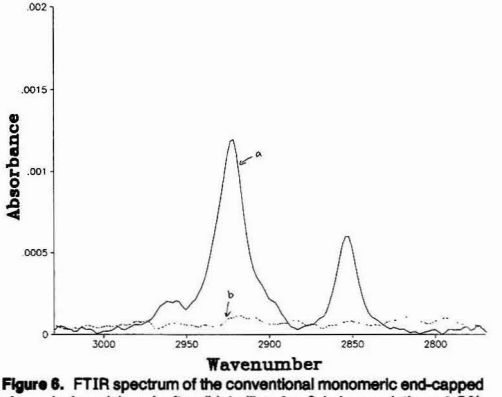

Figure 6. FTIR spectrum of the conventional monomeric end-capped phase before (a) and after (b) boiling for 3 h in a solution of 5% *n*-propanol in water at pH 12.

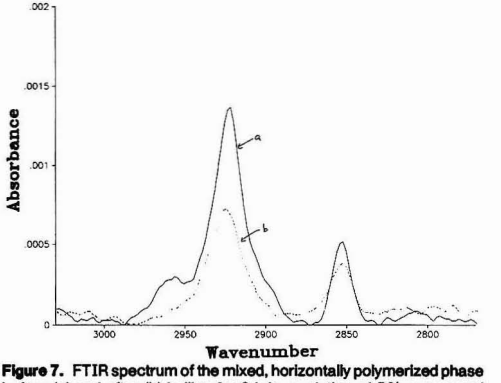

Figure 7. FTIR spectrum of the mixed, horizontally polymerized phase before (a) and after (b) boiling for 3 h in a solution of 5% *n*-propanol in water at pH 12.

the conventional and mixed, horizontally polymerized surfaces are summarized in Figures 6 and 7, respectively. Figure 6 confirms that the conventional monomeric surface was completely removed. Figure 7 shows that mixed, horizontally polymerized surface suffered approximately 50% hydrolysis over this 3-h boiling period. These results indicate that there

is also a dramatic improvement in stability to base hydrolysis using the new bonding scheme.

CONCLUSIONS

A hydrolytically stable monolayer surface can be made by covalently bonding a functional group of interest, diluted with a short-chain silanizing agent, to a silica surface. Both the reagents have trifunctional silanes, and horizontal polymerization occurs when only surface water is present. The new phase is considered pseudomonomeric because its business end is essentially the same as the monomeric phase, yet it is made from polymerizing reagents. The same bonding scheme is applicable to functional groups other than C_{18}, such as alkylamino, alkylhydroxyl, etc. The bonding scheme could be applied to the derivatization of capillary columns for capillary zone electrophoresis, where the surface reproducibility and hydrolytic stability would be improved.

The very impressive hydrolytic stability has been demonstrated using silica substrates that are flat. These phases are promising for high-performance chromatographic application if the bonding scheme is effective on rough silica surfaces. Horizontal polymerization is believed to work equally well on rough surfaces,[17] and experiments are underway to evaluate the improved stability of mixed, horizontally polymerized surfaces on chromatographic silica gel.

ACKNOWLEDGMENT

We thank Ms. Lois Weyer at Hercules, Inc. for use of the FTIR spectrometer. This work was supported by the Department of Energy (Grant No. DE-FG02-91ER14187) and the National Science Foundation (Grant No. CHE-9113544).

RECEIVED for review July 1, 1992. Accepted August 20, 1992.

Registry No. $PrSiCl_3$, 141-57-1; vitreous silica, 60676-86-0.

(17) Silberzan, P.; Leger, L.; Ausserre, D.; Benattar, J. J. *Langmuir* **1991**, *7*, 1647.

Quantitative Laser Mass Analysis by Time Resolution of the Ion-Induced Voltage in Multiphoton Ionization Processes

Israel Schechter,* Hartmut Schröder, and Karl L. Kompa

Max-Planck-Institut für Quantenoptik, D-8046 Garching, Germany

A simple instrumental setup for quantitative chemical analysis, based on the measurement of the time-resolved voltage induced on electrodes by MPI-generated charges, is suggested and evaluated. The method is suitable for on-line measurements and may achieve detectability close to the ppb range for highly efficient ionization (either by resonant MPI or by use of ps-lasers) and up to two parts in 10^7 (for nonresonant two-photon ionization by ns-lasers). The dynamical range of the detectable concentrations is considerably larger compared to other related techniques. With a KrF excimer laser used for ionization, the instrument can be used as an artificial nose for sensing organic compounds in atmospheric air. The method performs best in the determination of the mass and number of ions in a monocomponent system; however, simple binary mixtures can be resolved as well. The measurements reported here are carried out at pressures up to 10^{-3} mbar, using an unfocused laser beam. The "heart" of the method is a chemometric set of algorithms that extracts the information on the masses and number of ions out of the easily obtained signal.

INTRODUCTION

Laser Multiphoton Ionization (MPI) processes have been extensively applied to analytical chemistry in a variety of sophisticated methods. The general techniques have been reviewed,[1,2] as well as recent developments[3-6] and applications to mass spectrometry.[7]

In most of the commonly used techniques, the ions are produced by focusing a laser beam into the sample. They are detected by a time-of-flight mass spectrometer or a quadrupole filter. Thus, a very high mass resolution is achieved. However, there are several difficulties concerning the quantification in these systems, most of them imposed by the ion detection system and the poorly defined interaction volume. In spite of these difficulties, useful quantitative results may be obtained by using internal or external calibration methodology. However, in these methods multiple experiments are required.

Usually, the ions are detected by electron multipliers. They hit a conversion dinode and produce secondary electrons. These electrons are then multiplied until a gain of order of 10^4–10^8 is obtained. The other versions, the Channeltron or the channel plate multipliers, are also used. These methods, as well as several other closely related methods, have some disadvantages concerning the quantification of the results.

The conversion gain (ion to electrons) depends both on the ion species and on their velocity.[8] As a result, in the dc operating mode, the detection sensitivity significantly varies from mass to mass.[9] Furthermore, multipliers suffer from gradual long-term gain deterioration, due to frequently venting the system. This is inevitable in some analytical systems where the sample must be frequently changed.[9] The last problem, however, can be minimized by various experimental setups, where the sample can be introduced without the need to vent the instrument.

Another problem concerning the application of standard multipliers to ion detection in MPI analysis (in the pulse counting mode) is their limited dynamic range. At high count rates, the dead-time losses impose an upper limit to an accurate measurement. For a modern and fast amplifier the limit is reached already at 10^8 counts/s. This is a severe limitation for the nonlinear MPI processes, where the ion flux may differ by many orders of magnitude from one sample to another. It should be noted that the short laser pulses may easily produce very high ion fluxes. This limitation is being avoided in continuous ion-current measurements.

The first step toward the quantification of MPI analysis is to measure the absolute number of produced ions. Using the electron multiplier for the ion detection, one has to estimate the efficiency of the ion collection through the ion optics and to properly calibrate the detector. In addition, the ion flux must be kept below the saturation of the detector.

Even when the number of ions is properly calibrated, it is still difficult to evaluate the actual concentration of neutral species. For this purpose one has to know the MPI cross-section, the effective detection volume (which depends on the ion optics) and the effective interaction or ionization volume (which depends on the laser beam–lens system). To fulfill these two requirements is a very difficult task for a focused laser beam. The beam profile has to be measured at various positions along the axis and also outside in the wings. By focusing, one can easily reach the saturation regime of the MPI process. In this case, the expression for the interaction volume involves a power series in volume integrals of higher powers of laser intensity, which slowly converges.[10-12] Another difficulty for the interpretation of the data is caused by the mixed order processes that may occur in the focused beam. Much theoretical and experimental research has been carried out in order to investigate the focusing effects of laser beams on the MPI processes, and these problems are still not completely solved.[12-17] The problem of depletion of neutrals

(1) Letokhov, V. S. *Laser Analytical Spectrochemistry*; Adam Hilger: Bristol, PA, 1986.
(2) Lambropoulos, P., Smith, S. J. Eds. *Multiphoton Ionization*; Proceedings of the 3rd International Conference, Iraklion, Crete, Greece, Sept 1984; Spring-Verlag: Berlin, 1984.
(3) *Laser Applications to Chemical Analysis*; 1990 Technical Digest Series; Optical Society of America: Washington, DC, 1990; Vol. 2.
(4) Bieske, E. J.; Uichanco, A. S.; Rainbird, M. W.; Knight, A. E. W. *J. Chem. Phys.* **1991**, *94*, 7029.
(5) Niles, S.; Prinslow, D. A.; Wight, C. A.; Armentrout, P. B. *J. Chem. Phys.* **1990**, *93*, 6186.
(6) Okada, T.; Andou, H.; Moriyama, Y.; Maeda, M. *Appl. Phys. Lett.* **1990**, *56*, 1380.
(7) Burlingame, A. L.; Millington, D. S.; Norwood, D. L.; Russel, D. H. *Anal. Chem.* **1990**, *62*, 268R.
(8) Rudat, M. A.; Morrison, G. H. *Int. J. Mass Spectrom. Ion Phys.* **1978**, *27*, 249.
(9) Benninghoven, A.; Rüdenauer, F. G.; Werner, H. W. *Secondary Ion Mass Spectrometry*; Wiley: New York, 1987.
(10) Boulassier, J. C. *Nouv. Rev. Opt.* New York, **1976**, *7*, 329.
(11) Cervenan, M. R.; Isenor, N. R. *Opt. Commun.* **1975**, *13*, 175.
(12) Sogard, M. R. *J. Opt. Soc. Am.* **1988**, *5B*, 1890.
(13) Gandhi, S. R.; Bernstein, R. B. *Chem. Phys.* **1986**, *105*, 423.

0003-2700/92/0364-2787$03.00/0

in the focused volume has to be considered as well.[18] Concerning the MPI of organic molecules, one must be aware of the fragmentation that may take place at the high-intensity regions of the focus. In addition, the small interaction volume achieved by focusing may lower the detectability.

The focusing-based methods, although having many disadvantages, are imposed by the ion detection system. This is because the inherent mass resolution is only obtainable for small well-defined regions from which the ions can be extracted with high efficiency. It should be also noticed that typical detectors used in time of flight or quadrupole mass spectrometers need a high-vacuum environment. The high-vacuum systems complicate the operation and slow down the rate of sample exchange.

Nevertheless, when high mass resolution is desired, these traditional techniques are the best. The here proposed setup is suitable when quantification is needed, as well as ascertaining the mass of the substrate, and where only a few ionizable components are present in the mixture. It is characterized by its simplicity, low cost, and its possibility to operate on-line in a large dynamic range. A similar simplified method for measuring MPI cross-sections has been recently developed[19] and may be used for quantification when the cross-sections are unknown. We have applied this technique to measure the three photon ionization cross-sections of Xe at 266 nm.

In this context we emphasize that many organic compounds of interest may be easily ionized at low laser intensities and detected in regular air due to the high difference in ionization potentials. The atmospheric gases have ionization potentials of over 12 eV, while only 6–10 eV are needed for ionization of most of the organic compounds. This means that as far as nonresonant ionization is considered, a KrF laser pulse at 248 nm (5 eV) will ionize most of the organic compounds by two-photon ionization, while a three-photon process with a much lower probability is needed for the atmospheric gas ionization.[20-24]

Taking into account the low laser intensities that have to be applied to organic molecules (in order to prevent fragmentation), the probability to ionize the carrier gas is negligible. Considering the resonance effects, a proper wavelength should be used in order to keep the carrying gases in the low cross-section range. On the other hand, if a specific compound is looked for, the resonant ionization can be used to specifically increase its detectability by many orders of magnitude.

A simple estimation will emphasize the numerous ions produced by a nonresonant two-photon process: A typical KrF laser delivers an energy of 200 mJ over an area of 1 cm^2 in a 20-ns pulse. This yields a photon flux of 1.25×10^{25} photons cm^{-2} s^{-1}. The two-photon ionization probability for a typical cross-section of 10^{-49} cm^4 s is therefore 3×10^{-7}. Hence, at a pressure of 1 μbar we expect 7.5×10^6 ions/cm^3, which is many orders of magnitude over the sensitivity limit of our present apparatus (see below).

(14) Baravian, G.; Sultan, G. *Physica* **1985**, *128C*, 343.
(15) Lompre, L. A.; Mainfray, G.; Thebault, J. *Rev. Phys. Appl.* **1982**, *17*, 21.
(16) Hanazaki, I. *Appl. Phys. B* **1981**, *26*, 111.
(17) Francisco, J. S.; Steinfeld, J. I.; Gilbert, R. G. *Chem. Phys. Lett.* **1981**, *82*, 311.
(18) Chin, S. L.; Isenor, N. R. *Can. J. Phys.* **1970**, *48*, 1445.
(19) Schechter, S.; Schfoder, H.; Kompa, K. L. *Chem. Phys. Lett.* **1992**, *194*, 128.
(20) Boesel, U.; Neusser, H. J.; Schlag, E. W. *Chem. Phys.* **1981**, *55*, 193.
(21) Bischel, W. K.; Jusinski, L. E.; Spencer, M. N.; Eckstrom, D. J. *Diagnostics Development for E-Beam Excited Air Channels*; Technical Report No. 5; SRI Int.: Menlo Park, CA, 1985.
(22) Schlag, E. W.; Neusser, H. J. *Acc. Chem. Res.* **1983**, *16*, 355.
(23) Reilly, J. P.; Kompa, K. L. *J. Chem. Phys.* **1980**, *73*, 5468.
(24) Brophy, J. H.; Rettner, C. T. *Opt. Lett.* **1979**, *4*, 337.

Following, the proposed method for mass analysis and quantification is described. First, the theoretical part is developed. Then, the computer algorithms that have been developed for the experimental data analysis are described. The effect of various important factors on the final error of the determination is studied, using synthetic data that include various noise levels (ca. 70 000 simulated determinations have been carried out). Next, the experimental setup and the experimental conditions are described. The experimental results obtained from a few systems are reported.

GENERAL DESCRIPTION

The proposed method simplifies the presently existing techniques by three ways: First, applying a parallel unfocused beam eliminates the need to know the focus geometry precisely and provides a large interaction volume. Second, direct measurement of the ions at 100% collection efficiency is carried out. The signal measured is a voltage change between long electrodes, caused by charges induced during the ions' flight. It is recorded as a function of time on an oscilloscope or as a transient digitizer. To the best of our knowledge, this is the first time that this effect is used for analytical purposes. Third, the electrodes that are used are designed to enable measurements to be carried out at quite high pressures (10^{-3} mbar) compared to the traditional method. This avoids the need of a high-vacuum system and enables fast sample change. In an on-line setup, the sample is introduced continuously by a leak-valve, while the pumps maintain the needed pressure.

All the information about the masses, number of ions, and concentrations is achieved by a set of chemometric algorithms. Thus, the "hard work" is carried out by the computer rather than by a sophisticated experimental setup.

Apparatus. The apparatus consists of two long electrodes (a few centimeters apart) located in a vacuum tube. A UV parallel laser pulse passes between the electrodes and ionizes the sample. The ions are accelerated to the electrodes by a bias voltage. The induced voltage change across the electrodes as a function of time is recorded by a digital signal analyzer and then processed on a computer. More details are given in the Experimental Section.

Signal from a Monocomponent Sample. When a charged particle moves between two electrodes, a voltage is being induced in the electrodes. The observed signal is a potential difference between the electrodes as a function of time. The information on the number of ions, as well as on their masses, is to be extracted from this signal. A rapid rise is observed just after the laser pulse due to the fast electrons (low mass) that reach the positive electrode. If no other sources of electrons are expected, then this signal should be ne/C volts, where n is the number of ions produced, e is the electron charge, and C is the capacitance of the system (electrodes plus wiring). Next, a rise in the signal is observed due to the ions flight to the negative electrodes. This signal is caused by the electrostatic charges induced in the electrodes during the flight time. Since the ions are accelerated, the signal is parabolic in time. The maximum signal, $2ne/C$ volts, is observed when the ions reach the electrode. The time corresponding to this signal, t_{max}, is simply the flight time and is given by

$$t_{max} = \sqrt{2hdm/e\Delta V} \quad (1)$$

where d is the distance between the electrodes, h is the flight distance of the ions (usually, $h = d/2$, but not necessarily), m is the ion's mass, and ΔV is the bias voltage. After the maximum signal is reached, a regular RC exponential decay

is observed (R is the overall resistance). When the RC decay is neglected, the signal as a function of time is

$$V(t) = P_e + P + \frac{P}{t_{max}^2} \times t^2 \quad \text{for} \quad t < t_{max} \tag{2}$$

where $P = ne/C$ and P_e is the signal from extra electrons produced by stray light or other sources. In many cases, P_e is negligible, but not always.

However, the actual signal is the convolution of eq 2 and the exponential RC decay

$$V(t) = (P_e + P)e^{-t} + \int_0^t \frac{\partial V}{\partial s} e^{-(t-s)}\, ds \tag{3}$$

and the result is

$$V(t) = (P_e + P)e^{-t} + \frac{2P}{t_{max}^2}(e^{-t} + t - 1) \quad \text{for} \quad t \le t_{max} \tag{4a}$$

$$V(t) = \left[P_e + P + \frac{2P}{t_{max}^2}(t_{max}e^{t_{max}} - t_{max} + 1)\right]e^{-t} \quad \text{for} \quad t > t_{max} \tag{4b}$$

The time is in units of RC (for simplicity and generality).

Signal from a Mixture. When two components are simultaneously ionized, the time domain of the signal can be divided into three parts:

(I) $0 \le t < t_1$ (II) $t_1 \le t < t_2$ (III) $t_2 \le t < \infty$

t_1 is t_{max} for the first component and t_2 is t_{max} for the second one. Let us define the functions:

$$f_i(t) = \frac{2P_i}{t_i^2}(e^{-t} + t - 1)$$

$$g_i(t) = \frac{2P_i}{t_i^2}(t_i e^{t_i} - t_i + 1)e^{-t}$$

$$h(t) = (P_e + \sum_i P_i)e^{-t} \tag{5}$$

where i indicates component i in the mixture.

For a two-component mixture, the signal as a function of time is

$$\begin{aligned} V(t) &= h(t) + \sum_i f_i(t) \quad \text{range I} \\ &= h(t) + g_1(t) + f_2(t) \quad \text{range II} \\ &= h(t) + \sum_i g_i(t) \quad \text{range III} \end{aligned} \tag{6}$$

This expression may easily be generalized for more components; however, we shall restrict the demonstration to two components only. The signal profile depends on the number of ions, the masses of the ions, the electric field between the electrodes, the flight distance, the RC constant, and extra electrons produced (if present). Figure 1 shows several simulated examples of the signal at various R values. The resistance is usually provided by the internal characteristics of the oscilloscope that measures the signal. The break points are at t_1 and t_2. At higher R values the convolution of RC decay is less pronounced and the signal may be approximated by eq 2; however, at lower R the effect of the convolution is clearly observed. In this figure, as well as in some of the following ones, Gaussian noise has been added to some of the simulated signals. It has been produced by the Box–Müller method that provides normally distributed deviates with zero mean and unit standard deviation.[25] In addition to the Gaussian noise, the smearing out of the signal, due to the finite laser beam radius and due to some unperfectness of the beam alignment, have been simulated.

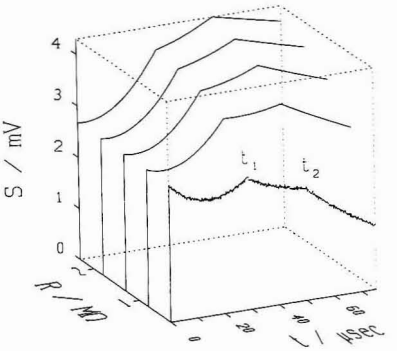

Figure 1. Signal as a function of time for a mixture of mass 100 amu and mass 300 amu, at various resistance values (in the range 0.3–2.3 MΩ) (eq 6). The number of ions of each component is 10^6. The capacitance is 150 pF, and ΔV is 18 V. The noise simulates a normal noise plus other smearing effects. At lower R, the overall signal is lower, but sometimes the break points are better resolved.

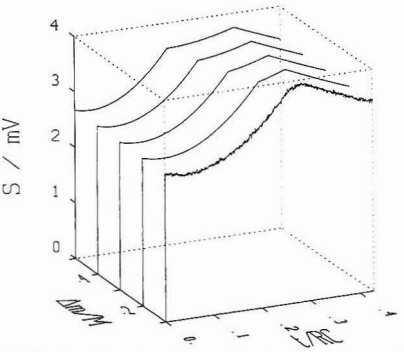

Figure 2. Signal as a function of reduced time for various mass mixtures (eq 6). The sum of the masses is 400 amu. R = 1 MΩ, and 25% of extra electrons are introduced. The noise is generated by σ_V = 20 μV and σ_h = 1%.

Principle of Mass Resolution and Quantification. The principle of the proposed procedure is to analyze the above mentioned generated data and to extract the desired information on masses and number of ions out of it. The information is included in the values of t_1 and t_2, as well as in the overall shape of the time function. The measured signal is to be fitted to the theoretical functions with the masses and the number of ions as parameters. The error-compensating fitting process is expected to provide better results than a direct inspection of the signal.

The first step in such a procedure is to resolve the break points t_1 and t_2. In order to understand the various factors that influence the resolution, we shall first describe how the various parameters affect the signal.

Figure 2 shows the signal for various values of $\Delta m/M$, where Δm is the difference between the ion masses and M is their sum. It can be seen that as Δm decreases, the time between

(25) Press, W. H.; Flannery, B. P.; Teukolsky, S. A.; Vetterling, W. T. *Numerical Recipes in Pascal*; Cambridge University Press: Cambridge, U.K., 1989.

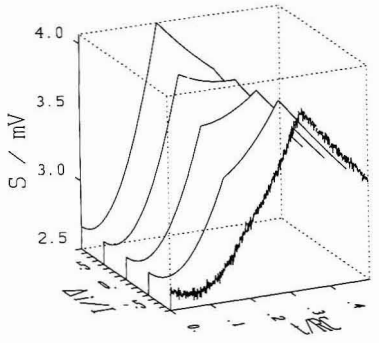

Figure 3. Signal as a function of reduced time, for various number of ions in the mixture (eq 6). The masses are 100 and 300 amu. The total number of ions is 2×10^6. Note how the resolution is more difficult at the two extremes (90% and 10% in the mixture).

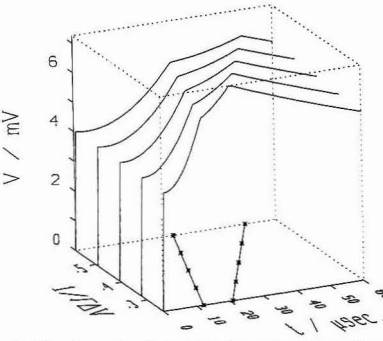

Figure 4. Signal as a function of time for various bias voltages. The projections of the break points form lines in the $1/\sqrt{\Delta V}-t$ plane. This procedure may be used for improving the results or for ascertaining the existence of unclear break points.

t_1 and t_2 also decreases. Therefore the break points become more and more difficult to be observed, especially when the signal is noisy. The time corresponding to the mean mass, however, is easily observed. As expected, the resolution of t_1 and t_2 depends also on the number of ions of the various species. The signals as a function of $\Delta i/I$ are shown in Figure 3. Δi is the difference between the number of ions and I is their sum (The masses are kept unchanged). As one of the ions diminishes, the resolution of its break point becomes more and more difficult, which emphasizes the needed of a computer algorithm to achieve the best possible resolution. Such an algorithm can do much better than the human eye.

As already mentioned, resolving the break points is of importance since one can find the masses of the ions directly from eq 1. In some cases this is an easy task. However, usually this is not sufficient for the analytical chemist who must be sure whether there are additional invisible break points, and above all, to find the best possible result out of the given signal. This is achieved by a computer algorithm that is described in the following. Even when the times t_1 and t_2 are resolved, one can still improve the quality of the results by plots of t_i vs $1/\sqrt{\Delta V}$. According to eq 1 these are straight lines and the masses can be found from their slopes. Figure 4 shows signals at various $1/\sqrt{\Delta V}$ values and the lines obtained for t_1 and t_2.

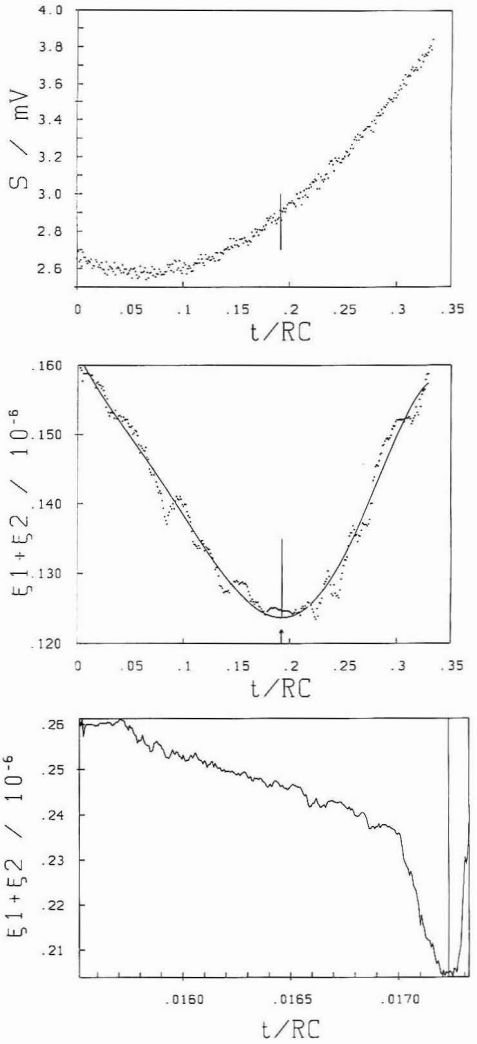

Figure 5. Demonstration of the resolution ability of the algorithm. (a, Top) noisy signal from a mixture of $\Delta I/I = 0.96$. The line shows the location of the break point which cannot be easily resolved. (Only a part of the signal is shown.) (b, Middle) function of $\xi_1 + \xi_2$, produced by the algorithm and a polynomial fit. The long line indicates the minimum of the polynomial and the arrow indicates the location of the real break point. (c, Bottom) function of $\xi_1 + \xi_2$ obtained by the algorithm for a high $\Delta I/I$ (0.98) and low $\Delta m/M$ (6×10^{-3}). The vertical line shows the location of the real break point, which is close to the minimum of $\xi(t)$.

ALGORITHMS

Several computer algorithms are described in this section. Combinations of these algorithms may be used in various experimental conditions. Afterward, a "recipe" or an "overall algorithm" describing when and how to use the various algorithms, is provided.

All—Finding a Break Point Corresponding to t_1 or t_2. This algorithm is of much importance to the suggested method

since it enables one to computerize and automate the analysis. Furthermore, it improves the resolution and the sensitivity of the method much over the limit of human eye analysis.

Let us analyze the signal in time interval a to c. Let $V_1(t)$ be the theoretical expected function in the range a to t_{BP}, and $V_2(t)$, that in the range t_{BP} to c, where t_{BP} is the unknown break point. For each experimental data point, b, in the range $\{a, c\}$, find the least-squares fit of $V_1(t)$ in the range $\{a, b\}$ and of $V_2(t)$ in the range $\{b, c\}$. ξ_1 is the result sum of the least squares in the range $\{a, b\}$, and ξ_2, that in the range $\{b, c\}$. Note $\xi = \xi_1 + \xi_2$ thus obtained for each point b. Fit a polynomial (of degree 6) to the points $\xi(t)$. Find the minimum of this polynomial. The time corresponding to that minimum is the estimate of t_{BP}, the break point.

Various algorithms have been tested and the one described above has been found to be the best for our purpose. The least-squares fit is a multidimensional one and has been performed by the modified Levenberg–Marquardt algorithm,[26,27] which proved many times to fastly converge in multidimensional fits, e.g.[28-30] Note that a couple of such fits must be carried out for each point of the experimental signal.

In order to demonstrate the power of this algorithm, it has been applied to a very noisy signal (Figure 5a), where the breakpoint cannot be resolved by eye. Figure 5b shows the $\xi(t)$ points obtained by the proposed algorithm, the polynomial fit, its minimum, and the true break point. In this case, the main problem has been caused by the high noise level and the values of $\Delta i/I = 0.96$ (note that $\Delta i/I = 1$ is the limit where there is just one component in the mixture) and $\Delta m/M = 0.5$. When a better signal is provided, a more complicated case can be handled. As an example, the resolution of 1% single-deuterated benzene in pure (unlabeled) benzene is presented. σ_V, the standard deviation of the voltage readings, has been 25 μV. σ_h, the standard deviation of the distance of the laser beam from the electrodes, has been 0.5% (it also represents the spread due to the finite laser cross-section). In this case, $\Delta i/I = 0.98$ and $\Delta m/M = 6 \times 10^{-3}$. The resolution, achieved by the proposed algorithm, is presented in Figure 5c. If the ξ points are just in the vicinity of the break point, they can be fitted by a low-degree polynomial. However, in order to include cases where the points are calculated in a large range (e.g., Figure 5c), a higher polynomial has been used.

Al2—Finding the Parameters by Direct Least-Squares Fit in the Three Ranges. The masses and the number of ions can be calculated by least-squares fit of the functions to the data in the three time ranges. In range I the fit function is

$$V_I(t) = x_1 e^{-t} + x_2(e^{-t} + t - 1) \tag{7}$$

And the fit provides the value of x_1 and x_2 where

$$x_1 = P_1 + P_2 + P_e$$

$$x_2 = \frac{2P_1}{t_1^2} + \frac{2P_2}{t_2^2} \tag{8}$$

In range II the function is

$$V_{II}(t) = x_3 e^{-t} + x_4(e^{-t} + t - 1) \tag{9}$$

and the fit provides the values of x_3 and x_4 where

$$x_3 = P_1 + P_2 + P_e + \frac{2P_1}{t_1^2}(t_1 e^{t_1} - t_1 + 1)$$

$$x_4 = 2P_1/t_1^2 \tag{10}$$

In range III the function is

$$V_{III}(t) = x_5 e^{-t} \tag{11}$$

and the fit provides the value of x_5 where

$$x_5 = P_1 + P_2 + P_e + \frac{2P_1}{t_1^2}(t_1 e^{t_1} - t_1 + 1) + \frac{2P_2}{t_2^2}(t_2 e^{t_2} - t_2 + 1) \tag{12}$$

Equations 8, 10, and 12 are to be solved for the values of t_1, t_2, P_1, and P_2. The solution requires a numerical minimization. This algorithm needs a prior estimate of t_1 and t_2. As a result, it provides a better approximation of these values, and then the masses are calculated. The initial estimates may be the observed value, just by inspection or, in case that this is not possible, just any two values in the reasonable range. This algorithm takes advantage of the information in all ranges; therefore, it is better than just reading t_1 and t_2 from the data. In case the exact locations of t_1 or t_2 are not clear, but well resolved, one has to exclude from the data some parts around the unclear break point and perform the fit without these uncertain points.

Al3—Finding the Masses by the Intercepts of the Functions. Fit the parametric functions V_I, V_{II}, and V_{III} as in Al2. Calculate the intercept of V_I and V_{II}, and get t_1, and the intercept V_{II} with V_{III} for t_2. Calculate the masses from the break points. Calculate P_1 and P_2 by the found t_1 and t_2 and by the values of x_4 (eq 10) and x_2 (eq 8).

Overall Algorithm. Several ways have been proposed for extracting the information out of the signal. The way one should follow depends on the noise level of the data, on the clearness of the break points, and on the reproducibility of the results. Al1 is the most computer-time-consuming and should be used in the case of unclear break points. Al3 is somewhat more expensive than Al2. The recipe of the algorithms usage is as follows: (a) When the signal has a low noise level and the break points are clear, Al2 should be used. (b) When the signal has a high noise level but has the break points can be observed, Al3 should be used. (c) When the signal has a low noise level but the break points are not clear, Al1 should be first used to find t_1 and t_2. Then Al2 should be applied, using t_1 and t_2 as initial estimates. (d) When the signal has a high noise level and unclear break points, first Al1 should be applied to find out t_1 and t_2. Then Al3 should be applied, using t_1 and t_2 as initial estimates of the break points. (e) At high experimental RC constants, Al3 should be preferred over Al2. (f) The results can be improved by repeating the measurements at various ΔV values. At each voltage, t_1 and t_2 are found by the previously proposed recipe. Then, the mass is calculated by the slope of the plots of the break points as a function of $1/\sqrt{\Delta V}$. This procedure, of repeating the measurements at various ΔV, may also help to better resolve the break points and to eliminate false break points that may appear due to the signal noise.

EVALUATION OF THE ALGORITHM

In this section the effect of various parameters and experimental conditions on the error of the determination is studied. Since many parameters are involved, it is desired to view the error as a function of all of them, in a multidimensional space. However, we can simultaneously view only two parameters, therefore several couples of variables have

(26) Levenberg, K. Q. *Appl. Math.* **1944**, 2, 164.
(27) Marquardt, D. *J. Soc. Ind. Appl. Math.* **1963**, *11*, 431.
(28) Mottola, H. A. *Kinetic Aspects of Analytical Chemistry*; Wiley: New York, 1988.
(29) Pardue, H. L. *Anal. Chim. Acta* **1990**, *237*, 207.
(30) Schechter, I. *Anal. Chem.* **1991**, *63*, 1303.

been chosen. The errors have been estimated as a function of these variables, accumulated in matrices, and presented in perspective view.

Numerous experiments are needed in order to cover the combined ranges of the important parameters. The experiments in this section (ca. 70 000) have been carried out by computer simulations. First, the experimental data have been simulated with a set of parameters. A Gaussian noise, at various variances, has been added to the data. The smearing out of the signal due to unperfect alignment of the laser beam and due to the diameter of the beam, has also been incorporated into the simulations: For each such simulated point, a different t_{max} has been used for calculation. The value of that t_{max} has been randomly selected in the right range and distribution, in order to simulate the above mentioned effects. This procedure is equivalent to calculation of random trajectories starting at the various possible initial conditions. Then, the algorithm has been applied in order to recover the initial parameters (masses and number of ions). Since in some experimental setups the number of electrons is higher than the number of ions, we have included this effect in the simulations. For a two-component system, each experiment provides four results and four estimated errors, corresponding to the masses and number of ions. Moreover, for each experiment all the suggested algorithms have been applied. Since the number of results is enormous, only the most significant ones are presented in the following.

***RC* Characteristics.** As can already be seen from Figure 1, the signal is much affected by the *RC* constant. The capacitance can be controlled by the design of the electrodes and by the overall length of the wires. The resistance is usually determined by the instrumental characteristics, and its value is around 1 MΩ.

At higher noise levels, the main effect of the capacitance is to reduce the signal-to-noise ratio. As can be seen in Figure 6a, the error of the determination increases with the capacitance. Almost no influence of *R* values is observed. In the experiments of Figure 6a, the algorithm Al2 has been applied for the determination.

At low niose levels, there is an additional interesting effect: Reducing the *RC* constant increases the information content of eqs 4 (at the limit of very high *RC*, eq 4b becomes a constant independent of time, and eq 4a becomes a parabola). Therefore, algorithm Al2 yields in this case somewhat better results at lower *RC* values. This case is presented in Figure 6b, where the noise level is lower than in Figure 6a and the determination has been carried out by algorithm Al2. Here, in contrast to Figure 6a, the error is low at small values of *R*, even at the highest capacitance. In this figure, only the error in the determination of the number of ions has been presented, but similar results have been obtained for the determination of the mass. However, there are still high errors at high *RC* constants. Applying algorithm Al3, which finds the break points by the intercept of the functions overcomes that problem at high *RC*, as can be seen in Figure 6c. The three parts of Figure 6 demonstrate the combined effect of signal-to-noise ratio, *RC* values and the algorithm that is being used.

Effects of $\Delta i/I$ and the Noise Level. As previously mentioned, when the number of ions diminishes, their determination becomes more difficult and inaccurate. In a series of computer experiments, the value of $\Delta i/I$ has been changed from +0.96 to −0.96. The first limit corresponds to 2% in the mixture and the last one to 98%. The standard deviation of the noise has been varied from 0 to a reasonable value for an oscilloscope. Figure 7 shows the error in the determination of m_2. Very similar results have been obtained for n_2. A mirror picture of these results has been obtained

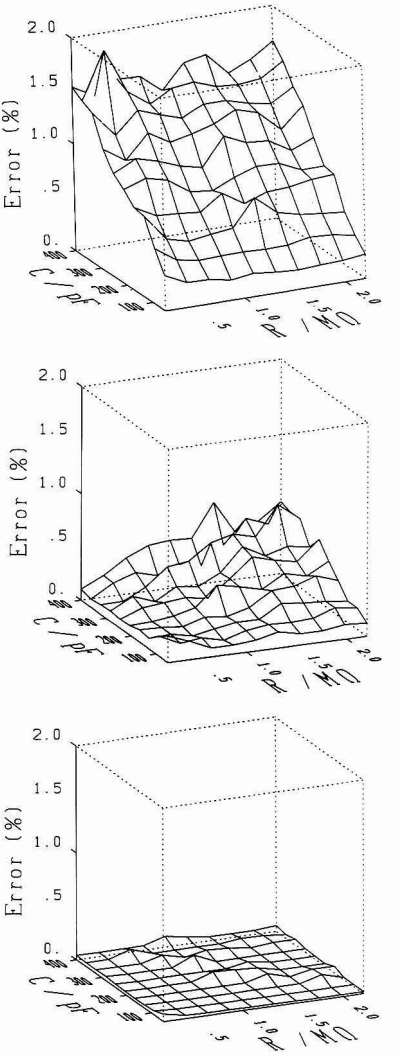

Figure 6. Influence of the *RC* characteristics and of the algorithm used. The plots show the error in the determination as a function of *R* and of *C* in the interesting range. (a, Top) the normal noise level is 0.1 mV, and the results are obtained by algorithm Al-2. (b, Middle) the normal noise level is 0.01 mV, and the results are obtained by algorithm Al-2. (c, Bottom) the normal noise level is 0.01 mV, and the results are obtained by algorithm Al-3.

for the error in the determination of m_1 and n_1 (the high error being at negative $\Delta i/I$). The results have been obtained by an automatic process that applies algorithms All and Al3. The results at the higher $\Delta i/I$ limits could be improved (by a factor of 2) by carefully viewing the plots of $\xi(t)$ rather than letting the computer to analyze it. The reason is that sometimes the automatic-fitted polynomial to the ξ points introduces a local minimum far away from the location that one would find by a simple inspection of the data. The general conclusion is that when the system is operated close to its limitations, one can obtain better results by supervising the

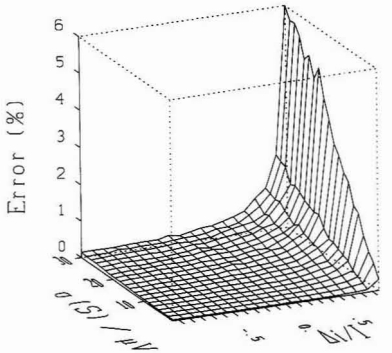

Figure 7. Error in the determination of m_2 as a function of the noise level and $\Delta I/I$. The mass is 100 amu, and the total number of ions is 2×10^6. The highest $\Delta I/I$ shown is 0.96. The results are obtained by AI-1 and AI-3. Algorithm AI-3 alone provides higher errors at high values of $\Delta I/I$ and a somewhat more spiky surface at the lower ranges.

computer program by observing the $\xi(t)$ function. This conclusion has been demonstrated by a computer subroutine that plotted $\xi(t)$ and the fitted polynomial for each experiment.

Effects of $\Delta m/M$ and the Noise Level. When the analyzed masses are similar, it becomes difficult to observe the break point. The error is mainly manifested by a poor determination of the number of ions of each species, although the sum is well determined. Figure 8a shows the error in the determination of the number of ions as a function of $\Delta m/M$ and the noise level of the readings. The lowest $\Delta m/M$ shown is 0.005 (1 amu at masses around 100 amu) and the highest noise level shown is far above a regular noise of an oscilloscope. The error in the determination of the masses is, as expected, much better, and is shown in Figure 8b. At low $\Delta m/M$ it is difficult to distinguish between the break points t_1 and t_2, but the average location is clearly defined, as can be seen from Figure 2. Concerning the mass determination, the error is mainly caused by the noise level. The results obtained for the other mass have been somewhat higher, up to 1%.

Limits of the Detection. The low-limit of the detection depends on the efficiency of the ionization and on the minimal number of ions that can be detected by the apparatus. In contrast to related methods which count the ions by electron multiplier, there is no upper limit in our method, since the detector cannot be practically saturated.

The ionization efficiency is described by the generalized MPI cross-section, Γ, which is defined for a kth-order process by[31]

$$N_i = n_0 \Gamma_k \tau_k v_k F^k \qquad (13)$$

where N_i is the number of produced ions, n_0 is the neutral density (cm^{-3}), τ_k and v_k are the kth-order interaction time and volume, and F is the photon flux ($cm^{-2}\ s^{-1}$). A typical cross-section for a nonresonant two-photon ionization is ca. $10^{-49}\ cm^4\ s$.[32] For a resonant, or close to resonant, process the cross-section would be higher by many orders of magnitude. The photon flux is very important, since it appears in eq 13 at the kth power. For instance, everything being the same, but switching from a ns-laser to a ps-laser increases the number of ions per pulse by 3 orders of magnitude for a two-photon process and by 6 orders of magnitude for a three-photon process. Ionization of many organic molecules with millijoule

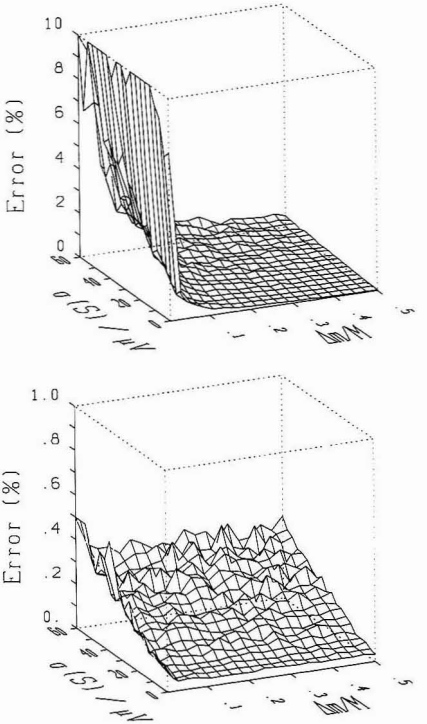

Figure 8. Error in the determination as a function of $\Delta m/M$ at various noise levels. (a, Top) error in the determination of the number of ions (n_1). It is affected mainly by the $\Delta m/M$ value and increases rapidly. (b, Bottom) error in the determination of the mass (m_2). It is mainly affected by the noise level and is still acceptable even at the highest noise level.

pulse energies by a two-photon process and a ps-laser has an efficiency close to 100%. Similar efficiencies are obtained by a resonant ionization with a ns-laser.[20,33,34] In the worst case, of a completely nonresonant two-photon ionization, using a ns-laser, one still can ionize ca. one part of 10^6 molecules, as has been previously discussed.

The second factor is the minimum number of ions that can be detected. This is basically determined by the signal-to-noise ratio. In a system of an overall capacitance of 80 pF, 1000 ions induce a voltage difference of 4 μV. In the simplest apparatus that detects the signal by an analog storage oscilloscope, equipped with a differential amplifier (10 μV/division), ca. 10 000 ions are needed for a reasonable determination. Using a good preamplifier connected directly to the electrodes and shielding the system may reduce the minimum detectable ions to 1000. However, the overall limitation is caused by the noise level. Figure 9 shows the error in the determination as a function of the number of ions at several capacities of the system.

It should be noted that the previously mentioned low voltages correspond to the detection limits only. As has been shown in the Introduction, a regular KrF excimer laser easily produces 10^5–10^7 ions/cm^3, which means that the regular signals can be measured by a current analog or digital storage oscilloscope and other transient recorders.

(31) Morellec, J.; Normand, D.; Petite, G. *Adv. At. Mol. Phys.* **1982**, *18*, 97.
(32) Lambropoulos, P. *Adv. At. Mol. Phys.* **1976**, *12*, 87.
(33) Klimcak, C.; Wessel, J. *Appl. Phys. Lett.* **1980**, *37*, 138.
(34) Stuke, M. *Appl. Phys. Lett.* **1984**, *45*, 1175.

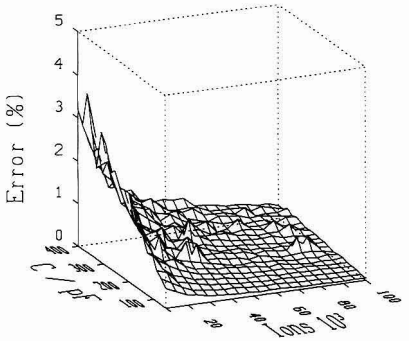

Figure 9. Error in the determination as a function of the absolute number of ions and the system's capacitance. Such plots may show the limits of the detection for several systems. An experimental system of ca. 100 pF needs ca. 10 000 ions for a good determination.

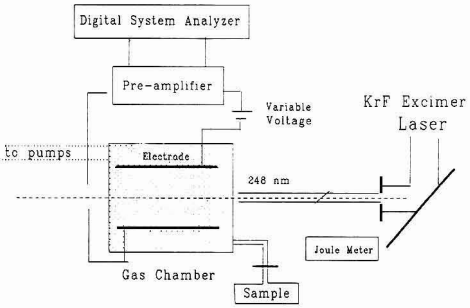

Figure 10. Experimental setup. The overall capacitance is 95 pF. The data are recorded on a DSA for single pulses and analyzed on a computer.

Thus, the theoretical limits of the detection (at 10^{-3} mbar) obtained by combining the previously discussed factors, are ca. two parts in 10^{11} for the very high ionization efficiency,[24] and as low as 2 parts in 10^7 for the nonresonant ionization by a ns-laser.

EXPERIMENTAL SECTION

The experimental setup is schematically shown in Figure 10. The light source has been an KrF Excimer laser (Lambda Physik EMG 150 NSC, divergence <0.2 mrad, band width <1 cm^{-1}). It has delivered pulses of ca. 250 mJ at 1 Hz and a wavelength of 248 nm (5 eV). An aperture of ca. 0.1 mm has been used in order to cut a narrow beam, and a piece of quartz, obliquely located in the beam, has attenuated the energy to the desired values. The beam has not been focused.

The stainless steel ionization tube has been sealed by UV-transparent windows. The two long electrodes have been mounted on Vespel holders and connected to BNC outputs. Additional small electrodes have been located close to the windows in order to trap possible charges originating at the windows or out of the long collecting electrodes. The parallel laser beam has been symmetrically aligned between the electrodes. The sample gas has been introduced to the chamber through a leak-valve. To simulate on-line measurements, the pumps have been continuously operated against the leak of the sample, maintaining constant pressures in the range 10^{-3}–10^{-6} mTorr. The pressures have been monitored by a capacitance manometer directly mounted on the chamber. The electrodes have been connected to a differential preamplifier and displayed on a 400-MHz digital signal analyzer (Tektronix, DSA601) triggered by the laser. When a differential oscilloscope is used, there is no need of the preamplifier. The wiring has been well shielded by stainless steel tubes. The bias voltage has been supplied by batteries located inside the shielding tubes. The voltage has been varied by connecting various numbers of batteries in series.

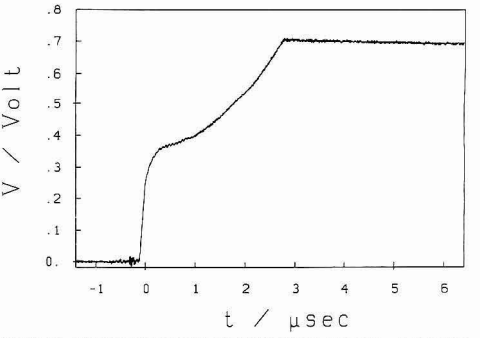

Figure 11. Digitized waveform obtained for pure benzene. It consists of 2048 data points. Even more data points, still from a single laser shot, may be obtained when necessary.

The signals have been recorded for single pulses (no simple integration could be done, due to the fluctuations in the laser pulse energy). The waveforms have been accumulated in the DSA's memory and then transferred to a personal computer. Most of the digitized waveforms consist of 2048 time points. However, much denser samplings have been carried out when necessary (the upper limit is 1-GHz sampling rate). The data analysis has been carried out on an IBM 3090 computer. All software was written in FORTRAN 77, and compiled by VS-FORTRAN Version 2 Compiler.

EXPERIMENTAL RESULTS AND DISCUSSION

Two systems have been chosen to demonstrate the applicability of the apparatus and the algorithm: the resolution of the natural isotope ^{13}C in benzene and analysis of a mixture of benzene and fluorobenzene. Many MPI experiments have been carried out with benzene; see, e.g. refs 20, 21, 23, 35, and 36. Benzene is resonantly ionized at 248 nm, so the unfocused laser beam has to be attenuated (has been kept below 10^6 W cm^{-2}). It has been found that best results are obtained at low energies, far below the saturation limit. It has been shown that at such low energies there is almost no fragmentation.[20-23,37] Low signals (10 mV at most before amplifications) kept the preamplifier far from its limitations, thus providing an undistorted waveform.

Figure 11 shows the digitized waveform obtained for pure benzene. The zero time has been assigned to the steepest ascent. This waveform consists of 2048 points. Most of the points overlap and cannot be resolved by eye; therefore, the true standard deviation is lower than the eye impression. The sampling resolution in the vertical mode (of ca. 0.4%) can be observed, especially at the decay time after 3 µs. Noisy oscillations that appear around the zero time are probably induced by the laser discharge and electronics. The baseline can still be accurately determined; however, the data at the first microsecond may be inaccurate. Detailed analysis of the oscillations shows one dominant frequency thus, in principle, the oscillations could be filtered out. In this particular case, we have just started the data analysis after the first microsecond, since the "interesting" information is

(35) Rossi, M. J.; Helm, H. *J. Chem. Phys.* **1987**, *87*, 902.
(36) Müller, G.; Fan, J. Y.; Lyman, J. L.; Schmidt, W. E.; Kompa, K. L. *J. Chem. Phys.* **1989**, *90*, 3490.
(37) Bernstein, R. B. *J. Phys. Chem.* **1982**, *86*, 1178.

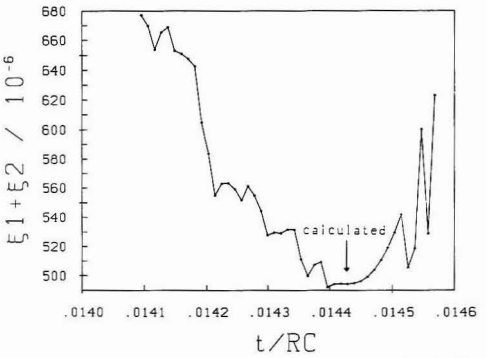

Figure 12. Function $\xi(t)$ obtained by the algorithm to resolve the ^{13}C benzene. The arrow shows the calculated location of the minimum.

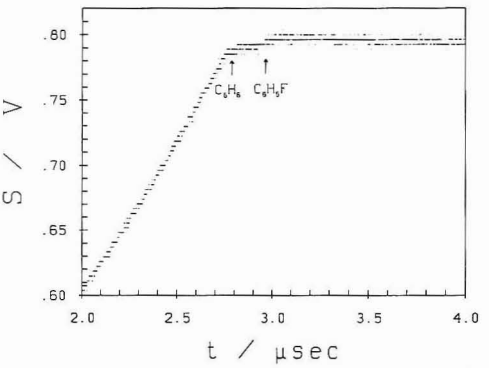

Figure 13. Signal from a mixture of benzene and fluorobenzene, in the vicinity of the break point. The numerous data points enable the algorithms to resolve the masses at a good precision.

expected to be at the break points around 3 μs. However, for further research, this technical problem will be solved.

The algorithm has been applied in order to resolve the ^{13}C molecules in benzene. This problem is characterized by a difficult combination of small value of $\Delta m/M$ and high value of $\Delta i/I$. The results in the vicinity of the break point are presented in Figure 12. The arrow points at the calculated location of the minimum. The relative deviation in the mass determination is twice the relative deviation in t_{max}; therefore, the error of the resolution has been in this case 1.4%. However, it should be emphasized that the main component (mass 78) has been perfectly determined by the shape of the waveform. This determination is at the limit of the particular setup; therefore the quantitative results for the isotopic variant have not been satisfactory (11% instead of the expected 6.7%). Imposing the correct masses and using algorithm Al3 provide a better result (7.2%). A higher error in the determination of the ions, compared to the determination of the masses, has been already predicted (see discussion on the effect of $\Delta m/M$ and Figure 8a,b). Poor reproducibility has been obtained in this limit case.

The next example has been the analysis of the mixture of benzene in fluorobenzene. This mixture can be resolved much easier. Figure 13 shows the digitized results. In this case the time points have been sampled in the vicinity of the break points which can be observed just by inspection. The number of ions of benzene is much higher than that of fluorobenzene. The equal distance between the digitized points at the vertical axis represents the sampling boxing in this coordinate. Most of the points cannot be observed by eye, due to overlapping; however, the computer algorithm uses all of them. The results show a ca. 1% error for the mass determination.

These experimental results prove the feasibility of the proposed method and also point out its major limitations, as have been previously predicted by simulations. It is clear that, for a monocomponent system, the analysis is simple, and its accuracy is determined by the previously described factors. A two-component system can be resolved as demonstrated in the experiment. As the masses are more similar and as the concentration of one of the components diminishes, the determination becomes more difficult and the errors are higher. Again, the more quantitative analysis of these effects is discussed in previous sections.

The method can be applied to more than two components as well. Each additional component possesses a break point in the measured signal. These cases will be studied in the future. However, it is clear that as the number of components is higher, the resolution is more difficult. It seems now that for a many-component mixture, only a very simple mass combination can be resolved by this method.

Other general experimental problems are the fragmentation by the laser light and the metastable ions formed during the flight time. These problems have not been studied here. The fragmentation has been prevented by using a very low laser flux. However, there are cases where fragmentation cannot be avoided. If the fragmentation is very fast, then the method can treat it as an additional component. A low level of fragmentation during the flight time can be ignored and treated like an additional noise in the signal (that can be handled by the numerical algorithms). However, an extended fragmentation, occurring at a distribution of times after the laser pulse, cannot be treated by this method. In general, to apply this method, fragmentation has to be avoided as much as possible, by applying low laser intensities. In many cases dealing with big molecules, this task can be accomplished due to the relatively short flight time.

It is well-known, in the time-of-flight instruments, that the mass resolution is mainly limited by the temporal duration of the laser pulse, the spatial region of ionization, and the initial velocity of the ions. In our case, the temporal duration of the laser is much shorter than the differences in t_{max}. The spatial region of ionization is determined by the laser beam. It has been minimized by means of an iris. As described in a previous section, the effect of the definite ionization region can be treated like a special kind of noise. However, this definite region, as well as the initial velocity distribution, limits the resolution by making the observation of the break points in the signal more and more difficult. Some of these factors are simulated in the previous calculations, in order to predict the overall effect on the error in the determination.

CONCLUDING REMARKS

A new, on-line, analytical method based on the MPI process has been described. The method is greatly simplified by using an unfocused laser beam and by a direct measurement of the ions. The proposed ion and mass detection enables measurement in a large dynamic range, and the need of a high-vacuum system is avoided. The price of the experimental simplification is that the signal has to be analyzed by a computer. The required computer algorithms have been developed and evaluated.

The method is quantitative, provided that the cross-sections for the ionizations are given. However, a related simplified method for ionization cross-section measurements has been recently developed[19] and we hope that more and more absolute ionization cross-sections will be available. It should be emphasized that, in contrast to the regular setups, by using

the proposed method, one can easily find the concentration from the number of ions (provided directly by the method) and the corresponding ionization cross-section. The parallel beam creates a large and simple interaction volume and avoids the difficult analysis of the focus regime. The described method carries out the analysis by using the information from a single laser pulse. Thousands of data points are recorded after one pulse, which usually provides good input for the error-compensating algorithm. However, information of many pulses can be used as well to improve the results in several ways: The waveforms may be stored and boxed according to the laser energy pulse and then be integrated. Another possibility is just to record the various energies of the pulses and analyze each of them separately. Then the data can be processed by statistical algorithms. Concerning the mass determinations, one can vary the bias voltage from pulse to pulse and calculate with a better accuracy the masses by a plot of t_{max} vs $1/\sqrt{\Delta V}$. The results are independent of energy fluctuations, as long as the energy is kept under the fragmentation level.

In this paper the method has been proposed and the algorithms evaluated. Experimental examples have been provided by using the first prototype. However, further improvements are needed in order to introduce it to general usage. Some improvements are still needed in the electronics. An especially designed differential amplifier connected directly to the chamber could be used, instead of the general purpose amplifier. A more compact system can reduce the capacitance by a factor of 2, thus increasing the sensitivity (the actual capacitance is ~95 pF, most of it due to the wiring). Another improvement can be introduced by properly reducing or filtering out some of the oscillatory noise observed in the waveform. Smaller windows in the chamber could improve the shielding.

The limitations of the technique have been discussed, and the expected error as a function of the various parameters has been predicted. In view of these limitations, it should be mentioned that this instrument is not to replace the traditional MS apparatus. It cannot provide a full mass spectra of complicated mixtures. Nevertheless, it can be used as a part of an alarm system for organic gases in air or for other environmental analyses where a simple and low-cost technique is required. Further investigation of more complex mixtures and the effects of metastable ions is planned.

A somewhat different use of this system is for monitoring a specific mass. In this case, it would be better to ionize at a resonance frequency. In this mode, one can scan lots of data just in the vicinity of the expected t_{max} that corresponds to the monitored mass. The method would be suitable for a mode of operation where continuous monitoring is needed, and the computer algorithms are mainly used to ascertain the mass and to resolve it from time-dependent mixtures. Such a system can be easily automated, due to its large dynamic range.

RECEIVED for review March 2, 1992. Accepted August 17, 1992.

Mass Spectrometric Analysis of Rubber Vulcanizates by Laser Desorption/Laser Ionization

Keith R. Lykke,*,†,‡ Deborah Holmes Parker,†,‡,§ Peter Wurz,†,‡ Jerry E. Hunt,‡ Michael J. Pellin,†,‡ Dieter M. Gruen,†,‡ and John C. Hemminger§

Materials Science and Chemistry Divisions, Argonne National Laboratory, Argonne, Illinois 60439, and Department of Chemistry, University of California, Irvine, California 92717

Robert P. Lattimer

The B. F. Goodrich Co., Research & Development Center, Brecksville, Ohio 44141-3289

Three different vulcanized rubbers have been studied by laser desorption/laser ionization mass spectrometry. Analysis of these vulcanizates by various conventional mass spectrometric methods has been difficult because of the complexity of their mass spectra. The major thrust of the present work is to show that different wavelengths for the postionization step allow selectivity which provides important additional information about the chemical makeup of these complex materials. Near-UV wavelengths selectively ionize aromatic additives, far-UV wavelengths photoionize other nonaromatic species, and VUV wavelengths access all of the desorbed species. The ability to vary these different parameters allows a specificity that rivals other techniques for surface and bulk analysis of polymers and their additives.

INTRODUCTION

Laser desorption (LD) has proven to be a viable means to introduce nonvolatile surface species into the gas phase.[1-13] Other methods, such as thermal desorption and ion bombardment,[14] often tend to thermally decompose the molecules or fragment the molecular species with the incident primary ions. Thus, the fragments are not easily identified with the molecular structure of the original surface which, in very important cases, is polymeric in nature. For laser desorption/laser ablation, the amount of fragmentation depends on the energy absorbed by the surface, the wavelength of the laser beam, and the pulse length of the laser.[15-17] However, by optimizing the laser parameters for a particular analysis system such as a polymer, conditions are achieved that induce very little fragmentation of the polymer itself or its additives. The most widely utilized technique for monitoring the laser desorbed species is prompt-ion mass spectrometry, that is, detection of ions produced directly by the laser desorption process.[1,18,19] This technique has proven to be quite useful in many instances, but it does suffer from severe matrix effects due to the strong dependence of surface ionization and surface neutralization on both substrate chemistry and the nature of the desorbate. These matrix effects arise from the two physical processes involved: laser desorption and ionization of the desorbed species. The first effect depends mainly on the absorbed energy and volatility of the sample while the second effect depends principally on the ionization potential of the desorbed species. In this paper, we report on a method to alleviate some of the inherent matrix effects by analyzing the *neutrals* that are contained in the laser-desorbed plume.[6,8,9,12] This is accomplished with a second laser beam of variable wavelength and intensity. We show that the ability to vary these different parameters allows specificity and detection sensitivity that rivals other techniques for surface and bulk analysis of polymers and their additives. The samples employed to demonstrate these capabilities are three different vulcanized rubbers that have been previously studied mass spectrometrically.[20-23]

Raw rubbers are usually mixed with various additives which produce certain characteristics in the polymer. These additives include vulcanizing agents, fillers, pigments, plasticizers, antioxidants, and antiozonants. Vulcanization cross links the rubbers to impart strength and elasticity and restricts viscous flow. Carbon black acts as a filler in the rubbers studied here, and there are no other pigments in them. A few antioxidants and antiozonants are present in the vulcanizates at the parts per hundred level. These constitute some of the more important species for analysis and are the focus in the

† Materials Science Division, Argonne National Laboratory.
‡ Chemistry Division, Argonne National Laboratory.
§ Department of Chemistry, University of California.

(1) Furstenau, N.; Hillenkamp, F.; Nitsche, R. *Int. J. Mass Spectrom. Ion Processes* **1979**, *31*, 85–91.
(2) Asamoto, B.; Young, J. R.; Citerin, R. J. *Anal. Chem.* **1990**, *62*, 61–70.
(3) Asamoto, B.; Bryan, S. R.; Judy, C. L.; Linton, R. W.; Hagenhoff, B.; Deimal, M.; Benninghoven, A. *SIMS VII*, **1990**.
(4) Becker, C. H.; Jusinski, L. E.; Moro, L. *Int. J. Mass Spectrom. Ion Processes* **1990**, 495, R1–R4.
(5) von der Linde, D.; Danielzik, B. *IEEE J. Quantum Electron.* **1989**, *25*, 2540.
(6) Pallix, J. B.; Schühle, U.; Becker, C. H.; Huestis, D. L. *Anal. Chem.* **1989**, *61*, 805–811.
(7) Meijer, G.; de Vries, M. S.; Hunziker, H. E.; Wendt, H. R. *J. Chem. Phys.* **1990**, *92*, 7625.
(8) Nogar, N. S.; Estler, R. C.; Miller, C. M. *Anal. Chem.* **1985**, *57*, 2441–2444.
(9) Otis, C. E. *Appl. Phys.* **1989**, *B49*, 455.
(10) Lubman, D. M.; *Lasers and Mass Spectrometry*; Oxford University Press: New York, 1990.
(11) Li, Y.; McIver, R. T.; Hemminger, J. C. *J. Chem. Phys.* **1990**, *93*, 4719.
(12) Hunt, J. E.; Lykke, K. R.; Pellin, M. J. *Methods and Mechanisms for Producing Ions from Large Molecules*; Plenum Press: Minaki, Canad, 1990.
(13) Engelke, F.; Hahn, J. H.; Henke, W.; Zare, R. N. *Anal. Chem.* **1987**, *59*, 909–912.
(14) Gardella, J. A.; Pireaux, J.-J. *Anal. Chem.* **1990**, *62*, 645A–660A.
(15) Lazare, S.; Granier, V. *Laser Chem.* **1989**, *10*, 25.
(16) Feldmann, D.; Kutzner, J.; Laukemper, J.; MacRobert, S.; Welge, K. H. *Appl. Phys.* **1987**, *B44*, 81–85.
(17) Srinivasan, R.; Braren, B. *Chem. Rev.* **1989**, *89*, 1303.
(18) Johlman, C. L.; Wilkins, C. L.; Hogan, J. D.; Donovan, T. L.; Laude, D. A.; Youssefi, M.-J. *Anal. Chem.* **1990**, *62*, 1167–1172.
(19) Huang, L. Q.; Conzemius, R. J.; Junk, G. A.; Houk, R. S. *Anal. Chem.* **1988**, *60*, 1490–1494.
(20) Lattimer, R. P.; Harris, R. E. *Mass Spectrom.* **1985**, *Rev. 4*, 369–390.
(21) Lattimer, R. P.; Harris, R. E.; Rhee, C. K. *Anal. Chem.* **1986**, *58*, 3188.
(22) Lattimer, R. P. *Rubber Chem. Technol.* **1988**, *61*, 658.
(23) Lattimer, R. P.; Harris, R. E. *Rubber Chem. Technol.* **1989**, *62*, 548.

0003-2700/92/0364-2797$03.00/0

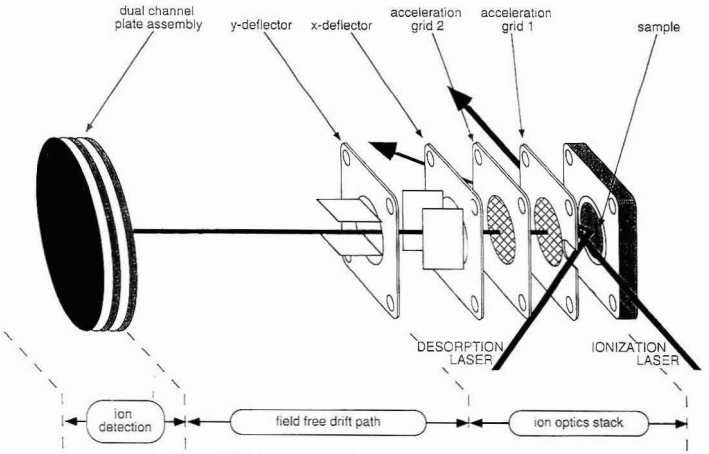

Figure 1. Schematic of the laser desorption time-of-flight apparatus. The sample is mounted on a rapid sample transfer rod and loaded into the system and then the rod is retracted. The sample is typically at 8 kV and grid 1 is at 7.6 kV for postionization or 0 kV for prompt-ion detection. The laser beams enter and exit the apparatus through fused silica windows.

present study. Antioxidants and antiozonants are added to polymers to prevent deterioration due to oxidative degradation of polymer bonds. Other species present in some polymers include flame retardants, mostly halogen-containing compounds that chemically deprive the flame of oxygen; plasticizers that soften brittle polymers and lower processing temperatures; UV stabilizers that protect the polymer from harmful effects of the near UV; mold releases that coat mold surfaces to prevent sticking and to ease removal of the part from the mold; mildicides and fungicides that control microbial attack at the surface of polymers; dyes and pigments that impart color to the polymer; and lubricants that act to reduce friction between polymer molecules (internal) and to reduce friction at interfaces (external).

Few methods exist that can detect and characterize such a wide diversity of molecular species at surfaces, especially when the species are present in only minor concentrations. One currently used method is prompt ion detection following laser desorption. A more elegant method is laser desorption to volatilize the surface molecular species into a neutral plume, followed by laser (species-sensitive) ionization. This method decouples the desorption and the ionization step, allowing each process to be independently optimized. In this paper, we compare these two approaches using well-characterized vulcanizate samples. (We will not discuss in detail the various physical and chemical aspects of the vulcanizates. The interested reader is encouraged to consult ref 21 for details.) Special emphasis is placed on the various possibilities of postionization of the neutral plume. Analysis with the proper choice of laser wavelength and intensity provides information about the polymer that cannot be obtained by other means. This is especially true if the postionization process is combined with high-resolution mass spectrometry. First, we discuss the experimental aspects of this work including the mass spectrometer, the lasers utilized for desorption and ionization, and the details of data capture and manipulation. Then, the results are presented and discussed. Finally, the implications of this new technique are summarized, and future directions for this research are proposed.

EXPERIMENTAL SECTION

The laser desorption/time-of-flight (LD–TOF) apparatus has been discussed in detail previously.[12,24] The mass spectrometer consists of a sample surface, an acceleration field, and a field-free region with an ion detector at the end of the flight path (see Figure 1). The TOF mass spectrometer can be operated in two different modes. First, for measuring the mass spectrum of direct laser desorbed ions (ions produced by the desorption laser alone), the sample is held at 8 kV and the grids are held at ground. Second, for postionization experiments, a two-step acceleration is used with the sample at 8 kV, the first grid at 7.6 kV, and the second grid at ground. In practice, the extraction potentials in the ion source are adjusted to optimize the mass resolution of the ions formed by photoionization of desorbed neutral molecules. The overall flight path length is 120 cm with acceleration distances of 4 mm in each of the two acceleration regions. The accelerated ions are detected using a dual-channel-plate detector with a modest postacceleration potential. Data are recorded in a transient recorder with a maximum time resolution of 5 ns. Further processing of the data is accomplished in a PC-based software system. The typical operating vacuum is $\sim 2 \times 10^{-9}$ Torr. The mass resolution ($m/\Delta m$) of the apparatus is approximately 1000 (fwhm at $m/z \sim 700$ amu) using a 5-ns laser pulse, while a $\leq$ 70-ps, 266-nm laser pulse yields a resolution exceeding 1500 with the same apparatus.

The vulcanizate samples were prepared in two distinct ways for the analysis described in this paper. For *direct analysis*, a piece of the 2-mm-thick polymer was cut into a 1-cm^2 piece, and the front side was scraped in air with a razor blade to expose a fresh surface and placed immediately (within less than 1 min) into the TOF mass spectrometer via a rapid sample transfer system. These samples were held in place on the sample stub with a press-fit ring holding a copper foil with a 4-mm-diameter hole cut out of the center. For the *extract analysis*, the vulcanizate was allowed to dissolve in the particular solvent for a number of days, and the extract was pipetted ($\sim$100 μL) onto a polished-stainless-steel stub, evaporated to dryness, and inserted into the TOF mass spectrometer for later analysis. We varied the number of days of sample extraction and noticed no difference in the mass spectra although the solutions became more concentrated for longer extraction periods. A motor-driven micrometer mirror mount permitted the desorption laser beam to be rastered over the entire surface. This capability allows

(24) Lykke, K. R.; Pellin, M. J.; Wurz, P.; Gruen, D. M.; Hunt, J. E.; Wasielewski, M. R. *Mater. Res. Soc. Symp. Proc.* **1991**, *206*, 679.

control over the measurement position and provides fresh surface exposure from shot to shot, an important consideration for reliable surface analysis.

Various lasers are used for desorption and ionization. Typically, the 532-nm-focused output (or 266-nm-doubled output) of a Q-switched, mode-locked Nd^{3+}:YAG laser (<100-ps pulse duration) is the desorption beam, followed by one of a number of frequencies generated with a Q-switched Nd^{3+}:YAG laser (~5-ns pulse duration). These wavelengths (and energies) include 1064 nm (the fundamental, 1.16 eV), 532 nm (2nd harmonic, 2.33 eV), 355 nm (3rd harmonic, 3.49 eV), 266 nm (4th harmonic, 4.66 eV), and 212 nm (5th harmonic, 5.83 eV). In addition to these easily generated laser wavelengths, we have available a 3rd harmonic frequency-tripling cell to produce 118-nm radiation (9th harmonic, 10.5 eV). This is described in more detail below. We also use a XeCl excimer laser (308 nm, 4 eV) for desorption or for postionization. The lasers are independently triggered, allowing their relative timing to be adjusted. An iris is used to pick out the central portion of the desorption laser beam, and a series of neutral density filters, or a polarizer in a rotation stage, is used to regulate the beam intensity. The desorption laser is obliquely incident on the sample as shown in Figure 1. The energy of the desorption laser is typically less than 0.01 mJ/pulse with an irradiated area of $<10^{-3}$ cm^2. The ionization laser intensity can be continuously varied using a set of mirror-image beam splitters (one high reflector at a specified wavelength, one uncoated) rotated in opposite senses to keep the beam from deviating in position and direction.

The 118-nm radiation is produced by frequency tripling the third harmonic of a Nd^{3+}:YAG laser in a Xe/Ar mixture. This mixture is optimized by photoionizing acetone with the 118-nm radiation and maximizing the $m/z = 58$ signal in the TOF mass spectrometer. We estimate the intensity of the generated VUV radiation to be ~100 nJ (~10^{11} photons/pulse). The 118-nm beam is separated from the 355-nm laser beam using the dispersion of a MgF_2 lens.[25-28] The two beams are separated by ~2 mm at the sample position. By translating the desorption laser spot ~2 mm on the sample, either 118-nm positionization or 355-nm postionization is obtained. The position of the desorption laser spot is monitored in real time with a video camera. This allows a simple method for quickly acquiring both the 355-nm data and the 118-nm data. Recently, we have installed a translatable 355-nm-high reflector inside of the vacuum system before the TOF ion optics. This allows for total rejection of the 355-nm beam.

RESULTS AND DISCUSSION

The three different types of analysis presented in this paper are laser desorption, laser desorption/laser ionization, and laser ionization alone. Each particular type of analysis has its own merits, and there have been numerous discussions of each (see Introduction for references). Prompt ions, produced by laser desorption, can be detected with high sensitivity and, in many cases, can give a broad overall understanding of the composition of the surface. However, detection of prompt ions from laser desorption suffers from extreme matrix effects. Thus, the measured ion abundances have little or no relation to the quantitative composition of the surface. The ions with the lowest ionization potential (for positive ion desorption) or the highest electron affinity (for negative ion desorption) are usually the ions detected with low laser fluence. However, at higher laser fluences, many of the species present at the surface are detected. At these fluxes, however, fragmentation of desorbing molecules often becomes a dominant channel. For most investigations performed in our laboratory, prompt ions are detected first (both positive and negative ions) to determine the overall makeup of the surface. Many times this will suffice to detect an unknown additive in a polymer. However, after this initial examination, a postionization analysis is usually performed to obtain a more comprehensive characterization of the sample.

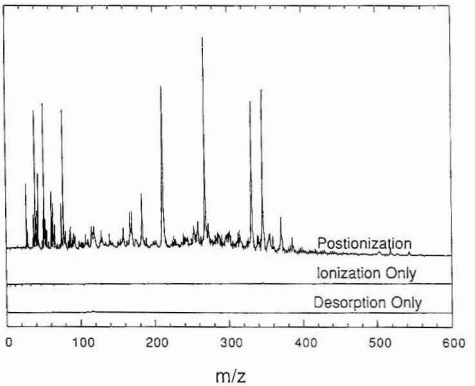

Figure 2. Direct analysis of vulcanizate B. The spectra taken with desorption only (postionization laser blocked) and ionization only (desorption laser blocked) yield a very weak signal and are shown as dashed and dotted lines near the zero signal level. The large peaks in the postionization spectrum 355 nm are indicative of certain additives in this vulcanizate (see text for details). The spectra are offset for clarity.

Postionization Experiments. Figure 2 displays a typical LD-TOF spectrum for vulcanizate B (direct analysis). This spectrum was acquired using the 308-nm excimer laser for desorption, followed by 355-nm light for ionization. Detection via resonantly enhanced multiphoton ionization (REMPI)[29] allows a few of the additives present in the polymer to be preferentially detected over the ubiquitous hydrocarbons in the polymer. A detailed discussion of the vulcanizates and the additives is presented in ref 21. Also included in Figure 2 are spectra obtained with the desorption laser blocked (ionization only) or with the ionization laser blocked (desorption only), showing that this surface analysis method is a probe of the desorbed *neutral* species only. The analysis is much less matrix-dependent than prompt-ion mass spectrometry because the desorption laser provides the energy for neutral particle removal only, without the extra energy needed for direct ionization. In addition to diminishing the matrix effect introduced by the surface, less laser fluence is required for the removal of particles, thus reducing the chance for fragmentation.

Figure 3 is an expansion of a postionization spectrum, accentuating the additive-rich portion of the mass spectrum for vulcanizate B. The higher ionization laser fluence utilized in this spectrum yields more fragmentation than shown in Figure 2 (see later). The molecular weight is labeled for each of the large peaks. Mass 268 is the parent peak for the antiozonant HPPD (see Table I), and $m/z = 211$ is characteristic of the fragment for HPPD. Poly-TMDQ (antioxidant) yields the mass peaks at $m/z = 346$ (parent) and 331 (methyl loss). Some of the other ions present are tentatively assigned to $m/z = 167$ (mercaptobenzothiazole $M^{+\cdot}$), $m/z = 169$ (PhNH-$Ph^{+\cdot}$), and $m/z = 183$ (Ph-NH-Ph-NH^+).

We will not discuss the laser desorption process itself in detail in this paper since numerous reviews in the literature

(25) VonDrasek, W. A.; Okajima, S.; Hessler, J. P. *Appl. Opt.* **1988**, *27*, 4057–4061.
(26) Van Bremer, S. E.; Johnston, M. V. *J. Am. Soc. Mass Spectrom.* **1990**, *1*, 419–426.
(27) Laporte, P.; Subtil, J. L.; Courbon, M.; Bon, M.; Vincent, L. *J. Opt. Soc. Am.* **1983**, *73*, 1062–1069.
(28) Steenvoorden, R. J. J. M.; Kistemaker, P. G.; de Vries, A. E.; Michalak, L.; Nibbering, N. M. M. *Int. J. Mass Spectrom. Ion Processes* **1991**, *107*, 475–489.
(29) Lustig, D. A.; Lubman, D. M. *Int. J. Mass Spectrom. Ion Processes* **1991**, 107, 265–280.

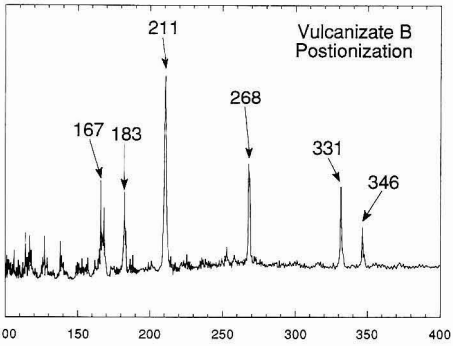

Figure 3. Expansion of the middle mass range for 355-nm postionization of vulcanizate B (direct analysis). The mass range emphasizes the two different additives, HPPD and poly-TMDQ. (See text for details.)

Table I. List of Molecular Additives Detected[a]

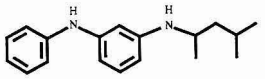

HPPD
MW=268)

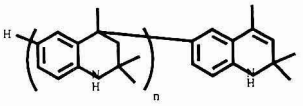

Poly-TMDQ
MW=173 + 173n

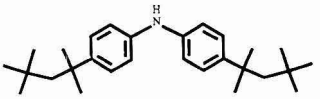

DODPA

molecular additive	molecular weight	vulcanizate
DOPPD *N,N'*-bis(1-methylheptyl)-*p*-phenylenediamine	332	A
DODPA di-*tert*-octyldiphenylamine	393, (322)	A
poly-TMDQ poly(2,2,4-trimethyl-1,2-dihydroquinoline)	346, 331	B
HPPD *N*-(1,3-dimethylbutyl)-*N'*-phenyl-*p*-phenylene-diamine	268, (211), (183), (169)	B, C

[a] Vulcanizate A is based on natural rubber, vulcanizate B is a styrene–butadiene rubber, and vulcanizate C is a *cis*-polybutadiene rubber. Fragments observed in mass spectra are listed in parentheses.

already exist.[17,30,31] Two different schools of thought have evolved concerning laser desorption/laser ablation of polymeric species and each seems to be valid under specific conditions. Particle removal results from either desorption due to electronic excitation to an antibonding state of the polymer, followed by bond breaking, or from thermal desorption caused by local heating of the laser-irradiated area. In terms of *surface* species, the thermally activated desorption model can be applicable. However, species in the near-surface region are only accessable via laser ablation/bond breaking (electronic excitation) since the thermal desorption process would tend to decompose some of the higher-molecular-weight additives present.

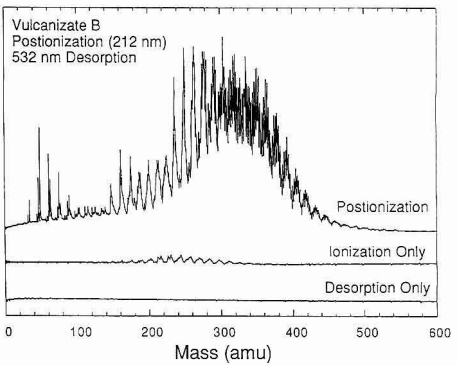

Figure 4. Postionization of vulcanizate B utilizating 212-nm radiation for the ionization laser. Also shown are ionization only (desorption laser-blocked) and desorption only (ionization laser-blocked). Compared with the 355-nm postionization data, the 212-nm radiation yields molecular ions characteristic of the bulk of the polymer and not just additives.

We have explored many different wavelengths for laser desorption and have not observed any differences in the product distribution. Furthermore, we operate the desorption laser at very low fluences. For direct-ion desorption, the laser fluence is adjusted to slightly above the desorption threshold for ion production. The laser fluence can be lowered below this ion-product threshold but still above the lower threshold for neutral particle production. This indicates that the polymer is probably ablated by a thermal desorption mechanism. However, the heating rates are much faster than in a typical thermal programmed desorption (TPD) experiment. In TPD, the heating rates are typically ~1–10 K/s, and the surface (and near-surface) species may either react with other species, dissociate on the surface, or diffuse from the bulk. In laser desorption, the heating rates may approach 10^9 K/s and the desorption channel may dominate other effects due to the desorption preexponential factor. That is, a higher energy pathway may be available simply due to a higher rate of the process.

Since thermal desorption is relatively matrix-independent, most of the observed matrix dependence arises from surface ionization processes. The ionization process can be accomplished in a controlled manner by choosing the proper wavelength (and energy density, vide infra) of the postionization laser in a laser desorption/positionization experiment. To illustrate this point, another set of mass spectra utilizing 212-nm light for ionization is displayed in Figure 4. The desorption-only and ionization-only scans are also shown for consistency. Background gas (pump oil) in the vacuum system is more efficiently ionized by 212-nm radiation than by 355-nm radiation, and ions appear at m/z ~150–300 amu in the ionization-only spectrum. However, a comparison of the ionization only and the postionization scans show that the signals from the rubber vulcanizate and additives dominate

(30) Avouris, P.; Walkup, R. E. *Annu. Rev. Phys. Chem.* **1989**, *40*, 173–206.
(31) King, D. S.; Cavanagh, R. R. *Adv. Chem. Phys.* **1989**, 45.

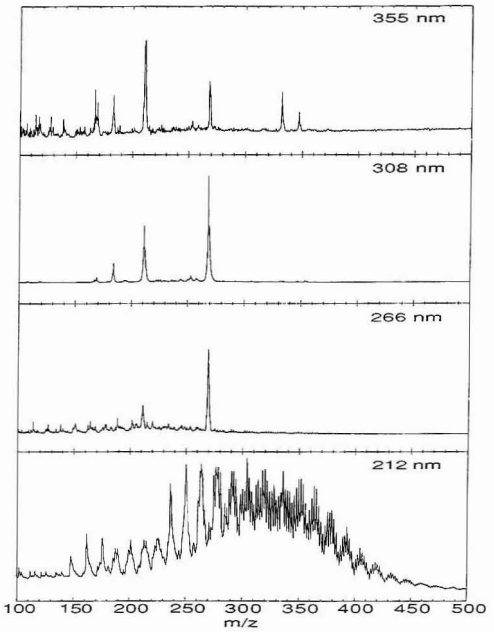

Figure 5. These four panels display postionization data at four different wavelengths for direct analysis of vulcanizate B. Each of the wavelengths accentuates different characteristic species in the vulcanizate.

the background signals. Much more ionization of the processing oils and paraffin wax and less selectivity of the additives occurs for 212-nm photoionization. The 212-nm radiation is absorbed by most of the species, and the ~11.7 eV available for (1 + 1) ionization will ionize most of the species that absorb at 212 nm. Therefore, the selectivity of the 355-, 308-, and 266-nm light (caused by π-π^* transitions in the additives) is absent in the 212-nm case.

Figure 5 displays a panel of the direct analysis experiments of vulcanizate B for wavelengths ranging from 355 to 212 nm. This figure demonstrates that different ionization laser wavelengths access different polymer additives, although there is some overlap between wavelengths. Radiation at 355 nm selectively ionizes the additives that contain aromatic groups, and the 212-nm radiation tends to ionize almost everything except for the small ablation fragments from the polymer. Figure 6 is a spectrum of the same sample utilizing 118-nm ionization, 308-nm desorption, again by direct analysis. The low-mass species are considerably enhanced relative to the high-mass species observed with the longer wavelengths. This is because of the difference in the optical absorption strength for the different species. That is, the small molecular weight fragments from the SBR (styrene–butadiene rubber) surface do not have large oscillator strengths for one photon absorption for $\lambda > 200$ nm. The larger additives observed have large oscillator strengths for one photon absorption (π-π^* transitions), and thus (1 + 1) REMPI is allowed. In summary, the 355-nm light preferentially accentuates the additives in the polymer (selective), the 212-nm light ionizes most of the other large species, while the 118-nm light can be utilized to characterize the majority of the desorbed material (nonselective ionization). This makes the combination of using 118-, 212-, and 355-nm radiation for positionization an extremely powerful technique.

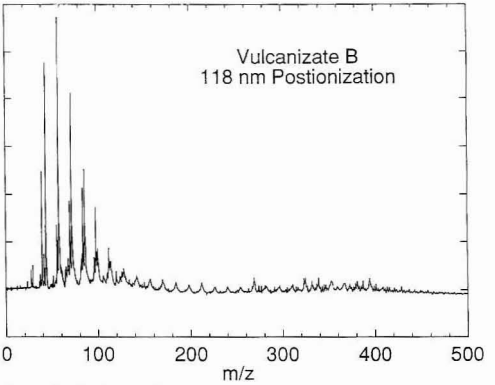

Figure 6. Postionization of vulcanizate B using 118-nm (10.5 eV) radiation. The low-mass region is probably caused by the rubber backbone and is present in higher abundance than the additives that were accentuated with the longer postionization wavelengths.

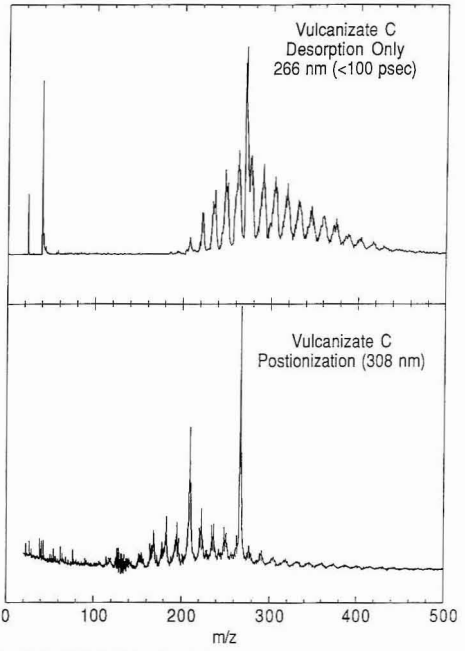

Figure 7. Comparison of postionization with 308-nm (bottom panel) and 266-nm prompt-ion desorption (positive ions, top panel) of vulcanizate C. The 308-nm postionization data were obtained utilizing 266-nm desorption (macropulse from the Q-switched mode-locked Nd:YAG laser). The 266-nm desorption laser pulse for prompt-ion detection is <100 ps in duration. The additives present in the vulcanizate are emphasized in the postionization scan. However, the prompt-ion spectrum does display many mass peaks characteristic to this polymer. The two peaks at low mass in the prompt-ion spectrum are sodium (m/z = 23) and potassium (m/z = 39 and 41).

Prompt Ions. A widely used procedure for analyzing polymers is direct laser ablation and monitoring the prompt ions produced. Figure 7 displays an analysis of vulcanizate C employing this scheme compared with postionization. The desorption pulse (266 nm, <70 ps) produces positive and negative ions directly, given enough laser fluence. The top panel in the figure is the positive-ion spectrum, and the 308-

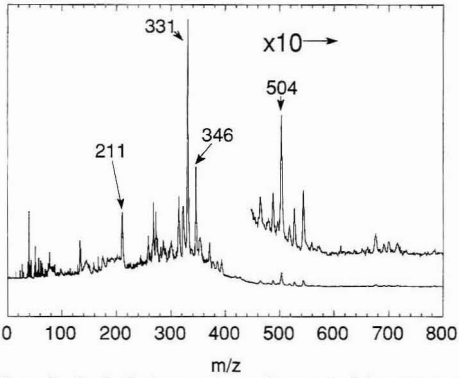

Figure 8. Postionization spectrum of an acetonitrile extract of vulcanizate B. The desorption pulse is the frequency-quadrupled (266 nm) macropulse from the Q-switched mode-locked Nd:YAG laser, and the postionization wavelength is 118 nm. The major peaks visible at high mass are attributable to poly-TMDQ.

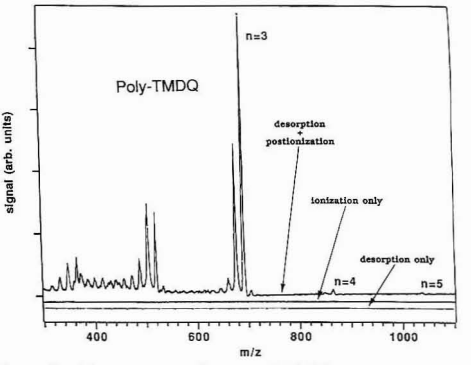

Figure 9. Mass spectra of pure poly-TMDQ acquired utilizing postionization (308-nm desorption, 248-nm postionization, top spectrum), ionization with 248 nm only (middle spectrum), and desorption with 308 nm only (bottom spectrum).

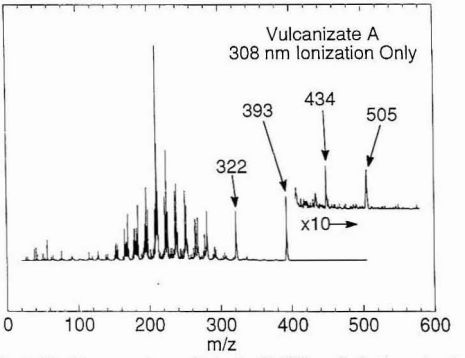

Figure 10. Mass spectrum obtained with 308-nm ionization-only of vulcanizate A (direct analysis). The gas-phase species detected are provided by evaporation from the near-surface region of the polymer and the strongest signals disappear within ~5 min after inserting the sample into the vacuum system.

nm postionization spectrum is displayed in the bottom panel for comparison. The two peaks at low mass in the desorption-only spectrum (m/z = 23, 39) correspond to Na and K ions, respectively. These two positive ions appear in most direct desorption experiments since the ionization potential for each species is so low (5.1 eV for Na and 4.3 eV for K). In fact, these low-mass alkali-metal prompt ions tend to overwhelm the higher-mass species in direct desorption experiments. However, the higher-mass ions between 200 and 400 amu are caused by ionization of the various surface species, such as processing oils and some of the additives.

Extract Analysis. An additional method for polymer analysis is the use of extract pretreatment of the polymer. In this case, we utilize two different solvent pretreatments—acetone and acetonitrile. The first sample investigated is vulcanizate B extracted in acetonitrile. The TOF mass spectrum is shown in Figure 8. The desorption wavelength is 266 nm (picosecond desorption) and postionization is achieved utilizing 118 nm (one-photon ionization). As is clearly evident, higher-molecular-weight species are detected and are attributable to some of the various additives present in the vulcanizate. Most of the (m/z > 400) ions are ascribed to poly-TMDQ additives present at the < 3% level in the bulk vulcanizate. As already pointed out in ref 21, higher-mass species can be observed in extracts that cannot be seen by direct analysis. The low-mass alkyl fragment ions are not observed to any degree in this spectrum in spite of the detectability by one-photon ionization. This is because acetonitrile extracts organic stabilizers in preference to processing oils.[32] Similar mass spectra were recorded following acetone extraction.

Since poly-TMDQ is observed as an additive in most of the vulcanizate B spectra, the laser desorption process was studied in more detail using pure poly-TMDQ as a desorption surface. The pure poly-TMDQ was dissolved in dichloromethane and evaporated on the stainless-steel sample probe. Figure 9 shows the signal obtained from desorption only, ionization only, and positionization. A few points need to be made concerning these spectra. The lack of signal from the ionization-only experiment is indicative of the low volatility of this hindered amine stabilizer. The main peaks in the desorption + postionization spectrum at m/z = 865, 692, 519, 346 are caused by the molecular ion of this oligomeric additive (see Table I). The mass peaks ~16 units below these main peaks originate from demethylation of the parent peak in the ionization process. The peaks ~16 amu above the parent peaks are attributed to oxidation products. In our earlier work,[12] velocity distributions for laser-desorbed neutrals of these samples were obtained and helped to define the pulse delay between desorption and ionization. In practice, this delay is optimized empirically by varying the time delay and observing the signal on a fast oscilloscope.

Ionization Only. If a polymer additive is volatile enough, its presence can be ascertained via ionization-only spectra. That is, the additive evaporates from the near-surface region for a certain amount of time, and the ionization laser alone will yield a reasonable amount of signal to obtain an analysis of the additive present. Figure 10 is a representative 308-nm ionization-only spectrum from vulcanizate A (direct analysis). The major high-mass peaks are from DODPA (see Table I). DODPA is an antioxidant and forms two dominant photoions, m/z = 393 ($M^{+\cdot}$) and 322 ($M - C_6H_{11}$)$^+$. A DODPA impurity, originally seen in vulcanizate A by Lattimer et al.,[21] was also seen in the postionization spectrum. This impurity (tri-*tert*-octyldiphenylamine) yields the ions observed at m/z = 505 ($M^{+\cdot}$) and 434 ($M - C_5H_{11}$)$^+$. By postionization (266-nm desorption, 308-nm postionization, Figure 11), the DODPA peaks are accentuated relative to the rest of the species.

(32) Carlson, D. W.; Hayes, M. W.; Ransaw, H. C.; McFaddon, R. S.; Altenau, A. G. *Anal. Chem.* **1971**, *43*, 1874–1876.

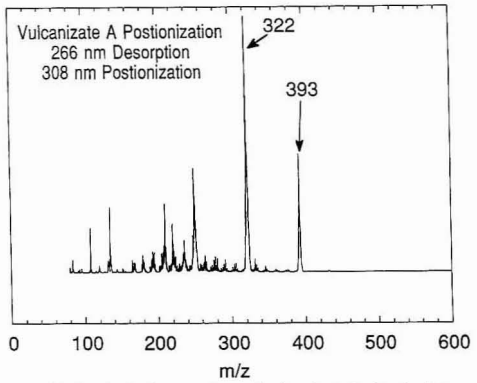

Figure 11. Postionization spectrum of vulcanizate A after the intense ionization-only signals have disappeared. The strongest peaks are characteristic of DODPA.

A unique approach for characterizing a polymeric additive is through multiphoton dissociation/ionization. In this type of experiment, the molecular ion and the associated fragments are detected following intense photon fluxes. Ionization spectra of gas-phase species from vulcanize B are shown in Figure 12. The most intense peaks in the spectrum for low laser fluence are indicative of the polymeric additive HPPD (see Table I for the molecular weights and proper chemical names for the given additives). These species are probably ionized via (1 + 1) ionization at 308 nm (4 eV) and are thus more efficiently ionized than the other species present. This type of ionization scheme (utilizing 250–350 nm) accentuates the aromatic species. Many more fragment peaks are evident in the lower portion of the figure (high fluence). These fragment peaks are due both to fragmentation of the HPPD additive and to fragments from other species present in the gas phase from the ablation of the vulcanizate.

CONCLUSIONS

We have demonstrated that LD–TOF can provide important analytical information about industrially important materials, such as vulcanizate rubbers. The selectivity of the technique allows for a determination of many of the additives present in the vulcanizates. Although not demonstrated in the present experiments, this technique is an extremely sensitive method for detecting surface and near-surface species. In fact, the laser desorption/laser ionization experiments reported in this work left no visible damage on the sample surface. These techniques should be directly applicable to the industrial workplace. A systematic study of the quantification of the detection of additives in polymers is needed. If the detection for direct analysis is shown to be quantifiable, then an "on-line" laser desorption apparatus could be adapted to test for the amount of incorporation of polymeric additives. In addition, segregation phenomena can

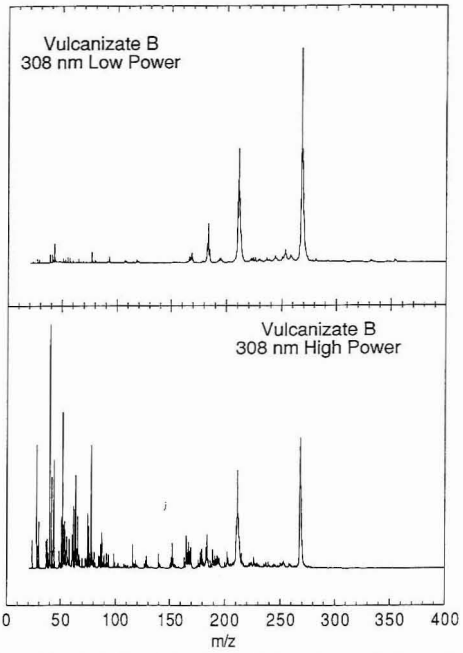

Figure 12. Illustration of the effect of intense laser radiation on the mass spectra of postionization of vulcanizate B (308 nm, direct analysis). The "low-power" spectrum (top panel) displays the peaks characteristic of the HPPD additive and very little else. The "high-power" spectrum (bottom panel) shows peaks characteristic of the HPPD additive along with mass peaks from cracking of the polymer backbone.

be probed with this apparatus and will allow a careful examination of various processes involved in the mixing of polymers and additives. Closely related to this is the investigation of diffusion-related phenomena. Diffusion to the surface (blooming) of polymers is an important process, both technologically and scientifically. A future direction of the research reported here is the detailed study of these diffusion processes in model systems. Once these model systems are understood on microscopic and macroscopic levels, the possibility exists to transfer this knowledge into real-world problems.

ACKNOWLEDGMENT

This work was supported by the U.S. Department of Energy, BES-Materials Sciences and Chemical Sciences, under Contract W-31-109-ENG-38.

RECEIVED for review April 7, 1992. Accepted August 20, 1992.

Registry No. DOPPD, 103-96-8; DODPA, 15721-78-5; TMDQ (homopolymer), 26780-96-1; HPPD, 793-24-8.

^{252}Cf Plasma Desorption Mass Spectrometry in the Synthesis of Porphyrin Model Systems

Jonathan S. Lindsey*

Department of Chemistry, Carnegie Mellon University, 4400 Fifth Avenue, Pittsburgh, Pennsylvania 15213

Tanuja Chaudhary and Brian T. Chait

The Rockefeller University, 1230 York Avenue, New York, New York 10021

^{252}Cf plasma desorption mass spectrometry has been used in the characterization of more than 100 synthetic porphyrins ranging in mass from 614 u for tetraphenylporphyrin to over 2000 u for some porphyrin model systems. In virtually every case, ^{252}Cf plasma desorption mass spectrometry yielded an intense ionized molecule ion [$M^{\cdot+}$ and/or $(M + H)^+$], irrespective of the groups appended to the porphyrin. The appended groups include carboxylic acids, amides, imides, chloroacetamides, Fmoc-protected amino acids, aromatic amines, nitriles, alkynes, alkenes, esters, active esters, benzyl ethers, acetals, dithioacetals, ketones, imines, phenols, quinone, hydroquinone, ferrocene, cyanine dyes, trimethylsilyl protecting groups, nitro groups, and combinations of these functionalities. Metalloporphyrins and porphyrin–porphyrin dimers are also analyzed with ease. Resolved isotopic peaks were observed for porphyrins with molecular weights below 1000, and unresolved isotopic peaks yielding average masses were observed for porphyrin compounds with higher molecular weights. The limited resolution in the higher molecular weight range does not lessen the utility of the method because the observation of the molecule ions [$M^{\cdot+}$ and/or $(M + H)^+$] provides unambiguous evidence concerning the success of the synthesis. The ^{252}Cf plasma desorption mass spectra of porphyrins are not complicated by chemical transformations. This method is ideally suited for rapid analysis of synthetic porphyrins and provides a powerful tool for chemists engaged in the synthesis of complex organic molecules.

INTRODUCTION

The increasing complexity of porphyrin model systems places a premium on methods for analysis and characterization. The analytical issue in porphyrin synthesis generally is not the identification of an unknown substance, but rather the confirmation that the synthesis has proceeded as expected. Chromatographic methods such as TLC provide information concerning product homogeneity, and absorption and fluorescence spectroscopy establish the integrity of the porphyrin chromophore. These techniques require small amounts of material and are performed rapidly but are insufficient to confirm the product identity. Electronic spectra in particular provide little information about the groups appended to the meso-positions, which often constitute much of the total mass in porphyrin model systems. Indeed, the essential porphyrin framework consists of only 24 atoms (e.g., porphine, $C_{20}H_{14}N_4$, molecular mass = 310 u), but typical porphyrin model systems range in mass from 700 to above 2000 mass units. ^{1}H NMR spectroscopy provides detailed structural information pertaining to the groups around the periphery of the porphyrin but often requires extensive interpretation of spectra derived from concentrated samples.

A number of different mass spectrometric methods have been applied to the analysis of porphyrinic molecules over the years.[1-3] These have focused largely on characterizing porphyrins derived from natural sources, although a few early reports concern synthetic porphyrins.[4] More recently, synthetic porphyrins have been examined by an assortment of mass spectrometric methods, including chemical ionization MS,[5] laser photodissociation tandem MS,[6] laser desorption fourier transform MS,[7] electrospray MS,[8] and fast atom bombardment MS.[9-13] The latter method has been used most extensively, and several groups have investigated the demetalation and redox reactions of metalloporphyrins that occur in the fast atom bombardment MS sample matrices.[10,11,14,15] Over the past 12 years we have utilized ^{252}Cf plasma desorption mass spectrometry (PDMS) for the characterization of more than 100 synthetic porphyrins encompassing a variety of model system architectures. The mass spectra are collected in 1–30-min runs on a few nanomoles of the porphyrin sample. We have found that porphyrins ionize readily by ^{252}Cf plasma desorption to form relatively stable intact molecule ions [$(M + H)^+$ and/or $M^{\cdot+}$]. Though the peripheral groups constitute the bulk of the mass in most of the porphyrin model compounds studied, the intact molecule ion was readily identifiable in nearly every case, thereby providing unambiguous confirmation of the success of the synthesis. Taken together, the universal applicability and rapid analysis make ^{252}Cf PDMS a powerful method for assessing the outcome of syntheses of porphyrin model

* To whom correspondence should be addressed.

(1) Smith, K. M. In *Porphyrins and Metalloporphyrins*; Smith, K. M., Ed.; Elsevier: Amsterdam, 1975; pp 381–398.
(2) Budzikiewicz, H. In *The Porphyrins*; Dolphin, D., Ed.; Academic Press: New York, 1978; Vol. III, pp 395–461.
(3) Gallegos, E. J.; Sundararaman, P. *Mass Spectrom. Rev.* **1985**, *4*, 55–85.
(4) Adler, A. D.; Green, J. H.; Mautner, M. *Org. Mass Spectrom.* **1970**, *3*, 955–962. Meot-Ner, M.; Green, J. H.; Adler, A. D. *Ann. N. Y. Acad. Sci.* **1973**, *206*, 641–648. Meot-Ner, M.; Adler, A. D.; Green, J. H. *Org. Mass Spectrom.* **1974**, *9*, 72–79.
(5) Van Berkel, G. J.; Glish, G. L.; McLuckey, S. A.; Tuinman, A. A. *J. Am. Chem. Soc.* **1989**, *111*, 6027–6035.
(6) Fukuda, E. K.; Campana, J. E. *Anal. Chem.* **1985**, *57*, 949–952.
(7) Brown, R. S.; Wilkins, C. L. *Anal. Chem.* **1986**, *58*, 3196–3199.
(8) Van Berkel, G. J.; McLuckey, S. A.; Glish, G. L. *Anal. Chem.* **1991**, *63*, 1098–1109.
(9) Rubino, F. M.; Mascaro, P.; Banfi, S.; Quici, S. *Org. Mass Spectrom.* **1991**, *26*, 161–166.
(10) Naylor, S.; Lamb, J. H.; Hunter, C. A.; Cowan, J. A.; Sanders, J. K. M. *Anal. Chim. Acta* **1990**, *241*, 281–287.
(11) Musselman, B. D.; Watson, J. T.; Chang, C. K. *Org. Mass Spectrom.* **1986**, *21*, 215–219.
(12) Kurlansik, L.; Williams, T. J.; Strong, J. M.; Anderson, L. W.; Campana, J. E. *Biomed. Mass Spectrom.* **1984**, *11*, 475–481.
(13) Zhang, M. Y.; Liang, X. Y.; Chen, Y. Y.; Liang, X. G. *Anal. Chem.* **1984**, *56*, 2288–2290.
(14) Naylor, S.; Hunter, C. A.; Cowan, J. A.; Lamb, J. H.; Sanders, J. K. M. *J. Am. Chem. Soc.* **1990**, *112*, 6507–6514.
(15) Schurz, H. H.; Busch, K. L. *Energy Fuels* **1990**, *4*, 730–736.

0003-2700/92/0364-2804$03.00/0

Chart I. Structural Diagrams for Tetraarylporphyrins (X Substituent, See Table I) and Tetraalkylporphyrins (R Substituent, See Table I)[a]

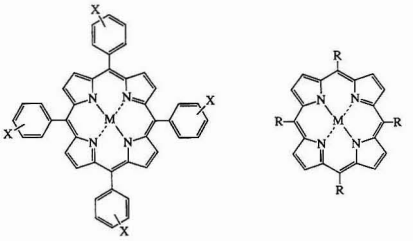

Tetra-aryl-porphyrin Tetra-alkyl-porphyrin

[a] The porphyrins are analyzed as the free base (M = H, H) unless a metal (M, usually Zn) is indicated in the molecular formula.

compounds, i.e. recognizing when synthetic errors or incomplete reaction has occurred, or conversely, when the target material or intermediate has been correctly synthesized. In this paper we summarize the application of ^{252}Cf PDMS in porphyrin synthetic chemistry, thus complementing prior studies that have used this method for the characterization of chlorophyll samples.[16-18]

EXPERIMENTAL SECTION

Porphyrin solutions were prepared at $\sim 10^{-4}$ M in solvents (such as CH_2Cl_2/methanol (1:1) or acetone) suitable for electrospray deposition[19] onto the mass spectrometer sample probe. Approximately 0.1 mL of the porphyrin solution was electrosprayed over the course of 5–10 min onto a 1-cm^2 area aluminized Mylar film. The porphyrin sample was clearly visible as a colored deposit.

The technique of ^{252}Cf plasma desorption mass spectrometry has been described previously.[20] The mass spectra were obtained with the Rockefeller University ^{252}Cf fission fragment time-of-flight mass spectrometer.[18,21] In these studies we concentrated almost exclusively on positive ion spectra. The ion acceleration voltage was 10 kV. An electrostatic particle guide maintained at −30 V with respect to the 3-m flight tube was used to increase the ion transport efficiency to the detector. The ^{252}Cf source with a strength of ~20 mCi yielded a flux of approximately 2000 fission fragments per second through the sample foil. The ever-present ions at m/z 1 (H^+) and 23 (Na^+, from adventitious trace impurities) were used to calibrate the masses observed with the positive ion spectra.

RESULTS

We outline our results as follows. First we present an overview of the typical spectral patterns obtained with porphyrins as a function of increasing molecular weight of appended groups. Next we describe a specific application of the method in the synthesis of a family of porphyrin cage molecules. Then we highlight issues in the characterization of diverse porphyrin compounds and model systems that, with only a few exceptions, have been synthesized using a biomimetic porphyrin reaction strategy.[22,23] Finally, we describe the characterization of porphyrin–porphyrin dimers.

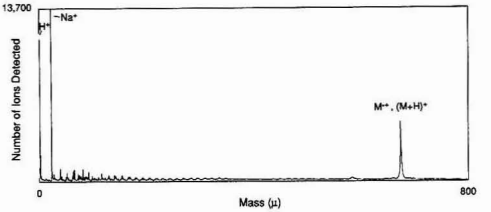

Figure 1. ^{252}Cf plasma desorption mass spectrum of *meso*-tetra(*p*-tolyl)porphyrin.

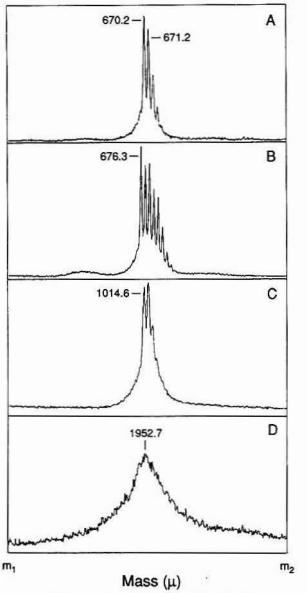

Figure 2. Spectra of the molecule ion region for four compounds. (A) *meso*-Tetra(*p*-tolyl)porphyrin. (B) The zinc chelate of *meso*-tetraphenylporphyrin. (C) *meso*-Tetrakis(4-(*n*-BuO_2C)C_6H_4)porphyrin. (D) *meso*-Tetrakis(4-(Fmoc-Pro-NH)C_6H_4)porphyrin.

1. Typical Spectral Patterns. The mass spectrum of *meso*-tetra(*p*-tolyl)porphyrin (4, Chart I, X = 4-CH_3) exhibits dominant peaks from the intact porphyrin ion (Figure 1) as well as a large number of less intense peaks arising from the fragmentation of the ionized molecule ion. The intense peaks arising from the intact porphyrin exhibit sufficient resolution to allow analysis of each of the isotopic components (Figure 2A). The lowest isotopic component[24] (A + 0) for the molecule containing $C_{48}H_{38}N_4$ ($M^{\cdot+}$) has a mass of 670.3 u and a calculated relative abundance of 57%.[25] The calculated relative abundance of the A + 1 component is 31%, which

(16) Hunt, J. E.; Macfarlane, R. D.; Katz, J. J.; Dougherty, R. C. *Proc. Natl. Acad. Sci. U.S.A.* **1980**, *77*, 1745–1748.
(17) Chait, B. T.; Field, F. H. *J. Am. Chem. Soc.* **1982**, *104*, 5519–5521.
(18) Chait, B. T.; Field, F. H. *J. Am. Chem. Soc.* **1984**, *106*, 1931–1938.
(19) McNeal, C. J.; Macfarlane, R. D.; Thurston, E. L. *Anal. Chem.* **1979**, *51*, 2036–2039.
(20) Macfarlane, R. D.; Torgerson, D. F. *Science* **1976**, *191*, 920–925.
(21) Chait, B. T.; Agosta, W. C.; Field, F. H. *Int. J. Mass Spectrom. Ion Phys.* **1981**, *39*, 339–366.
(22) Lindsey, J. S.; Schreiman, I. C.; Hsu, H. C.; Kearney, P. C.; Marguerettaz, A. M. *J. Org. Chem.* **1987**, *52*, 827–836.
(23) Lindsey, J. S.; Wagner, R. W. *J. Org. Chem.* **1989**, *54*, 828–836.
(24) The lowest isotopic component (A + 0) contains all ^{12}C, ^{14}N, ^{16}O; A + 1 contains one atom of ^{13}C with the remainder ^{12}C, ^{14}N, ^{16}O, etc.
(25) McLafferty, F. W. *Interpretation of Mass Spectra*, 3rd ed.; University Science Books: Mill Valley, CA, 1980.
(26) Atamian, M.; Donohoe, R. J.; Lindsey, J. S.; Bocian, D. F. *J. Phys. Chem.* **1989**, *93*, 2236–2243.
(27) Collman, J. P.; Gagne, R. R.; Reed, C. A.; Halbert, T. R.; Lang, G.; Robinson, W. T. *J. Am. Chem. Soc.* **1975**, *97*, 1427–1439.
(28) Kathawalla, I. A.; Anderson, J. L.; Lindsey, J. S. *Macromolecules* **1989**, *22*, 1215–1219.

Table I. Symmetric *meso*-Porphyrins

compd	aryl substituent (X)	position	formula	calcd	obsd
1	H		$C_{44}H_{30}N_4$	614.2	614.3
2[a]	H		$C_{44}H_{28}N_4Zn$	676.2	676.3
3	H		$C_{44}H_{30}{}^{15}N_4$	618.2	618.2
4	CH_3	4	$C_{48}H_{38}N_4$	670.3	670.2
5	CH_3	2,4,6	$C_{56}H_{54}N_4$	782.4	782.4
6	NO_2	2	$C_{44}H_{26}N_8O_8$	794.2	794.2
7	NH_2	2	$C_{44}H_{34}N_8$	674.3	674.4
8	Ph	4	$C_{68}H_{46}N_4$	918.4	918.6
9	$HOCH_2CH_2O$	4	$C_{52}H_{46}N_4O_8$	854.3	854.5
					836.7[b]
10	dithiolane	3	$C_{56}H_{46}N_4S_8$	1030.1	not res[c]
				1031.2 av	1031.4
11	dithiolane	4	$C_{56}H_{46}N_4S_8$	1030.1	not res
				1031.2 av	1031.4
12	*n*-Bu-O_2C	4	$C_{64}H_{62}N_4O_8$	1014.5	1014.6
13	PhenO_2C	3	$C_{80}H_{54}N_4O_{12}$	1262.4	not res
				1263.2 av	1262.8
14	CH_3O_2C	4	$C_{52}H_{38}N_4O_8$	846.3	846.3
15	*t*-BuO_2C	4	$C_{64}H_{62}N_4O_8$	1014.5	not res
				1015.1 av	1015.6
					791.3[b]
16	NC	4	$C_{48}H_{26}N_8$	714.2	714.3
17	CH_2CHCH_2O	4	$C_{56}H_{46}N_4O_4$	838.4	838.5
18	$-OCH_2O-$	3,4	$C_{48}H_{30}N_4O_8$	790.2	790.3
19	acetal	4	$C_{68}H_{70}N_4O_8$	1070.5	1070.9
20	molecular cleft	3	$C_{92}H_{90}N_8O_{16}$	1562.6	not res
				1563.7 av	1564.4
					1586.7[d]
					1608.7[d]
21[a]	$CH_3(CH_2)_9O$	4	$C_{84}H_{108}N_4O_4Zn$	1300.8	not res
				1303.2 av	1303.1
22	Fmoc-Pro-NH	4	$C_{124}H_{102}N_{12}O_{12}$	1950.8	not res
				1952.2 av	1952.7
23	$(CH_3)_3SiCC$	4	$C_{64}H_{62}N_4Si_4$	998.4	998.3
	porphine meso substituent (R)				
24	$CH_3(CH_2)_4$		$C_{40}H_{54}N_4$	590.4	590.5
25	$CH_3(CH_2)_9$		$C_{60}H_{94}N_4$	870.7	870.9
26	$PhCH_2$		$C_{48}H_{38}N_4$	670.3	670.3
27	PhCO		$C_{48}H_{30}N_4O_4$	726.2	726.2

[a] Zinc chelate. [b] More intense than the molecule ion. [c] Not resolved. [d] Sodium-cationized species. Literature sources: **1**, **9–14**, **16–19**, **24**, **25**;[22] **3**;[26] **5**;[23] **6**, **7**;[27] **8**;[28]; **20**;[29] **15**, **21–23**, **26**, **27**;[30] compounds unspecified are available from commercial sources.

would yield a peak with approximately half the intensity of the A + 0 component. However, the observed peak at 671.2 u has an intensity fully 0.9 times that of the A + 0 peak, indicating the presence of protonated species $(M + H)^+$ in addition to the radical cation $M^{\bullet+}$. The peak at 671.2 u is attributed to the superposition of the A + 1 component of the $M^{\bullet+}$ species and the A + 0 component of the $(M + H)^+$ species. Nonetheless, the molecular ion ($M^{\bullet+}$) is clearly identifiable in the mass spectrum. The accuracy of mass analysis is high; the difference between the observed molecular mass and the calculated mass for the A + 0 component is only 0.1 u (Table I).

The mass spectrum of the zinc chelate of *meso*-tetraphenylporphyrin (**2**), is shown in Figure 2B. The spectrum exhibits a more complex pattern of peaks than the free base porphyrin (**1**) due to the three major isotopes of zinc (^{64}Zn, 48.6%; ^{66}Zn, 27.9%; ^{68}Zn, 18.8%). However, the lowest isotopic component (all ^{12}C, ^{64}Zn) is readily observable. As the mass of the porphyrin model compound increases, the individual components become more difficult to resolve. For example, the monoisotopic component of *meso*-tetrakis(4-(butoxycarbonyl)phenyl)porphyrin (**12**) (1014.6 u) can still be partially resolved from the higher components at 1015.5 and 1016.5 u (Figure 2C). A porphyrin bearing even larger substituents, such as the tetrakis(Fmoc-proline)porphyrin (**22**, Chart II), yields a mass spectrum without a resolved monoisotopic molecule ion peak (Figure 2D). Instead, an envelope is observed resulting from the superposition of isotopic components of the radical cation and protonated species. In this case, the calculated average mass for the radical cation is 1952.2 u and the observed mass is 1952.7 u (Table I). The peak of the envelope is shifted to higher mass than that calculated because of the admixture of protonated and radical cation species. The magnitude of this shift, in all cases studied, is at most 1 mass unit, although in general smaller shifts are observed (Table I). The peaks remain intense, and the loss of isotopic resolution does not greatly diminish the utility of the mass spectral method in confirming the identity of synthetic target compounds.

Almost all of the 100 compounds that we studied yielded a dominant intact ionized porphyrin peak. In a few cases fragment ions with intensities greater than that of the intact ionized molecule were observed, although the $M^{\bullet+}$ and/or the $(M + H)^+$ ion (which we collectively term the molecule ions) was always present in good yield. In a few other cases, sodium cationization of the molecule yielded higher mass peaks of greater intensity than the molecular ion. Those instances involving intense fragmentation or cationization are indicated below.

2. Synthesis of Porphyrin–Quinone Compounds. A cofacial porphyrin–quinone cage molecule was synthesized

(29) Lindsey, J. S.; Kearney, P. C.; Duff, R. J.; Tjivikua, P. T.; Rebek, J., Jr. *J. Am. Chem. Soc.* **1988**, *110*, 6575–6577.

(30) Unpublished results of J. S. Lindsey, T. E. Johnson, R. W. Wagner, and P. Sreedharan obtained at Rockefeller University and at Carnegie Mellon University.

Chart II. A Selection of Substituents Appended to the Porphyrin Compounds

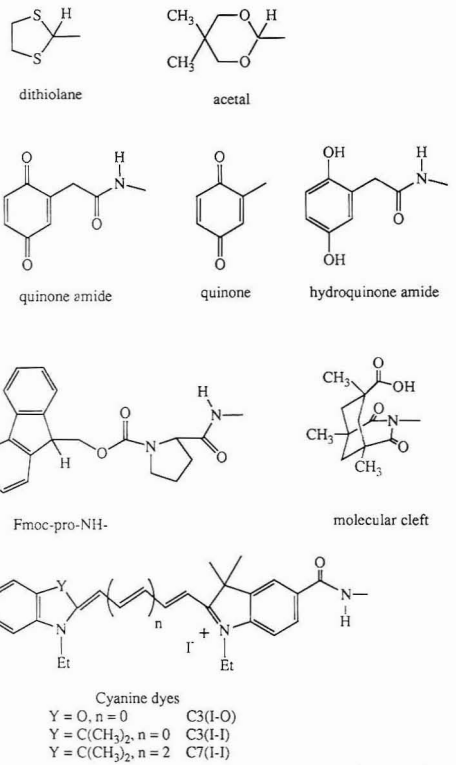

in order to examine photoinduced electron transfer reactions, as occur in the photosynthetic reaction centers.[31,32] A successful synthetic approach involved the condensation of a tetraaminoporphyrin with a tetraformyl quinone (Scheme I). The condensation was performed at room temperature with 0.5 mM porphyrin and quinone. Absorption spectroscopy of reaction aliquots taken over the course of 24 h showed the growing-in of a peak at 330 nm, indicative of Schiff base formation, but providing no distinction among possible intramolecularly-bonded (cage) and intermolecularly-linked (polymeric) porphyrin–quinone products.[33,34] A small sample of the crude reaction mixture (**28**), without purification, was analyzed by mass spectrometry (Figure 3). The peaks at 1367.1, 1384.9, and 1403.2 u are assigned to the porphyrin–quinone cage molecules with 4, 3, and 2 Schiff bases formed, respectively (Table II). These peaks can only derive from cage self-assembly, not intermolecular polymerization. The existence of these peaks indicated the porphyrin–quinone cage had formed; this incisive analysis encouraged subsequent studies of this promising self-assembly process.[34] Treatment of the porphyrin–quinone reaction mixture with $NaBH_3CN$ in order to reduce the Schiff bases gave rise to a new porphyrin component (**29**). Mass spectral analysis of this component confirmed that all four Schiff bases had been reduced as

(31) Lindsey, J. S.; Delaney, J. K.; Mauzerall, D. C.; Linschitz, H. *J. Am. Chem. Soc.* **1988**, *110*, 3610–3621.
(32) Delaney, J. K.; Mauzerall, D. C.; Lindsey, J. S. *J. Am. Chem. Soc.* **1990**, *112*, 957–963.
(33) Lindsey, J. S.; Mauzerall, D. C. *J. Am. Chem. Soc.* **1982**, *104*, 4498–4500.
(34) Lindsey, J. S. *New J. Chem.* **1991**, *15*, 153–180.

Scheme I. Self-Assembly of the Porphyrin–Quinone Cage Molecule PQ(4)[a]

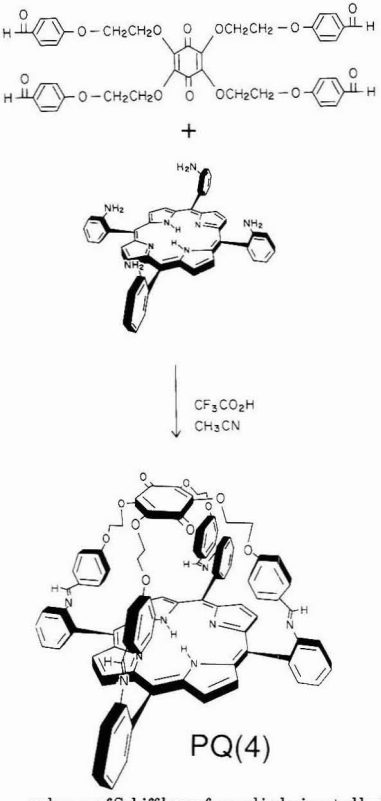

[a] The number, n, of Schiff bases formed is designated by PQ(n), where n = 1, 2, 3, or 4. Only PQ(4) is shown.

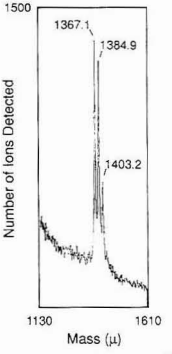

Figure 3. Partial mass spectrum of an unpurified sample (**28**) from the synthesis of a cofacial porphyrin–quinone, PQ(4).

evidenced by a peak at 1375.5 u, 8 mass units higher than the tetra-Schiff base product PQ(4), as expected (Table II). *We know of no other analytical method that provides such direct confirmation of the success of syntheses of this complexity.*

The mass spectral method proved equally valuable for assessing reactions involving modification of the porphyrin–quinones.[31] For example, the zinc–porphyrin–quinone (ZnPQ, **31**, Chart III, R = H, M = Zn) was treated with acetic

Table II. Porphyrin–Quinones

compd		formula	calcd	obsd
28	PQ(n) condensation[a]			
	PQ(4)	$C_{86}H_{62}N_8O_{10}$	1366.5	not res
			1367.4 av	1367.1
	PQ(3)	$C_{86}H_{64}N_8O_{11}$	1384.5	not res
			1385.5 av	1384.9
	PQ(2)	$C_{86}H_{66}N_8O_{12}$	1402.5	not res
			1403.5 av	1403.2
29	PQ	$C_{86}H_{70}N_8O_{10}$	1374.5	not res
			1375.5 av	1375.5
30	PQH_2	$C_{86}H_{72}N_8O_{10}$	1376.5	not res
			1377.5 av	1377.9
31[b]	ZnPQ	$C_{86}H_{68}N_8O_{10}Zn$	1436.4	not res
			1438.9 av	1438.8
32[b]	$ZnPQ(Ac)_4$	$C_{94}H_{76}N_8O_{14}Zn$	1604.5	not res
			1607.0 av	1606.9
				1629.6[c,d]
33[b]	$ZnPA_4(Ac)_4$	$C_{84}H_{72}N_8O_8Zn$	1384.5	not res
			1386.9 av	1386.5
34[b]	$ZnPQ(palm)_2$	$C_{118}H_{128}N_8O_{12}Zn$	1912.9	not res
			1915.6 av	1915.2
35[b]	$ZnPQ(palm)_3$	$C_{134}H_{158}N_8O_{13}Zn$	2151.1	not res
			2154.1 av	2155.5
				2177.4[c,e]
36[b]	$ZnPQ(palm)_3(Ac)_1$	$C_{136}H_{160}N_8O_{14}Zn$	2193.1	not res
			2196.1 av	2196.2
				2218.9[c,d]
37	chlorin–quinone CQ_α	$C_{86}H_{72}N_8O_{10}$	1376.5	not res
			1377.5 av	1377.9
38	chlorin–quinone CQ_β	$C_{86}H_{72}N_8O_{10}$	1376.5	not res
			1377.5 av	1377.8

[a] A sample from the crude reaction mixture was analyzed and found to contain PQ(4), PQ(3), and PQ(2) components. [b] Zinc chelate. [c] Sodium-cationized species. [d] More intense than the molecule ion. [e] Less intense than the molecule ion. Literature sources: **28, 29**;[33] **30–33, 37, 38**;[31] **34–36**.[30]

anhydride in order to acylate the four amines in the bridging groups. Mass spectrometry was used to confirm that all four amines were acetylated (R = Ac). A complicating feature in the mass spectrum of $ZnPQ(Ac)_4$ (**32**) was the observation of a peak at 1629.6 u, which surpassed the molecular ion peak (1606.9 u) in intensity (Figure 4). The higher mass peak arose by Na^+ addition to the porphyrin. This effect was eliminated by soaking the sample foil in distilled water for 10 min.[35] Reanalysis of the sample showed the near total disappearance of the Na^+ addition peak and enhanced intensity of the molecular ion peak (Figure 4).

Other members of the porphyrin-quinone family were characterized with similar ease (Table II). In general, reaction products were examined by chromatography (TLC or HPLC), and purified components were analyzed by PDMS. However, even partially purified products (such as chromatography fractions) could be examined profitably in order to gain quick feedback concerning the success of a synthetic reaction. For example, ZnPQ (**31**) was treated with palmitic anhydride in an effort to prepare a tetrapalmitoyl derivative $ZnPQ(palm)_4$ that would be sufficiently amphipathic to orient spontaneously at the lipid–water interface. The amidation reaction was sluggish, and new porphyrin components were isolated by chromatography and characterized by PDMS (Table II). The products with two and three palmitoyl groups (**34, 35**) were easily identified by the 238-u increment per added palmitoyl group. Prolonged treatment yielded a single component which upon mass spectral analysis was identified as $ZnPQ(palm)_3$ (**35**) rather than the expected $ZnPQ(palm)_4$. Because we sought to acylate all four amines, the product $ZnPQ(palm)_3$ was treated with excess acetic anhydride, forming $ZnPQ(palm)_3(Ac)_1$ (**36**) with characteristic peak at 2196.2 u (calcd av 2196.1 u) and with a more intense Na^+ addition peak at 2218.9 u (Table II).

(35) Aduru, S.; Chait, B. T. *Anal. Chem.* **1991**, *63*, 1621–1625.

Chart III. Porphyrin-Quinone Derivatives $MPQ(R)_4$ and Related Porphyrin-Anisyl derivatives $MPA_4(R)_4$[a]

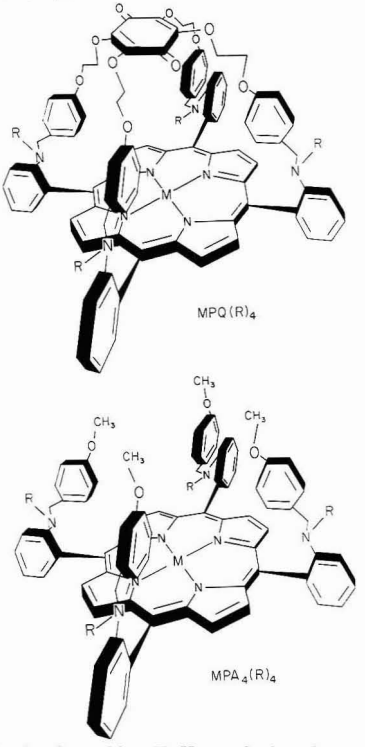

[a] The free base (M = H, H) porphyrin–quinone without derivatized bridge nitrogens (R = H) is designated PQ. Conversion of the quinone to the hydroquinone gives PQH_2. The zinc chelate, ZnPQ, can be acetylated (R = Ac), giving the tetraacetylated derivative, $ZnPQ(Ac)_4$. The porphyrin–tetraanisyl compound PA_4 and its derivatives are named in similar fashion.

In another series of experiments, the porphyrin–quinone (**29**) was treated with potassium azodicarboxylate to achieve reduction at the β-pyrrole positions, yielding the chlorin–quinone parallel and perpendicular isomers.[31] A number of products were formed in the reaction, requiring separation by HPLC. Absorption spectroscopy was used to distinguish chlorins from porphyrins and bacteriochlorins. Chlorin-containing fractions were then analyzed by PDMS to find which one contained the CQ isomers. The fraction that gave the CQ molecule ion (calcd av 1377.5 u) was subjected to further chromatography, ultimately resolving two closely-chromatographing components. Both exhibited typical chlorin absorption and fluorescence spectra. Upon mass spectral analysis, both components exhibited essentially identical molecule ion peaks (1377.9 u, 1377.8 u; calcd av 1377.5 u) and very similar fragmentation patterns, thus these components were necessarily the chlorin–quinone isomers (**37, 38**) and not synthetic byproducts which contained the chlorin macrocycle (Table II). Insufficient material was obtained for ^1H NMR characterization; however, the sensitivity of PDMS and the ease of interpretation led to unambiguous identification of the chlorin–quinones.

3. Synthetic Porphyrins. We have prepared a diverse collection of porphyrins in exploring the scope of a new synthetic method for preparing porphyrins (Table I). Mass

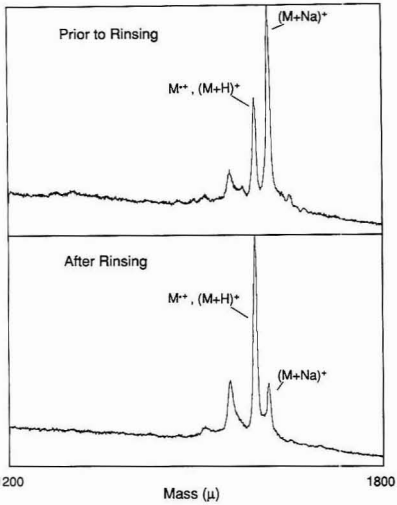

Figure 4. The mass spectrum of ZnPQ(Ac)$_4$ (**32**) shows Na^+ addition (top). After rinsing the sample film in water and reanalysis, the Na^+ is largely removed, yielding a more intense molecular ion peak.

Chart IV. Facial and Peripheral Encumberance of the Porphyrin Achieved by 2,4,6-Trisubstitution of Each Phenyl Ring with Bulky Benzyloxy Groups[a]

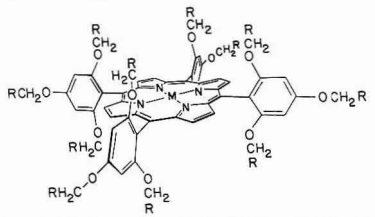

[a] Other substitution patterns include 2,6- or 3,5-disubstitution (not shown).

spectral analysis of the porphyrins yielded intense peaks corresponding to the intact ionized molecule, almost without regard to the molecular entities attached to the porphyrin macrocycle, making the interpretation of the spectra straightforward. Although information can be gleaned from examination of the fragmentation patterns, the presence of the intact molecule ion is sufficient to address the question of whether a porphyrin synthesis has proceeded as anticipated. Some examples included in Table I are particularly noteworthy. The molecular cleft porphyrin (**20**) underwent a small amount of sodium cationization but the molecule ion peak remained strong. The *tert*-butyl porphyrincarboxylate (**15**) yielded an intense fragment corresponding to the porphyrin carboxylic acid, but the molecule ion was still clearly observable. The *meso*-tetraalkylporphyrins (**24**, **25**) undergo significant fragmentation at the C_α–C_β bond (vide infra), but the molecule ion peaks are intense, and the *meso*-alkylporphyrins are as amenable to mass spectrometric analysis as are the *meso*-arylporphyrins. The mass spectrometric method is also well-suited for characterizing isotopically-enriched porphyrins, such as ^{15}N-TPP (**3**) (Table I).

Facially-Encumbered Porphyrins. A number of facially-encumbered porphyrins (Chart IV), prepared as components of a solid-state light-harvesting apparatus, were analyzed by

Table III. Facially-Encumbered Porphyrins[36]

compd	R	position	formula	calcd	obsd
39	H	2,6	$C_{52}H_{46}N_4O_8$	854.3	854.4
40	C_6H_5	2,6	$C_{100}H_{78}N_4O_8$	1462.6	not res
				1463.7	1464.1
41[a]	C_6H_5	2,6	$C_{100}H_{76}N_4O_8Zn$	1524.5	not res
				1527.0 av	1526.4
42	4-BrC_6H_4	2,6	$C_{100}H_{70}Br_8N_4O_8$	2085.9	not res
				2094.9 av	2094.9
43	4-$CH_3C_6H_4$	2,6	$C_{108}H_{94}N_4O_8$	1574.7	not res
				1575.9 av	1575.7
44	4-$CH_3O_2CC_6H_4$	2,6	$C_{116}H_{94}N_4O_{24}$	1926.6	not res
				1928.0 av	1928.1
45	C_6F_5	2,6	$C_{100}H_{38}F_{40}N_4O_8$	2182.2	not res
				2183.3 av	2183.0
46	C_6H_5	3,5	$C_{100}H_{78}N_4O_8$	1462.6	not res
				1463.7 av	1463.6
47	4-$CH_3O_2CC_6H_4$	3,5	$C_{116}H_{94}N_4O_{24}$	1926.6	not res
				1928.0 av	1927.8
48	C_6H_5	2,4,6	$C_{128}H_{102}N_4O_{12}$	1886.8	not res
				1888.1 av	1887.8
49	C_6F_5	2,4,6	$C_{128}H_{42}F_{60}N_4O_{12}$	2966.2	not res
				2967.6 av	2968.1

[a] Zinc chelate.

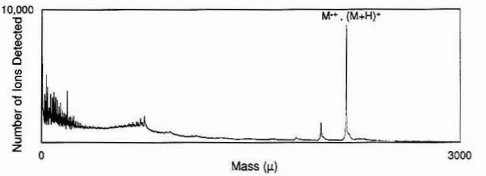

Figure 5. Mass spectrum of *meso*-tetrakis(2,6-bis((pentafluorobenzyl)-oxy)phenyl)porphyrin (**45**). The most intense peak in the mass spectrum is that of the molecule ion, in spite of the fact that the porphyrin skeleton ($C_{20}H_{10}N_4$, 306 u) comprises only 15% of the total mass (2182.2 u).

mass spectrometry (Table III).[36] The presence of 8 or 12 benzyloxy groups attached to the porphyrin gives molecular weights in the 1400–3000 range (**40**–**49**). Surprisingly, the projection of bulky benzyloxy groups over the face of the porphyrin does not impede analysis by mass spectrometry, in spite of the fact that in the bulkiest compounds the porphyrin chromophore only constitutes 10–20% of the total mass. Indeed, this family of porphyrins yielded intense molecule ion peaks in 2–30-min runs as easily as porphyrins without facial encumberance. The octakis- and dodecakis-(benzyloxy)porphyrins underwent significantly more fragmentation than the simpler octamethoxyporphyrin (**39**), but the fragmentation yielded a broad spectrum of nondistinct peaks of lesser intensity than the molecule ion peak, thus not interfering with a clear identification of the intact molecular ion (Figure 5). A particularly interesting porphyrin is the octabromo derivative (**42**). Although the calculated A + 0 mass is 2085.9, the isotopes of bromine result in a calcd av mass of 2094.9 u (Table III). The apex of the experimental peak was measured at 2094.9 u.

Hybrid Porphyrins. The condensation of two aldehydes (A and B) with pyrrole, in principle, yields four hybrid porphyrins (AB_3, cis and trans A_2B_2, and A_3B) and the two parent porphyrins (A_4 and B_4). In general the chromatographic elution order of the porphyrins occurs in accord with the differing polarities of the two aldehydes used in the mixed aldehyde condensation. Mass spectrometry was used to confirm the identity of the porphyrins isolated by chroma-

(36) Wagner, R. W.; Breakwell, B. V.; Ruffing, J.; Lindsey, J. S. *Tetrahedron Lett.* **1991**, *32*, 1703–1706.
(37) Atamian, M.; Wagner, R. W.; Lindsey, J. S.; Bocian, D. F. *Inorg. Chem.* **1988**, *27*, 1510–1512.

Table IV. Hybrid Porphyrins

compd	porphine meso substituents (R) 5	10	15	20	formula	calcd	obsd
			Alkyl–Aryl and Phenyl–Aryl Hybrid Porphyrins				
50	Ph	Ph	Ph	Ar	$C_{46}H_{32}N_4O_2$	672.3	672.1
51	Ar	Ph	Ar	Ph	$C_{48}H_{34}N_4O_4$	730.3	730.2
52	Ar	Ar	Ph	Ph	$C_{48}H_{34}N_4O_4$	730.3	730.2
53	Ar	Ar	Ar	Ph	$C_{50}H_{36}N_4O_6$	788.3	788.2
54	Ar	Ar	Ar	*n*-pentyl	$C_{49}H_{42}N_4O_6$	782.3	782.3
55	*n*-pentyl	Ar	*n*-pentyl	Ar	$C_{46}H_{46}N_4O_4$	718.4	718.4
56	*n*-pentyl	*n*-pentyl	Ar	Ar	$C_{46}H_{46}N_4O_4$	718.4	718.4
57	*n*-pentyl	*n*-pentyl	*n*-pentyl	Ar	$C_{43}H_{50}N_4O_2$	654.4	654.5
58	C_6H_5CO	*p*-tolyl	*p*-tolyl	*p*-tolyl	$C_{48}H_{36}N_4O$	684.3	684.3
59	$PhCH_2CH_2$	Ph	Ph	Ph	$C_{46}H_{34}N_4$	642.3	642.4 551.2[d]
			Monofunctionalized Porphyrins				
	5 4-aryl substituents (X)	10,15,20 meso substituents (R)					
60[a]	cyanine C3(I–O)	Ph			$C_{69}H_{56}N_7O_2$	1014.5 1015.1 av	not res 1015.3
61[a]	cyanine C3(I–I)	Ph			$C_{72}H_{62}N_7O$	1040.5 1041.2 av	not res 1041.4
62[a]	cyanine C7(I–I)	Ph			$C_{76}H_{66}N_7O$	1092.5 1093.3 av	not res 1093.4
63	$ClCH_2CONH$	Ms			$C_{55}H_{50}ClN_5O$	831.4	831.3
64	$PhthCH_2$	Ms			$C_{62}H_{53}N_5O_2$	899.4	899.4
65[b,c]	H_2N	Ph			$C_{44}H_{29}N_5Zn$	691.2	691.2
66	CH_3O_2C	Ms			$C_{55}H_{50}N_4O_2$	798.4	798.3
67	$(CH_3)_3Si(CH_2)_2O_2C$	Ms			$C_{59}H_{60}N_4O_2Si$	884.4	884.4
68	HO_2C	Ms			$C_{54}H_{48}N_4O_2$	784.4	784.3
69	$HO_2CCH(CH_3)NHCO$	Ms			$C_{57}H_{53}N_5O_3$	855.4	855.4
70	Fmoc-Pro-NH	Ms			$C_{73}H_{66}N_6O_3$	1074.5	1074.5
71	H-Pro-NH	Ms			$C_{58}H_{56}N_6O$	852.5 853.0 av	not res 853.5
72[b]	c-$C_5H_{10}NCO$	Ms			$C_{59}H_{55}N_5OZn$	913.4	913.4
73	SuO_2C	Ph			$C_{48}H_{33}N_5O_4$	755.3	755.4
74	dithiolane	*n*-pentyl			$C_{44}H_{52}N_4S_2$	700.4	700.4
75	$PhenO_2C$	*n*-decyl			$C_{65}H_{84}N_4O_3$	968.7	968.7
76	$(CH_3)_3SiCC$	2,4,6-$MeO_3C_6H_2$			$C_{58}H_{56}N_4O_9Si$	980.4	980.3
77	$(CH_3)_2N$	C_6F_5			$C_{46}H_{20}F_{15}N_5$	927.1	927.2
78	quinone amide	*p*-tolyl			$C_{55}H_{41}N_5O_3$	819.3	819.3
79	hydroquinone amide	*p*-tolyl			$C_{55}H_{43}N_5O_3$	821.3	822.3
80[b]	quinone amide	*p*-tolyl			$C_{55}H_{39}N_5O_3Zn$	881.2	881.4
81	quinone	Ph			$C_{50}H_{32}N_4O_2$	720.3	720.4
			Multifunctionalized Porphyrins				
	5 4-aryl substituents (X)	10,15,20 4-aryl substituents (X)					
82	Fc-	quinone			$C_{72}H_{44}N_4O_6Fe$	1116.3 1117.0 av	not res 1117.9
83	t-Bu-O_2C-	Fmoc-Pro-NH			$C_{109}H_{92}N_{10}O_{11}$	1716.7 1717.9 av	not res 1718.8[e]
84	HO_2C-	Fmoc-Pro-NH			$C_{105}H_{84}N_{10}O_{11}$	1660.6 1661.8 av	not res 1662.3

[a] The formula and calculated masses are for the porphyrin–dye cation without a counterion. [b] Zinc chelate. [c] Ortho substituted, not para. [d] More intense than the molecule ion. [e] May be protonated. Abbreviations: Su, succinimidyl; Phen, phenacyl; Phth, phthalimido; Fc, ferrocenyl. Literature sources: **50–57**;[37] **58–59, 63, 64, 66–84**;[30] **65**;[31] **60–62**.[38]

tography (for aldehydes with different molecular weights), although no mass spectral distinction was possible for the cis- and trans-disubstituted porphyrins. The mass spectrometric method was successfully applied to porphyrins bearing a wide variety of groups, including carboxylic acids, protected amino acids, active esters, dithioacetals, aromatic amines, quinone, ferrocene, and trimethylsilyl protecting groups (Table IV). The clear distinction observed between porphyrin–quinone (**78**) and porphyrin–hydroquinone (**79**) molecules, in spite of the only 2-u mass difference, enabled the ferreting out of reduced (**79**) and oxidized (**78**) species from crude reaction mixtures.

Porphyrins bearing *meso*-alkyl groups undergo fragmentation at the C_α–C_β bond, often forming fragment ion peaks of greater intensity than that of the porphyrin molecular ion. This fragmentation pattern mirrors the well-known benzylic fragmentation of β-pyrrole substituted porphyrins.[1,2] In a series of pentyl–aryl hybrid porphyrins (Table IV), the monopentylporphyrin (**54**) gave a molecular ion (782.3 u) and a single fragment at 725.2 u; the latter derives from benzyl-like cleavage of the C_α–C_β bond and loss of a butyl fragment. Similarly, the cis and trans porphyrins (**55, 56**), the tripentylporphyrin (**57**), and the tetrapentylporphyrin (**24**) each gave a molecular ion peak and fragments due to successive loss of two, three, and four substituents, respectively. The monophenethylporphyrin (**59**) undergoes C_α–C_β cleavage to yield two benzylic fragments. The high-mass fragment (porphyrin – benzyl (551.2 u)) was the most intense peak in the spectrum (with the exception of that of H^+), and the second most intense peak was due to the porphyrin molecular ion (642.4 u). The occurrence of fragmentation does not greatly complicate the interpretation, and in no cases have

we observed fragmentation of such intensity that the molecular ion could not easily be identified.

Several porphyrin cyanine dyes (**60–62**) were prepared as model systems for visible light harvesting (Chart II).[38] The cyanine dyes are ionic, consisting of a cationic organic dye and an anionic counterion. Though the initial counterion in the synthesis was iodide, ion exchange during normal handling can lead to a final product with several different counterions, potentially complicating analysis by NMR spectroscopy. Mass spectrometry cleanly sidesteps this pitfall because the negatively-charged counterions are not detected in the positive ion spectra. Each of the porphyrin cyanine dyes (**60–62**) gave a strong ion peak consistent with the calculated average mass of the porphyrin cyanine dye minus a counterion (Table IV). The mass spectra were readily interpreted, thus confirming the success of the synthesis. In contrast, the ^{1}H NMR spectra proved extremely difficult to interpret due to the large number of distinct protons in the asymmetric porphyrin and asymmetric cyanine dye. Further complications of interpretation were attributed to ion pairing of several different counterions with the cationic dyes in the nonpolar NMR solvents.

The porphyrin–indotricarbocyanine dye (**62**) gave a molecular ion peak at 1093.4 u, a fragment peak of lesser intensity at 556.6 u, and the intervening spectral region was almost devoid of peaks. The peak at 556.6 u derives from cleavage of the porphyrin–phenyl C–C bond, yielding the charged dye fragment ($C_{38}H_{41}N_3O$). A smaller fragment peak at 546.7 u (half the mass of the molecular ion) may arise from the doubly charged molecular ion. The cyanine dye bears one intrinsic positive charge, and ionization of the porphyrin would yield the doubly charged molecule. For the carbocyanine dye–porphyrins (**60, 61**), no peaks characteristic of the doubly-charged molecular ion were detected that were of greater intensity than fragments in the appropriate spectral region.

Strapped Porphyrins. The positioning of straps across adjacent *meso*-phenyl groups represents an attractive architecture for porphyrin model systems. We prepared a series of strapped porphyrins (Chart V) in order to study the effect of strap structure on porphyrin formation, as well as to obtain porphyrins bearing redox-active groups.[39] The porphyrins with straps at the ortho positions form atropisomers (with the two straps on the same face or on opposite faces of the porphyrin) which are separable chromatographically. The meta-strapped porphyrins can form atropisomers in principle, but in practice we have only observed one meta-strapped porphyrin chromatographic component in the synthesis of each meta-strapped porphyrin.[39] The ^{1}H NMR spectra of the meta-strapped porphyrins are complicated, apparently due to the slow interconversion of the atropisomers. Variable-temperature NMR experiments were performed to investigate the interconversion processes, but given the complexity of the spectra and the dynamics of the molecular processes (which differed depending on the nature of the strap), NMR spectroscopy was not very potent for providing confirmation that the syntheses had succeeded.

Mass spectrometry played a crucial role in the characterization of the strapped porphyrins (Table V). In the spectra of the *o*- and *m*-alkoxy-strapped porphyrins (**85–93**), peaks of low intensity were frequently observed at masses two, three, and $^3/_2$ times that of the molecular ion. These are attributed to the singly-charged dimer, the singly-charged trimer, and the doubly-charged trimer of porphyrins, respectively. A small amount of noncovalent dimer formation is frequently observed with porphyrins upon mass spectral analysis, but

Chart V. Strapped Porphyrins[a]

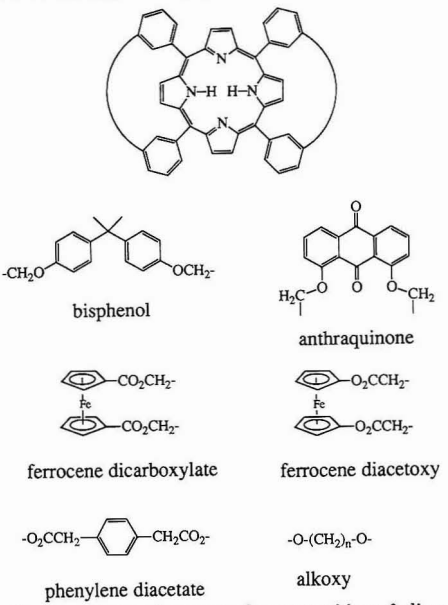

[a] The straps that are shown span the meta positions of adjacent phenyl groups. Only the alkoxy chain has been used to span ortho positions (not shown).

these are the only examples, to our knowledge, of noncovalent trimers formed from tetraphenylporphyrins. The prevalence of these higher mass peaks was in accord with the poor solubility of the *o*- and *m*-alkoxy-strapped porphyrins. In two cases (meta-C_5 (**89**), meta-C_7 (**91**)) we observed higher mass components (+312.7 u, +340.7 u, respectively) that could be attributed to the monostrapped porphyrin with two free aldehyde groups (identical in architecture to the cis-Ar_2-monostrapped porphyrins, Chart VI, and formed by failure to close the second strap). Though the intensity of these peaks was low (~10% of the molecular ion), their presence led us to reevaluate the synthetic method and purification procedures.

Hybrid-strapped porphyrins (**99–101**) also were prepared by condensing two different linked dialdehydes, yielding, for example, a strapped porphyrin (**101**) bearing a ferrocene in one strap and an anthraquinone in the other strap (Table V).[39] The observation of an intense peak at 1177.3 u coincided with the calculated average mass of 1177.0 u for the ferrocene–porphyrin–quinone (**101**), providing quick confirmation of the successful synthesis and isolation of the desired target. Similar mixed aldehyde condensations were performed in the synthesis of cis-disubstituted porphyrins (Chart VI). The mass spectra (Table V) provided unambiguous identification of the target molecules.

4. Porphyrin–Porphyrin Dimers. A building block approach was exploited to prepare porphyrin–porphyrin dimers for studies of visible light harvesting (Chart VII). Coupling of a monocarboxyporphyrin with a monoprolylporphyrin (**71**) yielded a number of chromatographic components. Analysis by mass spectrometry of each major component readily identified the component consisting of the zinc porphyrin/free base porphyrin dimer (**113**, Table VI). The mass spectrum showed a peak due to the dimer at 1683.1 u (calcd av mass, 1683.4 u) and a sizeable fragment peak at 803.3 u (Figure 6). The latter is easily assigned to the fragment

(38) Lindsey, J. S.; Brown, P. A.; Siesel, D. A. *Tetrahedron* **1989**, *45*, 4845–4866.
(39) Wagner, R. W.; Brown, P. A.; Johnson, T. E.; Lindsey, J. S. *J. Chem. Soc., Chem. Commun.* **1991**, 1463–1466.

Table V. Strapped Porphyrins

compd	position	formula	calcd	obsd
		$-O(CH_2)_nO-$ Straps		
ortho straps	*n*			
85	5	$C_{54}H_{46}N_4O_4$	814.4	814.4
86	7	$C_{58}H_{54}N_4O_4$	870.4	870.5
87	8	$C_{60}H_{58}N_4O_4$	898.4	898.6
88	10	$C_{64}H_{66}N_4O_4$	954.5	955.4
meta straps	*n*			
89	5	$C_{54}H_{46}N_4O_4$	814.4	814.4
90	6	$C_{56}H_{50}N_4O_4$	842.4	842.4
91	7	$C_{58}H_{54}N_4O_4$	870.4	870.4
92	8	$C_{60}H_{58}N_4O_4$	898.4	898.4
93	10	$C_{64}H_{66}N_4O_4$	954.5	954.6
meta straps	name			
94	bisphenol	$C_{78}H_{62}N_4O_4$	1118.5	not res
			1119.3 av	1119.6
95[a]	bisphenol	$C_{78}H_{60}N_4O_4Zn$	1180.4	not res
			1182.7 av	1182.4
96	phenylenediacetate	$C_{68}H_{50}N_4O_8$	1050.4	1050.5
97	ferrocenedicarboxylate	$C_{72}H_{50}N_4O_8Fe_2$	1210.2	not res
			1210.8 av	1211.7
98	ferrocene diacetoxy	$C_{72}H_{50}N_4O_8Fe_2$	1210.2	not res
			1210.8 av	1211.8

compd	strap 1	strap 2	formula	calcd	obsd
		Hybrid-Strapped Porphyrins (All Meta)			
99	ferrocenedicarboxylate	$-O(CH_2)_8O-$	$C_{66}H_{54}N_4O_8Fe$	1054.3	not res
				1054.9 av	1055.0
100	anthraquinone	$-O(CH_2)_8O-$	$C_{68}H_{52}N_4O_6$	1020.4	1020.5
101	ferrocenedicarboxylate	anthraquinone	$C_{74}H_{48}N_4O_8Fe$	1176.3	not res
				1177.0 av	1177.3

	$-O(CH_2)_nO-$ strap		4-ZC_6H_4			
compd	*n*	position	(Z)	formula	calcd	obsd
			Cis-Ar_2-Strapped Porphyrins			
102	5	ortho	CH_3O_2C	$C_{53}H_{42}N_4O_6$	830.3	830.3
103[a]	5	ortho	CH_3O_2C	$C_{53}H_{40}N_4O_6Zn$	892.2	892.4
104	5	ortho	$CH_3(CH_2)_7O$	$C_{65}H_{70}N_4O_4$	970.5	970.6
105	5	ortho	$(CH_3)_2N$	$C_{53}H_{48}N_6O_2$	800.4	800.6
106	8	meta	CH_3O_2C	$C_{56}H_{48}N_4O_6$	872.4	872.4

[a] Zinc chelate. Literature sources: **85–101**;[39] **102–106**.[30]

Chart VI. Porphyrins Bearing a Single Strapping Unit and Cis-Substituted Z Groups (for Substituent Z, See Table V)

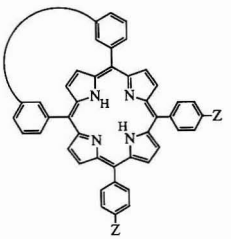

derived from cleavage at the carbonyl–phenyl bond, liberating the zinc–trimesitylmonophenylporphyrin fragment ($C_{53}H_{45}N_4Zn$, calcd av 803.3 u). Similarly, the free base porphyrin/free base porphyrin dimer (**114**) fragmented at the same bond site, yielding a fragment at 740.1 u ($C_{53}H_{47}N_4$, calcd av 739.9 u; data not shown). The region between the molecule ion and the major fragment peak was almost devoid of peaks in both spectra, rendering the analysis very straightforward. The free base/free base porphyrin dimer (**114**) was analyzed on a nitrocellulose layer[40,41] rather than aluminized Mylar, but no decrease in the extent of fragmentation was detected.

Porphyrin–porphyrin dimers (**107–112**) in a gable-type configuration[42] incorporating zinc, iron, or manganese were also analyzed by PDMS (Table VI). Sample preparation and analysis in PDMS are sufficiently mild that porphyrin demetalation does not occur. The biszinc chelate (**108**) was prepared with the bridging ligands dipyridylmethane or 1,3-bis(*N*-imidazolyl)propane. The mass spectra of these bisporphyrin complexes gave the molecule ion with loss of the linker, and in both cases the peak due to the protonated linker (dipyridylmethane, 171.0; bis(imidazolyl)propane, 177.0) was observed. The manganese and iron chelates each have a fifth ligand site, which in the bisporphyrins was occupied by chloride. The mass spectra of the bismanganese chelate (**109**) showed no molecule ion; instead molecule ions with loss of one and two chloride atoms were observed. The bisiron chelate (**110**) gave an observable molecule ion, but the peaks due to loss of one and two chloride atoms were more intense (Figure 7). However, each component in the cluster of peaks

(40) Jonsson, G. P.; Hedin, A. B.; Hakansson, P. L.; Sundqvist, B. U. R.; Save, B. G. S.; Nielsen, P. F.; Roepstorff, P.; Johansson, K. E.; Kamensky, I.; Lindberg, M. S. L. *Anal. Chem.* **1986**, *58*, 1084–1087.

(41) Chait, B. T. *Int. J. Mass Spectrom. Ion Processes* **1987**, *78*, 237–250. Chait, B. T.; Field, F. H. *Biochem. Biophys. Res. Commun.* **1986**, *134*, 420–426.

(42) Tabushi, I.; Sasaki, T. *Tetrahedron Lett.* **1982**, *23*, 1913–1916. Tabushi, I.; Kugimiya, S.; Kinnaird, M. G.; Sasaki, T. *J. Am. Chem. Soc.* **1985**, *107*, 4192–4199.

(43) Unpublished results of T. Sasaki and I. Tabushi obtained at Kyoto University.

Table VI. Porphyrin Dimers

compd	Ar_1	Ar_2	spacer	rM_1	M_2	formula	calcd	obsd
				Gable Porphyrins[a]				
107	Ph	Ph	gable	H,H	H,H	$C_{82}H_{54}N_8$	1150.4	1150.3
108	Ph	Ph	gable	Zn	Zn	$C_{82}H_{50}N_8Zn_2$	1274.3	not res
							1278.1 av	1278.4
109	Ph	Ph	gable	Mn-Cl	Mn-Cl	$C_{82}H_{50}N_8Mn_2Cl_2$	1326.2	not res
							1327.9 av	no molecule ion
								1292.9 (2)
								1257.2 (1)
110	Ph	Ph	gable	Fe-Cl	Fe-Cl	$C_{82}H_{50}N_8Fe_2Cl_2$	1328.2	not res
							1329.7 av	1330.0 (4)
								1294.5 (2)
								1259.1 (1)
								1181.6 (3)
								1103.3 (5)
111	Ph	*p*-tolyl	gable	H,H	H,H	$C_{85}H_{60}N_8$	1192.5	not res
							1193.4 av	1193.6
112	Ph	*p*-tolyl	gable	Fe-Cl	Fe-Cl	$C_{85}H_{56}N_8Fe_2Cl_2$	1370.3	not res
							1371.8 av	1371.8 (3)
								1336.8 (2)
								1301.4 (1)
				Building Block Porphyrin Dimers				
113	Ms	Ms	proline	Zn	H,H	$C_{112}H_{100}N_{10}O_2Zn$	1680.7	not res
							1683.4 av	1683.1
114	Ms	Ms	proline	H,H	H,H	$C_{112}H_{102}N_{10}O_2$	1618.8	not res
							1620.0 av	1620.2
115	Ar[c]	Ar[c]	alkyne	H,H	H,H	$C_{102}H_{80}N_8O_{12}Zn$	1672.5	not res
							1675.1 av	1675.0

[a] The gable porphyrins were prepared by Professor Tomikazu Sasaki (University of Washington). [b] The numbers in parentheses indicate the relative order of intensity of the peaks. [c] Ar = 2,6-$(MeO)_2C_6H_3$. Literature sources: **107, 108, 110–112;**[42] **109;**[43] **113–115.**[30]

Chart VII. Porphyrin Dimers with Various Spacers and Differential Metalation (M_1, M_2)[a]

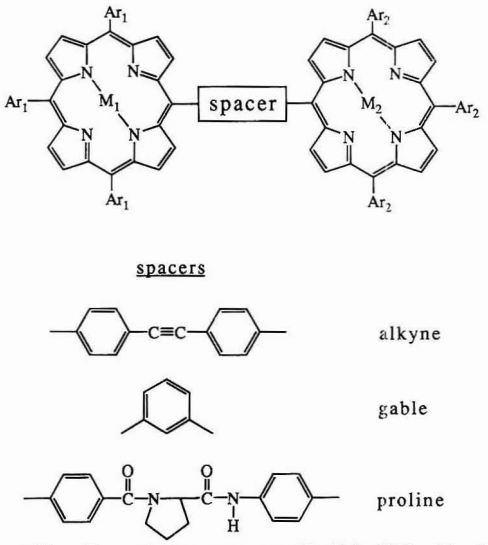

[a] The gable porphyrins were prepared by Tabushi, Sasaki and co-workers.[42]

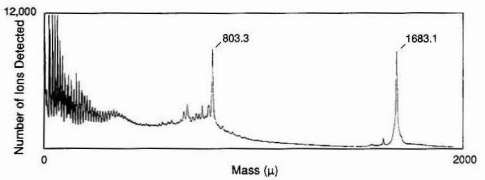

Figure 6. The mass spectrum of a porphyrin–porphyrin dimer (113) shows the intact molecule ion peak (1683.1 u) and a sizeable fragment peak (803.3 u). The lower mass fragments exhibit the characteristic oscillation of intensity with a 14-u periodicity.

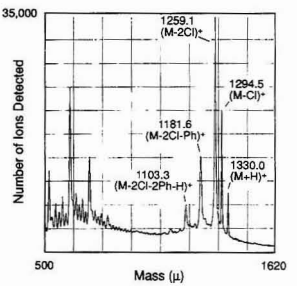

Figure 7. The mass spectrum of a gable porphyrin (110) shows several peaks clustered near the molecule ion, due to loss of ligands bound to the metals.

was readily assigned to fragments derived from loss of chloride or phenyl moieties, not demetalation of the porphyrin.

CONCLUSIONS

^{252}Cf PDMS is applicable to porphyrin model systems spanning an enormous range of architectures and functional group diversity. The method is especially well-suited for characterizing chromatographic fractions and partially purified components, thereby allowing reactions to be easily followed. The mass spectra are collected quickly and are readily interpreted, enabling rapid feedback concerning the outcome of a synthetic reaction. Taken together, these features make this method an extremely powerful tool for research in the synthesis of bioorganic porphyrin model systems. Our experience with porphyrin model systems leads us to believe that similar strategies employing ^{252}Cf PDMS

would accelerate progress in many other areas of synthetic organic chemistry.

ACKNOWLEDGMENT

This work was supported by NIH grants to J.S.L (GM-36238) and to B.T.C. (RROO 862) and by the Rockefeller University Graduate Program. The spectra were collected at The Rockefeller University Mass Spectrometric Biotechnology Research Resource, which is supported in part by the Division of Research Resources, National Institutes of Health. We thank Tomikazu Sasaki (University of Washington) for permission to show the data of the gable porphyrins.

RECEIVED for Review May 27, 1992. Accepted July 31, 1992.

Chiral Recognition and Enantiomeric Resolution Based on Host–Guest Complexation with Crown Ethers in Capillary Zone Electrophoresis

Reinhard Kuhn* and Fritz Erni

Analytical Research and Development, Sandoz Pharma Ltd., CH-4002 Basel, Switzerland

Thomas Bereuter and Johannes Häusler

Institute for Organic Chemistry, University of Vienna, A-1090 Wien, Austria

A chiral crown ether is successfully used as a pseudostationary phase in capillary zone electrophoresis to separate optically active amines. On the basis of the results obtained from the separation of more than 20 amines, two recognition mechanisms are proposed: (I) the four crown ether substituents act as chiral barriers for the guest molecules and (II) lateral electrostatic interactions occur between host and guest. These results are confirmed by thermodynamic studies on the host–guest complexes. Best resolutions are achieved if the chiral center is adjacent to the amine functionality. However, even racemates with a chiral center in the δ-position to the amine could be resolved excellently. For the separation of aliphatic amino acids a method has been developed allowing detection by an indirect detection mode.

INTRODUCTION

Crown ethers discovered in 1967 by Pedersen[1,2] are macrocyclic polyethers which are able to form stable and selective complexes with alkali, alkaline-earth, and primary ammonium cations. These ligands are usually classified in the family of coronands. A second, more sophisticated generation of macrocycles are the cryptands of Lehn[3,4] and spherands of Cram.[5,6] In modern chemistry all these compounds are of great importance in biological studies, e.g. as enzyme models,[7] in the synthesis, e.g. for phase-transfer catalysis,[8] and in analytical chemistry. For instance, complex formation of crown ethers can be utilized in ion chromatography,[9] for the extraction of heavy metals,[9] and in electrochemical sensors.[10,11] Cram and co-workers[12,13] were the first to recognize the potential of optically active crown ethers for the separation of enantiomers in liquid chromatography. The staggered arrangement of the binaphthyl rings in the structure of Cram's crown ethers behaves like a chiral barrier for the enantiomers. Separations of a variety of optically active amines using chiral crown ether stationary phases in HPLC have been reported subsequently.[14–18] Chiral separations by capillary electrophoresis (CE) have been accomplished by utilizing solubilization with optically active micelles,[19] ligand-exchange complexation,[20] or host–guest complexation with cyclodextrins.[21] In capillary zone electrophoresis (CZE) we described the use of a chiral crown ether for the separation of racemic amino acids for the first time.[22] A comprehensive review of this topic is presented in ref 23.

The focus of this study is to investigate the chiral recognition mechanism between 18-crown-6 tetracarboxylic acid (18C6H$_4$) with several optically active amines by means of open-tube capillary zone electrophoresis. Appropriate separation methods are developed which allow "baseline" resolution for racemic mixtures.

EXPERIMENTAL SECTION

Methods. Capillary electrophoresis was carried out using a P/ACE 2000 capillary electrophoresis instrument (Beckman Ins., Palo Alto, CA). Separations were performed at 25 °C in a fused silica capillary tube (50 cm × 75-μm i.d., Polymicro Corp., Phoenix, AZ) applying a potential of 15 kV. All experiments described in Table I were carried out in Tris/citrate (10 mM, pH 2.2) as carrier electrolyte with 10 mM 18C6H$_4$. For the temperature variations a system consisting of 30 mM 18C6H$_4$ in water was used. Separations with indirect detection were performed in benzyltrimethylammonium chloride (6 mM)/Tris (5 mM) adjusted with citric acid to pH 2.2. To this buffer was added 15 mM 18C6H$_4$.

* Author to whom correspondence and reprint requests should be addressed.

(1) Pedersen, C. J. *J. Am. Chem. Soc.* **1967**, *89*, 2495, 7017.
(2) Pedersen, C. J. Nobel Lecture, December 8, 1987, reprinted in *J. Incl. Phenom.* **1988**, *6*, 337.
(3) Dietrich, J.-M.; Lehn, J.-M.; Sauvage, J.-P. *Tetrahedron Lett.* **1969**, 2885 and 2889.
(4) Lehn, J.-M. Nobel Lecture, December 8, 1987, reprinted in *J. Incl. Phenom.* **1988**, *6*, 351.
(5) Kyba, E. P.; Siegel, M. G.; Sousa, L. R.; Sogah, G. D. Y.; Cram, D. J. *J. Am. Chem. Soc.* **1973**, *95*, 2691.
(6) Cram, D. J. Nobel Lecture, December 8, 1987, reprinted in *J. Incl. Phenom.* **1988**, *6*, 397.
(7) Sasaki, S.; Koga, K. *J. Incl. Phenom.* **1989**, *7*, 267.
(8) Weber, W. P., Gokel, G. W., Eds. *Phase Transfer Catalysis in Organic Synthesis, Reactivity and Structure Concepts in Organic Chemistry 4*, Springer-Verlag: New York, 1977.
(9) Blasius, E.; Janzen, K. P. Analytical Applications of Crown Compounds and Cryptands. In Dewar, M. J. S., Dunitz, J. D., Haffner, K., Heilbronner, E., Ito, S., Lehn, J.-M., Niedenzu, K., Raymond, K. N., Rees, C. W., Schäfer, K., Wittig, G., Eds. *Topics in Current Chemistry, Vol. 98, Host Guest Complex Chemistry I*; Springer-Verlag: New York, 1981.
(10) Thoma, A. P.; Viviani-Nauer, A.; Schellenberg, K. H.; Bedekovic, D.; Pretsch, E.; Prelog, V.; Simon, W. *Helv. Chim. Acta* **1979**, *62*, 2303.
(11) Bussmann, W.; Lehn, J.-M.; Oesch, U.; Plumeré, P.; Simon, W. *Helv. Chim. Acta* **1981**, *64*, 657.
(12) Kyba, E. P.; Timko, J. M.; Kaplan, L. J.; de Jong, F.; Gokel, G. W.; Cram, D. J. *J. Am. Chem. Soc.* **1978**, *100*, 4555.
(13) Sousa, L. R.; Sogah, G. D. Y.; Hoffman, D. H.; Cram, D. J. *J. Am. Chem. Soc.* **1978**, *100*, 4569.
(14) Hilton, M.; Armstrong, D. W. *J. Liq. Chromatogr.* **1991**, *14* (1), 9.
(15) Armstrong, D. W.; Ward, T.; Czech, B.; Bartsch, R. *J. Org. Chem.* **1985**, *50*, 5557.
(16) Zukowski, J.; Pawlowska, M.; Pietraszkiewicz, M. *Chromatographia* **1991**, *32*, 82.
(17) Udvarhelyi, P. M.; Watkins, J. C. *Chirality* **1990**, *2*, 200.
(18) *Daicel Crownpak CR(+) instruction Manual*, Daicel (Europe): Düsseldorf, Germany, 1990.
(19) Otsuka, K.; Kowahara, J.; Tatekawa, K.; Terabe, S. *J. Chromatogr.* **1991**, *559*, 209.
(20) Gassmann, E.; Kuo, J. E.; Zare, R. N. *Science* **1985**, *230*, 813.
(21) Fanali, S. *J. Chromatogr.* **1991**, *545*, 437.
(22) Kuhn, R.; Stoecklin, F.; Erni, F. *Chromatographia* **1992**, *33*, 32.
(23) Kuhn, R.; Hoffstetter-Kuhn, S. *Chromatographia*, in press.

0003-2700/92/0364-2815$03.00/0

Table I. Separation Data for Optically Active Amines on Chiral 18C6H$_4$

no.	name	structure	t_R[a] (min)	α	R_s	no.	name	structure	t_R[a] (min)	α	R_s
1	GlyPhe		45.13	1.141	3.09	14	histidine		14.94	1.016	0.54
2	tryptophan		25.56	1.055	3.13	15	3-amino-3-phenylpropionic acid		28.75	1.090	2.50
3	phenylglycine		59.11	no separation		16	norephedrine (1*R*,2*S*)/(1*S*,2*R*)		15.48	1.072	1.83
4	phenylalanine		29.56	1.059	3.75	17	*erythro*-2-amino-3-phenylbutyric acid		24.75	1.043	2.17
5	tyrosine		25.92	1.051	2.65	18	*threo*-2-amino-3-phenylbutyric acid		23.41	1.032	1.69
6	Dopa		29.18	1.053	2.78	19	threonine		24.73	1.078	3.42
7	*p*-aminophenylalanine		36.86	1.076	3.17	20	GlyGlyLeu	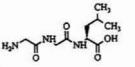	46.18	1.034	0.70
8	ephedrine		10.30	no separation		21	valine		26.69	1.086	1.42
9	phenylalaninol		13.47	1.070	1.85	22	leucine		33.33	1.130	1.75
10	phenylethylamine		17.36	no separation		23	alanine		26.23	1.071	0.79
11	naphthylethylamine		22.56	1.241	1.79	24	norvaline		31.73	1.054	0.79
12	noradrenaline		32.99	1.023	0.59	25	isoleucine		31.52	1.106	1.68
13	normetanephrine		28.36	1.037	0.60						

[a] Retention time of the first eluted enantiomer.

An appropriate amount of each sample was dissolved in diluted phosphoric acid or methanol/water and injected hydrodynamically for 1 s. The solutes were detected by UV absorption at 254 nm for direct detection and at 214 nm in the indirect detection mode. A Perkin-Elmer CLAS/2000 system was used for data acquisition.

Materials. All reagents were of analytical grade if not otherwise stated. Citric acid, benzyltrimethylammonium chloride (98%), 18-crown-6 tetracarboxylic acid (18C6H$_4$, 98%), phosphorous acid (85%), and tris(hydroxymethyl)aminomethane (Tris) were obtained from Merck (Darmstadt, Germany). All α-amino acids, *p*-amino-D,L-phenylalanine, D,L-2-amino-3-phenylbutyric acid (67% threo, 33% erythro), D,L-Dopa, glycyl-D,L-phenylalanine (GlyPhe), (±)-normetanephrine hydrochloride (98%), (±)-norephedrine, and (±)-2-amino-4-phenylbutyric acid were purchased from Sigma Chemicals (St. Louis, MO). (−)- and (+)-ephedrine (purum), (±)-2-amino-1-phenyl-1-propionic acid (purum), D,L-noradrenaline (purum), (*R*)-(+)- and (*S*)-(−)-1-(1-naphthyl)ethylamine (NEA; >99.5%), (*R*)-(+)- and (*S*)-(−)-phenylethylamine (>99%), 4-amino-D,L-phenylalanine hydrochloride (purum), and D- and L-phenylalaninol (purum) were from Fluka (Buchs, Switzerland). D,L-Phenylglycine (99%) was obtained from Janssen Chimica (Berse, Belgium) and D,L-3-amino-3-phenylpropionic acid (98%) and (±)-normetanephrine hydrochloride (98%) were from Aldrich Chemicals (Steinheim, Germany). Glycylglycyl-D,L-leucine (GlyGlyLeu) was purchased from Bachem Feinchemicalien (Bubendorf, Switzerland).

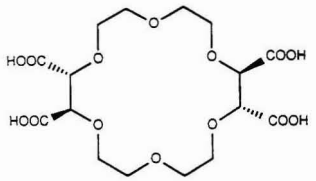

Figure 1. Chemical structure of 18-crown-6-tetracarboxylic acid.

RESULTS AND DISCUSSION

Scope. Chiral 18-crown-6 tetracarboxylic acid derived from tartaric acid was first synthesized by Lehn and co-workers[24,25] (see Figure 1). The polyether ring forms the shape of a cavity which is able to form stable complexes, particularly with potassium, ammonium, and protonated alkylamine cations. The six oxygens of the ring system are in the interior of the cavity and roughly define a plane.[12] Ammonium or primary amines held inside the cavity are bound by three $^{+}NH\cdots O$ hydrogen bonds in a tripod arrangement. However, since these host–guest complexes do not show chiral recognition, secondary lateral interactions between the substituents of the crown ether ring and the ligands are necessary for chiral discrimination. With respect to the structure of $18C6H_4$, we propose two different recognition mechanisms. First, the crown ether substituents, arranged perpendicularly to the plane formed by the ring system,[25,26] act like steric barriers dividing the space available for the substrate into two cavities. Also perpendicular to the plane is the $C^*–^{+}NH_3$ bond of a complexed primary amine. The three remaining substituents of C* are distributed among the two cavities. If C* is chiral, transient diastereomers are formed with different complex formation constants depending on the size and steric arrangement of the substituents. On the other hand, a second mechanism can be discussed that is caused by electrostatic interactions (ionic or hydrogen bonds) of the crown ether substituents with functional groups of the guest molecule. Even repulsion forces of carboxylate groups between host and guest should have an influence on the complex formation constant and on the enantioselectivity.

Resolution of Chiral Amines. We investigated the chiral resolution of a series of different optically active amines in capillary zone electrophoresis to elucidate the recognition mechanism. In the chosen pH range, $18C6H_4$ added to the buffer electrolyte is slightly negatively charged and migrates as an anion in the opposite direction to the solutes. Separation is based on a different steric arrangement of the host–guest complexes which forms diastereomers with disparate complex formation constants and different electrophoretic mobilities. More than 20 optically active amines were investigated and compared with respect to retention time, separation factor, and resolution. The results are summarized in Table I. It should be mentioned that better results could be obtained for a specific separation problem by individually optimizing the separation conditions. The separation factor (α) is supposed to be independent of migration time and reflects the chiral recognition. In general, only small but significant differences of α for the various compounds could be calculated. Most enantiomers were "baseline separated" mainly because of the high efficiency achieved in CZE.

Armstrong and co-worker[27] studied the influence of distance between the amine function and chiral center of dipeptides in HPLC using a chiral crown ether with hydrophobic substituents as stationary phase. While good resolution was found for those solutes where the amine group was adjacent to the stereogenic center, dipeptides of the glycyl amino acid type were not resolved or showed poor resolution. We observed that glycyl-D,L-phenylalanine (1, GlyPhe) was excellently resolved although the chiral center is in the δ-position to the primary amine. Molecular models of the $18C6H_4$–GlyPhe complex indicate that chiral recognition occurs predominantly by hydrogen bonds rather than by steric barrier mechanisms. A possible arrangement of the host–guest complex is shown in Figure 2a. Recognition is probably based on hydrogen bonds between the acidic functional group of the dipeptide with the crown ether side chains, indicated by the arrow in Figure 2a. Even the tripeptide GlyGlyLeu (**20**), which has its asymmetric center seven bonds from the amine, was recognized by the selector, although resolution was poor under the given conditions.

On the other side, nonpolar substituents like methyl, phenyl, or naphthyl groups are not able to bind with the polar crown ether substituents. Recognition is based on mere steric barrier mechanisms and, therefore, dependent on the size of the substituents. (±)-Phenylethylamine (**10**), for example, could not be separated because of too small substituents whereas the naphthyl analogue 11 was excellently resolved with a separation factor of 1.24. A stereoscopic image (Figure 2b) shows spatial hindrances by the crown ether substituents indicated by an arrow.

A representative electropherogram of a separation of aromatic amines with $18C6H_4$ is shown in Figure 3a. Chiral recognition of D,L-tryptophan is probably based on both polar interactions and steric barrier mechanisms. A second ammonium function as in *p*-aminophenylalanine (**7**) represented an additional anchoring group for the crown ether and caused, therefore, longer migration times and a slightly improved separation factor compared to phenylalanine (**4**). The method described showed sufficient selectivity to resolve all four stereoisomers of 2-amino-3-phenylbutyric acid (**17** and **18**) in one single run. Most aromatic amines except phenylglycine (**3**), phenylethylamine (**10**), and histidine (**14**) were baseline separated. While **3** and **10** were not recognized owing to the size of substituents, **14** was poorly resolved under the given test conditions. Complete separation of histidine was achieved by changing the pH from 2.2 to 5.0. Poor resolution was also found for the amines **12** and **13** which both have their chiral centers in the β-position to the amine. Although α values of 1.023 and 1.037 were found to be promising for satisfactory separation, incomplete resolution of enantiomers resulted in an unexpected loss in efficiency.

Aliphatic amino acids and the tripeptide (compounds **19**–**25**) could be detected by an indirect detection mode using benzyltrimethylammonium chloride (BTA) as tracer in the running buffer. An example is given in Figure 3b with the separation of D,L-threonine (**19**). Negative peaks originate from the threonine enantiomers which displace BTA in the running buffer and thus decrease the absorbance. Amino acids with bulky substituents showed improved separation factors in comparison with those with small substituents, e.g. leucine (**22**) compared to valine (**21**). Branched alkyl groups gave better α values than their straight-chain isomers (see leucine–isoleucine and valine–norvaline).

Obviously, the complexation of the ammonium cation is mandatory for chiral recognition as demonstrated with (±)-ephedrine (**8**). This separation failed because of an extremely

(24) Behr, J.-P.; Girodeau, J.-M.; Heyward, R. C.; Lehn, J.-M.; Sauvage, J.-P. *Helv. Chim. Acta* **1980**, *63*, 2096.
(25) Behr, J.-P.; Lehn, J.-M.; Vierling, P. *Helv. Chim. Acta* **1982**, *65*, 1853.
(26) Gehin, D.; Kollmann, P. A.; Wipff, G. *J. Am. Chem. Soc.* **1989**, *111*, 3011.
(27) Hilton, M.; Armstrong, D. W. *J. Liq. Chromatogr.* **1991**, *14* (20), 3673.

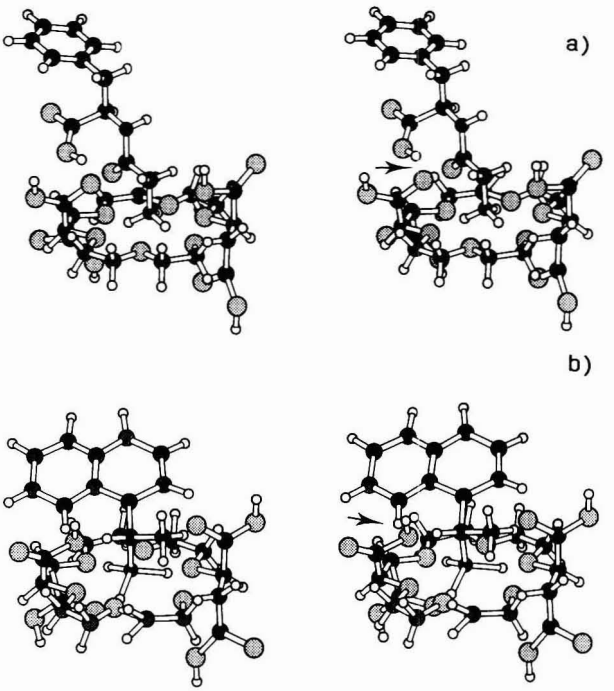

Figure 2. Stereoscopic image of a host–guest complex of $18C6H_4$ with (a) glycylphenylalanine and (b) naphthylethylamine. Arrows indicate position of possible hydrogen bonds (a) and spatial hindrance by the carboxylic acids of the crown ether (b). Key for the symbols: hydrogens are white, oxygens light, carbons dark and nitrogens black.

weak complex formation of $18C6H_4$ with the secondary amine, which does not fit into the crown ether cavity. As a consequence ephedrine eluted faster than its demethyl analogue, norephedrine (**16**), which was strongly retained by the crown ether complex.

Calculation of Thermodynamic Parameters for Chiral Recognition. For enantiorecognition based on two mechanisms: (i) steric barrier of the host carboxylic acid groups for naphthylethylamine and (ii) Coulombic interactions in the case of GlyPhe, thermodynamic parameters of the complexation reaction should differ significantly. These parameters are accessible by the separation factor α[28,29] which is related to $\Delta_{\pm}(\Delta G)$, the difference in the molar Gibbs energy of the two enantiomers, by eq 1

$$-\Delta_{\pm}(\Delta G) = RT \ln \alpha \tag{1}$$

where T is the absolute temperature and R is the gas constant (8.3143 J K^{-1} M^{-1}). Now, with

$$\Delta_{\pm}(\Delta G) = \Delta_{\pm}(\Delta H) - T\Delta_{\pm}(\Delta S) \tag{2}$$

where $\Delta_{\pm}(\Delta H)$ is the enthalpy difference of the complex formations and $\Delta_{\pm}$ (ΔS) is the difference in the entropy, it follows combining eqs 1 and 2

$$\ln \alpha = -\frac{\Delta_{\pm}(\Delta H)}{RT} + \frac{\Delta_{\pm}(\Delta S)}{R} \tag{3}$$

Equation 3 should enable $\Delta(\Delta H)$ and $\Delta(\Delta S)$ to be determined from the slope and the intercept of a plot of ln α versus $1/T$ (Van't Hoff plot). Figure 4 displays Van't Hoff plots of naphthylethylamine (NEA), GlyPhe, tryptophan, and phenylalanine in the temperature range 20–40 °C. Regression analysis gave correlation coefficients better than 0.993. An increase of temperature caused a decreased separation factor of NEA, Try, and Phe but improved α of the dipeptide. Hence, the positive and negative slopes found with NEA and GlyPhe, respectively, confirm that two chiral recognition mechanisms exist. The curve obtained for GlyPhe was unexpected. So far such shapes were only measured in gas chromatography.[30] Within a 95% confidence range, straight lines and thermodynamic data of Try and Phe are identical. Therefore, complex formation constants and chiral recognition for both amino acids should not differ significantly.

Although the separation factor α represents the chiral recognition based on lateral interactions of the host–guest complex, mere complexation of the amine with the polyether cavity also effects α. Therefore, the total Gibb's energy of the complexation $\Delta_{\pm}(\Delta G_{tot})$ calculated by eq 2 consists of two components: (i) a polyether cavity factor $\Delta_{\pm}(\Delta G_{cav})$ and (ii) the lateral interaction $\Delta_{\pm}(\Delta G_{lat})$ of the ligand without polyether participation.[31]

$$\Delta_{\pm}(\Delta G_{tot}) = \Delta_{\pm}(\Delta G_{cav}) + \Delta_{\pm}(\Delta G_{lat}) \tag{4}$$

Table II summarizes the thermodynamic data calculated from Figure 4 according to eqs 2 and 3. It has to be noted here that $\Delta(\Delta H)$ is assumed to be independent of temperature in the range studied and that extrapolation to the intercept

(28) Akanya, J. N.; Taylor, D. R. *Chromatographia* **1988**, *25*, 639.
(29) Schurig, V.; Weber, R. *J. Chromatogr.* **1981**, *217*, 51.
(30) Watabe, K.; Charles, R.; Gil-Av, E. *Angew. Chem.* **1989**, *101*, 195.
(31) Dutton, P. J.; Fyles, T. M.; McDermid, S. J. *Can. J. Chem.* **1988**, *66*, 1097.

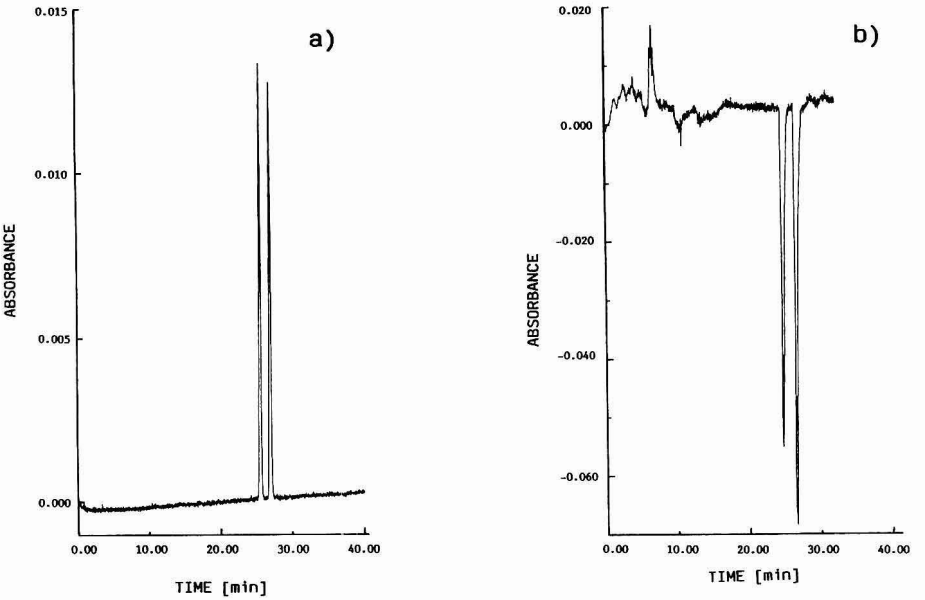

Figure 3. Chiral separation of D,L-tryptophan (a) and D,L-threonine (b) with L-threonine in excess.

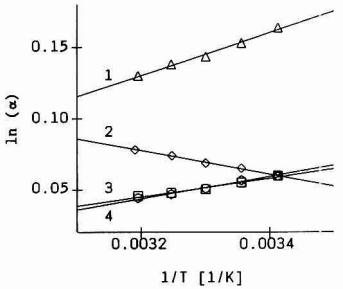

Figure 4. Van't Hoff plots of naphthylethylamine (1), glycylphenylalanine (2) tryptophan (3), and phenylalanine (4). Temperatures were 20, 25, 30, 35, and 40 °C.

Table II. Thermodynamic Data Calculated from the Straight Lines in Figure 4

compound	$\Delta_{\pm}(\Delta G)^{298}$ (J mol^{-1})	$\Delta_{\pm}(\Delta H)$ (J mol^{-1})	$\Delta_{\pm}(\Delta S)$ (J K^{-1} mol^{-1})
naphthylethylamine	−369	−1232	−2.9
GlyPhe	−161	+703	+2.9
Try	−140	−647	−1.7
Phe	−133	−550	−1.4

at infinite temperature is linear. While large errors were supposed to exist in such a procedure for HPLC,[28] our data enabled us to estimate the thermodynamic values with sufficient precision. Though accuracy of these data does not permit a sophisticated interpretation, obvious effects can be discussed. According to eq 1 the difference in the Gibb's energy is always negative since α is defined arbitrarily by the term t_2/t_1, where t_2 represents the migration time of the second eluted enantiomer and t_1 the migration time of the antipode. $\Delta(\Delta G)$ of naphthylethylamine enantiomers was the highest measured, although a large negative term $T\Delta(\Delta S)$ represented an unfavorable influence of the entropy on $\Delta(\Delta G)$ and thus on the separation. Usually Gibbs energy of the inclusion complex formation is associated with a favorable proportion of enthalpy and an unfavorable entropy proportion. This holds, for example, for the complex formation of the crown ether with NEA. The entropy value is influenced by a number of factors. A major contribution to the entropy is that hydrate water surrounding polar groups of host and guest is highly ordered and becomes disordered in particular if lateral hydrogen bonds are formed during complex formation. Simultaneously, there are losses in the translational and rotational degrees of freedom because of the association of host and guest. These two opposite effects are usually balanced, with the consequence that the contribution of entropy to the complex formation may be very small. In the case of the 18C6H$_4$–GlyPhe complexation the contribution by the release of hydrate water dominates over that caused by the loss of a degree of freedom. This effect should be more pronounced for the enantiomer which forms the stronger lateral hydrogen bonds with the host. Since the positive term $\Delta(\Delta H)$ does not contribute to the separation, α is controlled mainly by the entropic contribution, $T\Delta(\Delta S)$. The positive $\Delta(\Delta S)$ value in the case of GlyPhe is supposed to be characteristic for the recognition mechanism based on electrostatic interactions. If the chiral separation is based on both mechanisms, one should be able estimate from $\Delta(\Delta H)$ and $T\Delta(\Delta S)$ which mechanism dominates. In the case of Try and Phe a barrier mechanism dominates because $\Delta(\Delta G)$ is negative owing to the contribution of $\Delta(\Delta H)$.

CONCLUSIONS

The paper demonstrates the versatility of 18C6H$_4$ as chiral selector for the separation of enantiomers in capillary zone electrophoresis. Host–guest complexation with the crown ether depends on primary ammonium groups of the ligands and thus increases the appliciation range of CZE for chiral separations. Twenty-five optically active amines were screened with a uniform separation system. Approximately 90% of all compounds were recognized by the chiral selector and 60% were at least baseline resolved. Although separation factors of the enantiomers were small in general, most amines

were well separated because of the high efficiency of capillary zone electrophoresis. Best results were obtained if the chiral center of the molecule was adjacent to the primary amine, but excellent resolution was found even with a asymmetric center in the δ-position. Despite the suitability of the crown ether for the resolution of many amines, predictions based on the chemical structure of the guests are difficult.

CZE has proven to be extremely useful for mechanistic studies because all measurements can be performed under defined conditions and in pure aqueous solutions. On the basis of molecular models of complexes with naphthylethylamine and glycylphenylalanine, two different recognition mechanisms were proposed. It is very likely that in most separations barrier mechanisms dominate over electrostatic interactions as demonstrated with tryptophan and phenylalanine. By varying the pH value of the carrier electrolyte the mechanism could presumably be influenced in the opposite way. Thermodynamic studies have proven particularly useful to permit an additional insight into the chiral recognition and support the existence of two different separation mechanisms. While a temperature increase usually decreases the separation of enantiomers, it improved the separation in the case of GlyPhe.

RECEIVED for review March 5, 1992. Accepted July 31, 1992.

Solute Retention Mechanism in Semipermeable Surface Chromatography

Hongqi Wang, Carla Desilets,† and Fred E. Regnier*

Chemistry Department, Purdue University, West Lafayette, Indiana 47907

The retention mechanism of both small analytes and proteins was examined on two types of semipermeable surface sorbents (SPS). One type was created through the adsorption of poly(oxyethylene) (POE)-based nonionic surfactants onto reversed-phase chromatography columns. The second type was based on a mixed alkylsilane/POE-silane bonded phase on porous silica. Retention behavior of low molecular weight analytes on SPS columns was divided into three groups; polar species that are retained by hydrogen bonding to POE, amphipathic species which partition at the alkyl/POE interface, and hydrocarbons that penetrate the alkane surface layer. Proteins and peptides are generally unretained under physiological conditions. In contrast, changes in the structure of either the polypeptide or sorbent surface under denaturing conditions cause substantial retention of proteins and peptides.

INTRODUCTION

Small molecules in biological fluids and cellular extracts are often analyzed by reversed-phase chromatography (RPC), ideally by direct injection. Unfortunately, the presence of macromolecular components that foul reversed-phase columns often necessitates sample pretreatment. Several papers[1-5] have appeared in the past decade that describe methods and media to overcome this problem, the central concept in these reports being that macromolecular interference can be eliminated by shielding the stationary phase from contact with large molecules on the basis of molecular size or some other mechanism.

The first of these differential access media was the internal surface reversed-phase (ISRP) media of Pinkerton.[6,7] Through the use of hydrolytic enzymes, a 50–100-Å pore diameter sorbent was created with a hydrophobic interior and a hydrophilic exterior. Proteins were excluded from the hydrophobic interior and eluted from the column without retention. In contrast, small molecules had access to the entire surface of the particle and were retained predominantly by hydrophobic interaction with the reversed phase on the internal surface of the sorbent.

Coating a small pore diameter alkylsilane derivatized silica with a large protein, such as serum albumin, that is both strongly adsorbed and sterically excluded from the interior of the sorbent[8] is another method of preparing an ISRP packing material. Adsorbed serum albumin does not elute from columns when they were operated with less than 10% organic modifier in the mobile phase. Serum proteins are precluded from contacting the sorbent surface while small drug molecules readily gain access to the alkylsilane phase.

Shielding the stationary phase from contact with macromolecules by incorporating the stationary phase into a polymer on the sorbent surface is yet another technique by which differential access media have been created.[9,10] Shielding in these materials appears to be based on both size and hydrophobic character of solutes. Through the use of a polymeric surface layer consisting of both hydrophobic and hydrophilic monomers, hydrophobic monomers are internalized in the surface layer and cannot come in direct contact with the solution. Retention is based on the distribution of solutes between this internal hydrophobic environment and the more polar mobile phase. Apparently small hydrophobic species gain access to stationary phase groups more readily than proteins.

Still another family of media that discriminate between solutes on the basis of both size and hydrophobicity has been prepared by adsorbing nonionic surfactants to the surface of alkylsilane derivatized silica.[11] Depending on the size of the poly(oxyethylene) head group, approximately one surfactant molecules is adsorbed for every 3–10 alkylsilane residues. This semipermeable surface layer has also been produced by using a mixed alkylsilane and poly(oxyethylene)silane bonded phase.[11] A hydrophilic, arboreal surface layer is apparently created by polyoxyethylene through which molecules must diffuse to reach the alkylsilane layer below.

Ideally, the selectivity of differential access reversed-phase media would be identical to that of alkylsilane-based reversed-phase materials. This would mean that methods developed on alkylsilane-based columns could be transferred directly to differential access sorbents without the need to reoptimized the separation. On the basis of commercial literature, the selectivities of differential access media of the ISRP and shielded phase types differ among themselves and from simple alkylsilane-based reversed phase media.

The objective of this paper is to examine the retention characteristics of the third type of restricted access media, the semipermeable surface reversed-phase sorbents (SPS). The paper will focus on how the selectivity of these materials relate to conventional reversed-phase columns in small molecule and protein retention.

EXPERIMENTAL SECTION

Materials. The measurement of chromatographic retention of small analytes was performed on the same column described by Desilets.[11] The nonionic surfactants employed in this study are listed in Table I. These water-soluble members of the TWEEN series (see Figure 1 for chemical structures) were used because they can be reproducibly adsorbed onto reversed-phase packings from aqueous solution. All surfactant samples were

† Present address: U.S. Army Institute of Dental Research, Walter Reed Army Medical Center, Bldg. 40, Washington, D.C. 20307.

(1) Westerlund, D. *Chromatographia* **1987**, *24*, 155–164.
(2) Shibabi, Z. K. *J. Liq. Chromatogr.* **1988**, *11*, 1579–1583.
(3) Pinkerton, T. C. *Am. Clin. Lab.* **1989**, *8*, 32–35.
(4) Wong, S. H. Y. *J. Pharm. Biomed. Anal.* **1989**, *7*, 1011–1016.
(5) Takeda, N.; Niwa, T.; Maeda, K.; Shibabi, M.; Tatematsu, A. *J. Chromatogr.* **1988**, *431*, 418–423.
(6) Hagestam, I. H.; Pinkerton, T. C. *Anal. Chem.* **1985**, *57*, 1757–1763.
(7) Cook, S. E.; Pinkerton, T. C. *J. Chromatogr.* **1986**, *368*, 233–248.
(8) Chang, J. P. *J. Chromatogr.* **1984**, *317*, 157–163.
(9) Gisch, D. J.; Hunter, B. T.; Feibush, B. *J. Chromatogr.* **1988**, *433*, 264–268.
(10) Gisch, D. J.; Feibush, B.; Hunter, B. T.; Ascah, T. L. *Biochromatography* **1989**, *4*, 206–210.
(11) Desilets, Carla; Regneir, Fred E. *J. Chromatogr.* **1991**, *544*, 25–39.

0003-2700/92/0364-2821$03.00/0

Table I. Surfactants Used in This Study

commercial name	code[a]	m	n
G7606J	P-10-SM-12	10	12
TWEEN	P-20-SM-12	20	12
G4280	P-80-SM-12	80	12

[a] Surfactants are coded based on their chemical structures (see Figure 1): poly(oxyethylene) (m) sorbitan monoalkylates (n) or poly(oxyethylene) (m) alkyl ether (n). Letters "m" and "n" denote number of oxyethylene units per head group and number of carbon atoms per hydrocarbon tail, respectively.

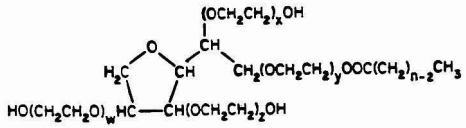

Figure 1. Chemical structure of TWEEN series of poly(oxyethylene) monoalkylates. $m = w + x + y + z$ = number of oxyethylene units (OCH_2CH_2).

kindly provided by ICI Specialty Chemicals Division, ICI Americas (Wilmington, DE) and were used as received.

The retention behavior of small peptides and proteins was studied on the SPS column and conventional C_8 columns. These columns were gifts from the Regis Chemical Co. (Morton Grove, IL). The SPS packing was a 100-Å pore diameter and 5-μm particle size with a C_8 alkylsilane and 5-kD poly(ethylene glycol) mixed bonded phase. This material was packed in a 4.6- × 150-mm column. A 4.6- × 150-mm Rexchrom S5-100-C-8 column was used for conventional reversed-phase separations.

Proteins and peptides were obtained from Sigma Chemical Co. (St. Louis, MO). A trypic digest of bovine serum albumin (BSA) was prepared according to commonly used procedures[12] with a minor modification. In brief, a mixture of BSA and trypsin (BSA:trypsin = 100:1 in moles, pH 8.2) was incubated at 37 °C for 3 h. Digestion was stopped by adding trifluoroacetic acid (TFA) to the reaction mixture.

Small analytes were of reagent grade or higher quality. Methanolic stock solutions of analytes were diluted to desired concentrations using filtered eluent. Inorganic reagents were of analytical grade or comparable quality. HPLC-grade trifluoroacetic acid (TFA) (Pierce, Rockford, IL) and acetonitrile (American Burdick & Jackson, Muskegon, MI) were used in the gradient elution separations of peptides and proteins.

Apparatus. Meaurement of chromatographic retention of small analytes was performed using a single minipump (Model 396, LDC-Milton Roy, Riviera Beach, FL) at 1.0 mL/min. The system contained a 10-port manual injection valve with 25- and 100-μL sample loops (Model C10-U, Valco Instruments, Houston, TX) and was connected to a fixed wavelength (254 nm) detector (Model 153, Beckman, Berkeley, CA).

Chromatographic retention measurements of small peptides and proteins were carried out on an HP1090 liquid chromatograph (HP1090 Series M, Hewlett-Packard Co., Palo Alto, CA) equipped with a diode array UV absorbance detector, a Hewlett-Packard ChemStation computer (Model HP 9000/300), a Hewlett-Packard printer (Thinkjet), and a Hewlett-Packard plotter (Model 7440A).

Procedures. *Measurements of chromatographic retention for small molecules* was accomplished using the equipment and reagents as described above on uncoated (control) and surfactant-coated C_8 or C_{18} columns of either 5- or 15-cm length. Analyte concentration was generally kept in the 20–200 μg/mL range. Isocratic separations were performed using an eluent consisting of 50 mM phosphate buffer (pH 6.5) with 3% 1-propanol. To maintain reproducible retention of small molecules, columns were usually recoated after each liter of eluent was used.[11]

Retention and Recovery of Polypeptides on SPS Columns under Near Physiological Conditions. The Regis SPS column and 1 mg/mL protein solutions were used in this study. Protein solutions were injected onto the column at pH 7.0 (50 mM phosphate buffer). Adsorbed protein was detected by eluting the column with a 30-min gradient ranging from phosphate buffer to 60% acetonitrile in phosphate buffer. Because ovalbumin was never retained under any circumstance, it was used as a totally recovered standard in frontal assays measuring the recovery of bovine serum albumin (BSA). It was found that the Regis SPS column adsorbed 91 μg of BSA per milliliter of packing material (Data not shown).

Peptide and Protein Retention Mechanism on SPS. Polypeptide retention was examined under both denaturing and nondenaturing conditions. Three small peptides and eight proteins were dissolved in 0.05 M phosphate buffer (pH 7.0) at a concentration of 0.5–5 mg/mL and used as the sample in these studies. Denaturing mobile phases were those commonly used in reversed-phase chromatography of peptides. Denaturing mobile phase A was 0.1 M trifluoroacetic acid (TFA). Denaturing mobile phase B was 60% acetonitrile in 40% double deionized water. Both mobile phases were degassed by sonication.

Under denaturing conditions, all the peptides and proteins were injected onto both the C_8 and the SPS column under the same condition. A 60-min gradient was used from buffer A to buffer B. The tryptic digested BSA sample was also run on both columns and eluted in a 100-min gradient from buffer A to buffer B.

Elution under physiological conditions was achieved using 0.05 M phosphate buffer (pH 7.0) as buffer A. Adsorbed proteins and peptides were eluted using a gradient from buffer A to 75% acetonitrile in double deionized water (buffer B). Peptides and proteins were first injected under physiological conditions, and the column was eluted for 10 min with buffer A. Adsorbed proteins were then eluted in a 30-min gradient from mobile phase A to B.

Small peptides were also examined on the SPS column under near physiological conditions (phosphate buffer, pH 7.0) and denaturing condition (0.1% TFA, pH 2.3). Retention behavior of small peptides was studied using isocratic elution under both conditions.

Hydrophobic Interaction Chromatography (HIC). Ammonium sulfate (2.0 M) in 0.05 M phosphate buffer (pH 7.0) was used as buffer A and 0.05 M phosphate buffer as buffer B in HIC separations. Proteins samples were made up in buffer A and eluted in a 30-min gradient from buffer A to B.

Table II. Stationary-Phase Compositions of Uncoated and Tween-Coated C_8 Reversed-Phase Column

	control (uncoated C_8)	P-10-SM-12	P-20-SM-12	P-80-SM-12
oxyethylene units (μmol/m²)[a]	0	14.3	16.4	18.4
TWEEN $-CH_2-$ (μmol/m²)[a]	0	17.16	9.83	2.82
total $-CH_2-$ (μmol/m²)[b]	26.08	43.24	35.91	28.90
L_a (μmol/m²)[c]	3.26	1.83	2.44	3.03

[a] The amount of surfactants adsorbed are calculated from the data obtained by frontal loading of surfactants and subsequent elemental analysis. See ref 11 for details. [b] The total hydrocarbon content is the sum of contributions from the alkylsilane and alkyl tail of the surfactant. Ligand density of the C_8 packing, based on elemental analysis, is 3.26 μmol/m². [c] The calculation of available reversed-phase ligand density (L_a) in μmol/m² was based on two assumptions as described in the Results and Discussion.

RESULTS AND DISCUSSION

Retention Mechanism of Small Analytes. The question being examined in this paper is the relationship of the chromatographic characteristics of semipermeable surface (SPS) columns to the reversed-phase columns from which they are derived. Desilets[11] made the important observation that the stationary phase in SPS columns is a composite of both the alkylsilane bonded phase and adsorbed surfactant. Quantitative analysis of these sorbents shows (Table II) that surfactant adsorption increases both the hydrocarbon and oxyethylene content of the stationary phase. Hydrocarbon content in micromoles of $-CH_2-$ groups/m² is the sum of contributions from the alkylsilane and alkyl tail of the

(12) Smyth, D. G. *Methods Enzymol.* **1967**, *11*, 214–231.

Table III. Capacity Factors (k') of Model Analytes on C_8 Reversed-Phase Columns Coated with TWEEN[a]

analytes	k' control (uncoated C_8)	P-10-SM-12	P-20-SM-12	P-80-SM-12
group I				
benzyl alcohol	2.48	0.96	1.28	1.62
phenobarbital	9.91	4.30	6.44	8.42
phenyl acetate	7.72	3.70	4.00	4.40
methyl benzoate	22.21	13.50	14.00	14.20
acetophenone	8.60	4.00	4.20	4.50
dimethyl terephthalate	68.86	19.70	23.0	25.67
group II				
phloroglucinol	0	1.80	2.95	2.99
aniline	1.41	1.60	1.90	1.98
phenol	2.67	4.45	5.81	6.44
group III				
anisole	12.08	14.70	14.60	13.30
benzene	7.78	13.00	12.20	9.90
toluene	26.86	42.30	39.00	31.40
ethyl benzene	82.49	122.70	112.30	94.30

[a] 50 mM phosphate buffer (pH 6.5) with 3% 1-propanol was used as the elution solvent.

surfactant. Oxyethylene content in micromoles of $-CH_2-CH_2O-$ units/m^2 is derived entirely from surfactants. Table II shows that the $-CH_2-$ content of SPS columns is greater than that of the parent C_8 reversed-phase column in all cases. Furthermore, it is seen that the hydrocarbon content of an SPS column prepared with a surfactant having a small poly(oxyethylene) head groups is greater than that of surfactants with large head groups. This may be attributed to the inverse relationship between packing density and head group size of surfactants.[11] In contrast, oxyethylene density is less dependent on head group size. Oxyethylene density increases only slightly with surfactant head group size. Desilets has shown that this is because poly(oxyethylene) head group distribution across the surface of a reversed phase column approaches a monolayer.[11]

There is the possibility that amphophilic solutes, much like surfactants in an SPS column, will partition between the alkylsilane bonded phase and mobile phase at the hydrocarbon/solvent interface. This would mean that the surfactant and amphophilic solutes are competing for the same surface binding sites at the interface. Surfactant adsorption would decrease the number of binding sites available for amphophilic solutes. This possibility was addressed by computing the "available reversed-phase ligand density" of SPS sorbents. Computation of reversed-phase ligands available at the interface was based on two assumptions: the first, that surfactant adsorption reduced the amount of reversed phase at the interface, and the second, that alkylsilanes are stoichiometrically paired with the alkyl tail of adsorbed surfactant. Available reversed-phase ligand density (L_a) (μmol/m^2) was calculated by subtracting the density of adsorbed surfactant from the ligand density of the parent reversed-phase sorbent.

Capacity factors (k') were measured for 13 small solutes of varying hydrophobicity on TWEEN-coated reversed-phase columns. Results from C_8 coated columns are listed in Table III. This data from both coated and uncoated (control) columns suggested that analyte retention behavior fell into three categories related to surfactant head group size and functional group polarity as will as seen below. Aromatic esters, phenobarbital, and benzyl alcohol fell into one group which will be referred to a "group I". Phenolics and aromatic amines fell into another group designated as "group II". Finally, aromatic hydrocarbons were placed in "group III" based on their similar behavior.

The chromatographic behavior of all analytes examined was altered by surfactant adsorption. How this occurs is an important question that will be addressed below. One possibility is that the surfactant limits access of the analyte to the alkylsilane bonded phase. In this case (case I), it would be expected that the capacity factor (k') of an analyte would be reduced. Limiting access to the stationary phase essentially reduces the amount of stationary phase. Another possibility is that the adsorbed surfactant itself acts as the stationary phase. Capacity factor would be increased in this case (case II) because the amount of stationary phase increases. Still another possibility (case III) is that the alkylsilane bonded phase and surfactant act in concert to create a new stationary phase. Again, k' would increase by the creation of stationary phase. All of these cases deal with either the creation or deletion of stationary phase, i.e. alterations in the phase ratio. There would be the possibility that analyte retention is due to multiple retention mechanisms (case IV). A typical case would be where an analyte is already retained on a reversed-phase column and the addition of surfactant creates a new stationary phase. In this case, the analyte would be retained by two mechanisms. The possibility also exists that the surfactant could alter the retention mechanism in the initial retention mode. Both of these cases would be the result of altering the distribution coefficient (K_d) in addition to the phase ratio.

Capacity factor (k') reduction subsequent to surfactant adsorption was characteristic of the group I analytes: benzyl alcohol, phenobarbital, phenyl acetate, methyl benzoate, acetophenone, and dimethyl terephthalate. This behavior would be typical of case I above and may be explained in the following way. Because surfactants are tightly adsorbed to reversed-phase columns and the poly(oxyethylene) head groups distribute across the alkyl surface in a near monolayer,[11] access to the interface is greatly reduced. Amphophilic analytes which adsorb preferentially at the stationary phase/solvent interface must compete with the surfactant for binding sites. This will reduce both the amount of stationary phase available to analytes and their distribution coefficient. Acting in concert, these two variables diminish k' of the group I analytes on SPS columns.

It is seen in Table III that the capacity factor (k') of both the group II and group III analytes are increased by adsorbed surfactants. This is characteristic of cases II–III above. There is however, an important distinction between these two groups which shows that they are retained by different mechanisms. The capacity factor of the group II analytes increases sharply with surfactant addition and is essentially independent of surfactant head group size. It is seen in Figure 2 that the behavior of phloroglucinol correlates relatively well with oxyethylene density. This is characteristic of case II. The fact that both group II analytes and poly(oxyethylene) head groups are rich in hydroxyl and ether groups suggests that hydrogen bonding can play a role in retention on surfactant loaded columns. This explanation is supported by the fact that these solutes are known to be soluble in and form complexes with poly(ethylene glycol).[11] Further support for this hypothesis comes from the similarity of C_8 and C_{18} columns with group II analytes despite a 1.6-fold difference in their carbon content (data not shown). Among the group II members there is probably a difference in retention mechanism representative of case IV. Aniline and phenol, in contrast to phloroglucinol, are retained on the reversed-phaes column in the absence of adsorbed surfactant. Because they too are amphiphilic in character, it is probable that they are also retained in a mechanism similar to that of group I analytes. Adsorbed surfactant initiates adsorption by a second retention mechanism through hydrogen bonding. In view of the fact that the surfactant, alkylsilane, and analyte are in intimate contact at the surface, it is possible that analyte

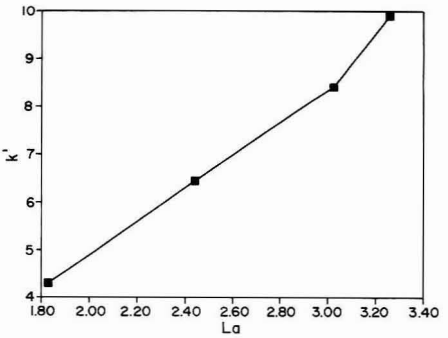

Figure 2. Retention behavior of "group I" solutes on uncoated (control) and surfactant-coated packing as a function of the "available reversed-phase ligand density" (L_a) in μmol/m^2. Data for phenobarbital is representative. Column packed with C_8 reversed-phase silica were coated with TWEEN surfactants as described by Desilets et al.[11]

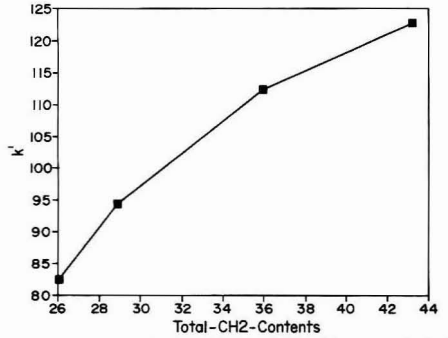

Figure 3. Retention behavior of "group III" solutes on surfactant-coated packing as a function of the total $-CH_2-$ units. Data for ethylenebenzene is representative.

contact with the hydrocarbon stationary phase and oxyethylene head groups occurs simultaneously. Under these circumstances, the presence of surfactant would induce a new retention mechanism that would alter retention by changing both the distribution coefficient (K_d) and the phase ratio.

Behavior of the hydrocarbonaceous group III analytes on SPS columns differs from the very polar group II analytes in that their capacity factor (k') increases more with the adsorption of surfactants having small head groups that large. This behavior correlates well with the hydrocarbon content of SPS columns (Figure 3). It appears that the alkylsilane bonded phase and hydrocarbon tail of the adsorbed surfactant are working in concert to create a new hydrocarbonaceous stationary phase (case III). Hydrocarbon analytes cross the stationary phase/solvent interface and gain access to the entire hydrocarbon stationary phase.

The data presented above show how solute retention in surfactant-coated reversed-phase sorbents occurs among the stratified layers formed by the surfactant. Furthermore, it is seen that retention and selectivity can be manipulated by changing surfactant head group size. In view of the fact that adsorbed surfactants are similar to adsorbed solvents, it is possible that these results applying to reversed-phase chromatography in general. If this is the case, then it may be concluded that (i) mobile-phase additives play an active role in creating the stationary phase and (ii) part of their role in

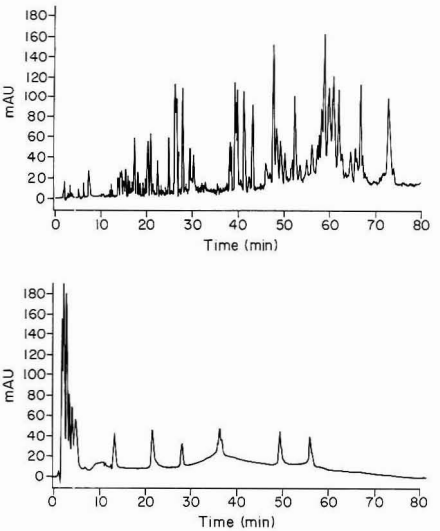

Figure 4. Retention behavior of trypsin digested BSA on C_8 and SPS (poly(ethylene glycol)-coated) column. Trypsin digested BSA was separated on C_8 (top chromatograph) and SPS (bottom chromatograph) under the same condition as described in the experimental section.

modulating selectivity is at the level of altering the stationary phase.[13,14]

Retention of peptides. Tryptic digests of proteins are known to range from small hydrophilic dipeptides to large hydrophobic oligopeptides of 20–30 residues[12] and are commonly resolved by reversed-phase chromatography.[12] A tryptic digest of bovine serum albumin (BSA) was used to test the size discriminating properties of the covalently bonded poly(oxyethylene) SPS column. This digest contains more than 50 peptides, some of which are very hydrophobic. When the peptide mixture was loaded onto the SPS column at either pH 3.0 or 7.0 and subsequently gradient eluted from 0.1% trifluoroacetic acid (TFA) to 0.1% TFA in 60% aqueous acetonitrile, only a few peptides were detected to have been adsorbed to the SPS column (Figure 4). This establishes that solute discrimination on the SPS sorbent occurs with analytes below a kilodalton in size.

Retention of Proteins. Protein structure is sensitive to environmental conditions. Extremes in pH or the presence of organic solvents can cause proteins to denature and become more hydrophobic without precipitating. These denatured proteins are much more strongly retained on reversed-phase chromatography columns than native proteins.

It is often the case in reversed-phase chromatography that organic solvents and other protein-denaturing mobile-phase additives must be used to affect the elution of low molecular weight analytes. The question addressed below was the effect denaturing mobile phases have on the adsorption of proteins to the commercial SPS column. Such adsorption is often referred to in the literature as "nonspecific adsorption". Adsorption of eight proteins and three peptides under nondenaturing conditions served as the control.

When the test proteins were applied under nondenaturing conditions, i.e. 50 mM phosphate buffer at pH 7.0, none were adsorbed except bovine serum albumin (BSA) as seen in

(13) Snyder, L. R. In *High Performance Liquid Chromatography-Advances and perspectives*: Horvath, Cs., Ed.; Academic Press: New York, 1980; Vol. 1, pp 208–316.

(14) Jamdera, P.; Churacek, J. *Gradient Elution in Liquid Chromatography. Theory and Practice*; Elsevier: Amsterdam, 1985; Chapter 4.

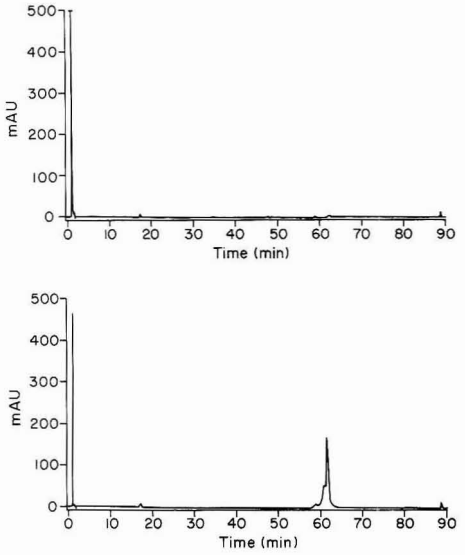

Figure 5. Protein recovery on SPS (polyethylene glycol coated) column. Data are shown for ovalbumin (upper) and BSA (lower) on SPS column when injected at near physiological conditions as described in the experimental section.

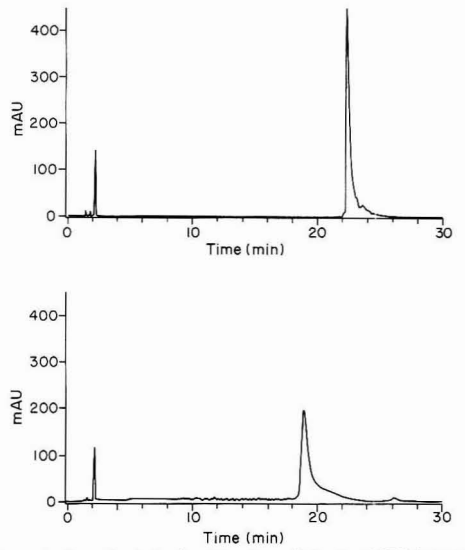

Figure 6. Retention behavior of insulin on C_8 (top) and SPS (bottom) under reversed-phase conditions as described in the Experimental Section.

Figure 5. Approximately 90 μg of BSA was adsorbed per milliliter of column volume. This behavior was not observed with the surfactant coated reversed-phase column (data not shown) and is interpreted to mean that the Regis SPS column had some small imperfections in the coating.

Multiple proteins were retained when administered to the SPS column under denaturing conditions (Figure 6). However, retention time of the model proteins was longer on a C_8 reversed-phase column than the SPS column in all cases. These results are interpreted in the following way. The results imply that the poly(oxyethylene) (POE) phase is either more extended under denaturing conditions or hydrophobic regions in denatured proteins displace the POE and come in contact with the underlying C_8 phase. In either case, denatured proteins bind to the SPS columns. This means that protein adsorption could be substantial when samples are applied to SPS columns under denaturing conditions. It is clearly undesirable to apply serum samples under denaturing conditions. Samples should be applied to the SPS column under nondenaturing conditions even when it is necessary to elute analytes with a denaturing mobile phase. This is easily achieved by mobile phase programming.

Denaturing mobile phases can also have an effect on retention of small peptides as seen when glycylphenylalanine and glycylglycylphenylalanine were examined at pH 7.0 and pH 2.3. Both peptides were nonretained at pH 7.0 but eluted with k' values of 6.5 and 8.5, respectively, at pH 2.3. Because conformational changes will not play a role in the retention of small peptides, these differences could be due to changes in stationary phase structure and/or the effective charge on the peptides. Since the effective charge difference itself normally will not cause such a big change (6- or 8-fold increase in k' value), this further suggests that under physiological conditions that the POE layer is more compact than at pH 2.3.

Protein retention was also examined in the presence of high concentrations of salt, i.e. 2.0 M $(NH_4)_2SO_4$, at pH 7.0. No separation or retention of the model proteins was observed (data not shown). These results indicate that SPS columns are of no utility in hydrophobic interaction chromatography of proteins.

CONCLUSIONS

These studies show that the chromatographic behavior of low molecular weight analytes on surfactant-coated and poly(oxyethylene) (POE)-derivatized reversed-phase columns is different than on normal reversed-phase columns. Furthermore, these differences are related to analyte structure and fall into several classes. Based on the fact that the retention of hydroxyl and amine-rich species is proportional to the surface density of POE, it is concluded that a significant portion of their chromatographic behavior is due to hydrogen bonding with the POE layer. In contrast, more amphipathic species partition at the interface between the alkylsilane bonded phase and the polar POE layer. Finally, it is concluded that hydrocarbon analytes gain access to more of the hydrocarbon bonded phase at the stationary phase/solvent interface of a sorbent and that their chromatographic behavior is more closely related to the total hydrocarbon content of column.

It is concluded that in contrast to small analytes, access of polypeptides to the alkylsilane bonded phases under physiological conditions is diminished by the presence of a poly(oxyethylene) polymer layer at the sorbent surface. In contrast, retention of proteins and some peptides under denaturing conditions increases. This is due either to modification of (i) solute conformation, (ii) stationary-phase conformation, or (iii) conformational changes in both the solute and stationary phase.

ACKNOWLEDGMENT

We thank the Regis Co. for kindly providing the columns, Tim Nadler for his assistance in operating the HP ChemStation, and Judy Heine for her typing of the manuscript.

RECEIVED for review March 20, 1992. Accepted August 24, 1992.

High-Performance Liquid Chromatographic Method for the Determination of Ultratrace Amounts of Iron(II) in Aerosols, Rainwater, and Seawater

Zhen Yi, Guoshun Zhuang,†,‡ Phyllis R. Brown,* and Robert A. Duce†,§

Department of Chemistry and Center for Atmospheric Chemistry Studies, Graduate School of Oceanography, University of Rhode Island, Kingston, Rhode Island 02881

A reversed-phase high performance liquid chromatography method was developed to determine concentrations of iron(II) in Chinese loess, aerosols, rainwater, and seawater. This method was isocratic, rapid, sensitive, and reproducible. Iron(II) forms a stable complex ion with the reagent ferrozine, $[Fe(FZ)_3]^{2+}$ in a pH range of 4–10. By measuring the absorbance of $[Fe(FZ)_3]^{2+}$ at 254 nm, iron(II) concentrations were determined. $[Fe(FZ)_3]^{2+}$ was separated from ferrozine and was detected in 6 min. Reversed-phase C_{18} solid-phase extraction cartridges, which were used for the sample preparation, concentrated the $[Fe(FZ)_3]^{2+}$ and increased sensitivity of the analysis. A detection limit of 0.1 nM Fe(II) was obtained. Retention time, addition of known amount of standard, and peak area ratios were used for peak identification of $[Fe(FZ)_3]^{2+}$. There was no interference from Fe(III), Ni(II), Co(II), and Cu(I). The recovery of 10^{-9}–10^{-10} M $[Fe(FZ)_3]^{2+}$ using the preconcentration step was in the range of 92–99%. The Fe(II) concentration in remote marine aerosols has been determined for the first time by using this new method.

INTRODUCTION

The determination of Fe(II) is of considerable interest in research in both atmospheric chemistry and oceanography. It has recently been suggested that iron, a micronutrient required by organisms, may be the limiting factor for primary biological productivity in some open ocean regions, including high latitude and equatorial upwelling regions, where other major nutrients (nitrate and phosphate) are abundant.[1-4] In clouds, fog, and rainwater the photoreduction of Fe(III) to Fe(II) has also been proposed as a major source of aqueous hydroxyl radical ($OH^•$),[5-7] which is a key radical in atmospheric photochemistry and plays a central role in the atmosphere in the oxidation of many tropospheric trace gases[8] and species in solution in atmospheric waters.

Although there are a number of papers that deal with the total iron in the ocean and in the atmosphere, only a few have reported the concentration of Fe(II).[9-13] In investigations of Fe(II) in the ocean and atmosphere a major obstacle in the analytical methods used has been the detection limits. The total dissolved iron concentration in the open ocean is generally less than 1 nmol/kg.[1,3,4,14,15] Thus, methods for the determination of Fe(II) in samples from the open ocean require very low detection limits. Recently, a technique of flow injection analysis with chemiluminescence detection was reported for the determination of subnanomolar levels of Fe(II) in seawater.[16] Since there was no separation of Fe(II) and Fe(III) in the analyses, the measured Fe(II) concentrations must be corrected for the chemiluminescence produced by the Fe(III).

Waite and Morel[13] reported a controlled potential coulometric procedure combined with a masking technique to determine the Fe(II) in seawater at the nanomol level. A colorimetric method using ferrozine (FZ) (3-(2-pyridyl)-5,6-diphenyl-1,2,4-triazine-*p,p'*-disulfonic acid) has been used for measuring Fe(II) since 1970.[11,12,17-20] The colorimetric reagent FZ forms a stable complex ion, $[Fe(FZ)_3]^{2+}$, with Fe(II) in a pH range of 4–10 but not with Fe(III). However, the detection limits of these reported methods are not satisfactory for the measurement of Fe(II) in the open ocean. Recently King et al.[21] reported a colorimetric methods for the determination Fe(II) in seawater at the nanomol level using FZ immobilized on a reversed-phase C_{18} Sep-Pak cartridge. This method is only marginally satisfactory for the measurement of Fe(II) at the less than 1-nmol level. FZ has a significant absorbance at the wavelength that was used for determination of Fe(II). In previous methods in which FZ was used as a reagent, the excess FZ in the reaction mixture was not separated from the $[Fe(FZ)_3]^{2+}$ complex ions that were formed, and the absorbance from the FZ itself and from other constituents in the samples (e.g., seawater) was measured by a blank determination. Since it is impossible to determine the concentration of FZ that is not complexed in the unknown sample solutions, the excess FZ can cause considerable error in a system with very low Fe(II) concentrations. To date there has been no

† Center for Atmospheric Chemistry Studies, Graduate School of Oceanography.

‡ Present address: Environmental Sciences Program, University of Massachusetts at Boston, 100 Morrissey Blvd., Boston, MA 02125-3393.

§ Present address: College of Geosciences and Maritime Studies Texas A&M University, College Station, TX 77843.

(1) Martin, J. H.; Gordon, R. M. *Deep Sea Res.* **1988**, *35*, 177–196.
(2) Martin, J. H.; Fitzwater, S. E. *Nature* **1988**, *321*, 341–343.
(3) Martin, J. H.; Gordon, R. M.; Fitzwater, S. E.; Broenkow, W. W. *Deep Sea Res.* **1989**, *36*, 649–680.
(4) Martin, J. H.; Gordon, R. M.; Fitzwater, S. E. *Nature* **1990**, *345*, 156–158.
(5) Graedel, T. E.; Weschler, C. J.; Mandich, M. L. *Nature* **1985**, *317*, 240–242.
(6) Weschler, C. J.; Mandish, M. L.; Graedel, T. E. *J. Geophys. Res.* **1986**, *91*, 5189–5204.
(7) Faust, B. C.; Hoigne, J. *Atmos. Environ.* **1990**, *24A*, 79–89.
(8) Davis, D.; Niki, H.; Mohnen, V.; Liu, S. *Global Tropospheric Chemistry, A Plan for a Action*; National Academy Press: Washington, DC, 1984; pp 78–87.
(9) Behra, P.; Sigg, L. *Nature* **1990**, *344*, 419–421.
(10) Landing, W. M.; Westerlund, S. *Mar. Chem.* **1988**, *23*, 329–343.
(11) Hong, H. S.; Kester, D. R. *Limnol. Oceanogr.* **1986**, *31*, 512–524.
(12) Hong, H. S.; Kester, D. R. *Coastal Shelf Sci.* **1985**, *21*, 449–459.
(13) Waite, T. D.; Morel, F. M. *Anal. Chem.* **1984**, *56*, 787–792.
(14) Landing, W. M.; Bruland, K. W. *Geochim. Cosmochim. Acta* **1987**, *51*, 29–43.
(15) Symes, J. L.; Kester, D. R. *Mar. Chem.* **1985**, *17*, 57–74.
(16) Elrod, V. A.; Johnson, K. S.; Coale, K. H. *Anal. Chem.* **1991**, *63*, 893–898.
(17) Stookey, L. C. *Anal. Chem.* **1970**, *42*, 779–781.
(18) Gibbs, M. M. *Water Res.* **1979**, *13*, 295–297.
(19) Gibbs, M. M. *Anal. Chem.* **1976**, *48*, 1197–1201.
(20) Boyle, E. A.; Edmond, J. M.; Sholkovitz, E. R. *Geochim. Cosmochim. Acta* **1977**, *41*, 1313–1324.
(21) King, D. W.; Lin, J.; Kester, D. R. *Anal. Chim. Acta* **1991**, *247*, 125–132.

0003-2700/92/0364-2826$03.00/0

method reported for the measurement of Fe(II) using high-performance liquid chromatography (HPLC). Here, we report a method for measurement of Fe(II) in environmental samples by derivatizating the Fe(II) with ferrozine and isolating the Fe(II)–FZ complex by reversed-phase HPLC.

EXPERIMENTAL SECTION

Apparatus. A Perkin-Elmer Series 3B liquid chromatograph (Perkin-Elmer Corp., Norwalk, CT) was used. All analyses were performed on a 250- × 4.6-mm, 5-μm Supelco LC-18 column (Supelco Inc., Bellefonte, PA). Detection was performed by means of a Perkin-Elmer LC-95 UV/visible spectrophotometer detector. Injections were made via a Waters Model U6K injector (Waters Chromatography Division of Millipore Corp., Milford, MA). Peak heights were recorded with a strip chart Omniscribe recorder (Houston Instruments, Austin, TX). Peak areas were electronically integrated with a Hewlett-Packard 3390A reporting integrator.

Chemicals and Supplies. The chromatographic standard was ferrous ammonium sulfate hexahydrate ($Fe(NH_4)_2(SO_4)_2 \cdot 6H_2O$) obtained from Sigma Chemical Co. (St. Louis, MO). The monosodium salt of ferrozine, sodium dodecyl sulfate (SDS), and tetrabutylammonium phosphate (TBA) were also obtained from Sigma. Sodium chloride (99.999%) was obtained from Aldrich Chemical Co. (Milwaukee, WI). Sep-Pak C18 cartridges were obtained from Waters. Methanol was purchased from Fisher Scientific (Fair Lawn, NJ). Mobile phases which were prepared with doubly distilled deionized water (DDH_2O) were filtered through a 0.45-μm Nylon 66 membrane filter (Alltech Associates Inc., Deerfield, IL). All standard and sample solutions were stored in Teflon vials.

Chromatographic Conditions. The mobile phase was 400 mL of an aqueous solution containing 0.0500 g of SDS, 0.5000 g of NaCl, 0.0100 g of TBA, and 100 mL of methanol. A flow rate of 1.0 mL/min was used. The injected volume of each sample was 50 μL. The temperature was 20 ± 1 °C.

Sample Preparation. The sample and standard preparation was performed in Class 100 clean laboratories at the University of Rhode Island.

I. Standard Solutions. A 0.0392-g sample of $Fe(NH_4)_2(SO_4)_2 \cdot 6H_2O$ was dissolved in 100 mL of DDH_2O, and the concentration of Fe^{2+} was 10^{-3} M; 0.100 mL of 10^{-3} M Fe^{2+} was immediately added to 0.400 mL of 10^{-3} M FZ and diluted to 10 mL. The concentration of $[Fe(FZ)_3]^{2+}$ was 10^{-5} M. The 10^{-5} M $[Fe(FZ)_3]^{2+}$ standard solution was then diluted with DDH_2O to 5×10^{-6}, 10^{-6}, 5×10^{-7}, 10^{-7}, 5×10^{-8}, 10^{-8}, 5×10^{-9}, and 10^{-9} M.

II. Aerosol Samples. A 2- or 4-cm^2 aliquot of an aerosol sample collected on a filter over the North Pacific Ocean was leached in 0.2 mL of doubly distilled hydrochloric acid (DDHCl) and 2.0 mL of DDH_2O for at least 3 h. After the sample was filtered through a 0.4-μm Nuclepore filter, 25% NH_3 was added to the filtrate to adjust the pH to the range of 4–6; 0.1–0.2 mL of a 10^{-3} M solution of FZ was then added to the sample.

III. Chinese Loess. Chinese loess was the major source of the mineral aerosols over the North Pacific. To determine the relationship of Fe(II) in mineral aerosols and its source, the Fe(II) in Chinese loess was also measured. A 1.0- or 2.0-mg sample was leached in 0.2 mL of HCl and 2.0 mL of DDH_2O for at least 3 h. The sample was then treated the same way as the aerosol sample.

IV. Rain and Seawater. The samples were prepared by using a reversed-phase C18 Sep-Pak cartridge for the solid phase extraction procedure. Rainwater samples were collected from Narragansett, a coastal area of Rhode Island. Coastal seawater samples were collected from Narragansett Bay, RI. As soon as a sample was collected, it was filtered with a 0.4-μm Nuclepore filter. The rainwater or seawater (100–500 mL) was passed through the pre-prepared Sep-Pak cartridge at a rate of 10 mL/min. Each Sep-Pak cartridge had been cleaned with 10 mL of methanol and 10 mL of DDH_2O and then loaded with 2 mL of 10^{-3} M FZ. A 5–10-mL aliquot of DDH_2O was used to rinse the Sep-Pak. The complex $[Fe(FZ)_3]^{2+}$ and FZ were eluted with 1 mL of methanol. A 4-mL portion of DDH_2O was added to the eluent in order to make the ratio of methanol to water in the eluent the same as that in the mobile phases, and this eluent was used for injection in the HPLC system.

V. Blank Samples. A blank Whatman 41 filter of the type used for aerosol sampling was used as a blank sample for aerosols, and DDH_2O was used as a blank sample for rain and seawater. The procedures for blank sample preparation were the same as those described in sections II and IV.

Sample Recovery. The recovery of Fe(II) from the Sep-Pak was determined by addition of known amounts of Fe(II) standards to sample matrixes of rainwater or deionized water. The complex ion, $[Fe(FZ)_3]^{2+}$, was extracted using the sample preparation procedure described in section IV.

Detection Limit. To determine the detection limit, a 10^{-10} M standard $[Fe(FZ)_3]^{2+}$ solution was prepared by the dilution of 1 mL of 5×10^{-8} M $[Fe(FZ)_3]^{2+}$ standard solution to 500 mL with DDH_2O. After 1 mL of 10^{-3} M FZ was passed through a Sep-Pak, 500 mL of 10^{-10} M $[Fe(FZ)_3]^{2+}$ was passed through the Sep-Pak prepared with FZ. The Sep-Pak was then rinsed with 5 mL of H_2O. The $[Fe(FZ)_3]^{2+}$ adsorbed on the Sep-Pak was eluted with 1 mL of methanol. The methanol in the eluent was evaporated with helium gas to ~0.2 mL, and DDH_2O was added to 1 mL. A 50-μL portion of the sample was then injected into the HPLC system.

Peak Identification. Identification of the peaks of interest was based on retention time, co-injection of standards with the samples, and determination of the ratios of peak area at various wavelengths (254, 270, 290, 310, 330, 350, 450, 546, and 562 nm) to the peak area at 230 nm.

Interferences. Interferences from Fe(III), Ni(II), Co(II), and Cu(I) were tested. Solutions of 10^{-5} M Fe(III), Ni(II), Co(II), and Cu(I) were prepared from Fe, Ni, and Co standard solutions (NBS) and CuBr, respectively; 0.1 mL of 10^{-3} M FZ was added to 5 mL of 10^{-5} M Fe(III), Ni(II), Co(II), and Cu(I), respectively. The pH of the Fe(III) solution was ~4.0, and the pH of the Ni(II), Co(II) and Cu(I) solutions was 5.5. Since Cu(I) is light- and air-sensitive, the Cu(I) solution was wrapped with aluminum foil, and FZ was added into 10^{-5} M Cu(I) solution immediately after CuBr was dissolved in DDH_2O.

A capillary electrophoresis (CE) method for cations[22,23] was also used to determine Fe(II), and the results were compared with those obtained by HPLC. A Waters Quanta 4000 capillary electrophoresis system, equipped with a positive voltage power supply, was used in this study. Details were in the literature.[22,23]

RESULTS AND DISCUSSION

The peaks of $[Fe(FZ)_3]^{2+}$ and FZ were baseline resolved (Figure 1). By measuring the absorbance of $[Fe(FZ)_3]^{2+}$ at 254 nm, iron(II) concentrations were determined. $[Fe(FZ)_3]^{2+}$ was separated from ferrozine and was detected in 6 min. The peaks prior to 5 min are not identified. The retention times, peak areas, and peak shapes were reproducible on 10 samples of a 10^{-7} M standard solution; the relative standard deviation of the retention times and the peak areas were 0.6% and 4.3%, respectively. There was a good linear response (regression coefficient = 0.997) in the concentration range of 10^{-5}–10^{-8} M.

If Sep-Pak C_{18} solid phase extraction cartridges were used, the detection limit was 10^{-10} M. When the Sep-Pak extraction procedures were not used, the detection limit at 254 nm was decreased to 10^{-8} M, and the mass detection limit was 0.028 ng. Even though the wavelength 562 nm has been reported as the best,[21] baseline noise was greater at 562 nm. In addition, the peak areas at 230, 310, 290, 330, and 254 nm are greater than that at 562 nm (Table I). Therefore, detection limits were lower at the wavelengths 230, 310, and 254 nm than at 562 nm. Since some models of UV/visible detectors can only be used at one wavelength (usually at 254 nm), the wavelength of 254 nm was chosen in this work.

(22) Weston, A.; Brown, P. R.; Jandik, P.; Jones, W. R.; Heckenberg, A. L. *J. Chromatogr.* **1992**, *593*, 289–295.
(23) Weston, A.; Brown, P. R.; Heckenberg, A. L.; Jandik, P.; Jones, W. R. *J. Chromatogr.* **1992**, *602*, 249–256.

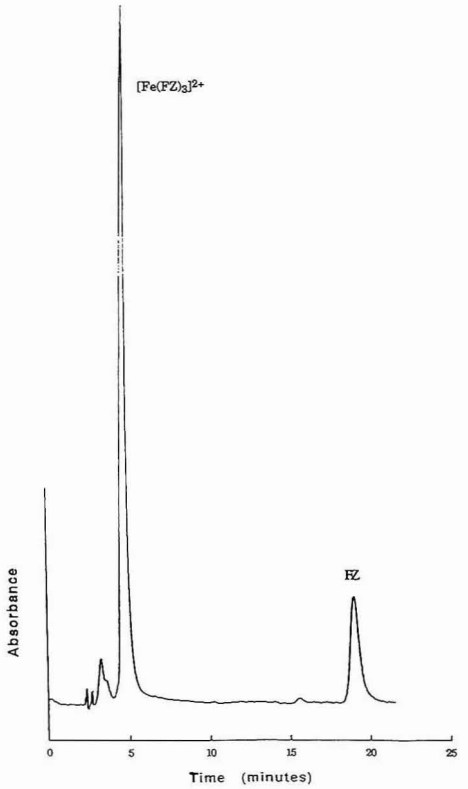

Figure 1. A chromatogram of 20 μL of 5 × 10^{-6} M $[Fe(FZ)_3]^{2+}$ standard solution. Chromatographic conditions are described in the Experimental Section. UV/vis detector, 254 nm; sensitivity, 0.01 AUFS (Absorbance Unit Full Scale); response time, 500 ms.

Table I. Peak Area Ratios ($R = A_{x\ nm}/A_{230\ nm}$) for a Standard Solution and a Sample Solution at Various Wavelengths

	standard solution[a]		sample solution[b]	
wavelength (nm)	$area_{x\ nm}$	ratio ($A_{x\ nm}/A_{230\ nm}$)	area	ratio ($A_{x\ nm}/A_{230\ nm}$)
230	9 227 400		7 080 300	
254	4 641 900	0.50	3 581 100	0.51
270	4 581 300	0.50	3 574 400	0.50
290	6 741 300	0.73	5 343 100	0.75
310	6 993 200	0.76	5 462 900	0.77
330	5 074 900	0.55	3 940 100	0.56
350	3 323 400	0.36	2 592 500	0.37
450	1 016 800	0.11	862 340	0.12
564	2 218 300	0.24	1 809 200	0.26
562	2 881 300	0.31	2 341 500	0.33

[a] Standard solution: 50 μL of 5 × 10^{-6} M $[Fe(FZ)_3]^{2+}$. [b] Sample: 50 μL of aerosol sample solution from an aerosol sample collected at Enewetak, an island in the North Pacific (sample ID EN162).

The important advantage of our HPLC method is that the $[Fe(FZ)_3]^{2+}$ complex can be separated from the excess ferrozine and other constituents in the solution. As mentioned above, in previous methods the absorbance from the excess FZ, as measured in a blank of FZ, had to be subtracted from the total absorbance of the sample. In a system with very low Fe(II) concentrations, this calculation could cause considerable error in the Fe(II) concentrations. For example, when a 5 × 10^{-6} M Fe(II) standard reacted with 2 × 10^{-5} M FZ solution was measured at 562 nm, the excess FZ concentration was 5 × 10^{-6} M. The ratio of the peak area of $[Fe(FZ)_3]^{2+}$ to the peak area of FZ was ~10. As reported in the measurement of Fe(II) in seawater in which a C_{18} Sep-Pak preconcentration step was used,[21] the concentration of FZ was ~10^{-3} M and the measured Fe(II) concentration was only ~4 nM. In this case the absorbance from the excess FZ was much greater than that of Fe(II). Therefore, the calculation of Fe(II) obtained by subtracting the FZ "blank" from the total absorbance may cause considerable error. Fortunately, with our HPLC method, $[Fe(FZ)_3]^{2+}$ was completely separated from FZ and other constituents in the samples, and thus there was no interference from the FZ peak. In blank samples for Chinese loess, aerosol, rainwater, and seawater, $[Fe(FZ)_3]^{2+}$ was not detectable. To determine if any Fe(II) was released from Sep-Pak cartridges during the sample preparation, 1000 mL of double distilled H_2O was used as a blank to pass through the same type of Sep-Pak cartridge, and there was no detectable Fe(II) ferrozine complex peak due to Fe released from the Sep-Pak cartridge.

It was reported that Cu(I), Co(II), and Ni(II) are the only metals other than Fe which may form colored complexes with FZ.[17,24] When 0.1 mL of 10^{-3} M FZ was added to 5 mL of 10^{-5} M Ni(II), Co(II), and Cu(I) solutions, there are no additional peaks to respond the possible Ni(II), Co(II), and Cu(I) ferrozine complexes either in the range of Fe(II) peak or in other ranges of the chromatograms even up to 2 h after the addition of FZ. It was also found that when 0.1 mL of 10^{-3} M FZ was added to 5 mL of 10^{-5} M Fe(III) solutions, there is no Fe(II) peak to respond the possible reduction of Fe(III) by FZ to Fe(II) in the range of the Fe(II) peak even up to 2 h after the addition of FZ. Only 0.1% of 18 μM Fe(III) was reduced by FZ to Fe(II) 2 h after addition of FZ. Since all the samples were analyzed within 30 min of addition of FZ, there would be no error caused by reduction of Fe(III) to Fe(II). Similarly, because there is no interference from the presence of Ni(II), Co(II), and Cu(I), these ions which may form colored complexes with FZ would not cause any errors in the Fe(II) concentrations in any of the samples.

Peak identification of $[Fe(FZ)_3]^{2+}$ was carried out by retention time, by addition of known amount of standard, and by comparison of peak area ratios at various wavelenghs.[25] The ratios of peak areas at various wavelengths to the peak area at 230 nm for a standard solution and for an aerosol sample solution (sample ID: EN 162) are shown in Table I. The $[Fe(FZ)_3]^{2+}$ peak was identified when the ratios for the standard solution and for the sample were similar or identical. These results indicate that there was little or no absorption due to other substances, such as possible organic compounds, in the aerosol samples. It would be unlikely that the organic compounds would have the same absorbance ratios at so many different wavelengths.

The recovery of 10^{-8}–10^{-10} M $[Fe(FZ)_3]^{2+}$ by preconcentration with the Sep-Pak C_{18} cartridge was in the range of 92–99% (Table II).

To determine if any Fe(II) was produced due to the reduction of Fe(III) in aerosol samples by other factors during the storage, a standard Fe(III) solution was added to several blank Whatman 41 filters (~1 μmol/cm^2 filter, ~5–400 times higher than that in the measured aerosol samples). These filters were measured for Fe(II) by the same procedures used for measuring Fe(II) in the aerosol samples 7, 14, 35, and 91 days after addition of Fe(III). In all of these cases there was

(24) Bet-Pera, F.; Jaselakis, B. *Analyst* **1981**, *106*, 1234–1237.
(25) Krstulovic, A. M.; Rosie, D. M.; Brown, P. R. *Anal. Chem.* **1976**, *48*, 1383–1386.

Table II. Recovery Efficiency of Fe(II) Measured by Preconcentration with C18 Sep-Pak Cartridges

added concn (nM)	measured concn (nM)	recovery concn (nM)	recovery (%)
10	10.6	9.4[a]	94
5	6.0	4.8[a]	96
1	2.12	0.92[a]	92
0.1	0.099	0.099[b]	99

[a] The recovery was determined by addition of known amounts of newly prepared fresh Fe(II) standards to a rainwater sample. The recovered Fe(II) concentration is the measured Fe(II) concentration minus the Fe(II) concentration in the rainwater sample (1.2 ± 0.4 nM; n = 4). [b] The recovery was determined with 0.1 nM Fe(II) standard in the iron-free deionized water. The recovered Fe(II) concentration is the measured Fe(II) concentration.

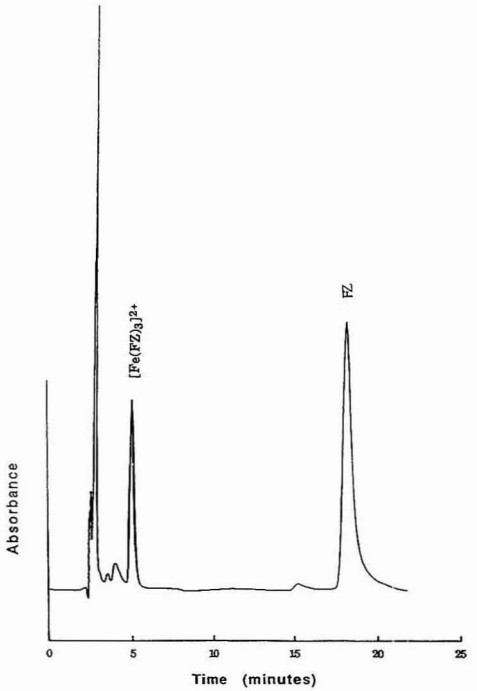

Figure 2. A chromatogram of an aerosol Whatman 41 filter sample (EN 161). Sample preparation and chromatographic conditions are described in the Experimental Section. UV/vis detector, 254 nm; sensitivity, 0.05 AUFS; response time, 500 ms.

no detectable Fe(II) (i.e., Fe(II) <0.028 ng).

In a blind study, the concentrations of Fe(II) in a standard solution and in a blind sample solution were determined by our HPLC method and the results compared to those obtained by CE method for cations.[22,23] The results obtained by the CE method supported our results; the concentrations of Fe(II) in both the standard and sample solutions were within 3% of the concentrations obtained by HPLC. However, the limit of detection of the CE method was only 10^{-5} M compared to the detection limit of 10^{-8} M by the HPLC method.

Examples of chromatograms for aerosol, rainwater, and seawater are shown in Figures 2–4, and the results of the determination of Fe(II) concentrations in some environmental samples are presented in Table III. The Fe(II) concentration in remote marine aerosols has been determined for the first time by using this new method.[26] Fe(II) in aerosol samples collected from Enewetak, a remote island in the North Pacific,

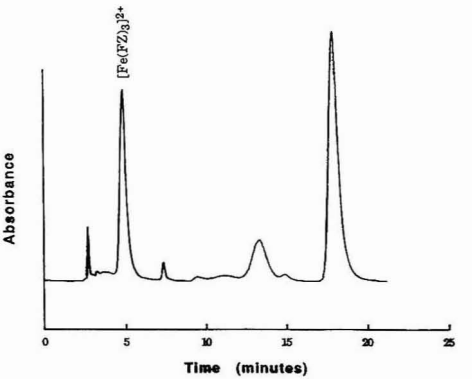

Figure 3. A chromatogram of rainwater collected from Narragansett, RI, (sampling date 12/8/1990). Sample preparation and chromatographic conditions are described in the Experimental Section. Fe(II) in rainwater was preconcentrated 50 times with C18 Sep-Pak. UV/vis detector, 254 nm; sensitivity, 0.02 AUFS; response time, 500 ms.

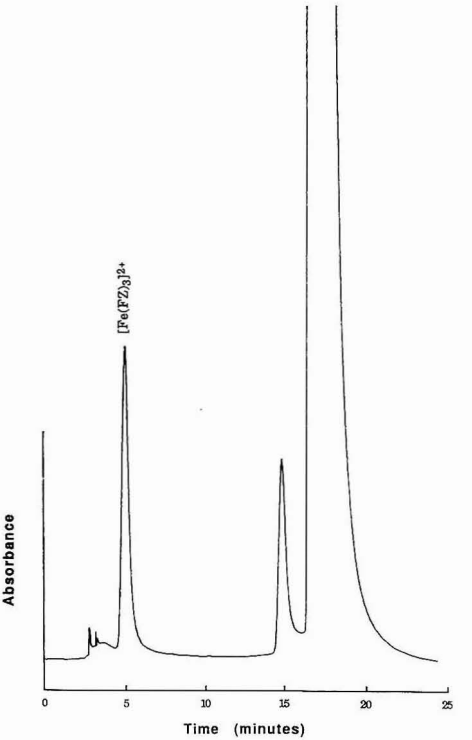

Figure 4. A chromatogram of seawater collected from Narragansett Bay, RI, (sampling date 3/6/1991, 1500). Sample preparation and chromatographic conditions are described in the Experimental Section. Fe(II) in seawater was preconcentrated 100 times with C18 Sep-Pak. UV/vis detector, 254 nm; sensitivity, 0.005 AUFS; response time, 500 ms.

(26) Zhuang, G.; Yi, Z.; Duce, R. A.; Brown, P. R. *Nature* **1992**, *355*, 537–539.

Table III. Fe(II) Concentrations in Chinese Loess, Aerosol, Rainwater, and Seawater

sample	concentration		Fe(II)/T(Fe) (%)
	Fe(II)	T(Fe)[a]	
Chinese loess	~0.015% (w/w)	~3% (w/w)	0.4 ± 0.3
aerosol (EN 161)	6.7 ± 0.6 ng/m^3	27 ± 3 ng/m^3	~25
rain (12/8/1990, from Narr., RI)	68 ± 6 nM	230 ± 25 nM	~30
seawater (3/6/91, from Narr. Bay)	29 ± 3 nM	72 ± 7 nM	~40

[a] T(Fe): The total Fe concentration in the sample was measured by atomic absorption spectrophotometer.

from April 30 to May 5, 1986, was 6.7 ± 0.6 ng/m^3 (~25% of the total Fe, 27 ± 3 ng/m^3). The Fe(II) concentration in rain samples has also been reported for the first time. The concentration of Fe(II) in a rain sample collected in Narragansett, RI, on December 8, 1990, was 68 ± 6 nM (~30% of the total Fe, 230 ± 25 nM). Fe(II) in a seawater sample collected from Narragansett Bay, RI, at 1500 on March 6, 1991, was 29 ± 3 nM (~40% of the total Fe, 72 ± 7 nM). The seawater sample was collected in the afternoon of a sunny day during spring. Kuma et al. [1992] also observed 20–40 nmol/kg Fe(II) in oxic surface 10-m-depth seawater collected from Funka Bay, Japan, from mid-March to early April during a spring bloom in 1987, 1988, and 1989. The high Fe(II) concentration observed may have resulted from photoreduction and microbial reduction of Fe(III) to Fe(II) in seawater. These findings will certainly require some interesting chemistry in either aerosol or seawater. The Fe(II) has been found to be sustained in remote marine aerosols for several years[26] since the pH of marine aerosols could be lower than 1.0,[27] while the half-life of soluble Fe(II) may be only a few minutes in oxygenerated seawater with pH ~8. We have discussed the possible photoreduction mechanism of Fe(III) to Fe(II) in marine aerosols during their long range transport.[26] Kuma et al.[28] and O'Sullivan et al.[29] have also discussed the possible photoreduction and microbial reduction of Fe(III) to Fe(II) in seawater. King et al. reported a mean Fe(II) concentration of 4.2 ± 0.4 nM in seawater samples collected from the same area of Narragansett Bay (21). In their method the ferrozine peaks were not separated from the $[Fe(FZ)_3]^{2+}$ complex. Since the concentration of FZ used in their analysis was much higher than the measured Fe(II) concentration and the difference between the total absorbance and the FZ absorbance was rather small, big errors in the measurements can result. Therefore, it was not surprising that our results were higher than the previous reported data. However, because we completely separated the $[Fe(FZ)_3]^{2+}$ from FZ and other constituents in the samples, we believe that our results are more reliable. In addition we were able to determine the low levels of Fe(II) down to 0.1 nM. Fe(II) in a Chinese loess sample collected from the central area of China was only ~0.015% (w/w) (~0.4 ± 0.3% of the total Fe in this sample).

(27) Zhu, X. R.; Prospero, J. M.; Savoie, D. L.; Brass, G. M. *EOS, Trans.* **1990**, *71*, 1226.
(28) Kuma, K.; Nakabayashi, S.; Suzuki, Y.; Kudo, I.; Matsunaga, K. *Mar. Chem.* **1992**, *37*, 15–27.
(29) O'Sullivan, D. W.; Hansen, A. K.; Miller, W. L.; Kester, D. R. *Limnol. Oceanogr.* **1991**, *36*, 1727–1741.

CONCLUSIONS

A reversed-phase high performance liquid chromatography analysis using a UV/visible spectrophotometer detector was developed to determine concentrations of iron(II) in Chinese loess, aerosols, rainwater, and seawater. The detection limit increased from 10^{-8} to 10^{-10} M by preconcentration of the samples using Sep-Pak C18 cartridges and the recovery of 10^{-8}–10^{-10} M $[Fe(FZ)_3]^{2+}$ was in the range of 92–99%. There was less baseline noise in the chromatograms at a wavelength of 254 nm, and peak areas were larger than those at 562 nm. Therefore, a better detection limit could be obtained by using 254 nm instead of 562 nm. There was no interference from Fe(III), Ni(II), Co(II), and Cu(I). Retention times, addition of a known amount of standard, and peak area ratios were used for peak identification of $[Fe(FZ)_3]^{2+}$.

ACKNOWLEDGMENT

This work was supported by a graduate fellowship awarded to Zhen Yi by University of Rhode Island in recognition of achievement and promise as a scholar and partially supported by NSF Grants OCE 87-15955 and ATM 87-02563 and ONR Grant N00014-90-J-1355. We thank the Perkin-Elmer Corp. for the use of the liquid chromatograph with a UV/visible spectrophotometer detector and Supelco Inc. for the column. We also thank Miss Andrea Weston for analysis of Fe(II) by CE and Waters Associate Inc. for the use of CE equipment. We also wish to thank the reviewers for their helpful comments and suggestions.

RECEIVED for review March 27, 1992. Accepted September 1, 1992.

Capillary Ultrafiltration: In Vivo Sampling Probes for Small Molecules

Michael C. Linhares and Peter T. Kissinger*

Purdue University, Department of Chemistry, West Lafayette, Indiana 47907

Capillary ultrafiltration is a novel sampling method convenient for low molecular weight substances in living biological systems. By application of a negative pressure across a hydrophilic membrane capillary, small molecules are actively "pulled" across the membrane and collected. By elimination of large molecules and cellular matter, the ultrafiltrate collected is well suited for further analysis by liquid chromatography, capillary electrophoresis, or mass spectrometry. Ultrafiltration probes (UF probes) provide a simple means to obtain a small-volume sample from subcutaneous tissue, blood, saliva, or any other biological fluid in vivo. The dependence of recovery on flow rate, temperature, membrane dimensions, and vacuum magnitude are considered. The relative merits of capillary ultrafiltration probes and microdialysis probes are considered. UF probe applications presented include in vivo monitoring of drug disposition in human saliva and in the subcutaneous space of awake, freely moving rats.

INTRODUCTION

Determination of low molecular weight substances in fully functioning biological systems is a goal long sought by scientists in pharmacology, toxicology, drug metabolism, and clinical chemistry, among other disciplines. A great deal of effort is directed at obtaining reproducible samples rapidly enough to follow the metabolic events of interest. In addition, removing undesirable components that might interfere with the determination of the analyte of interest is necessary. Although the ideal methodology does not exist at this time, microdialysis[1-5] and ultrafiltration[6,7] show great promise for in vivo monitoring.

Ultrafiltration has been used in vitro for sample preparation by means of centrifugal membrane filters for several decades. Capillary ultrafiltration probes provide a new format to address several of the problems associated with sampling in biological media. The concept was originally developed for in vivo use specifically as a part of a glucose monitoring system for diabetics.[6] Capillary ultrafiltration probes (UF probes) use a negative pressure gradient to create a flow of fluid across a hydrophilic membrane. The membrane excludes proteins and other cellular matter while allowing the extracellular fluid and small molecules or ions to pass through. This provides an ultrafiltrate that is well suited for analysis by liquid chromatography, capillary electrophoresis, or mass spectrometry. Since the process of ultrafiltration is a convective process, high relative recoveries are achieved for small analytes, typically greater than 90%. UF probes can be implanted in vivo in subcutaneous tissue for long periods of time, at least 6 months,[6] and provide clean samples rapidly (1–5 μL/min). The magnitude of analyte flux across the membrane is a function of temperature, pressure differential, membrane dimensions and material. A preliminary study of these parameters and the other practical factors affecting the use and implementation of UF probes for in vivo study are presented here.

It is beneficial to consider the differences and similarities of capillary ultrafiltration and capillary microdialysis for the sampling of small molecules in vivo. Microdialysis has proven to be an excellent sampling technique for in vivo sampling of the brain, liver, eye, and heart and subcutaneous area. It shows great promise for studies of the metabolism, pharmacokinetics, and bioavailability of therapeutic drugs.[1-5]

Due to their simplicity and ruggedness, UF probes have the potential to be used for many applications. Two initial areas of investigation were explored in this study. In vivo saliva collection is one area of interest. Saliva has been shown to be a good media to monitor some therapeutic drugs[8-10] and metabolites,[11] and has been shown to track the concentration of many small molecules in blood plasma quite well. The disposition of controlled release theophylline tablets was monitored in saliva by capillary ultrafiltration. Monitoring of therapeutic drug disposition in subcutaneous tissue is also well suited to study using the capillary ultrafiltration technique. The disposition of acetaminophen was observed in awake freely moving rats.

PRINCIPLES OF ULTRAFILTRATION

In ultrafiltration, a pressure gradient across a semipermeable membrane causes solvent (water) and small analytes to pass through the membrane leaving large substances behind. The flux (mol/(cm^2 s)) through the membrane is dependent on the size of the given analyte, the transmembrane pressure, the viscosity of the fluid (sample media), the membrane thickness, and the structure of the membrane. The flux dependence on the pressure gradient is nonlinear at lower vacuum gradients and becomes constant at higher gradients. The mathematical relationships and other features of the ultrafiltration process have been reviewed.[12] The influence of temperature is very critical during in vivo experiments in that membrane fluidity, solution viscosity, blood flow, and metabolic rates are all affected. Polyacrylonitrile membranes with reported molecular weight cutoffs (MWCO) of 30 000 were used in this study. Since the

(1) Lunte, C. E.; Scott, D. O.; Kissinger, P. T. *Anal. Chem.* **1991**, *63*, 773A–780A.
(2) Benveniste, H.; Hüttermeier, P. C. *Prog. Neurobiol.* **1990**, *35*, 195–215.
(3) Lonnroth, P.; Jansson, P. A.; Fredholm, B. B.; Smith, U. *Am. J. Physiol.* **1989**, E250–E255.
(4) Benveniste, H. *J. Neurochem.* **1989**, 1667–1679.
(5) Scott, D. O.; Sorenson, L. R.; Steele, K. L.; Puckett, D. L.; Lunte, C. E.; *Pharm. Res.* **1991**, *8*, (3), 389–392.
(6) Ash, S. R.; Janle-Swain, E. M. U.S. Pat. No. 4,854,322, 1989.
(7) Schramm, W. *Anal. Chim. Acta* **1991**, *246*, 517–528.
(8) Danhof, M.; Breimer, D. D. *Clin. Pharm.* **1978**, *3*, 36–57.
(9) Ritschel, W. A.; Tompson, G. A. *Methods Find Exp. Clin. Pharmacol.* **1983**, *5* (8), 511–525.
(10) Horning, M. G.; Brown, L.; Nowlin, J.; Lertratanangkoon, K.; Kellaway, P.; Zoin, T. E. *Clin. Chem.* **1977**, *23* (2), 157–164.
(11) Mucklow, J. C. *Ther. Drug. Monit.* **1982**, *4* (3), 229–247.
(12) Lloyd, D. R.; Meluch, T. B. *Material Science of Synthetic Membranes*; ACS Sympsium Sereis 269; American Chemical Society: Washington, DC, 1985.

0003-2700/92/0364-2831$03.00/0

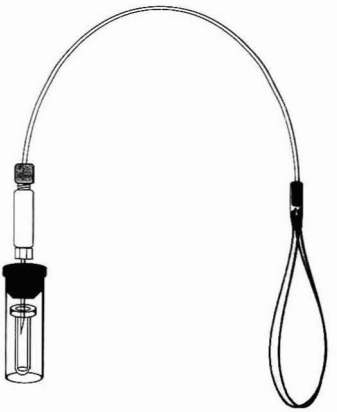

Figure 1. Schematic of a UF-3-7 PAN capillary ultrafiltration probe with a Vacutainer collection system.

membrane is under a vacuum, thick membranes, typically >40 μm of small internal diameter are more successful, in that the membrane does not collapse under the applied vacuum. Thicker membranes do, however, lower the flux and the recovery of some analytes due to interactions with the membrane structure. The UF probes utilized here have three membrane loops of 7–16 cm and provide flow rates of 2–5 μL/min. These are not intended to be the ultimate embellishment of this technique. Other formats are being utilized for other specific applications.

EXPERIMENTAL SECTION

Ultrafiltration Probes. Prototype ultrafiltration probes UF-3-7, UF-3-12, and UF-3-16 were provided by Bioanalytical Systems, BAS (West Lafayeete, IN). These probes consisted of three loops of polyacrylonitrile (PAN) membrane between 7 and 16 cm long. The PAN membrane is 310-μm o.d and 220-μm i.d. and has a reported 30 000 MWCO. A 1-cm length of the implanted membrane filter has an internal volume of 0.38 μL. The probes use Teflon tubing for connection to a vacuum source and use soft polyurethane connectors to allow for greater biocompatability and flexibility.[13] An example of a capillary ultrafiltration probe, with a Vacutainer collection vessel, is shown in Figure 1.

Vacuum Sources. Two primary methods were used to create the vacuum for ultrafiltration. A 2-mL Vacutainer (Becton/Dickinson, Rutherford, NJ) with approximately 1 -in. Hg works very well for collecting samples. A small 250-μL vial (Chromacol, 03-CVG, Trumbull, CT) is placed inside the Vacutainer, and the vacuum is replaced by using a 60-mL syringe. An example is shown in Figure 1. The second method is the use of a peristaltic pump. A peristaltic pump (Minipuls 2, Gilson, France) using 0.007-in. i.d. tubing can produce a variable but controlled flow which supports a pressure differential. The peristaltic pump is useful when it is desirable for the collection of samples to be continuously automated. A modified peristaltic pump tubing with 100-μm-i.d. fused-silica tubing inserted inside has provided an excellent system for automated collection with an internal volume less than 7 μL. Coupled to a CMA/140 fraction collector (BAS, West Lafayette, IN) it permits totally unattended operation of sample collection. The peristaltic pump was used for characterization and in vivo subcutaneous tissue studies, while the Vacutainer system was used only for in vivo saliva collection studies.

Ultrafiltration Characterization. A Metler AE 166 balance was used for weighing the ultrafiltrate samples during bulk flow determinations. Samples were collected for a specific time, usually 5 min, and weighed. Timing was done using a stopwatch. For temperature control a Pierce Reacti-therm (Rockford, IL) heating block was used. All in vitro solutions were constantly stirred using a magnetic stirring plate.

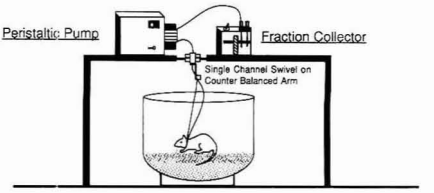

Figure 2. Schematic of the awake animal capillary ultrafiltration collection system.

Monitoring of Theophylline in Saliva. Experimental subjects fasted 12 h before the experiment and 2 h after dosing (Uniphyl 400-mg 24-h controlled release tablet) with 180 mL of water. After flushing the mouth with water and chewing on a piece of parafilm for about 1 min to stimulate saliva flow, samples were taken for 3 min, at 15-min intervals for 4 h. Samples were then directly analyzed by reversed-phase liquid chromatography.

In Vivo Monitoring of Acetaminophen in Subcutaneous Tissue. Long Evans rats (200–250 g) were anesthetized using ketamine/xylazine (0.1 mL/100 g). Either a UF-3-12 or UF-3-16 probe was implanted in the subcutaneous tissue of the back. The probe was sutured to the skin to secure it. The rats were placed in an BAS/CMA awake animal bowl. A collar was attached and secured through a wire theather to a single channel swivel attached to a counter-balanced arm. This arrangement allows for freedom of movement for the animal and is illustrated in Figure 2. After the rats recovered from surgery, between 8 and 12 h, the UF probe was attached to a peristaltic pump through the swivel. The pump was set to a flow rate of 44 μL/min; producing a vacuum to achieve an ultrafiltration rate of 2.4 ± 0.1 μL/min (n = 56). A stock solution of acetaminophen (1 mg/mL) was made in Ringer's solution, and 2.0 mg/kg was injected interperitoneally. Ultrafiltrates were collected continuously using a BAS/CMA 140 fraction collector and were directly analyzed by reversed-phase liquid chromatography.

Chromatography. Liquid chromatography was carried out with a BAS 200A liquid chromatograph (Bioanalytical Systems, West Lafayette, IN). Separations were carried out on a Biophase C_{18}, 3-μm, 100-mm by 3.2-mm column at 35 °C and 1 mL/min, except for subcutaneous acetaminophen determination which used a Biophase 250-mm by 4.6-mm octylsilane column. For the separation of theophylline in saliva a mobile phase of 100 mM phosphate buffer at pH 6.1 with 5% acetonitrile was used. Detection for theophylline was accomplished using the variable-wavelength UV detector set at 270 nm. For acetaminophen determinations the mobile phase consisted of 75 mM monochloroacetic acid (pH 3.1), 0.67 mM EDTA, and 2.5% acetonitrile was used. Electrochemical detection was accomplished using a 3-mm glassy-carbon electrode at +750 mV vs Ag/AgCl.

Capillary Electrophoresis. An in-house-built capillary electrophoresis system was used for all experiments. Brij 35/akylsilane capillaries prepared according to the method of Towns and Regnier[14] were used for separations. The 75-μm-i.d. capillaries were 50 cm long, with detection at 25 cm. Detection was accomplished by UV absorption at 214 nm. Injections were done by hydrodynamic syphon for 10 s at 20 cm. Samples were electrophoresed under a potential of 300 V/cm.

Reagents. Acetaminophen, theophylline, and protein standards were purchased from Sigma (St. Louis, MO) and used as received. All buffer reagents were reagent grade and purchased from Aldrich Chemical (Milwaukee, WI). HPLC grade acetonitrile (Baxter) was used. All solutions were made with double distilled deionized water and filtered using 0.22-μm Nylon filters.

(13) Szycher, M.; Siciliano, A. A.; Reed, A. M. *Medical Des. Mater.* **1991**, *18*, 19–25.

(14) Towns, J. K.; Regnier, F. E. *Anal. Chem.* **1991**, *63*, 1126–1132.

Table I. Comparison of Ultrafiltration and Microdialysis as in Vivo Sampling Methods

	microdialysis	ultrafiltration
sample condition	physiological saline solution–ready for analysis	extracellular fluid– ready for analysis
sample dilution	yes, 5–30% conc recovery	relatively little, >90% conc recovery
spatial resolution	excellent	good in specific tissue
time resolution (typical)	1–5 min (both depend on the sample volume needed)	1–5 min
flow rate control	yes, very precise	limited ±5%
sample collection rate	0.1–10 μL/min	0.1–10 μL/min
mol wt range	recoveries drop exponentially with increasing mass	depends on membrane structure and compound of interest
mode of collection	passive-diffusion conc gradient	active-pressure gradient
awake animals	yes	yes
tissue restrictions	none	yes, requires large fluid turn over
ease of automation	fraction collection and on-line to instrument	fraction collection only

RESULTS AND DISCUSSION

Sampling and determining the extracellular concentration of small molecules in living biological systems present a huge problem. No single methodology is useful for all situations. Capillary ultrafiltration probes provide a solution to the problems of time-dependent sampling, rapid continuous sampling, enzymatic degradation of the sample, and sampling freely behaving animals. In addition to capillary ultrafiltration, microdialysis also provides these advantages.[1-5] Low relative recoveries due to sample dilution, delicate probes with rigid components, and uncertainties in calculating interstitial concentrations can present hurdles for microdialysis in some circumstances.[15] Capillary ultrafiltration may provide a solution to several of these concerns. Table I outlines the differences and similarities of these two in vivo sampling techniques.

UF probes provide a sample in which all high molecular weight components including enzymes, proteins, and cellular particulate matter are removed. In order to observe the effectiveness of capillary ultrafiltration to remove high molecular weight molecules, samples of proteins with varied molecular masses were ultrafiltrated and analyzed by capillary electrophoresis. The proteins included apoprotein (MW 6500), insulin (MW 5800), myoglobin, cytocrome *c*, ribonuclease, and serum albumin. Using the PAN membranes, no protein was ever seen in the ultrafiltrate. These results lead us to believe that the PAN membranes effective MWCO is much lower than 30 000 when used under a negative pressure and they are effective at removing any potentially interfering proteins.

Capillary ultrafiltration probes provide very high recoveries of small molecules. One concern with microdialysis is that very low relative concentration recoveries are achieved, since it is a diffusion-based technique using small probes. In vitro and in vivo recoveries are seldom identical due to the fact that diffusion of the analytes through the tissue is the limiting factor in the collection of the analyte.[16] Typical microdialysis recoveries are between 5 and 30% at flow rates of 1 μL/min. Ultrafiltration provides higher recoveries, typically greater than 90%, because the process includes an active transport of fluid across the membrane. Table II illustrates recoveries of several different small molecules of interest. The membrane only acts by a sieving mechanism and the pressure difference creates the flux across the membrane (rather than diffusion alone). Ideal (100%) recoveries are not obtained for all molecules. Water molecules and small ions are statistically more likely to pass through the membrane unobstructed and are less likely to experience hydrophobic or electrostatic interactions with the membrane. As a consequence recoveries are typically greater than 90% for small molecules. Variation in concentration of a analyte does not change the relative recovery. Table III illustrates recoveries for acetaminophen at several different concentrations. Using the students t test, these values are not statistically different.

Table II. Ultrafiltrate Recovery for Several Compounds of Interest

compd	% recovery ± SD[a]	compd	% recovery ± SD[a]
acetaminophen	97.6 ± 0.83	ascorbic acid	99.5 ± 1.05
cefazolin	95.2 ± 1.83	glucose	98.0 ± 1.00
theophylline	100.2 ± 0.80	amoxicillin	97.3 ± 1.36
tryptophan	92.7 ± 0.095		

[a] $n = 5$ for all analytes. All samples were prepared in Ringer's solution, and experiments were performed at 27 °C with constant stirring. Each analyte concentration was between 1 and 5 μg/mL.

Table III. Comparison of Ultrafiltration Recoveries with Variation in Concentration of Analyte

conc of acetaminophen, μg/mL	% recovery ± SD[a]	conc of acetaminophen, μg/mL	% recovery ± SD[a]
10	99.7 ± 0.90	0.5	100.7 ± 1.41
5	100.7 ± 1.3	0.25	100.4 ± 2.3
1	98.6 ± 1.27		

[a] $n = 5$ for all concentrations. All samples were prepared in Ringer's solution, constantly stirred, and performed at 27 °C.

Capillary ultrafiltration can be used for in vivo sampling in awake animals. Ultrafiltration probes are well suited for use in tissues that have a high fluid turnover and are not substantially affected by loss of fluid. A typical ultrafiltration capillary removes extracellular fluid at 50 (nL/min)/mm of membrane. UF probes can provide constant sampling rates in subcutaneous tissue. Using UF-3-16 PAN a flow rate of 2.4 ± 0.1 μL/min ($n = 56$) was obtained in subcutaneous tissue. Only tissue that can sustain these losses are potential sampling sites for ultrafiltration. Microdialysis probes are especially useful for small animals and organs. There is no net fluid loss from the tissue in microdialysis, and this is especially advantageous in organs that cannot sustain fluid loss. The effects of loss of extracellular fluid in relation to physiological response is unknown at this time.

UF probes are currently quite large compared to most microdialysis probes. Using polyacrylonitrile membrane material, fibers need to be at least 7–16 cm long to achieve

(15) Benveniste, H.; Jon Hanson, A.; Saabye, O.; Niels, *J. Neurochem.* **1989**, *52*, 6, 1741–1750.
(16) Bungey, P. M.; Morrison, P. F.; Dedrick, R. L. *J. Neurochem.* **1991**, *57*, 103–109.

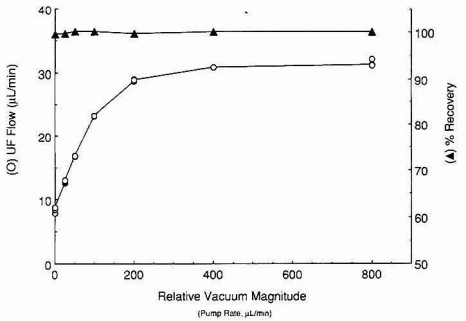

Figure 3. Ultrafiltrate flow (O) for a UF-3-7 PAN probe and relative recovery (▲) of acetaminophen at increasing vacuum (as indicated by nominal flow rate setting on a peristaltic pump).

practical in vivo flow rates (1–5 µL/min), whereas microdialysis capillaries under 1 cm in length are quite common. Since UF probes remove extracellular fluid from the animal, the temperature and activity of the animal are important. In anesthetized animals the drop in body temperature and circulation of fluids can cause decreased ultrafiltration rates. The ultrafiltration flow has been found to change linearly in vitro at a rate of 0.3 (µL/min)/°C for a UF-3-7 probe ($n = 3$).

In ultrafiltration the flow rate is dependent on the dimensions of the membrane (membrane surface area) and differential pressure, while relative recovery is not. This is illustrated in Figure 3, which shows both the dependence of UF flow on vacuum magnitude for a UF-3-7 PAN probe and the constant recovery of acetaminophen obtained at these vacuum magnitudes. As it is illustrated, the UF flow is dependent on vacuum magnitude but is limited by the flux of water across the membrane. The probe size or membrane surface area and vacuum magnitude are the factors that limit UF flow. If more rapid sample collection rates are required, a larger membrane surface area can be used. In microdialysis the relative recovery is exponentially related to the perfusion flow rate since the transport is mediated by diffusion. The sampling rate is therefore limited by the volume of sample needed for analysis. Most microdialysis experiments are carried out at flow rates less than 3 µL/min for this reason.

Capillary ultrafiltration can be carried out continuously in awake animals for extended periods of time with fully automated systems. Microdialysis has become very popular due to the ability to sample awake animals continuously and conduct lengthy experiments with either on-line analysis or automated sample collection systems. Capillary ultrafiltration probes can function similarly. UF probes implanted in subcutaneous tissue can be attached to a peristaltic pump and fraction collector, enabling samples to be automatically collected. Ultrafiltration can be more difficult with on-line chromatographic systems due to "outgassing" (bubble segmented flow in the collection line).

Therapeutic Drug Monitoring in Saliva. Saliva is a biological fluid that has great promise as a therapeutic drug monitoring medium.[8-10] For many drugs, metabolites, and biomolecules the saliva concentrations are a good representation of blood plasma levels.[9] Ultrafiltration probes are well-suited for sampling in saliva. The UF-3-7 PAN probes provide a rapid in vivo sampling method that is not invasive, avoids the unpleasantness of expectorating into a cup, and can provide 20 µL of "clean" microbe and protein-free sample in 4 min. This allows for more simplified assay methods and direct injection of the ultrafiltrate.

To demonstrate this concept, the monitoring of the common broncial dialator theophylline in saliva is presented. A

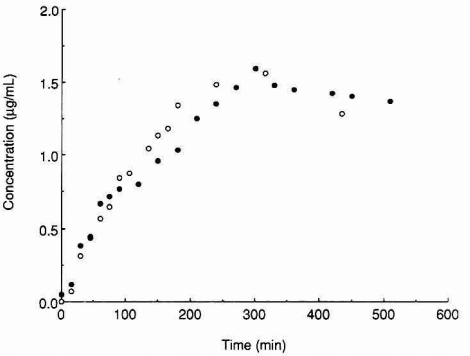

Figure 4. Two examples of in situ monitoring of theophylline in saliva after dosing with a controlled release 400 mg of Uniphyl tablet using capillary ultrafiltration. Both curves were done on the same subject on separate days.

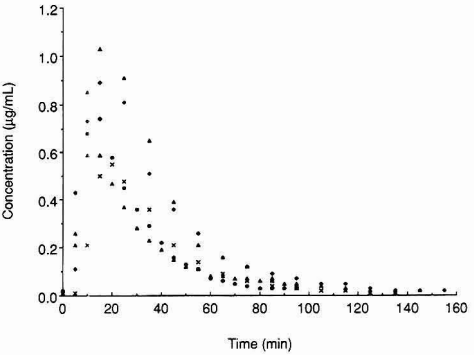

Figure 5. Disposition curves for five different rats dosed with 2.0 mg/kg acetaminophen obtained using capillary ultrafiltration probes implanted in the subcutaneous tissue.

pharmacokinetic model for theophylline using saliva as a monitoring medium has been reported.[17] Using UF-3-7 PAN probes theophylline concentration was followed in saliva. Two representative disposition curves are presented in Figure 4. This was only a preliminary study to explore the possible utility of UF probes, not to determine pharmacokinetic parameters for the dosage form used.

In Vivo Monitoring of Acetaminophen. The monitoring of the disposition of APAP in subcutaneous tissue in awake rats is presented. Ultrafiltration probes were implanted into the subcutaneous tissue along the back of five rats for these experiments. The animals were anesthetized before implantation and then allowed to recover for 8–12 h prior to dosing interperitonealy (2.0 mg/kg). The dynamics of acetaminophen was monitored while the animals were awake and freely moving. The results from five different animals are shown in Figure 5. These results compare very well with microdialysis experiments monitoring acetaminophen in the jugular vein of rats.[5]

CONCLUSIONS

Capillary ultrafiltration probes provide an alternative sampling technique for small molecules in living biological

(17) Ogilvie, R. I. *Clin. Pharmacokinet.* **1978**, *3*, 267–293.

systems. UF probes remove large molecules, enzymes, and cellular matter that can degrade analytes and instrument performance, while providing high recoveries of small molecules. UF probes are made from biocompatable, soft components and can be implanted in awake animals for extended periods. UF probes are ideal for monitoring drug disposition in subcutaneous tissue and can be used in situ for saliva collection. In addition to the experiments presented here the dynamics of cefazolin, amoxicillin, theophylline, glucose, lactic acid, and pyruvate have been monitored in vivo by ultrafiltration and will be presented in future publications.

ACKNOWLEDGMENT

We wish to thank Dr. Elsa Janle and Terri Clark of Bioanalytical Systems for helpful discussions and providing samples of ultrafiltration probes for this work.

RECEIVED for review April 14, 1992. Accepted September 1, 1992.

Flow Field-Flow Fractionation of Polymers in Organic Solvents

J. J. Kirkland*,† and C. H. Dilks, Jr.†

E. I. DuPont de Nemours Company, Central Research and Development Experimental Station, Building 228/240A, P.O. Box 80228, Wilmington, Delaware 19880-0228

Previous flow field-flow fractionation (FlFFF) studies have used aqueous mobile phases in separations, thereby limiting the applicability of the method. We now have performed FlFFF with totally organic mobile phases, so that organic-soluble synthetic polymers can be characterized with this approach. Mixtures of poly(ethylene oxide) standards were fractionated in a channel using an unmodified regenerated cellulose ultrafiltration membrane with methanol as the mobile phase. Polystyrenes were fractionated in tetrahydrofuran after silanizing the membrane. Quantitative molecular-weight-distribution results were obtained by using published Mark–Houwink constants to calibrate the system. These studies demonstrate the potential of FlFFF to provide important information on polymers and particulates in nonaqueous as well as aqueous environments.

INTRODUCTION

Flow field-flow fractionation (FlFFF) provides high-resolution separations for characterizing a wide range of macromolecules and colloidal particles.[1-4] This method has been called the most generally useful of any of the field-flow fractionation (FFF) family.[5,6] FlFFF can be used to measure the particle size and particle-size distribution of 0.02- to >1-μm particles, and the molecular weight (MW) and molecular-weight distribution (MWD) of soluble polymers in the 10^4–10^7 range. Separations are based on physical first principles, so that no standard samples are required for calibration. The method is based on a quantitative theory of retention and band broadening that permits the direct measurement of solute diffusion coefficients.[2,4-7]

FlFFF separations are carried out in a thin channel formed with a semipermeable membrane as the accumulation wall. A liquid flow within the channel generates a laminar flow profile within the narrow space formed between parallel plates. The force field needed for the separation is provided by simultaneously flowing this same liquid across the channel thickness and through the semipermeable accumulation-wall membrane. As a result of this cross-flow force field, larger sample components move close to the semipermeable membrane accumulation wall. These components are intercepted by slower flow streams next to this wall. Larger components then are eluted after smaller components that are further from the wall and subjected to faster flow streams down the channel. Elution in FlFFF is directly related to component size or hydrodynamic volume.

FlFFF has been performed in channels made with parallel plates using two semipermeable membranes[2,3] or in a porous hollow fiber.[8,9] However, the best separations have been carried out in so-called asymmetrical channels that use only a single semipermeable membrane.[4-7,10] In recent studies we described the apparatus and techniques for performing FlFFF separations using exponentially-decreasing force fields during the separations.[6] In this way, a wide range of components (relative MW range >600) can be separated in a convenient time with a single experiment.

Besides providing direct measurements of diffusion coefficients, FlFFF also can be used to calculate the sizes of particles, using the well-known Einstein–Stokes equation.[6,7] Recent studies showed that FlFFF also can provide MW and MWD data on polymers by converting measured diffusion coefficients using published Mark–Houwink constants for polymers.[11]

Previous FlFFF separations were performed with aqueous mobile phases, largely because of limitations from available semipermeable ultrafiltration membranes. In this study we demonstrate the feasibility of FlFFF separations with organic solvents. Modification of conventional ultrafiltration membranes was required for some polymers.

EXPERIMENTAL SECTION

Apparatus. The equipment used during this study was the same as previously described,[6] with recent minor modifications.[11] The rectangular asymmetrical channel was formed with a Teflon fluorocarbon polymer spacer so that the final channel thickness was 0.0254 cm. The separating channel was 41.0 × 2.0 cm, and the sample focusing distance was 4.3 cm. The glass plate originally forming the top wall of the channel was replaced with a similar stainless steel metal plate. This modification allowed the insertion of standard HPLC-type stainless steel connecting fittings that are better suited for operation with organic solvents. Detection was with a Model 903 Optilab refractometer (Wyatt Technology Corporation, Santa Barbara, CA) or a Spectroflow Model 783 variable-wavelength absorption detector (Kratos Analytical, Ramsey, NJ).

Sample injection was carried out in a manner similar to that described by Litzen and Wahlund.[4] Typically, the sample in the sample loop was pumped into the channel injection port at 0.06 mL/min for 4.0 min. During this time inlet flow was set at 1.0 mL/min and the channel outlet back flow was 9.0 mL/min to focus the sample in a narrow band.[6] After sample injection, focusing was continued with the same conditions for another 4.0 min. Fractionations then were performed by setting the cross-flow V_c and the channel outflow V_{out} at the desired flow rates. Programmed separations were performed by the exponential force-field decay method[6] using the desired exponential time constant τ for the decay and an optional time delay τ prior to the force field decay.

† Current address: Rockland Technologies, Inc., 538 First State Blvd., Newport, DE 19804.

(1) Giddings, J. C.; Yang, F. J. F.; Myers, M. N. *Science* **1976**, *193*, 1244.
(2) Giddings, J. C.; Yang, F. J. F.; Myers, M. N. *Anal. Chem.* **1976**, *48*, 1126.
(3) Giddings, J. C.; Myers, M. N.; Caldwell, K. D.; Fisher, S. R. *In Methods of Biochemical Analysis*; Glick, D., Ed.; John Wiley: New York, 1980; Vol. 26, p 89.
(4) Litzen, A.; Wahlund, K.-G. *J. Chromatogr.* **1989**, *461*, 73.
(5) Litzen, A.; Wahlund, K.-G. *J. Chromatogr.* **1989**, *476*, 413.
(6) Kirkland, J. J.; Dilks, C. H., Jr.; Rementer, S. W.; Yau, W. W. *J. Chromatogr.* **1992**, *593*, 339.
(7) Wahlund, K.-G.; Giddings, J. C. *Anal. Chem.* **1987**, *59*, 1332.
(8) Jönsson, J. A.; Carlshaf, A. *Anal. Chem.* **1989**, *61*, 11.
(9) Carlshaf, A.; Jönsson, J. A. *J. Chromatogr.* **1989**, *461*, 89.
(10) Litzen, A.; Wahlund, K.-G. *J. Chromatogr.* **1991**, *548*, 393.
(11) Kirkland, J. J.; Dilks, C. H., Jr.; Rementer, S. W. *Anal. Chem.* **1992**, *64*, 1295.

0003-2700/92/0364-2836$03.00/0

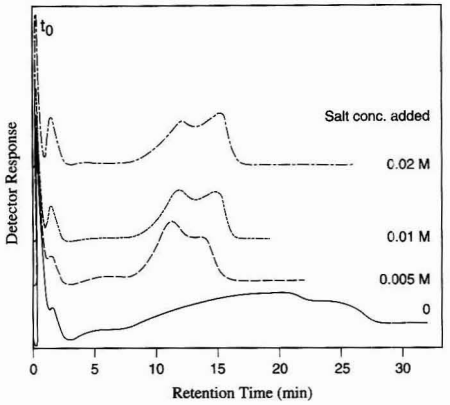

Figure 1. Effect of ammonium acetate on the fractionation of a MW 252 000 poly(ethylene oxide) standard in methanol. Cross flow, 3.0 mL/min, constant; channel outlet flow, 1.0 mL/min; temperature, 22 °C; sample, 0.10 mL, 0.1% in methanol; detector, refractive index.

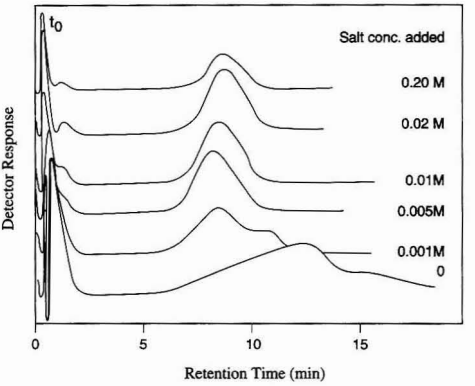

Figure 2. Effect of ammonium acetate for the fractionation of a MW 86 000 poly(ethylene oxide) standard in methanol. Conditions as in Figure 1, except cross flow, 6.0 mL/min.

As in previous studies, fractionation data were collected with a PE/Nelson ACCESS*CHROM data handling system (Nelson Analytical, Inc., Cupertino, CA). Software for the MW and MWD outputs was developed in-house using FORTRAN 77 on a VAX 3100 computer (Digital Equipment Corporation, Maynard, MA).[6] Mark–Houwink constants used for MW calculations were from the literature.[12]

Reagents and Chemicals. Poly(ethylene oxide), polystyrene, and poly(methyl methacrylate) standards were from Polymer Laboratories, Inc. (Amherst, MA) or DuPont Instruments (Wilmington, DE). HPLC-grade solvents used for mobile phases were from EM Science (Gibbstown, NJ). Fresh tetrahydrofuran was used to avoid safety problems and possible detector baseline drift due to the formation of peroxides in this solvent when exposed to air. Tergitol TMN-3 was from Union Carbide Corp. (Danbury, CT).

Semipermeable Membranes. A type PLGC regenerated cellulose ultrafiltration membrane (Millipore Corporation, Bedford, MA) was used as the material for the accumulation wall of the channel. This membrane was modified for part of the studies by flowing a mixture of 1% (volume) bis(trimethylsilyl)trifluoroacetamide and 0.25% (volume) trimethylchlorosilane (Hüls America, Bristol, PA) in dry acetonitrile overnight at 0.5 mL/min through the channel with the mounted regenerated cellulose membrane at ambient temperature. The channel then was thoroughly purged before use with tetrahydrofuran to eliminate excess reactant silanes.

THEORY

Retention theory for FlFFF has been detailed in previous publications and will not be repeated here.[1-7] Briefly, with a rectangular asymmetrical channel and a constant force field (cross flow), solute diffusion coefficients can be approximated with the expression[7]

$$D_s = \left(\frac{W^2}{6t_R}\right) \ln\left[\frac{z/L - (V_c + V_{out})/V_c}{1 - (V_c + V_{out})/V_c}\right] \quad (1)$$

here D_s is the solute diffusion coefficient, cm²/s; W is the channel thickness, cm; t_R is the retention time of the component, s; z is the focusing distance from the channel inlet, cm; L is the channel length, cm; V_c is the cross-flow flow rate, mL/min; and V_{out} is the flow rate of the channel effluent, mL/min. With eq 1 and known operating parameters, the diffusion coefficients of components are approximated without the need for standards. By measuring the diffusion coefficients at each elution time over the component peak envelope, diffusion-coefficient distributions for the sample can be obtained.[6]

For samples with a wide MWD, it sometimes is desirable to use force field programming during the separation. We have found that an exponential-decay program is convenient in such cases.[6] Calculations of diffusion-coefficient distributions with exponential-decay force field programming are performed using an iterative numerical process with eq 3 of ref 6.

Measured diffusion coefficients can be converted to molecular weights as previously described[11] by using a form of a relationship developed by Rudin and Johnston.[13] This expression relates the effect of diffusion coefficients, the hydrodynamic volume, and the intrinsic viscosity on polymer MW. Therefore, with polymer Mark–Houwink constants, measured diffusion coefficients were used to calculate polymer MW values. The reduced expression for this calculation is[11]

$$M_v = \left[\left(2.915\,22 \times 10^{-10} \frac{T}{D_s \eta_o}\right)^3 / K\right]^{1/(1+a)} \quad (2)$$

where M_v is the viscosity average molecular weight of the polymer; T is the temperature, K; η_o is the viscosity of the liquid mobile phase, poise (=10^{-1} Newton s/m²); and K (dL/g) and a are the Mark–Houwink constants for the polymer/solvent system.

RESULTS AND DISCUSSION

Initial experiments were conducted with the unmodified regenerated cellulose membrane. Tests quickly showed that polystyrene and poly(methyl methacrylate) standards were strongly (sometimes irreversibly) sorbed to this membrane from nonprotic organic solvents such as toluene, methyl ethyl ketone, and dioxane. Addition of 3% ethanol to toluene and 0.1% Tergitol TMN-3 (surface-active agent) to dioxane gave no improvement. We conclude that the sorptive forces associated with the unmodified regenerated cellulose membrane were too strong to allow proper elution of many polymers with solvents used typically for dissolution and analysis.

However, we found that the polar polymer, poly(ethylene oxide) (PEO), was eluted normally from the unmodified membrane with the protic solvent, methanol, under certain

(12) Kurata, M.; Tsunashima, Y. In *Polymer Handbook*, 3rd ed.; Brandrup, J., Immergut, E. H., Eds.; John Wiley: New York, 1989; p VII/1.

(13) Rudin, A.; Johnston, H. K. *J. Polym. Sci., Part B: Polym. Lett.* **1971**, *9*, 55.

Table I. Effect of Salt on FlFFF of Poly(ethylene oxide) Standards[a]

reported MW	V_c, mL/min	V_{out}, mL/min	M NH_4Ac	R value	measured[c] diff coeff, $D_s \times 10^6$, cm^2/s	calculated MW[d]	apparent polydispersity[e]
86 000	4.0	1.0	0	0.28		97 300	1.14
	6.0	1.0	0.001	0.24		90 300	1.09
	6.0	1.0	0.001	0.24		92 900	1.10
	6.0	1.0	0.005	0.25		82 300	1.05
	6.0	1.0	0.01	0.25		86 700	1.04
	6.0	1.0	0.02	0.24		92 000	1.04
	6.0	1.0	0.20	0.24	0.42	90 900	1.04
	6.0	1.0	0.20	0.24		93 100	1.04
18 000	8.8	1.0	0.2	0.54	1.14	14 200	1.08
	8.8	1.0	0.2	0.56		13 300	1.09
	9.3[f]	0.5	0.2			18 200	1.20

[a] Mobile phase, methanol; temperature, 22 °C; viscosity of methanol, $\eta_0 = 0.54$ cP; see Figures 1–3 for illustrative fractograms. V_c held constant during runs except for f. [b] $R = t_0/t_R$. [c] Sampling and focusing in Experimental Section. [d] Mark–Houwink constants, $K = 8.52 \times 10^{-4}$ dL/g, $a = 0.57$. [e] Polydispersity, M_w/M_n. [f] Exponential force-field program, $\tau = 7.0$ min.

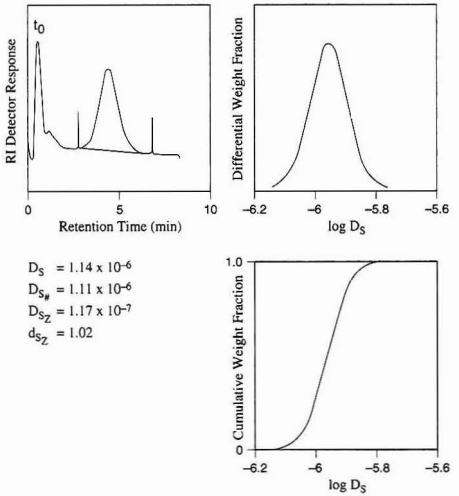

Figure 3. Diffusion coefficient distribution of MW 18 000 poly(ethylene oxide) standard. Conditions as in Figure 1 except cross flow, 8.8 mL/min; ammonium acetate, 0.2 M in methanol mobile phase.

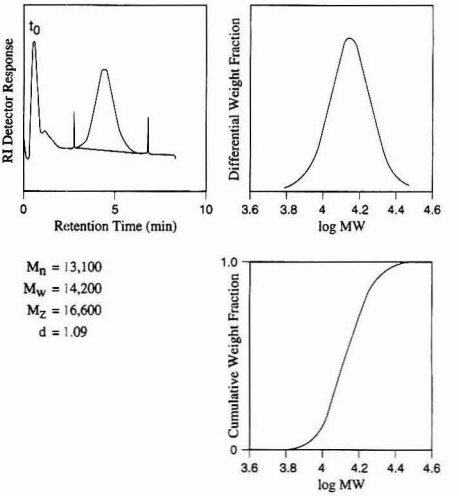

Figure 4. Molecular weight distribution of MW 18 000 poly(ethylene oxide) standard. Conditions as in Figure 3, except Mark–Houwink constants, $K = 8.52 \times 10^{-4}$, $a = 0.57$.

conditions. Test with a MW 252 000 PEO standard with unmodified methanol as the mobile phase initially produced puzzling results. Fractionations showed a very broad peak with calculated MW values that were more than twice the reported value when using Mark–Houwink values reported for PEO/pure methanol systems. We suspected a deleterious interaction of the polymer with itself, or with the semipermeable membrane. A soluble salt, ammonium acetate, then was the added in increasing concentrations to the methanol mobile phase. The effect was to reduce retention and sharpen the band. However, the PEO standard gave a bimodal peak with salt concentrations up to 0.02 M. Figure 1 shows the fractograms obtained in this study, with the baselines offset for clarity. The reason for the apparent bimodality of this PEO standard under these conditions is not yet known. It could, however, involve a polymer interaction effect at the sample concentrations that were used. Interestingly, the first eluting "hump" of this distribution shows a molecular weight that closely corresponds to the reported M_w value for this polymer standard.

A similar study was performed with a MW 86 000 PEO standard with ammonium acetate added to the mobile phase at concentrations up to 0.2 M. The composite fractograms in Figure 2 show that the initial broad peak in pure methanol was significantly sharpened with increasing salt concentrations. Reasonable calculated MW values and expected polydispersity values were obtained only with salt concentrations of at least 0.01 M, as tabulated in Table I. Also given in Table I are the calculated diffusion coefficients, MW, and polydispersity data obtained on this sample. Also shown are data on a MW 18 000 PEO standard with ammonium acetate in the mobile phase. Figures 3 and 4 show the diffusion coefficient distribution and molecular weight distribution, respectively, for the MW 18 000 PEO standard fractionated in methanol containing 0.2 M ammonium acetate.

The MW values in Table I were calculated using Mark–Houwink constants for PEO/methanol systems without salt.[12] While these calculated values may not reflect an accurate MW calibration, the results do provide a comparison of the salt effect in this system. For example, the polydispersity (M_w/M_n) values in Table I show a significant decrease with increasing salt concentration, in keeping with the sharpening of the bands with increasing amounts of salt. At least 0.01 M of salt was required to obtain a constant polydispersity value of 1.04. The higher polydispersity value for the programmed fractionation of the 18 000 MW sample in Table I probably is a result of the increased instrumental band broadening of this lower-resolution separation. Higher res-

Table II. FlFFF of Polystyrene Standards[a]

reported MW	V_c, mL/min	V_{out}, mL/min	R value[b]	measured[c] diff coeff, $D_s \times 10^6$, cm²/s	calculated MW[d]	% diff	polydispersity[e]
50 000	8.8	1.0	0.42	0.92	34 100	−31.2	1.10
	9.3	0.5	0.59	0.86	38 000	−24.0	1.34
87 000	8.8	1.0	0.23	0.47	96 900	+11.4	1.11
	8.8	1.0	0.22	0.47	95 900	+10.2	1.08
	9.3	0.5	0.31	0.44	107 000	+23.0	1.06
100 000	8.8	1.0	0.22	0.46	103 400	+3.4	1.07
	8.8	1.0	0.20	0.43	108 000	+8.0	1.07
233 000	3.0	1.0	0.24	0.40	179 000	−23.0	1.41
	3.0	1.0	0.24	0.40	177 000	−24.0	1.41
	4.0	1.0	0.10	0.29	242 000	+3.9	1.20
515 000	2.0	1.0	0.17	0.17	547 000	+6.2	1.01
	1.0	1.0	0.27	0.19	471 000	−8.5	1.02
					rel std dev	14.7	

[a] Mobile phase, tetrahydrofuran; temperature, 22 °C; viscosity of tetrahydrofuran, η_o = 0.46 cP. V_c held constant during runs as shown. [b] $R = t_0/t_R$. [c] Sampling and focusing conditions in Experimental Section. [d] Mark–Houwink constants, $K = 1.40 \times 10^{-4}$ dL/g; $a = 0.70$. [e] Polydispersity, M_w/M_n.

olution constant-field fractionations predictably produced lower polydispersity values. D_s values in Table I were calculated for only one run each for the two PEO standards.

This study strongly suggests that there is a significant interaction of the PEO standards with the regenerated cellulose membrane. Addition of a soluble salt at appropriate concentrations apparently eliminates this deleterious effect so that normal retention presumably takes place. These results suggest that FlFFF retention theory predictably holds for nonaqueous as well as aqueous systems, providing forces causing unwanted retention are absent.

The elution of a mixture of PEO standards in methanol with 0.2 M ammonium acetate using exponential-decay force-field programming is illustrated in Figure 5. This programmed separation is comparable to that previously shown with a totally aqueous mobile phase.[6]

To enable the predicted elution of polymers with nonprotic solvents, we chemically modified the semipermeable membrane to reduce deleterious sorptive effects. A mixture of bis(trimethylsilyl)trifluoroacetamide and trimethylchlorosilane is a known agent for silanizing the hydroxy groups on sugars and carbohydrates.[14] Therefore, this reaction was used in an attempt to deactivate the membrane surface for desired FlFFF separations. Although no effort was made to optimize this reaction, the resulting modified membrane immediately exhibited significantly lowered sorptive characteristics toward polymers in our FlFFF apparatus.

The silanized membrane permitted the normal elution of polystyrene standards with tetrahydrofuran as the mobile phase, as shown in Table II. Molecular weights calculated with Mark–Houwink constants with a variety of operating conditions show differences from reported values that are comparable to those found by FlFFF for several polymer standards in totally aqueous mobile phase systems.[11] Results were also comparable to those found for MW measurements by thermal FFF using Mark–Houwink constants.[15] Of course, differences are dependent both on the accuracy of the Mark–Houwink constants used for the calculations and the reliability of MW data on the standards. Still, the data in Table II again confirm the ability of FlFFF to produce useful quantitative information with totally organic mobile phases. Diffusion coefficient calculations suggest a precision of about 8% for D_s measurements with the limited data from this system.

(14) Horning, M. G.; Boucher, E. A.; Moss, A. M. *J. Gas Chromatogr.* **1967**, *5*, 297.
(15) Kirkland, J. J.; Rementer, S. W. *Anal. Chem.* **1992**, *64*, 904.

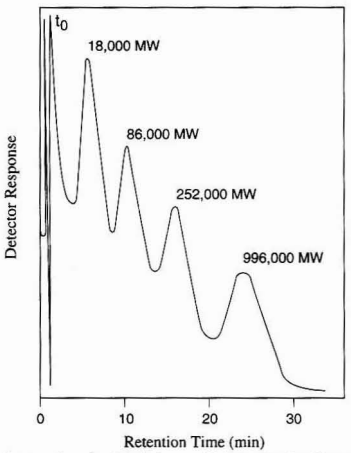

Figure 5. Separation of poly(ethylene oxide) standards with exponential-decay programmed force field in methanol. Conditions: mobile phase, methanol with 0.2 M ammonium acetate; temperature, 22 °C; initial cross flow, 9.2 mL/min; exponential decay constant, 6.0 min; channel outlet flow, 0.5 mL/min; sample, 0.10 mL, 0.1% each in methanol; refractive index detector.

Note that the values for the MW 50 000 PEO standard in Table II show the largest error. The low retention level of this polymer in this system at the highest available force field produced an R (~0.6) value that forced the software to calculate in a region of poor applicability.[6] Accurate calculations require that R values of <0.3 are obtained in the separation. Figure 6 shows the programmed exponential-decay force-field separation of a mixture of polystyrene standards using tetrahydrofuran as the mobile phase. Unfortunately, the modified membrane failed after about 3 weeks of continuous use. Examination of this membrane after failure suggested that the modified cellulose membrane had been partially dissolved by the tetrahydrofuran mobile phase during use.

In all of the studies with nonaqueous mobile phases, we unexpectedly found that peaks were broader than in comparable separations with totally aqueous mobile phases. A definitive explanation for this effect is not yet apparent. It was anticipated that organic phases would actually produce sharper bands because of lower viscosity and improved mass-transfer effects. A study of injection, focussing and relaxation

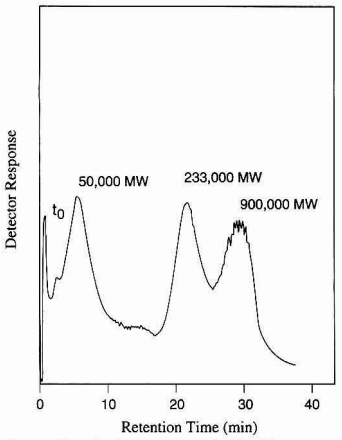

Figure 6. Separation of polystyrene standards with exponential-decay programmed force field in tetrahydrofuran. Conditions: mobile phase, tetrahydrofuran; temperature, 22 °C; initial cross flow, 8.8 mL/min; exponential decay constant, 10.0 min with 10.0 min delay; channel outlet flow, 1.0 mL/min; sample, 0.25 mL, 0.5% each; UV detector, 260 nm, 0.05 AUFS.

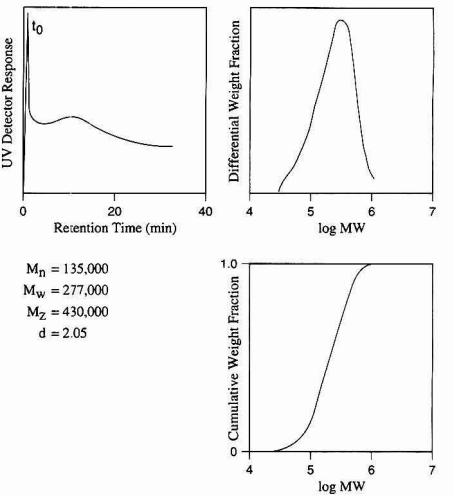

Figure 7. Molecular weight distribution of Dow 1683 polystyrene with exponential-decay force field in tetrahydrofuran. Conditions as in Figure 6.

effects did not explain the apparent anomaly. Optimum conditions were essentially the same as those previously found for aqueous separations. We speculate that some deleterious effect involving the membrane might be involved. As noted below, there are indications that the silanization method used did not create the desired fully reacted, energy-homogeneous membrane surface. Alternatively, polymer interaction effects could be the cause.

The utility of FlFFF for characterizing broad MW organic-soluble standards was illustrated with the Dow 1683 polystyrene. This sample has been widely defined by other methods as having a number-average MW (M_n) of 100 000 and a weight-average MW (M_w) of 250 000. The results of this characterization are shown in Figure 7. The M_w value found in this analysis is about 10% higher than reported. However, this is within the limits previously found for analyses carried out using Mark–Houwink constants for calibrating FlFFF systems for water-soluble polymers[11] and thermal FFF systems for organic-soluble polymers.[15] Relatively higher M_n values were the result of some overlap with the channel dead volume peak, t_0, with the particular nonoptimized programmed force-field conditions used for this analysis. The accuracy of MW calculations is a direct function of the accuracy of D_s measurements for the polymer under the experimental conditions used (eqs 1 and 2).

Attempts to generate data on poly(methyl methacrylate) standards with tetrahydrofuran as the mobile phase produced erratic results. Initial injections of this polymer gave anticipated peaks. However, subsequent injections of the same polymer standard produced smaller and smaller peaks. These results were experienced at the time that the modified membrane began to fail, so are not indicative of the true capability of the method. It is also possible that the treatment to deactivate the membrane was not sufficient for this polymer. A more vigorous reaction or a different deactivation process may be useful in extending the range of polymers that can be characterized with cellulose-based membranes.

CONCLUSIONS

This study has shown that flow FFF can be carried out with totally organic solvents to enable the characterization of organic-soluble polymers. Solute diffusion coefficients are the fundamental data that are available from flow FFF measurements. However, molecular weights and molecular weight distributions can be determined by converting these diffusion coefficients with published Mark–Houwink constants for polymer/solvent systems. Results obtained on organic-soluble polymers show variations from reported values that are equivalent to those previously reported in the FlFFF characterization of water-soluble polymers and thermal FFF of organic polymers. Our studies indicate that better ultrafiltration membranes are needed for the flow FFF of organic-soluble polymers. Suitable membranes may involve rigid inorganic structures that are deactivated by known surface modifications. Such developments could lead to the broad application of the flow FFF method for characterizing a wide range of both water-soluble and organic-soluble macromolecules.

RECEIVED for review April 17, 1992. Accepted August 31, 1992.

Determination of Intracellular Species at the Level of a Single Erythrocyte via Capillary Electrophoresis with Direct and Indirect Fluorescence Detection

Barry L. Hogan and Edward S. Yeung*

Department of Chemistry and Ames Laboratory–USDOE, Iowa State University, Ames, Iowa 50011

Intracellular contents reflect the specific history of a cell including innate physiological heterogeneity as well as differing levels of exposure to environmental influences. A method capable of analyzing a variety of species from within a single human erythrocyte is demonstrated. Guided by a microscope, individual cells can be drawn into open capillaries of 10-μm i.d. On contact with a low ionic strength buffer solution, the cell lyses and releases its intracellular fluid. The ionic components are then separated by capillary electrophoresis. For glutathione, microderivatization with a fluorescent reagent can be accomplished in vitro with monobromobimane. The effects of extracellular oxidizing and reducing agents on the glutathione levels can thus be followed. For sodium and potassium, or any other ionic species, charge displacement of a fluorescent cation results in indirect fluorescence detection. The two detection modes are suitable for intracellular components present at low-attomole and sub-femtomole levels, respectively.

An understanding of the effects of external stimuli, such as exposure to anticancer agents and exogenous toxins, upon specific cellular strains is important in fields such as cell biology, pharmacology, and toxicology.[1] Alternatively, the discovery and study of inherent differences in the composition of morphologically identical cells could help elucidate the correlation between a specific cellular trait, such as disease resistance, and the presence of certain species within a cellular subclass.[2] An analytical procedure capable of providing insight into the biochemical composition of a selected single mammalian cell could accelerate progress toward these goals.

We have devised a simple analytical scheme capable of separating and detecting either nonfluorescent or fluorescent species within the cytoplasm of a single human erythrocyte. The instrument is based upon a capillary electrophoresis (CE) separation system coupled with either a laser-based indirect or direct fluorescence detection scheme. The high separation power of CE allows discrimination against the complicated cell matrix and provides positive identification of the analytes based on retention times. We are able to monitor nonfluorescent species such as sodium and potassium and fluorescent derivatized species such as the physiologically important peptide, glutathione (GSH). A membrane-mediated approach makes derivatization of single cell contents practical without tedious microchemistry or pooling of the heterogeneous cell contents of many cells. As a practical application of single-cell CE, human erythrocytes were subjected to modeled oxidative stress by the application of externally applied reagents. We can follow statistically valid modulations in the quantity of glutathione present in human erythrocytes before and after application of the cell-affecting reagents. We believe that this is the first report of the separation and quantitation of individual species at the mammalian erythrocyte level. In light of the extremely small cell volume of the erythrocyte (87 fL), it is clear that single-cell analysis of the majority of mammalian cells is possible and practical.

EXPERIMENTAL SECTION

Instruments. The CE separation system used here has similarities to previously described instruments.[3] Excitation is provided by 4 mW of combined 350–360-nm radiation from an Ar ion laser (Coherent Innova 90, Palo Alto, CA). A 6-mm focal length glass lens (Edmund Scientific, Barrington, NJ) is used to focus the beam within the 10-μm capillary. A 20× microscope objective (Edmund Scientific) is used to collect the fluorescent image. A R928 photomultiplier (Hamamatsu) is used to detect the fluorescence signal. The instrumental configuration of the capillary and electrodes has been rearranged to allow open continuous operation of the grounded end of the CE capillary in a buffer vial under the field of view of a microscope (100× magnification, Series 10 Microstar). The grounded end of the capillary and the ground electrode are both mounted in 3D micromanipulators (The Micromanipulator Co., Models 412 and 512). The configuration of the grounded injection region is shown in Figure 1. This arrangement allows precise movement of the CE capillary while the capillary orifice is being viewed through the microscope. During CE separations, the capillary and ground electrodes are positioned within a small buffer vial. The buffer vial consists of the bottom 10–15 mm of a 20-mL sample vial firmly bonded to a microscope slide. For cell injections or injections of standards, the capillary and ground electrode are manipulated upwards slightly, and the appropriate solutions are positioned upon the microscope stage.

Cell Selection and Injection. A 20-μL drop of the cell suspension to be sampled is placed on a clean microscope slide in place of the CE running buffer vial. Best results are obtained with low to moderate cell densities (≤1/500 that of whole blood) and small drop volumes which reduce convective disturbances. An individual erythrocyte is selected for injection by manually positioning the orifice of the capillary close to the cell of interest with the aid of the microscope and the micromanipulators. A pulse of vacuum from the opposing capillary orifice is then applied. Electroosmosis can in principle be employed to introduce cells though this method suffers from the inability to rapidly adjust the magnitude of the injection velocity or to reverse the flow direction. A 1-m column of 10-μm internal diameter typically requires only 350 mmHg vacuum for a few seconds to induce an erythrocyte to enter the capillary. A 20-mL sample vial made airtight with a septum and an autosampler cap serves as the high-voltage buffer reservoir. The capillary is inserted through the flexible septum with the aid of a hypodermic needle. A manually controlled 20-mL gastight syringe interfaced to the high voltage vial via a Luer-lock hypodermic needle provides the pressure or vacuum required to modulate the motion of fluid within the capillary. The entire process of cell selection and injection typically consumes 2–5 min.

Once an individual erythrocyte is within the fused silica capillary, the cell membrane typically adheres to the capillary

(1) Parce, J. W.; et al. *Science* **1989**, *246*, 243–247.
(2) Salgame, P.; et al. *Science* **1991**, *254*, 279–282.
(3) Kuhr, W. G.; Yeung, E. S. *Anal. Chem.* **1988**, *60*, 2642–2646.

0003-2700/92/0364-2841$03.00/0

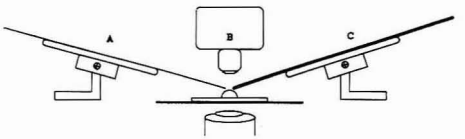

Figure 1. Closeup of the cell injection region of the CE system. A = ground electrode; B = 100× microscope; C = CE capillary. A cell is selected for injection by manually positioning the orifice of the capillary close to the cell of interest and then applying a pulse of vacuum to the capillary.

walls, immobilizing the cell. The capillary can now easily be manipulated up out of the cell solution, and the CE running buffer solution can be replaced under the capillary. Lysis of the cell to release the intracellular contents is now desired. Additional cell lysate solutions (1% SDS, digitonin or dilute buffer) may be introduced over the cell for this purpose. We have found the resumption of the electrophoretic separation with the capillary in CE running buffer also destroys cell integrity. Upon lysis, the intracellular contents migrate toward the optical detection window.

Direct Fluorescence Detection. Fused silica columns (Polymicro Technologies, Phoenix, AZ) of 1-m total length (50 cm to detector) were used without modification. The CE running buffer was 20 mM sodium phosphate, pH 8.8. A voltage of −20 kV was applied. One 400-nm longpass filter (GG-400, Melles Griot) was used in combination with two 470-nm (Edmund Scientific, Barrington, NJ) interference filters.

Erythrocytes in EDTA were obtained from an apparently healthy adult male. Whole blood was stored at 4 °C for 4–5 days without additives. No marked hemolysis was observed. The erythrocytes were prepared by removing plasma contamination by repeated washes/centrifugations using 135 mM NaCl, 20 mM phosphate, pH 7.4, as the washing buffer. Whole blood (40 μL) was added to 7 mL of wash buffer and inverted gently. After centrifugation (1100 rpm for 6 min), the supernatant was removed, and fresh wash buffer was added. Process was repeated several times for a plasma removal factor of 10^6. Monobromobimane (mBBr) derivatization was carried out as in ref 10, with 12 μmol of mBBr/mL of packed cells at 37 °C for 60 min. Cells were washed before and after derivatization.

GSH Modulation Experiments. Modulation conditions and format were similar to those of standard macroscopic intracellular GSH experiments.[4,5] Cells were washed free of plasma before incubation. Cells were derivatized with 24 μmol of mBBr/mL of packed cells for 60 min at 37 °C after incubation with modulation reagents. Cells were washed before the next incubation step proceeded.

Indirect Detection. Applied voltage is 20 kV. One 400-nm longpass filter (GG400, Melles Griot) was used with two 515-nm (Edmund Scientific, Barrington, NJ) interference filters. The requirement of very low ionic strength cell suspension solutions and the tendency of cationic species to interact with the silica column walls call for the use of column deactivation procedures. Previous work demonstrated the sensitivity required for detection of cytoplasmic cations;[6] however, that method was not compatible with the high osmotic strength cell wash solutions necessary or the cell matrix itself. To alleviate these effects, a hydrophobic coating is bonded to the column walls[7] and a cationic surfactant is included in the CE running buffer. The surfactant adheres to the wall coating and minimizes cationic interactions with the column. These methods dramatically improved single-cell CE's reproducibility and its ability to withstand the heavy cell matrix effects encountered.

2% OV-17v coated CE columns were prepared according to published methods.[7] 6-Aminoquinoline (6-AQ) (500 μM) and 200 μM cetyltrimethylammonium bromide, pH 3.8, make up the CE running buffer. Cells are washed as with direct detection with 8% glucose/500 μM 6-AQ, pH 6.5. Other conditions are identical to those of direct detection.

Data Collection. Data was collected with an IBM-compatible AT clone through a Data Translation (Marlboro, MA) DT2802 analog to digital interface.

Reagents. Unless specified otherwise, all reagents were obtained from Sigma Chemical (St. Louis, MO). 6-Aminoquinoline and cetyltrimethylammonium bromide were obtained from Aldrich Chemical (Milwaukee, WI). OV-17v was obtained from Petrarch Systems, Bristol, PA. Monobromobimane was obtained from Molecular Probes (Eugene OR). Diamide is the trivial name for diazenedicarboxylic acid bis(*N*,*N*-dimethylamide).

RESULTS AND DISCUSSION

Detection of low concentrations of cell constituents within the subpicoliter detection volumes used here requires highly sensitive detection such as that provided by laser-based fluorescence methods.[8] Unfortunately, only a minority of interesting analytes fluoresce appreciably naturally. Several possibilities exist for overcoming this limitation at these small volumes. Common derivatization methods miniaturized to the single erythrocyte scale may eventually be feasible yet certainly still present formidable technical challenges.[9] Pooling the contents of multiple cells defeats the purpose of a single-cell analysis technique by homogenizing the contents of possibly heterogeneous cells. Alternative detection methods such as electrochemical detection are suitable in some instances, but ultimately also detect only a given subset of potentially interesting species. In considering these options, one can see that much room exists for new solutions to the problem of microderivatization.

Microderivatization of living cells is a unique challenge which can be approached in methods unsuitable for other samples. One such approach is to use the cell's semipermeable membrane to regulate the flux of species through the "reaction vessel", i.e. the cell itself. Small nonpolar derivatization reagents applied to the macroscopic exterior phase surrounding the cell readily partition through the lipophilic cell membrane where they are available for reaction with the appropriate analyte functionalities. The exterior phase with its excess reagents and contaminants can be completely removed via centrifugation. The derivatized product, if larger or more polar than the original reagent, will not migrate back out through the cell membrane. No tedious microchemistry is required, and no loss of correlation between individual cellular identities and cellular biochemical information is seen. A limitation is that not all functionalities possess favorable reaction kinetics with known derivatization reagents at physiological conditions. A number of interesting intracellular species should be accessible, however. Intracellular thiols and cytosolic proteins are known to react with reasonable rates near physiological pH conditions.[10,11] Membrane-mediated microderivatization is similar to concepts employed in fluorescence microscopy and flow cytometry, and some reagents used in those fields may be immediately useful. Reactive fluorescent probes, such as dichlorotriazinylaminofluorescein (DTAF) are suitable for reaction with the ε-amino group of lysine side chains and N-terminal α-amino groups of cytosolic proteins with acceptable yields (40–70%) at room temperature in reaction times of 1 hour or less at

(4) Kosower, N. S.; Kosower, E. M.; Zipser, Y.; Faltin, Z.; Shomrat, R. *Biochim. Biophys. Acta* **1981**, *640*, 748–759.
(5) Dolphin, D.; Avramovic, O.; Poulson, R. *Glutathione: Chemical, Biochemical and Medical Aspects*; Wiley: New York, 1989; Part B, pp 330–340.
(6) Gross, L.; Yeung, E. S. *Anal. Chem.* **1990**, *62*, 427–431.
(7) Dluzneski, P. R.; Jorgenson, J. W. *J. High Resolut. Chromatogr. Chromatogr. Commun.* **1988**, *11*, 332–336.
(8) Sweedler, J. V.; Shear, J. B.; Fishman, H. A.; Zare, R. N.; Scheller, R. H. *Anal. Chem.* **1991**, *63*, 496–502.
(9) Kennedy, R. T.; Oates, M. D.; Cooper, B. R.; Nickerson, B. V.; Jorgenson, J. W. *Science* **1989**, *246*, 57–63.
(10) Kosower, N. S.; Kosower, E. M.; Newton, G. L.; Ramney, H. M. *Proc. Natl. Acad. Sci. U.S.A.* **1979**, *76*, 3382–3386.
(11) Blakeslee, D.; Baines, M. G. *J. Immunol. Methods* **1976**, *13*, 305–320.

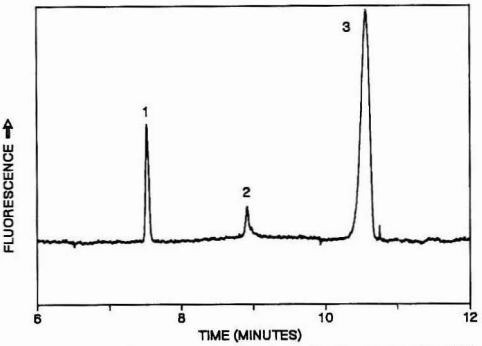

Figure 2. Electropherogram of mBBr-derivatized contents of a single human erythrocyte using direct fluorescence detection. The peaks are: 1 = peak associated with unreacted mBBr; 2 = unidentified intracellular thiol; 3 = GSH.

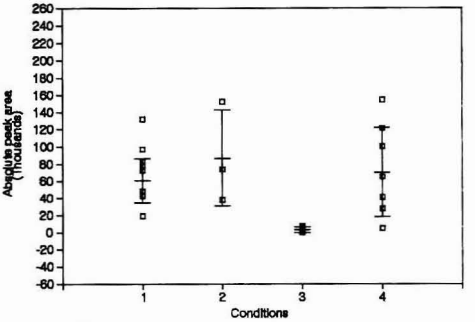

Figure 3. GSH determinations in single erythrocytes. Bars represent average GSH peak area and standard deviation. Conditions: 1 = derivatization of cells with mBBr; 2 = 0.3 μmol of diamide/mL of packed cells; mBBr derivatization; 3 = 1 μmol of diamide/mL of packed cells; mBBr derivatization; 4 = 1 μmol of diamide/mL of packed cells; then 5 mM DTT followed by mBBr derivatization. A statistically significant (95% confidence) difference exists between the means of GSH levels of conditions 1–3 and 4–3. No statistical difference between means 1–4.

physiological pH.[11] Delivery of such probes can be accomplished via esterification of polar moieties to allow penetration into the cell where nonspecific esterases activate the reagent.[12] The fluorescein-based structure of this and other reagents should permit highly sensitive detection of derivatized species.

As an example of the utility of this concept, monobromobimane (mBBr) was used to derivatize thiol-containing species within functioning erythrocytes at physiological conditions.[6] Cellular thiols have an important function in the biology of cells, being involved with cell proliferation,[13] cellular transport mechanisms,[14] and DNA synthesis.[15] Numerous environmental toxins such as heavy metals,[11] oxidants,[16] and metabolites of toxic chemicals[17] can modulate cellular thiols. GSH has been reported to constitute over 95% of nonprotein thiols in macroscopic cell lysates[18] and is accordingly of special significance. In particular, GSH metabolism is an important determinant in the control of cellular response to various types of drugs and radiation.[19] Figure 2 shows the electropherogram of intracellular thiols at the single erythrocyte level. The high separation efficiency of CE and the specificity of the derivatization reaction allows positive identification of GSH. Injection of the matrix fluid showed no trace of derivatized GSH. For future work, improved detection of other trace thiols could be achieved by use of optimized fluorescein-based thiol reagents and specific laser lines.

We also studied the effects of diamide and dithiothreitol (DTT) as model oxidative and reductive agents upon the total GSH present within given cells. Figure 3 gives the graphical results of this experiment. The reagents induced a statistically valid modulation between high and low GSH levels in the cells by the alternate oxidation and reduction of intracellular GSH and the corresponding disulfide, GSSG. More subtle doses of diamide (condition 2) were unable to produce statistically significant changes in GSH content, as expected.

In order to understand the role of GSH within a functioning cell, some method of artifically changing its concentration is desired. Known levels of GSH can then be correlated with observed cellular properties. Diamide is a convenient and effective species for modulating the intracellular GSH level of functional cells.[18,20] Diamide oxidizes GSH to its disulfide, GSSG. This species is then unavailable for reaction with the thiol-specific derivatizing reagent, mBBr. The ability to monitor changes in intracellular GSH levels via exposure to diamide implies a similar ability to monitor the modulation effects of more complex and interesting stimuli such as exposure to chemotherapeutic agents or ionizing radiation at the single cell level. Dithiothreitol is a well-known agent for the reduction of intracellular thiols.[21] Its effect here is to reduce GSSG to the thiol, GSH. This reaction increases GSH levels at the expense of GSSG levels, and consequently, larger concentrations of GSH are available for derivatization with mBBr. The restoration of GSH–mBBr levels seen upon incubation of cells with DTT following incubation with diamide (condition 4) demonstrates that the low intracellular GSH levels seen in condition 3 are due to the conversion of GSH to GSSG and are not due to such factors as cell lysis or leakage. As GSH levels have been reversibly cycled through high to low to high states, cellular integrity must be maintained throughout the entire process.

Single-cell monitoring provides information about the cell to cell variation of measured quantities within the sampled group of cells. Statistics can provide reasonable estimates of the cell population mean[22] provided that the distribution is Gaussian. It can be seen that qualitative determinations of the population mean will require very few samples, while sample size increases accordingly with the accuracy desired for the measurement. Four single-cell measurements currently require 1 h or less of contiguous experimental time. It should be noted that no effort was made here to optimize throughput, and recent advances in ultra-high speed CE[23] or the use of parallel experimental apparatus may permit even more rapid analysis times. The degree of accuracy required for biological applications will vary, yet it is of interest to

(12) Bronner-Fraser, M. *J. Cell Biol.* **1985**, *101*, 610–617.
(13) Hammett, F. S. *Protoplasma* **1929**, *7*, 297–322.
(14) Kwock, L.; Wallach, D. F. H.; Hefter, K. *Biochem. Biophys. Acta* **1976**, *419*, 93–103.
(15) Holmgren, A. *Biochem. Soc. Trans.* **1977**, *5*, 611–612.
(16) Arrick, B. A.; Nathan, C. F.; Griffith, O. W.; Cohn, Z. A. *J. Biol. Chem.* **1982**, *257*, 1231–1237.
(17) Pfeifer, R. W.; Irons, R. In *Immunotoxicology and Immunopharmacology*; Dean, J., Munson, A., Luster, M., Eds.; Raven Press: New York, 1978; pp 255–262.
(18) Kosower, N. S.; Kosower, E. M. *Int. Rev. Cytol.* **1978**, *54*, 109–160.
(19) Dolphin, D.; Avramovic, O.; Poulson, R. *Glutathione: Chemical, Biochemical and Medical Aspects*; Wiley: New York, 1989.
(20) Kosower, N. S.; Kosower, E. M.; Wertheim, B.; Correa, W. S. *Biochem. Biophys. Res. Commun.* **1969**, *37*, 593–596.
(21) Kosower, N. S.; Kosower, E. M. *Glutathione: Chemical, Biochemical and Medical Aspects*; Dolphin, D., Avramovic, O., Poulson, R., Eds.; Wiley: New York, 1989; Part B, p 325.
(22) Mendenhall, W. *Introduction to Probability and Statistics*; Duxbury Press: Boston, 1983; pp 280–285.
(23) Monnig, C. A.; Dohmeier, D. M.; Jorgenson, J. W. *Anal. Chem.* **1991**, *63*, 807–810.

Table I. Averaged Total GSH Content from Six Separate Single Erythrocyte Separations and Comparison with Expected Macroscopic Literature Values

	amount present (amole)	concentration (M)
single-cell GSH	68 ± 48	(7.5 ± 0.55) × 10^{-4}
macroscopic values	191 ± 36	(2.20 ± 0.41) × 10^{-3}

[a] See ref 39. Intracellular concentrations are based upon 87-fL cell volumes,[40] manufacturer's specifications of column internal diameters, and absence of injection bias for standard samples. The calibration curve for free GSH–mBBr conjugate was linear with r^2 of 0.994 and a LOD of 5.9 amol (4.8 × 10^{-8} M) based upon S/N of 3.

note that a number of toxic agents are known to decrease intracellular GSH levels by 70% before critical depletion occurs and the onset of irreversible intracellular damage begins.[24]

It is important to note that the purpose of single-cell studies is not so much to predict the average cell contents, but to assess individual differences. We made multiple injections of single erythrocytes derivatized with mBBr to assess the variability of contents in single cells. Table I shows the results of these GSH determinations. Figure 3 and Table I show that there are large variations among cells that cannot be explained by differences in sampling or measurement. In fact, the distribution in Figure 3 appears to be non-Gaussian. Several sources of variability contribute to the observed deviation. These are variations in actual cell volume from mean values, nonuniformity in the extent of the derivatization reaction, variability in membrane permeability, and deviations in intercellular thiol content and status. We note, however, that erythrocytes are remarkably uniform in volume. We believe that the last two sources, the specific cellular properties of the sampled cells, play a significant role in the observed scatter of experimentally determined GSH quantities. This underscores the value of single-cell analysis. Our conclusion is based upon several factors. The first is our knowledge of the "all or nothing" cell injection method used in that a cell's entry into the capillary can be visually confirmed. As the cells are packaged as individual biological quanta, all of the cell's contents are injected together. The fact that multiple cells are not injected is similarly confirmed. We also note that all cells of a given experiment are derivatized under identical conditions in the same macroscopic solution. This should greatly reduce any imprecision based upon changes in reaction conditions. Finally, repeat injections of standards produce peak areas reproducible to ±2%.

The mean GSH levels in Table I are substantially lower than literature values. The present scheme is only applicable to soluble material released on lysis. GSH may be tied up in other cellular compartments and therefore not measured here. We attempted to totally dissociate any bound GSH conjugate from the cellular matrix by injecting a running buffer containing 1% SDS over the immobilized cell. For a limited numbers of trials, no dramatic increase in detected GSH was seen. We also note that uncertainties exist in estimating the quantity (volume) of standards injected. Hysteresis in electroinjection and inaccuracy in the column internal diameter as quoted by the manufacturer can both lead to errors in quantitation. It is not uncommon to have a time constant of 1–2 s in high-voltage power supplies, adding 50% to the amount of standards injected. Also, a 20% error in estimating the column diameter will lead to a 40% error in injection volume. It is apparent that better calibration is needed to provide reliable absolute GSH values.

(24) Smith, C. V.; Mitchell, J. R. *Glutathione: Chemical, Biochemical, and Medical Aspects*; Dolphin, D., Avramovic, O., Poulson, R., Eds.; Wiley: New York, 1989; Part B, pp 3–8.

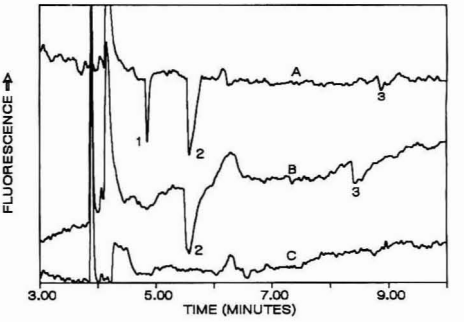

Figure 4. Electropherograms using indirect fluorescence detection. A = 2-s electroinjection of 45 μM standards. 1 = LI (11.7 fmol injected); 2 = Na (10.7 fmol); 3 = K (6.5 fmol); B = 1 human erythrocyte injected; C = blank of extracellular matrix. The calibration curve for electroinjected LiCl standards was linear from 5.0 × 10^{-6} to 8.4 × 10^{-4} M with r^2 of 0.996 (n = 20). We determined the peak area precision of 2-s 60 μM LiCl standard injections to be 2.0% RSD with a retention time precision of 0.22% RSD (n = 7).

We recognize that derivatization methods, regardless of the degree of refinement, will not be useful in all instances. A significant number of analytes inherently lack useful detection properties and do not possess the functionalities appropriate for derivatization, or those functionalities are inaccessible due to experimental restrictions. We have achieved the separation and detection of two underivatized nonfluorescent species, sodium and potassium, from the cytoplasm of single human erythrocytes via indirect fluorescence detection. Indirect fluorescence detection records the passage of a nonfluorescent analyte through the detection zone by the charge displacement effects of the analyte upon the fluorescent comigrating buffer ions.[25] Indirect detection methods permit the sensitive detection of species which have no inherently useful detection properties and offer the potential for general detection of charged species. Of particular interest are those intracellular species which possess no useful detection properties, such as inorganic ions. Other biologically important anionic species such as glutamate, aspartate, lactate, and pyruvate are all also amenable to indirect detection though further increases in instrumental sensitivity will be required to reliably quantify them within an erythrocyte. Figure 4 shows the results of a determination of sodium and potassium from a single erythrocyte. Since these two ions have quite distinct mobilities and are present as major components in erythrocytes, identification by migration times is adequate in this study. By inspection of the peak area of the potassium standard, it can be seen that the sampled potassium is present at quite reasonable physiological levels. The intracellular sodium, however, appears to be present at substantially larger than expected levels as the peak area of the injected sodium standard represents 5 times the expected level of intracellular sodium. Our comparisons are based upon macroscopic literature values for intracellular sodium and potassium concentrations[26,27] and estimates of erythrocyte cell volume.[28] A coeluting system peak[29] can be seen as a shoulder on the sodium peak and is the main contributor to this unexpected increase. This system peak appears even when pure lithium or potassium standard

(25) Yeung, E. S.; Kuhr, W. G. *Anal. Chem.* **1991**, *63*, 275A–282A.
(26) Hald, P. M.; Heinsen, A. J.; Peters, J. P. *J. Clin. Invest.* **1947**, *26*, 983–990.
(27) Hald, P. M.; Eisenmann, A. J. *J. Biol. Chem.* **1937**, *118*, 275–288.
(28) Weinstein, R. S. In *The Red Blood Cell*; Surgenor, D. M., Ed.; Academic Press: New York, 1974; p 232.
(29) Poppe, H. *J. Chromatogr.* **1990**, *506*, 45–60.

is injected. A correction must therefore be applied or else a different buffer system should be used for the determination of intracellular sodium.

Human erythrocytes prove difficult analysis targets as the cationic electrolytes quickly dissipate upon immersion of the cell into solutions of low ionic strength.[30] Porcine erythrocytes do not demonstrate this property so readily and are useful for developmental studies. In our laboratory, similar results are seen upon injection of single porcine erythrocytes.

This work is a step toward a viable analysis of the intracellular composition of single mammalian cells. Several other groups have utilized capillary separations with electrochemical and fluorescence detection to study trace organic species within the cytoplasm of invertebrate neurons.[5,31-37] Most recently, Cooper et al. demonstrated analysis of femtomole levels of catecholamines within mammalian adrenomedullary cells.[38] Differentiating features of the present work are its ability to analyze cells of a volume similar to that of an erythrocyte (which is about 1000 times smaller than a typical invertebrate neuron and 20 times smaller than an adrenomedullary cell), the ease of cell manipulation, the absence of dilution before injection, and the interchangeable detection concepts of microderivatization (specific) and indirect fluorescence (universal). We believe that a substantial advantage would be gained by the development of coherent methodologies whereby investigators could readily analyze a wide variety of intracellular species via the more appropriate of two detection schemes with only trivial instrumental modifications. The limitations of single-cell CE are seen as the requirement for low ionic strength solutions for indirect detection and restrictions on reaction conditions for microderivatization. On-column derivatization methods involving nonphysiological conditions could provide additional flexibility in the types of species amenable to this approach.

We anticipate that single-cell CE will be useful in such tasks as correlating the relationships between cellular function and biochemical composition and for elucidation of the mechanistic effects of drug candidates upon specific cellular subsets. Single-cell CE would be especially useful in instances where investigators are interested in the effects of extracellular influences upon multiple specific intracellular species. This type of information is difficult to obtain with methods such as flow cytometry and fluorescence microscopy. It is important to note that single-cell CE allows for the physical separation of the derivatized products whereas methods such as flow cytometry typically provide information in terms of total protein content or total DNA content, for instance. Single-cell CE may also be useful as a technique to provide compositional information on rare cell types sorted and partially characterized by higher throughput techniques such as flow cytometry. This method should also be useful for monitoring the purity and yield of recombinantly derived protein products quickly and with good sensitivity in small numbers of cells from mammalian cell culture. The power of separation at the single erythrocyte level could provide, in effect, a multiparametric description of the cell's biochemical status with each relevant separated species contributing an additional dimension of information. These additional dimensions of information should allow elucidation of substantially more subtle and complex effects than possible by monitoring the response of a single cellular characteristic to a given stimuli.

ACKNOWLEDGMENT

The authors would like to thank Philip Haydon and Stephen Ford for their helpful advice and generous gifts of time and porcine erythrocytes. The Ames Laboratory is operated by Iowa State University for the U.S. Department of Energy under contract No. W-7405-Eng-82. This work is supported by the Director of Energy Research, Office of Basic Energy Sciences.

RECEIVED for review May 1, 1992. Accepted August 24, 1992.

Registry No. GSH, 70-18-8; Na^+, 7440-23-5; K^+, 7440-09-7; mBBr, 71418-44-5.

(30) Passow, H. In *The Red Blood Cell*; Bishop, C., Surgenor, D. M., Eds.; Academic Press: New York, 1964; pp 106–109.
(31) Wallingford, R. A.; Ewing, A. G. *Anal. Chem.* **1988**, *60*, 1972–1975.
(32) Kennedy, R. T.; St. Claire, R. L.; White, J. G.; Jorgenson, J. W. *Mikrochim. Acta* **1987**, *II*, 37–45.
(33) Kennedy, R. T.; Jorgenson, J. W. *Anal. Chem.* **1989**, *61*, 436–441.
(34) Oates, M. D.; Cooper, B. R.; Jorgenson, J. W. *Anal. Chem.* **1990**, *62*, 1573–1577.
(35) Zare, R. N. *Abstracts of Papers of the American Chemical Society* **1991**, *201*, 71.
(36) Olefirowicz, T. M.; Ewing, A. G. *Anal. Chem.* **1990**, *62*, 1872–1876.
(37) Olefirowicz, T. M.; Ewing, A. G. *Chimia* **1991**, *45*, 106–108.
(38) Cooper, B. R.; Jankowski, J. A.; Leszczyszyn, D. J.; Wightman, M. R.; Jorgenson, J. W. *Anal. Chem.* **1992**, *64*, 691–694.
(39) Jocelyn, P. C. *Biochem. J.* **1960**, *77*, 363–368.
(40) Weinstein, R. S. In *The Red Blood Cell*; Surgenor, D. M., Ed.; Academic Press: New York, 1974; p 232.

Separation of Boron-Complexed Diol Compounds Using High-Performance Capillary Electrophoresis

James P. Landers,* Robert P. Oda, and Mark D. Schuchard

Department of Biochemistry and Molecular Biology, Mayo Foundation and Mayo Clinic, Rochester, Minnesota 55905

In this study, borate is shown to be key in the high-performance capillary electrophoretic (HPCE) separation of several biologically-active molecules differing only by a single hydroxyl group with no change in net charge. Separation of several paired compounds is minimal or nonexistent in 100 mM tricine buffer at pH 8.4, while identical analysis with 100 mM borate buffer led to baseline resolution in less than 10 min, most likely due to complexation of borate with the molecules containing a *cis*-diol. In contrast, baseline separation of tyrosine from the *cis*-diol-containing compounds dopa and dopamine is achieved with either buffer system because of differences in their charge due to the *p*-hydroxyl group of the benzene ring. The equilibrium complexation of borate with cytidine can be monitored by HPCE through a borate concentration-dependent change in the borate–cytidine complex migration time (MT). A semilogarithmic plot of the change in MT versus borate concentration suggests an equilibrium dissociation constant for the complex of 15 mM, a value consistent with literature values for borate–ribose complex formation.

INTRODUCTION

High-performance capillary electrophoresis (HPCE) is a relatively new analytical technique that is useful for the separation of a diverse array of molecules including ions,[1] small organic molecules,[2,3] sugars,[4,5] peptides,[6] oligonucleotides,[7] and proteins.[8–12] Electrophoretic separation is carried out in a fused-silica capillary (typically 375-μm o.d. × 50-μm i.d.) which, even under high current, efficiently dissipates generated Joule heat, thus avoiding many of the problems known to plague slab gel electrophoresis.[13] Of the many advantages of HPCE analysis, one is the ability to easily resolve sample mixtures under denaturing or nondenaturing conditions. In both of these modes, separation results from two independent processes. The first is electrophoretic migration of the analytes, based primarily on differences in the charge-to-mass ratios. The second results from the negative charge of the inner surface of the capillary by the silica. During electrophoresis the negative charge acts as a pumping mechanism to propel cations through the capillary and causes a net movement of fluid from the inlet to the outlet. This process, termed electroosmotic flow (EOF), drives the movement of all molecules (positive, neutral, and negative) toward the cathode, with separation ultimately being determined by differences in the charge of the molecules.

The choice of buffer for the separation of analytes by HPCE is very important. Buffers must be of adequate ionic strength in order to provide optimal buffering capacity at the desired pH, yet not produce excess Joule heat (from increased current) under high fields. One buffer that has proven adequate for separations carried out in the pH 8–9 range is sodium borate.[13–21] In addition to its buffering ability, borate has long been known to form stable complexes with *cis*-diols.[14–17] This characteristic of borate has been exploited for the chromatographic separation of certain biologically-active molecules containing *cis*-diols[22–25] that are of basic scientific[26,27] and clinical[28] interest. Honda and co-workers were the first to explore the use of borate for the separation of sugars, focusing on the analysis of derivatized monosaccharides and oligosaccharides.[17,18] Novotny and co-workers furthered this with HPCE analysis of fluorescently-labeled sugars.[4,5] Most recently, the concept of HPCE analyses of borate-complexed sugars has been extrapolated to glycoproteins.[29]

While several borate–diol complexes have apparently been isolated,[30–32] characterization of the complexation process has been limited.[14] The exploitation of borate–diol complexation for chromatographic separations of certain biologically-active

* To whom correspondence should be addressed.

(1) Jones, W. R.; Jandik, P.; Pfeifer, R. *Am. Lab.* **1991**, *23*, 40–46.
(2) Carney, S. L.; Osborne, D. J. *Anal. Biochem.* **1991**, *195*, 132–140.
(3) Landers, J. P.; Schuchard, M.; Subramaniam, M.; Sismelich, T.; Spelsberg, T. C. *J. Chromatogr.* **1992**, *603*, 247–257.
(4) Lui, J.; Shirota, O.; Novotny, M. *Anal. Chem.* **1991**, *63*, 413–417.
(5) Lui, J.; Shirota, O.; Wiesler, D.; Novotny, M. *Proc. Natl. Acad. Sci. U.S.A.* **1991**, 2302–2306.
(6) Grossman, P. D.; Colburn, J. C.; Lauer, H. H. *Anal. Biochem.* **1989**, *179*, 28–33.
(7) Karger, B. L.; Cohen, A. S.; Guttman, A. *J. Chromatogr.* **1989**, *492*, 585–614.
(8) Gordon, M. J.; Lee, K.-J.; Arias, A. A.; Zare, R. N. *Anal. Chem.* **1991**, *63*, 69–72.
(9) Wiktorowicz, J. E.; Colburn, J. C. *Electrophoresis* **1990**, *11*, 769–773.
(10) Towns, J. K.; Regnier, F. E. *Anal. Chem.* **1991**, *63*, 1126–1132.
(11) Mazzeo, J. R.; Krull, I. S. *BioTechniques* **1991**, *10*, 638–645.
(12) Bolger, C. A.; Zhu, M.; Rodriguez, R.; Wehr, T. *J. Liq. Chromatogr.* **1991**, *14* (5), 895–906.
(13) Landers, J. P. *BioEssays* **1991**, *13*, 253–258.
(14) Advis, J. P.; Hernandez, L; Guzman, N. A. *Peptide Res.* **1989**, *2*, 389–394.
(15) Guzman, N. A.; Berck, C. M.; Hernandez, L.; Advis, J. P. *J. Liq. Chromatogr.* **1990**, *13*, 3843–3858.
(16) Hoffstetter-Kuhn, S.; Paulus, A.; Gassmann, E.; Widmer, E. M. *Anal. Chem.* **1991**, *63*, 1541–1547.
(17) Honda, S.; Iwase, S.; Makino, A.; Fujiwara, S. *Anal. Biochem.* **1989**, *176*, 72–77.
(18) Honda, S.; Makino, A.; Suzuki, S.; Kakehi, K. *Anal. Biochem.* **1990**, *191*, 228–234.
(19) Kenndler, E.; Schwer, C.; Fritsche, B.; Pohm, M. *J. Chromatogr.* **1990**, *514*, 377–382
(20) Otasuka, K.; Terabe, S.; Ando, T. *J.* Chromatogr. **1985**, *332*, 219–226.
(21) Wallingford, R. A.; Ewing, A. G. *Anal. Chem.* **1989**, *61*, 98–100.
(22) Sienkiewicz, P. A.; Roberts, D. C. *J. Inorg. Nucl. Chem.* **1980**, *42*, 1559–1575.
(23) Roy, G. L.; Laferriere, A. L.; Edwards, J. O. *J. Inorg. Nucl. Chem.* **1957**, *4*, 106–114.
(24) Conner, J. M.; Bulgrin, V. C. *J. Inorg. Nucl. Chem.* **1967**, *29*, 1953–1961.
(25) Tanner, D. W.; Bruice, T. C. *J. Am. Chem. Soc.* **1967**, *89*, 6954–6971.
(26) Weith, H. L.; Wiebers, J. L.; Gilham, P. T. *Biochemistry* **1970**, *9*, 4396–4401.
(27) Schott, H.; Rudloff, E.; Schmidt, P.; Roychoudhury, R.; Kossel, H. *Biochemistry* **1973**, *12*, 932–938.
(28) Moyer, T. P.; Jiang, N.-S.; Tyce, G. M.; Sheps, S. G. *Clin. Chem.* **1979**, *25*, 256–263.
(29) Landers, J. P.; Madden, B. J.; Oda, R. P.; Spelsberg, T. C. *Anal. Biochem.* **1992**, *205*, 115.
(30) Pailer, I. M.; Fenzl, W. *Monatsh. Chem.* **1961**, *92*, 1294–1299.
(31) Kliegel, W. *Organomet. Chem. Rev.* **1972**, *A8*, 153–181.
(32) Musgrave, O. C.; Park, T. O. *Chem. Ind. (London)* **1955**, 1552.

0003-2700/92/0364-2846$03.00/0

molecules has been a logical step.[26,27,33] Weith and co-workers[26] showed that borate could be covalently bound to various cellulose matrices and used for the column chromatographic separation of nucleic acid components, sugars, and other polyols. Schott and co-workers[27] extended this approach by linking borate to a methacrylic acid backbone which proved to be functional for the complexation with *cis*-diols of ribonucleoside 5′-phosphates, 3′-ribonucleotide-terminated oligodeoxynucleotides, and tRNAs. Since binding and dissociation of the active components was both pH- and salt-concentration-dependent, a simple and effective chromatographic technique for the separation of tRNA from aminoacyl–tRNA resulted. On the basis of the success of borate complexation with the *cis*-diols of nucleosides, a similar approach was taken with the isolation of catecholic substances.[34] Moyer and co-workers[28] exploited the fact that borate could be linked to get matrices[35] and employed this as part of an initial purification procedure for urinary catecholamines which were quantified by reversed-phase HPLC.

The present study describes the utility of borate as a buffer system for the HPCE separation and analysis of biologically-active molecules containing *cis*-diols from molecules differing only by a single hydroxyl group. These molecules include norepinephrine and its methylated metabolite, chloramphenicol and the diacetyl derivative, cytidine and deoxycytidine, and tyrosine, dopamine, and dopa (dihydroxyphenylalanine).

EXPERIMENTAL SECTION

Materials. Boric acid, borax (sodium tetraborate), norepinephrine, normetanephrine, 1-(4-hydroxy-3-methoxyphenyl)-2-aminoethanol [DL-4-hydroxy-3-methoxy-α-(aminomethyl)benzyl alcohol], diacetylchloramphenicol, tricine [*N*-tris(hydroxymethyl)methylglycine], dopa (3,4-dihydroxyphenylalanine), dopamine, cytidine, and deoxycytidine were obtained from Sigma (St. Louis, MO). Tyrosine and phenylalanine were obtained from Pierce (Rockford, IL). Mesityl oxide, a neutral marker, was part of a Micro-coat protein analysis kit from Applied Biosystems (Foster City, CA). Dimethylformamide (DMF) was purchased from J. T. Baker Chemical Co. (Phillipsburg, NJ). Sodium chloride and sodium sulfate were purchased from Fisher Scientific (Fairlawn, NJ).

Buffer and Sample Preparation. The borate running buffer was made by titrating 25 mM sodium tetraborate with 100 mM boric acid, to pH 8.4. The tricine running buffer (100 mM) was adjusted to pH 8.4 with NaOH. All buffers were made with Milli-Q (Millipore, Bedford, MA) water, and filtered through an 0.2-μm filter (Gelman) before use. All samples were dissolved in the running buffer used and filtered through an 0.22-μm microcentrifuge filter (Millipore, Bedford, MA).

Instrumentation. HPCE was carried out on a Beckman P/ACE System 2050 (Beckman Instruments, Fullerton, CA), interfaced with an IBM 55SX computer utilizing System Gold software (V. 6.01) for control and data collection. Peak migration times were obtained through the System Gold software.

Capillary Electrophoresis Separation Conditions. New capillaries were conditioned by a 20 column volume rinse with 0.1 M NaOH, water, and finally with running buffer. For a typical analysis, the following method was used: a three-column volume rinse with running buffer, 3-s pressure injection of sample, 3-s pressure injection of neutral marker (mesityl oxide or DMF), separation at 25 kV (constant voltage), a three-column volume wash with 0.1 M NaOH followed by a three-column volume rinse with running buffer. Polyimide-coated, fused-silica capillaries were 50-μm i.d., and either 57 or 47 cm in length (50 and 40 cm, respectively, to the detector). Polarity was such that the inlet was the anode and the outlet was the cathode. The capillary temperature was maintained at 28 °C. Detection was measured by absorbance at 200 nm.

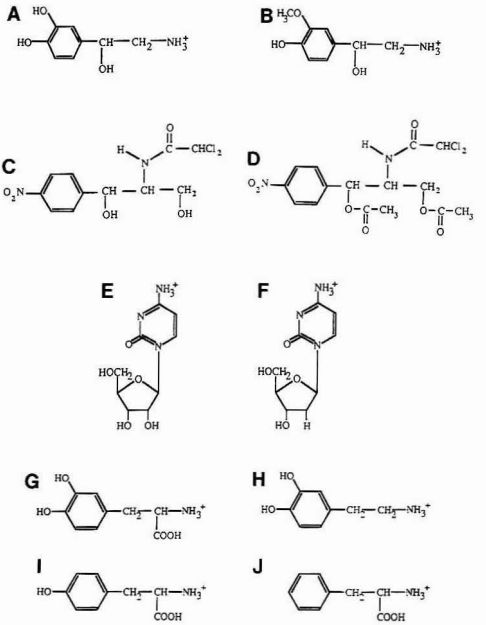

Figure 1. Fully protonated chemical structures: (A) norepinephrine; (B) normetanephrine; (C) chloramphenicol; (D) diacetylchloramphenicol; (E) cytidine; (F) deoxycytidine; (G) dopa; (H) dopamine; (I) tyrosine; (J) phenylalanine.

Equilibrium Studies. Solutions varying in borate concentration were prepared by mixing stock solutions (100 mM) in the correct proportions with tricine solutions (100 or 33 mM). Salt solutions (sodium sulfate and sodium chloride) were made in 100 mM borate and added with the borate solution to maintain ionic strength. Samples were injected in 33 mM tricine.

RESULTS AND DISCUSSION

The utility of borate for the HPCE separation of diol-containing compounds is evaluated in this study with several low molecular weight compounds of biological relevance. The compounds include norepinephrine, and its metabolite normetanephrine, which results from the enzymatic methylation of the hydroxyl group at the meta position; deoxycytidine and cytidine; chloramphenicol, a wide spectrum antibiotic that, in chloramphenicol-resistant strains of bacteria, is enzymatically acetylated to the 1,3-diacetylchloramphenicol metabolite; the amino acids tyrosine and phenylalanine and the enzymatic metabolites 3,4-dihydroxy-L-phenylalanine (L-dopa) and dopamine. The fully protonated form of each of these is given in Figure 1. Inherent in each of these systems is at least one compound containing an intact diol. On the basis of the structure of these molecules and their associated charge at pH 8.4, predictions can be made regarding their migration relative to EOF which is determined by the migration of a neutral marker, mesityl oxide or DMF (Table I). The net positive charge of norepinephrine and normetanephrine at pH 8.4 indicates that they should both migrate ahead of EOF. However, normetanephrine should migrate slower than norepinephrine as a result of its slightly larger mass. Figure 2 shows this to be the case when separation is carried out in 100 mM tricine buffer at pH 8.4 where both are observed to migrate faster than EOF (2.70 min) with

(33) Igloi, G. L.; Kossel, H. *Methods Enzymol.* **1987**, *155*, 433–449.
(34) Higa, S.; Suzuki, T.; Hayashi, A.; et al. *Anal. Biochem.* **1977**, *7* (1), 18–24.
(35) Porath, J. *Methods Enzymol.* **1974**, *34*, 13–35.

Table I. Predicted Migration in the Absence of Borate and the Change in Net Charge Associated with Borate Complexation

analyte	migration vs EOF pH 8.4 (no borate)	net charge at pH 8.4 tricine	borate
norepinephrine	faster	+1	0
normetanephrine	faster	+1	+1
cytidine	equal	0	−1
deoxycytidine	equal	0	0
chloramphenicol	equal	0	−1
diacetylchloramphenicol	equal	0	0
dopa	equal	0	−1
dopamine	faster	+1	0
tyrosine	equal	0	0

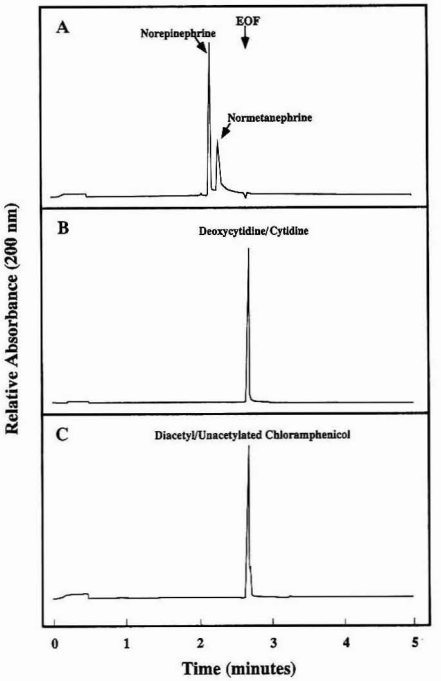

Figure 2. High-performance capillary electrophoretic separation in tricine buffer: (panel A) norepinephrine and normetanephrine; (panel B) cytidine and deoxycytidine; (panel C) chloramphenicol and diacetylchloramphenicol. All stock solutions (≈5 mM in water) were diluted 10-fold in 100 mM tricine buffer, pH 8.4, and pressure injected for 3 s into an uncoated fused-silica capillary of dimensions 57 cm × 50 μm containing 100 mM tricine, pH 8.4. Separation was carried out by applying a constant voltage of 25 kV, 40 μA.

norepinephrine being the fastest migrating species. For both the cytidine/deoxycytidine and chloramphenicol/diacetylchloramphenicol systems, all molecules are uncharged (neutral) at pH 8.4 and, hence, in tricine buffer, they migrate with EOF (figures 2B,C) and are unresolved.

In 100 mM borate buffer at the same pH, the migration patterns change markedly (Figure 3). The separation of norepinephrine and normetanephrine is markedly improved (baseline resolved by 0.6 min) and the order reversed, with norepinephrine migrating slower than both normetanephrine and EOF (Figure 3A). The comigration of the cytidine/deoxycytidine (Figure 2B) and chloramphenicol/diacetyl chloramphenicol (Figure 2C) systems in tricine is contrasted by excellent separation of the paired compounds in borate

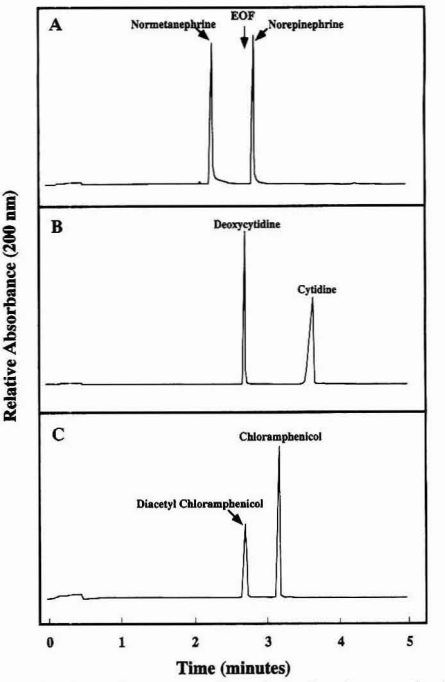

Figure 3. High-performance capillary electrophoretic separation in borate buffer: (panel A) norepinephrine and normetanephrine; (panel B) cytidine and deoxycytidine; (panel C) chloramphenicol and diacetylchloramphenicol. All stock solutions (≈5 mM in water) were diluted 10-fold in 100 mM borate buffer, pH 8.4, and pressure injected for 3 s into an uncoated fused-silica capillary of dimensions 57 cm × 50 μm containing 100 mM borate, pH 8.4. Separation was carried out by applying a constant voltage of 25 kV, 16 μA.

(Figures 3B,C). There is clearly a preferential retardation of the migration of norepinephrine, cytidine, and chloramphenicol, all of which contain a diol moiety in their structure. In contrast, normetanephrine, deoxycytidine, and diacetylchloramphenicol, all of which lack the diol moiety, migrate with a velocity that is seemingly unaltered. It appears that borate is playing a role in the separation through the formation of a borate–*cis*–diol complex with norepinephrine, cytidine, and chloramphenicol. In addition to the slight increase in molecular mass, complexation imparts an additional negative charge to the molecule, due to ionization of one of the free hydroxyl groups of borate ($pK_a = 9.14$; ionic strength 0.1, 20 °C).[36] Complexation results in a change in the charge-to-mass ratio substantial enough to allow for the separation of analytes which are poorly separated (or not separated) under nonborate conditions. Table I outlines the complexation-induced changes in charge associated with each of the analytes in the two buffer systems.

In contrast to the systems described above, separation of a mixture containing tyrosine and its metabolites, dopamine and dopa, was not particularly advantageous in borate buffer (Figure 4). In tricine at pH 8.4, dopamine is positively charged and migrates faster than EOF (mesityl oxide) while both tyrosine and dopa migrate slower than EOF. Dopa appears to be more negatively charged than does tyrosine, probably

(36) Weast, R. C. *Handbook of Chemistry and Physics*, 61st ed.; CRC Press, Boca Raton, FL 1980; p D-167.

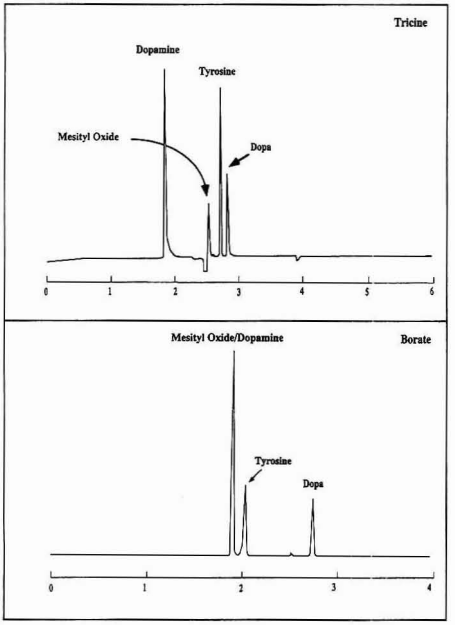

Figure 4. High-performance capillary electrophoretic separation of tyrosine, phenylalanine, dopamine, and dopa. Separation was carried out at pH 8.4 in an uncoated fused-silica capillary of dimensions 57 cm × 50 μm containing either (panel A) 100 mM tricine or (panel B) 100 mM borate. Sample was injected by pressure for 3 s, and constant voltage was applied at 25 kV (42 and 16 μA, respectively). Sample concentrations were ≈0.5 mM for each component.

as a result of ionization of the *p*-OH group, as expected from the pK_a of each compound (pK_a for the *p*-OH: tyrosine, 10.13; dopa, 9.88).[37] In borate buffer at the same pH, the separation of tyrosine and dopa is enhanced, as would be expected from complexation with borate. The corresponding complexation of dopamine with borate negates the positive charge on the amine and results in the comigration of dopamine with EOF. Therefore, while tyrosine–dopa separation is enhanced, the resolution of dopamine and tyrosine is decreased. Interestingly, addition of phenylalanine to this mixture showed that it was not separable from tyrosine under borate and nonborate conditions (data not shown). This differs from the separation of tryptamine from 5-hydroxytryptamine (serotonin) under the same conditions where hydroxytryptamine is found to migrate later than tryptamine and closer to EOF (data not shown). The tryptamine and serotonin separation is probably due to the low pK_a of the hydroxyl group on serotonin.[38] Serotonin is also known to be unstable under basic conditions which may be due to oxidation to a quinone imine structure. Hence, the possibility that the resolved peak is an oxidation product cannot be ruled out.

The nature of the complex between borate and a *cis*-diol has been studied extensively. Recorded studies date back as far as 1842 when Biot[39] showed that addition of sugar to a borate solution led to increased acidity. This observation led to studies which attempted to elucidate the structural aspects of borate in the free and complexed form. Branch and co-workers[40] postulated that, on the basis of the F-strain of bonds, a trigonal phenylboronate could be converted to the tetrahedral phenylborate under alkaline conditions. In 1955, Daniel and Brown showed that, in the borate–diol complex, borate took on a tetrahedral conformation.[41] This was supported by several studies[42,43] which demonstrated that borate was indeed a reactive species and reacted quantitatively with diols in a pH-dependent manner. In studies focused on resolving monosaccharides,[4,5,17] borate has been proposed to interact with the hydroxyl groups of C_3 and C_4 in a tetrahedral configuration, a logical structure based on the fact that boron has a coordination number of 4.[44] A similar complexation of borate, in a tetrahedral configuration, with the C_2–C_3 diol of the ribose ring of cytidine would be predicted. With this structure, and at a pH of 8.4, it is reasonable to expect that at least one of the uncomplexed hydroxyl groups is partially ionized ($pK_a \approx 9.14$), thus imparting a negative charge to the compound with which it is complexed. This explains the decreased migration of the diol-containing compounds in borate but not tricine buffer.

Knowledge of the interaction of borate with diols has resulted in its more recent employment as a buffer for HPCE. Wallingford and Ewing[21] were one of the first to exploit this characteristic for HPCE purposes showing that borate could specifically alter selectivity in the separation of catecholamines in phosphate–SDS–borate micellular electrophoresis. The ability of borate to complex with the diols of sugars has led to its use in the HPCE analysis of saccharides. Borate has been shown to be an important component in the HPCE separation of monosaccharides and oligosaccharides as well as the separation of glycosylated from nonglycosylated peptides.[16] As an extension of the work of Honda and co-workers,[17,18] Novotny and co-workers[4,5] demonstrated that fluorescently-labelled glucosamine and galactosamine, which differ only by orientation of the hydroxyl group on C_4 and hence should not be separable, were baseline resolved in borate but not in a different buffer at the same pH. They suggest that steric differences at this position on the sugar may result in differential complexation of borate with the sugar. This borate-dependent separation of free carbohydrates in solution appears to also be relevant to carbohydrate moieties linked to proteins. We have recently shown that borate may be a key player in the high-resolution separation of proteins with varying carbohydrate structures.[29] Analysis of purified ovalbumin by HPCE results in the resolution of five major and 10–12 minor peaks. This correlates well with the study by Honda and co-workers[18] who have shown that ovalbumin oligosaccharides migrate as five major isoforms by HPCE analysis. Borate has also been shown to be useful in the HPCE separation of neuropeptides,[14] urine constituents,[15] oligosaccharides,[16–18] plant hormones,[19] amino acids,[20] and catechols.[21]

From a chemical equilibria perspective, HPCE shows potential for the analysis of borate complexation with *cis*-diols in equilibrium-driven processes. Unlike the monitoring of the conversion of chloramphenicol to acetylchloramphenicol in an enzyme-catalyzed reaction where the loss of the substrate corresponds stoichiometrically with the appearance of the product,[3] the complexation of borate with a diol-containing structure is governed by equilibria between the complexed and uncomplexed forms. Figure 5 shows that this

(37) Sober, H. A. *CRC Handbook of Biochemistry*, 2nd ed.; Chemical Rubber Co.: Cleveland, OH, 1970; pp B-17 and 18.
(38) Strecher, P. G.; Windholz, M.; Leahy, D. S. *The Merck Index*, 8th ed.; Merck and Co., Inc.: Rahway, NJ, 1968; p 943.
(39) Biot, M. *Compt. Rend. Acad. Sci., Paris* **1842**, *14*, 49–59.
(40) Branch, G. E. K.; Yabroff, D. L.; Bettoman, B. *J. Am. Chem. Soc.* **1934**, *56*, 937–941.
(41) Daniel, M.; Brown, W. C. *J. Am. Chem. Soc.* **1955**, *77*, 3756–3763.
(42) Knoeck, J.; Taylor, J. K. *Anal. Chem.* **1969**, *41*, 1730–1734.
(43) Onak, T. P.; Landesman, H.; Williams, R. E.; Shapiro, I. J. *Phys. Chem.* **1959**, *63*, 1533–1535.
(44) Boeseken, J. *Adv. Carbohydr. Chem.* **1949**, *4*, 189–219.

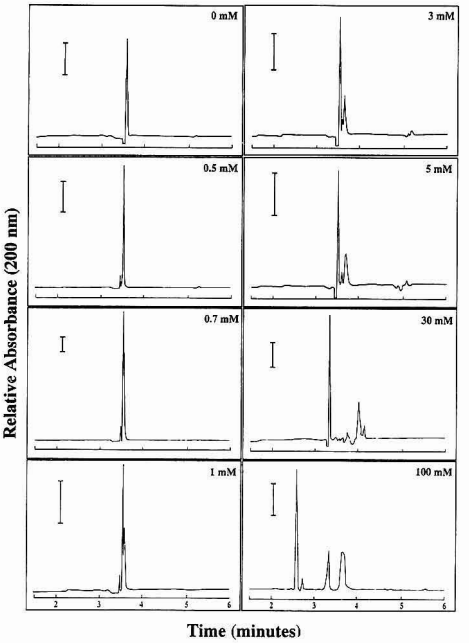

Figure 5. Borate concentration-dependent change in cytidine migration time. Separation was carried out at pH 8.4 in an uncoated fused-silica capillary of dimensions 57 cm × 50 μm containing 100 mM buffer composed of varying combinations of tricine and borate ([borate] given in upper right-hand corner of each profile). Sample (cytidine, 822 μM; deoxycytidine, 873 μM; dissolved in the running buffer) was injected by pressure for 3 s, and constant voltage was applied at 25 kV (40 μA for buffer up to 30 mM borate; 16 μA for 100 mM borate). The bar in the upper left of each panel represents 0.005 AU.

equilibria can be observed in a concentration-dependent manner. Borate-complexed cytidine (≈0.8 mM) begins to resolve from deoxycytidine when the borate concentration in the separating buffer reaches a concentration of ca. 1 mM and is clearly separated from the deoxycytidine at a concentration of 3 mM. Increasing the borate concentration greater than 3 mM results in further retardation of cytidine migration until complete complexation is obtained at a concentration of 100 mM. The identity of the somewhat broader peak migrating later than the cytidine is not known with certainty, although a polyborate–cytidine complex certainly is possible.

Literature describing affinity constants for borate complexation with diols is sparse. Antikainen and Huttunen[45] reported that borate–D(+)-ribose complexation was associated with an equilibrium constant (K_{eq}) on the order of 13 mM (25 °C; ionic strength = 0.1). Knowing that the degree of borate complexation was a function of borate concentration in the running (and sample) buffer, the magnitude of borate complexation was found to be directly reflected in retardation of cytidine migration (as per Figure 5). Plotting the difference in migration time (ΔMT) between deoxycytidine and the borate–cytidine complex against the log of the concentration of borate results in a sigmoidal saturation curve (Figure 6). Interestingly, with this particular data, the concentration of borate at which the borate–cytidine complex has been retarded

(45) Antikainen, P. J.; Huttunen, E. *Suomen Kem.* **1973**, *B46*, 184–190.

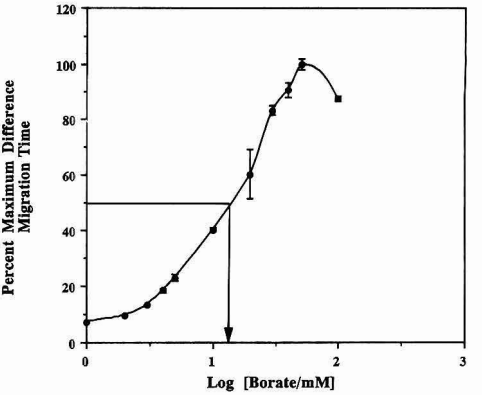

Figure 6. Effect of borate on cytidine migration: semilogarithmic plot of ΔMT versus borate concentration. The *y*-axis represents the absolute difference between cytidine migration time (MT) and that of deoxycytidine (=EOF) in minutes. The line through the points is a computer interpolation of the data, and the error bars represent the standard deviation with three separate experiments.

to 50% of the maximum retardation is found to be 14.4 mM and, thus, represents the K_{eq} for the equilibrium interaction of borate with cytidine. These data were obtained at constant voltage (25 kV) where the current was observed to drop from ca. 42 μA at 40 mM borate (60 mM tricine) to 16 μA with 100 mM borate, probably as a result of the lower ionic strength of borate as a buffer. This accounted for a dramatic shift in the peaks over this range (Figure 5) and the "dip" in the sigmoidal curve in Figure 6. To overcome potential artifacts resulting from borate-concentration-dependent changes in current, several approaches were explored. First, titration of 100 mM tricine with borate was carried out under a constant current of 15 μA. Under these conditions, a maximum voltage of 9.5 kV was reached, resulting in a longer run time (ca. 12 min) and a K_{eq} of 8.4 mM (data not shown). A second approach was to maintain a voltage of 25 kV without exceeding a maximum current of 16 μA. This was done by titrating 33 mM tricine with borate and gave a K_{eq} of 18 mM (data not shown). A final approach was to increase the ionic strength of the borate solution by addition of either sodium sulfate (6 mM) or sodium chloride (28 mM) to allow for titration at constant current (43 μA at 25 kV). This yielded K_{eq}'s of 20 and 18 mM, respectively (data not shown). The mean K_{eq} (±sd) for titrations with all of the approaches is 15.8 ± 4.6 mM. This value for the interaction of borate with cytidine is in excellent agreement with the literature value of 13 mM for interaction of borate with ribose.[44]

CONCLUSIONS

It is clear that the advantage of using a borate buffer system in HPCE is not limited to its ability to produce relatively low current at millimolar concentrations. The affinity of borate for complexation with compounds containing a *cis*-diol results in a substantial change in the charge-to-mass ratio of the complexed compound due to the free ionized hydroxyl group of borate that exists at pH 8.4. The complexation is key in the free solution separation of diol-containing molecules from those that would not typically be separable by HPCE with other buffer systems and underscores the sensitivity of HPCE for resolving molecules which differ only slightly in structure and have identical net charge. Finally, the ability to monitor the borate concentration-dependent complexation highlights the possibility that HPCE may provide a unique

approach for studying the equilibrium association of borate with *cis*-diols.

ACKNOWLEDGMENT

The authors would like to thank Colleen Allen for her excellent clerical assistance and both the Medical Research Council (Canada) and Mayo Medical Ventures for support of this work. We also thank C. Senoff, Department Chemistry and Biochemistry, University of Guelph, Ontario, Canada, for helpful discussions on borate–diol complexes and T. C. Spelsberg for his encouragement and facilities to conduct these studies.

RECEIVED for review May 13, 1992. Accepted August 24, 1992.

Large-Volume Injection in Capillary Supercritical Fluid Chromatography

Robert M. Campbell,* Hernan J. Cortes, and L. Shayne Green

The Dow Chemical Company, Analytical Sciences, 1897A Building, Midland, Michigan 48667

A system was developed to introduce large sample volumes (100 μL or more) into a capillary supercritical fluid chromatograph (SFC). Capillary columns of 50-μm internal diameter (i.d.) were used without a noticeable decrease in chromatographic efficiency and resolution. The sample introduction system consisted of a series of valves which were operated to effect sampling into an inlet column, followed by a solvent elimination step. A SF extraction step was then used to refocus the analytes at the head of the capillary SFC column. Chromatography of the refocused analytes was accomplished with pressure programming of the CO_2 mobile phase. Narrow bands were obtained in the final SFC analytical step for a variety of analytes including alkanes, synthetic triglycerides, polymer additives, and polyglycols in solvents such as methylene chloride, chloroform, acetonitrile, and water. A peak with greater than a ten to one signal to noise ratio was obtained for a 100-μL injection of a 10 parts per billion (ppb) solution of tribehenin (C22:0) using flame ionization detection (FID). Triton X-100 in water was analyzed at the 3 ppm level using a 100-μL injection. Injection reproducibility at 1 ppm for 10-μL injections of Irganox 1076 polymer additive was 0.16% relative, based on the raw peak areas. The large-volume injection system described allowed sensitivity increases of 1000-fold, coupling with liquid chromatography, injection of a large variety of solvents, including water, and a 10-fold improvement in reproducibility.

INTRODUCTION

Capillary supercritical fluid chromatography (SFC) has been used by the analytical community to solve problems, conduct research, and monitor industrial production processes. Many problems which would have been difficult or impossible to approach with conventional chromatographic techniques are readily amenable to capillary SFC. The combination of advantages of high chromatographic efficiency, predictable elution of increasing molecular weight, high inertness, and sensitive, universal detection for organic compounds has made SFC a valuable tool in industry, academia, and government. Compound classes such as polyglycols, polymer additives, waxes, lipids, reactive intermediates including epoxies, peroxides, and isocyanates are frequently easier and better analyzed by capillary SFC with FID than by any other method.[1]

Columns of 50-μm i.d. are needed in capillary SFC to provide high chromatographic efficiency.[1] With these narrow diameters, even small amounts of injected solvent can flood the column, spreading the sample bands and resulting in broadened, distorted peaks. Consequently, injection is usually done in a split mode with injected quantities in the nanoliter range.[1,2] Such small injected volumes limit the sensitivity of the technique to 10–20 parts per million (ppm) using conventional split or timed-split injection for organic compounds detected by flame ionization (FID).

To overcome this sensitivity limitation, a variety of injection techniques for SFC have been investigated in order to allow larger volumes to be introduced into the SFC. These techniques include direct injection using an uncoated inlet,[2,3] solvent venting,[3-5] solvent dilution,[6] density gradient focusing,[7] solvent back-flush,[7] and combinations of these.[8] SFC injection methods have been recently reviewed.[9]

Due to the small injection volumes and split injection mode used in SFC, analytical precision values obtained are seldom better than 3–5% relative, for raw peak areas.[2] Although better precision can be obtained with internal standard methods, the precision obtained in SFC is a significant limitation of the technique.

The development of a large volume injection system for capillary SFC also has utility in the field of multidimensional separations.[10] Systems coupling microcolumn liquid chromatography (LC) to capillary gas chromatography (GC)[11-13] and to conventional LC[14,15] have been demonstrated for a variety of applications. However, a need remains for the capability to separate analytes of interest from a complex matrix in a multidimensional approach where the second dimension is SFC. Other workers have investigated LC–SFC[16-18] and the application of the principles demonstrated in this paper to the on-line coupling of LC to SFC were recently reported.[19]

Several on-line systems have been reported in which samples were SF extracted and the extractables deposited at

* To whom correspondence should be addressed.

(1) Lee, M. L.; Markides, K. E. *Analytical Supercritical Fluid Chromatography and Extraction*; Chromatography Conferences, Inc.: Provo, UT, 1990.

(2) Richter, B. E.; Knowles, D. E.; Anderson, M. R.; Porter, N. L.; Campbell, E. R.; Later, D. W. *HRC & CC, J. High Resolut. Chromatogr. Chromatogr. Commun.* **1988**, *11*, 29.

(3) Berg, B. E.; Greibrokk, T. *HRC & CC, J. High Resolut. Chromatogr. Chromatogr. Commum.* **1989**, *12*, 322.

(4) Ashraf, S.; Bartle, K. D.; Clifford, A. A.; Davies, I. L.; Moulder, R. *Chromatographia* **1990**, *30*, 618.

(5) Koski, I. J.; Markides, K. E.; Lee, M. L. *J. Microcolumn Sep.* **1991**, *3*, 521–529.

(6) Hirata, Y.; Kadota, Y.; Hondo, T. *J. Microcolumn Sep.* **1991**, *3*, 17.

(7) Lee, M. L.; Xu, B.; Huang, E. C.; Djordjevic, N. M.; Chang, H. C.; Markides, K. E. *J. Microcolumn Sep.* **1989**, *1*, 7.

(8) Liu, Z.; Farnsworth, P. B.; Lee, M. L. *J. Microcolumn Sep.* **1991**, *3*, 435.

(9) Koski, I. J.; Lee, M. L. *J. Microcolumn Sep.* **1991**, *3*, 481–90.

(10) Cortes, H. J. In *Multidimensional Chromatography*; Cortes, H. J., Ed.; Marcel Dekker: New York, 1990; pp 251–300.

(11) Cortes, H. J.; Olberding, E. L.; Wetters, J. H. *Anal. Chim. Acta* **1990**, *236*, 173.

(12) Cortes, H. J.; Pfeiffer, C. D.; Richter, B. E. *HRC & CC, J. High Resolut. Chromatogr. Chromatogr. Commun.* **1985**, *8*, 469–474.

(13) Cortes, H. J.; Green, L. S.; Campbell, R. M. *Anal. Chem.* **1991**, *63*, 2719–2724.

(14) Cortes, H. J.; Bormett, G. E.; Graham, J. D. *J. Microcolumn Sep.* **1992**, *4*, 51.

(15) Takeuchi, T.; Assai, U.; Haraguchi, H.; Ishii, D. *J. Chromatogr.* **1990**, *499*, 549.

(16) Lurie, I. S. *LC-GC* **1988**, *6*, 1066.

(17) Moulder, R.; Bartle, K. D.; Clifford, A. A. *Analyst*, **1991**, *116*, 1293–1298.

(18) Hirata, Y. *J. Microcolumn Sep.* **1990**, *2*, 214.

(19) Cortes, H. J.; Campbell, R. M.; Himes, R. P.; Pfeiffer, C. D. *J. Microcolumn Sep.* **1992**, *4*, 239–44.

0003-2700/92/0364-2852$03.00/0

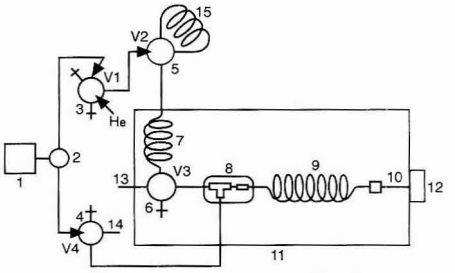

Figure 1. Schematic diagram of the large-volume injection CSFC system: (1) SFC pump; (2) tee; (3) 10-port switching valve; (4) 4-port switching valve; (5) 10-port switching valve; (6) 8-port switching valve; (7) capillary inlet column; (8) SFC interface; (9) capillary SFC column; (10) frit restrictor; (11) GC oven; (12) FID; (13) vent; (14) vent; (15) sample loop.

the head of the SFC column.[20-23] These systems required manually opening the extraction vessels between analyses and were not amenable to automated analysis. Since these systems were designed primarily for solid samples, they did not readily accommodate analyses of liquid samples.

In this report we describe a system which allows introduction of large liquid volumes into capillary SFC which is accomplished through solvent elimination followed by refocusing of the analytes by pressurizing the inlet and depositing the analytes in a narrow band at the head of the SFC column. The large volume injection SFC system described herein yielded high sensitivity and improved reproducibility.

EXPERIMENTAL SECTION

Reagents and Chemicals. The SFC system, including injection steps, was operated with SFE/SFC (FID and ECD) grade CO_2 (Scott Specialty Gases, Plumsteadville, PA) which was further purified by passing it through a charcoal (SKC, Eighty Four, PA) trap, 30-cm × 9-mm i.d., followed by an alumina (Bio-Rad, Richmond, CA) trap, 80-cm × 9-mm i.d., which was heated to 75 °C during pump filling. All solvents were HPLC grade or better (Fisher, Pittsburgh, PA). Methylene chloride was pesticide grade (Burdick and Jackson, Muskegon, MI). Synthetic triglycerides and Triton X-100 were obtained from Sigma Chemical Co., St. Louis, MO. Irganox 1076, 1330, and 1010 were obtained from Ciba-Geigy, Basel, Switzerland.

Instrumentation. The system used is similar to that previously reported.[19] The CSFC injection system consisted of a series of switching valves mounted on a Model 5890 gas chromatograph (Hewlett-Packard, Avondale, PA). A schematic diagram of the system is shown in Figure 1. The carrier fluid, CO_2, was supplied with a syringe pump, 1 (Model 100D, Isco, Lincoln, NE). Valve VI (Model N10WT, Valco, Houston, TX) allowed selection of either helium purge gas or liquid CO_2 and was connected to valve V2 with $^1/_{32}$-in.-o.d. stainless steel tubing. The helium purge gas was supplied at 40 psi, and at this pressure its volumetric flow rate through the inlet column was approximately 2 mL/min. Valve V2 (Model N10WT, Valco, Houston, TX) was equipped with a stainless steel sample loop, 15, of either 10 or 100 μL and was connected to valve V3 (Model C8WE, Valco, Houston, TX) with the sample inlet column, 7. Valve V3, the inlet column, interface, and analytical column were mounted inside the oven. Valves V1, V2, and V4 were located outside the oven. Fill and waste lines were installed in the appropriate ports of valve V2. The inlet column was either a 15-m × 0.15-mm-i.d. fused-silica tube (Polymicro Technologies, Phoenix, AZ) or a 6-m- × 0.28-mm-i.d. Silcosteel tube (Restek, Bellefonte, PA) or a 5-m- × 0.18-mm-i.d. fused-silica column coated with a 0.2-μm film of methylsilicone (Rt_x-1, Restek, Bellefonte, PA). The outlet of this tube was connected to valve V3 which was in turn connected to the SFC column, interface, 8, via a linear restrictor, 30-cm × 20-μm i.d. × 90-μm o.d. (Polymicro Technologies, Phoenix, AZ). A vent tube (20-cm × 250-μm i.d. fused silica, Polymicro) was connected to the port adjacent to the inlet column and a plug was installed in the port adjacent the restrictor. The linear restrictor was inserted through a glass-lined tee (Model SUT/16/005/005, Scientific Glass Engineering, Inc., Austin, TX) and into the interface tube, 20-cm × 100-μm i.d. (deactivated, Dionex/Lee Scientific, Salt Lake City, UT). The third leg of the tee was connected to valve V4 (Model C4W, Valco, Houston, TX) with a stainless steel tube 20-cm × 0.02-in. (508-μm) i.d. The outlet end of the interface tube was connected to the SFC analytical column, 9, 10-m × 50-μm i.d. (SB-PHENYL-5, Dionex/Lee Scientific, Salt Lake City, UT) with a stainless steel butt-connector (MVSU 004, SGE, Austin, TX). The analytical column was equipped with a frit restrictor which was affixed with a pressed-fit connector. The outlet of the analytical column restrictor was installed in the flame ionization detector (FID). Carbon dioxide was supplied to valve V4 via a 40-cm × 0.01-in.-(254-μm) i.d. stainless steel tube. A short fused-silica tube was installed in valve V4 as vent and the other port was plugged.

Data were collected and processed with a computer-based chromatography data system (Access*Chrom, PE Nelson, Cupertino, CA).

Procedure. A sample was injected on the system and analyzed as follows. The loop of valve V2 was filled with sample with a syringe. With valve V1 positioned to select helium, valve V4 positioned to supply CO_2 to the analytical column, and valve V3 in the vent position, valve V2 was switched to put the loop in the helium flow stream. The system was held in this position for a period of time, usually 5 min, sufficient to allow the solvent to evaporate. The oven was held at 100 °C. Valves V4, V3, and V1 were then switched rapidly in succession, in that order. This supplied CO_2 to the inlet column, vented the interface and analytical column, and diverted the outlet of the inlet column from waste to the restrictor and interface. The CO_2 pressure was ramped at 53 atm/minute from 80 to 400 atm and held for a period of time (usually 5 min) in order to transfer the analytes from the inlet column to the interface. The CO_2 was decompressed through the linear restrictor and vented as a gas while the analytes were deposited in the interface. The pump pressure was then decreased to 80 atm, and valves V4, V1, and V3 were switched. This supplied CO_2 to the interface and analytical column and vented the inlet column. The pressure was then ramped at 12.8 atm/min to 400 atm and held for 6 min. The analytes were eluted from the analytical column and detected by the FID.

RESULTS AND DISCUSSION

This injection system was designed to handle volumes ranging from 1 μL to hundreds of microliters. Volumes less than 1 μL can be injected using direct injection with an uncoated inlet. As described in the Experimental Section, the sample was introduced into a capillary inlet where, through the action of helium gas and heat, the solvent was eliminated. A capillary column provides a more efficient separation of analyte from solvent than simple evaporation in a vial under a nitrogen gas stream. The use of this type of inlet system allows the application of all the solvent removal and analyte retention mechanisms which have been used in large-volume injection in GC[10] to injection in SFC.

During the solvent elimination step, the solutes are spread over a wide band in the inlet column due to flooding of the column by the large amount of solvent. The solutes must be refocused into a narrow band prior to chromatography on the narrow-bore CSFC column. This was accomplished by fully exploiting the properties of CO_2 as a supercritical fluid. The analytes deposited on the walls of the inlet were dissolved in

(20) Jackson, W. P.; Markides, K. E.; Lee, M. L. *HRC & CC, J. High Resolut. Chromatogr. Chromatogr. Commun.* **1986**, *9*, 213.
(21) Anderson, M. R.; Swanson, J. T.; Porter, N. L.; Richter, B. E. *J. Chromatogr. Sci.* **1989**, *27*, 371.
(22) Xie, L. Q.; Markides, M. L.; Lee, M. L. *J. Chromatogr. Sci.* **1989**, *27*, 365.
(23) Koski, I. J.; Jansson, B. A.; Markides, K. E.; Lee, M. L. *J. Pharmaceut. Biomed. Anal.* **1991**, *9*, 281–290.

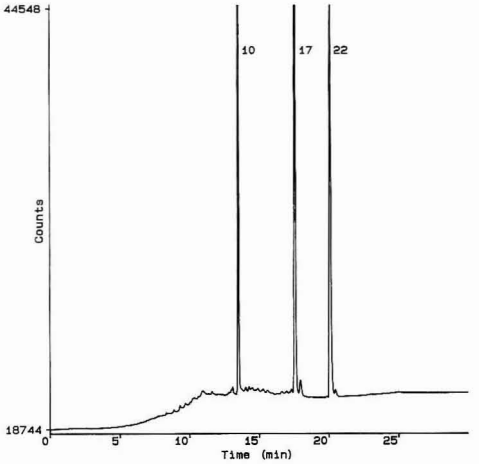

Figure 2. LVI/CSFC chromatogram of synthetic triglycerides: (10) tridecanoin (C10:0); (17) triheptadecanoin (C17:0); (22) tribehenin (C22:0). Conditions: injection volume, 10 μL; concentration, 1 μg/mL; solvent, chloroform. Inlet column, 15-m × 150-μm i.d. fused silica; oven temperature, 100 °C; inlet He purge time, 5 min; inlet pressure program, 80–400 atm at 53 atm/min, 6-min hold. Conditions for analytical column: 10-m × 50-μm i.d., 5% phenylmethylsilicone, 0.25-μm film thickness; oven temperature, 100 °C; pressure program, 80–400 atm at 12.8 atm/min, 6-min final hold; detection, FID.

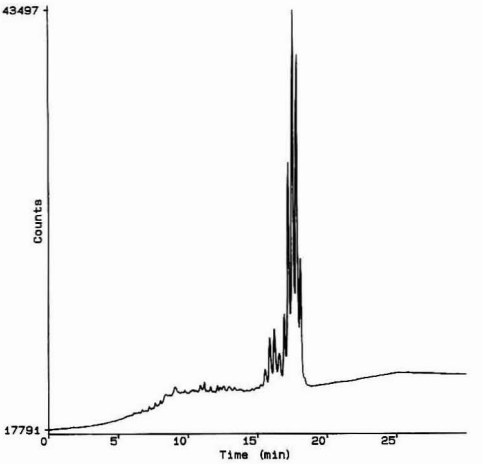

Figure 3. LVI/CSFC chromatogram of pentaerythritol tetrastearate (PETS). Conditions: injection volume, 10 μL; concentration, 5 μg/mL; solvent, chloroform; inlet column, 6-m × 0.29-mm i.d. Silcosteel; inlet pressure program final time, 8 min. Other conditions are as in Figure 2.

supercritical CO_2, transported through a restrictor, and deposited in the interface. The CO_2 decompressed through the restrictor and changed phase from a high-density, supercritical fluid to a low-density gas. Since the analytes were not soluble in the low-density, gaseous CO_2, they deposited in a narrow band at the outlet of the restrictor. It is important that the dead volume in the interface be minimized in order to prevent band broadening prior to the SFC analytical step which was accomplished using a 100-μm-i.d. interface tube with a 90-μm-o.d. restrictor tube.

In early experiments, a large background was seen in the chromatograms.[19] This problem was alleviated by using a better grade of CO_2, careful cleaning of the system components, and the use of heated traps during pump filling, as described in the Experimental Section. It was important to use a low pump filling rate (1–2 mL/min) to obtain clean CO_2 in this system. The heated trap caused the CO_2 to expand to a low density at this pressure, and the impurities were then no longer soluble in the fluid and deposited on the packed bed. If the filling rate was too high, the heater capacity was exceeded and impure liquid CO_2 flowed into the pump, resulting in high backgrounds.

A typical chromatogram obtained using the described system is shown in Figure 2. The chromatogram represents a 10-μL injection of synthetic triglycerides, tridecanoin (C10:0), triheptadecanoin (C17:0), and tribehenin (C22:0) dissolved in chloroform at the 1 μg/mL level (ppm). Although actual column efficiencies could not be measured due to pressure programming, peak widths obtained were equivalent to those obtained with conventional split or timed-split injection. Another measure of the injection performance is resolution of closely related isomers. A chromatogram of pentaerythritol tetrastearate (PETS) polymer additive is shown in Figure 3. Resolution of the PETS isomers in this 10-μL injection of a 5 ppm solution was as good as that obtained using conventional split injection under similar chromatographic conditions.

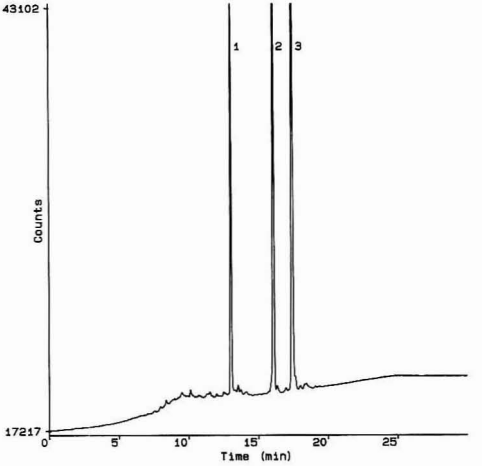

Figure 4. LVI/CSFC chromatogram of Irganox 1076 (1), 1330 (2), and 1010 (3). Conditions: injection volume, 10 μL; concentration, 1 μg/mL except Irganox 1010 which was 2 μg/mL; solvent, chloroform. Other conditions are as in Figure 2.

The injection system was also applicable to compounds of intermediate polarity. Figure 4 shows the SF chromatogram of a 10-μL injection of hindered phenol polymer additives. Irganox 1076 and 1330 were injected at a concentration of 1 ppm, while Irganox 1010 was at the 2 ppm level. Resolution and peak shape were equivalent to those obtained with conventional injection typically restricted to much higher concentration levels (100–200 ppm). The capability to analyze dilute solutions of polymer additives is important since many of the additives are found in polymers at trace levels.

A 10-μL injection of Triton X-100 polyglycol at the 30 ppm level in chloroform is presented in Figure 5. This was injected at a level which is much lower than the percent levels which are usually necessary in split injection. Although the pressure

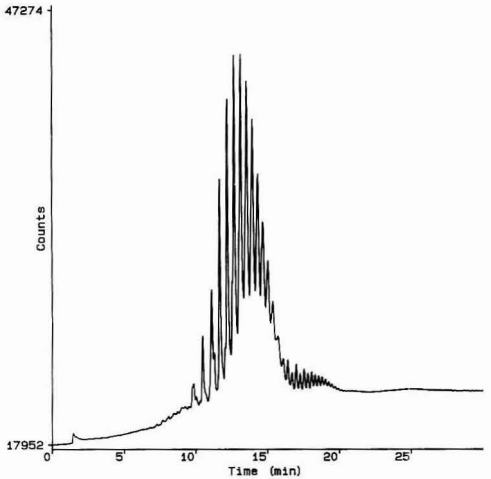

Figure 5. LVI/CSFC chromatogram of Triton X-100. Conditions: injection volume, 10 μL; concentration, 30 μg/mL; solvent, chloroform; inlet column, 6-m × 0.28-mm i.d. Silcosteel; inlet pressure program final time, 10 min. Other conditions are as in Figure 2.

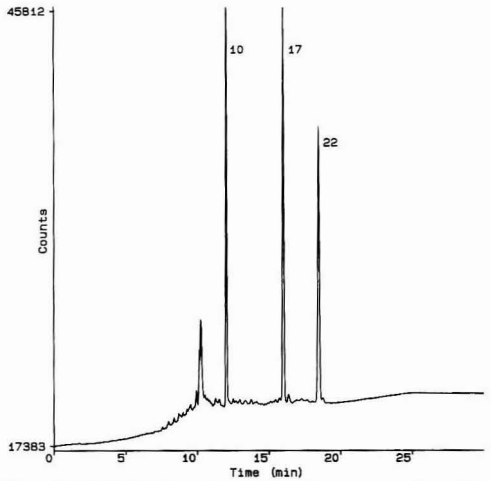

Figure 6. LVI/CSFC chromatogram of synthetic triglycerides: tridecanoin (10); triheptadecanoin (17); tribehenin (22). Conditions: injection volume, 100 μL; concentration, 0.1 μg/mL; solvent, methylene chloride; inlet He purge time, 20 min; inlet pressure program final time, 10 min. Other conditions are as in Figure 2.

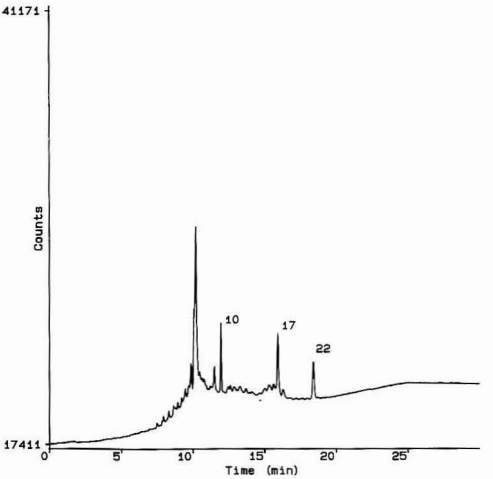

Figure 7. LVI/CSFC chromatogram of synthetic triglycerides. Conditions: concentration, 0.01 μg/mL (10 ppb). Other conditions are as in Figure 6.

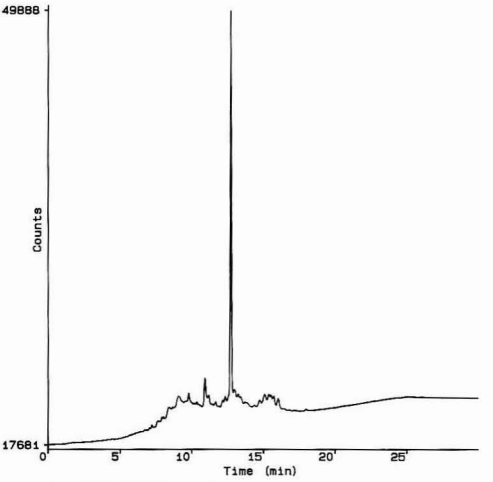

Figure 8. LVI/CSFC chromatogram of Irganox 1076. Conditions: injection volume, 10 μL; concentration, 1 μg/mL; solvent, water with 0.2% (w:w) acetic acid; inlet column, 5-m × 0.18-mm i.d. methylsilicone capillary, 0.2-μm film; inlet He purge time, 10 min; inlet pressure program final time, 18 min. Other conditions are as in Figure 2.

program was not optimized here for resolution of all the isomers, peak shapes are not significantly worse in width or symmetry than what is seen in conventional split injection SFC. Further optimization of the pressure program and other column/inlet conditions will likely result in improved resolution for this material. This demonstrates the applicability of the large-volume injection system to polyglycols.

Injection volumes much larger than 10 μL were also possible with this system, making trace analysis a reality for capillary SFC. Figure 6 shows a 100-μL injection of the triglycerides in methylene chloride at the 0.1 ppm level. Figure 7 shows the same triglycerides injected at the 10 parts per billion (ppb) level, again with 100 μL injected. The signal to noise level was greater than 10 for tribehenin, suggesting that detection limits of less than 10 ppb are possible. Larger injection volumes may be feasible and it appears that sensitivity with the reported injection technique may only be limited by the background level of impurities in the sample.

In addition to organic solvents, aqueous samples were also introduced into the system. Figure 8 shows the injection of 10 μL of Irganox 1076 in water at the 1 ppm level. A small amount (0.2%) of acetic acid was added to the sample to prevent adsorption of the analyte onto the walls of the glass vial and injection syringe. As can be observed, peak shapes obtained were not affected by the type of solvent introduced. Figure 9 represents a chromatogram of a 100-μL injection of triglycerides in water at the 0.1 ppm level, while Figure 10 represents a chromatogram of 100 μL of water containing Triton X-100 polyglycol nonionic surfactant at the 3 ppm

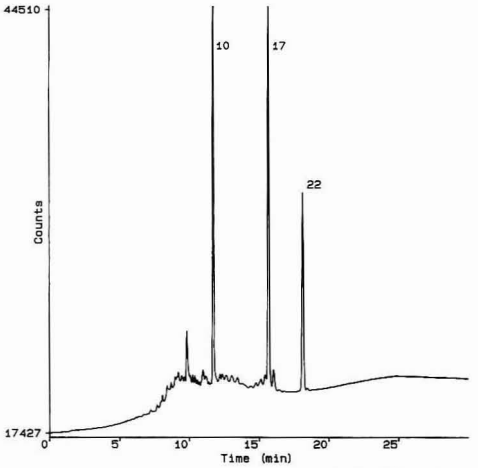

Figure 9. LVI/CSFC chromatogram of synthetic triglycerides. Conditions: injection volume, 100 μL; concentration, 0.1 μg/mL; solvent, water with 0.2% acetic acid. Other conditions are as in Figure 8.

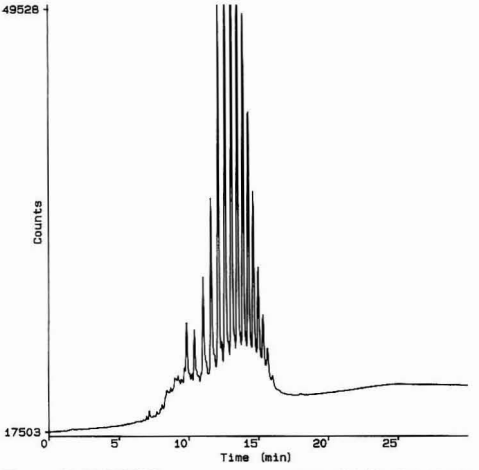

Figure 10. LVI/CSFC chromatogram of Triton X-100. Conditions: injection volume, 100 μL; concentration, 3 μg/mL, solvent, water. Other conditions are as in Figure 8.

level. The results obtained demonstrate the applicability of the technique for the analysis of trace level components in aqueous media. Samples such as process streams, waste streams, or blood plasma, for example, will likely be candidates for analysis using the reported approach.

A coated column was used as the inlet column for the aqueous injections. The separation mechanism employed in the inlet column during aqueous injections was different from that used in the organic solvent injections. In the organic solvent injections, the introduction temperature was above the boiling point of the solvent, and the solvent was evaporated in the uncoated inlet tube and exited as a vapor. The solutes were retained on the basis of differential volatility. In the aqueous case, the sample was forced through an inlet column coated with methyl silicone stationary phase with the temperature below the boiling point of water. The water exited the inlet column as a liquid, rather than a vapor as in the organic solvent case. The organic analytes in the aqueous solution were trapped in the silicone stationary phase through a partitioning mechanism, analogous to open tubular reversed-phase liquid chromatography. The separation between the water solvent and the organic solutes was based on water/silicone partitioning coefficients rather than on volatility.

Table I. Raw Areas and Precision Results for Irganox 1076 and Triheptadecanoin at 1 ppm and 10-μL Injections in Chloroform

	peak area (counts)		
run	Irganox 1076	triheptadecanoin	ratio
1	182 258	184 762	0.9864
2	182 366	183 186	0.9955
3	182 178	186 438	0.9772
4	182 176	185 296	0.9832
5	182 418	185 574	0.9830
6	181 704	186 860	0.9724
7	182 174	185 008	0.9847
8	182 768	186 336	0.9809
av	182 255	185 433	0.9829
% RSD[a]	0.16	0.63	0.69

[a] RSD = relative standard deviation.

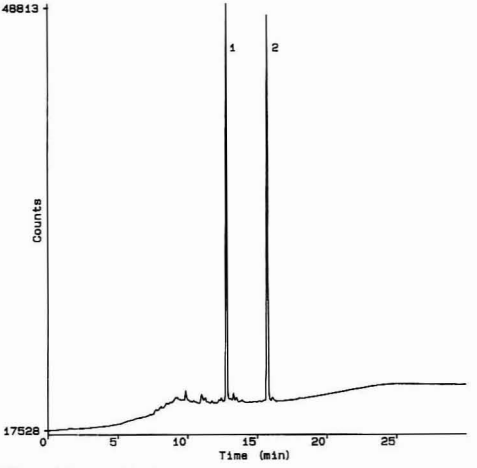

Figure 11. LVI/CSFC chromatogram of Irganox 1076 and triheptadecanoin. Conditions: injection volume, 10 μL; concentration, 1 μg/mL; solvent, chloroform; inlet column, 6-m × 0.28-mm i.d. Silcosteel; inlet pressure program final time, 10 min. Other conditions are as in Figure 2.

One important benefit obtained using the system described is in injection precision. Conventional split injection techniques yield precision values in the range 3–5% RSD for the raw peak areas. Using this large-volume injection, however, much better precision than this was obtained. Table I lists the results of a series of eight 10-μL injections of Irganox 1076 and triheptadecanoin at the 1 ppm level. A representative chromatogram from this series is shown in Figure 11. An RSD value of 0.16% was obtained for Irganox 1076, while triheptadecanoin yielded an RSD value of 0.6%. The results obtained represent a 10-fold increase in injection precision over conventional split and timed split techniques.

It should be noted that the precision values reported here do not necessarily reflect a maximum level of precision possible with this system. As in any technique, the actual precision obtained will be affected by the type of analyte, the matrix, sample type, concentration, analysis conditions, etc. Further

work on the optimization of this system will likely yield even better precision values.

The precision of the peak area ratios as would be used in internal standard methods was about the same as the raw area precision. Since the two compounds used in this case were of different compound classes and did not have closely related retention times, the relative precision obtained is not a good indicator of what will be possible with this injection system.

The same set of valves, including valve V3 in the oven, was used over a period of months for hundreds of injections without leakage or failure. The oven temperature was typically at 100 °C, although some injections were made at 80 or 120 °C.

In this report we have described a large-volume injection system and have shown that it brings four important advances to CSFC injection technology. First, with analyses down to 10 ppb, sensitivity has been improved 1000-fold over conventional split techniques. Second, LC was coupled to CFSC for improved specificity and trace analysis of complex samples.[19] Third, aqueous samples can be injected without prior extraction or prior removal of the water matrix. Fourth, with large-volume injections using a sample loop, a 10-fold improvement of injection precision was realized over conventional split techniques in CSFC. In addition, since the system is operated completely with switching valves, it can be easily automated. With this injection system, the major limitations which have heretofore been associated with CSFC injection were overcome.

ACKNOWLEDGMENT

The authors wish to thank R. P. Himes and C. D. Pfeiffer for helpful discussions and their kindly assistance.

RECEIVED for review June 1, 1992. Accepted September 1, 1992.

Laboratory Evaluation of Polyurethane Foam–Granular Adsorbent Sandwich Cartridges for Collecting Chlorophenols from Air

Gregory W. Patton,[†,‡] Laura L. McConnell,[†,§] Mark T. Zaranski,[†,∥] and Terry F. Bidleman*[,†,⊥,£]

Department of Chemistry, Marine Science Program, and Belle W. Baruch Institute for Marine Biology and Coastal Research, University of South Carolina, Columbia, South Carolina 29208

Adsorbent traps containing 5–6 g of Tenax-GC sandwiched between two 3-cm-thick polyurethane foam (PUF) plugs were used to collect six di- to tetrachlorophenols from 285–380 m³ of analyte-spiked air. Laboratory experiments were conducted by vaporizing known quantities of chlorophenols into a clean airstream for sampling by a General Metal Works PS-1 high-volume air sampler at 20 °C. Chlorophenols were Soxhlet extracted from the adsorbent traps, derivatized with acetic anhydride, and analyzed by gas chromatography using electron capture detection. Collection efficiencies, determined by mass balance of the quantities introduced and recovered, averaged 63–96% for individual compounds, with an overall mean of 83%. The PUF–Tenax traps should be suitable for ambient air sampling at air volumes up to at least 380 m³ with air temperatures ≤20 °C.

INTRODUCTION

Chlorophenols are a group of semivolatile organic compounds that are used as pesticides, bactericides, wood preservatives, and synthetic intermediates. They are also byproducts of the chlorine bleaching process used in pulp and paper mills. Most chlorophenols are on the U.S. Environmental Protection Agency priority pollutant list, and reliable air collection methods are needed for these compounds. Recently, chlorophenols have been investigated as indicator parameters for polychlorinated dibenzodioxins and furans from municipal waste combustion.[1] Little information on chlorophenols in ambient air is available, but measurements in Portland, OR,[2] Windsor, Ontario,[3] and Hamburg, Germany,[4] showed low ng/m³ concentrations.

Vapor pressures of di- through tetrachlorophenols range from about 13 to 0.4 Pa at 20 °C (see Table I) and are similar to those of chlorobenzenes and two-ring aromatic hydrocarbons. Semivolatile organic compounds in this volatility range are poorly collected by high-volume air samplers using polyurethane foam (PUF) alone as an adsorbent. Collection of these semivolatile compounds is greatly improved by using granular adsorbents with higher specific surface areas such as Tenax-GC or XAD-2, either alone[6-8] or sandwiched between two PUF slices.[9,10] We have demonstrated that a high-volume air sampler equipped with PUF–granular adsorbent sandwich cartridges can be used to collect two-ring aromatic hydrocarbons, chlorobenzenes, and hexachlorocyclohexanes (HCHs).[11] The objective of this study was to evaluate PUF–Tenax-GC as a solid-phase adsorbent for high-volume air sampling of chlorophenols.

Table I. Chlorophenol Quantities Used in Collection Experiments

compd	μg	$p_L°$, (Pa) (20 °C)[a]
2,6-DCP	0.35–4.8	8.2
2,4-DCP	0.37–4.8	13.1
3,4-DCP	0.30–5.8	*b*
2,4,5-TCP	0.24–23	4.1
2,4,6-TCP	0.17–3.2	2.6
2,3,4,5-TeCP	0.077–1.7	*b, c*

[a] Reference 5. [b] Value not available. [c] $p_L°$ for 2,3,4,6-TeCP = 0.44 Pa.

EXPERIMENTAL SECTION

Sampling Train and Test Procedures. A description of the apparatus used for collection efficiency studies is given in Zaranski et al.[11] Briefly, a General Metal Works, Inc. PS-1 high-volume sampler was modified by attaching a stainless steel mixing chamber to the top of the filter head assembly. Air entering the mixing chamber was cleaned by passage through a glass-fiber filter followed by an activated charcoal bed. A mixture of chlorophenols (0.077–23 μg each) in 25–50 μL of methanol or hexane was injected into a heated glass port, vaporized, and swept into the clean airstream. The outlet of the mixing chamber led into the PS-1 sampler containing two PUF–granular adsorbent traps, each with 5.8-cm i.d. The sandwich traps were filled with 5–6 g of Tenax-GC (35/60 mesh, Alltech Associates) between two 3-cm-thick PUF slices (density = 0.022 g/cm³, Product No. 3014, Olympic Products Corp., Greensboro, NC). Intact traps were precleaned before use by Soxhlet extraction with 15% ethyl ether in petroleum ether (15% EE/PE) and then dried and stored as previously described.[11]

After injection of test compounds, air was pulled through the mixing chamber at 0.1–0.3 m³/min to sweep the chlorophenols from the mixing chamber into the adsorbent bed. The pressure

† Department of Chemistry, University of South Carolina.
‡ Present address: Battelle, Pacific Northwest Laboratories, P.O. Box 999, Richland, WA 99352.
§ Present address: Agricultural Research Service, U.S. Department of Agriculture, Beltsville, MD 20705.
∥ Present address: TMS, Division of Coast-to-Coast Analytical Services, 7726 Moller Rd., Indianapolis, IN 46268.
⊥ Marine Science Program, University of South Carolina.
£ Present address: Atmospheric Environment Service, 4905 Dufferin St., Downsview, Ontario M3H 5T4, Canada.

(1) Öberg, T.; Bergström, J. *Chemosphere* **1989**, *19*, 337.
(2) Leuenberger, C.; Ligocki, M. P.; Pankow, J. F. *Environ. Sci. Technol.* **1985**, *19*, 1053–1058.
(3) Dann, T. Detroit Incinerator Monitoring Program Data Report #4, PMD-90-8; River Road Environmental Technology Center, Environment Canada Conservation and Protection: Ottawa, 1990; Appendix B-G.
(4) Bruckmann, P.; Kersten, W.; Funcke, W.; Balfanz, E.; König, J.; Theisen, J.; Ball, M.; Päpke, O. *Chemosphere* **1987**, *17*, 2363–2380.
(5) Weast, R. C.; Astle, M. J.; Beyer, W. H. *Handbook of Chemistry and Physics*, 65th ed.; CRC Press: Boca Rotan, FL, 1984; p D-204.
(6) Billings, W. N.; Bidleman, T. F. *Environ. Sci. Technol.* **1980**, *14*, 679–683.
(7) Billings, W. N.; Bidleman, T. F. *Atmos. Environ.* **1983**, *17*, 383–391.
(8) Arey, J.; Atkinson, R.; Zielinska, B.; McElroy, P. A. *Environ. Sci. Technol.* **1989**, *23*, 321–327.
(9) Lewis, R. G.; Jackson, M. D. *Anal. Chem.* **1982**, *54*, 592–595.
(10) Zaranski, M. T.; Bidleman, T. F. *J. Chromatogr.* **1987**, *409*, 235–242.
(11) Zaranski, M. T.; Patton, G. W.; McConnell, L. L.; Bidleman, T. F.; Mulik, J. D. *Anal. Chem.* **1991**, *63*, 1228–1232.

0003-2700/92/0364-2858$03.00/0

drop behind the adsorbent cartridges was measured with the Magnehelic gauge on the PS-1 sampler and related to flow rate using the PS-1 orifice calibrator. Experiments were carried out in a controlled-temperature room at 20 ± 2 °C.

In some experiments, chlorophenols were vaporized from a spiked glass-fiber filter (10-cm diameter) instead of being injected into the mixing chamber. The mixing chamber was removed and the spiked filter was inserted into the standard PS-1 holder in front of the PUF–adsorbent cartridges. The mixing chamber with its prefilter assembly was reattached to scrub laboratory air entering the system.

Seventeen collection experiments were run at air volumes of 285–380 m^3. Sixteen of the runs used duplicate front and back cartridges containing 5–6 g of Tenax between PUF slices, the other run used 10 and 3 g in the front and back traps.

Chlorophenols used were 2,4-dichlorophenol (2,4-DCP), 2,6-DCP, 3,4-DCP, 2,4,5-trichlorophenol (2,4,5-TCP), 2,4,6-TCP, and 2,3,4,5-tetrachlorophenol (2,3,4,5-TeCP). Chlorophenol standards were made from reagent-grade compounds that were purchased from chemical supply houses and used without further purification. The amounts used for collection experiments ranged from 0.077 to 23 μg (Table I).

Analytical Methods. Analytes were extracted from intact adsorbent cartridges using 15% EE-PE in a specially designed Soxhlet apparatus built by the University of South Carolina glass shop. The solvent was concentrated by flash evaporation at room temperature to about 10–20 mL, transferred to graduated centrifuge tubes, and evaporated to 5 mL with nitrogen that had been filtered through Tenax-GC.

Chlorophenols were separated from base–neutral compounds and derivatized for analysis by gas chromatography (GC) using the following procedure, adapted from Chau and Coburn[12] and Abrahamsson and Xie:[13] The sample extract (5 mL) was shaken for 3.0 min with 5.0 mL of 0.1–0.2 M Na_2CO_3 in a 16- × 125-mm culture tube having a polytetrafluoroethylene-linked screw cap. The phases were separated, and the organic layer was saved for the analysis of base–neutral compounds (e.g., chlorobenzenes, HCHs, aromatic hydrocarbons). The aqueous layer was skaken with 2 mL of hexane, and the hexane was added to the base–neutral fraction. A 1-mL aliquot isoocante was added to the tube containing the aqueous phase, 50–200 μL of acetic anhydride was added, and the tube was immediately capped and shaken for 3.0 min. This step (extractive acetylation) derivatized the chlorophenols to their corresponding acetates and extracted them into the organic layer for GC analysis. For each collection experiment, an isooctane solution containing the target chlorophenols was derivatized in the same manner as the sample extracts and used as an external standard.

GC analysis using a ^{63}Ni electron capture detector (GC-ECD) was carried out on Carlo Erba 4160 or Varian 3700 chromatographs. A 25-m bonded phase fused-silica column (polydimethylsiloxane, 5% phenyl) was used for chlorophenol acetate analysis. Samples were injected splitless (Grob technique, 1–2-μL volume, 30-s split time) using the following program: Inject at 65 °C, hold 1.0 min, program at 7 °C/min to a final temperature of 260 °C. Other GC conditions were as follows: carrier gas, H_2 at 30–40 cm/s; injector 240 °C; detector 320 °C. Chromatographic data were collected and processed with a Hewlett-Packard 3390A or Shimadzu Chromatopac CR3A integrator.

RESULTS AND DISCUSSION

Analytical Method and Blank Values for Chlorophenols. To evaluate analyte losses during extraction and evaporative concentration steps, phenols containing 2–4 chlorines were spiked onto Tenax-GC in paper thimbles or PUF–Tenax-GC traps and Soxhlet extracted with 15% EE-PE. The spiked compounds showed recoveries of 83–95% (Table II).

The effect of acidity on chlorophenol acetate yield was evaluated over a pH range of 4.6–9.7. The equilibrium pH (pH of the aqueous phase following the extractive acetylation) was adjusted by changing the concentration of the Na_2CO_3 solution from 0.1 to 1.0 M. A 5-mL aliquot of each Na_2CO_3 solution was spiked with chlorophenols, 1 mL of isooctane, and 100 μL of acetic anhydride. Normalized acetate yields relative to the maximum yield for each compound are shown in Figure 1a. Overall yields of chlorophenol acetates were best at pH 4.6–6.0 and remained above 75% through the entire pH range for 2,4-DCP, 3,4-DCP, and 2,4,5-TCP. A slight reduction to 70% for 2,3,4,5-TeCP yields was observed at pH 9.3–9.7. The production of acetates was greatly reduced at 9.3–9.7 for 2,6-DCP and 2,4,6-TCP. The chlorophenols with substitution in the 2,6-positions were more sensitive to pH effects. In the acetylation reaction both chlorophenol and water compete for the acetic anhydride. For successful derivatization to occur, the acetylation rate must be fast compared to the hydrolysis rate of acetic anhydride. The 2,6-position chlorophenols may be sterically hindered in their ability to react with acetic anhydride. An additional experiment was run using the previous conditions, except that the amount of acetic anhydride was increased to 200 μL. Increasing the acetic anhydride resulted in a lower equilibrium pH for the solutions and a pH range of 4.0–8.3. Normalized acetate yields (Figure 1b) were good throughout the entire pH range with results ranging from 0.74 to 1. The equilibrium pH was 4.5–4.7 for all collection runs.

Table II. Recovery of Chlorophenols from Spiked Adsorbents[a]

	Tenax (3 g) in paper thimbles[b]		PUF–Tenax traps[c]	
compd	quantity (μg)	recovery (% mean ± sd)[d]	quantity (μg)	recovery (% mean + sd)
2,6-DCP	0.51	91 ± 5	0.51–3.1	83 + 14
2,4-DCP	0.48	94 ± 5	0.48–2.9	85 + 20
3,4-DCP	0.97	95 ± 12	0.52–5.9	87 + 18
2,4,6-TCP	0.23	93 ± 2	0.23–1.4	86 + 16
2,4,5-TCP			0.24–18.6	84 + 12
2,3,4,5-TeCP	0.11	93 ± 3	0.11–0.64	84 + 27

[a] 50 – 150 μL of acetic anhydride used. [b] $n = 5$. [c] $n = 9$; except for 2,4,5-TCP where $n = 7$. [d] sd = standard deviation.

Analytical blanks (cleaned and stored adsorbent traps) for PUF–Tenax-GC were <2 ng for the DCPs, 1 ng for 2,4,6-TCP, and <1 ng for 2,3,4,5-TeCP. Blank levels were low relative to the amounts of analytes typically seen in ambient air and remained low even after storage in a freezer for 4 months.

Collection Efficiencies. Ten experiments were performed in which chlorophenols were introduced into the mixing chamber (M experiments in Table III). Average recoveries of 2,4-DCP and 2,6-DCP were 87–96%. Losses were greater for the less volatile 3,4-DCP, 2,4,6-TCP, and especially 2,3,4,5-TeCP (mean = 63% ± 26%). The lower recoveries of the less volatile chlorophenols may have been caused by loss of analytes in the sample inlet and mixing chamber. For one experiment (Table III, 347 m^3), the injection port and mixing chamber were rinsed with PE following the run and the extracts collected were analyzed for chlorophenols. Percentages found in the injection port–mixing chamber were <1% for 2,4-DCP and 2,6-DCP, 6% for 3,4-DCP, 3–5% for 2,4,6-TCP and 2,4,5-TCP, and 30% for 2,3,4,5-TeCP. Because the injection port temperature was not monitored, variations in temperature may explain the low and variable recoveries of chlorophenols in some experiments.

To avoid losses to the inlet system, seven runs were performed in which the chlorophenols were spiked onto a glass-fiber filter in front of the adsorbent traps (F experiments,

(12) Chau, J. S. Y.; Coburn, J. A. *J. Assoc. Off. Anal. Chem.* **1974**, *57*, 389–393.

(13) Abrahamsson, K.; Xie, T. M. *J. Chromatogr.* **1983**, *279*, 199–208.

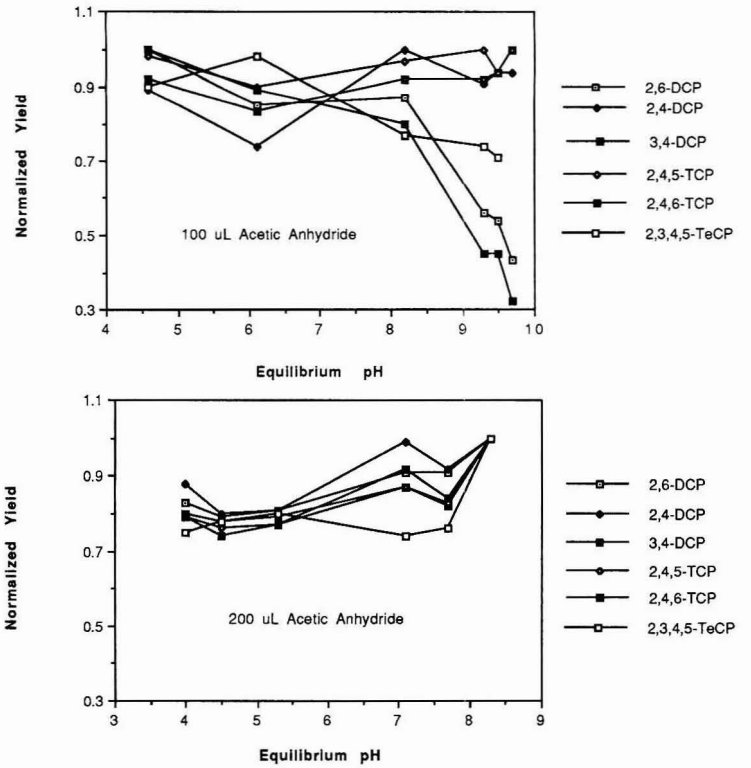

Figure 1. (a, Top) Chlorophenol acetate yield relative to equilibrium pH using 100 μL of acetic anhydride with 0.1–1.0 M Na_2CO_3. (b, Bottom) As in (a) except 200 μL of acetic anhydride.

Table III. Percentage Recovery of Chlorophenols for PUF–Tenax Collection Runs[a]

m^3	spike[b] method	2,6-DCP	2,4-DCP	3,4-DCP	2,4,5-TCP	2,4,6-TCP	2,3,4,5-TeCP
285	M	48	53	55		25	29
314	M	58	66	31		27	18
334	M	109	112	111		89	97
346[c]	M	106	149	116		106	65
347[d]	M	82	74	68	83	82	87
353	M	105	118	100		95	85
358	M	94	109	85		90	66
374	M				87		
374	M	91	87	73	101	79	70
380	M	92	93	66	63	63	53
mean[e]	M	87 ± 21	96 ± 30	78 ± 27	84 ± 16	73 ± 29	63 ± 26
288	F	87	84	86		73	75
289	F	60	55	90	96	83	84
296	F	73	73	92	73	95	71
296	F	98	78	85	69	82[f]	74
318	F	76	69	80	73	94	88
350	F	65	82	107	138[f]	104	90
374	F	88	125	105	87	100	84
mean[e]	F	78 ± 14	81 ± 22	92 ± 10	89 ± 26	90 ± 11	81 ± 7.2

[a] Based on the sum of quantities found in both traps, separate cartridges, Tenax = 5–6 g front, 5–6 g back. [b] Spike method: M = injected into mixing chamber, F = volatilized from a glass-fiber filter. [c] Separate cartridges, Tenax = 10 g front, 3 g back. [d] Includes the amount recovered from rinses of the injection port and mixing chamber. [e] Mean ± standard deviation. [f] Front trap and filter only, contaminant on back trap.

Table III). Collection experiments were then run in the normal fashion, and the spiked filters as well as sorbent traps were analyzed. The F runs showed significantly improved precision (lower variance, F-test, $p < 0.05$) for 3,4-DCP, 2,4,6-TCP, and 2,3,4,5-TeCP. In addition, the F runs yielded higher recovery for 2,3,4,5-TeCP (Mann-Whitney U-test, $p < 0.05$, omitting the mixing chamber rinse experiment).

Analyte migration (breakthrough) beyond the front adsorbent trap was monitored using the back adsorbent trap. Breakthrough was calculated as $100(T_2/T_1)$, where T_2 and T_1

Table IV. Breakthrough of Test Compounds from Front to Back Traps

	$100(T_2/T_1)^a$		
compd	mean	sd	no. of samples
2,6-DCP	8.6	±9.1	14
2,4-DCP	7.0	±6.2	14
3,4-DCP	4.4	±7.1	14
2,4,6-TCP	4.3	±7.2	13
2,4,5-TCP	1.6	±1.8	6
2,3,4,5-TeCP	1.9	±3.1	14

[a] T_1 and T_2 = quantities on front and back traps, respectively.

are the quantities found on the back and front traps, respectively. Mean breakthrough for the chlorophenols ranged from 1.6 to 8.6 and are given in Table IV. The results showed greater breakthrough for the more volatile chlorophenols, but the most volatile compound (2,6-DCP) had a mean breakthrough of only 8.6 ± 9.1. The di- through tetrachlorophenols are effectively retained by PUF–Tenax at air volumes up to at least 380 m^3 at 20 °C. Analyte breakthrough increases with temperature, thus ambient air collection at temperatures higher that 20 °C may need smaller sample volumes or greater quantities of Tenax-GC.

ACKNOWLEDGMENT

Although the research described in this paper has been funded in part by the U.S. Environmental Protection Agency through Contract CR811662, it has not been subjected to Agency review and therefore does not necessarily reflect the views of the Agency, and no official endorsement should be inferred. Additional support for this work was provided by the Battelle Memorial Institute, Columbus Division, under Agreement No. M-3937 (0781)-838. Mention of trade names of commercial products does not constitute endorsement or recommendation for use. Contribution No. 954 of the Belle W. Baruch Institute.

Received for review June 10, 1992. Accepted September 1, 1992.

Analysis of Phosphite Polymer Stabilizers by Laser Desorption/Electron Ionization Fourier Transform Ion Cyclotron Resonance Mass Spectrometry

Xinzhen Xiang,[†] James Dahlgren,[§] William P. Enlow,[§] and Alan G. Marshall*[,†,‡]

Departments of Chemistry and Biochemistry, The Ohio State University, 120 West 18th Avenue, Columbus, Ohio 43210, and General Electric Company, Parkersburg Center, Fifth and Avery Streets, Parkersburg, West Virginia 26102

Detection and quantitation of phosphite antioxidants in polymers is a challenging analytical problem: infrared absorption at realistic antioxidant concentration (250 ppm to 2%) may be obscured by absorption from the polymer itself, and the antioxidant tends to fragment extensively in mass spectrometric analysis. In this work, ULTRANOX 626 diphosphite [bis(2,4-di-*tert*-butylphenyl)pentaerythritol diphosphite] and its corresponding diphosphate oxidation product, XR-2502, as well as the phosphite additive, WESTON 618 diphosphite (distearyl pentaerythritol diphosphite) have been successfully analyzed by Nd:YAG laser desorption 1.064 μ) electron ionization Fourier transform ion cyclotron resonance mass spectrometry (LD/EI/FT/ICR/MS). For each of the isolated additives, the molecular ion (M^+) was observed as the predominant species with virtually no fragmentation. Moreover, abundant molecular ions were detected for ULTRANOX 626 diphosphite in a mixed polymer of poly(ethylene terphthalate), polypropylene, and acrylonitrile–butadiene–styrene at additive concentration as low as 0.1% by direct analysis of the polymer film when the probe was heated to about 200 °C prior to laser desorption. The elevated sample temperature appears to increase the free volume of the polymer, in turn facilitating release of laser desorbed/ionized additives. LD/EI/FT/ICR/MS thus offers a sensitive and accurate means for detecting nonvolatile phosphite additives at typical concentration in solid polymers, without the need for any chemical pretreatment.

INTRODUCTION

As industrial thermoplastics are melt processed, they undergo oxidation reactions leading to changes in molecular weight and color. Phosphite antioxidants[1-4] are generally considered to be secondary antioxidants, and their function is to control polymer molecular weight and color. Phosphite stabilizers are used in most common thermoplastics at levels from 250 ppm to 2%. Typical phosphite loadings are often less than 1000 ppm. Phosphite stabilizers react with hydroperoxides, peroxy radicals, alkoxy radicals, and olefinic and carbonyl moieties; in addition, phosphites form coordination complexes with metals, changing their potential activity.[5,6]

Since the additive level in the polymer affects its stability, the analysis of polymer additives immediately poses two basic analytical questions: first, how much of the additive got into the polymer during compounding; and second, how much of the additive that was added remains as the original phosphite form? Conventional methods for isolation and detection of phosphite additives include extraction/liquid chromatography, X-ray fluorescence, ash/UV analysis, and/or Fourier transform infrared (FT/IR) spectroscopy.[6] However, FT/IR analysis of the intact polymer may be precluded for polymers which themselves have strong infrared absorption. X-ray fluorescence and the ash/UV method suffer from their incapability of differentiating the original phosphite from other forms of phosphorus-containing components which are generated in the stabilization process. Extraction-based analysis may not necessarily give an accurate measure of the additive concentration in the original polymer due to incomplete extraction or reactions due to extraction technique.

Mass spectroscopy has obvious advantages of high sensitivity and selectivity, providing structural information and the prospect of direct detection of the molecular or pseudomolecular [e.g., $(M + H)^+$] ion by various "soft" ionization methods. Laser desorption (LD),[7,8] secondary ion mass spectrometry (SIMS),[9-12] fast atom bombardment (FAB),[13] plasma desorption (PD),[14,15] and electrospray (ESI)[16,17] ionization have been used to detect and identify various nonvolatile compounds in polymers.[18-22] For example, Lat-

* Author to whom correspondence may be addressed.
† Department of Chemistry, The Ohio State University.
‡ Department of Biochemistry, The Ohio State University.
§ General Electric Company.

(1) Schwetlick, K. *Pure Appl. Chem.* **1983**, *55*, 1629–1636.
(2) Schwetlick, K.; König, T.; Rüger, C.; Pionteck, J.; Habicher, W. D. *Polym. Degrad. Stab.* **1986**, *15*, 97–108.
(3) Schwetlick, K.; Pioteck, J.; Koenig, T.; Habicher, W. D. *Eur. Polym. J.* **1987**, *23*, 383–388.
(4) Pobedimskii, D. G.; Kurashov, V. I.; Kirpichnikov, P. A. *J. Polymer Sci.: Polym. Chem. Ed.* **1983**, *21*, 55–66.
(5) Tannahill, M. M.; Enlow, W. P. GE Specialty Chemicals Technical Bulletin. Limitations of Liquid Chromatographic and FTIR Determinations for Ultranox® 626 in Polyolefins; GE Plastics, 1988.
(6) Reeder, M.; Enlow, W.; Borkowski, E. In *Polyolefins VI International Conference*; Society of Plastic Engineers: Houston, TX, 1989; pp F181.
(7) Hillenkamp, F. *Int. J. Mass Spectrom. Ion Phys.* **1982**, *45*, 305–313.
(8) Hillenkamp, F. *Int. J. Mass Spectrom. Ion Processes* **1987**, *78*, 53–68.
(9) Benninghoven, A.; Japers, D.; Sichtermann, W. *Adv. Mass Spectrom.* **1978**, *7B*, 1433–1436.
(10) Lodding, A. R.; Fisher, P. M.; Odelius, H.; Norén, J. G.; Sennerby, L.; Johansson, C. B.; Chabala, J. M.; Levi-Setti, R. *Anal. Chim. Acta* **1990**, *241*, 299–314.
(11) Pauw, D. E. *Mass Spectrom. Rev.* **1986**, *5*, 191–212.
(12) Pachuta, S. J.; Cooks, R. G. *Chem. Rev.* **1987**, *87*, 647–669.
(13) Barber, M.; Bordoli, R. S.; Sedgwick, R. D.; Tyler, A. M. *J. Chem. Soc., Chem. Commun.* **1981**, 325–327.
(14) Torgerson, D. F.; Skowronski, R. P.; Macfarlane, R. D. *Biochem. Biophys. Res. Commun.* **1974**, *60*, 616–621.
(15) Sundqvist, B. U. R.; Macfarlane, R. D. *Mass. Spectrom. Rev.* **1985**, *42*, 421–460.
(16) Whitehouse, C. M.; Dreyer, R. N.; Yamashita, M.; Fenn, J. B. *Anal. Chem.* **1985**, *57*, 675–679.
(17) Fenn, J. B.; Mann, M.; Meng, C. K.; Wong, S. F. *Mass Spectrom. Rev.* **1990**, *9*, 37–70.
(18) Lattimer, R. P.; Harris, R. E. *Mass Spectrom. Rev.* **1985**, *4*, 369–390.
(19) Lattimer, R. P.; Harris, R. E.; Rhee, C. K.; Schulten, H.-R. *Anal. Chem.* **1986**, *58*, 3188–3195.
(20) Hsu, A. T.; Marshall, A. G. *Anal. Chem.* **1988**, *60*, 932–937.
(21) Asamoto, B.; Young, J. R.; Citerin, R. J. *Anal. Chem.* **1990**, *62*, 61–70.

0003-2700/92/0364-2862$03.00/0

timer et al.[18,19] reported the use of mass spectrometry for the analysis of rubber additives by direct rubber analysis and by prior extraction. Hsu et al.[20] applied laser desorption Fourier transform ion cyclotron resonance mass spectrometry (LD/FT/ICR/MS) to identify dyes in poly(methyl methacrylate). More recently, Asamoto et al.[21] and Johlman et al.[22] have analyzed polymer additives by LD/FT/ICR/MS. Although the latter results show that LD/FT/ICR/MS can offer high mass range and highly abundant pseudomolecular ions [usually $(M + K)^+$], mass spectrometry has in general not been notably successful for detecting molecular ions from phosphite additives.

In this work, we focus on the detection of phosphite additives by laser desorption followed by electron ionization (LD/EI/FT/ICR/MS). The mass spectra of the three compounds, ULTRANOX 626 diphosphite, its corresponding diphosphate, XR-2502, and WESTON 618 diphosphite are presented. (ULTRANOX and WESTON are registered trademarks of GE Specialty Chemicals, Inc.) The feasibility of direct analysis of a phosphite additive in a polymer thin film is demonstrated for phosphite additives in polypropylene (PP), poly(ethylene terphthalate) (PET), and acrylonitrile–butadiene–styrene (ABS) polymers.

ULTRANOX® 626 diphosphite (MW 604)

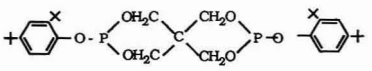

XR - 2502 (MW 636)

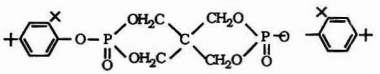

WESTON® 618 diphosphite (MW 732)

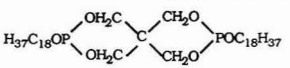

EXPERIMENTAL SECTION

Materials. All samples reported in this work were provided by GE Specialty Chemicals. The preparation of samples of the pure additives was as follows: typically ~20 mg of pure additive was dissolved in 1 mL of methylene chloride and added dropwise to the mass spectrometer probe tip. Subsequent evaporation of the solvent left a uniform thin sample film on the probe tip. Polymer samples were prepared by hot pressing to form a thin film which was then affixed to the probe tip.

Mass Spectrometry. FT/ICR mass spectra were obtained on a standard 3.0 T Extrel 2000 FT/ICR mass spectrometer (Extrel FTMS, Madison, WI) modified with Helix CryoTorr 8 Cryopumps (CTI Corp., MA) in place of the usual diffusion pumps on both the source and analyzer sides of the dual trap. Laser desorption was produced by a Continuum Model YG-660A Nd:YAG laser operated at 1.064 μm, at a power level of ~50 mJ in 10 ns. Details of the mechanical and electronic interface between the mass spectrometer and a Continuum Model YG-660 Nd:YAG are described elsewhere.[23] Since laser irradiation typically produces ~1000-fold excess of neutrals over ions, best results were obtained by ionizing the laser-desorbed neutrals by means of an electron beam (70 eV, 5-ms duration, emission current of 5 μA measured just behind the filament) passing through the ICR ion trap. Creasy[24] has used the same LD/EIFT/ICR/MS technique for the analysis of neutral oligomers. The trapping voltage was typically 2 V. A delay of 3–5 s after ion formation allowed neutrals to be pumped away before excitation/detection. Broadband frequency sweep excitation for 3.8 ms at a sweep rate of 200–400 Hz μs^{-1} was followed by collection of a 16K time-domain transient, digitized in direct-mode at a bandwidth of 2000 kHz, padded with an additional 16K of zeroes, and discrete Fourier transformed (without apodization) followed by magnitude calculation to produce an 8K magnitude-mode FT/ICR mass spectrum.

Scheme I

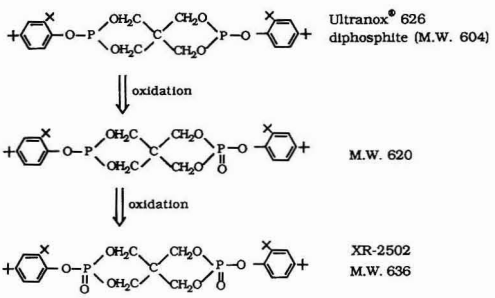

RESULTS AND DISCUSSION

Mass Spectra of Pure Additives. The LD/EI/FT/ICR mass spectrum of the ULTRANOX 626 diphosphite additive is shown in Figure 1a. The molecular ion (M^+) at mass-to-charge (m/z) 604 is the principal ionic species, in contrast to the pseudomolecular ($M + K^+$) ion observed in highest abundance for other kinds of additives[21,22] by LD/FT/ICR/MS (i.e., no electron ionization following laser desorption). By optimizing the laser power (to ~50 mJ in ~10 ns in this case), it is possible to generate abundant molecular ions with virtually no fragmentation; higher laser power induces significant fragmentation.

Scheme I shows the two-stage oxidation of ULTRANOX 626 diphosphite to form the diphosphate compound, XR 2502. The LD/EI/FT/ICR mass spectrum in Figure 1b shows the predominant molecular ion signal (m/z 636) for the diphosphate, XR 2502, along with residual signals from incompletely oxidized phosphite precursor at m/z 620 (half-oxidized monophosphate) and m/z 604 (unoxidized phosphite).

Figure 1c shows the LD/EI/FT/ICR mass spectrum of a second phosphite additive, WESTON 618 diphosphite. Although the molecular ion (m/z 732) is readily observed, its abundance is lower than for ULTRANOX 626 diphosphite or XF 2502, presumably because WESTON 618 diphosphite has saturated C_{18} hydrocarbon chains in place of aromatic rings and therefore fragments more easily. Similar behavior has been reported for other phosphite additives.[21,22]

Phosphite/Phosphate Ratio. Since only the phosphite form of the additive is effective as an antioxidant, it is clearly useful to determine the ratio of phosphite to phosphate, in order to find out how much of the original additive is still in its active (phosphite) form. To that end, Figure 2 shows an LD/EI/FT/ICR mass spectrum of a 1:1 mixture of the phosphite additive, ULTRANOX 626 diphosphite, and its corresponding diphosphate, XR 2502. Since both the diphos-

(22) Johlman, C. L.; Wilkins, C. L.; Hogan, J. D.; Donovan, T. L.; Laude, D. A., Jr.; Youssefi, M.-J. *Anal. Chem.* **1990**, *62*, 1167–1172.

(23) Liang, Z.; Ricca, T. L.; Marshall, A. G. *Rapid Commun. Mass Spectrom.* **1991**, *5*, 132–136.

(24) Creasy, W. R. In *Proceedings of the 38th ASMS Conference on Mass Spectrometry and Allied Topics*; American Society Mass Spectrometry: Tucson, AZ, 1990; pp 850–851.

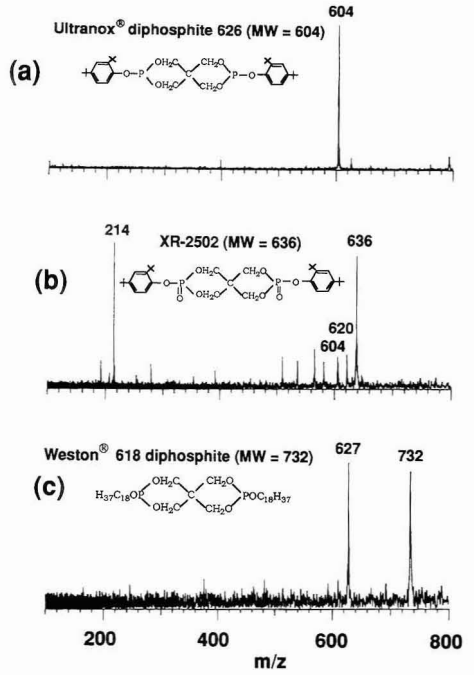

Figure 1. LD/EI/FT/ICR mass spectra of pure additives: (a) ULTRANOX 626 diphosphite; (b) XR 2502; (c) WESTON 618 diphosphite. Note the prominent molecular ion in each case.

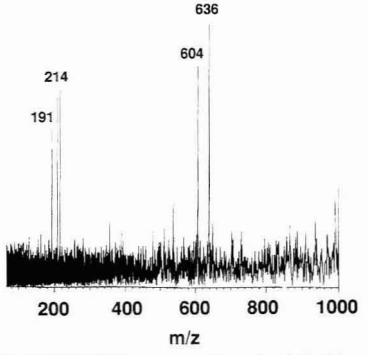

Figure 2. LD/EI/FT/ICR mass spectrum of a 1:1 mixture of the diphosphite additive, ULTRANOX 626 diphosphite, and its corresponding diphosphate, XR2502. Note the comparable abundances of the phosphite and phosphate molecular ions.

phite and diphosphate ions are present in comparable abundance, it appears that the compounds have comparable ionization efficiencies and may thus be quantitated by use of suitable standard mixtures.

Spectra of ULTRANOX 626 Diphosphite in Polymers. Finally, for maximum practical utility, it is important to be able to detect the phosphite additives present in an already cast polymer. For example, Figure 3a shows the LD/EI/FT/ICR mass spectrum of ULTRANOX 626 diphosphite (~0.1% w/w) in polypropylene. Although no fragment ions from the polymer itself are observed under these conditions (due to

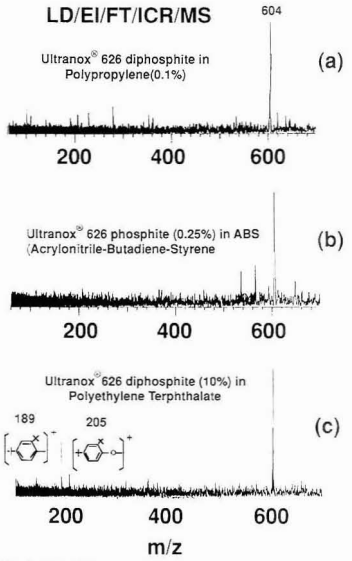

Figure 3. LD/EI/FT/ICR mass spectra of ULTRANOX 626 diphosphite in various solid polymers: (a) 0.1% in polypropylene; (b) 0.25% in acrylonitrile–butadiene–styrene; (c) 10% in polyethylene terphthalate. No pretreatment or extraction was necessary to produce these spectra.

low laser power and high molecular weight of the polymer), molecular ions from the additive in both diphosphite (m/z 604) and diphosphate (m/z 636) form are clearly detectable at ~0.05% each. The signal magnitude increases significantly when the probe is heated to about 200 °C prior to laser desorption. Heating evidently increases the free volume of the polymer to facilitate laser desorption/ionization of the additives. Abundant ions at m/z 191 and 205 correspond to the following fragments:

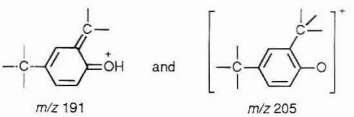

The fragment at m/z 205 is an obvious phosphite bond cleavage product; the other fragment was confirmed to be $C_{13}H_{19}O^+$ (191.143 u) by accurate-mass measurement (191.145 u) by internal calibration against ions of seven m/z ratios from perfluorotri-*n*-butylamine.

LD/EI/FT/ICR mass spectra of the same additive present at higher concentrations in poly(ethylene terphthalate) and acrylonitrile–butadiene–styrene (ABS) polymers are shown in Figures 3b,c. This time, there does not appear to be significant oxidation of the additive, since no signals from the phosphate or diphosphate oxidation products are observed.

Spectra of WESTON 618 Diphosphite in Polymers. Although the LD/EI/FT/ICR mass spectrum of WESTON 618 (5%) in acrylonitrile–butadiene–styrene (ABS) polymer (not shown) did not show a molecular ion, its corresponding oxidation product (m/z 764) was observed, along with several fragment ions.

In summary, the above results clearly show that LD/FT/ICR/MS provides for simple and direct identification of the molecular ions of phosphite additives and their oxidized phosphate forms. Moreover, these additives may be detected

sensitively and accurately in solid polymers without any prior sample pretreatment. Sensitivity (~0.1% additive in solid polymer) is superior to FTIR detection, and is moreover applicable to polymers whose own IR absorption may preclude FT/IR detection of additives.

ACKNOWLEDGMENT

This work was supported by the NSF (CHE-8721498, CHE-90-21498) and The Ohio State University.

RECEIVED for review March 30, 1992. Accepted July 10, 1992.

Registry No. PP (homopolymer), 9003-07-0; PET (SRU), 25038-59-9; ABS (copolymer), 9003-56-9; ultranox 626 diphosphate, 26741-53-7; ultranox 626 diphosphate, 97994-11-1; weston 618 diphosphite, 3806-34-6.

CORRESPONDENCE

Mass Spectrometry of Synthetic Polymers by UV–Matrix-Assisted Laser Desorption/Ionization

Ute Bahr,* Andreas Deppe, Michael Karas, and Franz Hillenkamp

Institut Für Medizinische Physik und Biophysik, Universität Münster, Robert-Kochstr. 31, 4400 Münster, FRG

Ulrich Giessmann

Finnigan MAT, P.O. Box 144062, 2800 Bremen 14, FRG

Mass spectrometry has become a viable technique for characterization of low molecular weight synthetic polymers. The power of this method compared to more classical techniques of polymer analysis is the fast and accurate determination of the absolute molecular weight distribution. Moreover, data on the sequence of repeat units, polymer additives and impurities, and structural information can be obtained.[1] The main barriers for mass spectrometry of high molecular weight compounds, caused by the low volatility and/or thermal lability of those substances, have been overcome to a considerable extent by the development of soft ionization techniques. Secondary ion mass spectrometry (SIMS) in combination with time-of-flight (TOF) mass analyzers has been used for molecular weight determination of polymers in the mass range m/z 500–10 000 Da, mainly from thin films.[2,3] Beside desorption of intact oligomer ions, fragmentation of the polymer chain is observed. Molecular weight distribution of oligomers has also been obtained by field desorption (FD),[4,5] fast atom bombardment,[6] electrohydrodynamic,[7,8] plasma desorption,[9] and electrospray ionization mass spectrometry.[10] Whereas CO_2-laser desorption, combined with either a time-of-flight or a fourier-transform mass analyzer, yields abundant molecular ion peaks for a number of polymers in the mass range up to 10 000 Da,[11,12] UV-laser desorption was limited to polymer masses of 1000–2000 Da.[13,14] The accessible mass range has been considerably extended by the development of the matrix-assisted laser desorption/ionization (MALDI) technique.[15,16] Sample molecules are embedded in small, highly absorbing organic compounds which induce an efficient transfer of the laser-pulse energy to the sample and a soft desorption process. Until now this method has been exclusively used for analysis of biopolymers. Another matrix technique for MALDI has been introduced by Tanaka et al.[17] Using a fine metal powder dispersed in glycerol as the matrix desorption of protein molecular ions as well as of PEG 20000 was achieved. In this short communication, application of MALDI to synthetic polymers is reported. It will be shown that this method is capable of producing mass spectra from a number of different polymers with molecular weights between 1000 and at least 70 000.

EXPERIMENTAL SECTION

Instruments. Two time-of-flight mass spectrometers were used for the analyses. One is a modified LAMMA 1000 laser microprobe instrument (Leybold Heraeus), equipped with a nitrogen laser delivering 3-ns laser pulses at a wavelength of 337 nm (VSL 337 ND, Laser Science Inc.). The laser is focused onto the sample to a spot of about 30-μm diameter. The second instrument is a laser desorption mass spectrometer (Vision 2000, Finnigan MAT, Bremen) equipped with a Nd-YAG-laser with 8-ns pulse length (Spektrum GmbH, Berlin) and a focus diameter on the sample of about 70 μm. The frequency-tripled output of the laser, 355 nm, is used for ion generation. Both instruments are equipped with a reflectron and used for ion detection a secondary electron multiplier (Hamamatsu, R2362) with separate conversion dynodes for postacceleration of the heavy ions. An instrumental mass resolution of up to 3500 (fwhm) (for the Vision 2000) and 500 (for the LAMMA 1000) can be obtained for ions below 5000 Da, provided sample and preparation allow for MALDI under optimal conditions. In the experimental set-up used for these investigations, the mass resolution above 10 000 Da is reduced to values of ≤200 in both instruments due to both electrons and secondary ions yielded after postacceleration of primary ions. Signals are registered by a transient recorder (LeCroy 9400 or 9450, respectively). Spectra shown have been accumulated from typically 30–50 laser shots. For calculation of the average molecular weights, peak intensities were determined using in-house-generated software. The program integrates the area under each peak envelope after drawing a base line between adjacent peak valleys. The integrated peak areas, reflecting the number of ions (N_i) are used with the isotope-averaged molecular weight of the oligomer (M_i) to calculate the number average (M_n) and weight average (M_w) using the following

(1) Smith, C. G.; Nyquist, R. A.; Smith, P. B.; Pasztor, A. J., Jr.; Martin, S. J. *Anal. Chem.* **1991**, *63*, 11R.
(2) Leyen, D. V.; Hagenhoff, B.; Niehuis, E.; Benninghoven, A.; Bletsos, I. V.; Hercules, D. M. *J. Vac. Sci. Technol. A* **1989**, *7*, 1790.
(3) Bletsos, I. V.; Hercules, D. M.; v. Leyen, D.; Hagenhoff, B.; Niehuis, E.; Benninghoven, A. *Anal. Chem.* **1991**, *63*, 1953.
(4) Lattimer, R. P.; Schulten, H.-R. *Int. J. Mass Spectrom. Ion Phys.* **1985**, *67*, 227.
(5) Rollins, K.; Scrivens, J. H.; Taylor, M. J.; Major, H. *Rapid Commun. Mass Spectrom.* **1990**, *4*, 355.
(6) Lattimer, R. P. *Int. J. Mass Spectrom. Ion Processes* **1983**, *55*, 221.
(7) Lai, S.-T.; Chan, K. W. S.; Cook, K. D. *Macromolecules* **1980**, *13*, 953.
(8) Chan, K. W. S.; Cook, K. D. *Org. Mass Spectrom.* **1983**, *18*, 1736.
(9) Feld, H.; Leute, A.; Zurmühlen, R.; Benninghoven, A. *Anal. Chem.* **1991**, *63*, 903.
(10) Wong, S. F.; Meng, C. K.; Fenn, J. B. *J. Phys. Chem.* **1988**, *92*, 546.
(11) Ijames, C. F.; Wilkins, C. L. *J. Am. Chem. Soc.* **1988**, *110*, 2687.
(12) Cotter, R. J.; Honovich, J. P.; Olthoff, J. K.; Lattimer, R. P. *Macromolecules* **1986**, *19*, 2996.
(13) Mattern, D. E.; Hercules, D. M. *Anal. Chem.* **1985**, *57*, 2041.
(14) Holm, R.; Karas, M.; Voigt, H. *Anal. Chem.* **1987**, *59*, 371.
(15) Hillenkamp, F.; Karas, M.; Beavis, R. C.; Chait, B. *Anal. Chem.* **1991**, *63*, 1193A.
(16) Karas, M.; Bahr, U.; Giessmann, U. *Mass Spectrom. Rev.* **1991**, *10*, 335.
(17) Tanaka, K.; Wak, H.; Ido, Y.; Akita, S.; Yoshida, Y.; Yoshida, T. *Rapid Commun. Mass Spectrom* **1988**, *2*, 151.

0003-2700/92/0364-2866$03.00/0

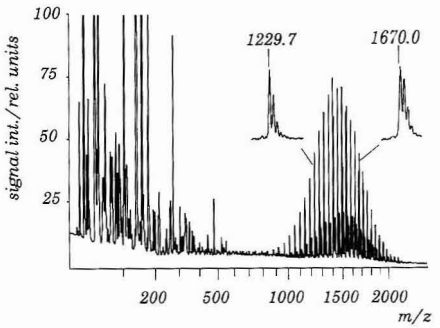

Figure 1. Matrix-LDI spectrum of PEG 1470. Instrument: Vision 2000. Matrix: DHB, 355-mm wavelength.

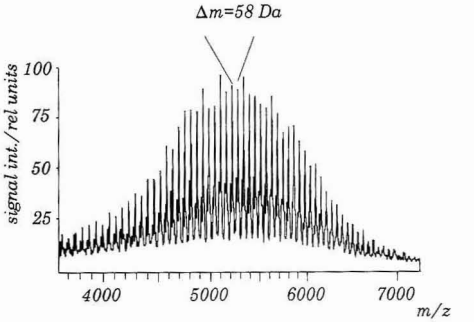

Figure 2. Matrix-LDI spectrum of PPG 5300. Instrument: Vision 2000. Matrix: DHB, 355-nm wavelength.

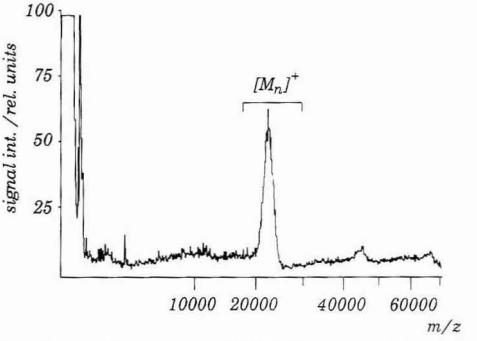

Figure 3. Matrix-LDI spectrum of PEG 23000. Instrument: LAMMA 1000. Matrix: DHB, 337-nm wavelength.

equations:

$$M_n = \Sigma N_i M_i / \Sigma N_i$$

$$M_w = \Sigma N_i M_i^2 / \Sigma N_i M_i$$

For polymer distributions where the single polymers are not resolved, M_n and M_w are determined by numerical integration. Moreover, the maximum (M_p) and the centroid mass (M_c) are determined.

Sample Preparation. All polymers investigated were from commercial sources and used as received. Poly(ethylene glycols) (PEG) PEG-1470, PEG-4250, PEG-7100, PEG-12600, and PEG-23000 were obtained from Boehringer, Mannheim, PEG-35000 from Merck, PEG 40000, Poly(propylene glycol) (PPG) PPG-1150, PPG-5300, polystyrene (PS) 46000 and 70000, poly(methyl methacrylate) (PMMA) 3500 and 7100 from Polymer Standard Service, Mainz, PS-1300, PS-1700, PS-3000, PS-5000, PS-7000, PS-10000, PS 20000 from Machery & Nagel, PS-32660 from Aldrich.

Samples of PEG were dissolved in H_2O, PPG in a mixture of water/ethanol, 1:1 (v/v), and PMMA in acetone, all at a concentration of 5 g/L.

2,5-Dihydroxybenzoic acid was used as a matrix for PEG and PPG analysis at a concentration of 10 g/L in water/ethanol 9:1. A 0.5-μL sample of polymer solution was mixed on a polished silver target with 2 μL of matrix solution and dried in a gentle stream of air. In some cases, 1 μL of alkaline salts solution (LiCl, NaCl, KCl, about 0.1 M) was added to increase the yield of cationized species, or for a more homogeneous cationization.

For PS analysis 5 g/L was dissolved in 2-nitrophenyl octyl ether as matrix, together with 5 g/L silver trifluoroacetate for cationization. Typically 500 ng of polymer were used for a single preparation.

RESULTS AND DISCUSSION

In the positive ion spectra of all polymers investigated, exclusively cation-attached molecular ions of the individual oligomers are observed; no fragmentation occurs. Without addition of alkaline salts, Na^+- and K^+-attached species are recorded; cations presumably stem from salt impurities in the sample or matrix. Addition of small amounts of either NaCl or KCl results in nearly exclusive attachment of Na^+ or K^+, respectively.

A number of PEGs with average molecular weights between 1470 and 35 000 have been examined. Figure 1 shows the mass spectrum of PEG 1470. In the lower mass range only peaks for matrix ions appear. Na^+- and K^+-attached oligomeric molecules, ranging from 900 to 2100 Da reflect the molecular weight distribution. The mass resolution of the instrument (Vision 2000) is sufficient to resolve single isotope peaks. The precision of mass determination using small masses for calibration is 0.01%. Since no fragmentation is observed, an average molecular weight can easily be calculated. The number average molecular weights (M_n) as determined from the peak areas are 1460 for the measurement with the Vision 2000 instrument and 1464 for the LAMMA 1000, which agree well and indicate a good reproducibility. Although mass spectra from PEG distributions up to about m/z 2000 can be obtained by UV laser desorption without matrix, MALDI-MS gives an increase in signal intensity of at least a factor of 10. PEGs above 2000 Da cannot be analyzed without matrix.

Figure 2 shows the MALDI spectrum of PPG 5300 obtained with the Vision 2000 instrument. Only the mass region of the polymer distribution is shown. Oligomer ions from Na^+ and K^+ attachment with the expected mass difference of 58 Da between oligomers are resolved. Again no fragmentation occurs and the low mass range shows only peaks for matrix ions.

Figure 3 shows the mass spectrum of PEG 23000 obtained with the LAMMA 1000 instrument. In this case the resolution is not sufficient to resolve adjecent oligomers with a difference of 44 mass units. The polymer distribution ranges from ca. 20 000 to 25 000 Da which corresponds to a degree of polymerization between ca. 454 and 568. The maximum of the distribution is at 22 930 Da and the centroid mass (M_c) at 22 950 Da. The base-line level in the spectrum is apparently lowered at the high mass side of the polymer distribution. This effect is often observed; a saturation of the detector, caused by the large number of analyte ions, seems unlikely because this effect should then be even more pronounced for the much larger number of low mass ions. Metastable decay which could account for the observed effect and increased signal level at the low mass side cannot be excluded, but seems

Table I. Molecular Weight Averages[a] of Different PEGs and PPGs

polymer	M_n	M_w	M_w/M_n	M_p	M_c	method[b]
PEG 1470	1460	1493	1.02	1468	1494	LD-MS (Vision)
	1464	1507	1.03	1460	1490	LD-MS (LAMMA)
	1382	1443	1.05	1468		GPC/SEC
	1300					VPO
PEG 4250	3957	4018	1.02	4150	4085	LD-MS (LA)
	3958	4059	1.03	4246		GPC/SEC
	4100					VPO
PEG 7100	6655	6865	1.03	7300	7021	LD-MS (Vi)
	6874	7043	1.03	7179		GPC/SEC
	6600					VPO
PEG 12600	12426	12492	1.01	12790	12740	LD-MS (LA)
	11843	12320	1.04	12634		GPC/SEC
	11500					MO
PEG 23000	22115	22190	1.01	22850	22770	LD-MS (LA)
	20040	21228	1.06	22906		GPC/SEC
PEG 35000	36250*[c]	36400*	1.01*	36990*	26980*	LD-MS (LA)
PEG 40000	36842	37039	1.01	37900	37530	LD-MS (LA)
	36500	41500		40000		GPC
		41400				LS
PPG 1150	1047*	1081*	1.03*	1025*		LD-MS (Vi)
PPG 5300	5157	5227	1.01	5280	5240	LD-MS (Vi)

[a] M_w/M_n = polydispersity, M_p = peak molecular weight, M_c = centroid mass. [b] GPC/SEC = gel permeation chromatography/size exclusion chromatography; VPO = vapor pressure osmometry; MO = membrane osmometry; LS = light scattering; LA, Vi = measurement with LAMMA 1000, Vision 2000. [c] Values marked with an asterisk (*) are average values of 4–6 individual measurements.

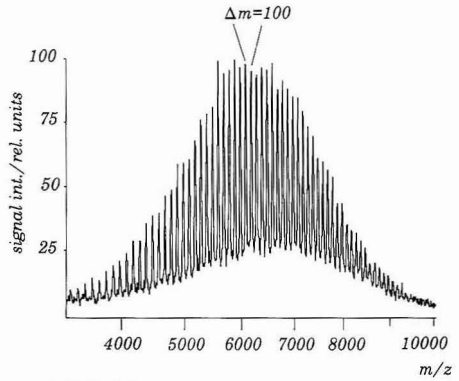

Figure 4. Matrix-LDI spectrum of PMMA 7100. Instrument: Vision 2000. Matrix: DHB, 355-nm wavelength.

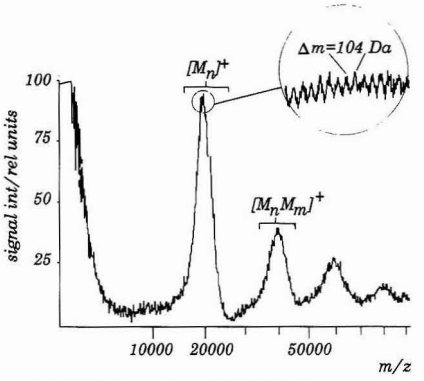

Figure 5. Matrix-LDI spectrum of PS 20000. Instrument: LAMMA 1000. Matrix: 2-nitrophenyl octyl ether, wavelength: 337 nm. Mixed oligomers up to tetramers are observed in the spectrum.

to play a minor role under our conditions because measurements of polymers up to 46 000 Da on a linear time-of-flight instrument gave comparable peak shapes. Moreover, the good agreement of our determined molecular weights with the suppliers values support this assumption. It is more likely that this effect reflects low molecular weight components of the sample.

Table I gives the average molecular weights for the PEGs and PPGs investigated with MALDI together with the values given by the supplier as obtained by different methods. Values marked with asterisk are mean values of 4–6 measurements. They gave a standard deviation of ≤3% for M_n and M_w. The values for M_n and M_p as obtained by MALDI-MS agree quite well with the values specified by the manufacturers and obtained by gel permeation chromatography (GPC) and vapor pressure osmometry (VPO). Deviations are 5–10% for M_n and 2–6% for M_p. The reproducibility and accuracy of MALDI-MS is thus comparable to other mass spectrometric techiques, like TOF-SIMS[3] and FD-MS.[5]

Incorrect results can arise from metastable decay of the high-mass molecules as discussed earlier or from mass discrimination, due to decreasing detection probability with increasing mass. Indeed, a shift of the mean molecular weight toward lower masses has been observed for PS 1300. This effect is due to a decrease in ion–electron conversion with increasing mass at the conversion dynode in front of the secondary electron multiplier. Variation of the postacceleration voltage of the conversion dynode between 3 and 20 kV shows an increase in M_n from 3 to 12 kV of about 10%; above 12 kV it remains constant within the accuracy of the method.[18] Similar observations can be made for other low to medium mass polymers. For the higher mass polymers measured the limited signal even at highest detection potential does not permit such a check. Some discrimination as a function of mass cannot be excluded in these cases. For water-soluble polymers like PEG dihydroxybenzoic acid or other matrices used for MALDI of proteins like sinapinic acid are appropriate matrices. As long as matrix and polymer show a good miscibility in the condensed phase, they can also be used for substances which are insoluble in water, such as PMMA. PMMA 3500 and PMMA 7100 (Figure 4) give good spectra with DHB as matrix. Polystyrenes, mixed with DHB,

(18) Deppe, A., Bahr, U., Hillenkamp, F. Unpublished results.

Table II. Molecular Weight Averages[a] of Different PS Standards

polymer	M_n	M_w	M_w/M_n	M_p	M_c	method
PMMA 3500	3622	3824	1.06	3532	3757	LD-MS (Vi)
PMMA 7100	6395	6583	1.03	6410	6560	LD-MS (Vi)
PS 1300	1440	1528	1.06	1430	1464	LD-MS (Vi)
PS 1700	1883	1957	1.03	1800	1880	LD-MS (Vi)
PS 5000	5184	5302	1.02	5165	5213	LD-MS (Vi)
PS 7000	7048	7152	1.02	7039	7088	LD-MS (Vi)
PS 10000	9750	10294	1.06	10266	9740	LD-MS (LA)
PS 20000	19337	19509	1.01	19740	19650	LD-MS (LA)
PS 32600	33020	33230	1.01	32900	32850	LD-MS (LA)
PS 46000[b]	46760	47319	1.01	47119	46700	LD-MS (LA)
	42000	43500	1.03	46000		GPC
PS 70000[b]	73914	74518	1.01	75000	74250	LD-MS (LA)
	66000	67500	1.03	70000		GPC
		69000				LS

[a] M_w/M_n = polydispersity, M_p = peak molecular weight, M_c = centroid mass. [b] Only these polymers are specified by the manufacturer.

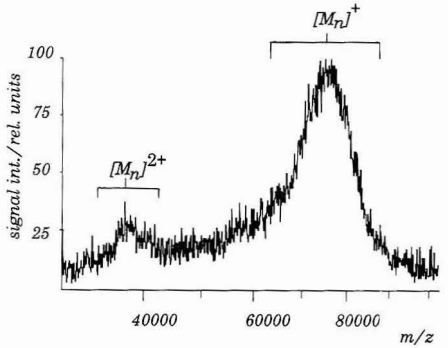

Figure 6. Matrix-LDI spectrum of PS 70000. Instrument: LAMMA 1000. Matrix: 2-nitrophenyl octyl ether, 337-nm wavelength.

on the contrary show a separation of matrix crystals and polymer under microscopic observation. No results can be obtained from such preparations. For polystyrenes, nitrophenyl octyl ether, a highly viscous liquid, was therefore used as matrix. Figure 5 gives a positive ion spectra of silver-cationized polystyrenes PS 20000. In addition to the singly charged oligomers dimer, trimer and tetramer oligomer ion distributions up to 80000 Da are also observed. The mass of the repeat unit (m/z 104) can still be extracted from the spectrum. Table II lists the results of all polystyrenes and PMMAs investigated.

Figure 6 shows the LD spectrum of PS 70000, the largest polymer successfully investigated so far by the authors. The maximum of the distribution is at about 75 000 and the centroid at 74 250; M_n is calculated to 73 914 Da. Although the signal to noise ratio is worse compared to other spectra, the signals can still be evaluated. Good spectra have also been obtained for other polymers such as poly(methyl methacrylate) sodium salts and poly(acrylic acids).

CONCLUSION

The results show that characterization of various polymers with molecular weights up to almost 80 000 can be obtained with good quality by MALDI.

Compared to MALDI of biopolymers where protonated species with molecular weights up to 300 000 are easily produced, the analysis of synthetic polymers causes several problems. The main problem in the MALDI analysis of synthetic polymers, still to be overcome, is the search for optimal matrices. There is good reason to believe that good miscibility of matrix and polymer in the condensed form is the prerequisite for a good matrix, as has been found to be true for protein desorption. Matrices working well for polar biopolymers will not be optimal for nonpolar synthetic polymers. Most of the protein matrices also actively exclude ionic components such as alkali ions, which, however, are needed for the cationization of synthetic polymers. It is not clear at this point if and how the two essential steps in MALDI, the desorption of the large species and their cationization, can both be optimized in one given system. Another limiting factor in the MALDI of synthetic polymers is the wide polymer distribution. Unlike for proteins, the total available charge produced during MALDI will be distributed over a large number of different ions. This may eventually lead to an upper mass limit, at which the single oligomer ion peaks become be indistinguishable from noise. The somewhat higher concentration of the polymers, as compared to that for optimal protein desorption, may already point in this direction.

ACKNOWLEDGMENT

Financial support of the Deutsche Forschungsgemeinschaft and the Bundesministerium für Forschung und Technologie is gratefully acknowledged.

RECEIVED for review April 8, 1992. Accepted August 13, 1992.

Registry No. PEG, 25322-68-3; PPG, 25322-69-4; PMMA, 9011-14-7; PS, 9003-53-6.

Direct Detection of Laser-Induced Capillary Vibration by a Piezoelectric Transducer

Tamao Odake, Takehiko Kitamori, and Tsuguo Sawada*

Department of Industrial Chemistry, Faculty of Engineering, The University of Tokyo, 7-3-1 Hongo, Bunkyo, Tokyo 113, Japan

For its extremely high separation efficiency, with the theoretical plate number presently reaching nearly 10^6, capillary zone electrophoresis (CZE) is a powerful separation method, especially for biological materials.[1-6] The method has another merit that sampling volume can be reduced to less than a nanoliter. This merit can be taken an advantage especially in ultramicroanalysis. However, conventional absorbance detectors are not sensitive enough for such small sampling volumes due to the short optical path. Several highly sensitive spectrometric detection methods have been proposed as on-column methods, including direct[7-11] and indirect laser induced fluorometry[12-14] and a laser-induced photothermal beam deflection method.[15-17] The authors have already proposed another highly sensitive detection method, i.e. capillary vibration induced by laser (CVL), and details of the signal generation and detection mechanisms have been given in the literature.[18,19] The lower limit of detection for this method was an absorbance of about 10^{-5}. While, the detection limit of typical UV–vis absorbance detectors equipped with commercialized CZE instruments is about 10^{-3} in absorbance. Therefore, the CVL method was about 2 orders of magnitude more sensitive than conventional absorbance detectors. The CVL method was applied to a detector for CZE, and underivatized amino acids of femtomole level were detected.[19]

In the previous reports, the capillary vibration was caused by local tension fluctuation of the capillary irradiated by an intensity-modulated excitation laser beam. Analytes in the capillary tube absorbed this laser beam and generated heat periodically according to the photothermal effect, which made the capillary tension fluctuate locally. This vibration emitted an acoustic wave, which was detected by an optical beam deflection (OBD) method.[20] In this case, the probe laser beam passed just above the vibrating capillary and was deflected by the acoustic wave.

As described in this report, the capillary vibration is directly detected by a piezoelectric transducer (PZT). The energy conversion process in this direct detection method does not involve energy transfer from mechanical vibration energy to acoustic wave energy, so this method is expected to be more sensitive than the OBD detection. Furthermore, for PZT detection, alignment of the probe beam is not required. Therefore, the instrumentation of PZT detector is much simpler than that of OBD detector.

EXPERIMENTAL SECTION

The experimental arrangement was almost the same as in the previous report.[18,19] One of the holders which supported the capillary tube (50-μm i.d., 150-μm o.d.) was replaced by a PZT disc (20 mm in diameter, 2 mm thick) as shown in Figure 1. The excitation beam was an argon ion laser beam of 488-nm wavelength and 100-mW output power. The beam intensity was modulated by a light chopper. The beam was focused with a 50-mm focal length lens on the capillary tube, which was tensioned by a hanging weight. The generation mechanism of the capillary vibration was the same as before, and the capillary vibrated like a string between the two supports, one of which was the PZT detector. Mechanical vibration of the capillary was directly detected by the PZT detector. The PZT output was amplified by a 40-dB preamplifier and fed into an autophase lock-in amplifier. The liquid samples were aqueous solutions of sunset yellow dye (absorption peak at 482 nm). The sample concentrations were adjusted by stepwise dilution with distilled water to have absorption coefficients in the range of 1.7×10^{-3} to 1.7×10^{-2} cm^{-1}.

RESULTS AND DISCUSSION

Typical examples of vibration signals obtained from the PZT detector are shown in Figure 2. The samples were distilled water and sunset yellow dye solution of 5.0×10^{-3} cm^{-1} absorption coefficient, which corresponded to absorbance of 2.5×10^{-5} for 50-μm-i.d. capillary tubes. Stable signals were acquired for both samples. These results confirmed the principle of this photothermal detection method of optical absorption, as described in the previous experiments.[18,19] The mechanical energy of vibration of the capillary was directly transferred to the PZT disc and converted into an electrical signal by the piezoelectric effect.

Figure 3 shows frequency characteristics of the signal magnitude. The resonant peak appeared at 604 Hz. The resonance corresponded well with the natural frequency of the capillary calculated[18] from the length of the vibrating part and the applied tension. This resonant peak also verified the string-like vibration of the capillary. Use of this resonance for analytical applications could not be recommended for the following reasons. First, as pointed out previously, the signal-to-noise ratio was not satisfactory at this resonant frequency, because noise induced by mechanical factors occurred at the natural frequencies of the vibration system. Second, the peak was too sharp (the full width of the half maximum was 7.5 Hz), and it was difficult to keep the resonating conditions.

* To whom all correspondence should be addressed.

(1) Cobb, K. A.; Novotny, M. *Anal. Chem.* **1989**, *61*, 2226–2231.
(2) Kennedy, R. T.; Oates, M. D.; Copper, B. R.; Nickerson, B.; Jorgenson, J. W. *Science* **1989**, *246*, 57–63.
(3) Drossman, H.; Luckey, J. A.; Kostichka, A. J.; D'Cunha, J.; Smith, L. M. *Anal. Chem.* **1990**, *62*, 900–903.
(4) Cohen, A. S.; Terabe, S.; Smith, J. A.; Karger, B. L. *Anal. Chem.* **1987**, *59*, 1021–1027.
(5) Ewing, A. G.; Wallingford, R. A.; Olefirowicz, T. M. *Anal. Chem.* **1989**, *61*, 292A–303A.
(6) McCormick, R. M. *Anal. Chem.* **1988**, *60*, 2322–2328.
(7) Cheng, Y.-F.; Dovichi, N. J. *Science* **1988**, *242*, 562–564.
(8) Amankwa, L. N.; Scholl, J.; Kuhr, W. G. *Anal. Chem.* **1990**, *62*, 2189–2193.
(9) Sweedler, J. V.; Shear, J. B.; Fishman, H. A.; Zare, R. N.; Scheller, R. H. *Anal. Chem.* **1991**, *63*, 496–502.
(10) Swerdlow, H.; Zhang, J. Z.; Chen, D. Y.; Harke, H. R.; Grey, R.; Wu, S.; Dovichi, N. J.; Fuller, C. *Anal. Chem.* **1991**, *63*, 2835–2841.
(11) Jorgenson, J. W.; Lukacs, K. D. *Anal. Chem.* **1981**, *53*, 1298–1302.
(12) Kuhr, W. G.; Yeung, E. S. *Anal. Chem.* **1988**, *60*, 1832–1834.
(13) Kuhr, W. G.; Yeung, E. S. *Anal. Chem.* **1988**, *60*, 2642–2646.
(14) Garner, T. W.; Yeung, E. S. *J. Chromatogr.* **1990**, *515*, 639–644.
(15) Yu, M.; Dovichi, N. J. *Anal. Chem.* **1989**, *61*, 37–40.
(16) Bruno, A. E.; Paulus, A.; Bornhop, D. J. *Appl. Spectrosc.* **1991**, *45*, 462–467.
(17) Bornhop, D. J.; Dovichi, N. J. *Anal. Chem.* **1987**, *59*, 1632–1636.
(18) Wu, J.; Kitamori, T.; Sawada, T. *Anal. Chem.* **1990**, *62*, 1676–1678.
(19) Wu, J.; Odake, T.; Kitamori, T.; Sawada, T. *Anal. Chem.* **1991**, *63*, 2216–2218.
(20) Murphy, J. C.; Aamodt, L. C. *J. Appl. Phys.* **1980**, *51*, 4580–4588.

0003-2700/92/0364-2870$03.00/0

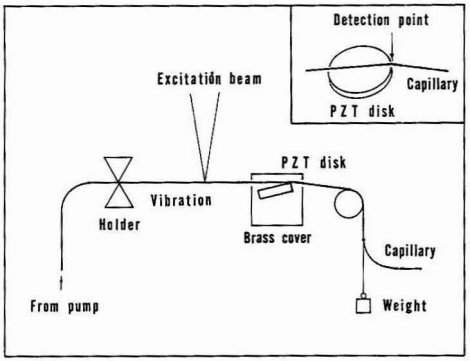

Figure 1. Experimental arrangement of the direct detection system for CVL with a PZT detector. Insert: enlargement of the detector.

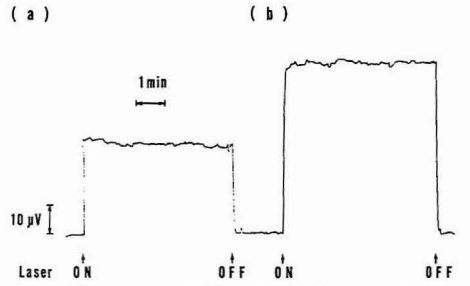

Figure 2. Typical examples of signals. (a) Distilled water, and (b) sunset yellow dye solution of 2.5×10^{-5} absorbance.

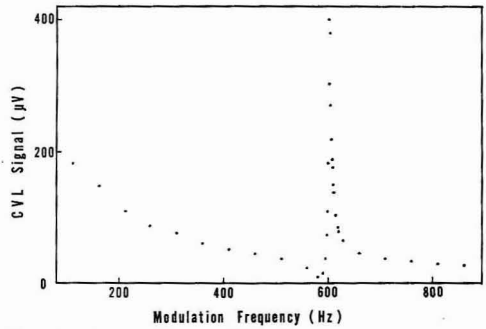

Figure 3. Frequency characteristics of the signal magnitudes.

Therefore, a nonresonant frequency at 710 Hz was used in the following experiments.

The dependence of signal magnitudes on dye concentration was measured. For 50-μm-i.d. capillary, absorbances of the prepared samples corresponded to 8.4×10^{-6} to 8.4×10^{-5} absorbance. The signal magnitudes showed linearities for absorbances of the sample as often occurs with the photothermal effect (correlation coefficient was 0.99), because

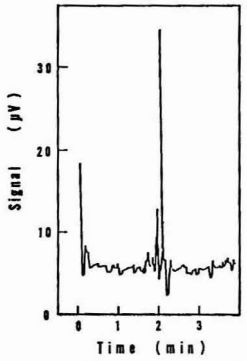

Figure 4. Electropherogram of riboflavin obtained with the CVL method. Separation voltage was 20 kV.

absorbances of the samples were sufficiently low. The detection limit (S/N = 2) of absorbance was calculated as 8.5×10^{-7} for the 50-μm capillary. For sunset yellow dye solution, the lower limit of detection for concentration was calculated to be 6.8×10^{-9} M. Considering the optical sampling volume estimated to be 1.0×10 L, the detection limit of absolute amount was 6.8×10^{-20} mol. Considering that the detection limit reported previously in the OBD method was 1.5×10^{-5} for the same capillary, the PZT detection was proved to be at least 1 order of magnitude more sensitive than the OBD method.

Comparing the energy conversion process of the two detection methods of CVL, energy loss in the PZT detection process is smaller. Energy conversions from optical to thermal and to mechanic energy of vibration by the photothermal effect are common for both methods. However, the mechanical energy is directly converted to electric energy in the PZT detection, while there are two processes before the final conversion for the OBD detector, i.e. acoustic emission of vibrations and interaction between the acoustic wave and the probe beam. Therefore, the total energy loss in the PZT detecting process is considered to be smaller than for OBD detection, and this results in superior sensitivity.

As the PZT detector is very sensitive to any electric field because it is electrically equivalent to the combination of a capacitor and a resistor, poor base-line stability and noise due to the separation current and electrophoresis potential are possible. However, for the experimental results (Figure 4) from applying this method as a CZE detector, no serious effect from the separation current was observed. In this experiment the sample was riboflavin (200–300 fmol) and the separation conditions were the same as in the previous report.[19] In addition to the superior sensitivity, the direct detection method does not need optical alignment for probing. This results in favorable reproducibility and simpler instrumentation.

RECEIVED for review May 15, 1992. Accepted August 24, 1992.

Registry No. Sunset yellow, 2783-94-0; riboflavin, 83-88-5.

TECHNICAL NOTES

Protein-Based Capillary Affinity Gel Electrophoresis for the Separation of Optical Isomers

Staffan Birnbaum† and Staffan Nilsson*

Department of Pure and Applied Biochemistry and Department of Technical Analytical Chemistry, P.O. Box 124, University of Lund, Lund S-22100, Sweden

INTRODUCTION

Chiral separation and synthesis are currently of utmost concern, particularly for the preparation and analysis of pharmaceutical compounds. Biological receptors, often the targets of these compounds, discriminate between the enantiomers and thus the optical isomers of a racemic drug will often exhibit completely different pharmacological effects. Methods for chiral separation and analysis include liquid (LC), gas (GC) as well as supercritical fluid (SFC) chromatography in which the chiral selector has either been used in conjunction with the mobile or stationary phase. Among the various chiral stationary phases (CSP) investigated, immobilized protein phases such as ovomucoid, α-acid glycoprotein, as well as bovine serum albumin (BSA) and its proteolytic peptide fragment have been used.[1-4] The efficiency of the BSA-based LC methods has, however, been relatively poor.[5] In addition, the large size of the protein chiral selector limits the capacity of the stationary phase.

Capillary electrophoresis (CE) is a technique which has developed considerably during the past years.[6-8] CE distinguishes itself from other liquid-phase separation methods in that extremely high efficiency is obtained. Furthermore, CE can be viewed as a microanalytical procedure and is advantageous when, for example, the availability of sample, mobile phase, or separation phase are limited.

In order to circumvent the low efficiency displayed by protein-based liquid chromatography separation of enantiomers, we have investigated CE as a means of achieving enhanced theoretical plate number characteristics for protein-based chiral separation. Though we solely report here the use of BSA as chiral selector, we are firmly convinced that the method is generally applicable for other protein-based affinity separations using capillary electrophoresis. In addition, the method used here to prepare the separation phase involves no inert carrier support; only the chiral selector BSA cross-linked with glutaraldehyde is employed, thus maximizing the potential capacity of the separation phase.

In this note, we describe the preparation, utilization, and performance characteristics of high-performance electrophoresis performed in capillaries filled with gels consisting of BSA cross-linked with glutaraldehyde for the separation of tryptophan enantiomers. The methodological description significantly extends the application area of CE to separation methods based on affinity interactions, exemplified here by the optical resolution of D- and L-tryptophan on immobilized BSA as the separation phase. We term this method as capillary affinity gel electrophoresis (CAGE). Electrophoretic separation methods based on ligands included in polyacrylamide gel-filled capillaries have been reported for enantiomeric separation of dansylated amino acids as well as for DNA restriction fragment separations.[9,10]

EXPERIMENTAL SECTION

Apparatus. During these studies, a Waters Quanta 4000 capillary electrophoresis instrument (Millipore Inc., Bedford, MA) was employed. Analytes were detected on-column at a wavelength of 214 nm. The temperature was 25 °C. The electropherograms were recorded and stored on a NEC personal computer with the MAXIMA 825 software program (Millipore Inc., Bedford, MA).

Procedure. A detection window was prepared on the polyimide-clad fused-silica capillary tubing (75 μm × 40 cm, Polymicro Technologies Inc., Phoenix, AZ) 7 cm from one end of the capillary by quickly flaming an approximately 1-cm portion of the tubing. A typical preparation of the BSA-filled capillary was done as follows and is summarized in Figure 1. The capillary was washed with 10 mL each of water, 0.5 M NaOH, water, and finally 0.05 M potassium phosphate/acetate buffer pH 5.0 with a peristaltic pump. Five pars 5% (w/v) BSA in 0.05 M phosphate/acetate, pH 5.0, was mixed with two parts 25% (v/v) glutaraldehyde and eight parts 0.05 M phosphate/acetate buffer, pH 5.0. The mixture was immediately pumped (circa 10 μL/min) into the buffer-filled capillary from the injection end of the capillary. The capillary was disconnected from the peristaltic pump when the BSA/glutaraldehyde mixture had reached approximately 2 mm from the detection window. The capillary ends were then held level until after gelation (usually circa 10 min). Thus, the detection window region of the capillary contained phosphate/acetate buffer and not BSA gel.

The gel-filled capillary was subsequently preconditioned by exposing the capillary to a potential of 2 kV overnight with the cathode at the injection side and the anode at the detection side of the capillary in 50 mM potassium phosphate buffer, pH 7.5. Electrophoresis of samples was subsequently performed (6 kV) with the capillary in reverse direction to that used during preconditioning. Samples were electrokinetically introduced (5 s, 4 kV) from a buffer with half the ionic concentration of the running buffer (50 mM potassium phosphate, pH 7.5).

Chemicals. BSA (Product No. A7030, Lot No. 57F-0404) was purchased from Sigma (St. Louis, MI). Glutaraldehyde (Product

* To whom correspondence should be addressed at the Department of Technical Analytical Chemistry.
† Department of Pure and Applied Biochemistry.

(1) Kirkland, K. M.; Neilson, K. L.; McCombs, D. A. *J. Chromatogr.* **1991**, *545*, 43–58.
(2) Hermansson, J. *Trends Anal. Chem.* **1989**, *8*, 251–259.
(3) Andersson, S.; Allenmark, S.; Erlandsson, P.; Nilsson, S. *J. Chromatogr.* **1990**, *498*, 81–91.
(4) Erlandsson, P.; Nilsson, S. *J. Chromatogr.* **1989**, *482*, 35–51.
(5) Erlandsson, P.; Hansson, L.; Isaksson, R. *J. Chromatogr.* **1986**, *370*, 475–483.
(6) Hjérten, S. *J. Chromatogr.* **1983**, *270*, 1–6.
(7) Karger, B. L.; Cohen, A. S.; Guttman, A. *J. Chromatogr.* **1989**, *492*, 585–614.
(8) Ewing, A. G.; Wallingford, R. A.; Olefirowicz, T. M. *Anal. Chem.* **1989**, *61*, 292A–303A.
(9) Guttman, A.; Paulus, A.; Cohen, A. S.; Grinberg, N.; Karger, B. L. *J. Chromatogr.* **1988**, *448*, 41–53.
(10) Guttman, A.; Cooke, N. *Anal. Chem.* **1991**, *63*, 2038–2042.

0003-2700/92/0364-2872$03.00/0

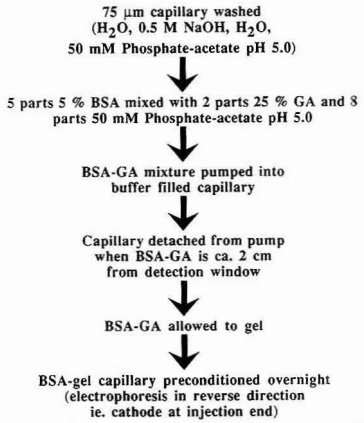

Figure 1. Flow diagram for preparation of BSA-filled capillary.

No. 12179), potassium phosphate, and sodium acetate were obtained from Merck (Darmstadt, FRG).

RESULTS AND DISCUSSION

Preparation of Capillaries Filled with BSA Gel. Initially, conditions were investigated for gelation of BSA cross-linked with glutaraldehyde. Various BSA and glutaraldehyde concentrations as well as various pH and ionic strengths were tested. It was found that an opaque off-white gel formed after approximately 3 min at room temperature when 50 μL of BSA (50 mg/mL) in 0.05 M potassium phosphate/acetate buffer (pH 5.0) was mixed with 100 μL of 5% (v/v) glutaraldehyde in 0.04 M potassium phosphate/acetate buffer (pH 5.0).

Our first trials at running electrophoresis through the gel-filled capillaries resulted in the formation of bubbles within the capillaries, primarily within the buffer region of the capillary, soon after current was applied. After various attempts to alleviate this difficulty, we finally found that reversing the direction of current (simply by inverting the capillary so that the anode was now at the detection window end of the capillary) and exposing the BSA-filled capillary overnight to a potential of 2 kV eliminated the incessant occurrence of bubble formation in the capillaries when samples were subsequently electrophoresed in the correct direction.

Enantiomeric Separation of Tryptophan with Capillary Affinity Gel Electrophoresis. The optical isomers of tryptophan were introduced by electrophoretic migration and separated, as shown in Figure 2A. We presume that the migration of tryptophan depends on electroosmotic flow in the gel-filled capillary, as the isoelectric point of tryptophan is 5.9 and of BSA is 4.9, the pH of the mobile phase was 7.5, and the electrophoresis was performed with the cathode at the detection end of the capillary. Identification of the enantiomers was subsequently accomplished by introduction and electrophoresis of solely the D isomer under similar conditions (Figure 2B). The theoretical plate number, N, calculated using the peak width at the base, obtained in this case was circa 85 000.[11] The N values for the present version of a capillary affinity gel electrophoretic separation of the isomers are thus significantly higher than those obtained from high-performance liquid affinity chromatography separations

(11) Snyder, L. R.; Kirkland, J. J. *Introduction to Modern Liquid Chromatography*; J. Wiley: New York, 1979.

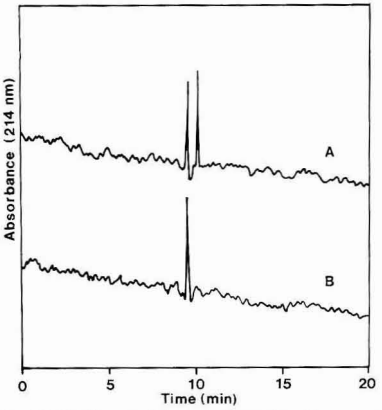

Figure 2. (A) Capillary affinity gel electrophoretic separation of tryptophan enantiomers. Sample was DL-tryptophan (10 μM in 25 mM potassium phosphate pH 7.5). (B) Identification of racemate. Sample was D-tryptophan (5 μM in 25 mM potassium phosphate pH 7.5). Conditions: constant applied electric field, 150 V/cm, 80 μA; gel length = 32 cm, total length = 40 cm; buffer 50 mM potassium phosphate (pH 7.5); sample injection, 100 V/cm, 5 s.

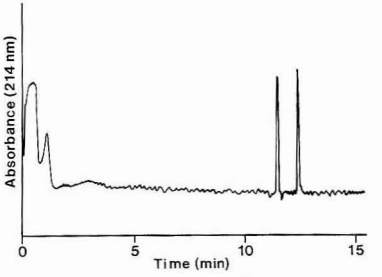

Figure 3. Capillary affinity gel electrophoretic separation of tryptophan enantiomers. Sample was DL-tryptophan (10 μM in 25 mM potassium phosphate pH 7.5). Conditions: constant applied electric field, 125 V/cm; gel length = 32 cm, total length = 40 cm; buffer 50 mM potassium phosphate (pH 7.5); sample injection, 100 V/cm, 3 s.

on immobilized BSA.[5] The resolution, R_s, defined as

$$R_s = \frac{t_2 - t_1}{(w_1 + w_2)/2}$$

where t is the elution time and w, the peak width at the base (i.e. the length of the baseline intercepted by the tangents drawn to the inflection points), was 3.0 for the separation shown in Figure 2A which is comparable to BSA-based LC separation. Using another capillary preparation, an even better resolution was obtained, as shown in Figure 3, with a resolution value of 6.0 and an N value of 91 000.

One of the limitations of protein-based chiral stationary phases in LC is their limited capacity due to the high molecular weight of the selector. Using the quantities employed here, we see that the BSA concentration within the capillary is circa 0.25 mM. For satisfactory separation, the concentration of the molecules to be separated should be considerably lower than 0.25 mM (assuming that a one to one interaction between BSA and the optical isomer exists and, in addition, that probably not all BSA molecules are available for interaction). Generally, at least 1 order of magnitude less is prescribed. Thus, a capacity of 25 μM sample is possible, which we also observed in practice. With UV detection at 214 nm, as used here, the lowest L-tryptophan concentration which can be

detected is 1 μM at a signal to noise ratio of 2. The range of concentrations separated and analyzed was thus 1–25 μM.

Sample Injection and Separation Conditions. DL-Tryptophan was introduced electrophoretically, and the enantiomers were subsequently separated at 6 kV typically in 10–11 min (Figure 2A). The pH and ionic strength of the running buffer were varied. As the pH of the running buffer was changed from 7.0 to 8.0, we found no significant change in separation performance except at pH close to 8.0 when the difference in migration time for the enantiomers decreased. The best separation results were obtained at an ionic strength of 25–50 mM for the running buffer. The ionic strength of the sample buffer was also varied, and we found that sample injection from a buffer with an ionic strength half that of the separation buffer gave better resolution and higher efficiency, presumably due to sample stacking.[12]

In conclusion, we have shown the feasibility of employing protein gels for affinity separation in capillary electrophoresis. Specifically, we have used the protein, in this case BSA, as the chiral selector for the separation of tryptophan enantiomers with very high efficiency compared to the analogous protein-based LC separations.[5] In addition, the method employed for preparing the separation phase, i.e. gel formation through chemical cross-linking, allows a high concentration of the affinity selector to be immobilized. The protein (BSA) itself is the sole component (except for bifunctional cross-linking agent glutaraldehyde) in the separation phase without any other inert support material.

In the future, we see that the interactive methods described here in which immobilized protein phases are used in CE expands the application field of CE to new practical separation endeavors (such as antibody-based separations) as well as to fundamental protein interaction studies, particularly with respect to weak affinity interaction.[13] The minimal volumes and amounts of components used in CE induce the initial screening of exclusive proteins (i.e. proteins of limited availability) as potential chiral selectors, for example for drug enantiomer separation. The method described here has the potential to be applicable for all types of affinity-based separations which include cross-linkable specific binding partners.

ACKNOWLEDGMENT

We gratefully acknowledge the financial support from the Crafoord, Lars Hiertas Memorial, and Carl Tryggers Foundations. We thank Hans Olof Nilsson for his technical assistance. The results described here were, in part, presented at the Euchem Conference on Capillary Electroseparations, December 9–11, 1991, Storlien, Sweden, and at the 4th International Symposium on High-Performance Capillary Electrophoresis, February 9–13, 1992, Amsterdam, The Netherlands.

RECEIVED for review April 7, 1992. Accepted September 1, 1992.

(12) Burgi, D. S.; Chien, R.-L. *Anal. Chem.* **1991**, *63*, 2042–2047.
(13) Zopf, D.; Ohlson, S. *Nature* **1990**, *346*, 87–88.

Extraction of Metal Ions from Liquid and Solid Materials by Supercritical Carbon Dioxide

K. E. Laintz† and C. M. Wai*

Department of Chemistry, University of Idaho, Moscow, Idaho 83843

C. R. Yonker and R. D. Smith

Chemical Sciences Department, Battelle Pacific Northwest Laboratory, Richland, Washington 99352

Supercritical fluid extraction (SFE) of organic compounds has been the subject of many studies in recent years.[1,2] A suitable solvent for this purpose is carbon dioxide due to its moderate critical constants (T_c = 31.1 °C, P_c = 72.8 atm), inertness and easy availability in purified form. Little information is available in the literature regarding SFE of metal ions. Direct extraction of metal ions by supercritical carbon dioxide is known to be highly inefficient because of the charge neutralization requirement and the weak solute–solvent interactions. However, if metal ions are bound to organic ligands, their solubility in supercritical carbon dioxide may be significantly increased. A widely used chelating agent for trace metal extraction known in the literature is diethyl dithiocarbamate (DDC) which forms stable complexes with over 40 metals and nonmetals.[3] Recently, Laintz et al. have shown that metal–DDC complexes have limited solubilities in supercritical carbon dioxide.[4,5] If fluorine is substituted for hydrogen in the ligand, as in the case of bis(trifluoroethyl) dithiocarbamate (FDDC), the resulting metal–FDDC complexes exhibited significantly high solubilities in supercritical carbon dioxide.[5] The solubilities of a number of metal–FDDC complexes in supercritical carbon dioxide are in the order of 10^{-3} M at 50 °C and 100 atm which is about 2–3 orders of magnitude greater than the nonfluorinated analogues. The solubility of metal–FDDC in supercritical CO_2 appears adequate for analytical applications. However, the feasibility of applying FDDC for metal extraction using supercritical CO_2 as a solvent has not been demonstrated. This paper describes an experimental approach for the extraction of Cu^{2+} from an aqueous solution and from a silica surface using a supercritical carbon dioxide fluid containing LiFDDC as an extractant.

EXPERIMENTAL SECTION

Lithium bis(trifluoroethyl) dithiocarbamate was synthesized according to a procedure outlined in the literature.[6] The starting material, bis(trifluoroethyl)amine, was obtained from PCR Chemicals. Other chemicals used in the synthesis, including *n*-butyllithium (2.5 M in hexane), carbon disulfide and isopentane, were obtained from Aldrich Chemical Co. (Milwaukee, WI). An aqueous Cu^{2+} solution was prepared by dissolving a known amount of solid $Cu(NO_3)_2$ (Mallinckrodt Inc., St. Louis, MO) in deionized water. For the extraction of Cu^{2+} from a solid matrix, $Cu(NO_3)_2$ adsorbed on silica was used as obtained from Aldrich as 30% by weight $Cu(NO_3)_2$ adsorbed on Celite. Weighing of the solid materials was done using a Cahn microbalance (Cerritos, CA) which allows for accuracy in the range of 10^{-3} mg.

The apparatus for the SFE experiments is shown in Figure 1. SCF-grade CO_2 (Scott Specialty Gases, Plumsteadville, PA) was delivered to the system using a microprocessor controlled Varian (Sunnyvale, CA) 8500 high-pressure syringe pump. The system pressure was monitored to ±1 psi using a Setra Systems (Acton, MA) pressure transducer. The supercritical CO_2 was passed through solid LiFDDC contained in a 10 mL stainless steel high pressure cylinder, which functioned as the ligand extraction vessel. The fluid phase containing the dissolved FDDC was subsequently introduced into a high-pressure stainless steel view cell containing either the aqueous Cu^{2+} solution or the solid $Cu(NO_3)_2$ adsorbed on silica. The 14.9-mL cell was fitted with 1.27-cm quartz windows. A gas tight seal was achieved by the compression of gold-plated stainless steel "V" rings between the cell and the windows. Mixing of the two phases was accomplished by stirring with a Teflon-coated stir bar driven by a magnetic motor. The view cell was electrically heated using an Omega (Stamford, CT) Model CN2001P2 microprocessor-based temperature controller. The portion of the system that included the view cell and stirrer motor was placed within a Varian Cary Model 2200 UV–vis spectrophotometer equipped with a DS-15 data station to monitor the formation of $Cu(FDDC)_2$ in the supercritical CO_2 phase.

RESULTS AND DISCUSSION

Using the high-pressure view cell, direct measurement of the rate of extraction of Cu^{2+} can be achieved using Beer's law based upon attenuation of the UV–vis beam focused on the supercritical fluid phase. For the extraction of Cu^{2+} from Celite, about 1–6 mg of the solid material was placed in the view cell. Supercritical CO_2 containing LiFDDC at different pressure was introduced and the absorbance of $Cu(FDDC)_2$ at 416 nm, the peak maximum of the characteristic charge transfer absorbance for the Cu^{2+} complex, was monitored as a function of time.[4] The solubility of FDDC in supercritical CO_2 at 50 °C and 100 atm has been reported to be in the order of 4.7×10^{-4} M.[4] Under our experimental conditions, the molar ratio of FDDC to Cu^{2+} would range roughly from 7:1 to 40:1, which is a significant excess for 2:1 complex formation. Since the quantity of the solid material involved in these experiments is small, no stirring was applied. In the absence of LiFDDC, no detectable amount of Cu^{2+} was extracted by supercritical CO_2 after 30 min. The rate of extraction of Cu^{2+} at 35 °C with different densities of CO_2 containing LiFDDC is shown in Figure 2. Rapid transfer of Cu^{2+} from the silica surface to supercritical CO_2 was observed within the first few minutes of contact followed by a gradual increase to approach a saturation value in the fluid phase. At a CO_2 density of 0.29 g/cm^3 (or P = 75.8 bar), the concentration of $Cu(FDDC)_2$ in the fluid phase approached a saturation value of 9.7×10^{-6} M after 60 min, corresponding to about 17% of the total Cu adsorbed on the solid phase. The percent of Cu^{2+} extracted was based on the concentration of Cu^{2+} in the supercritical fluid phase as $Cu(FDDC)_2$ divided by the concentration of Cu^{2+} in the original sample. When the CO_2 density was increased to 0.37 g/cm^3 (P = 79.3 bar), the concentration of

† Current address: Department of Chemistry, Japan Atomic Energy Research Institute, Tokai-mura, Ibaraki-ken, Japan.

(1) Hawthorne, S. B. *Anal. Chem.* **1990**, *62*, 633A.
(2) Eckert, C. A.; Van Alsten, J. G.; Stoicos, T. *Environ. Sci. Technol.* **1986**, *20*, 319.
(3) Wai, C. M. In *Preconcentration Techniques for Trace Elements*; Alfassi, Z. B., Wai C. M., Eds.; CRC Press: Boca Raton, FL, 1991; Chapter 4, p 111.
(4) Laintz, K. E.; Wai, C. M.; Yonker, C. R.; Smith, R. D. *J. Supercrit. Fluids* **1991**, *4*, 194.
(5) Laintz, K. E.; Yu, J. J.; Wai, C. M. *Anal. Chem.* **1992**, *69*, 6960.
(6) Sucre, L.; Jennings, W. *Anal. Lett.* **1980**, *13*, 497.

0003-2700/92/0364-2875$03.00/0

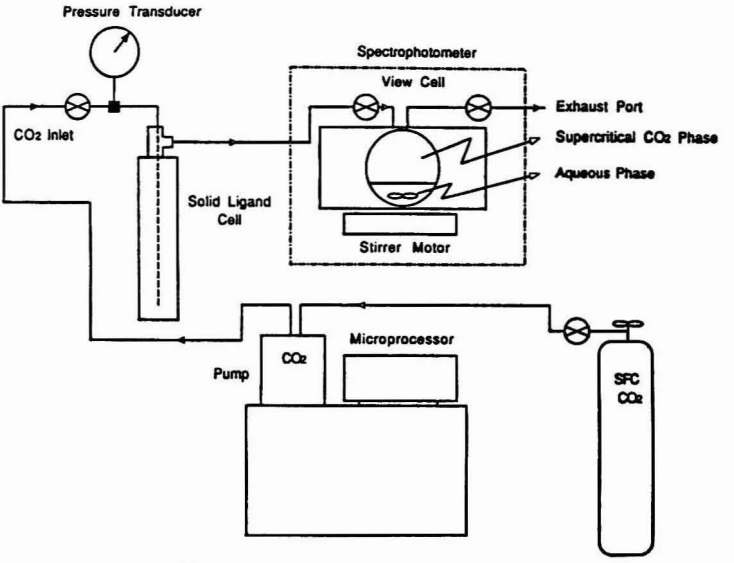

Figure 1. Apparatus for the extraction of Cu^{2+} with supercritical CO_2.

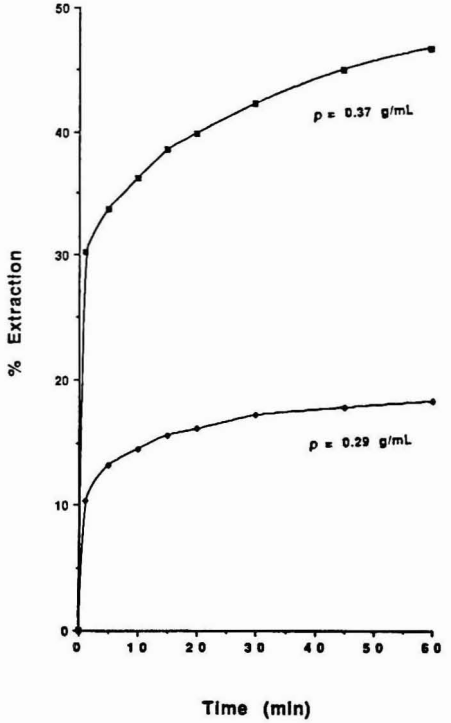

Figure 2. Rate of extraction of Cu^{2+} adsorbed on Celite with supercritical CO_2 containing LIFDDC at 35 °C and different density.

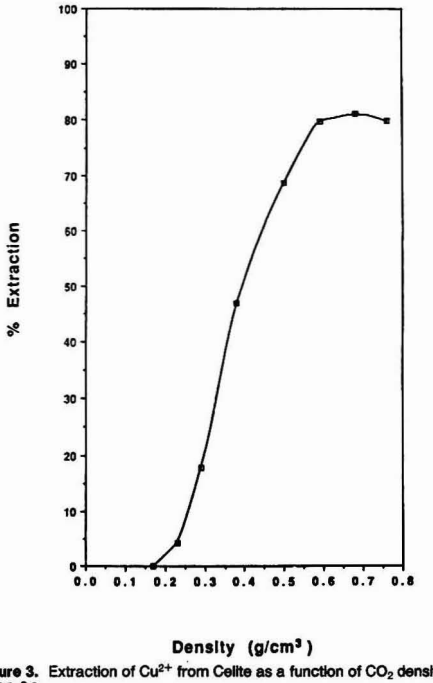

Figure 3. Extraction of Cu^{2+} from Celite as a function of CO_2 density at 35 °C.

$Cu(FDDC)_2$ in the fluid phase reached a value of 2.5×10^{-5} M, corresponding to about 46% of the total Cu on Celite.

Figure 3 shows the percent of Cu^{2+} extracted from the silica surface surface of a single sample after 1 h of contact at different CO_2 densities. As shown in Figure 3, the efficiency of extraction increases very rapidly when the pressure of CO_2 exceeds the P_c. The percent of extraction reaches a limit of

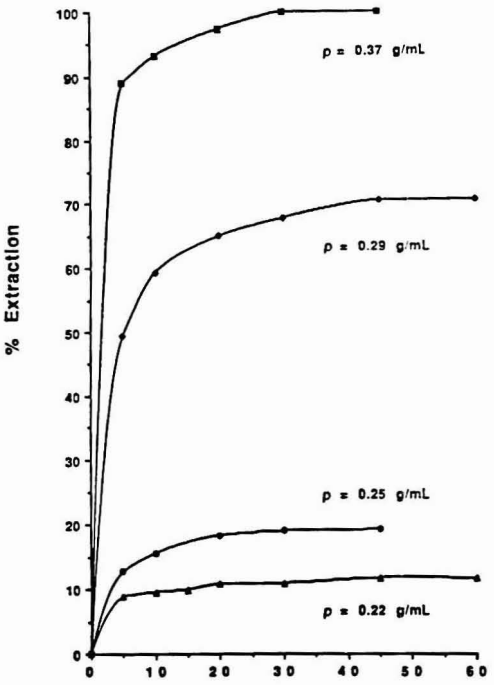

Figure 4. Rate of extraction of Cu^{2+} from aqueous solution with supercritical CO_2 containing LIFDDC at 35 °C as a function of density.

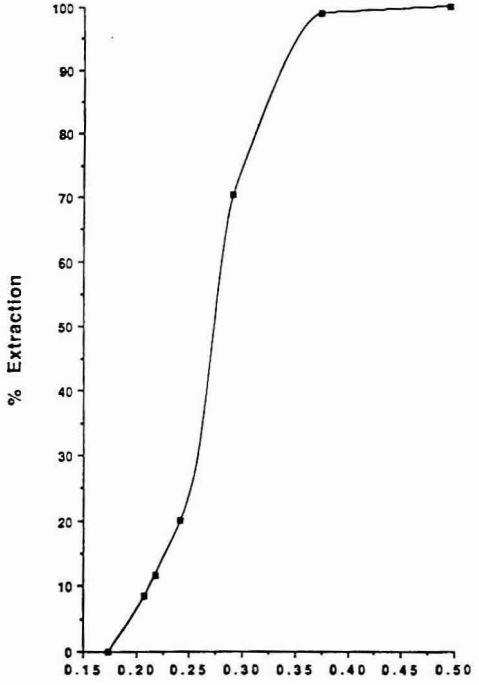

Figure 5. Extraction of Cu^{2+} from aqueous solution as a function of supercritical CO_2 density at 35 °C.

about 80% of total Cu in the Celite at a density of about 0.6 g/cm³ t 35 °C. It is possible that this unextracted 20% may represent Cu of different chemical forms in the sample which are not accessible for complexation with FDDC in supercritical CO_2 or it may represent different forms of Cu^{2+} which do not absorb at 416 nm.

For the extraction of Cu^{2+} from water, 5 mL of a 5×10^{-5} M solution of $Cu(NO_3)_2$ was placed in the bottom of the view cell. The volume of solution in the cell was such that it did not interfere with the beam from the spectrophotometer. The aqueous phase was stirred with a mini-stir bar with a speed of about 120 rpm. Since $Cu(FDDC)_2$ has a dark brownish-green color in solution, the extraction progress was easily visually monitored. Spectrophotometric quantitation was done by measuring the charge-transfer absorption of the complex at 416 nm in supercritical CO_2. The rates of extraction of Cu^{2+} from aqueous solutions at 35 °C are shown in Figure 4. Rapid transfer of Cu^{2+} from the aqueous phase into supercritical CO_2 was observed in all experiments. Initially, CO_2 below the critical pressure at 62 bar (density 0.17 g/cm³) was delivered to the ligand extraction vessel and then introduced into the view cell. No detectable $Cu(FDDC)_2$ was observed in the fluid phase even after 1 h. Upon increasing the pressure to 69 bar (density 0.22 g/cm$_3$), 12% of the Cu^{2+} was extracted into the supercritical CO_2 phase. The rate of extraction in this case is again fast, requiring only several minutes to approach the saturation value. Further pressure increments to 72.4 and 75.8 bar showed extractions of the $Cu(FDDC)_2$ complex at 20% and 70%, respectively. Quantitative extraction of the Cu^{2+} from the aqueous phase was readily achieved upon an increase of pressure to 79.3 bar, corresponding to a CO_2 density of 0.37 g/cm³. The percent extraction of Cu^{2+} at different densities of supercritical CO_2 is shown in Figure 5. The efficiency of extraction increases nearly exponentially with respect to density.

The extraction efficiency was also found to increase with temperature. These experiments were carried out under constant density instead of constant pressure because in the latter case change in temperature would affect density and consequently extraction efficiency. When the logarithm of the equilibrium distribution coefficient D, which is defined as the ratio of $Cu(DDC)_2$ in CO_2 over total Cu^{2+} in the aqueous phase, was plotted against $1/T$ (K), a linear relationship was observed (Figure 6). The negative slope suggests an endothermic process with a ΔH of 4.4 ± 0.4 kJ/mol for the extraction of Cu^{2+} at a constant density of 0.22 g/cm³. An increase in temperature by 10 °C from 35 to 45 °C at this density would increase the D value by about a factor of 1.7. According to these results, extraction of Cu^{2+} by FDDC in supercritical CO_2 should be favored at higher temperatures and pressures above the critical point.

When no stirring was applied to the liquid phase, the rate of extraction was much slower. For example, at 35 °C and a density of 0.25 g/cm³, extraction of 7% of Cu^{2+} from the aqueous phase into supercritical CO_2 would generally require about 1 h as compared to the experiments with stirring where 20% extraction was achieved in 20 min (Figure 4). Because it is difficult to perform experiments without any disturbance of the two phases in our system, the results of the extraction experiments without stirring are generally not reproducible. Analysis of kinetic data also appears complicated since it

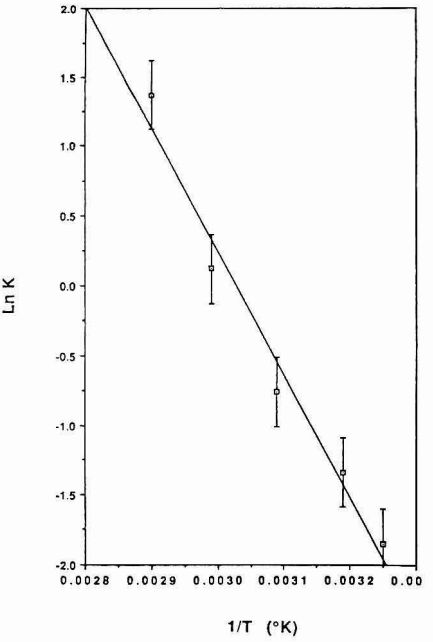

Figure 6. Plot of ln D versus $1/T$ for the extraction of Cu^{2+} from aqueous solution with supercritical CO_2 at a constant density of 0.22 g/cm^3.

involves both the diffusion and the mass transport process in the extraction experiments. Nevertheless, the rate of extraction of Cu^{2+} from water into supercritical CO_2 is still fast, requiring about 10 min in most cases to approach a saturation value with moderate stirring as shown in Figure 4.

This study has demonstrated that metal ions dissolved in aqueous solution or adsorbed on the silica surface can be effectively extracted by supercritical CO_2 containing a suitable chelating agent such as FDDC. The choice of ligand is obviously important for this extraction technique. FDDC happens to be moderately soluble in supercritical CO_2 and complexes effectively with many metal ions to form chelates which have sufficient solubility in the fluid phase. Using supercritical CO_2 as a solvent for metal extraction can avoid organic solvent waste generation and exposure of personnel to harmful vapors. With a simple extractor design shown in this study, rapid extraction of Cu^{2+} by supercritical CO_2 from both the liquid and the solid material can be achieved. If a ligand is specific for certain metals, selective extraction by supercritical fluids may also be accomplished. This type of selective chelation–supercritical fluid extraction approach offers a host of potential applications for preconcentration of trace metals for analytical purposes and in separation processes including toxic metal waste treatment.

ACKNOWLEDGMENT

This material is based on work supported by the Idaho EPSCoR Program of the National Science Foundation under Grant No. RII-8902065 and by the Center for Hazardous Remediation Research of the University of Idaho. C.R.Y. and R.D.S. were supported by the Director, Office of Energy Research, Office of Basic Science, Chemical Sciences Division of the U.S. Department of Energy under contract DE-AC06-76RLO 1830.

RECEIVED for review April 17, 1992. Accepted July 15, 1992.

Signal-to-Noise Enhancement of Neutral-Ion Correlation Measurements for Tandem Time-of-Flight Mass Spectrometry

F. H. Strobel and D. H. Russell*

Department of Chemistry, Texas A&M University, College Station, Texas 77843

INTRODUCTION

Tandem time-of-flight (TOF) mass spectrometry is a developing area with excellent potential for ultra-high-sensitivity analysis and structural characterization of complex biological molecules. Pulsed ionization methods such as pulsed Cs^+ liquid-SIMS, are not directly compatible with scanning instruments, but such methods are compatible with tandem TOF. In addition, several laboratories have demonstrated that pulsed ionization methods, specifically pulsed liquid-SIMS,[1] multiphoton ionization (MPI), and laser desorption ionization, especially matrix-assisted laser desorption ionization (MALDI),[2] are inherently more sensitive than continuous ionization methods, and recent work has demonstrated that MALDI combined with tandem TOF mass spectrometry is an ultra-high-sensitivity analysis method.[3] The added sensitivity of pulsed ionization is particularly advantageous to tandem mass spectrometry and the development of ultra-high-sensitivity (10^{-18} to 10^{-15} M) biological mass spectrometry.[3] On the other hand, instrumentation for performing tandem TOF mass spectrometry experiments is still early in the development stages,[4] and optimum methods for performing such experiments have not been established.

In a recent paper we described a magnetic sector/reflectron-TOF instrument under development in our laboratory[5] and reported data obtained using neutral-ion correlation measurements.[6] The neutral-ion correlation experiment permits a continuous ionization source to be used on the magnetic sector/reflectron-TOF instrument. Although we successfully demonstrated the instrument concept, the signal-to-noise (S/N) ratio of the collision-induced dissociation (CID) spectra was disappointing. The major factor limiting the S/N ratio of the CID spectra is the background of neutrals formed by neutralization of the incident ions upon collision with the target gas. The neutrals are formed by either endothermic charge-transfer reactions between the incident ion and the target gas[7] or by CID to form product ions that are not sampled by MS-II, e.g., low m/z fragment ions such as H^+ that are not efficiently transmitted by MS-II or CID reactions involving large scattering angles and the fragment ions are scattered outside the acceptance angle of the spectrometer. The latter process seems an unlikely explanation because both the ion and neutral formed by CID would be scattered, and the efficiency for neutral collection should also be low, which it is not.

In this paper we report a method for improving the S/N ratio by reducing the background signal, e.g., reducing N. The method used to reduce N is taken from nuclear chemistry and is generally referred to as "pile-up rejection."[8] In the neutral-ion correlation experiment, the occurrence of a dissociation reaction of the mass-selected ion is indicated by the neutral product striking a detector positioned behind the reflectron,[5,6] and the ion is detected by a detector positioned to receive the reflected ions. Thus a dissociation reaction yields two products, e.g., an ion and a neutral, that must be correlated. As with all event correlation experiments it is important to keep the flux of the events low in order to minimize the number of "false" correlation events, e.g., background signals from uncorrelated events. The devices used for this experiment and data obtained in this manner are described in the following sections.

EXPERIMENTAL SECTION

The apparatus used in this study has been described previously.[5] Briefly, the instrument consists of a Kratos MS-50 high-resolution mass spectrometer that has been modified by addition of a reflectron TOF that acts as MS-II for tandem mass spectrometry experiments. The Kratos MS-50 operates as supplied by the vendor, and the R-TOF is a single-stage reflectron designed specifically for tandem mass spectrometry.[9] The TOF electronics are standard LeCroy TDC components that are interfaced to an IBM-PC compatible computer by using a National Instruments, Inc. GPIB card. The TOF spectra are displayed using software compiled in our laboratory.

The samples used in this study were obtained from Sigma Chemical Co. and were used without purification or preparation steps. The samples were ionized by continuous Cs^+ ion liquid SIMS, and all other aspects of the experiments were performed as described in our earlier report.[5]

RESULTS AND DISCUSSION

To illustrate the neutral-ion correlation/pile-up rejection experiment, three spectra for Leu-enkephalin are contained in Figure 1. Figure 1A contains the metastable ion spectrum obtained by using neutral-ion correlation, and Figure 1B contains the metastable ion spectrum obtained by using neutral-ion correlation/pile-up rejection. The fragment ions are identified using the notation suggested by Roepstorff and Fohlman.[10] The spectrum contained in Figure 1A required 60 000 dissociation events to yield a S/N ratio of 20:1 (based on signal amplitude and noise defined by the background fluctuations) for the most abundant fragment ion. The spectrum contained in Figure 1B required 10 000 dissociation events to yield a S/N ratio of >100:1 for the most abundant fragment ion; however, the uncertainty of the peak height is determined by $N^{1/2}$, where N is the number of counts associated with the peak height. Thus neutral-ion correlation/pile-up rejection improves the S/N by a factor of 5 and reduces the required number of events by a factor of 6. The collision-induced dissociation spectrum for the $[M + H]^+$ ion of Leu-enkephalin is shown in Figure 1C. This spectrum was

(1) Tecklenburg, R. E., Jr.; Castro, M. E.; Russell, D. H. *Anal. Chem.* **1989**, *61*, 153. (b) Olthoff, J. K.; Cotter, R. J. *Nucl. Instrum. Methods Phys. Res., Sect. B* **1987**, *B26*, 566.
(2) Hillenkamp, F.; Karas, M.; Beavis, R. C.; Chait, B. T. *Anal. Chem.* **1991**, *63*, 1193A.
(3) Strobel, F. H.; Solouki, T.; White, M. A.; Russell, D. H. *J. Am. Soc. Mass Spectrom.* **1991**, *2*, 91.
(4) Stults, J. T.; Enke, C. G.; Holland, J. F. *Anal. Chem.* **1983**, *55*, 1323. (b) Stults, J. T.; Holland, J. F.; Watson, J. T.; Enke, C. G. *Int. J. Mass Spectrom. Ion Processes* **1986**, *71*, 169. (c) Glish, G. L.; Goeringer, D. E. *Anal. Chem.* **1984**, *56*, 2291. (d) Glish, G. L.; McLuckey, S. A.; McKown, H. S. *Anal. Instrum.* **1987**, *16*, 191.
(5) Strobel, F. H.; Preston, L. M.; Washburn, K. S.; Russell, D. H. *Anal. Chem.* **1992**, *64*, 754.
(6) Della-Negra, S.; Le Beyec, Y. *Anal. Chem.* **1985**, *57*, 2035. (b) Tang, X.; Ens, W.; Standing, K. G.; Westmore, J. B. *Anal. Chem.* **1988**, *60*, 1791.
(7) Bricker, D. L.; Russell, D. H. *J. Am. Chem. Soc.* **1986**, *108*, 6174. (b) Bricker, D. L.; Russell, D. H. *Anal. Chim. Acta* **1985**, *178*, 117.
(8) Williams, O. M.; Sandle, W. J. *J. Phys. E* **1970**, *3*, 741.
(9) Strobel, F. H.; Russell, D. H. Manuscript in preparation.
(10) Roepstorff, P.; Fohlman, J. *Biomed. Mass Spectrom.* **1984**, *11*, 601.
(11) Holmes, J. L. *Mass Spectrom. Rev.* **1989**, *8*, 513.

0003-2700/92/0364-2879$03.00/0

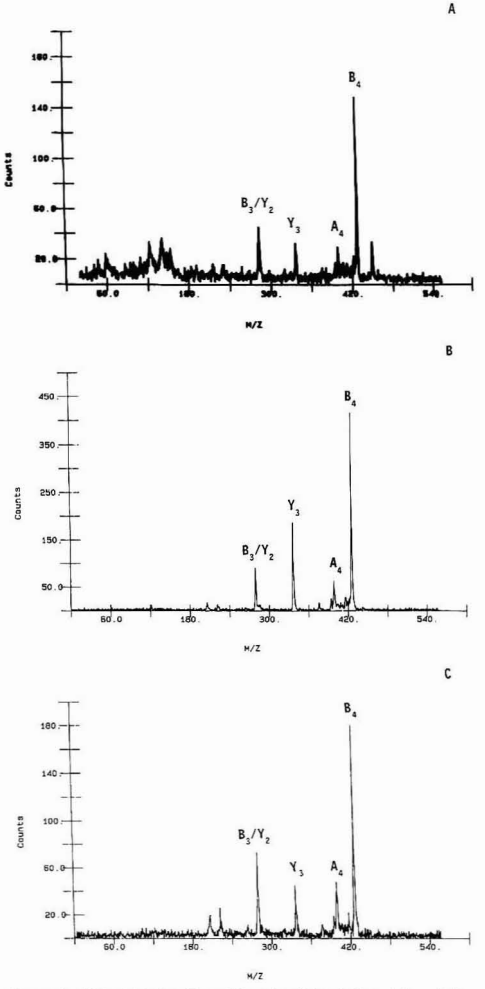

Figure 1. Metastable ion (A and B) and collision-induced dissociation (C) spectra for the $[M + H]^+$ ion of Leu-enkephalin obtained by neutral-ion correlation (A) and neutral-ion correlation/pile-up rejection (B and C).

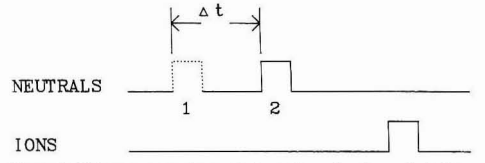

Figure 2. Pulse sequence for neutrals and ions showing arrival of two neutrals (1 and 2) that yields false correlation signals.

obtained by using neutral-ion correlation/pile-up rejection and an attenuation of the incident ion beam of 30%. Note that the CID spectrum has a higher noise level than the metastable ion spectrum. The noise level of the CID spectrum is greater because fewer dissociation events are averaged due to a high number of background events that contribute false correlations. Nonetheless, the S/N for the CID spectrum is greatly improved over that obtained without using pile-up rejection.[5]

To understand the advantages of pile-up rejection for neutral-ion correlation measurements, it is instructive to examine the factors that limit the S/N for Figure 1A. As the mass-selected ion (mass selected by MS-I) traverses the field-free region between MS-I and MS-II, fast neutrals are produced by two processes, reactions 2 and 3.

$$m_1^+ + m_g \rightarrow [m_1^+] + m_g \quad (1)$$

$$[m_1^+] + m_g \rightarrow F_i^+ + F_j^0 \quad (2)$$

$$m_1^+ + m_g \rightarrow m_1^0 + m_g^+ \quad (3)$$

Reaction 1 corresponds to collisional activation (CA) and subsequently leads to collision-induced dissociation (CID; reaction 2), thus producing a fragment ion (F_i^+) and a fragment neutral (F_j^0) of the incident ion, denoted m_1^+. Reaction 3 produces an ion (the original target atom) and a neutral (m_1^0) but the ion has near-thermal kinetic energy and is not extracted from the collision cell; thus the only detectable product (detectable in the tandem mass spectrometry experiment) of reaction 3 is the fast-neutral. (m_1^0 denotes a neutral species, and whether the neutral is an intact molecule or a fragment of the molecule is now known; however, results from neutralization–reionization experiments suggest that both intact molecules and fragments are formed.[11]) Reaction 2 yields a fast-ion and a fast-neutral, and both fragments retain the initial velocity of m_1^+. In the neutral-ion correlation experiment detection of F_j^0 is the "start" signal for the time-of-flight clock for the ion detector. The arrival time of F_i^+ at the ion detector is delayed in time relative to the neutral because the flight path of the ion is greater; thus the difference in arrival time of the neutral and ion can be used for TOF analysis of the ionic products of reaction 2. The occurrence of reaction 2 is confirmed by correlation of an ion with a neutral, whereas fast-neutrals formed by reaction 3 do not correlate with an ion.

The primary source of background signal associated with coincidence measurements arises when the count rates for "true" coincidence signals are low and the count rate of "false" coincidence signals is high. For example, false coincidence gives rise to signal distortion if a neutral formed by reaction 3 strikes the detector (a start signal for the ion TOF clock) and within the ion acquisition time window a second neutral formed by reaction 2 strikes the detector, the TOF measurement for the ion is in error by Δt, the difference in arrival time between neutral 1 and neutral 2 (Figure 2). Because Δt is random, the end result is noise in the ion TOF spectrum. In addition, the probability for background signal in a coincidence experiment is directly proportional to the time window allowed for detection of F_i^+, which is determined by the flight time of the ion. Typically, time windows of 10–100 μs are required for acquisition of the full range MS-II mass spectrum for ion energies of 1–8 keV and m/z values of 100–5000 for m_1^+. Such a large time window for the MS-II mass spectrum limits the maximum allowable ion current for m_1^+ to approximately 10 000–50 000 neutrals/s. Data acquisition rates of 10–50 kHz exceeds the capabilities of the instrument hardware; thus it is necessary to acquire a statistical sampling of the actual number of neutrals formed. Because the number of products formed by reaction 3 far exceeds the number of products from reaction 2, signal-averaging is not an efficient means for improving the S/N ratio. Although the S/N ratio can be improved by summing together narrow segments of the TOF spectrum, e.g., sampling a narrow time window, this method increases the total data acquisition time for the experiment. In addition, this procedure is practical only if

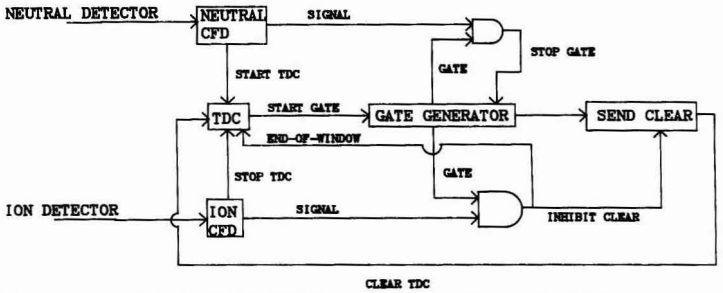

Figure 3. Schematic drawing for the circuitry to eliminate false correlated signals and improve the signal-to-noise ratio for the metastable ion and collision-induced dissociation spectra.

the signal for m_1^+ is constant in time; e.g., often times the liquid-SIMS spectrum changes (in terms of analyte versus matrix background signal)[12] as the sample is depleted, and thus the time-averaged spectra are composite MS-II spectra for analyte and matrix background ions.

The pile-up rejection S/N enhancement can be accomplished in two ways: (i) acquire and store all the neutral-ion arrival events and process the data off-line,[13] or (ii) develop a hardwired system for performing the experiment on-line. We chose to use an on-line system because this permits evaluation of the tandem mass spectrometry data as the data are being acquired. On-line evaluation of the data is important because some samples yield acceptable S/N ratios with minimum acquisition times, either because the dissociation efficiency is high or a large amount of sample is available, but other samples require much longer acquisition times to achieve acceptable S/N levels. The on-line experiment is performed by the circuitry shown in Figure 3. This circuitry signals the computer that valid data have been obtained. Valid data are defined by (i) a signal for ion arrival within the ion flight time window and (ii) a second neutral not detected within the ion flight time. The signals from the neutral and ion detectors are used as inputs to two constant-fraction discriminators (CFD) (Canberra 2126 and 2128). Each CFD has four outputs (two NIM and two TTL). One output on the neutral CFD is used to start the TDC (LeCroy 4208), and one output of the ion detector is used as the TDC stop. The TDC then sends a signal through its "busy" output which starts a gate generator (LeCroy 2323A). The signal from the two CFD's are "ANDed" with the gate generator output. At the end of the gate a signal would normally clear the TDC; however, if a signal is obtained by the ion detector during the gate period, two events occur. The first process sends a signal to the TDC, which indicates valid data have been received. The second process inhibits the signal which clears the TDC. If a second neutral is received, the gate is stopped so that no signals from the ion detector are processed as valid data.

CONCLUSIONS

The studies to date clearly illustrate the potential for tandem TOF mass spectrometry for ultra-high-sensitivity analysis[3] and structural characterization of biological molecules.[5] Although neutral-ion correlation methods can be used for acquisition of metastable ion and collision-induced dissociation (CID) spectra, the background signal from neutralization of the incident ion by collisions with residual gases or the CID target gas reduces the S/N ratio for the product ions. Consequently, neutral-ion correlation/pile-up rejection, a method for rejection of spectral data from events where false coincidence signals limit the S/N ratio, dramatically improves the data and reduces the time required for data acquisition. For example, neutral-ion correlation/pile-up rejection improved the S/N ratio for the metastable ion spectrum of the $[M + H]^+$ ion of Leu-enkephalin by a factor of 5. In addition, because the acquisition rates are limited by the computer (50 Hz) and not the rate of dissociation events (1000–50 000 Hz), the acquisition time is reduced by a factor of 6. A comparable improvement is also obtained for the CID spectrum of Leu-enkephalin $[M + H]^+$ ions.

ACKNOWLEDGMENT

This work is sponsored by the U.S. Department of Energy, Division of Chemical Sciences, Office of Basic Energy Sciences (Grant No. DE-FG05-85ER-13434), and the U.S. Department of Energy, University Research Instrumentation Program (Grant No. DE-FG05-89ER75502).

RECEIVED for review May 1, 1992. Accepted August 20, 1992.

Registry No. Leu-enkephalin, 58822-25-6.

(12) Caldwell, K. A.; Gross, M. L. *Proceedings of the 39th American Society for Mass Spectrometry Annual Conference on Mass Spectrometry and Allied Topics*, Nashville, TN, May 19–24, 1991; ASMS: East Lansing, MI, 1991; p 122–123.

(13) Huang, L. Q.; Conzemius, R. J.; Junk, G. A.; Houk, R. S. *Int. J. Mass Spectrom. Ion Processes* **1989**, *90*, 85. (b) Parks, M. A.; Gibson, K. A.; Quinones, L.; Schweikert, E. A. *Science* **1990**, *248*, 988. (c) Conzemius, R. J.; Svec, H. J. *Int. J. Mass Spectrom. Ion Processes* **1990**, *103*, 57.

Derivatization in Trace Organic Analysis: Use of an All-Glass Conical Reaction Vial

Samy Abdel-Baky,† Kariman Allam, and Roger W. Giese*

Department of Pharmaceutical Sciences in the Bouve College of Pharmacy and Health Sciences and Barnett Institute of Chemical Analysis and Materials Science, Northeastern University, Boston, Massachusetts 02115

As we have reported,[1,2] we are developing an analytical procedure for diol epoxide-polyaromatic hydrocarbon (DE-PAH) DNA adducts in which the isolated adducts are subjected to a sequence of three chemical steps prior to detection by gas chromatography–electron capture negative ion mass spectrometry (GC–ECNI-MS). The three steps are as follows: (1) acid hydrolysis to release the DE-PAH as a tetrol from the DNA, (2) oxidation of this tetrol with potassium superoxide to a corresponding dicarboxy-PAH, and (3) esterification of the latter compound with pentafluorobenzyl bromide.

During the course of progressively applying steps 2 and 3 of the method to lower amounts of an authentic tetrol (namely benzo[a]pyrene-7,8,9,10-tetrahydrotetrol), we encountered severe irreproducibility at the 100-pg level in terms of both losses and interferences. Here we report that this problem was due to microscopic, recalcitrant brown/black specks in the commercial vials employed for this purpose and the presence of PTFE liner/plastic caps. Reproducible results were achieved by employing an all-glass conical reaction vial fabricated in-house.

EXPERIMENTAL SECTION

General Information. The reagents, instrumentation, commercial vials, and reactions were described previously.[1,2] All solvents used for the following cleaning procedures were HPLC-grade.

All-Glass Reaction Vial. This was fabricated in-house from a 14/20 hollow, ground-glass stopper and a size 14/20, 7585 joint (outer member, medium length, 12-mm o.d.) obtained from ACE Glass (Vineland, NJ).

Vial Cleaning. Scrub each vial (commerical or home-made) with a test tube brush (Cat. No. 17030-006, VWR Scientific, Philadelphia, PA) in water:Micro (No. 6731, International Products Corp., Burlington, NJ), 90/10 v/v. Heat the vial at 60 °C for 2 h in a covered (Pyrex watch glass) beaker filled with 10% Micro cleaning solution, and leave at room temperature overnight. Wash the vials individually 10× with distilled water and keep in water for ≥2 h. Heat the vials in chromic acid[3] for 2 h at 60 °C, and leave at room temperature overnight. Wash the vials as before with water, and stack them upright in a Petri dish. Fill each vial with methanol, and 0.5 h later remove the methanol with a pipet attached to a vacuum source. Loosely cover the dish with aluminum foil, remove the residual methanol on a hot plate, and seal the vials after cooling to room temperature with a polytetrafluoroethylene (PTFE) linear/plastic cap or ground glass stopper, cleaned as described below, for storage until use.

Cap Cleaning. Rinse the caps briefly with water and keep in 10% Micro at room temperature for ≥24 h. Wash the caps individually with water and keep in water for ≥24 h. Heat the caps in methanol at 60 °C four times for 2 h each. Partly air-dry the caps upside down on a paper towel, transfer to and wrap loosely in aluminum foil, place in a 70 °C oven overnight, and store wrapped tightly until use.

PTFE-Liner Cleaning. Three-Step Method. The method is the same as above for the caps.

Six-Step Method. After 10% Micro and a water wash (see above), stir the liners in chromic acid at 50 °C for 1 h. Stir in 60 °C water 6×, 70 °C toluene 3×, and 50 °C methanol 3× (including 10 min of boiling in the last methanol), with 20 min for each step. Air-dry in the covered (loose aluminum foil) beaker, place in a 70 °C oven overnight, and store until use wrapped in aluminum foil.

RESULTS AND DISCUSSION

We decided to first examine whether the vials themselves were contributing to the irreproducibility that we had encountered at the 100-pg level of tetrol analyte, even though the vials were routinely cleaned with detergent, 3 M nitric acid (both at 60 °C for 8 h), and methanol. While the vials were always clean by ordinary visual inspection, closer examination with a hand-held magnifying lens (×5) revealed the presence of tiny brown and black specks, stuck to the inner wall, that varied vial-to-vial. New vials, examined as received from two other suppliers, were found to contain the specks. As implied above, the specks were recalcitrant to our existing cleaning procedure.

A second problem became apparent as well from use of the magnifying lens. When the plastic cap fitted with a PTFE liner was screwed down tightly (as necessary) onto a vial to seal the contents for the subsequent chemical reaction, white particles (having the shape of "shavings") were dislodged into the vial, obviously from abrasion of the PTFE-liner against the lid of the vial. This could be seen by placing some methanol in the vial, tightening down the PTFE-lined cap, inverting the vial to contact the liner with the solvent, and observing the sinking white particles with the magnifying lens.

The presence of the brown/black specks (at least at the magnifying lens level) was overcome by a different cleaning procedure (including the rigorous use of a micro test tube brush). The white particles were overcome by fabricating an all-glass vial consisting of a ground-glass stopper attached to a short, conical tube (see Figure 1). Apparently, a vial of this type and dimensions is not available commercially at the present time.

To compare the performance of the old (PTFE-lined plastic cap) and new (glass stopper) vials, both cleaned free of brown/black specks (the specks were never encountered in the glass-stoppered vials), we conducted three experiments in which only blank vials (no added tetrol) were tested. *Experiment I*: reactions 2 and 3 (see Introduction or Table I) were conducted sequentially in vials fitted with plastic caps and PTFE-liners, where these caps and liners had been separately cleaned with detergent, water, and hot methanol (three-step cleaning) prior to assembly. *Experiment II*: same as I except the liners were cleaned stepwise with detergent, water, chromic acid, water, hot toluene, and hot methanol (six-step cleaning). *Experiment III*: the caps and liners were cleaned as in II, but only reaction 3 was conducted. At the end of reaction 3 in each case, sample cleanup was performed as described,[2] followed by injection into the GC–ECNI-MS.

* Address reprint requests to this author.
† Current address: BASF Corp., Research Triangle Park, NC 27709-3528.

(1) Li, W.; Sotiriou, C.; Abdel-Baky, S.; Fisher, D. H.; Giese, R. W. *J. Chromatogr.* **1991**, *588*, 273–280.
(2) Allam, K.; Abdel-Baky, S.; Giese, R. W. *Anal. Chem.* **1992**, *64*, 238–239.
(3) Vogel, A. *Textbook of Practical Organic Chemistry*; John Wiley: New York, 1987; p 3.

0003-2700/92/0364-2882$03.00/0

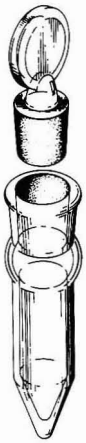

Figure 1. All-glass conical reaction vial that was fabricated in-house.

Table I. Interference Level by GC–ECNI-MS When Blank Reactions (No Analyte Added) Are Conducted in a Vial[a] Sealed with P, a PTFE-Lined Plastic Cap, or G, a Glass Stopper

experiment (reacn 2 = KO_2 oxidation; reacn 3 = pentafluorobenzylation)	contamination level: specific (pg/vial of a coeluting, unknown compound)[b]	contamination level: general (abundance × 10^{-3} at 10 min)[c]
I. reacns 2 and 3		
P (3-step cleaning)[a]	23 ± 35	144 ± 21
G	2.3 ± 1.3	58 ± 29
II. reacns 2 and 3		
P (6-step cleaning)[a]	8.1 ± 8.4	59 ± 14
G	4.2 ± 3.2	30 ± 22
III. reacn 3		
P (6-step cleaning)[a]	0.2 ± 0.2	18 ± 1
G	0.0	16 ± 2

[a] All vials were cleaned free of microscopically-visible brown/black specks prior to this experiment. [b] An amount is assigned to the unknown compound by assuming that it is contaminating analyte. [c] It is meaningful to compare the general abundance values because all of the MS measurements were made on the same day and the baseline for the instrument was constant throughout this day.

The results of these experiments are summarized in Table I. Both the magnitude of a specific interference peak (a contaminating peak that always coelutes with authentic analyte) and the abundance of the general background signal at an arbitrary retention time (but where major interfering peaks are absent) are presented as two measures of the contamination level. Most importantly, the specific interference was fully overcome only in the all-glass vial in experiment III-G (G = glass) where only reaction 3 was conducted. This interference shows up consistently once reaction 2 is done as well (2.3 ± 1.3 pg/vial in experiment I-G and 4.2 ± 3.2 pg/vial in experiment II-G). (An amount is assigned to the unknown interfering peak by assuming that it is contaminating analyte; see below.) The level of this interference is highest and most variable (23 ± 35 pg/vial) when reactions 2 and 3 are conducted sequentially in a commercial vial capped with a plastic cap and PTFE liner, where the last two components have been cleaned only with the three-step procedure (experiment I-P; *P* = plastic cap + PTFE liner). More thorough cleaning of the PTFE liner (experiment II-P) reduces the interference to 8.1 ± 8.4 pg/

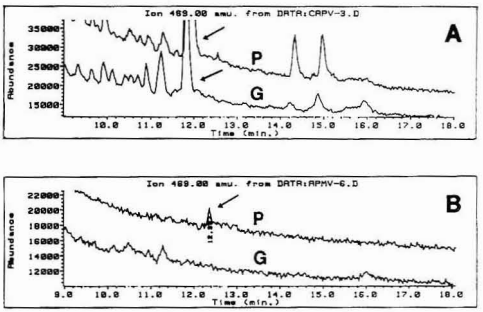

Figure 2. Representative GC–ECNI-MS selected ion (*m/z* 469) chromatograms for blank vials from (A) experiment II and (B) experiment III (see Table I). For each pair of chromatograms, trace P is from a vial sealed with a PTFE-lined plastic cap and trace G is from a vial sealed with a glass stopper. The unknown designated peak eluting near 12 min in each chromatogram (except trace G in (B), where the peak is absent) is considered a specific interference, as indicated in Table I, since it always coelutes with authentic product, 2,3-bis-(pentafluorobenzyl)pyrenedicarboxylate. (Largely because of variation in the vacuum of the MS, the retention time of the apparent analyte peak is not constant, but the coelution of this peak with true analyte was always confirmed by coinjecting authentic analyte.)

vial. Thus, both reaction 2 and the PTFE liner/plastic cap are origins of the specific interference.

We postulate, for two reasons, that the specific interference is due to the analyte or an analyte analog arising as a contaminant in the procedure. First, this interference shifts in its retention time exactly the same as the analyte when each is derivatized (after superoxide oxidation) with *p*-tetrafluorobenzyl bromide instead of pentafluorobenzyl bromide (data not shown). Second, benzo[*a*]pyrene, an ultimate parent compound for the analyte, is ubiquitous in the environment, and the superoxide step is known to convert a variety of oxidation products of benzo[*a*]pyrene to our intermediate product 2,3-pyrenedicarboxylic acid.[4]

Returning to Table I, we see that the general contamination level also is always lower, more or less, when the all-glass vial is used. To more directly show the type of data leading to Table I, selected ion chromatograms are shown in Figure 2 from representative, corresponding P and G vials utilized in experiment II (Figure 2A) and in experiment III (Figure 2B).

A possible limitation of the glass-stoppered conical vial for some reactions is that the seal is not as tight as that provided by a PTFE-lined plastic cap. The volume reduction was 25 → 20 μL for reaction 2 (conducted at room temperature for 18 h) and 50 → 21 μL (50 °C for 5 h) for reaction 3 in the all-glass vial. In this case, however, comparable volume reduction also takes place in the plastic cap/PTFE liner vial: 25 → 20 μL for reaction 2 and 50 → 35 μL for reaction 3. For the latter vial, the solvent loss apparently occurs through the spaces at the top of the capped vial, by absorption of solvent vapor into the PTFE liner and plastic cap, or by both.

As a less convenient alternative to the all-glass vial presented here to conduct a chemical reaction, a glass ampule (available commercially) or small tube can be flame-sealed under vacuum for this purpose (e.g. ref 5). Relative to a conventional vial, cleaning the all-glass vial is easier since the former involves three different components (vial, plastic cap, and PTFE liner).

The improved reproducibility for the blanks extends to our tetrol samples. When eight, 100-pg samples (as duplicates in four separate experiments) of tetrol were subjected to

(4) Sotiriou, C.; Li, W.; Giese, R. W. *J. Org. Chem.* **1990**, *55*, 2159–2164.
(5) Crain, P. F.; McCloskey, J. A. *Anal. Biochem.* **1983**, *132*, 124–131.

reactions 2 and 3, the overall absolute yield of product by GC–ECNI-MS was 36 ± 8% ($x \pm SD$). For the last duplicate tested, an isotopic internal standard[1] was included, which gave peak ratios (analyte/IS) of 1.81 and 1.80.

Thus, the all-glass vial is useful both in terms of its convenience and the reproducibility of the procedure that we tested.

ACKNOWLEDGMENT

This work was funded by Grant OH02792 from the Centers for Disease Control and in part under a contract from the Health Effects Institute (HEI), an organization jointly funded by the U.S. Environmental Protection Agency (EPA) (Assistance Agreement X-812059) and automative manufacturers. The specific grant was HEI Research Agreement 86-82. The contents of this paper do not necessarily reflect the views of the HEI, nor do they necessarily reflect the policies of the EPA or automotive manufacturers. Contribution No. 550 from the Barnett Institute.

RECEIVED for review May 15, 1992. Accepted August 17, 1992.

Laser Beam Probing in Capillary Tubes

François Maystre* and Alfredo E. Bruno

Analytical Research, Ciba-Geigy Ltd., CH-4002 Basle, Switzerland

INTRODUCTION

As on-column optical detection gains acceptance in various separation techniques, capillary optics has emerged as a new field[1-4] of importance within analytical chemistry. On-column detection is particularly important for microcolumn high-performance liquid chromatography (μ-HPLC) and for capillary electrophoresis (CE) because these separation techniques require detectors with volumes in the picoliter to nanoliter range. To date, on-column detectors for absorption,[2] fluorescence,[5] and refractive index[3,4] have been reported, using different light sources and different optical arrangements to bring light into the capillary bore and to collect it efficiently. From the optical point of view, the main difficulty in using a round capillary is that it acts upon the incoming beam like a thick cylindrical lens with a short focal length. This cylindrical lens effect transforms circular incoming beams into strongly elliptical outgoing beams, making light collection difficult. In addition, this cylindrical lens effect is associated with a strong astigmatism that makes further imaging of the probing zone difficult. One way to overcome this problem is to use capillaries with square cross-sections as proposed by Zare et al.[6] However, the handling of such capillaries presents increased difficulties, and manufacturing them with a narrow bore, while retaining a square cross-section with satisfactory optical quality, remains a problem.

In this technical note, we present the general formalism for paraxial capillary optics using transformation matrices. The particular case of capillaries for which the lens effect vanishes is discussed in detail. For such capillaries, the intensity distribution of the light beam remains practically unchanged after interacting with the capillary, thus making the illumination and collection optics much simpler to design. Furthermore, experimental results show that the required geometrical conditions are satisfied for some fused-silica capillaries employed in μ-HPLC and in CE.

The present scheme exploits the fact that, in most practical cases, the capillary is filled with a transparent liquid (mobile phase or buffer solution) which has a refractive index smaller than that of the capillary wall. Therefore the refractive powers of the outer interface (air–capillary wall) and of the inner interface (capillary wall–mobile phase) have opposite signs and act as converging and diverging lenses, respectively. By selecting the correct geometry for a capillary, it is thus possible to suppress the lens effect of the capillary.

THEORY

Geometrical Configuration. Figure 1 represents an axial (yz) and a side (xz) views of a transparent capillary tube onto which a laser beam is being focused. The optical z axis intercepts the capillary at a right angle so that the situation corresponds to the on-axis illumination of a thick cylindrical lens. The geometry is given by the outer radius, r_1, and the inner radius, r_2, of the tube. Material parameters of importance are the refractive index of the capillary wall, n_1, and the refractive index of the liquid within the tube, n_2. The tube is in air, so that the surrounding index of refraction, n_0, is 1. For the mathematical description, it is convenient to place the origin of the coordinate system at the external wall of the tube. In doing so, all the refracting surfaces are on the positive side of the propagation axis.

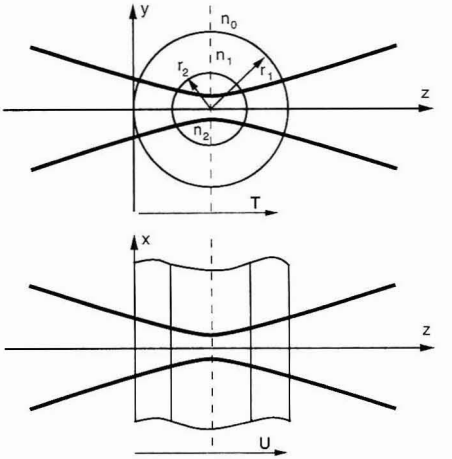

Figure 1. Axial and side view of a transparent capillary tube placed on the beam waist of a focused laser beam. r_1 and r_2 are the outer and the inner radius of the capillary whereas n_1 and n_2 are the refractive indices of the capillary wall and of the liquid in the bore, respectively. **T** and **U** are the paraxial transformation matrices for each principal plane.

In this analysis, it is assumed that the condition for paraxial optics is satisfied.[7] In practice, this assumption is correct if the fundamental mode of the laser beam is focused onto the capillary with a spot size a few times smaller than the bore diameter. Hence, the propagation of the beam through the tube can be described with paraxial transformation matrices[8] that are calculated from the geometry of the optical layout.

Transformation Matrices of the Capillary. As a detailed derivation of the transformation matrices of the capillary is beyond the scope of this paper, only the relevant results will be presented here. As shown in Figure 1, the two main radii of curvature of the optical surfaces lie in planes parallel and perpendicular to the capillary axis. Let **U** and **T** be the transformation matrices for the corresponding orthogonal components of the beam.[8] The matrix **U**, which accounts for the transformation in the plane parallel to the

(1) Synovec, R. E. *Anal. Chem.* **1987**, *59*, 2877–2884.
(2) Bruno, A. E.; Gassmann, E.; Pericles, N.; Anton, K. *Anal. Chem.* **1989**, *61*, 876–883.
(3) Bruno, A. E.; Krattiger, B.; Maystre, F.; Widmer, H. M. *Anal. Chem.* **1991**, *63*, 2689–2697.
(4) Krattiger, B.; Bruno, A. E.; Widmer, H. M.; Geiser, M.; Dändliker, R. Work done at Analytical Research, Ciba-Geigy Ltd., CH-4002 Basle, Switzerland. Submitted for publication in *Appl. Opt.*
(5) Amankwa, L. N.; Albin, M.; Kuhr, W. G. *Trends Anal. Chem.* **1992**, *11*, 114–120.
(6) Tsuda, T.; Sweedler, J. V.; Zare, R. N. *Anal. Chem.* **1990**, *62*, 2149–2152.
(7) Klein, M. V.; Furtak, T. E. *Optics*, 2nd ed.; John Wiley: New York, 1986; pp 141–151.
(8) Klein, M. V.; Furtak, T. E. *Optics*, 2nd ed.; John Wiley: New York, 1986; pp 151–164.

0003-2700/92/0364-2885$03.00/0

Table I. Values for r_1, r_2, and δ Assuming Complete Compensation for Fused-Silica Capillaries Filled with Water (i.e. $n_1 = 1.46$ and $n_2 = 1.33$)

inner diameter $2r_2$ (μm)	outer diameter $2r_1$ (μm)	astigmatism δ (μm)
10	47	28
30	141	85
50	235	141
70	329	198
100	471	283

capillary axis, corresponds to a pure translation of optical path length $2u$ and is readily found to be

$$\mathbf{U} = \begin{pmatrix} 1 & 0 \\ 2u & 1 \end{pmatrix} \tag{1}$$

with

$$u = \frac{(r_1 - r_2)}{n_1} + \frac{r_2}{n_2} \tag{2}$$

Derivation of the matrix **T**, which accounts for the transformation in the plane perpendicular to the capillary axis where the curvature is strongest, involves lengthy calculations. Ultimately, it can be put in the form of

$$\mathbf{T} = \begin{pmatrix} t & (t-1)/r_1 \\ (t+1)r_1 & t \end{pmatrix} \tag{3}$$

with

$$t = \frac{2(n_1 - n_2)}{n_1 n_2}\frac{r_1}{r_2} + \frac{2}{n_1} - 1 \tag{4}$$

It is important to note that by setting $t = 1$, the matrix **T** reduces to a pure translation of optical path length $2r_1$, namely

$$\mathbf{T} = \begin{pmatrix} 1 & 0 \\ 2r_1 & 1 \end{pmatrix} \tag{5}$$

Under this condition, eq 4 yields the desired requirement for a complete compensation of the opposite lens effects which can be written as

$$\frac{r_1}{r_2} = n_2\frac{n_1 - 1}{n_1 - n_2} \tag{6}$$

In most applications $n_1 > n_2$, so that the right-hand term of eq 6 is positive and leads to a mathematical solution that also has a physical meaning (i.e. $r_1 > r_2$). To illustrate these findings, consider a fused-silica capillary filled with water. The refractive indices are then $n_1 = 1.46$ and $n_2 = 1.33$. According to eq 6, complete compensation is obtained when $r_1/r_2 = 4.706$. For a capillary with a bore diameter of $2r_2 = 75$ μm, this corresponds to an outer diameter of $2r_1 = 353$ μm. These dimensions are close to the most commonly used capillaries in CE. Other fused-silica capillaries with dimensions satisfying the complete compensation conditions when filled with water are reported in Table I.

It is important to note that at complete compensation, the ratio of both radii of the capillary is given by eq 6. Therefore the optical path in the plane of the capillary (matrix **U**) becomes

$$2u = \rho = 2\frac{n_2(n_2 - 1) + (n_1 - n_2)}{n_2^2(n_1 - 1)}r_1 \tag{7}$$

This value does not match the optical path in the plane perpendicular to the capillary (matrix **T**). For a circular incoming beam, the output beam is then also circular but

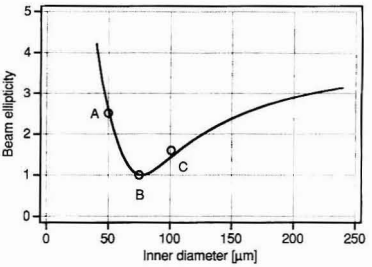

Figure 2. Ellipticity of the output beam produced by a water-filled fused-silica capillary having an external diameter of 363 μm as a function of its bore diameter when a laser beam with a spot size of $2\omega_0 = 32$ μm is focused on it. Open circles represent measured points for three commercially available capillaries. The outer and inner diameters of these capillaries are (left to right) (A) 361 μm, 50 μm; (B) 362 μm, 75 μm; (C) 367 μm, 101 μm.

with a pure astigmatism. As reported in Table I, the residual astigmatic distance

$$\delta = 2(r_1 - \rho) \tag{8}$$

is of the order of a few inner capillary diameters and thus only several times larger than the laser spot size.

EXPERIMENTAL SECTION

Experimental Setup. A set of commercially available fused-silica capillaries with different diameters (Polimicro Technologies, Phoenix, AZ) were prepared by removing the polyimide protective coating over a few millimetres and filling with HPLC-grade water. The beam of a 2-mW linearly polarized HeNe laser (Uniphase No. 1103P) was focused at a right angle on the capillary using a spherical lens with a focal length of $f = 30$ mm. The lens was mounted on a three-axis translation stage to facilitate the positioning of the laser beam with respect to the capillary. The spot size was measured without capillary to be $2\omega_0 = 32$ μm. The ellipticity (i.e. the ratio between the long axis and the short axis) of the cross-section of the output beam was measured with a ruler on a screen placed at a distance $d = 300$ mm away from the capillary.

RESULTS AND DISCUSSION

The experimental results for three capillaries with approximately the same outer diameters but different bore diameters are shown in Figure 2. For comparison, the ellipticity of the output beam was computed[9] using eqs 1 and 3, as shown in the Appendix. The measured values show good agreement with the theoretical curve, in particular if one takes into consideration the accuracy of the measurement procedure employed. As predicted by the theory, the capillary where $r_1/r_2 = 4.8$ and which is labeled B in Figure 2 best approximates the value for complete compensation (i.e. $r_1/r_2 = 4.7$), and practically no ellipticity is observed in the output beam. It is important to note that the theoretical curve has a relatively flat minimum and therefore the tolerances on the dimensions of the capillary are fairly large.

For a capillary specified to minimize ellipticity at a given refractive index value of the buffer, the tolerances on the refractive index are also fairly large. As an example, a capillary with outer and inner diameters of 353 and 75 μm, respectively (i.e. optimized for $n_2 = 1.33$ or water), produces an ellipticity of less than 1.07 over a refractive index range from 1.32 to 1.34. This indicates that refractive index changes due to eluting peaks, the use of different buffer solutions or the use

(9) Yariv, A. *Optical Electronics*, 3rd ed.; Holt-Saunders: New York, 1985; pp 32–34.

of a gradient elution techniques will have little effect on the ellipticity. Polyacrylamide gel-filled capillaries were also tested and displayed results close to water-filled capillaries, indicating that this gel has optical properties much like those of water.

CONCLUSIONS

The possibility of passing a laser beam perpendicularly through a transparent capillary tube without introducing ellipticity has been demonstrated. The important parameters are the ratio of the outer to inner diameters of the capillary and the refractive indices of the capillary wall and of the liquid in the bore. Using these findings, it is possible to design an on-column detection cell in which the light beam remains collimated within the bore. This results in a better defined probing volume with a well-controlled optical path length compared to what is obtained with conventional on-column cells.[10] For cells designed according to the above geometrical considerations, a substantial reduction of distorting refractive index effects and light scattering is also expected. This would allow for the development of more reliable fluorescence detectors with improved detection limits.

On-column multipass absorption cells with increased sensitivity[11] can be constructed using the described method. Such cells constitute a good way of boosting the sensitivity of detectors and will be of particular significance when very narrow bore capillaries (e.g. with inner diameter smaller than 50 μm) become standard in capillary electrophoresis.

(10) Stewart, J. E. *Appl. Opt.* **1981**, *20*, 654–659.
(11) Wang, T.; Aiken, J. H.; Huie, C. W.; Hartwick, R. A. *Anal. Chem.* **1991**, *63*, 1372–1376.

ACKNOWLEDGMENT

We would like to thank H. M. Widmer for supporting this research and E. Verpoorte for critically reviewing the manuscript.

APPENDIX

Ellipticity of the Output Beam. With the propagation matrices given in eqs 1 and 3, the cross-section of the output beam is readily computed. In general, this cross-section is elliptical and the ratio between the long axis a and the short axis b is

$$\frac{a}{b} = \sqrt{1 + \left(\frac{k\omega_0^2}{2}\right)^2 \left(\frac{t-1}{r_1}\right)^2} \qquad \text{(A1)}$$

where $k = 2\pi/\lambda$ is the free space wave number and $2\omega_0$ is the spot size (diameter) of the incoming laser beam.

RECEIVED for review May 20, 1992. Accepted August 12, 1992.

Registry No. Silica, 60676-86-0.

AUTHOR INDEX

ChemStock

Chemical Inventory Database for the Macintosh

Watch for the DOS Version Fall '92

The perfect inventory system for small to mid-sized labs.

Combine the "chemistry-literate" *ChemStock* with the user-friendly Macintosh application features, and you have a program that responds quickly to a chemist's needs because it is set up to operate the way a chemist thinks!

- A few simple keystrokes allow you to check quantities, locations, suppliers...and more
- Searches and sorts by chemical name, formula, or by any other field in the chemical record
- Quickly reduces structural formulas to their molecular formulas for ease in searching and locating inventory
- Sorts and files using the "chemist's alphabet", i.e., by root name, excluding certain prefixes, numerals, or special characters

Best of all, you can transfer from your present system to *ChemStock* with a minimum of interruption if you are using a general database program such as Hypercard or a spreadsheet to manage your inventory. *ChemStock* will import those files with no re-entering of data to have you up and running fast!

Hardware: Any Macintosh, 1mb RAM, System 4.1 or higher

ISBN 0-8412-1926-5
List price: **$199.00** Member and Academic price: **$149.00**

To Order, Call TOLL-FREE **1-800-227-5558**
In Washington, DC: 202-872-6067
FAX: 202-872-6067

or WRITE:
American Chemical Society, Distribution Office, Dept. 38, 1155 16th Street, NW, Washington, DC 20036

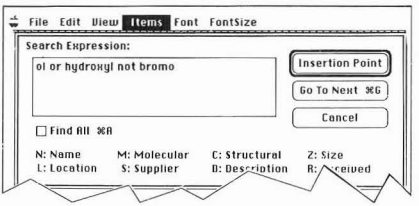

You can search for all compounds that contain a specific chemical subgroup using Boolean logic.

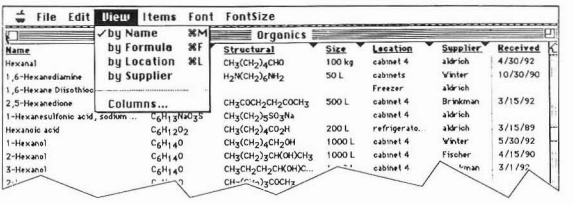

Pull up a product by name, and ChemStock *gives you all the information about it: chemical makeup, quantity on hand, supplier, and location.*

THE ACS GUARANTEE: If you are not completely satisfied with your purchase, or if a program does not meet your expectations, simply return your purchase within 30 days for a full refund.

ACS Software

Now the industry's premier GC system comes with an industry-leading warranty.

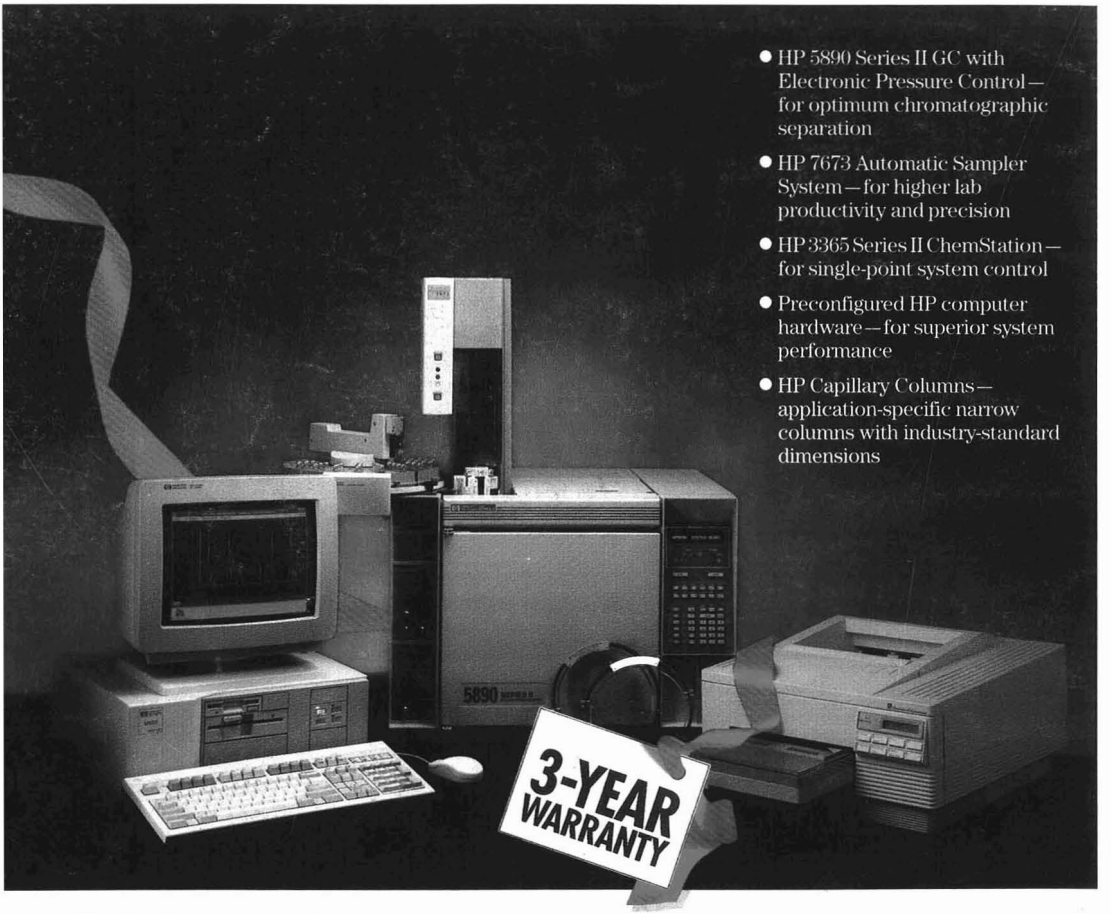

- HP 5890 Series II GC with Electronic Pressure Control—for optimum chromatographic separation
- HP 7673 Automatic Sampler System—for higher lab productivity and precision
- HP 3365 Series II ChemStation—for single-point system control
- Preconfigured HP computer hardware—for superior system performance
- HP Capillary Columns—application-specific narrow columns with industry-standard dimensions

Now there's one complete GC system you can buy with complete confidence: the automated HP 5890 Series II GC System. The only one from a single manufacturer with a 3-year limited hardware warranty* on all parts and labor.

The HP 5890 Series II sets the industry standard for performance. And with new Electronic Pressure Control (EPC) capabilities, your chromatography is improved, while the system is even easier to use.

Plus the system now features automatic cool on-column injection into 320- and 250-micron columns, for uncompromised sensitivity and precision.

For complete automation, the system's PC-based ChemStation gives you single-point chromatography control—from sample introduction through report generation. And you can get easy access to information anywhere in your lab or office, through the HP Unified Laboratory.

To maximize your laboratory uptime, the complete system is backed by HP's top-rated service and support team. For details, call **1 800 334-3110**, Ext. 220 today.

*Warranty valid only with the purchase of a complete automated GC system, consisting of all the equipment shown. Warranty does not cover columns, consumables, software or supplemental support.

HEWLETT PACKARD

Sales Representative: Circle Reader Service Card No. 46

Literature Circle Reader Service Card No. 47